Thermophysical Properties Measurement of Liquid Al and Al-Cu by the Discharge Crucible Method

by

Richard Seamus Patrick Flood

A thesis submitted in partial fulfillment of the requirements for the degree of

Master of Science

in

Materials Engineering

Department of Chemical and Materials Engineering
University of Alberta

ABSTRACT

The demand to develop Materials Genomics and Integrated Materials Computation requires the availability of high temperature property data of liquid metals. High temperature metallurgical processes, such as refining, casting, welding and additive manufacturing, can be optimized and operate more efficiently with the accurate knowledge of thermophysical properties of metals and alloys, such as viscosity, surface tension and density. As computing power and algorithms are constantly being improved, the accuracy of thermophysical property data has emerged as one of the limiting factors. Knowledge of these properties for materials such as Al and Al-alloys is a critical factor in numerical simulations and modelling, which are essential for not only the development but also the optimization of production processes.

This work reports on the simultaneous measurements of viscosity, surface tension and density of liquid Al and Al-Cu alloys using the discharge crucible method. The method is based on a mathematical formulation that describes the fluid dynamics of a liquid draining through an orifice under the influence of gravity. It is based on the Bernoulli formulation, but accounts for surface tension effects induced by Laplace pressure at the exit of the orifice. It is used to describe the liquid flow rate in terms of orifice exit radius, discharge coefficient, experimental head, and the three thermophysical properties. In gathering data of the experimental flow rate, viscosity, surface tension and density can be solved iteratively using a multiple non-linear regression. The results for Al and Al-22.5wt.%Cu as a function of temperature will be presented and compared to literature values obtained using classical methods and theoretical and empirical numerical models.

The results have achieved, with a varying degree of success, the goal of measuring the thermophysical properties of Al and Al-Cu. The results for viscosity and surface tension have

provided an important validation to the measurement technique and are in good agreement with published literature data and certain numerical models. Conversely, results for density were found to be much lower than reported in literature.

Through analysis, it was determined that wetting at the orifice affected the flow rate, since modelling of the flow did not account for accelerative losses created by the meniscus. Dimensionless number analysis identified that wetting had an immediate effect on the flow rate, becoming more dominant with drain time. This work recommends that efforts be made to further modify the discharge crucible formulation to account for wetting and validate the technique by measuring different liquid metals and alloys at various temperatures.

ACKNOWLEDGEMENTS

I would first like to thank my thesis supervisor, Dr. Hani Henein, for his support throughout the entirety of my thesis work. The door to Prof. Henein's office was always open whenever I ran into a trouble spot or had a question about my research. Thank you for your patience, even when I decided to take a non-conventional and lengthy route in completing my degree. I would also like to thank Dr. Qingxia Liu and Dr. Hongbo Zeng for agreeing to act as virtual examiners (thanks COVID-19), as well as Dr. Rajender Gupta for chairing

Sincere thanks to all current and former members of the Advanced Materials & Processing Laboratory, particularly Justin Forth, Dylan Rose, Lily Ren, and Dr. Abdoul-Aziz Bogno. If it were not for your help, I am not sure I would have ever finished this project. Watching liquid drain from a crucible is nearly as boring as watching paint dry, so I am grateful that each of you were always willing to keep me company. Not only did you all help with my experimental work but were also always available to discuss ideas and work through problems. Thank you to Les Dean, Walter Boddez, Herb Green, James McKinnon, Dave Parlin, and everyone at the CME Machine Shop for your technical support. Experiments at high temperatures are never easy, but with all of your help, designing and prototyping the experimental setup was much, much easier. Furthermore, many thanks to Lily Laser for your administrative support, and perpetually positive attitude. Additionally, I would also like to acknowledge NSERC and ESA for funding this project.

Finally, I must express my very profound gratitude to my parents, my sisters and the love of my life, Danielle, for providing me with unfailing support and continuous encouragement throughout my (many) years of study and the process of researching and writing this thesis. This accomplishment would not have been possible without all of you. Thank you.

TABLE OF CONTENTS

LIST OF FIGURES

LIST OF TABLES

NOMENCLATURE

a = Activity (no units)

A = Area (m^2)

A^k = Redlich-Kister parameters (no units)

$\hat{A}$ = Amplitude (m)

Bo = Bond number (no units)

Ca = Capillary number (no units)

C_p = Molar heat capacity (J/mol)

C_d = Discharge coefficient (no units)

d = Diameter (m)

E_a = Activation energy (J/mol)

E_k = Kinetic energy (μW)

F_A = Attractive force (N)

F_R = Repulsive force (N)

F_N = Net force (N)

F_σ = Pulling force (N)

Fr = Froude number (no units)

g = Gravitational acceleration (m/s^2)

G = Gibbs free energy (J)

h = Height, head or depth (m)

$\bar{h}$ = Effective height of capillary column (m)

$1/H$ = Shape factor of pendant drop method (no units)

ΔH = Enthalpy of mixing (J/mol)

I = Beam intensity (W/m^2)

l = Length (m)

${}^vL$ = Redlich-Kister parameters (J/mol)

m = Mass (kg)

M = Molar mass (kg/mol)

MSE = Mean square error

N_A = Avogadro's number (mol^{-1})

P = Pressure (Pa)

ΔP = Pressure different between two phases (Pa)

Q = Volumetric flow rate (m^3/s)

r = Radius (m)

r_o = Radius of the orifice (m)

R = Molar gas constant (J/mol·K)

R_M = Real component of mechanical impedance (N·s/m)

Re = Reynolds number (no units)

s = Specific entropy ($J/m^2 \cdot K$)

S = Entropy (J/K)

SE = Standard error

t = Time (s)

T = Temperature (K)

v or u = Velocity (m/s)

V = Volume (m^3)

V_0 = Intrinsic volume (m^3/mol)

V_{exp} = Experimental mass flux ($kg/m^2 \cdot s$)

We = Weber number (no units)

x = Concentration (mole fraction)

X = Width measurement of a liquid droplet (m)

z = Coordination number (no units)

Z = Height measurement of a liquid droplet (m)

η = Dynamic viscosity (Pa·s)

η_∞ = Arrhenius equation pre-exponential factor (Pa·s)

σ = Gas-liquid surface tension (N/m)

ρ = Mass density (kg/m^3)

τ = Shear stress (Pa·s)

ϕ = Fluidity (1/Pa·s)

υ = Kinematic viscosity (m^2/s)

f = Frequency (Hz)

μ = Chemical activity / potential (J/mol)

Γ = Excess surface concentration (mol/m^2)

ω = Chatain model interaction parameter (J/mol)

φ = Nearest neighbors bond energies (J/mol)

θ = Contact angle (degrees)

α_a = Absorption coefficient (m^2/kg)

ζ = Damping constant (s^{-1})

ε = Convergence tolerance (no units)

SUBSCRIPTS

A = Species A of binary mixture

B = Species B of binary mixture

d = Dynamic

i = Species i in multi-component mixture

m = At melting point (or liquidus)

M = Molar

s = Static

T = As a function of temperature

SUPERSCRIPTS

B = In the bulk

E = Excess

S = At the surface

CHAPTER 1 : INTRODUCTION

Aluminum is roughly a third of the weight of steel, which makes it particularly suitable for the automotive and aerospace industries. It is also used in the building, electrical, machinery, consumer durables, and packaging industries. It has high corrosion resistance, conductivity, impermeability, and strength, and is aesthetic, relatively inexpensive to produce, and essentially infinitely recyclable. One billion tonnes of Al has been produced since 1886, and three quarters of that metal is still in use [1]. Al and its alloys are generally first melted and then undergo different forming processes, such as casting, continuous casting, pressure die casting, metal injection molding, and additive manufacturing. In current practices, computer-based simulations enable the modelling of the casting, melting and remelting processes, as well as heat transport, solidification, shrinkage, residual stresses and welding [2]. Thermophysical properties are critical inputs for these simulation models. For example, viscosity is required to model convection and macro-segregation during solidification [3]. Surface tension is vital to the castability and mold filling ability of the metal or alloy [4], and also for modelling surface tension driven flow, i.e. the Marangoni effect, during welding [5]. And, density is a fundamental property often required to quantify other properties using theoretical or semi-empirical models.

These data are typically very difficult and time consuming to measure, and thus, there would be great benefit to industry if a complete database of these properties existed. This information would not only facilitate modelling for process optimization, but also the development of new, improved multi-component alloys. Industrial stakeholders are keen to develop this database, as more data could help them create alloys quicker, cheaper and with more environmental sustainability. Granted, this is easier said than done. Historically, there are wide discrepancies in the thermophysical property data reported in literature. For example, there is a spread of roughly 400% in the reported values for Al viscosity [6]. These discrepancies are mainly attributed to the nature of materials becoming highly reactive at high temperatures. Contamination is persistently an issue, and although there are a wide array of measurement methods to pick from, most fall victim to the same limitations. This is especially detrimental when measuring both viscosity and surface tension of Al-based liquids, as contamination, particularly with oxygen, has proven to drastically affect the values measured using conventional techniques. As computers and models

continue to improve, the accuracy of the thermophysical property measurements has become one of the limiting factors.

In recent years, the levitated drop (LD) method using electromagnetic levitation (EML) has become increasingly popular in measuring the viscosity, surface tension and density of metallic liquids. The reason for this is that it is a containerless method, and thus significantly reduces sources of contamination. It is also useful in that it is able to simultaneously measure multiple properties at once. However, the EML-LD method has a few critical flaws, such as the inability to measure viscosity terrestrially, evaporation of volatile elements, and poor control of oxygen partial pressure. To address the first limitation, an EML apparatus was installed on the International Space Station (ISS). Not surprisingly, this has a significant effect on the cost of each property measurement.

One, terrestrial-based, alternative to the LD method for the simultaneous measurement of viscosity, surface tension and density of metallic liquids is the discharge crucible (DC) method, which was developed by Roach and Henein at the University of Alberta in the early 2000s [7]. This will be the method used in this study. The DC method is a relatively simple way of measuring the thermophysical properties of high-temperature liquids and consists of a liquid draining from an orifice under the influence of gravity. The technique relies on solving a multiple non-linear regression, with the equations formulated based on simplistic force-balance analysis of the liquid after it exits the orifice. The DC method has been previously employed to measure the thermophysical properties of Al, Pb, Sb, Ga, and Zn [8]–[11] and various alloys, such as Al-Mg, Al-Zn, Al-Mg-Zn, Sb-Sn-Zn, Sb-Sn, Ga-Zn, Ga-Sn, Ga-Sn-Zn and Pb-Sb [8], [9], [12]–[14]. As a promising alternative to EML-LD, continued research must be conducted to understand the full capabilities of the DC method.

The main goal of this work is to replicate viscosity, surface tension and density measurements of liquid Al at different temperatures, and hence compare the results to those previously obtained using the DC method. Additionally, as part of the European Space Agency THERMOLAB project, a batch of samples were sent to the ISS for thermophysical property measurements. Included in this batch is an Al-Cu alloy, which is an important system in casting of light-weight alloys in the automotive industry [3] and, due to the presence of low temperature eutectic compositions, in lead-free soldering [15]. There is also motivation to create an accurate

and reliable set of thermophysical property data for the binary Al-Cu system to enable the prediction of the properties of ternary or higher order systems containing Al and Cu [3]. Thus, another objective of this study will be to measure an Al-Cu alloy, with the same composition of that being measured on the ISS, so that the results can be compared, which may ultimately validate the use of the DC method as an alternative to the ISS-EML-LD method used in space. Not only will the results of this study be eventually compared to results obtained using ISS-EML-LD, but also to other conventional methods, like the oscillating vessel, sessile drop, maximum bubble, gas bubble, rotational and pulse heating methods. Furthermore, the results from this study will be compared and validated against semi-empirical models used to predict viscosity, surface tension and density, and perhaps, by doing so, a better understanding of the effect of Cu on the thermophysical properties of Al may be gained.

Another objective of this study is to modify the current high-temperature DC apparatus to further reduce the oxygen content in the atmosphere, as well as to prototype a crucible made of a material more suitable for higher melting point metals and alloys, like Fe and alloyed steel. To do so, an oxygen getter was designed and implemented, and an Al_2O_3 crucible was used, as opposed to graphite, which had been used in all previous studies using the DC method. Finally, prior studies have suggested that the effectiveness of the DC method relies on the assumption that no wetting occurs at the exit of the orifice [7], [16]. However, due to the use of Al_2O_3 crucibles, it will be shown that this phenomenon will occur for Al and Al-Cu. The effect of wetting on the flow rate of the liquid exiting the orifice, and consequently on the accuracy of the property measurements, will be discussed in detail.

CHAPTER 2 : LITERATURE REVIEW

The knowledge of the thermophysical properties of metallic liquids is crucial in understanding and modelling various types of metallurgical processes. This chapter will describe several theoretical concepts relating to viscosity, surface tension and density. It will also discuss the fundamentals of each respective property, as well as provide a review of numerical models and experimental measuring techniques reported in literature. The effects of composition, temperature and operating conditions on the properties of metallic liquids will be discussed. Further, a thorough overview of methods able to simultaneously measure the viscosity, surface tension and density will be provided. This especially pertains to the DC method, which is the experimental method used in this work. Finally, a review of experimental literature data will be provided, including data on both Al and Al-Cu alloys

2.1 Viscosity of Metallic Liquids

Viscosity is a physical property that quantifies the resistance of a fluid to flow. It is often related to the "thickness" of a liquid. Consider a small volume of a fluid confined between two parallel plates, as shown in Figure 2.1.

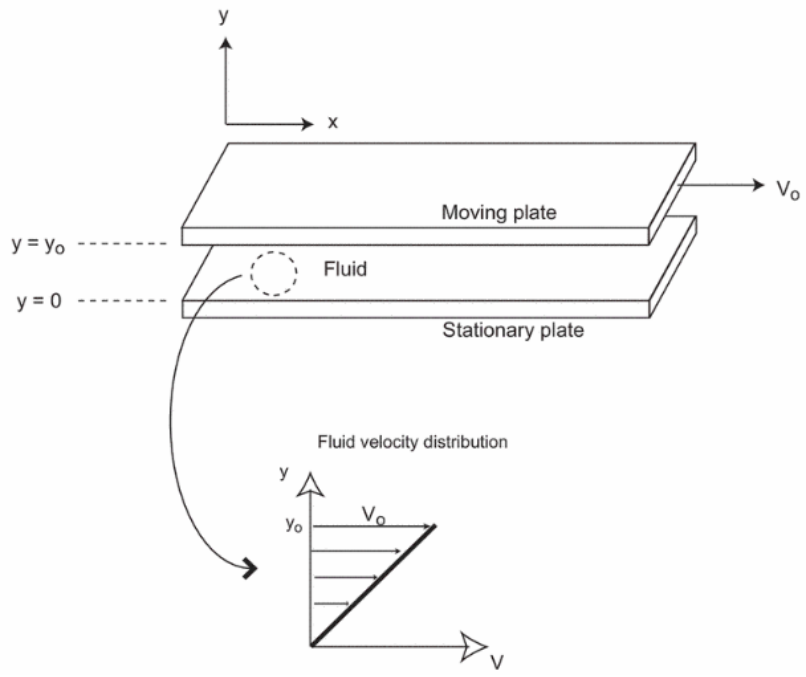

Figure 2.1: The sliding-plate experiment [17]

If the top plate slides in the x direction with velocity, v_o (m/s), a force is required to overcome the friction of the fluid between the plates. This force will differ with respect to different velocities, plate sizes, liquids, and distances between the plates. To simplify the matter, the distance between the plates can be ignored by measuring the force per unit area of the plate, or simply the shear stress, τ (Pa). It should be noted that at both fluid-solid boundaries, the fluid velocity is equal to the velocity of the solid surface. This is known as the no-slip condition; described by the fact that there is a thin layer fluid adsorbed to the solid surface, caused by molecular forces [18]. At low velocities, the velocity profile in the fluid between the plate is linear:

$$\mathrm{v} = \frac{v_o y}{y_o} \tag{2.1}$$

so that,

$$\frac{dv}{dy} = \frac{v_o}{y_o} \tag{2.2}$$

dv/dy (s^{-1}) is the velocity divided by a distance and is commonly referred to as the shear rate, rate of strain, and rate of shear deformation. The results for the experiment are generally shown on a plot of τ versus dv/dy. A straight line through the origin is called Newtonian because it is described by Newton's law of viscosity [19]:

$$\tau = \eta \frac{dv}{dy} \tag{2.3}$$

Where η is the dynamic viscosity of the fluid (Pa·s). It is generally assumed that all metallic liquids are Newtonian; but it should be noted that the above equation is only valid for laminar flow. There have been recent studies suggesting that certain liquid metals and alloys exhibit shear thinning and non-thixotropic flow behavior [20].

A similar equation is used for turbulent flow. Turbulent viscosities range from 10^4 to 10^6 times greater than when under laminar conditions [21]. The sliding-plate experiment is easy to understand both conceptually and mathematically, however, it is very difficult to perform [19]. There are other, more practical, experimental methods that are used to measure the viscosity of liquid metals which will be discussed in more detail in Section 2.1.2.

2.1.1 Numerical Calculation Models for Viscosity

The following section will review several theoretical and empirical models that predict the viscosity of both pure liquid metals and multicomponent systems. The models that will be discussed will include:

a) The Andrade and Arrhenius equations, and Hildebrand's free volume theory, which are classical models used to predict the viscosities of pure liquid metals at either their melting temperature or as a function of temperature.
b) The Hirai model, which was developed empirically using both the Andrade and Arrhenius equations, to predict both the viscosities of pure liquid metals, and liquid alloys.
c) Two unified equations developed by Kaptay, Buda and Bemko combine all three of the above-mentioned models and can be used to predict the viscosities of pure liquid metals and alloys.
d) The Moelwyn-Hughes model which thermodynamically calculates the viscosities of binary liquid metal systems, which was then modified to consider transport phenomena.
e) The Schick model and Zhang model used to predict viscosity of multi-component system exhibiting strong interactions between atoms.

Note that this is not a comprehensive list of all viscosity models, as there are multiple others that will not be discussed. For additional details on the other models, please refer to review publications by Brooks *et al.* [22], Budai *et al.* [23], Cheng *et al.* [24], Kaptay [25] and, Iida and Guthrie [26].

2.1.1.1 Andrade Equation

Andrade [27] presented an equation in 1934, which is used to calculate the viscosities of liquids at their melting points:

$$\eta_m = \frac{C_A (T_m M)^{1/2}}{{V_M}^{2/3}} \tag{2.4}$$

Which can also be expressed as:

$$\eta_m = C_A T_m^{1/2} \rho_m^{2/3} M^{-1/6} \tag{2.5}$$

Since:

$$V_M = \frac{M}{\rho} \tag{2.6}$$

Where C_A is the Andrade coefficient ($J^{1/2}$ $K^{-1/2}$ $mol^{-1/8}$), V_M is the molar volume (m^3/mol), M is the molecular weight (g/mol), ρ is the density (kg/m^3) and T_m is the melting temperature (K). It is based on the notion that momentum is transferred within atoms from neighboring atomic layers, and that the atomic vibration frequencies in liquid and solid metals are equal at their melting points. Iida *et al.* [26] reported an average value of 1.80 x 10^{-7} $J^{1/2}$ $K^{-1/2}$ $mol^{-1/8}$ for the C_A of liquid metals. The value was determined by dividing experimental viscosities of 45 liquid metals at their melting points by their respective value of $(T_m M)^{1/2} {V_M}^{-2/3}$, as shown in Figure 2.2. It should be noted that semiconductors, such as Ge, Se, Si and Te, were not included in the analysis as they exhibited outlying viscosity behavior [28].

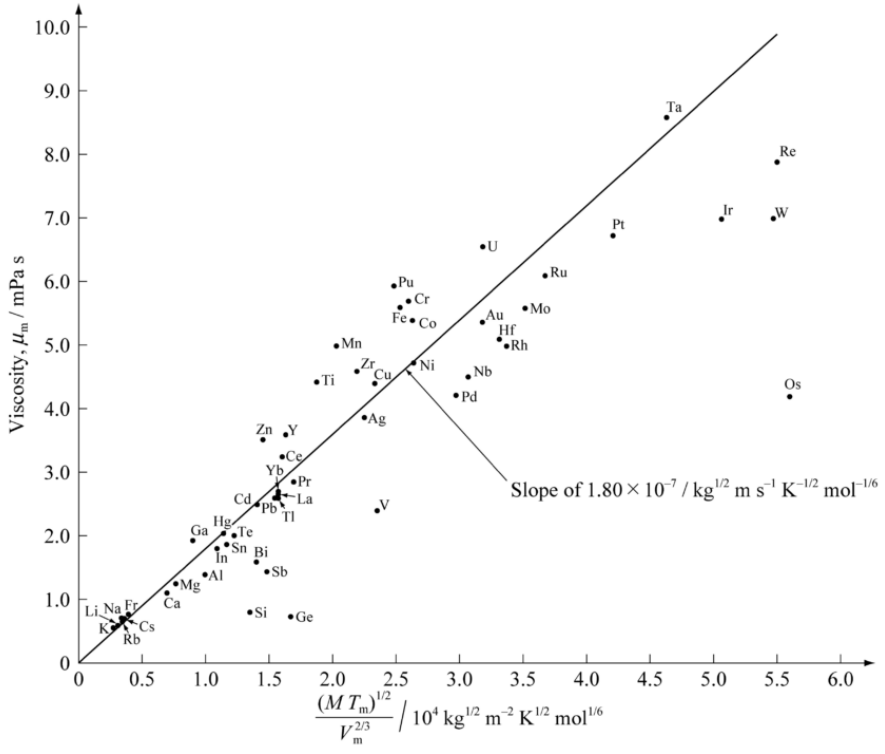

Figure 2.2: Andrade relationship for the melting-point viscosities of liquid metals [26]

Andrade [29] also formulated an equation to describe viscosity of metallic liquids as a function of temperature:

$$\eta = \frac{C_1}{V_m^{1/3}} \exp\left(\frac{C_2}{V_m T}\right) \tag{2.7}$$

Where C_1 and C_2 are material specific constants similar to the Arrhenius equation (discussed in Section 2.1.1.2). Chhabra *et al.* derived values for both C_1 and C_2 from experimental data for Ag, Al, Au, Bi, Ca, Cd, Co, Ca, Cu, Fe, Ga, Ge, Hg, In, K, Li, Mg, Na, Ni, Pb, Pu, Rb, Sb, Sn, Tl and Zn [30].

2.1.1.2 Arrhenius Equation

The Arrhenius equation is the most commonly used model to describe the temperature dependence of the viscosity of pure metals, and has also been used to describe the viscosities of some liquid alloys [21]:

$$\eta = \eta_\infty \exp\left(\frac{E_a}{RT}\right) \tag{2.8}$$

Where E_a is the activation energy for viscous flow (J/mol), R is the gas constant (8.3144 J mol^{-1} K^{-1}), T is the temperature (K), and η_∞ is the pre-exponential factor (Pa·s). In the same study discussed above, Chhabra *et al*. [24] determined the Arrhenius equation parameters for a variety of pure liquid metals [30]. For metals not included in the study, it is possible to back-calculate the constants for any metal using two measured viscosity points at two different temperatures.

2.1.1.3 Hirai Model

Hirai [31] developed a simple relationship for E_a (J/mol) in the Arrhenius equation (see Section 2.1.1.2), by plotting the value of E_a for various pure metals and alloys versus their melting temperatures, which is shown in Figure 2.3, and expressed as:

$$E_a = 2.65 T_m^{1.27} \ \text{(J mol}^{-1}\text{)} \tag{2.9}$$

Hirai calculated E_a by plotting the $\ln \eta$ vs $1/T$ (K^{-1}), which yields a slope of E_a/R (K^{-1}). For pure metals, the correlation coefficient was reported as 0.96 [31].

Hirai also suggested a way of combining both the Andrade and Arrhenius equations to express an equation that describes viscosity of liquid metals at their melting point. By substituting Equations 2.5 and 2.9 into Equation 2.8, an expression can be derived for η_∞ (Pa·s):

$$\eta_\infty = \frac{1.7\ x\ 10^{-7}\ \rho^{2/3} T_m^{1/2} M^{-1/6}}{\exp\left(2.65 T_m^{0.27}/R\right)} \tag{2.10}$$

Then, using Equations 2.8, 2.9 and 2.10, Hirai developed a modified Andrade equation, known as the Hirai model:

$$\eta_m = 1.7\ x\ 10^{-7} T_m^{1/2} \rho_m^{2/3} M^{-1/6}\ \text{(Pa·s)} \tag{2.11}$$

This equation best describes the viscosities of pure liquid metals; however, it can be used to predict the viscosities of any alloy. This is done by a simple weighted average of the ρ_m (kg/m^3) and M (kg/mol), with the T_m (K) acquired from a phase diagram. Furthermore, the Hirai model has been adopted to predict the viscosity as a function of temperature. Hirai showed that the predicted viscosities of several binary liquid alloys agree well with measured values [32].

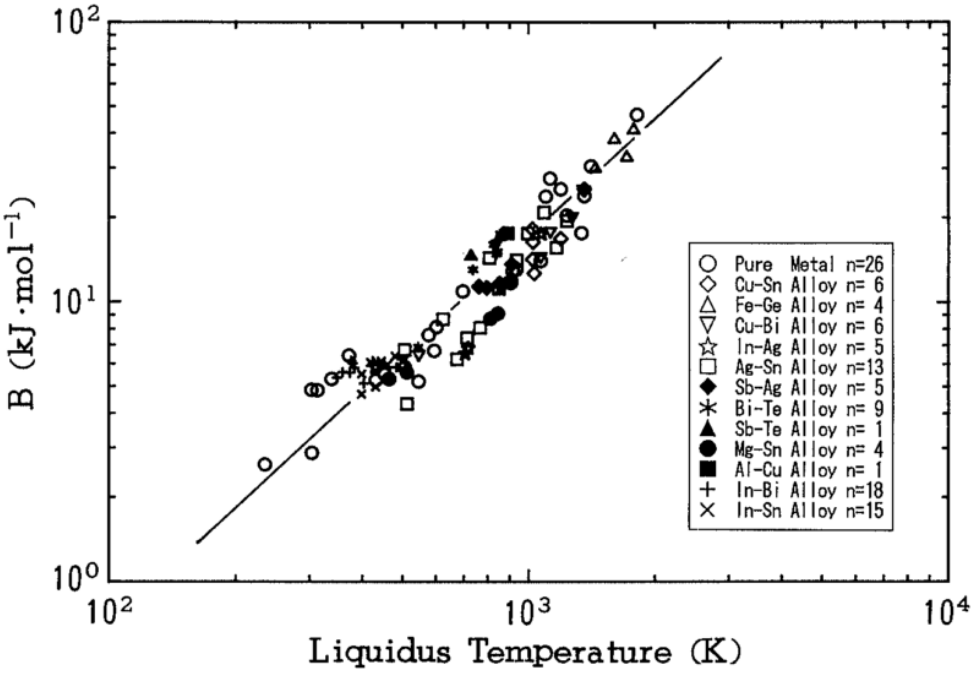

Figure 2.3: Relationship between pre-exponential factors from the Arrhenius equation and the liquidus temperature of various metals and alloys [31]

2.1.1.4 Hildebrand's Free Volume Theory

Hildebrand [33] published a paper in 1970 on "Motions of Molecules in Liquids: Viscosity and Diffusivity", where he modified an equation for the viscosity of liquids based on the principle that fluid flow is governed by the free space available. He reasoned that fluidity, $\phi = 1/\eta$ (1/Pa·s), should decrease with decreasing temperature, due to molecules becoming more closely packed. The fluidity should decrease to a point where they would be too crowded to permit free flow, and ϕ becomes zero. As such, he defined an equation describing the fluidity of a liquid:

$$\phi = \frac{1}{\eta} = B\left(\frac{V_M - V_0}{V_0}\right) \tag{2.12}$$

Where V_0 (m^3/mol) is the intrinsic volume where flow is stopped, V_M (m^3/mol) is the molar volume and B (1/Pa·s) is a characteristic constant. Both V_0 and B are constants independent of temperature, and Chhabra *et al.* [30] once again derived these constants for various different pure liquid metals from experimental viscosity data.

2.1.1.5 Kaptay's Unified Equation

Kaptay [25] presented a unified equation, using the Andrade equation and theories from both the activation energy and the free volume concepts. His study concluded that both the activation energy and free volume theories have identical roots, and their models lead to identical viscosity results. Thus, he developed a unified equation to describe the viscosity of all liquid metals as a function of temperature:

$$\eta = A_K \frac{M^{1/2}}{V_m^{2/3}} \exp\left(B_K \frac{T_m}{T}\right) \tag{2.13}$$

Where A_K and B_K are constants. The above-mentioned equation was tested on 15 liquid metals (101 individual measurements), and the average values for the constants A_K and B_K were found to be (1.80 ± 0.39) x 10^{-8} $(J/Kmol^{1/3})^{1/2}$ and 2.34 ± 0.20, respectively. With these values, he predicted the viscosities of 33 other liquid metals, and concluded that the equation worked on 28 metals (i.e. 85% of cases), failing only on single measurements of Hf, Mn, Pd, Pu and V.

2.1.1.6 Moelwyn-Hughes Model

Moelwyn-Hughes [34] proposed that the viscosities of binary liquid mixtures be described by:

$$\eta = (x_A\eta_A + x_B\eta_B)\left(1 - 2x_Ax_B\frac{\Delta u}{\kappa T}\right) \tag{2.14}$$

And:

$$\Delta u = \frac{\Delta H}{x_Ax_BN_A} \tag{2.15}$$

Where η_A and η_B are the viscosities of the pure liquid metals (Pa·s), x_A and x_B are the mole fractions of the pure liquid metals, κ is the Boltzmann constant, ΔH is the (integral) enthalpy of mixing (J/mol) and N_A is Avogadro's constant (mol^{-1}) . This equation can be represented by the excess viscosity ($\eta^E = \eta_A - [x_A\eta_A + x_B\eta_B]$):

$$\eta^E = -2(x_A\eta_A + x_B\eta_B)\frac{\Delta H}{RT} \tag{2.16}$$

This model was proven to be successful for certain metal alloys, but it failed to predict the lower viscosities of eutectic systems [22]. The above equation shows that the positive or negative deviation of viscosity solely depends on the sign of the enthalpy of mixing, which is untrue considering that viscosity is a transport coefficient and cannot exclusively be described by thermodynamics. In fact, when tested by Budai *et al.* [23], they concluded that the Moelwyn-Hughes model provides unreasonable predictions. Iida *et al*. [35] modified the Moelwyn-Hughes model to incorporate both the size and the mass of atoms:

$$\eta^E = (x_A\eta_A + x_B\eta_B)\left[-\frac{5x_Ax_B(d_A-d_B)^2}{x_Ad_A^2+x_Bd_B^2} + 2\left\{\left(1+\frac{x_Ax_B\left(m_A^{1/2}-m_B^{1/2}\right)^2}{\left(x_Am_A^{1/2}+x_Bm_B^{1/2}\right)^2}\right)^{1/2} - 1\right\} - \frac{0.12x_Ax_B\Delta u}{\kappa T}\right] \text{(in cP)} \tag{2.17}$$

Where, d is the diameter of an atom (m) (when calculating viscosities, use Pauling ionic radii) and m is the mass of the atom (kg).

2.1.1.7 Budai-Bemko-Kaptay Model

Budai, Bemko and Kaptay [23] conducted a thorough review of six different theoretical models and from that, they derived a new equation to describe the viscosities of any multicomponent liquid metal system, even if the viscosities of the pure liquid metals are unknown (unlike the Moelwyn-Hughes model). The equation is an extension of the Kaptay unified equation and was named the BBK model:

$$\eta = A\frac{(\sum x_i M_i)^{1/2}}{\left(\sum x_i V_{m,i} + \Delta V^E\right)^{2/3}} T^{1/2} \exp\left[\frac{B}{T}\left(\sum x_i T_{m,i} - \frac{\Delta H}{qR}\right)\right] \tag{2.18}$$

Where A and B are the same constants as in the Kaptay unified model, q is a semi-empirical parameter ($q \approx 24.4 \pm 2$), ΔV^E is the excess molar volume upon alloy formation (m^3/mol) which can be taken as zero when experimental data are not available. The BBK model was tested on 28 binary liquid metal systems and was found to agree very well with the Hirai model; however, the BBK model proved more reliable near eutectic compositions [23].

2.1.1.8 Schick Model

Schick [32] attempted to account for the effect of strong interactions between atoms on the viscosity of liquid metallic binary systems. It assumes that the activation energy, E_a (J/mol), is generally larger if unlike atoms are more attracted to each other. Hence, the activation energy can be expressed as a function of the enthalpy of mixing, ΔH (J/mol):

$$E_a = \sum x_i E_{a,i} - \Delta H + RT \sum x_i \ln x_i \tag{2.19}$$

And the pre-exponential factor, A (Pa·s) is given as:

$$\ln \eta_\infty = \sum x_i \ln \eta_i \tag{2.20}$$

Where η_i is the viscosity of the pure components. The Schick model has been successfully applied to the Al-Cu system and was able to predict an increase in viscosity at 60 weight percent Cu presumed to be caused by the strong interactions of the intermetallic phase β ($AlCu_3$) which congruently melts with the alloy.

2.1.1.9 Zhang Model

Unlike Schick, Zhang *et al.* [36] attempted to specifically consider the effects of "associates", i.e. clustering, in the liquid phase. They proposed a model that can be expressed in two parts: one for ideal mixing and other for the excess viscosity (using the Redlich-Kister polynomial):

$$\eta = \sum_{i=1}^{m} x_i \eta_i + \sum_{i} \sum_{j>i} x_i x_j \sum A^k \left(x_i - x_j\right)^k \tag{2.21}$$

Where A^k is determined experimentally. The Zhang model has successfully predicted the viscosities of Al-Cu, Al-Mg, Al-Si, Cu-Mg, Cu-Si, and Al-Cu-Si over the entire range of compositions [36].

2.1.2 Methods of Viscosity Measurement

There have been numerous efforts made to experimentally determine the viscosity of metallic liquids. There are reported viscosity values for 67 different liquid metals [21]. The main challenged associated with viscosity measurements of metallic liquids is preventing the sample from becoming contaminated at high temperature. There are many different methods used to determine the viscosity of liquids; however, due to constraints of high melting points, high chemical reactivity and low viscosities, there is only a limited number of techniques that apply to metallic liquids. Some of these techniques include:

(a) Capillary Method
(b) Oscillating Vessel Method
(c) Rotational Method
(d) Oscillating Plate Method

These methods will be described briefly, but for additional details please refer to "The Thermophysical Properties of Metallic Liquids" by Iida and Guthrie [21]. Further, review papers have been published on the viscosity measurement of metals and alloys by Brooks *et al.* [22] and Cheng *et al.* [24]. Also, note that the Saybolt viscometer will be presented in this section. It is not used for measuring the viscosity of metallic liquids, but rather low-temperature fluids, like oils. It will be discussed nonetheless as it shares similarities with the DC method (the primary method used in this work).

2.1.2.1 Capillary Method

The capillary method measures the time required for a definite volume of liquid to flow through a capillary under a specified pressure, using a setup shown in Figure 2.4.

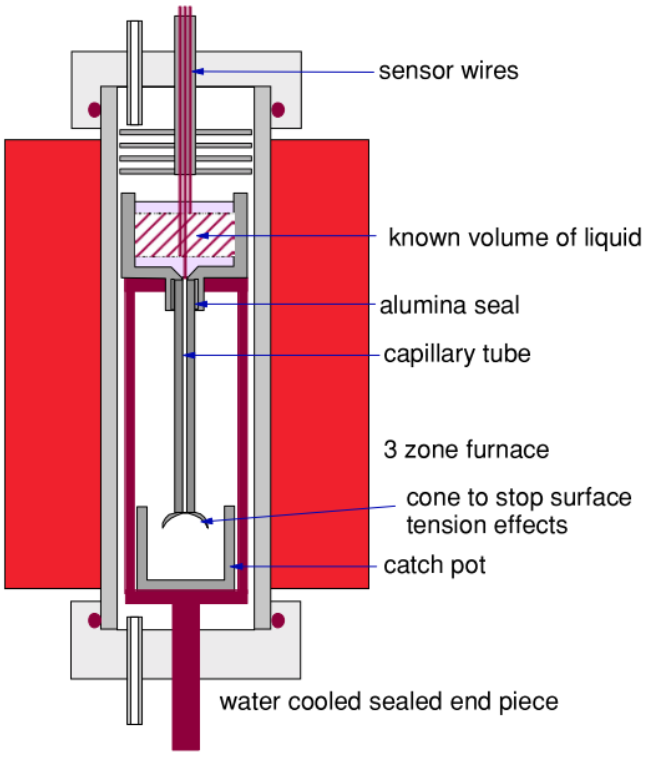

Figure 2.4: Schematic of a capillary viscometer [22]

The efflux time depends on the viscosity of the liquid. This measurement is based on the Hagen-Poisseulle formula of capillary flow:

$$\eta = \frac{\pi r^4 \rho g \bar{h} t}{8V(l + nr)} \Delta p - \frac{m_{CM} \rho V}{8\pi(l + n_{CM} r)t} \tag{2.22}$$

Where V is the liquid volume (m^3) discharged in time t (s), ρ is the liquid density (kg/m^3), r and l are the radius and length of the capillary (m), $\bar{h}$ is the effective height of the liquid column (m), and m_{CM} and n_{CM} are constants. This formula is only valid for laminar flow. To avoid errors of the dimension measurements, r, l, $\bar{h}$ and V are fixed, which reduces Equation 2.22 to:

$$\frac{\eta}{\rho} = \upsilon = C_1 t - \frac{C_2}{t} \tag{2.23}$$

Where ν is the kinematic viscosity (m^2/s), and C_1 and C_2 are constants. These constants are determined by calibration with liquids of known viscosity. To measure the viscosity of metallic liquids using the capillary method, a very fine and long tube is used (i.e. r < 0.015 to 0.2 mm, l > 70 to 80 mm) to ensure laminar flow by satisfying a low Reynolds number, Re, regime. The cleanliness of the metallic liquid is vital as small inclusions or oxides can cause blockage of the tube, which will have an enormous impact on the efflux time. It is very difficult to find a material for fine and long-bore tubes, as well as a material that will not contaminate the metallic liquid; therefore, the only capillary tubes used presently are heat-resistant quartz glass tubes. Consequently, the capillary method has only been applied to metallic liquids with melting points below approximately 1200°C (i.e. the maximum operating temperature of quartz products). The capillary method has been used to measure the viscosity of multiple low melting point metals, such as Pb, Sn and Cu, with an accuracy of ± 0.5% [21], [37].

2.1.2.2 Oscillating Vessel Method

The oscillating vessel method is comprised of a liquid placed in a vessel attached to a torsional suspension. An example of an oscillating vessel viscometer setup is given in Figure 2.5.

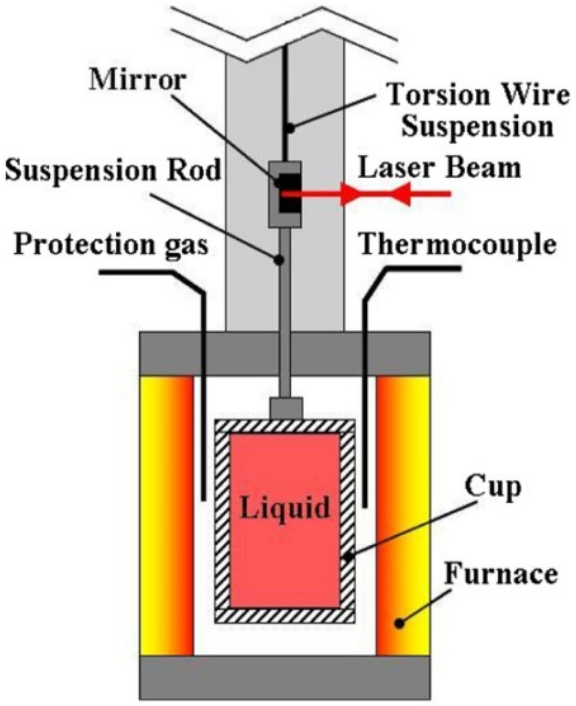

Figure 2.5: Schematic of an oscillating vessel viscometer [24]

The vessel oscillates about the vessel axis, and the oscillations eventually dampen due to viscous dissipation within the liquid. The viscosity is calculated from the decrease in the time period of the oscillations. The advantages of using this method for high temperature applications are that the shape of the vessel is relatively simple, and a closed vessel can be used. Additionally, the oscillation time period decrements can be measured very accurately. While experimentally straight forward, relating the measured parameters to the metallic liquid viscosity through second-order differentiation is mathematically challenging. The oscillating vessel method has been employed by numerous researchers; however, the errors have ranged between 1 to 5%, with discrepancies up to 50% between comparative experimental work [21]. Some examples of works done using the oscillating vessel viscometer include viscosity measurements of Hg, Sn, Al, Cu, Ni, Fe, Ni-based super alloys, steels, Al alloys LM25 [38], Al-Mg alloys [39], Fe-Ni, Fe-Co and Ni-Co binary alloys [40], and Cu-Sn, Ni-IN 718 and Co-X45 alloys [41].

2.1.2.3 Rotational Method

This method employs a rotating cylindrical vessel containing liquid, and an additional cylinder placed in the center of the vessel. A schematic of a rotational method apparatus is shown in Figure 2.6.

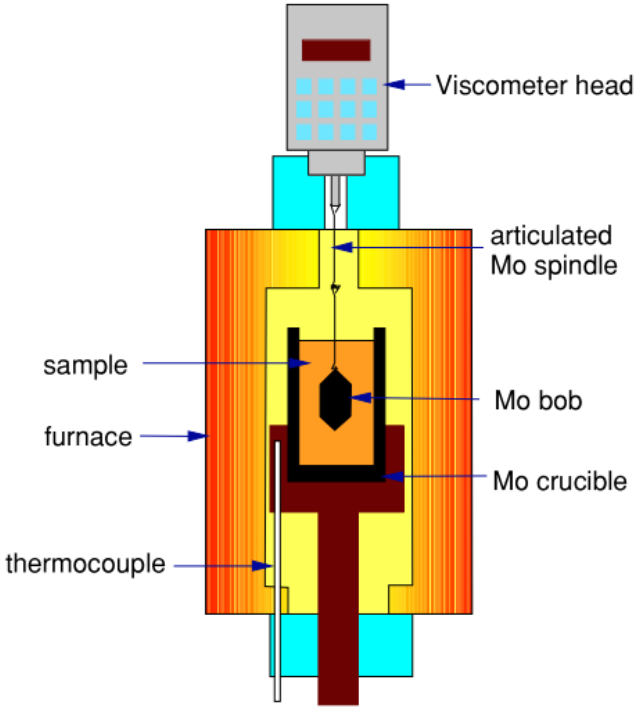

Figure 2.6: Schematic of a rotating bob viscometer [22]

The vessel spins with a constant angular velocity while the cylinder located inside the vessel remains fixed. Consequently, the viscous liquid exerts torque on the inner cylinder, and since the cylinder is suspended by a fibre, the force can be determined by measuring the angular displacement of the fibre. The viscosity of the liquid is then calculated from the torque. There are various types of rotational viscometers that have been developed using this basis, but they differ slightly, i.e. rotation of a sphere, rotation of a disk, and rotation of cylinder (outer cylinder fixed, inner cylinder rotated). For example, with the rotating bob viscometer, shown in Figure 2.6, the viscosity of the metallic liquid is determined by the torque generated on the rotor arm of the rotating bob. If the bob is rotated at a constant speed, the viscosity of the liquid can be calculated from the following equation:

$$\eta = \left(\frac{1}{r_1^2} - \frac{1}{r_2^2}\right)\frac{T}{8\pi^4 nh} \tag{2.24}$$

Where r_1 is the radius of the bob (m), r_2 is the radius of the crucible (m), T is the torque (N·m), n is the number of revolutions per second, and h in the height of the bob (m). The abovementioned equation is applicable for infinitely long rotating cylinder, and normally, the system is calibrated prior to taking measurements. The rotating cylinder method offers a larger viscosity range over the rotating bob method; however, typically rotating bob instruments are cheaper and more commercially available. The rotational method is primarily used for slag viscosity measurement, and when used for metals, the relatively low viscosity of metallic liquids prove to yield experimental difficulties. It is critical that the bob or cylinder rotates axisimetrically and concentrically within the liquid sample or else the apparent viscosity will be inaccurately inflated. To acquire necessary sensitivity to measure the low viscosity of metallic liquids, the clearance between the stationary and rotating parts must be kept small. This creates difficulties in maintaining the system coaxially. Nevertheless, the rotational method has been used to measure the viscosity of Al and binary Al alloys [42].

2.1.2.4 Oscillating Plate Method

The oscillating plate method relies on the principle that when a flat plate performing linear oscillations is immersed in a liquid, the motions are impeded by force created by the viscous liquid on the oscillating plate. A schematic of the oscillating plate method is given in Figure 2.7. If the plate is vibrated with a constant driving force, the amplitude of the plate will be reduced, depending on the viscosity of the liquid. The measurements of the amplitude of the plate in liquid is compared to the amplitude of the plate in air. The relation between amplitude and viscosity is described using the following equation [43]:

$$\rho\eta = \frac{R_M^2}{\pi f A^2}\left(\frac{f_a \hat{A}_a}{f \hat{A}_l} - 1\right)^2 \tag{2.25}$$

Where ρ is the density of the liquid (kg/m^3), $\hat{A}_l$ and $\hat{A}_a$ are the amplitudes in liquid and in air (m), respectively, f and f_a are the resonant frequencies in liquid and in air (Hz), respectively, R_M is the real component of the mechanical impedance (Ns/m), and A is the area of the oscillating plate

(m^2). It has been shown that the resonant frequency in air is the same as in liquid, thus the equation can be expressed as follows:

$$\rho\eta = \frac{R_M^2}{\pi f A^2}\left(\frac{A_a}{A_l} - 1\right)^2 \tag{2.26}$$

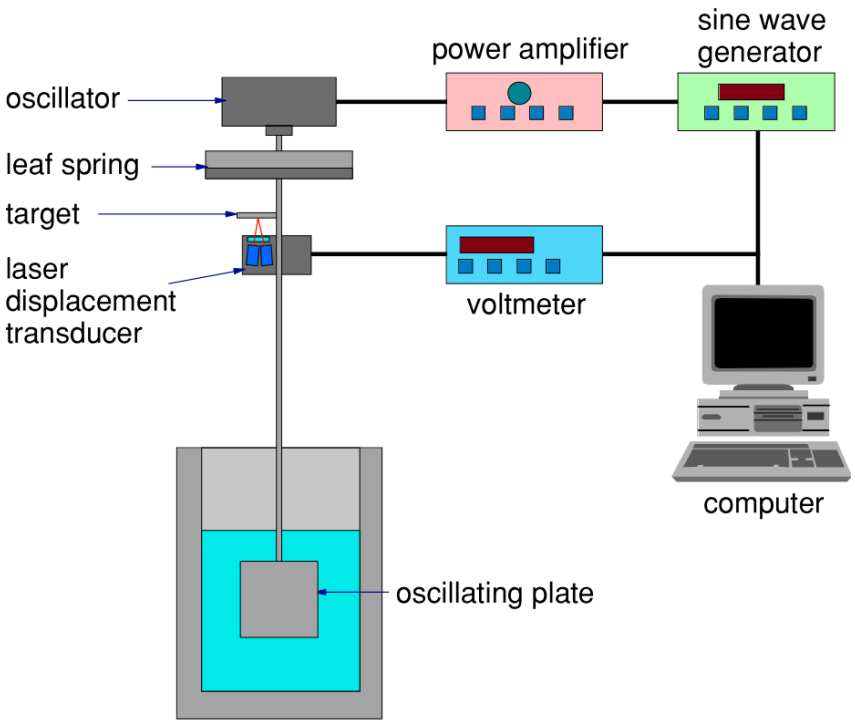

Figure 2.7: Schematic of a oscillating plate viscometer [22]

The advantages of using the oscillating plate method include relatively simple construction and operation, and the instantaneous and continuous measurement of ρη over a wide temperature range (since amplitudes can be measured while heating). When comparing this method with the rotating cylinder method, viscosities for slag systems were shown to typically agree within ±7% [44]. However, due to the low viscosity of metals, in theory, this method requires a very thin oscillating plate with a large area, which must be vibrated slowly, making this method impractical for metallic liquids.

Recently, Dubberstein *et al.* [45] developed a novel viscosity measurement method like the oscillating plate method able to measure the viscosity of high-temperature liquid metals and alloys.

Coined the vibrating finger viscometer; the authors were successful in measuring the viscosity of Au, Ag and Sn, with relative measurement error in high temperature below 30% [45].

2.1.2.5 The Saybolt Viscometer

A standard method to measure viscosity called the Saybolt viscometer has striking resemblances with the DC method (described in Section 2.4.3). It is important to understand how these methods differ, especially with respect to the effect of surface tension on a stream exiting an orifice. The Saybolt viscometer is part of a larger family of orifice viscometers, or efflux-type viscometers. Other efflux-type viscometers include the Redwood viscometer, the Engler viscometer, the Ford cup viscometer, the Shell cup viscometer, and the Zahn cup viscometer. These viscometers are simple, and are essentially comprised of a reservoir, orifice, and receiver. The concept of the orifice viscometer was based on the Hagen-Poisseulle Law, much like the capillary method, which states that the efflux time of a fixed volume liquid through a capillary is proportional to the kinematic viscosity. In practice, the flow within the short length of the orifice in these instruments failed to meet the requirement of the Hagen-Poisseulle Law. Alternatively, conversion tables and formulas are used to convert respective efflux time units to kinematic viscosity [46].

The Saybolt viscometer was first introduced as a standard by W.H. Herschel [47] in 1917. It became popular because it was used as the standard viscometer by chemists at Standard Oil Co. [46]. This method consists of a fluid loaded into a heated bath, then drained through a calibrated orifice into a capillary. The time it takes for 60 mL of fluid to collect into a graduated cylinder at specific temperature is the viscosity and the time are in units called Saybolt universal seconds (SUS) or Saybolt furol seconds (SFS). A schematic of the technique is illustrated in Figure 2.8. Both these units are used to characterize petroleum and bituminous products, but the Saybolt furol is recommended to be used on fluids with viscosities above 1000 SUS [48]. The Saybolt universal viscometer is generally used for lubricating oils, while the Saybolt furol viscometer is used for fuel oils [46]. Another type of orifice exists for asphalt. Several conversion tables have been established for converting viscosity in Saybolt Universal viscosity in SUS and Saybolt Furol viscosity in SFS to kinematic viscosity in centistokes (cSt) [49].

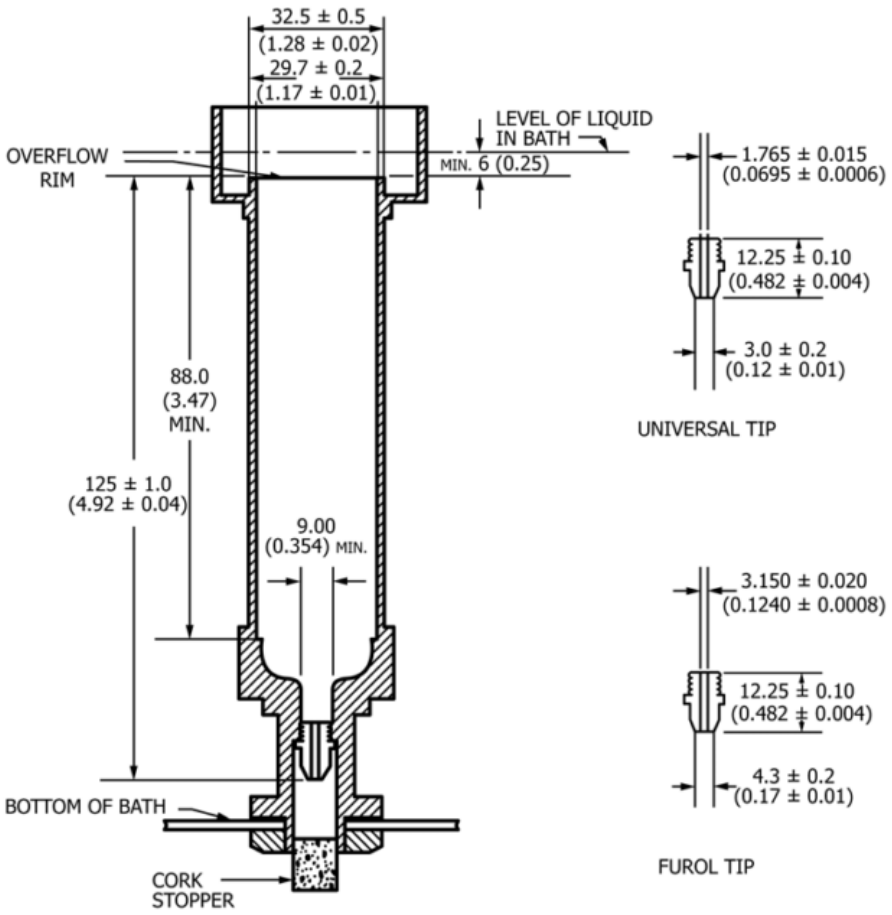

Figure 2.8: Saybolt viscometer with universal and furol orifice [48]

Several challenges arise when using the Saybolt viscometer, such as control of bath liquid level, cork stopper leakage and temperature control. One major issue was observed by Hershel when comparing tests with sucrose solutions to alcohol solutions. The tests with sucrose solutions, although consistent, were positioned lower on the calibration curve (kinematic viscosity versus time of discharge) than tests with alcohol solutions. It was believed that the difference was a result of difference in surface tension, i.e. sucrose solutions had a much higher surface tension. The effect of surface tension was not considered when formulating the Saybolt viscometer equations, and thus should only be used on fluids with surface tensions nearly equal to that of oils [47], [50]. To this date, no attempts have been made to address this issue, with the exception of the DC method [16].

2.2 Surface Tension of Metallic Liquids

The surface tension is a combination of two properties: cohesion and adhesion. Surface tension forces exist between liquid and gas, liquid and solid and solid and gas [51]. In this thesis, surface tension will refer solely to the liquid gas interface. Unlike most thermophysical properties, surface tension is a surface property, not a bulk property. Consider the net force, F_N (N), the repulsion force, F_R (N), and the attraction force, F_A (N), acting between adjacent atoms or molecules in the liquid, and both forces vary inversely with the interatomic or intermolecular separation distance, r (m) [52], [53]:

$$F_N = F_R + F_A \tag{2.27}$$

$$F_N = \frac{C}{r^n} - \frac{D}{r^m} \tag{2.28}$$

Where C and D are constants for a specific system (N·m), n is greater than m, and by convention, repulsion forces are positive and attraction forces are negative. The resultant force on the liquid atoms or molecules at the equilibrium spacing, r_o (m), is zero, as shown in Figure 2.9.

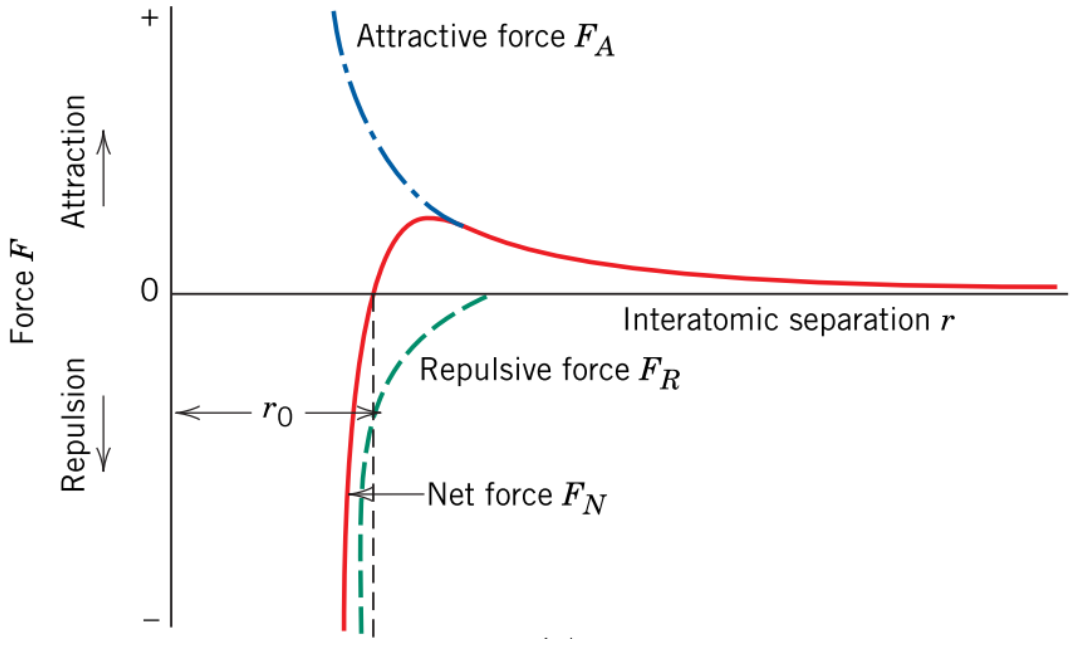

Figure 2.9: Dependence of repulsive, attractive, net forces on interatomic separation [52]

When r is greater than r_o, the resultant force is negative, and the molecules are attracted to each other. When r is smaller than r_o, the opposite occurs, and the molecules are repulsed from each other. As r increases, the net force increases until it reaches a maximum, at which point, it begins to decrease to zero as the spacing becomes infinite.

Within the bulk of the liquid, all atoms or molecules are attracted to each other with similar cohesive force, and thus, the overall force field acting on individual atom or molecule is balanced and uniform in all directions. At the free surface, or the interface between the liquid and gas, the adhesive forces acting between the liquid and gas molecules are much weaker than the cohesive forces acting within the bulk of the liquid, which causes an asymmetrical force imbalance at the surface of the liquid, as shown in Figure 2.10. The molecules at the interface of the liquid are pulled towards the bulk of the liquid, i.e. normal and inward from the surface, creating a state of tension at the surface. The free surface behaves much like a stretched thin elastic membrane [51].

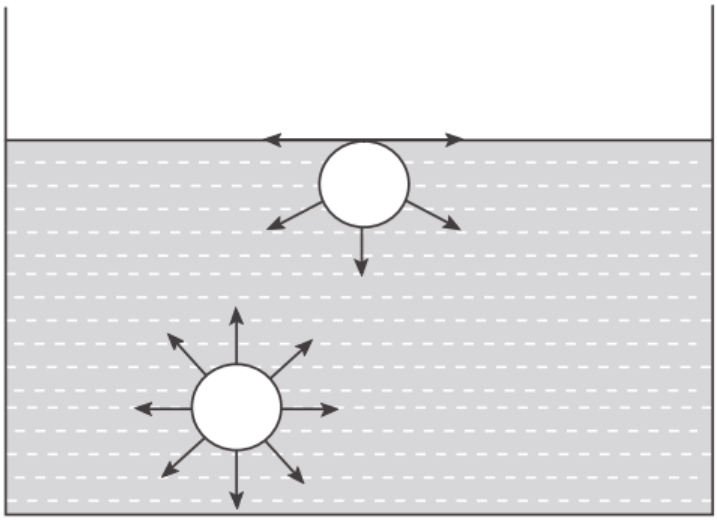

Figure 2.10: Forces acting on the molecules in different regions of a liquid [51]

The surface tension, σ (N/m), acts parallel to the liquid surface and can be calculated by dividing the pulling force, F_σ (N), by the length, l (m), over which it is acting:

$$\sigma = \frac{F_\sigma}{l} \tag{2.29}$$

As mentioned, surface tension can be described as a force per unit length with SI units of Newton per meter (N/m), or it can be expressed as free surface energy, which has SI units of Joules per

meter squares (J/m^2) [53]. An equation for surface tension can be derived thermodynamically by considering the change of Gibbs free energy assuming that the interface is flat, or planar:

$$dG = -SdT + VdP + \sum \mu_i dx_i + \sigma dA \tag{2.30}$$

Where G is the Gibbs free energy (J), S is the entropy (J/K), T is the temperature (K), V is the total volume of both phases (m^3), P is the pressure in both phases (Pa) (if the interface is planar both phases have the same pressure), μ_i and c_i are the chemical potential (J/mol) and concentration of the ith substance (mole fraction), respectively, and A is the surface area. Using Equation 2.30, the thermodynamic definition of surface tension can be written as:

$$\sigma = \left.\frac{\partial G}{\partial A}\right|_{T,P,x_i} \tag{2.31}$$

Therefore, the surface tension can be defined as the increase of Gibbs free energy per increase of the surface area at constant temperature, pressure and concentration [54].

A simple example of the effect of surface tension is shown in Figure 2.11. A pin floating on a liquid exerts a force, W (N), on the surface of the liquid. The surface gets depressed, and the weight of the pin is balanced by the vertical components of the two surface tension forces acting on either side of the pin [51].

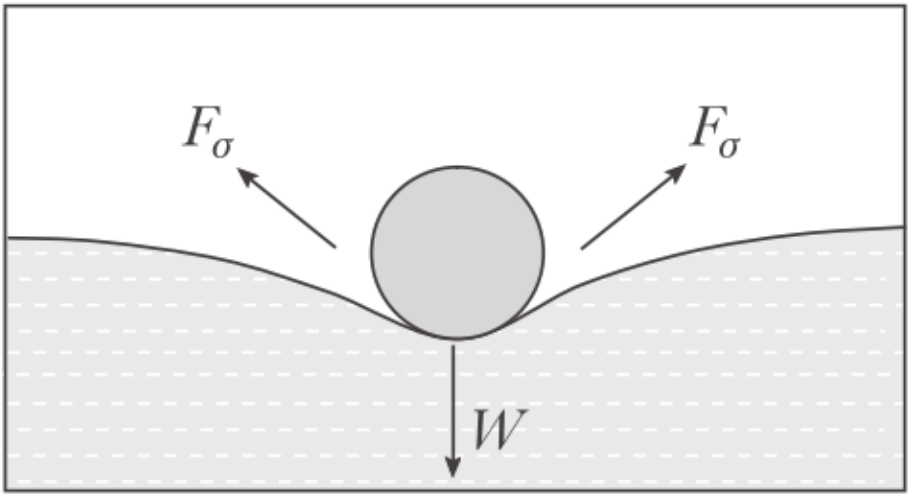

Figure 2.11: Demonstration of surface tension effect [51]

2.2.1 Gibbs Thomson Effect

The surface tension of a liquid is governed by the cohesive forces between the atoms at the free surface, which depends on the chemical composition. The plane that separates two phases is called an interface. An interface between a condensed phase and its own vapor, or an inert gas, is termed a surface. As previously mentioned, the surface is in a higher energy state than the bulk because coordination among the atoms are incomplete. Consequently, it is energetically favorable for foreign elements to segregate to the surface and form a layer [21] . These elements are known as surface active, or surfactants, and their preferential absorption to the liquid surface, even in relatively low levels, i.e. concentrations of ppm, can remarkably reduce the surface tension of the liquid. For example, in metallic liquids, O is very surface active, and almost impossible to eliminate while conducting surface tension measurements. Thus, surface tension data of pure liquid metals in literature differ depending on the O content in the metal or in the surrounding atmosphere. This is revealed in the case of pure liquid Fe, where added concentration of O significantly reduces the surface tension of the melt, as shown in Figure 2.12.

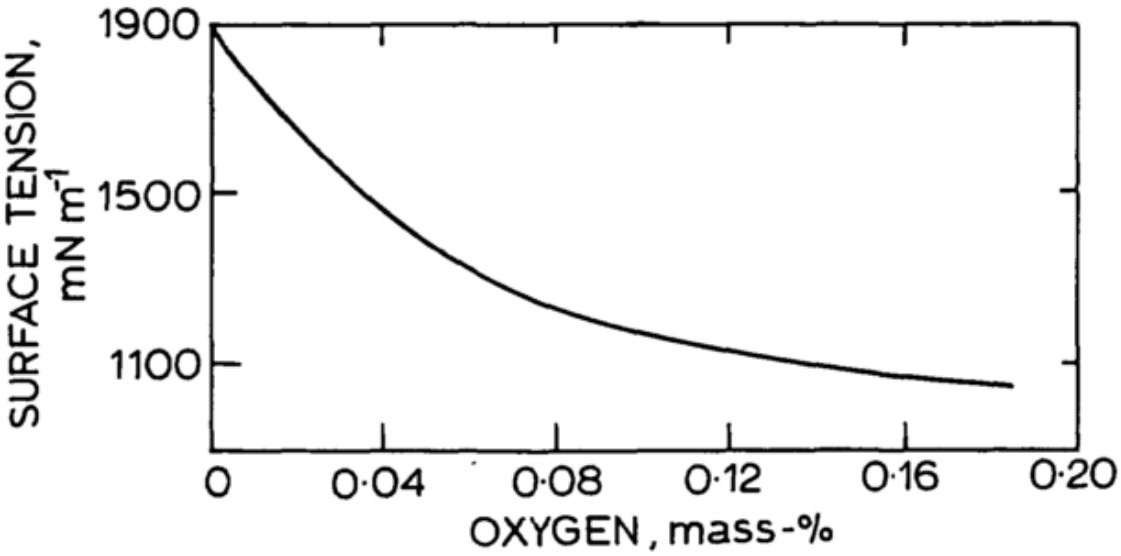

Figure 2.12: Variation of surface tension of molten Fe with O content [53]

The formation of a layer of solutes, or surface-active elements, on the surface of a condensed phase is called ‘adsorption’. The effect that the adsorbed surface-active solutes have on the surface tension of metallic liquids can be investigated by measuring the surface tension as a

function of solute concentration. The results can be interpreted by considering the thermodynamics of the interface. First, we must consider that the presence of an interface introduces an additional term to the function relating the changes in internal energy of the surface, U^s (J), with changes in surface volume, V^s (m^3), surface entropy, S^s (J/K), and molar quantities of species (mole fraction), i:

$$dU^s = -PdV^s + TdS^s + \sum \mu_i dx_i^s + \sigma dA^s \tag{2.32}$$

Since the interface has constant volume, Equation 2.32 can be reduced to:

$$dU^s = TdS^s + \sum \mu_i dx_i^s + \sigma dA^s \tag{2.33}$$

Equation 2.33 can then be integrated by keeping the intrinsic parameters T (K), μ_i (J/mol), and σ (N/m) constant:

$$U^s = TS^s + \sum \mu_i x_i^s + \sigma A^s \tag{2.34}$$

Then, differentiating Equation 2.34 results in:

$$dU^s = TdS^s + S^s dT + \sum \mu_i dx_i^s + \sum x_i^s d\mu_i + \sigma dA^s + A^s d\sigma \tag{2.35}$$

Equating Equation 2.32 to 2.35 leads to:

$$0 = S^s dT + \sum N_i^s d\mu_i + A^s d\sigma \tag{2.36}$$

At constant temperature, Equation 2.36 can be reduced to the Gibbs adsorption isotherm:

$$d\sigma = -\sum \Gamma_i d\mu_i \tag{2.37}$$

Where Γ_i is defined by $\Gamma_i = \frac{x_i^s}{A^s}$ (mol/m^2). The simplest use of the Gibbs adsorption isotherm is when you consider an isothermal two-component system (e.g. a solvent and a solute):

$$d\sigma = -\Gamma_{solvent} d\mu_{solvent} - -\Gamma_{solute} d\mu_{solute} \quad (2.38)$$

An ideal interface can be defined so that $\Gamma_{solvent} = 0$. Therefore:

$$d\sigma = -\Gamma_{solute} d\mu_{solute} \quad (2.39)$$

The chemical potential of the solute is given by:

$$\mu_{solute} = \mu^0_{solute} + RT \ln \frac{a_{solute}}{a_0} \quad (2.40)$$

Where a_{solute} is the activity of the solute and a_0 is a standard activity (i.e. 1mol/L). The equation above is then differentiated with respect to a_{solute}/a_0 at constant temperature:

$$d\mu_{solute} = RT \frac{da_{solute}}{a_{solute}} \quad (2.41)$$

By substituting this into Equation 2.38, the excess surface concentration of a solute of a binary system at constant pressure and temperature is given by:

$$\Gamma_{solute} = -\frac{d\sigma}{RTd(\ln a_{solute})} = -\frac{a_{solute}}{RT}\frac{d\sigma}{da_{solute}} \quad (2.42)$$

In dilute systems, the activity of the solute can be replaced by the solute concentration in terms or either weight percent or atomic percent.

This equation has significant importance when considering the effect of solute on the surface tension of metals. When a solute is enriched at the surface, i.e. Γ_{solute} is greater than zero, the surface tension decreases when the solute concentration is increased. This scenario describes what happens when metallic liquids contain surface-active elements. Contrarily, an increase in surface tension with increasing solute concentration indicates that the solute preferentially diffuses to the bulk of the metallic liquid, i.e. Γ_{solute} is less than zero [55]**.** To explain this conceptually, consider a liquid containing surface active solutes and the definition of surface tension being the increase of free energy required per unit surface area increase. The concentration of solute is higher at the surface than the bulk, i.e. the surface has an excess surface concentration larger than zero. If the surface area of the liquid is increased, it is necessary to remove solute atoms or molecules from

the bulk to the surface because the solute particles preferentially adsorb to the free surface. If the concentration of solute is increased in the bulk, the solutes have a higher chemical potential, thus it is easier to pull them from the bulk to create a new surface. Since it requires less energy to pull the solute from the bulk, the surface tension is lowered. Mills *et al.* [56] suggested that a thorough review of surface tension data of metals in literature is required to verify if the values reported represent "pure liquid metals", i.e. free of contamination by surface active agents.

2.2.2 Temperature Dependence

As previously discussed, the surface tension of a liquid can be determined by considering the free energy of the surface. The temperature dependence of surface tension is related to the surface entropy, and by manipulating the Gibbs adsorption isotherm (Equation 2.37) can be defined as [55]:

$$-\left.\frac{\partial S^s}{\partial A}\right|_{T,x_i^s} = \left.\frac{\partial \sigma}{\partial T}\right|_{A,x_i^s} \tag{2.43}$$

Or, if we define the specific surface entropy s^s (J/m^{2}K) [57]:

$$-s^s = \frac{d\sigma}{dT} \tag{2.44}$$

Rearranging Equation 2.44, and integrating on both side for a constant s^s gives:

$$\sigma = \sigma_m - s^s(T - T_m) \tag{2.45}$$

Where T_m the melting point (K), σ_m is the surface tension at the melting point (N/m) and dσ/dT is the surface tension temperature coefficient (N/m·K). Here, we can see that the surface tension of metallic liquids as a function of temperature is a linear relationship, and if typically represented by [21], [53], [54]:

$$\sigma_t = \sigma_m + \frac{d\sigma}{dT}(T - T_m) \tag{2.46}$$

The surface tension of liquids typically decreases with increasing temperature, or the temperature coefficient is negative. This phenomenon occurs because typically cohesive forces

weaken with an increase in molecular thermal activity. There are, however, a few rare circumstances in which liquids exhibit a positive surface tension coefficient [53]:

- Slags containing SiO_2: large complex molecules are formed creating unsatisfied bonds at the free surface as the temperature increases.
- Molten Fe containing chalcogens (O, S, Se, Te): these surface-active agents progressively desorb from the surface layer as the temperature increases.

2.2.3 Numerical Calculation Models for Surface Tension

This section will describe several analytical and empirical models that were developed to predict the surface tension of pure liquid metals and binary liquid alloys, at either melting temperature, or as a function of temperature. The models that will be discussed will include:

f) The Butler and Chatain models which are classical models in which the surface is described as a stacking of atomic layers.
g) The Egry model which incorporate theory on the depletion of surface-active elements at the surface due to the formation of intermetallic clusters.
h) Empirical models prosed by Allen and Kaptay which accurately calculate the surface tension of pure liquid metals as a function of the melting temperature.

These models will be described briefly, but for additional details, especially on how to derive each model, please refer to "Thermophysical Properties of Multicomponent Liquid Alloys" by Jürgen Brillo [32].

2.2.3.1 Butler Model

The Butler model was one of the first analytical models for the prediction of surface tension [58] . It differs from the Gibbs model (described in Section 2.2.1) by the definition of a "surface". The phase between the bulk liquid and gas phases is considered a separate thermodynamic phase consisting of a monolayer of atoms, which is in equilibrium with the bulk phase. The gas phase is ignored. The Butler model was originally developed for ideal solutions but failed to predict experimental data correctly because the excess Gibbs energy, ${}^{E}G$ (J), in most systems is not equal to zero. Therefore, for a binary alloy, or sub-regular solution, consisting of elements A and B, with

corresponding surface tensions, σ_i $(i = A, B)$ (N/m), the surface tension, σ (N/m), of the system can be predicted using the following equation [59]:

$$\sigma = \sigma_i + \frac{RT}{A_i}\ln\left(\frac{c_i^S}{c_i^B}\right) + \frac{1}{A_i}\left({}^{E}G_i^S\left(T, c_i^S\right) - {}^{E}G_i^B(T, c_i^B)\right) \tag{2.47}$$

Where R is the universal gas constant (J/mol·K), T is the temperature (K), c_i^B is the mole fraction of component i in the bulk phase, c_i^S is the mole fraction of component i in the surface phase, ${}^{E}G_i^B$ is the partial excess Gibbs energy in the bulk (J/mol), ${}^{E}G_i^S$ is the partial excess Gibbs energy of component i in the surface layer (J/mol), and A_i is the surface area in the monolayer of one mole of pure liquid substance (m^2/mol). The surface area can be calculated from the molar volume, $V_{M,i}$ (m^3/mol) , as follows [60].

$$A_i = 1.091 V_{m,i}^{2/3}(6.02 \times 10^{23})^{1/3} \tag{2.48}$$

The partial excess free energy ${}^{E}G_i^B$ can be derived by partial differentiation of the excess free energy ${}^{E}G^B$ with respect to concentration. Also, the partial excess free energy ${}^{E}G_i^S$ is generally unknown, but Tanaka and Iida [60] determined that it could be approximated as:

$${}^{E}G_i^S\left(T, c_i^S\right) \approx \beta \cdot {}^{E}G_i^B\left(T, x_i^S\right) \tag{2.49}$$

Where β is a factor that accounts for the reduced coordination of atoms in the surface layer. Tanaka and Iida [60] conducted a detailed analysis and suggested that a value of 0.83 be used as default for liquids with unknown surface layer structure.

To apply the Butler model, surface tension, density and the excess Gibbs energy of the bulk phase must be known. For binary alloys, temperature dependent parameters, ${}^{v}L_{A,B}(T)$, are used to calculate ${}^{E}G^B$ using the Redlich-Kister equation [61]:

$${}^{E}G^B(x_A^B, T) = x_A^B(1 - x_A^B)\sum_{v=0} {}^{v}L_{A,B}(T)(2x_A^B - 1)^v \tag{2.50}$$

2.2.3.2 Chatain Model

The Butler model has been heavily criticized as it is closer to a semi-empirical model than an analytical model. Some reasons for this criticism include: the factor β is arbitrary, the mono-layer assumption does not reflect reality in most systems, and the Butler model disagrees with the Gibb-adsorption isotherm. Thus, the Chatain model (Equation 2.51), or the multilayer model, was developed to remedy these issues, and rather than considering a sole monolayer as the surface, it considers a stack of atomic layers, each with different compositions. The surface tension of liquid binary alloys, consisting of elements A and B, can be calculated using the following expression [59]:

$$\begin{aligned} A \cdot \sigma = {} & c_A^{(1)} \cdot \varphi_{AA} + c_B^S \cdot \varphi_{BB} - z_v \omega \cdot \left(c_B^{(1)} - 2c_B^B c_B^{(1)} + c_B^{B^2} \right) - 2z_v \omega \\ & \cdot \sum_{j=1}^{k} \left(c_B^{(j)} - c_B^B \right) \left(c_B^{(j+1)} - c_B^B \right) - z_1 \omega \\ & \cdot \sum_{j=1}^{k} \left(c_B^{(j)} - c_B^B \right)^2 + RT \cdot \sum_{j=1}^{k} \left(c_B^{(j)} \cdot \ln\left(\frac{c_B^{(j)}}{c_B^B} \right) + c_A^{(j)} \cdot \ln\left(\frac{c_A^{(j)}}{c_A^B} \right) \right) \end{aligned} \tag{2.51}$$

Where $c_A^{(i)} = 1 - c_B^{(i)}$ and $c_A^{(B)} = 1 - c_B^{(B)}$ are the atom fractions of components A and B in the jth layer, and in the bulk (i.e. $c_A^{(j>k)} = c_A^{(B)}$, where k is selected such that the composition of the $(k+1)th$ layer is the same composition as the bulk), respectively, φ_{ij} (with $i, j = A, B$) is the nearest neighbor bond energies (J/mol), z_v is the number of neighbors of an atom in an adjacent layer, and z_1 is the number of neighbors in any given atom layer parallel to the surface. The atoms of the liquid are assumed to reside in lattice sites with a coordination number of $z = 12$, therefore, z_v=3 and $z_1 = 6$ [59]. The parameter ω (J/mol) characterizes the interaction between the components A and B, and is defined by:

$$\omega = \varphi_{AB} - [\varphi_{AA} + \varphi_{BB}]/2 \tag{2.52}$$

To apply the multilayer model, the surface tension is solved by minimizing Eq. 2.51 using a Monte-Carlo algorithm with random sampling [59].

2.2.3.3 Egry Model

Often, when systems form intermetallic compounds in the solid phase, surface-active agents are depleted from the surface. Egry [62] suggested that this can be explained by assuming that clusters of the intermetallic composition will also exist in the liquid phase. These clusters bind the surface active elements, which prevents them segregating to the surface, creating a competition between clustering and segregation. To account for this phenomenon, Egry proposed a simple model based on the Butler model for ideal solutions. For a binary alloy, consisting of elements A and B, with intermetallic compounds A_nB_m, the surface tension can be calculated as:

$$\sigma = \sigma_A \frac{c_A}{c_A + c_B \exp\left(-(A(\sigma_B - \sigma_A) - f(n+m)c_A^n c_B^m)/RT\right)} + \sigma_B \frac{c_B}{c_B + c_A \exp\left(-(A(\sigma_B - \sigma_A) - f(n+m)c_A^n c_B^m)/RT\right)} \tag{2.53}$$

Where R is the universal gas constant (J/mol·K), T is the temperature (K), c_A is the mole fraction of component A, c_B is the mole fraction of component B, f is an adjustable parameter describing the probability of finding a cluster in the liquid, and A is the molar area (m^2/mol), described by Equation 2.48. A major assumption in the above equation is that the clusters do not segregate to the surface. Also, it assumes that component A is surface active, i.e. $\sigma_A < \sigma_B$. In prior studies, the parameters σ_A, σ_B, and f were fitted to experimental surface tension data using the Levenberg-Marquardt algorithm [62], [63].

2.2.3.4 Empirical Models

Allen [64] developed a simple empirical model that relates the surface tension of a liquid metal at its melting point to the liquidus temperature, T_m (K), the density at the liquidus temperature, ρ_m (kg/m^3) , and its molar mass, M (kg/mol).

$$\sigma_{(T_m)} = 3.6T_m \left(\frac{M}{\rho_{(T_m)}}\right)^{-2/3} \tag{2.54}$$

The above expression was initially derived for pure liquid metals, but Egry *et al.* [63] found that it resulted in an excellent fit to experimental data obtained for Al-Ni and Al-Fe alloys, using density values from literature. This is shown in Figure 2.13.

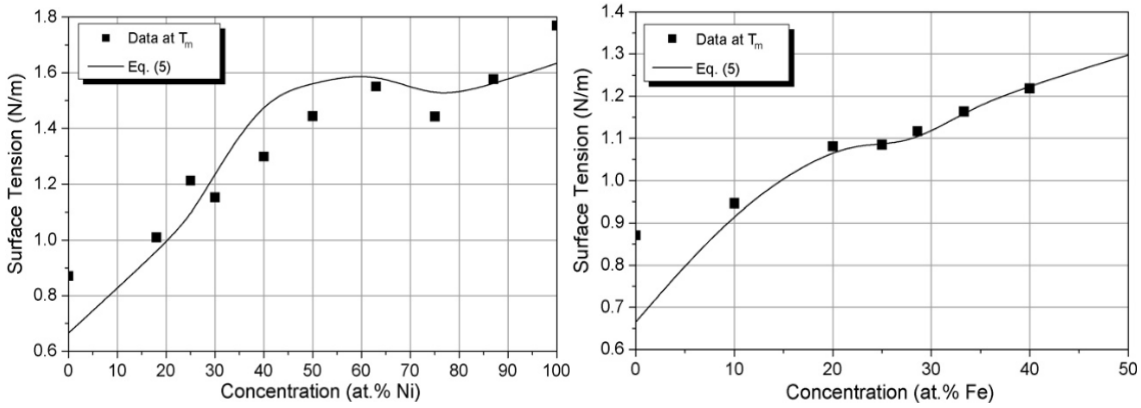

Figure 2.13: Comparison with the experimental data versus theoretical predictions for a) Al–Ni and b) Al-Fe at the liquidus temperature [63]

In addition, Kaptay [65] modelled the surface tension and surface tension temperature coefficient for pure liquid metals using the excess surface enthalpy, excess surface entropy and molar surface area; assuming that the outer two surface layers of the liquid metals are similar to the {111} fcc crystal plane. A simple empirical equation was presented based on calculated cohesive energies, which were also found to be proportional to the liquidus temperature. The following equation describes the surface tension of a pure liquid metals as a function of T_m (K):

$$\sigma_m \cong \alpha_K \frac{T_m}{(V_M)^{2/3}(N_A)^{1/3}} \tag{2.55}$$

Where V_M is the molar volume (kg/mol), N_A is Avogadro's number (mol^{-1}) and α_K is an empirical parameter which was found to equal 38(±10) J/K. In the same study Kaptay concluded that Equation 2.51 oversimplified the way in which cohesive enthalpy was expressed, and therefore, incorporated a second empirical parameter, β_K. To calculate the surface tension temperature coefficient, σ (N/m), the following equation was proposed:

$$\sigma_T \cong -\frac{(0.182 \pm 0.026)C_p - (1.2 \pm 2.3)}{(V_m)^{2/3}(N_A)^{1/3}} - \frac{2}{3}\beta\sigma_{(T_m)} \tag{2.56}$$

Where C_p is the molar heat capacity (J/mol) and β is the thermal expansion coefficient (K^{-1}) . The surface tension can be calculated assuming a linear relationship with temperature.

2.2.4 Methods of Surface Tension Measurements

There are a variety of methods used to determine the surface tension of liquid metals and alloys. There are reported surface tension values for 67 different liquid metals [21]. The main challenge associated with surface tension measurements of metallic liquids is preventing the sample from becoming contaminated at high temperature. As discussed in Section 2.2.1, the presence of surface active elements can drastically decrease the surface tension of liquids. This is practically impossible to prevent, especially with respect to O. The following methods will be discussed briefly:

(a) Sessile Drop Method
(b) Maximum Bubble Pressure Method
(c) Pendant Drop Method
(d) Drop Weight Method
(e) Maximum Drop Pressure Method
(f) Capillary Rise Method

Generally, sessile drop method, maximum bubble pressure method, and the levitated drop method (discussed in Section 2.4.2) are most frequently used at elevated temperatures. The pendant drop method and the drop weight method are used for high melting point refractory metals [21]. Note that more thorough reviews of surface tension measurement methods were compiled by Iida and Guthrie [21], Keen [53], and Mills and Su [56].

Most the methods outlined above are based on a force balance where surface tension plays a significant role. More specifically, they rely on the Young-Laplace equation (or simply Laplace) to describe the pressure difference across a curved interface. As previously discussed, if a fluid element is at a liquid-gas interface, there are forces exerted on the fluid element due to surface tension. The tension in the surface must be balanced by an equal and opposite force, and these stresses depend on the surface tension and the curvature of the surface [66]. In simpler terms, if in equilibrium a liquid-gas interface is curved, there is a pressure difference across it. This can be better described by considering an example of a rubber membrane stretched across a tube end, as shown in Figure 2.14.

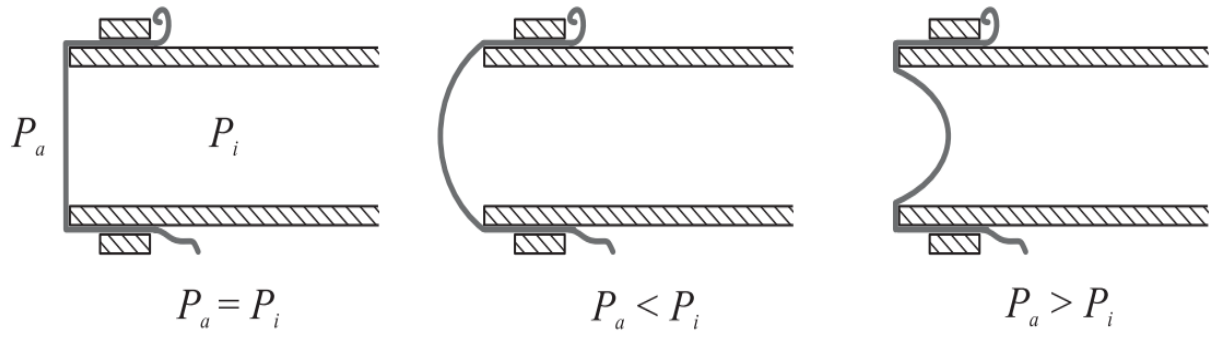

Figure 2.14: Effect of inner and atmospheric pressure on a rubber membrane at the end of a cylindrical tube [55]

If we close one end of the tub with a rubber membrane under tension, the membrane will be planar since the pressure both inside and outside the tube are atmospheric. Instead, if we blow air through the other end of the tube, the membrane will bulge outward, creating a curved interface, and the pressure inside the tube will be larger than outside. The opposite occurs if you suck the air. The Laplace equation related the pressure difference between the two phases, ΔP (Pa), with the surface tension and the curvature of the surface, i.e. the two principal radii of curvature, R_1 and R_2 (m) [55]

$$\Delta P = \sigma \left(\frac{1}{R_1} + \frac{1}{R_2} \right) \tag{2.57}$$

For a spherical surface R_1 and R_2 are equal, therefore:

$$\Delta P = \frac{2\sigma}{R} \tag{2.58}$$

And for a cylindrical surface $R_2 = \infty$, therefore:

$$\Delta P = \frac{\sigma}{R} \tag{2.59}$$

The curvature of both a spherical and a cylindrical surface is illustrated in Figure 2.15. Both relations are important for the methods described below.

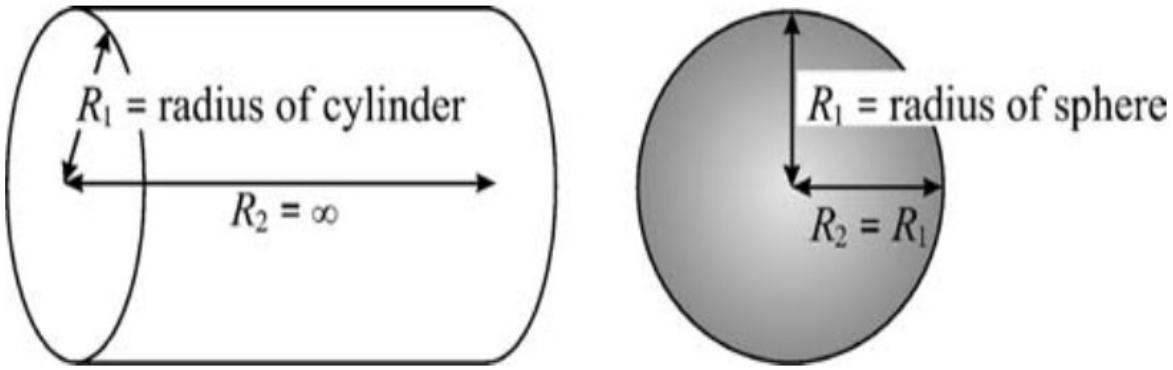

Figure 2.15: Illustration of the curvature of a cylinder and sphere [55]

2.2.4.1 Sessile Drop Method

This method measures the dimensions of a stationary liquid drop placed on a horizontal substrate, as shown by the drop equilibrium profile in Figure 2.16 [21].

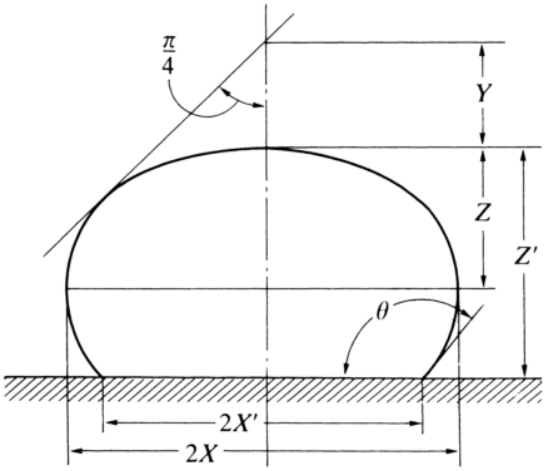

Figure 2.16: Measurements of sessile drop for surface tension calculations [21]

There are several ways to calculate the surface tension from the dimensions of the liquid drop. As an example, the surface tension of a metallic liquid can be obtained using the Bashforth and Adams equation [67]:

$$\sigma = \frac{g\rho b^2}{\beta} \tag{2.60}$$

Where g is the gravitational constant ($m^3/kg{\cdot}s$), ρ is the density of the liquid (kg/m^3), and from the measured X and Z values (m), b and β can be determined using the Bashforth and Adams tables. The density can be calculated using the volume and weight of the drop. The volume, V (m^3), of the drop can be calculated using the same parameters as above:

$$V = \frac{\pi b^2 X^2}{\beta}\left(\frac{2}{b} - \frac{2\sin\theta}{X} + \frac{\beta Z}{b^2}\right) \tag{2.61}$$

The most accurate results for surface tension are obtained when the ratio of X/Z are between 1.5 and 2.0. When the drop becomes more spherical, the accuracy is significantly reduced. The measurements should be made on the profiles of non-wetting sessile drops, since the overall accuracy of the technique is reduced for wetting drops. It is considerably difficult to accurately measure the drop dimensions, particularly dimension Z. This can contribute to error in the surface tension measurements. The dimensions of the drop are typically obtained from measuring photographed images; however, recent developments have employed computer curve fitting techniques along with higher resolution photography or video processing, which helps eliminate human error. Another issue arises from contamination between the substrate and the liquid drop. It should also be noted that only one measurement of surface tension can be made per drop. Nevertheless, the sessile drop method has several advantages over other methods, which includes accurate measurements over a wide range of temperatures, simultaneous measurement of contact angle, spreading coefficient, work of adhesion, and density, and relatively basic experimental equipment [21], [53], [68].

To further improve accuracy, large drop sizes should be used because the contour of the sessile drop is clearer, but in practice, with large drops it is challenging to attain asymmetry. To overcome this challenge, the constrained drop method, as shown in Figure 2.17, was developed, and confirmed by measuring the surface tension of low liquid metals, such as Fe, Co, Sn, Bi, and Pb. When comparing liquid Fe and Co surface tension results between the traditional and constrained methods, the traditional method yielded experimental scatter within ±6.8%, while the constrained method was within ±3.0% [69]

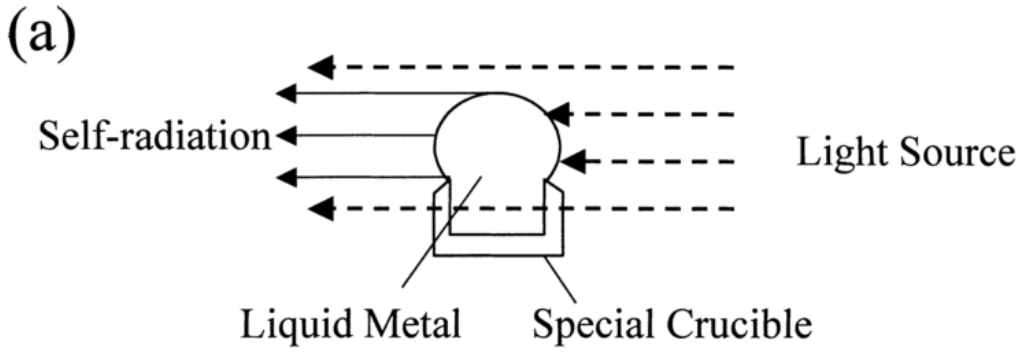

Figure 2.17: Schematic of the constrained drop method [69]

The sessile drop method has proven successful in measuring the surface tension of various pure metals, e.g. Fe, Si, Ni, Ag, Au, Sn [69]–[72], and alloys, e.g. Fe-Ni-O, Fe-Cr-Mn-Ni, and Al-Ni [73]–[75].

2.2.4.2 Maximum Bubble Pressure Method

The maximum bubble pressure (MBP) method is based on the immersion of a capillary tube with radius, r (m), into the fluid to a known depth, h (m). Inert gas is passed through the capillary tube and bubbles of gas will form from the tip of the capillary. The surface tension of a metallic liquid can be determined by measuring the pressure required to detach the bubble from the tip of the capillary tube. The MBP, P_M (Pa), is calculated from the sum of the static pressure needed to maintain the column of liquid at a certain depth, i.e. ρgh, and the Laplace pressure at the curved bubble surface, i.e. $\Delta P = 2\sigma/r$:

$$P_M = \rho gh + \Delta P = \rho gh + \frac{2\sigma}{r} \tag{2.62}$$

As pressure increases, the size of the bubble increases until a maximum bubble pressure is obtained, and its radius corresponds exactly to the radius of the capillary. A correction must be made to account for any bubble distortion that might be caused by gravitational effects. The Schrodinger equation is most commonly used to correct the experimental values [76][76]:

$$\sigma = \frac{r\Delta P}{2}\left(1 - \frac{2}{3}\frac{\rho gh}{3\Delta P} - \frac{1}{6}\left(\frac{\rho gh}{\Delta P}\right)^2\right) \tag{2.63}$$

The MBP method is an effective technique to measure the temperature dependence of surface tension as it can be carried out at high temperatures and over a large range of temperatures. It also facilitates the use of thermocouples [5]. It also proves to be very useful for measuring the surface tension of metals that are susceptible to surface contamination, e.g. alkali metals, Mg, Al, and Ca. The reason for this is that each successive measurement is made on a freshly bubbled surface; this significantly reduces surface contamination. However, trace levels of O in the inert gas will affect the surface tension results of the metallic liquid. There have been cases of initial wetting of the capillary tip by the metallic liquid (e.g. liquid Al on Al_2O_3) and as a result, the maximum pressure decreases, indicating an increase in the radius of the bubble detaching [78]. Obviously, this will cause significant errors in the surface tension measurements. An example of an experimental apparatus for the MBP is illustrated in Figure 2.18.

The MBP method has been successfully employed to measure the surface tension and the surface tension temperature coefficient of multiple liquid metals and alloys, like Fe-Cr-Mn-Ni alloy, TRIP/TWIP steel, [11], [70], [73], [79], [80]. A schematic of the experimental apparatus used by Yoshikawa to measure the surface tension of Fe-Si-C alloys is shown in Figure 2.18 [80].

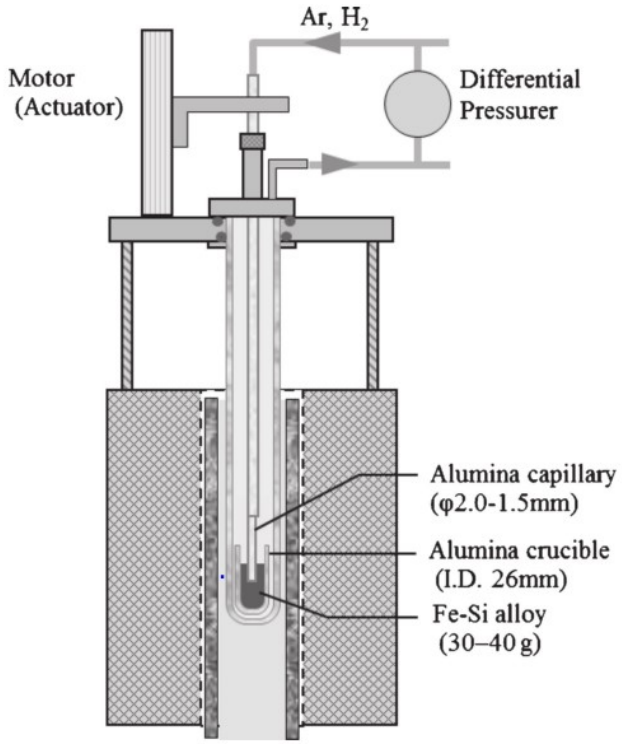

Figure 2.18: Experimental apparatus for the maximum bubble pressure method [80]

2.2.4.3 Pendant Drop Method

The pendant drop is essentially an inverted sessile drop. When a drop is suspended freely from the tip of a vertical capillary tube, it will adopt a shape typically as shown in Figure 2.19 [21]. This configuration results from a static force balance between surface tension and gravity. Thus, the surface tension of a metallic liquid can be calculated by:

$$\sigma = \frac{\rho g X^2}{H} \tag{2.64}$$

Where X (m) is the maximum drop diameter, and $1/H$ (is the shape factor for the drop, which is a funciton of X'/X. The values of $1/H$ have been experimetally determined, and typically vary between 0.2 and 1.0 [81].

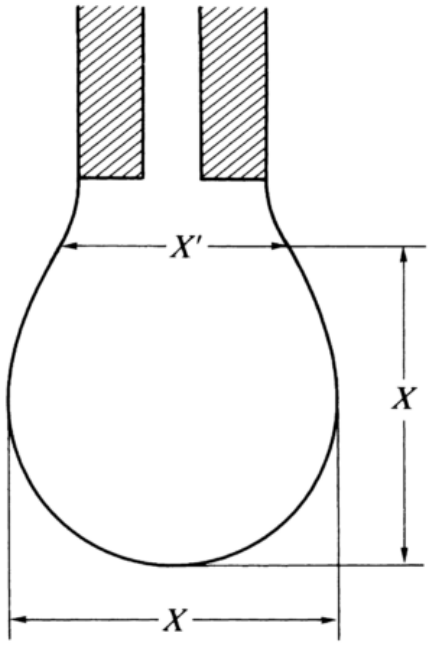

Figure 2.19: Measurements of pendant drop for surface tension calculations [21]

Like sessile drop, the pendant drop method presents difficulties involving chemical compatibiltity, errors in measurements of relatively small dimensions, and only being able to take one measurement per drop. Furthermore, any instabilities during the experiment could lead to the drop becoming detached from the capillary tube. The temperature range over which surface tension can be measured with the pendant drop method is considerably less than with the sessile drop

method [53]. An advange that the pendant drop offers is that rather than use a capillary tube, a drop can be formed from a rod of the same material. This is done by focusing a heat source on the rod, e.g. electron or laser beam, which produces a drop, and negates any contamination issues [82]. Unfortunately, often, the heat source can introduce instability and temperature uniformity problems. Only a few works have been conducted on the measurement of the surface tension of metallic liquids using the pendant drop method, and they are mostly limited to low melting temperature metals, like Ga [83], and Se [84]. Nevertheless, it has also be used to measured the surface tension of refractory metals [82], [85], [86], and Si-Ge alloys [87].

Giuranno *et al.* [88] developed a combined sessile drop and pendant drop method to measure the surface tension of metallic liquids at high temperatures, which allows the performance of both techniques under the same experimental conditions. This combined method has several advantages including short contact time, large drop comparable symmety, and reduction of surface primary oxide film. It has been successfully used to measure the surface tension of a class of reactive metal systems, the liquid γ-TiAl-based alloys, as well as pure Cu, Ni, Al, and Fe [89].

2.2.4.4 Drop Weight Method

Like the pendant drop method, the drop weight method relies on a liquid drop forming at the tip of a vertical cylindrical rod (wire), or capillary tube. However, it also relies on the theory that if the drop grows enough to the point that it detaches itself, the gravitational force acting on the drop at this point will be equal to the surface force. This is known as Tate's law [90]:

$$mg = \sigma 2\pi r \tag{2.65}$$

Where m (kg) is the mass of the drop and r (m) is the radius of the rod, or capillary tip. Tate's law only applies under ideal circumstances. The mechanism of a liquid drop forming and detaching, in reality, is much more complicated; the weight of the drop is always less than the ideal weight. As the drop grows, the neck of the liquid, which attaches the drop to the rod or capillary tip, progressively elongates until the drop detaches. This occurs because the neck is unable to support the mass of the growing drop, and results in early detachment, followed by several small satellite drops. Moreover, some of the liquid from the neck remains attached [53]. To correct for this phenomenon, Harkins and Brown [91] empirically developed a table of factors, C_{HB}, that corrects for the difference between ideal and actual weight. These factors are determined by

calibrating low temperature liquids, e.g. water, organics, so it is unclear if they translate well with respect to high temperature metallic liquids. By incorporating the correction factor, the surface tension can be calculated from:

$$\sigma = \frac{mg}{2\pi r C_{HB}} \tag{2.66}$$

The drop weight method shares many advantages and challenges with the pendant drop method. Both techniques can be used to measure the surface tension of metallic liquid by heating a metal rod and thus eliminating any contamination issues from a capillary tip. The drop weight method can only be used to measure the melting point surface tension of the metal, since the liquid drops are suspended by a solid of the same composition. It is, therefore, unable to measure surface tension temperature dependence. It is also important to control the rate of drop formation; this is difficult to regulate using the containerless method [53]. The drop weight method has been employed on liquid Hg and Sn [92], [93], and industrial alloys such as 316 stainless steel, Inconel 182 and 600, Cr-Mn-Ni steel alloys, and CMSW-4 super alloy [94]–[96]

2.2.4.5 Maximum Drop Bubble Method

The maximum drop bubble method involves measuring the pressure required to force a small liquid from the tip of a vertically, upwards-facing capillary tube. It shares very similar principals with the MBP technique. Its advantages include that it provides dynamic, uncontaminated surfaces, avoids introduction with contact angles, and has no theoretical uncertainty [21]. It is often used to measure the surface tension of highly reactive metals, but unfortunately, is limited to low melting point metals (e.g. maximum 750 °C) because designing the equipment for high temperatures proves to be quite challenging [21]. Successful surface tension results were obtained for liquid Hg, Cd, Zn, Pb, Sn and Bi [92]

2.2.4.6 Capillary Rise Method

This method applies the phenomenon of capillary action, i.e. the liquid level will rise in the tube due to the capillarity of the liquid. The liquid will exhibit a curved free surface, i.e. meniscus, within the capillary tube, as shown in Figure 2.20, creating a pressure difference between the liquid

and gas interface, as per the Laplace equation. From this, the surface tension can be calculated from the simple expression:

$$\sigma = \frac{\rho g h r}{2 \cos \theta} \tag{2.67}$$

Where h (m) is the difference in height between the liquid surface within the capillary and the surface of the bulk liquid outside the capillary, r (m) is the radius of the capillary, and θ is the contact angle between the liquid and the capillary wall [21].

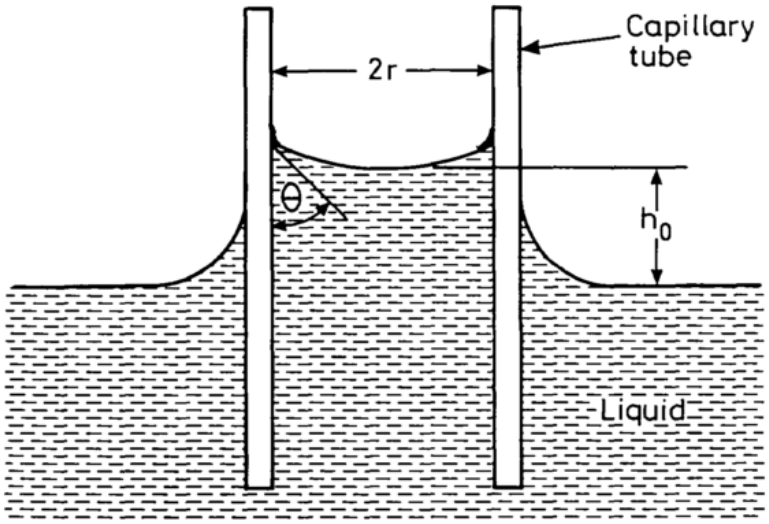

Figure 2.20: Capillary rise method for determining surface tension [53]

The capillary rise method has been extensively used to determine the surface tension of organic liquids and acqueous solutions [97], [98]. The method requires exact knowledge of contact angles, therefore, the lack of metallic contact angle data makes this method difficult to use for metallic liquid surface tension measurements [21], [53]. There are also obvious challenges associated with contamination from the reactive metal contact with the capillary tube, and the distorition and opacity of the meniscus within the tube, i.e. difficulties in height measurement [53]. Measurements have been obtained for low temperature metals and binary alloys, such as In, Sn and Pb [99].

2.3 Density of Metallic Liquids

Mass density (which will be referred to solely as density) is the mass per unit volume of a substance [100]. Most metallic liquids experience a volume increase, or density decrease, during the solid-liquid phase transformation. The volume jumps are characteristic of a first-order phase transition. Exceptions to this rule are semimetals, e.g. Ga, Si, Ge, and Bi, and Ce and Pl [21]. Density provides useful information on topics ranging from simple mass balance calculations in refining operations to knowledge of volume changes in metals and alloys at their melting temperatures, which is of vital importance for solidification processes. Furthermore, density is usually required in measuring other basic thermophysical properties, e.g. surface tension, viscosity, thermal conductivity, etc. [101]. As a result, researchers have conducted density measurements for more than 150 years on metallic liquids, including liquid metals, semimetals, semiconductors, and alloys.

There is plenty of density data available for pure liquid metals, but reliable density data only exists for common low melting temperature liquid metals and alloys, and further measurements are required on a multitude of more complex systems [101]. Often, metallic liquids are too chemically reactive, scarce or refractory for accurate experimental data to be obtained [21]. There are various methods to measure the density of metallic liquids, which rely on measurements of buoyancy, hydrostatic pressure, volume, or shape. These methods will be discussed in detail in Section 2.3.1.

Generally, within a limited temperature range, the density as a function of temperature, ρ, of metallic liquids can be expressed linearly [101]:

$$\rho = \rho_m + \frac{\partial \rho}{\partial T}(T - T_m) \tag{2.68}$$

Where ρ_m (kg/m^3) is the density at the melting temperature, T_m (K), and $\partial\rho/\partial T$ is the constant temperature coefficient (kg/m^3·K) . For multicomponent systems, the molar volume of the mixture, V_M, can be expressed using the following equation [101]:

$$V_M = \sum x_i \frac{M_i}{\rho_i} + V^E \tag{2.69}$$

Where ρ_i (kg/m^3) are the densities of the pure liquid metals, x_i are the respective molar concentrations, M_i (kg/mol) are the respective molar masses, and V^E (m^3/mol) is the excess volume. For thermodynamic ideal solutions, the atoms are randomly distributed, and V^E is equal to zero [102]. Therefore, the above equation reduces to:

$$V_M = \sum x_i \frac{M_i}{\rho_i} \tag{2.70}$$

Otherwise, a simple expression for V^E in ternary systems is given as [101]:

$$V^E(x_1, x_2, x_3, T) = \sum_{i}^{2} \sum_{j<1}^{3} x_i x_j V_{i,j} + x_1 x_2 x_3 V^T \tag{2.71}$$

Where $V_{i,j}$ is the binary contributions from components i and j, and V^T is the parameter for a possible ternary contribution.

2.3.1 Methods of Density Measurements

There are various methods that exist and have been employed to measure the density of metallic liquids. Much like surface tension and viscosity measurements, there are numerous challenges associated with density measurements at high temperatures. These include, but are not limited to, contamination, reactivity, and material selection. It is important to be cognizant of the most appropriate method to be employed depending on the system of interest. The following techniques will be summarized in the sections below:

(a) Archimedean Method
(b) Pycnometric Method
(c) Dilatometric Method
(d) Sessile Drop Method
(e) Maximum Bubble Pressure Method
(f) Gamma Radiation Attenuation Method

(g) Fast Pulse Heating Method

It should be noted that these methods are based on different principles, such as buoyancy, volume, hydrostatic pressure, etc. There are numerous review papers and/or books published on density measurements of metallic liquids. These include works published by [21], [103], [100], and [104].

2.3.1.1 Archimedean Method

This method is based on the Archimedes principle and measurements of buoyancy force. In the case of metallic liquids, a sinker is immersed in a liquid specimen attached to a counterweight or balance. When the sinker is immersed in the liquid, a new apparent weight, w_2 (kg), is observed, or an apparent loss of weight, $\Delta w = w_1 - w_2$ (kg). The weight loss is caused by buoyancy force exerted on the sinker by the metallic liquid sample. Note that an indirect Archimedean method exists where a metallic liquid is placed in a crucible, which is weighed while immersed in an inert liquid with known properties, e.g. inert fused salt. The advantage of this is that metallic solids can be measured, and so can the density gap at meting [103]. The density of a metallic liquid using the direct method is given by:

$$\rho = \frac{\Delta w + s}{g(V_s + V_w)} \tag{2.71}$$

And,

$$s = 2\pi r\sigma \cos\theta \tag{2.73}$$

Where V_s (m^3) is the volume of the sinker, V_w (m^3) is the volume of the wire, s is the surface tension correction factor, r (m) is the radius of the wire, σ (N/m) is the surface tension of the liquid and θ is the contact angle between the liquid and the wire. The magnitude of s is typically 0.5% of Δw for most liquid metals and suspensions [103]. Other corrections that must be considered include thermal expansion of the wire and sinker, which will affect their volumes [105].

The primary source of error in this method involves uncertainties with surface tension and contact angle measurements. Also, the Archimedean method requires a large volume of liquid sample, thus it is often difficult to achieve uniform temperatures and thermal gradient induced convection will exert unaccounted for forces on the sinker [103]. Another problem consists of

material selection; the sinker can be made of chemically resistant materials such has graphite, Al_2O_3 or ZrO_2, but generally metals are used for making the wire. This leads to reactivity between the metal wire and the metallic liquid which will obviously contaminate the sample, and reduce the volume of the wire [21]. Conversely, this method possesses several benefits, such as relative simplicity, and the ability to measure density of a wide range of temperatures.

Several workers from the early 1900s have used the Archimedean method to measure the density of metallic liquids [103]. More recently, Wang and Xian [106] have conducted high temperature Archimedean experiments on liquid Sn-Pb, Sn-Zn and Sn-Bi alloys to temperatures up to 250 °C. As well, Hitoshi *et al.* [107] used the Archimedean method to measure the density of molten Si from 1420 to 1650 °C, and Dang *et al.* [108] on hypereutectic Al-Si alloys at around 550 °C.

2.3.1.2 Pycnometric Method

This method consists of filling a vessel with a metallic liquid to an accurately determined volume, and then weighing the system once the liquid has solidified to room temperature. The advantages of using this method is that is provides accurate, absolute measurements, and that the principle and construction of the apparatus is relatively simple. For absolute density measurements, the volume of the vessel must be known with high confidence, i.e. the vessel must be machined with high precision. At higher temperature (i.e. above 1100°C) this is difficult because of limitations of container materials. The requirements for a high temperature pycnometer are high machinability, no reactivity with the liquid sample, refractoriness, and low, well-characterized thermal expansion. Depending on the application, materials such as graphite, quartz, refractory (e.g. Ta), and metal oxides (e.g. Al_2O_3) have been employed [21]. If the geometry of the vessel is irregular, the pycnometer must be calibrated with a liquid of known properties; often Hg [104]. Other issues include incomplete filling of the vessel at the sharp corners due to surface tension effects, and the inability to measure density at varying temperatures [21], [104].

Multiple pycnometry experiments have been carried out at high temperatures on low-melting temperature liquid metals, e.g. Sb, Zn, Cd, In, Tl, Bi, La, and Ce [104], [109], and liquid metal alloys, e.g. Zn-Sn, Cd-Sn, Cd-Pb, Zn-Pb, Cd-Tl, Pb-Bi, Zn-Al [110]–[112]. Recently, this method has been carried out on high-melting point metallic liquids. Sato *et al.* [113] performed

successful density measurements on Si at temperatures reaching 1580 °C using a pycnometer made of BN and Al_2O_3.

2.3.1.3 Dilatometric Method

The dilatometric method is an established method based on the principle that the volume of an accurately weighed sample will change if heated, and that this change in volume can be measured using a scale, or other. The density can then be calculated considering the bulk density of the sample at room temperature and the continuously measured volumetric expansion of the metallic liquid [21], [100]. There are multiple varieties of dilatometers used to measure the density metallic liquids; these include optical [114], laser [115], push rod [116], and capacitive [117]. An example of the push-rod dilatometer is given in Figure 2.21.

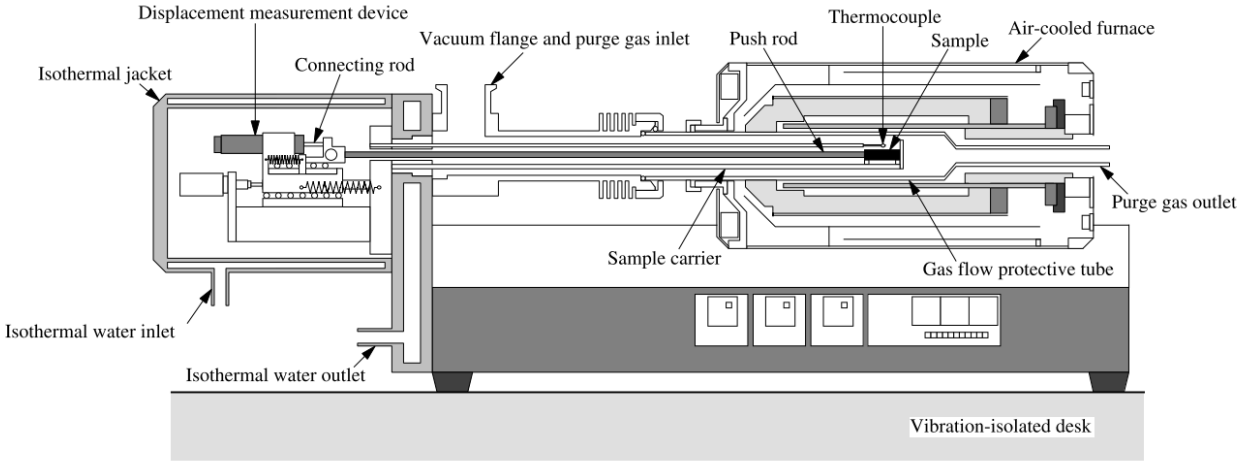

Figure 2.21: Experimental apparatus for the dilatometric method [113]

The advantages of using the dilatometric method includes simplicity, accuracy, continuous density measurements at varying temperatures, and it requires very little sample material. However, at high temperatures, the container must be made using compatible materials that are resistant to dissolution by liquid metals. Most often, these consist of refractories which are difficult to fabricate and machine accurately [104]. To resolve these issues, optical dilatometry is used in combination with the electromagnetic levitation. This recently combined technique has been used to measure the density of molten Cu, Ni, Fe and their alloys [118], [119].

2.3.1.4 Sessile Drop Method

The sessile drop method was previously described in Section 2.2.3.1. The shape of the drop, obtained using X-ray or CCD, is used to calculate the volume of the drop. The mass of the liquid drop is known; thus, density can be calculated. This method is considered very accurate if the drop is fully symmetrical, often achieved using the "large-drop method" [6]. Nevertheless, if non-symmetrical, algorithms can be used to calculate the best curve fit shape of the drop. Jimbo and Cramb [120] employed the sessile drop technique to measure the density of Fe-C alloys at temperatures ranging from 1250 to 1550 °C, and were able to achieve values within ±1.5 % of well-established literature values. A schematic of their experimental apparatus is shown in Figure 2.22. More recently, Mizukam *et al.* [121] conducted density measurements on carbon steel using the sessile drop method to temperatures reaching up to 1700 °C.

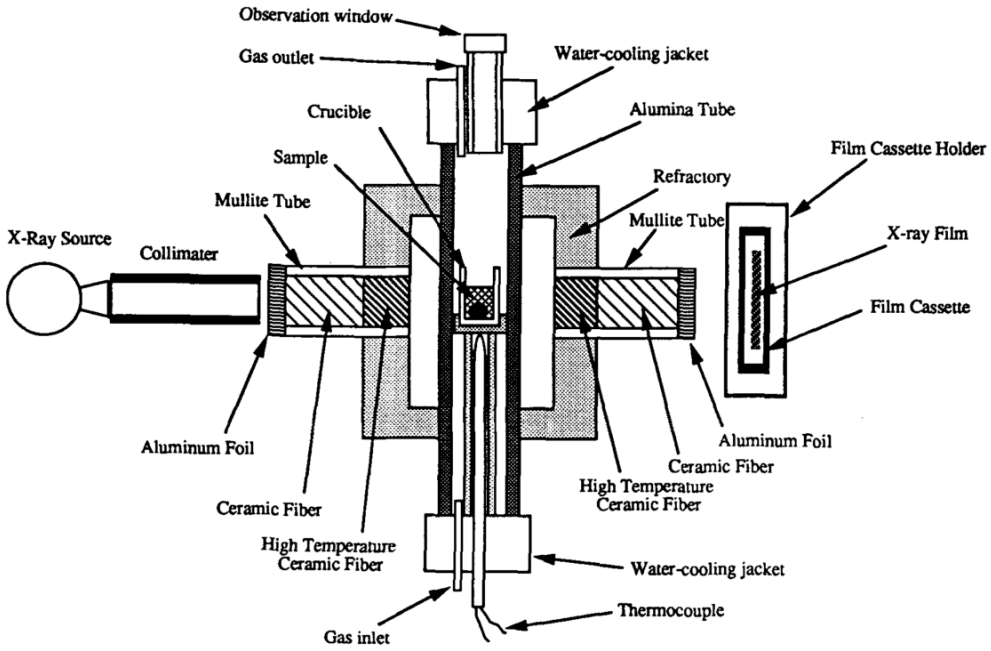

Figure 2.22: Schematic of the experimental sessile drop apparatus using X-ray devices [120]

2.3.1.5 Maximum Bubble Pressure Method

This technique based on hydrostatic pressure is identical to the technique described in Section 2.2.4.2. If you consider Equation 2.62, the second term in the equation, i.e. the surface tension effects, can be removed if you conduct measurements at different capillary depths. If the

maximum bubble pressures are P_{m1} and P_{m2} (Pa) at depths h_1 and h_2 (m), respectively. Equation 2.62 can be re-written as:

$$\rho = \frac{P_{m1} - P_{m2}}{g(h_1 - h_2)} \tag{2.74}$$

The MBP method is not as accurate as the pycnometric method, but is preferable for measurements at high temperatures [6]. It possesses an advantage over the Archimedean method in that it does not require knowledge of surface tension. This technique has recently be used to measure the density of Fe-Cr-Mo (AISI 4142), Fe-Cr-Ni (AISI 304), and Fe-Cr-Mn-Ni TRIP/TWIP high-manganese liquid alloys to temperatures up to 1650 °C [122]. It has also recently been used by the same author to measure the density of liquid Au, Ag and Sn [70]

2.3.1.6 Gamma Radiation Attenuation Methods

The gamma radiation attenuation method is based on the attenuation (i.e. reduction of amplitude) of a γ-ray beam passing through a metallic liquid. The incident beam emitted from a radiation source is attenuated relative to the mass of the liquid sample and recorded with a radiation counter. For a γ-ray beam with intensity I_0 (W/m^2) passing through a sample of length l (m), the attenuated beam intensity is given by:

$$I = I_0 e^{(-\alpha_a \rho l)} \tag{2.75}$$

Where α_a (m^2/kg) is the absorption coefficient per unit mass, which can be determined from absorption measurements on solid samples with easily calculated density values. The main advantage of using this technique is that since the radiation penetrates the bulk of the sample, surface tension effects and chemical contamination are not involved [6]. The γ-ray attenuation method has been used to measure the density of molten Mn, Fe, Ni, Cu, Al and Sn [123]. A similar technique using X-ray attenuation has been used on liquid Al alloys [124], and on Fe alloys in high-pressure geophysical environments [125], [126]. A schematic of this method if given in Figure 2.23.

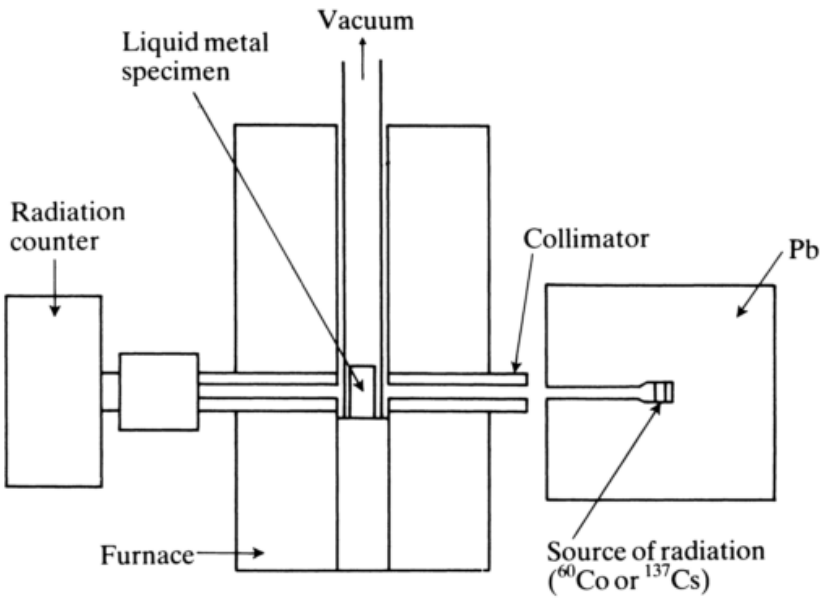

Figure 2.23: Schematic of the experimental set-up for gamma ray attenuation method [21]

2.3.1.7 Pulse Heating Method

The pulse heating method is a containerless technique restricted to electrically conducting materials. The sample is made into a thin-wire and a current pulse passes through the sample which is resistively heated past the liquidus temperature. The heating rate can reach up to 10^8 K/s and the sample temperature increases from room temperature to the boiling point in roughly 50 μs, at which point the wire explodes [127]. The method is so fast that measurements can be made on the "standing" liquid columns, and the geometry of the sample remains unaffected by gravity, instabilities, or other effects [100]. A high-speed pyrometer is used to measure the temperature, and the volume changes are registered using a CCD camera. Not only can pulse heating measure density, but also specific enthalpy, electrical resistivity, thermal conductivity, thermal diffusivity and temperature coefficient of thermal expansion [127].

Evidently, the main advantage of this method is that it avoids the negative effects of the sample being in contact with a vessel and/or substrate. It is also able to measure properties at extremely high temperatures. Recent measurements have been carried using pulse heating on Pt-Cu alloys [127] and Ni80Cr20 alloy [128]. These measurements agree well with static and quasi-static methods.

2.4 Simultaneous Property Measurement Methods

There are very few methods able to simultaneously measure the viscosity, surface tension and density of metallic liquids at high temperatures. In this section, three measurement methods will be described which include levitated drop, gas bubble viscometer and the discharge crucible. Furthermore, the advantages and disadvantages of each method will be described in detail to better understand the applicability of each method. It should be noted that the discharge crucible is the experimental method used in this work, so special attention will be made to highlight the fundamentals, formulation, computation, assumptions, and any prior work.

2.4.1 Gas Bubble Viscometer

The gas bubble viscometer was developed for metallic liquids at high temperatures by Friedrichs *et al.* [129]. It is based on the Test Method for Viscosity of Transparent Liquids by Bubble Time Method (ASTM D1545) which describes a procedure where the time at which bubbles rise through a transparent liquid can be used to estimate the viscosity of the liquid [130]. For high-temperature applications, inert gas bubbles (e.g. Ar bubbles) are produced through a capillary tube in the melt at a known depth. The departure time of the gas bubble is determined by the measurement of a pressure drop in the tube. The arrival time (i.e. the time when the bubble reaches the liquid surface) is determined by locating a laser beam on the surface of the liquid which is reflected to a diode. When the bubbles surface, the surface disturbance and accompanied intensity drop of the reflected laser is recorded. The difference of these two times is the bubble rise time. The viscosity of the metallic liquid is calculated based on the bubble velocity which is determined by the balance of forces acting on it, including inertial forces, capillary forces, buoyancy forces frictional (drag) forces. Since the mechanism of rise depends on the drag forces, represented by the drag coefficient, which is a function of Reynolds number, Re, viscosity can be calculated iteratively. A schematic of the experimental method is illustrated in Figure 2.24.

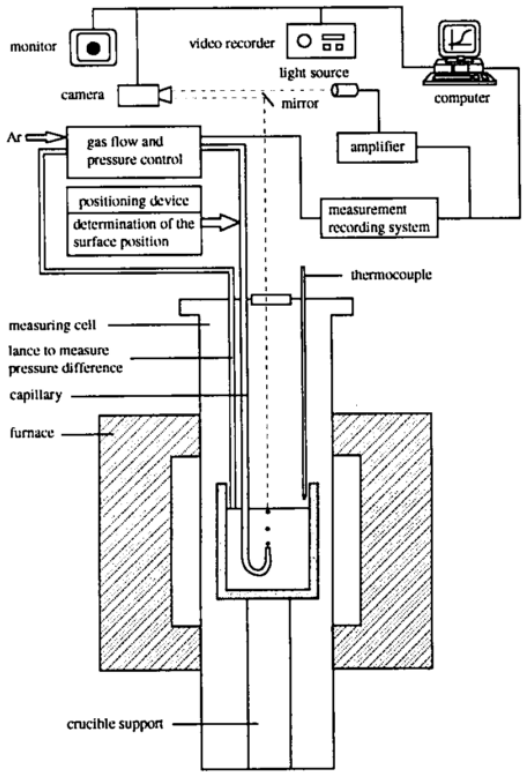

Figure 2.24: Schematic of the gas bubble viscometer [131]

The main advantage of using this technique is that since the pressure change at the capillary tube is measured at the time of detachment, the pressure required to detach the bubble from the capillary tip is also measured. Thus, the surface tension and density of the liquid can be calculated based on the MBP method. The gas bubble viscometer was first used to measure the viscosity, surface tension and density of liquid Cu, Sn and Pb at temperatures up to 1250 °C [129]. The results differed considerably from literature values (up to 21% for viscosity, 33% for surface tension and 53% for density). The authors proposed that the errors were due to a combination of influences such as vibrations affecting the laser beam, melt surface oxidation, poor wettability of the capillary tube (which could cause the formatting of larger bubbles susceptible to break-up), capillary orifice not being perfectly round, measurement of orifice and capillary depth not being accurate, etc. It has also been suggested that that shape of the gas bubble is a crucial parameter for predicting interfacial transport between gas bubbles and metallic liquids, and the gas bubble viscometer assumes that the bubbles remains spherical [129], [132]. The shape of the bubbles depends on several characteristics, namely diameter, mean rising velocity, gas holdup, bubble frequency, etc. [133]. If the bubbles deviate from spherical shape by elongation, the friction forces,

or viscous forces, acting on the bubbles will decrease. Obviously, the control of bubble shape is difficult, and will have a large impact of the accuracy of the metallic liquid viscosity measurements.

Friedrichs *et al.* [131] also used the gas bubble viscometer to take measurements of viscosity, surface tension, and density of Al-Cu alloys in the temperature range of roughly 690 to 1190 °C. Some results are shown in Figure 2.25. To date, no other measurements have been made using this technique.

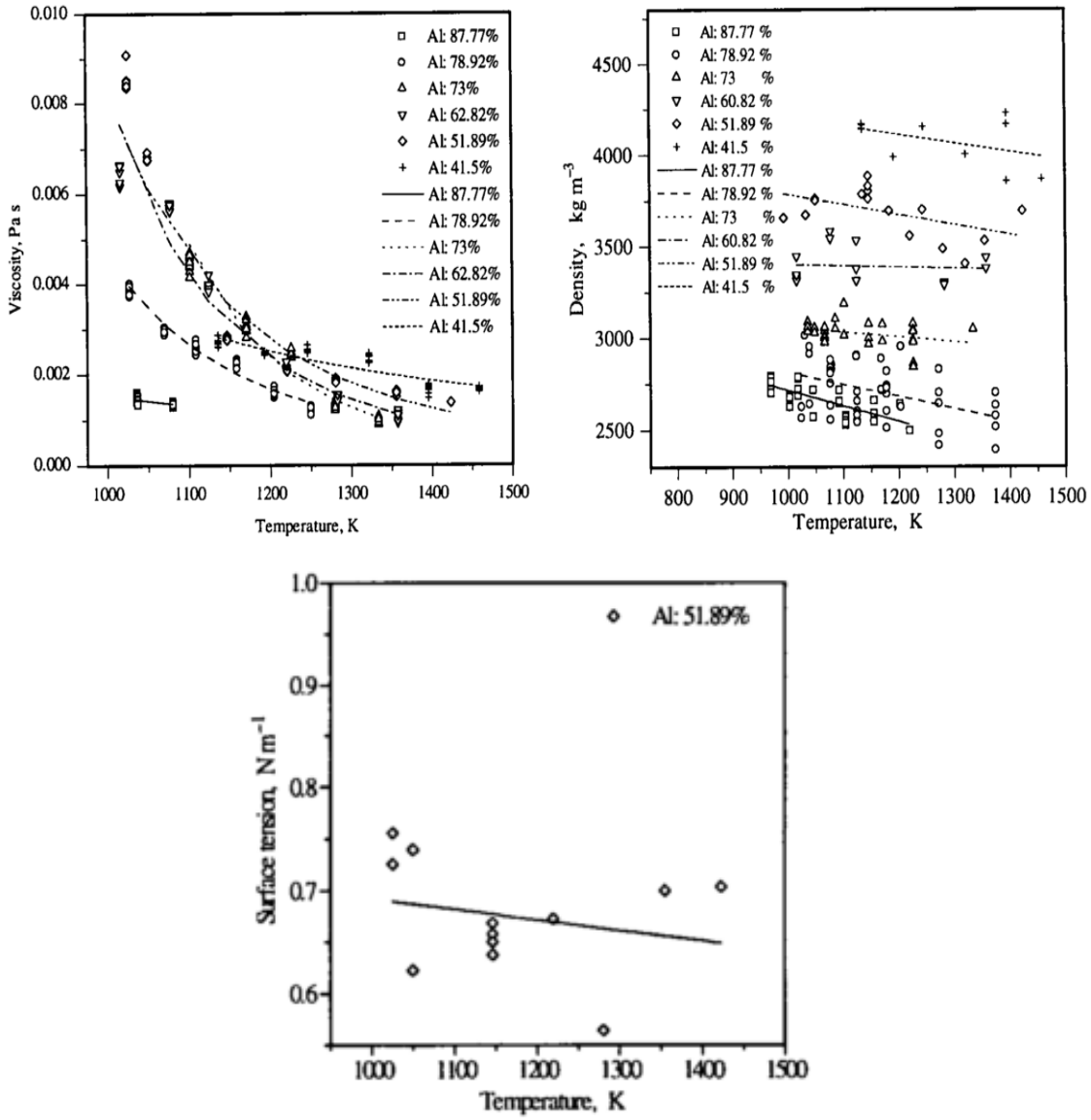

Figure 2.25: Results of viscosity, surface tension and density of Al-Cu alloys using the gas bubble viscometer [131]

2.4.2 Levitated Drop Method

The measurements of thermophysical properties of metallic liquids at high temperatures using conventional techniques are often complicated because of either chemical or dissolution reactions between the metallic liquid and the container holding the metallic liquid. Electrostatic (ESL), electromagnetic (EML), aerodynamic, and acoustic levitation offers an alternative containerless approach to measure the thermophysical properties of metallic liquid through the levitated drop (LD) method. A comparative summary of the main characteristics of each levitation technique is presented in Table 2-1 [134]

Of these levitation techniques, EML is the most popular and robust property measurement technique with regards to electrically conducting liquids, e.g. metallic liquids. Thus, it will be the focus of this section. The principle of containerless EML is well understood and based on Faraday's induction law. When an electrically conducting material is subjected to an alternating magnetic field, eddy currents are induced in the sample. The interaction between the eddy currents and the magnetic field creates a Lorentz force that opposes gravity and supports the sample without physical contact. Along with levitation, Joule, or Ohmic, heating occurs leading to the eventual melting of the sample. EML-LD has impressive analytical capabilities (as seen in Figure 2.26) able to measure many properties including viscosity, surface tension, density, specific heat, and electrical conductivity.

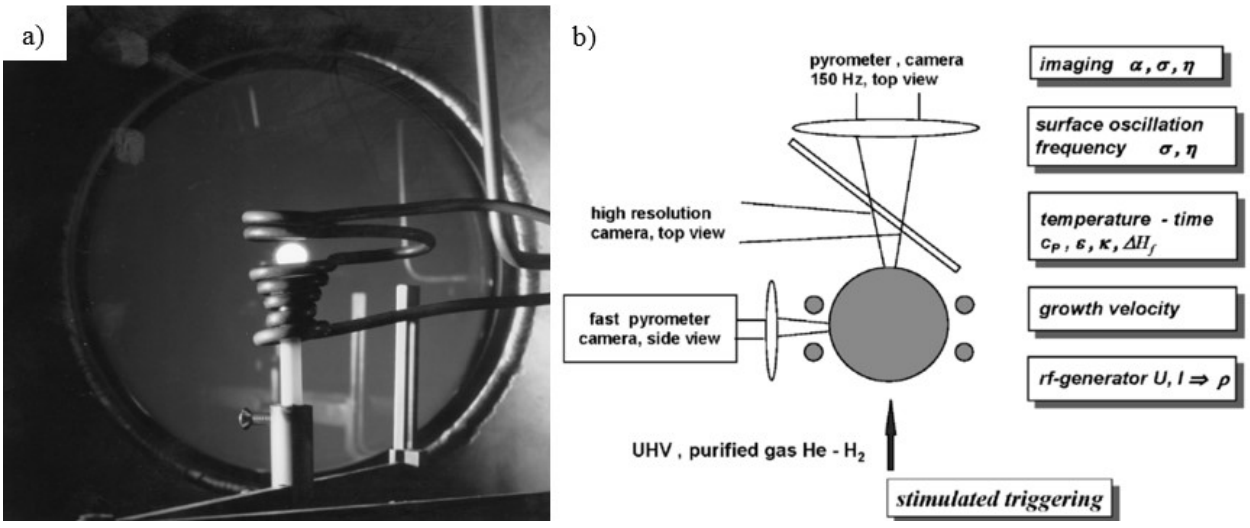

Figure 2.26: The levitated drop method shown by a) an image of a levitated specimen and b) a schematic of the method with analytical capabilities [135]

Table 2-1: Comparison of the characteristics of different levitation techniques [134]

Levitation technique	Material		Processing environment		Access to sample for diagnostics	Stability at high temperature	Comments
	Type	Size	High vacuum	Pressurized atmosphere			
Electrostatic	Conductor; semi-conductor; insulator	mm-size	Possible	Possible but pressure range limited by Paschen's rule	Excellent	Excellent	Rotation control; levitation and heating uncoupled; high speed feedback; complex system; costly; ISS operation to come soon
Electromagnetic	Conductor	cm-size	Possible	Possible	Fair	Good	Levitation initiation easy; large samples processed; levitation and heating coupled; somewhat complex; Sample deformation; rotation control difficult; inner flow; used on-board ISS
Acoustic	Conductor; semi-conductor; insulator	cm-size	Impossible	Possible	Good	Bad	Used on-based space shuttle; somewhat complex
Aerodynamic	Conductor; semi-conductor; insulator	mm-size	Impossible	Possible	Fair	Good	Simple system; inner flow; used during parabolic flights
Ultrasonic	Conductor; semi-conductor; insulator	cm-size	Impossible	Possible	Excellent	Good	Used on-based ISS; combustion experiments; complex system
Optical	Conductor; semi-conductor; insulator	Atoms to mm-size objects	Possible	Possible	Excellent	Excellent	Levitation and heating coupled Somewhat complex

An in depth description of how viscosity, surface tension and density are measured in metallic liquids will provided in this section. As well, a thorough analysis of the advantages and disadvantages of EML-LD.

2.4.2.1 Viscosity Measurement

The EML-LD method is now widely used for viscosity measurements of high melting point liquids. The method relies on the fact that the viscosity of the metallic liquid dampens the oscillations of the levitated drop. With the relationship between the viscosity and the damping constant, ζ (s^{-1}), the viscosity can be calculated using the following expression:

$$\zeta = \frac{20\pi r_o \eta}{3m} \tag{2.76}$$

Where r_o (m) is the radius and m (m) is the mass of the levitated drop. A pulse of power initiates the oscillations, and the oscillations are monitored with a video camera. Then, image analysis is used to measure the amplitude and decay time, as illustrated in Figure 2.27.

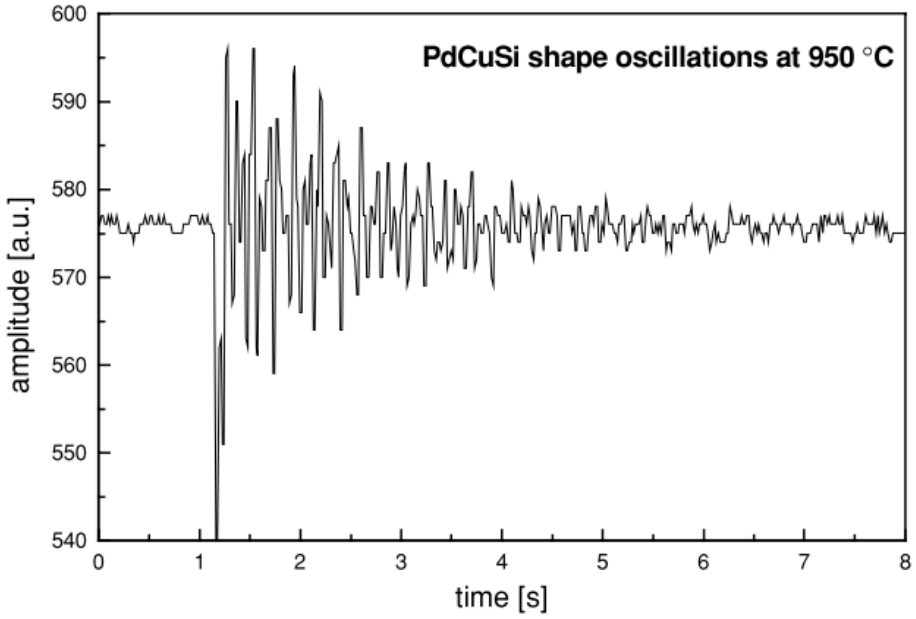

Figure 2.27: Example of damping of shape oscillations [22]

To apply the equation, the following conditions must be satisfied:

- The liquid drop must be spherical

- The oscillations must remain undisturbed for several cycles
- There must be no additional damping mechanisms

Often, these conditions are impossible to attain terrestrially (i.e. gravity deforms the sample), there are overlapping self-excited oscillations, and there is convection within the liquid drop induced by buoyancy-driven forces and/or the large electromagnetic forces that are required for terrestrial levitation. Thus, these experiments are often conducted under microgravity conditions, i.e. either parabolic flights or on the International Space Station (ISS) [22]. Another disadvantage includes the inaccuracies in noncontact temperature measurement when using a laser.

In the past decade, the LD method has been used to measure the viscosities of some 15 transition metals [21]. More recently, EML-LD has been conducted in microgravity conditions on Co-Pd and Pd-Cu-Si alloys on board the ISS [136], FeCr20Ni20 steel alloy on both a parabolic flight and on board the ISS [137], Ni-based superalloys on board a parabolic flight [138], high-Cr and Mn steels on board a parabolic flight [139], and Ni-Al catalytic precursor alloys on board a parabolic flight [140]

2.4.2.2 Surface Tension Measurement

EML-LD has also been widely used to measure the gas-liquid surface tension of levitated metallic liquids. The oscillations of the liquid drop, levitated in a high frequency magnetic field, are related to the surface tension though the Rayleigh's formula. If the radius, r (m), of the spherical drop undergoes oscillations of the form:

$$r = r_0\left(1 + \hat{A}\cos(ft)e^{-\zeta t}\right) \tag{2.77}$$

Where $\hat{A}$ (m) and f (Hz) are respectively the amplitude and frequency of the oscillation. The oscillation frequency is given by:

$$f^2 = \left(\frac{32\pi\sigma}{3m}\right) \tag{2.78}$$

Where σ (N/m) is the surface tension and m (kg) is the mass of the drop [136]. In practice, the levitated sample is melted and brought to a specified temperature, then the abovementioned form of oscillation is induced by superimposing a small sinusoidal electrical field on the levitation

magnetic field [21]. The influence of external electromagnetic and gravitational fields must be accounted for using an approximate correction factor; however, it is beneficial to conduct the experiments under microgravity, where the fields are negligibly small, so that Rayleigh's formula can be applied directly [136]. As previously mentioned, this method has an advantage of reducing contamination which often occurs through contact with substrates and/or capillary tubes when performing the sessile drop, the maximum bubble pressure, and the capillary ride methods. Consequently, as of recent time, the EML-LD method has become the standard for measuring the surface tension of metallic liquid, particularly high melting point metals and alloys [21].

Some recent surface-tension measurements made using EML-LD include, Au, Cu, Ni, Fe, [141], Fe-Ni and Ni-Co alloys [142], Cu-Co-Fe alloys [143], [144], Cu-Fe-Ni, Cu-Fe-Co, Cu-Co-Ni, Al-Cu-Ag alloys [145], Fe-O alloys [146], Fe-C alloys containing Si, Mn and S [147], low-alloyed carbon steel [148], 304 and 316 stainless steels [149], 430 stainless steel [150], and various other industrial high temperature alloys [135].

2.4.2.3 Density Measurement

The densities of levitated drops are typically measured using videography. In terrestrial experiments, the metallic samples are not perfectly spherical, but actually elongated by forces from both electromagnetic and gravitational fields. Nevertheless, the equilibrium shape remains rotationally symmetrical around the vertical axis (i.e. parallel to the gravity vector) thus, if images are taken perpendicular to the axis, the volume, V (m^3), of the sample can be calculated [145]. The sample is weighed before the experiment (i.e. the mass, m (kg) is known); therefore, density can be calculated from:

$$\rho = m/V \tag{2.79}$$

As opposed to direct images, shadowgraphs are obtained by illuminating the sample from behind using a monochromatic parallel laser light. This maintains a temperature-independent contrast. Moreover, potential asymmetrical surface oscillations are removed from analysis by taking multiple images (e.g. n = 1000) and averaging the edges of the sample. Also, the shape, or curvature, of the sample is fitted with a series of Legendre polynomials [118]. It has been reported that this procedure leads to less than 1% error in density measurements [145]. These experiments

can be performed on the ground, but microgravity conditions can improve the accuracy of the measurements [151]. A schematic of the experimental setup for EML-LD density measurements is shown in Figure 2.28.

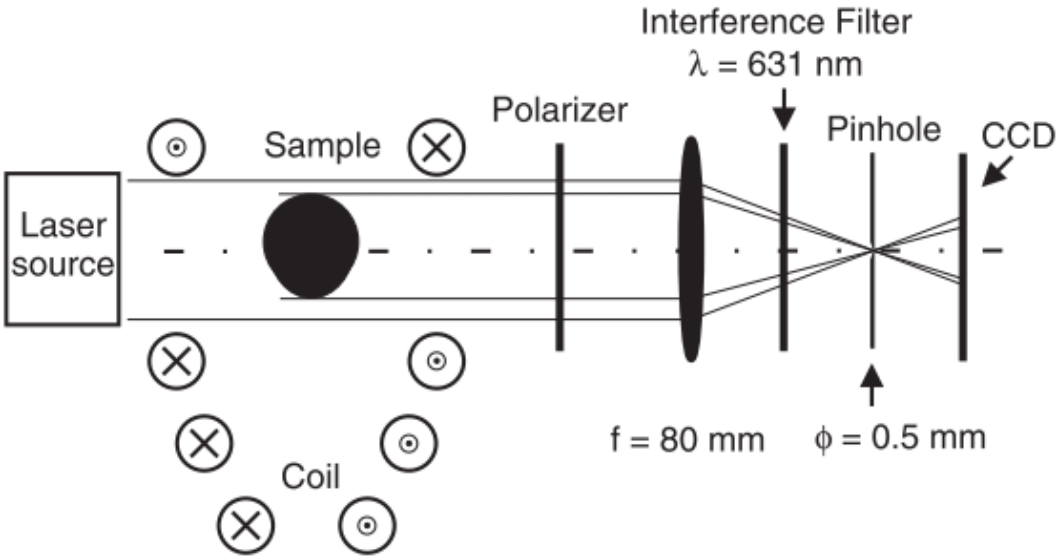

Figure 2.28: Schematic of electromagnetic levitated drop density measurements [101]

Density measurements have been recently carried using both ground-based experiments and experiments aboard the ISS. A multitude of pure liquid metals have been tested, including Cu, Ni, Fe, Ag, Al, Au, Co, Si [119], [145]; as well as various binary and ternary alloys, like Fe-Ni, Ag-Cu, Ag-Au, Al-Cu, Cr-Fe, Cr-Ni, Fe-Cu-Ni, Al-Cu, Cu-Co-Fe, Cu-Fe-Ni, Al-Cu-Ag, Co-Cu-Ni, Al-Cu-Si [101], [143], [152]–[158]. Further studies have been conducted on industrial alloys, such as a high-Cr steel alloy and a eutectoid Mn steel alloy [139]

2.4.2.4 Summary

EML-LD is a useful technique for containerless processing of metallic liquids. It provides a multitude of advantages compared to conventional thermophysical property measurement techniques. The biggest benefit, and most obvious, is that it eliminates any source of contamination which would arise using a substrate, capillary, crucible, etc. For extremely reactive metals (like Ti or Zr) it is in fact the only suitable option for property measurement [32]. Also, the electromagnetic inductive stirring within the sample ensures that the sample surface is continually being refreshed, reducing surface contamination [159]. Another significant advantage is that, due

to the absence of heterogeneous nucleation sites, deep undercoolings are possible [151]. Thus, LD can measure the thermophysical properties of high melting point metallic liquids, over a wide range of temperatures, including undercooled temperatures. Other advantages of EML-LD include intrinsic sample stability (i.e. magnetic field restores deviations of sample to equilibrium position), coupled inductive heating, temperature and composition homogeneity caused by internal fluid flow, and the ability to simultaneously measure surface tension, viscosity and density, plus other properties [160].

One major disadvantage, previously mentioned, is that it is impossible to accurately measure viscosity terrestrially. The presence of the gravitation field on earth distorts the sample sphericity, and thus, the shape oscillations, which makes quantitative analysis challenging. This is illustrated in Figure 2.29 by the splitting of a single frequency into five peaks combined with a shift to higher frequencies occurring terrestrially when conducting EML-LD experiments on an Au-Cu alloy [161]. The splitting of the frequency peak can be explained by the deformation of the droplet caused by the effects of a large electromagnetic field. The increase in oscillation frequencies occurs because the magnetic field and eddy currents which cause levitation act as pressure on the surface of the liquid drop, consequently increasing the surface tension value [162].

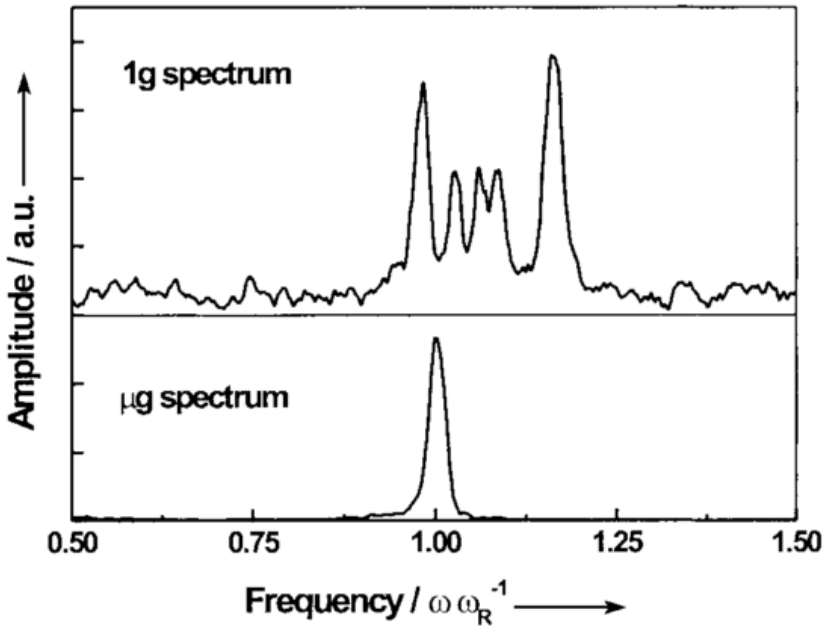

Figure 2.29: Oscillation spectrum of a liquid drop levitated on Earth (top) and in microgravity (bottom) [161]

Additionally, terrestrial EML thermophysical property measurements are further influenced by internal fluid flow caused by buoyancy and or positioning forces. For example, internal turbulent flow can excite surface oscillations, which can actually improve surface tension measurements. At the same time, these excitations might result in abnormally large amplitudes resulting in non-linear effects, reducing the overall precision of the measurement [163]. More importantly, fluid flow within the levitated drops will prevent the observation of decreasing oscillating amplitude, or oscillation dampening. Consequently, EML-LD viscosity measurements are impossible to perform on Earth [163]. It is possible to eliminate or reduce these issues by conducting experiments in microgravity; however, it is extremely costly, amongst other challenges, to conduct experiment on the ISS or using parabolic flights.

Another issue with EML-LD is evaporation of volatile elements, and ultimately, mass loss and compositional changes during measurements. Generally, "the mass loss that is encountered during evaporation is determined by three factors: the partial vapor pressure of an element, its transport to the surface, and the ratio of the surface area to the bulk volume" [164]. EML proves to contribute to several of these factors. In EML-LD measurements, the ratio of the droplet surface area to bulk volume is large, compared to conventional container measurement techniques. Also, as previously discussed, EML promotes internal convection, or stirring, which increases the rate at which the volatile elements are transported to the surface. At high temperatures, some metals have a high vapor pressure leading to a shift in the sample composition [165]. Recall that as the temperature of a liquid increases, the kinetic energy of its molecules also increases, which increases the number of molecules transitioning into a vapor, thereby increasing the vapor pressure. Materials with high vapor pressure are referred to as volatile. There are several cases of observed Al mass loss (or volatization) during EML processing at temperature above 1200 K. The evaporation of Al_2O_3 of course has an impact on composition and the measure properties [166] [153] [167]. Furthermore, there are also issues with evaporation where it has been observed that the flux condenses on the colder pyrometer window. This leads to decreases in radiation intensity reaching the pyrometer sensors, resulting in an erroneous decrease in measured temperature [166].

2.4.3 Discharge Crucible Method

The discharge crucible (DC) method, developed by Roach and Henein [7] at the University of Alberta, is a ground-based technique able to simultaneously measure the surface tension,

viscosity and density of metallic liquids in a simple, robust and cost-effective manner. A simple schematic of the method is shown in Figure 2.30.

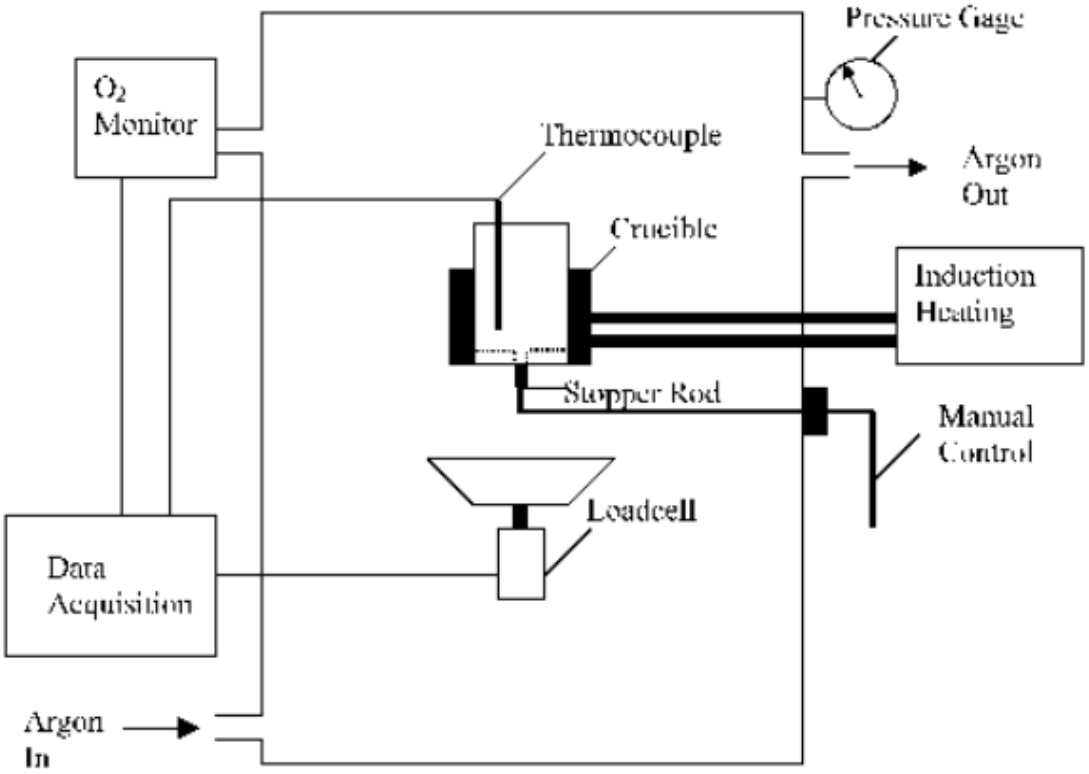

Figure 2.30: Schematic of the experimental discharge crucible apparatus [7]

The DC method is based on a new formulation which describes the fluid dynamics of a liquid draining through an orifice under the influence of gravity. This formulation differs from the classical formulation (i.e. Bernoulli equation) as it includes surface tension effects induced by Laplace pressure at the exit of the orifice. The model relates experimental values of head height and mass flow rate, with surface tension, viscosity, and density; and simultaneously calculates the unknown thermophysical properties using the Gauss-Newton algorithm. The following sections will describe aspects of the theoretical formulation, the computational process, and finally, a summary of published results obtained with the DC method.

2.4.3.1 Formulation

The Bernoulli formulation can be used to quantify the potential, kinetic and viscous forces of a fluid draining under the influence of gravity through an orifice; and results in a function that relates the flow rate, Q (m^3/s), with the head above the orifice discharge, h (m), as illustrated in Figure 2.31. It is assumed that a free jet will form when the vessel is filled with a fluid. This section will review two models, as originally described by Roach and Henein [7]: first model describing the flow without considering the effects of surface tension, and a second model which accounts for surface tension at the exit of the orifice,

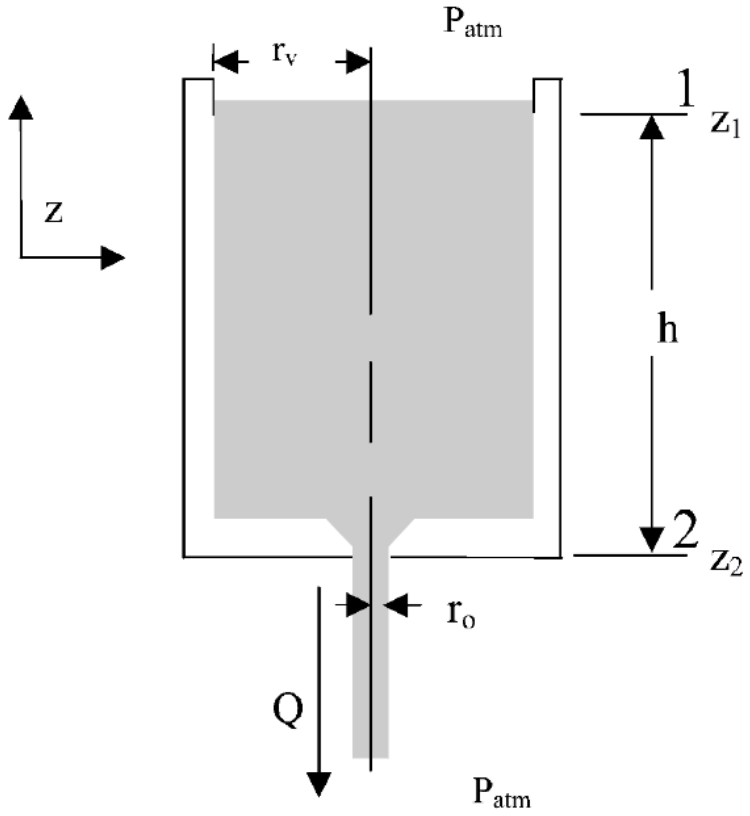

Figure 2.31: Schematic of draining vessel system depicting flow rate of a fluid through an orifice place at the bottom [7]

2.4.3.1.1 Classical Formulation: Bernoulli Equation Neglecting Surface Tension

Daugherty *et al.* [168] derived the Bernoulli equation for unsteady flow (i.e. velocity as a function of both position and time) along a streamline, which describes the conservation of energy of a small cylindrical element, as illustrated in Figure 2.32.

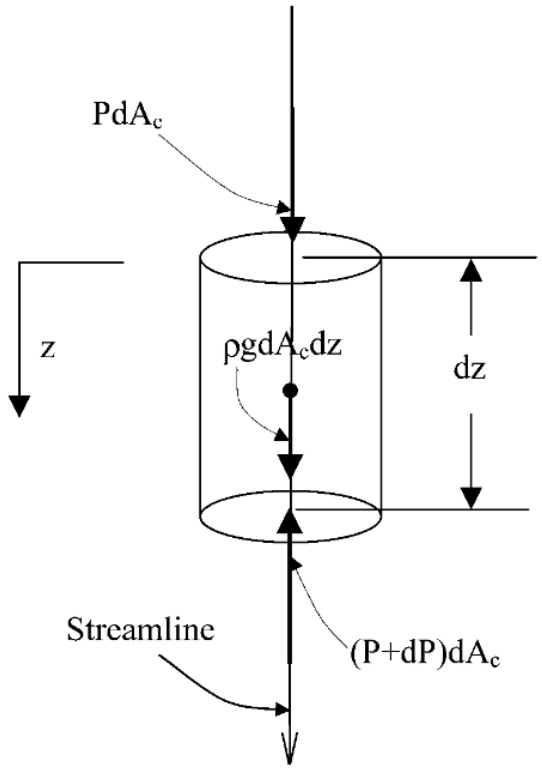

Figure 2.32: Control element of streamline neglecting frictional losses [168]

The following equation accounts for pressure forces ($-dPdA_c$), the weight ($\rho g dA_c dz$) and the change in momentum, i.e. mass multiplied by acceleration ($m\left(u\frac{\partial u}{\partial z}+\frac{\partial u}{\partial t}\right)$) of the cylindrical element:

$$-dPdA_c + \rho g dA_c dz = m\left(u\frac{\partial u}{\partial z}+\frac{\partial u}{\partial t}\right) \tag{2.80}$$

Where, P (Pa) is the pressure exerted at the inlet of the element, dP (Pa) is the change in pressure across the element, dA_c (m^2) is the cross sectional area of the element, ρ (kg/m^3) is the density of the element, g (m/s^2) is the gravitational acceleration, m (kg) is the mass of the element, and u (m/s) is the velocity of the element. The mass of the element can be expressed $m = \rho dA_c dz$, therefore, Equation 2.80 can be written as:

$$-dPdA_c + \rho g dA_c dz = \rho g dA_c dz\left(u\frac{\partial u}{\partial z}+\frac{\partial u}{\partial t}\right) \tag{2.81}$$

Then, by dividing Equation 2.81 by $-\rho dA_c$, rearranging the terms, and integrating between the limit points of 1 and 2, shown on Figure 2.31, yields:

$$\frac{(P_2 - P_1)}{\rho} - g(z_2 - z_1) + \frac{(u_2^2 - u_1^2)}{2} = -(z_2 - z_1)\left(\frac{\partial u}{\partial t}\right) \tag{2.82}$$

Where P_1 and P_2 (Pa) are the pressures exerted on the fluid at reference points 1 and 2, u_1 and u_2 are the velocities (m/s) of fluid at reference points 1 and 2, and $(z_2 - z_1)$ refers to the head of the fluid above the exit of the orifice, h (m). Note that the term $\partial u/\partial t$ is considered constant because the relationship between velocity and time at reference points 1 and 2 are essentially linear. This linear assumption was proven experimentally by Roach [77] using water at room temperature and is shown in Figure 2.33.

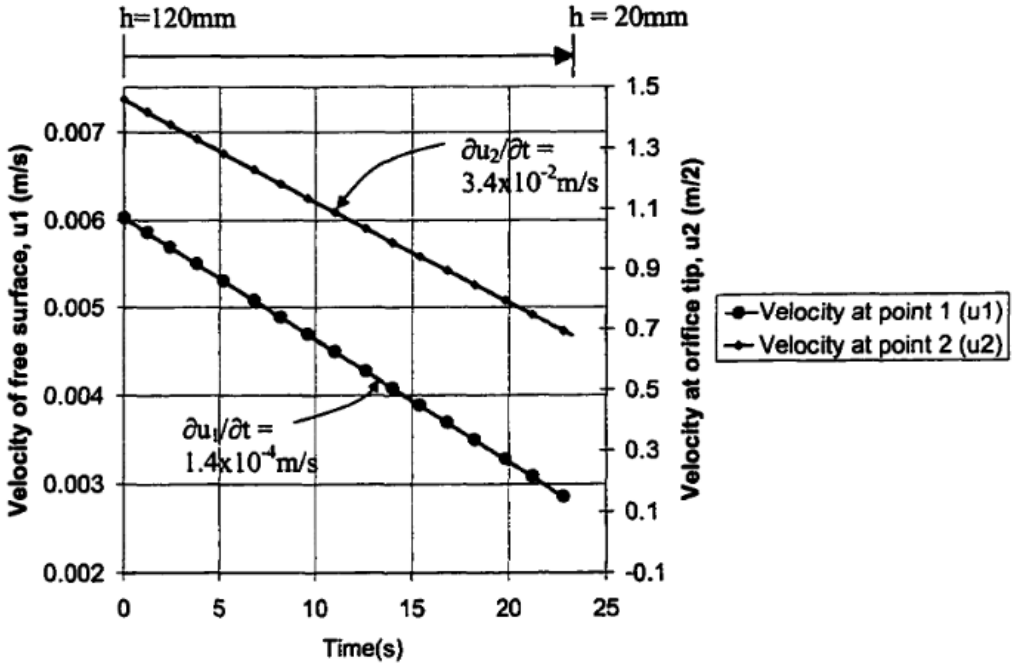

Figure 2.33: Velocity of reference point 1 and 2 as a function of time [77]

The above equation only describes the energy or force balance for inviscid flow. The viscosity effects, or frictional effects, will be included later through the addition of the discharge coefficient, C_d. Using the continuity equation, the velocity and reference point 1 can be expressed as $u_1 = (r_o^2/r_v^2)u_2$, and since $r_v >> r_o$, rearranging the terms of the velocity at reference point 2, Equation 2.77 can be written as:

$$u_2 = \sqrt{2g\left(h - \frac{(P_2 - P_1)}{\rho g} - \frac{h}{g}\left(\frac{\partial u}{\partial t}\right)\right)} \tag{2.83}$$

The accelerative head term, $\frac{h}{g}\left(\frac{\partial u}{\partial t}\right)$, within the vessel is neglected in the formulation. This assumption is validated later in this section. It is also assumed that there is no pressure difference between reference points 1 and 2, i.e. atmospheric pressure at the top free surface and bottom orifice tip, Equation 2.78 becomes:

$$u_2 = \sqrt{2gh} \tag{2.84}$$

Because friction is neglected in the formulation, u_2 is considered the theoretical maximum velocity of the stream at the exit of the orifice, and therefore, the maximum theoretical flow rate, Q_{theo} (m^3/s) , can be written as:

$$Q_{theo} = \pi r_o^2 \sqrt{2gh} \tag{2.85}$$

Now, C_d is used to characterize the frictional flow losses in the orifice, and can be defined as the ratio between the experimental flow rate, Q_{exp}, and Q_{theo}:

$$C_d = \frac{Q_{exp}}{\pi r_o^2 \sqrt{2gh}} \tag{2.86}$$

The precise value of C_d, or the frictional characteristics, depends on the specific geometry of the vessel used, and must always be less than 1. Many experiments have shown that C_d, depends only on the Reynolds number, Re [168]. Re is defined as:

$$Re = \frac{2\rho Q_{exp}}{\pi r_o^2 \eta} \tag{2.87}$$

Where ρ and η are the density and viscosity of the fluid, respectively. The assumptions made in this classical formulation include [77]:

1) The flow is quasi-steady state, i.e. the accelerative terms are neglected.
2) Viscous dissipation is neglected, i.e. loss of frictional energy when fluid is sheared.

3) The velocity at reference point 1, u_1, is much less than u_2.
4) The velocity profile at the orifice exit is flat.
5) The pressure at the inlet and outlet is at atmospheric pressure.

To validate the first assumption, an analysis of C_d and Re was conducted by comparing the formulation with quasi-steady state and unsteady state criteria [77]. If the accelerative head term, $\frac{h}{g}\left(\frac{\partial u}{\partial t}\right)$, is included in the formulation, and is considered within the vessel and orifice separately, the velocity at point 2 can be expressed as:

$$u_2 = \sqrt{2g\left(h - \frac{(P_2 - P_1)}{\rho g} - \frac{(h - z_o)}{g}\left(\frac{\partial u_1}{\partial t}\right) - \frac{(z_o)}{g}\left(\frac{\partial u_2}{\partial t}\right)\right)} \tag{2.88}$$

Where z_o (m) is the height of the orifice plate. This equation assumes that there is an instantaneous change in velocity from u_1 to u_2 at the entrance of the orifice. With this, the frictional characteristics of the vessel and orifice considering unsteady flow can be determined by calculating C_d:

$$C_d = \frac{Q_{exp}}{\pi r_o^2 \sqrt{2g\left(h - \frac{(P_2 - P_1)}{\rho g} - \frac{(h - z_o)}{g}\left(\frac{\partial u_1}{\partial t}\right) - \frac{(z_o)}{g}\left(\frac{\partial u_2}{\partial t}\right)\right)}} \tag{2.89}$$

The terms $\frac{\partial u_1}{\partial t}$ and $\frac{\partial u_2}{\partial t}$ were taken from Figure 2.1 using water at room temperature. With the same experimental data obtained by Roach [77], C_d was calculated using both Equation 2.81 and Equation 2.84, and plotted versus Re, as shown in Figure 2.36. The quasi-steady state assumption is valid since there is no difference in frictional characteristics when the accelerative head term is included in the formulation. Note that Figure 2.36 illustrates the relationship between C_d and Re when both neglecting and considering the effects of surface tension; these effects will be discussed in more detail in Section 2.4.3.1.2.

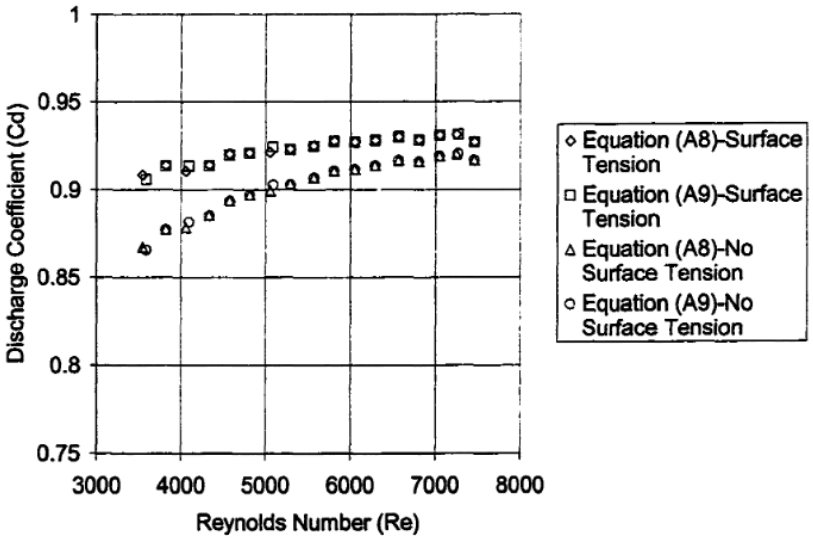

Figure 2.34: C_d versus Re curves neglecting and considering surface tension effects [77]

Using the classical Bernoulli formulation, Roach and Henein [7] conducted four separate experiments using the same experimental set-up to calculate the C_d versus Re of water and ethylene glycol at various temperatures. The results are plotted on Figure 2.35.

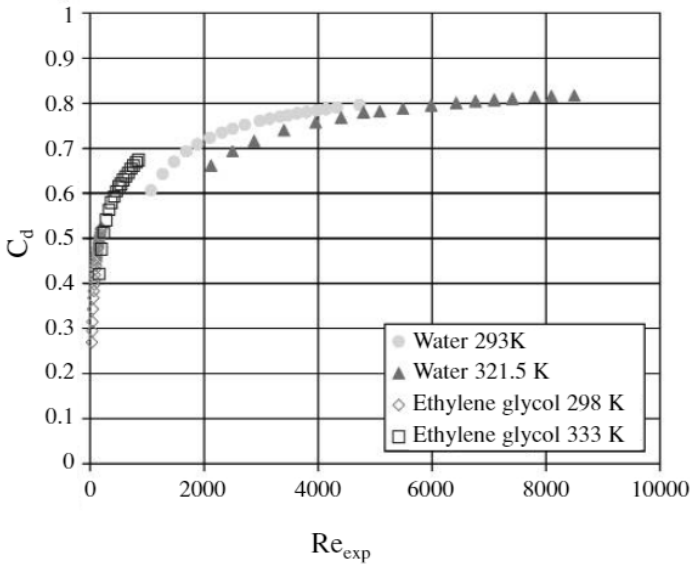

Figure 2.35: C_d versus Re for different liquids; surface tension not included in analysis [7]

The trend depicted in Figure 2.35 indicates that there are varying observed frictional characteristics when testing fluids with varying properties. Note that the properties of the fluids change at different temperatures. In theory, the individual curves should overlap, since the

relationship between C_d and Re is assumed to depend solely on the geometry of the vessel. Thus, it was concluded that there was an error in either the analysis, or the assumptions made in the initial formulation [7]. This was investigated further, and a new modified formulation is described in the following section.

2.4.3.1.2 Modified Formulation

To account for the discontinuity of the C_d versus Re curves presented in Figure 2.37, Roach and Henein speculated that there could be pressure induced at the outlet of the orifice cause by some interfacial phenomena [7]. As described in Section 2.2., pressure is exerted by surface tension, σ (N/m), at a curved interface separating a liquid from a gas, as quantified by the Laplace equation (Equation 2.54). In the case of the DC method, at the orifice tip (i.e. reference point 2), the liquid stream is assumed to be a perfect cylinder, thus, resulting in an induced pressure of the form:

$$P_2 = \frac{\sigma}{r_0} \tag{2.90}$$

By including the added pressure at the orifice tip into Equation 2.84, and assuming quasi-steady state conditions, the modified Bernoulli equation can be written as follows:

$$u_2 = \sqrt{2g\left(h - \frac{\sigma}{\rho g r_o}\right)} \tag{2.91}$$

Which can be expressed in terms of maximum theoretical flow rate:

$$Q_{theo} = \pi r_o^2 \sqrt{2g\left(h - \frac{\sigma}{\rho g r_o}\right)} \tag{2.92}$$

At which point, C_d can be calculated as:

$$C_d = \frac{Q_{exp}}{\pi r_o^2 \sqrt{2g\left(h - \frac{\sigma}{\rho g r_o}\right)}} \tag{2.93}$$

Using the same experimental data obtained for ethylene glycol and water at varying temperature from Section 2.4.3.1.1, C_d versus Re values were calculated using Equations 2.93 and 2.82, respectively. The values were plotted and are shown in Figure 2.36, and the C_d values appear to demonstrate a continuous dependence on the Re.

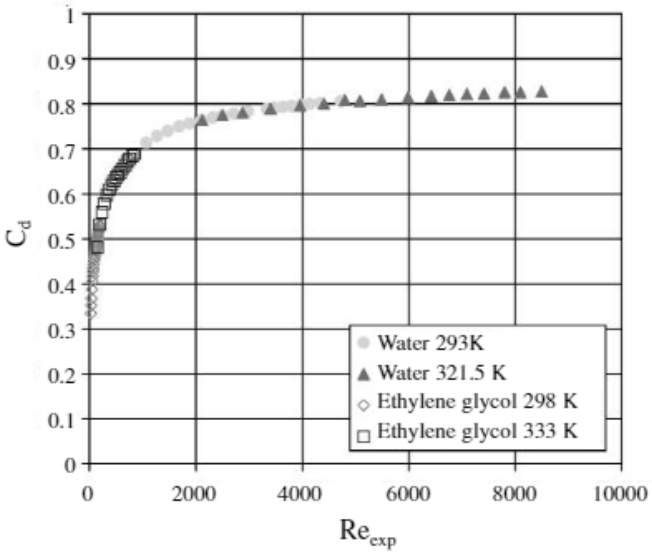

Figure 2.36: C_d versus Re calculated using the modified Bernoulli equation on water and ethylene glycol [7]

These results indicate that surface tension should be included in the Bernoulli formulation when quantifying the forces prevalent under the specific experimental conditions of the DC method.

2.4.3.2 Dimensionless Formulation

The equations presented in Section 2.4.3.1.2. can be generalized and written in dimensionless form. These dimensionless numbers can be insightful when designing an apparatus for high temperature fluids, or in identifying when the new formulation should be applied (i.e. considering surface tension effects) versus the classical formulation [7] .

Equation 2.93 can be written in dimensionless form so that:

$$\frac{\left(Q_{exp}/C_d \pi r_o^2\right)^2}{2gh} = 1 - \frac{\sigma}{\rho g r_o h} \tag{2.94}$$

Or,

$$\frac{u_{theo}^2}{2gh} + \frac{\sigma}{\rho g r_o h} = Fr + {}^{1}/_{Bo} = 1 \tag{2.95}$$

Where the Bond number, Bo, and the Froude number, Fr, are defined as:

$$Fr = \frac{u_{theo}^2}{2gh} = \frac{\left({}^{Q_{exp}}/_{C_d \pi r_o^2}\right)^2}{2gh} = \frac{\text{inertial forces}}{\text{potential forces}} \tag{2.96}$$

$$Bo = \frac{\rho g r_o h}{\sigma} = \frac{\text{potential forces}}{\text{surface forces}} \tag{2.97}$$

Upon inspection of Equation 2.95, since the sum of the $1/Bo$ and Fr numbers must equal to one, when the $1/Bo$ number increases, the Fr number must decrease. A small Bo number indicates that surface energy plays a big role in the system. Thus, the following criterion were proposed:

- As $1/Bo \rightarrow 0$ for a particular system, or $Fr \rightarrow 1$, flow rate and frictional characteristics can be approximated using the classical formulation outlined in Section 2.4.1.1.
- When $1/Bo \rightarrow 1$, or $Fr \rightarrow 0$, surface tension effects must be considered, as outlined by the modified formulation in Section 2.4.1.2.
- When $1/Bo \rightarrow > 1$, or $Fr < 0$, continuous flow has stopped and a different formulation must be used, i.e. dripping by capillary action [77].

This analysis proves useful when deciding to account for surface tension in the Bernoulli equation to calculate flow rate and frictional characteristics for DC measurements. Metallic liquids with a relatively high surface tension to density ratio (e.g. Al) exhibit a large $1/Bo$, indicating that the modified formulation should be used when calculating properties using the DC method, as illustrated in Figure 2.37.

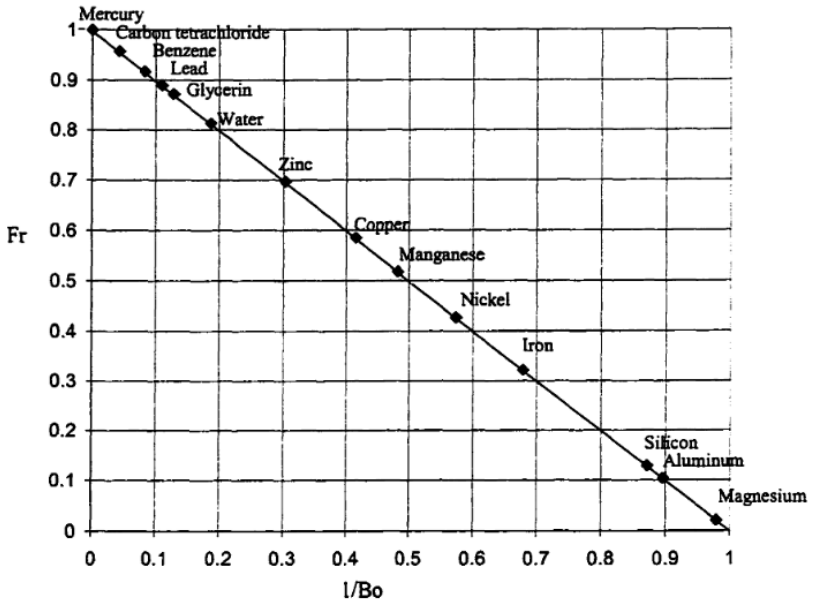

Figure 2.37: Fr versus 1/Bo for various liquids for a head and orifice radius of 0.01 m and 0.004 m respectively [77]

Furthermore, for design considerations, the dimensionless formulation can be useful when determining the radius of the orifice and minimum head of the experiments. If the radius of the orifice or the head are too large, the $1/Bo$ will approach zero, and the DC method should not be used to calculate surface tension (i.e. the classical formulation is valid). Contrarily, if the radius of the orifice or head are too small, the surface tension forces will exceed the potential forces, which will result in dripping. There is an obvious balance that should be accounted for during the design phase. Furthermore, by taking the ratio of Equation 2.91 and 2.84, the following equation can be useful with design:

$$\frac{u_{theo,\sigma}}{u_{theo,no\ \sigma}} = \frac{\sqrt{2g\left(h - \frac{\sigma}{\rho g r_o}\right)}}{\sqrt{2gh}} = \sqrt{1 - {}^{1}/_{Bo}} \tag{2.98}$$

Where $u_{theo,\sigma}$ and $u_{theo,no\ \sigma}$ are the velocities when considering surface tension and neglecting surface tension, respectively. So, when the Equation 2.98 approaches unity, surface tension should be neglected from the formulation [7]. However, to simultaneously solve surface tension, viscosity and density of a metallic liquid, it is important that surface tension is included in the

formulation; thus, Equation 2.98 can be used to design the orifice and height of the crucible so that favorable conditions are attained.

2.4.3.3 Computation

This section outlines the formulation of the model that simultaneously calculates surface tension, viscosity and density using a nonlinear regression analysis. First, the Gauss-Newton method to solve nonlinear least-squares problems will be described. Given m functions r = (r_1, …, r_m), which are called residuals, of n variables $\beta = (\beta_1, \dots, \beta_n)$, and if $m > n$, the Gauss-Newton algorithm iteratively finds the value of the variables that minimizes the sum of squares [169]:

$$\|r(\beta)\|^2 = \sum_{i=1}^{m} r_i^2(\beta) \tag{2.99}$$

In data fitting, the goal is to find variables β so that the model function $y = f(x_i, \beta)$ best fits some data points $(x_i y_i)$ therefore, $r_i(\beta)$is written as:

$$r_i(\beta) = y_i - f(x_i, \beta) \tag{2.100}$$

The method itself starts with an initial guess $\beta^{(0)}$, and then the variables are refined iteratively:

$$\beta \approx \beta^{(s+1)} = \beta^{(s)} + \Delta\beta \tag{2.101}$$

Where *s* is the iteration number, and $\Delta\beta$ is known as the shift vector. The residuals $r_i(\beta)$ are linearized near the current iterate $\beta^{(s)}$ using a first-order Taylor series expansion:

$$r_i\left(\beta^{(s+1)}\right) \approx \Delta y_i\left(\beta^{(s)}\right) + \sum_{j=1}^{n} J_{ij}\left(\beta^{(s)}\right) \cdot \left(\Delta\beta_j\right) \tag{2.102}$$

Where J_{ij}, the Jacobian matrix, and $\Delta y_i\left(\beta^{(s)}\right)$ are expressed as:

$$\Delta y_i\left(\beta^{(s)}\right) = y_i - f\left(x_i, \beta^{(s)}\right) \tag{2.103}$$

$$J_{i,j} = \frac{\partial r_i(\beta)}{\partial \beta_j} \tag{2.104}$$

Now, the nonlinear least-squares problem has been locally approximated to a linear least-squares problem, i.e. $r = Ax - y$. Thus, by applying the linear least-squares theory, the solution can be expressed by:

$$\Delta \boldsymbol{\beta}_j = \left(\boldsymbol{J_{i.j}}^T \boldsymbol{J}_{i.j}\right)^{-1} \boldsymbol{J_{i.j}}^T \Delta \boldsymbol{y_i} \tag{2.105}$$

The variables β are then updated, and iterations are repeated until convergence or it becomes unstable. There are several advantages to using the Gauss-Newton algorithm as an optimization method. For instance, it is not required to calculate the second-order derivatives. Also, for moderately-sized problems and when the model fits the data well, Gauss-Newton converges relatively quickly. However, it might not converge on problems that are very nonlinear or have large residuals. It also requires a good initial guess. Now, to set up the Gauss-Newton algorithm for the DC model, the residuals $r_i(\beta)$, for i =1 to m, and variables β, will be defined as:

$$r_i(\beta) = h_{i,exp} - f\left(Q_{i,exp}, \beta\right) \tag{2.106}$$

$$\beta = \begin{bmatrix} \sigma \\ \eta \\ \rho \end{bmatrix} \tag{2.107}$$

Where $h_{i,exp}$ is experimental head, $Q_{i,exp}$ is experimental volumetric flow rate, and are expressed in vector notation:

$$h_{exp} = \begin{bmatrix} h_{1,exp} \\ \cdot \\ \cdot \\ h_{i,exp} \\ h_{m,exp} \end{bmatrix} \tag{2.108}$$

$$Q_{exp} = \begin{bmatrix} Q_{1,exp} \\ \cdot \\ \cdot \\ Q_{i,exp} \\ Q_{m,exp} \end{bmatrix} \tag{2.109}$$

By rearranging Equation 2.93, the modified Bernoulli equation can be expressed as:

$$f(Q_{i,exp},\beta) = \frac{1}{2g}\left(\frac{Q_{i,exp}}{C_d \pi r_o^2}\right) + \frac{\sigma}{\rho g r_o} \tag{2.110}$$

A calibration of C_d versus Re of a specific orificed vessel can be obtained using liquids of known physical properties and applying Equations 2.87 and 2.93. Often water is used, which yields a function of the form:

$$C_d = a(Re)^3 + b(Re)^2 + c(Re) + d \tag{2.111}$$

Note that higher order polynomial curve fitting was implemented, but it was determined that precision was not improved [16]. By substituting Equation 2.111 into Equation 2.110, $h_{i,exp}$ can be written as:

$$f(Q_{i,exp},\beta) = \frac{1}{2g}\left(\frac{Q_{i,exp}}{(a(Re)^3 + b(Re)^2 + c(Re) + d)\pi r_o^2}\right) + \frac{\sigma}{\rho g r_o} \tag{2.112}$$

Which, when considering Equation 2.87, yields:

$$f(Q_{i,exp},\beta) = \frac{1}{2g}\left(\frac{Q_{i,exp}}{\left(a\left(\frac{2\rho r_o Q_{i,exp}}{\pi r_o^2 \eta}\right)^3 + b\left(\frac{2\rho r_o Q_{i,exp}}{\pi r_o^2 \eta}\right)^2 + c\left(\frac{2\rho r_o Q_{i,exp}}{\pi r_o^2 \eta}\right) + d\right)\pi r_o^2}\right)^2 + \frac{\sigma}{\rho g r_o} \tag{2.113}$$

The experimental flow rate, $Q_{i,exp}$, is a volumetric quantity that is determined from the dividing the mass flow rate data by the density of the liquid. Since density is an unknown variable, mass flux, $V_{i,exp}$, with units kg/m^{2}s, is introduced to replace $Q_{i,exp}$:

$$V_{i,exp} = \frac{\rho Q_{i,exp}}{\pi r_o^2} \tag{2.114}$$

Now, the residuals, $r_i(\beta)$,can be defined as:

$$r_i(\beta) = h_{i,exp} - f\left(V_{i,exp}, \beta\right) \tag{2.115}$$

And, Equation 2.113 can be expressed by:

$$f\left(V_{i,exp}, \beta\right) = \frac{1}{2g}\left(\frac{V_{i,exp}}{\left(a\left(\frac{2\rho r_o V_{i,exp}}{\pi r_o^2 \eta}\right)^3 + b\left(\frac{2\rho r_o V_{i,exp}}{\pi r_o^2 \eta}\right)^2 + c(\frac{2\rho r_o V_{i,exp}}{\pi r_o^2 \eta}) + d\right)\rho}\right)^2 + \frac{\sigma}{\rho g r_o} \tag{2.116}$$

In applying the Taylor series approximation, as described earlier, the Gauss-Newton equation can be set up as follows:

$$\Delta\boldsymbol{\beta}_{\boldsymbol{j}} = \left(\boldsymbol{J_{i,j}}^T \boldsymbol{J}_{\boldsymbol{i,j}}\right)^{-1} \boldsymbol{J_{i,j}}^T \Delta\boldsymbol{y_i} \tag{2.117}$$

Where,

$$\Delta\boldsymbol{\beta}_{\boldsymbol{j}} = \begin{bmatrix} \sigma^{(j+1)} - \sigma^{(j)} \\ \eta^{(j+1)} - \eta^{(j)} \\ \rho^{(j+1)} - \rho^{(j)} \end{bmatrix} \tag{2.118}$$

$$\boldsymbol{J}_{\boldsymbol{i,j}} = \begin{Bmatrix} \frac{\partial f\left(V_{1,exp}\right)}{\partial\sigma} & \frac{\partial f\left(V_{1,exp}\right)}{\partial\eta} & \frac{\partial f\left(V_{1,exp}\right)}{\partial\rho} \\ \vdots & \vdots & \vdots \\ \frac{\partial f\left(V_{i,exp}\right)}{\partial\sigma} & \frac{\partial f\left(V_{i,exp}\right)}{\partial\eta} & \frac{\partial f\left(V_{i,exp}\right)}{\partial\rho} \\ \frac{\partial f\left(V_{m,exp}\right)}{\partial\sigma} & \frac{\partial f\left(V_{m,exp}\right)}{\partial\eta} & \frac{\partial f\left(V_{m,exp}\right)}{\partial\rho} \end{Bmatrix}_j \tag{2.119}$$

$$\Delta\boldsymbol{y}_{\boldsymbol{i}} = \begin{bmatrix} h_{1,exp} - f\left(V_{1,exp}, \beta^s\right) \\ \vdots \\ h_{i,exp} - f\left(V_{i,exp}, \beta^s\right) \\ h_{m,exp} - f\left(V_{m,exp}, \beta^s\right) \end{bmatrix}_j \tag{2.120}$$

The partial derivatives of Equation 2.116, for substitution into Equation 2.119, with respect to σ, η and ρ are:

$$\frac{\partial f(V_{i,exp})}{\partial \sigma} = \frac{1}{\rho g r_o} \tag{2.121}$$

$$\frac{\partial f(V_{i,exp})}{\partial \eta} = \frac{V_{i,exp}^2}{\rho^2 g}\left(\frac{1}{\left(a\left(\frac{2r_oV_{i,exp}}{\eta}\right)^3 + b\left(\frac{2r_oV_{i,exp}}{\eta}\right)^2 + c\left(\frac{2r_oV_{i,exp}}{\eta}\right) + d\right)}\right)^3 \left(\frac{24a\left(r_oV_{i,exp}\right)^3}{\eta^4} + \frac{8b\left(r_oV_{i,exp}\right)^2}{\eta^3} + \frac{2c\left(r_oV_{i,exp}\right)}{\eta^2}\right) \tag{2.122}$$

$$\frac{\partial f(V_{i,exp})}{\partial \rho} = -\frac{1}{\rho^3 g}\left(\frac{V_{i,exp}}{\left(a\left(\frac{2r_oV_{i,exp}}{\eta}\right)^3 + b\left(\frac{2r_oV_{i,exp}}{\eta}\right)^2 + c\left(\frac{2r_oV_{i,exp}}{\eta}\right) + d\right)}\right)^2 - \frac{\sigma}{\rho^2 g r_o} \tag{2.123}$$

Recall that the iterations begin at $j = 0$, and initial guesses are made for $\sigma^{(0)}$, $\eta^{(0)}$ and $\rho^{(0)}$. The updated values are then calculated after each iteration:

$$\sigma^{(j+1)} = \sigma^{(j)} + \Delta\beta_1 \tag{2.124}$$

$$\eta^{(j+1)} = \eta^{(j)} + \Delta\beta_2 \tag{2.125}$$

$$\rho^{(j+1)} = \rho^{(j)} + \Delta\beta_3 \tag{2.126}$$

This entire process is repeated until convergence is attained, or when the following quantities are less than the specified tolerance, ε:

$$\varepsilon_{\sigma} = \frac{\sigma^{(j+1)} - \sigma^{(j)}}{\sigma^{(j+1)}} \tag{2.127}$$

$$\varepsilon_{\eta} = \frac{\eta^{(j+1)} - \eta^{(j)}}{\eta^{(j+1)}} \tag{2.128}$$

$$\varepsilon_{\rho} = \frac{\rho^{(j+1)} - \rho^{(j)}}{\rho^{(j+1)}} \tag{2.129}$$

When all three properties meet the convergence criteria, the regression ends, and the thermophysical properties of the liquid are given by $\sigma^{(j+1)}$, $\eta^{(j+1)}$ and $\rho^{(j+1)}$.

2.4.3.4 Summary

The DC method has been used to successfully measure the surface tension, viscosity and density of various pure low and high melting temperature liquids, like water, ethylene glycol, Al, Pb, Sb, Ga, and Zn [8]–[11]. It has also been used to determine the thermophysical properties of various alloys, such as Al-Mg, Al-Zn, Al-Mg-Zn, Sb-Sn-Zn, Sb-Sn, Ga-Zn, Ga-Sn, Ga-Sn-Zn and Pb-Sb [8], [9], [12]–[14]. There was initial skepticism with regards to low reported viscosity value (e.g. approximately 50% lower than values obtained in literature) for measurements on pure liquid Al, however, this was later attributed to high O content in the atmosphere [10]. A recent study repeated the experiments on Al, and reported viscosity values that aligned much closer to literature values [8].

As it stands, the DC method is one of few measurement techniques able to simultaneously measure the surface tension, viscosity, and density of metallic liquids; and, it is a relatively inexpensive technique compared to EML-LD, which requires microgravity conditions. It is also economical because of the simple design (e.g. there are no optical measurements required). There is a statistical advantage to using DC over other methods because a substantial quantity of data (i.e. experimental head and flow rate) is used to calculate the properties. Also, unlike conventional methods, the dynamic nature of the experiment produces an interface that is rapidly replenished, and thus, should in theory more closely reflect pure dynamic surface tension with minimal O contamination.

2.5 Thermophysical Property Studies on Selected Metallic Liquids

This section will review prior experiments conducted on the measurement of the surface tension, viscosity and density of pure liquid Al and liquid Al-Cu alloys. A thorough review of literature was performed, and all recent data reported.

2.5.1 Aluminum Literature Data

Experimental data for viscosity, surface tension and density of pure liquid Al from a variety of studies is discussed in this section. These values will be used to compare against the results found in this study. Also, reviews by Assael *et al.* [6] and Mills and Su [56] are discussed, and will be used as the baseline for comparisons with literature values. Frequently, the experimental viscosities of metallic liquids differ from the results given by theoretical calculations (described in Section 2.1.1). As such, experimental measurement methods are required to accurately determine the viscosity of liquid metals [77]. Unfortunately, the reliability of different measurement techniques should be scrutinized, as their accuracies vary in the range of 5 to 20%. In the case of Al, experimental values exhibit even higher discrepancies [21]. The differences in the results published for liquid Al could be caused by difficulties associated with conducting measurements at such high temperatures. These include the purity of the liquid sample, which can be significantly impacted by container in which it is being held, and the surrounding atmosphere. For example, Roach and Henein [7] conducted DC experiments on pure Al resulting in viscosity values approximately 50% lower than those published in literature. Later, Gancarz *et al.* [8] repeated the same experiments, also using the DC method, but with a higher purity Al sample, and a better control of the protective atmosphere. They obtained values very similar to those published in literature and attributed the difference to lower O content in the surrounding atmosphere [8].

A broad literature review was conducted on studies that measured the viscosity of liquid Al. The methods employed consisted primarily of the oscillating vessel method; however, studies were also conducted using the DC, rotational, and gas bubble viscometer methods. Note that there is no published viscosity data for Al using EML-LD, this is likely due to the challenges associated with conducting measurements terrestrially. Assael *et al.* [6] conducted a very thorough analysis of the viscosities of pure liquid Al and Fe. For Al, they assessed five different studies, which they deemed accurate, or primary datasets, and developed a standard reference correlation,

characterized by a standard deviation of 13.7%, at the 95% confidence level [6]. Table 2-2 summarizes literature results; highlighting the atmosphere, purity of sample, and container material employed. The results are presented through the constants of the Arrhenius equation.

Table 2-2: Viscosity of liquid Al published in literature

Authors	Year	Method	Atmosphere	Purity (wt.%)	Container	Temp. Range (K)	Arrhenius Constants		Quoted Uncertainty (%)
							A (Pa·s)	E_a (J/mol)	
Jones and Bartlett [42]	1952	OV	—	—	Graphite	933 - 1125	2.76×10^{-4}	22790	0.5
Yao and Kondic [170]	1952	OV	—	99.9935	Graphite	933 - 1053	1.28×10^{-4}	25999	—
Yamasaki *et al.* [171]	1993	OV	Argon	99.99	—	943 - 1080	2.01×10^{-4}	14342	—
Friedrichs *et al.* [131]	1997	GB	Argon	99.9	Steel	1073 - 1120	3.74×10^{-6}	50626	—
Andon *et al.* [172]	1999	—	Argon	—	Alumina	950 - 1110	2.69×10^{-4}	11016	—
Wang and Overfelt [173]	2002	OV	Vacuum	99.995	Graphite	950 - 1115	2.05×10^{-4}	14799	4
Park *et al.* [174]	2005	R	Argon	99.98	Graphite	933 - 1223	2.82×10^{-3}	3119	—
Roach and Henein [7]	2005	DC	Argon (20 ppm O_2)	99.95	Graphite	973 - 1165	5.75×10^{-4}	-946	7
Wang *et al.* [39]	2007	OV	Argon	—	—	950 -1115	9.00×10^{-4}	4776	—
Plevachuk *et al.* [165]	2008	OV	Helium	99.99	Boron Nitride	937 - 1173	1.60×10^{-4}	16599	3
Kobatake *et al.* [158]	2014	OV	Argon	—	Alumina	933 – 1250	2.81×10^{-4}	12300	6
Gancarz *et al.* [8]	2018	DC	Argon (<1 ppm O_2)	99.999	Graphite	963 - 1073	1.91×10^{-4}	14982	5

OV = oscillating vessel; R = rotational; GB = gas bubble viscometry; DC = discharge crucible

The viscosity results presented in Table 2-2 were plotted in Figure 2.38. The disagreement between measurements greatly reduces the reliability of the data, even though quoted uncertainties for these studies are less than or equal to 7%. These differences originate from inherent sources of error within each measurement technique, such as contamination, imaging, etc. The different challenges associated with each measurement method were highlighted in Section 2.1.2. Clearly, better agreement between studies is necessary. Also, as alluded earlier, control of the atmosphere is crucial in reducing contamination of the metallic liquid. Regrettably, most studies reviewed in Table 2-2 and Figure 2.38 fail to report oxygen content in the protective atmosphere. Only measurements made using the DC method report oxygen content; however, the values reported in these studies are much higher than required to reduce oxygen contamination in the highly reactive Al and Al alloys. Attempts were made in this study to further reduce the oxygen content and are discussed in Chapter 3.

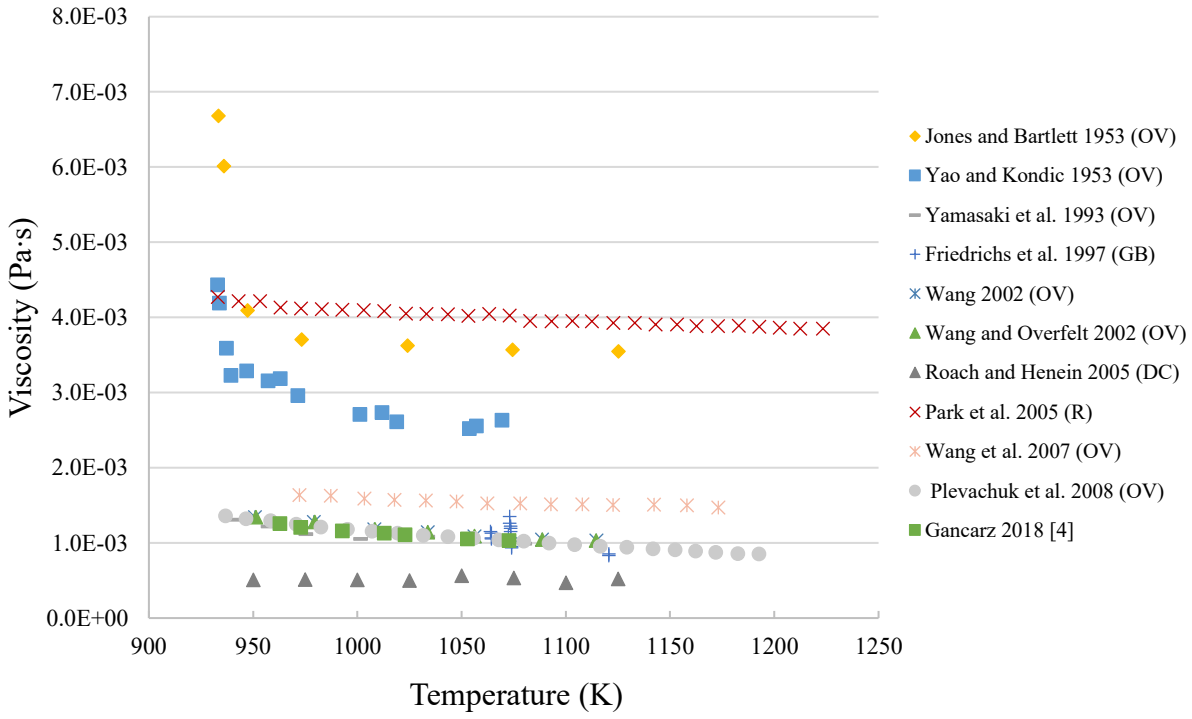

Figure 2.38: Experimental viscosity of Al published in literature

As discussed in Section 2.2.1, the presence of surface-active agents (e.g. O), can significantly reduce the surface tension of metallic liquids. Liquid Al reacts strongly with O, and will form a fine layer, or sometimes "islands", of oxide on the surface, drastically impacting the

surface tension. To avoid oxide contamination in liquid Al, an O partial pressure of 10^{-50} atm is required [175]. Obviously, this is nearly impossible to achieve experimentally; therefore, most values presented in Table 2-2 describe the surface tension of O saturated Al, with values in the 0.8 N/m range. Nevertheless, a few researchers have done excellent work to measure the viscosity of unoxidized Al. Gourmiri and Joud [176] used the sessile drop method to measure the surface tension of "pure" liquid Al. They were able to atomically clean the Al sample, with a combination of heating and Ar ion bombardment. Using Auger electron spectroscopy, the concentration of O at the surface was determined, and plotted against surface tension, as shown in Figure 2.39.

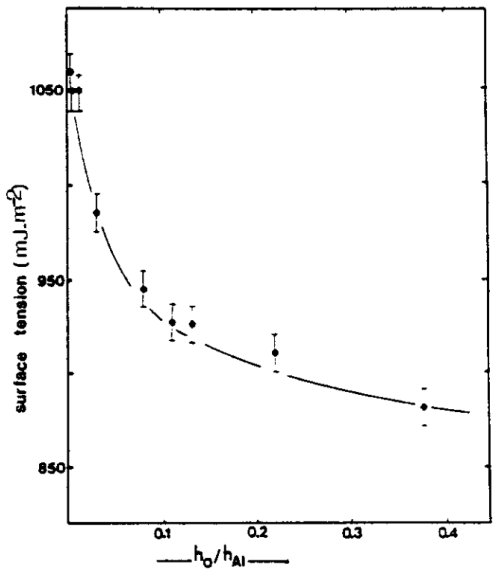

Figure 2.39: Surface tension of Al versus Auger peaks ratio [176]

Pamies *et al.* [177] used MBP to measure the viscosity of Al. They hypothesized that most of the O diffused through the system walls, and that severe purging of the system leads to rapid O saturation. To remedy this, they employed complete purging prior to capillary submersion, followed by a low purging flow rate, with rapid measurement time, and were able to obtain surface tension values at the Al melting temperature above 1.0 N/m at 973 K. They also noted that with time, the surface tension began to decrease, with full saturation occurring after two hours. Garcia-Cordovilla *et al.* [178] repeated this process, and obtained surface tension value of unoxidized Al of 1.091 N/m at 973 K. Lastly, Anson *et al.* [175] used sessile drop, with precise attention to avoid contamination, by using vacuum, a gas purifier, and electron-grade alumina substrate, and were able to obtain a surface tension value of 1.009 N/m at 953 K.

Of all the methods reviewed in Section 2.2.4, the sessile drop and maximum bubble pressure method are most frequently used for measuring surface tension of metallic liquid [21]. But, in recent years, EMD-LD has been adopted as the standard; this is reflected in Table 2-3.

Table 2-3: Surface tension of liquid Al published in literature

Authors	Year	Method	Atmosphere	Purity (wt.%)	Container	Temp. Range (K)	σ_m (N/m)	-dσ/dT (N/mK)	Quoted Uncertainty (%)
Eustathopoulos *et al.* [179]	1974	SD	Vacuum / Helium	99.99	Graphite	733 - 1293	0.870	1.95×10^{-4}	20
Laty *et al.* [180]	1977	SD	Argon	99.996	Boron Nitride	973 - 1123	0.865	1.50×10^{-4}	0.75
Laty *et al.* [180]	1977	MBP	Argon	99.996	Alumina	933 - 1200	0.868	1.50×10^{-4}	0.5
Friedrichs *et al.* [131]	1997	GB	Argon	99.9	Steel	985 - 1118	0.897	3.88×10^{-4}	3.9
Egry *et al.* [181]	2001	LD	Helium / Hydrogen	99.999 / 99	*Containerless*	933 - 1723	0.881	2.00×10^{-4}	—
Park *et al.* [174]	2005	DW	Argon	99.98	Graphite	973 - 1323	0.842	2.04×10^{-4}	—
Roach and Henein [7]	2005	DC	Argon (1 ppm O_2)	99.95	Graphite	973 - 1165	0.871	1.55×10^{-4}	2
Molina *et al.* [182]	2007	SD	Vacuum	99.999	Graphite	973 - 1273	0.883	1.85×10^{-4}	3
Kobatake *et al.*[183]	2015	LD	Argon / Helium (<1.0 Pa O_2)	—	*Containerless*	1300 - 1550	0.979	2.71×10^{-4}	6
Gancarz *et al.* [8]	2018	DC	Argon (<1 ppm O_2)	99.999	Graphite	963 - 1073	0.866	1.77×10^{-4}	0.1

SD = sessile drop; DW = drop weight; GB = gas bubble viscometry; LD = levitated drop; MBP = maximum bubble pressure; DC = discharge crucible

There has also been considerable effort in reducing contamination during measurements. All studies reported in Table 2-3 use high purity metals, protective atmosphere, and highly stable container materials or even occasionally containerless. However, they also fail to report O content in the atmosphere, with the exception of a few studies. This is especially important to do when measuring metals like Al that have high affinity for O. Mills and Su [56] conducted a review on the surface tension of various metallic liquids. Based on previous experiments, they proposed

equations for O saturated Al surface tension and "pure" Al surface tension, based on mean values. The respective equations for saturated and pure Al surface tension are given below.

$$\sigma = 875 - 0.18(T - 933) \tag{2.149}$$

$$\sigma = 1050 - 0.25(T - 933) \tag{2.150}$$

Where σ (mN/m) is the surface tension of Al as a function of temperature, and T (K) the temperature of the liquid. The data reviewed in Table 2-3 was plotted in Figure 2.40. The agreement between different studies, and different measurement techniques is good, and especially impressive considering the uncertainties quoted by each researcher. The key to further improving the reliability of the data is to report O contamination, and state whether the properties describe pure Al or O saturated Al.

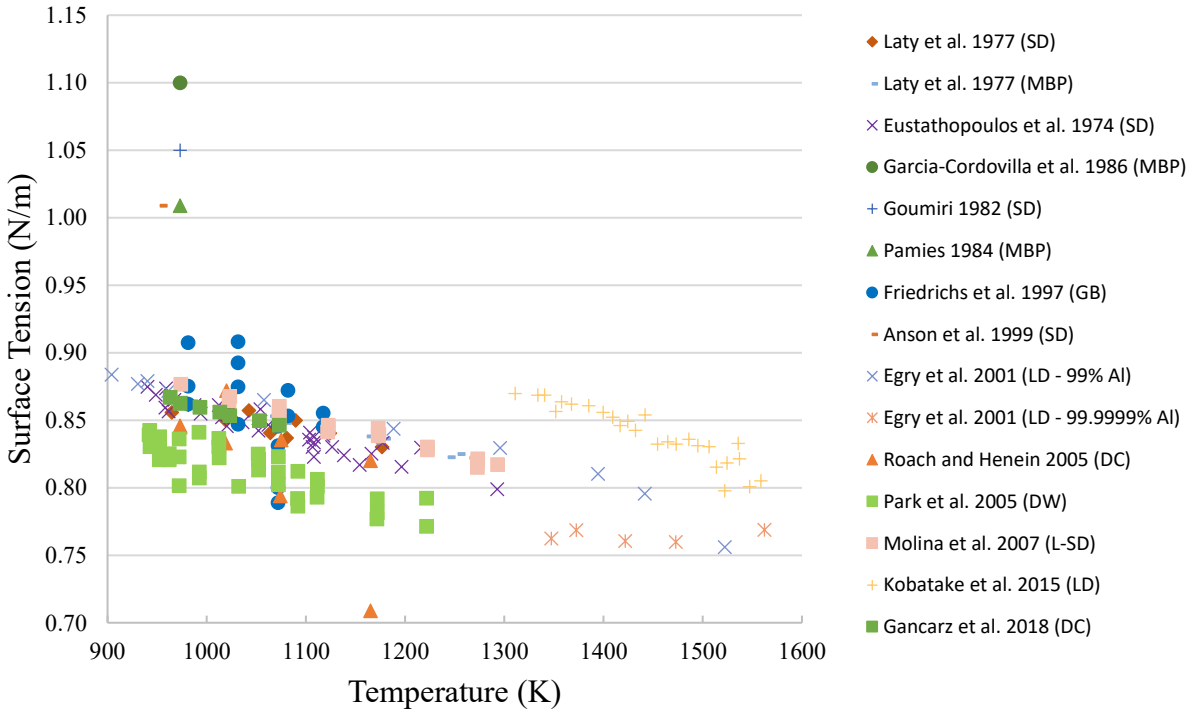

Figure 2.40: Experimental surface tension of Al published in literature

The density of liquid Al was measured by a variety of sources. Multiple methods were employed, like gamma-ray attenuation, x-ray attenuation, EML-LD, pulse heating, and DC. The constants that described the temperature dependence of density (see Equation 2.68) are listed in Table 2-4. The quoted uncertainties, also listed in Table 2-4, are very small. This highlights the

high accuracy of metallic liquid density measurements methods. Figure 2.41 shows the data from the studies reviewed in Table 2-4.

Table 2-4: Density of liquid Al published in literature

Authors	Year	Method	Atmosphere	Purity (wt.%)	Container	Temp. Range (K)	ρ_m (kg/m^3)	-dρ/dT (kg/m^3)	Quoted Uncertainty (%)
Drotning [184]	1979	γ-ray	Argon	99.999	Graphite	933 - 1973	2388	2.92×10^{-1}	0.2
Nasch and Steinemann [123]	1959	γ-ray	Argon	99.98	Alumina	933 - 1613	2375	2.33×10^{-1}	0.75
Friedrichs *et al.* [131]	1997	GB	Argon	99.9	Steel	985 - 1118	2221	1.54×10^{-1}	3.4
Smith *et al.* [124]	1999	x-ray	Helium	99.99	Graphite	975 - 1075	2380	3.50×10^{-1}	—
Sarou-Kanian *et al.* [185]	2003	LD	Argon / Helium	99.99	*Containerless*	2000-2300	2400	3.00×10^{-1}	1.5
Roach and Henein [7]	2005	DC	Argon	99.95	Graphite	973 - 1165	2390	1.50×10^{-1}	2
Schmitz *et al.* [167]	2012	LD	Argon	99.999	*Containerless*	1273 - 1850	2360	3.20×10^{-1}	0.5
Kobatake *et al.* [158]	2015	LD	Argon / Helium	—	*Containerless*	1050 - 1400	2420	3.0×10^{-1}	1
Peng *et al.*	2015	LD	Argon / Helium	99.9999	*Containerless*	933 - 1200	2290	2.51×10^{-1}	—
Leitner *et al.* [186]	2017	PH	Nitrogen	99.999	*Containerless*	640 - 1680	2397	3.00×10^{-1}	3.8
Leitner *et al.* [186]	2017	LD	Argon / Hydrogen	99.999	*Containerless*	986 - 1483	2304	2.47×10^{-1}	—
Gancarz *et al.* [8]	2018	DC	Argon	Argon (<1 ppm O_2)	Graphite		2383	3.11×10^{-1}	0.05

γ-ray = γ-ray attenuation; x-ray = x-ray attenuation; GB = gas bubble viscometry; LD = levitated drop; PH = pulse heating; DC = discharge crucible

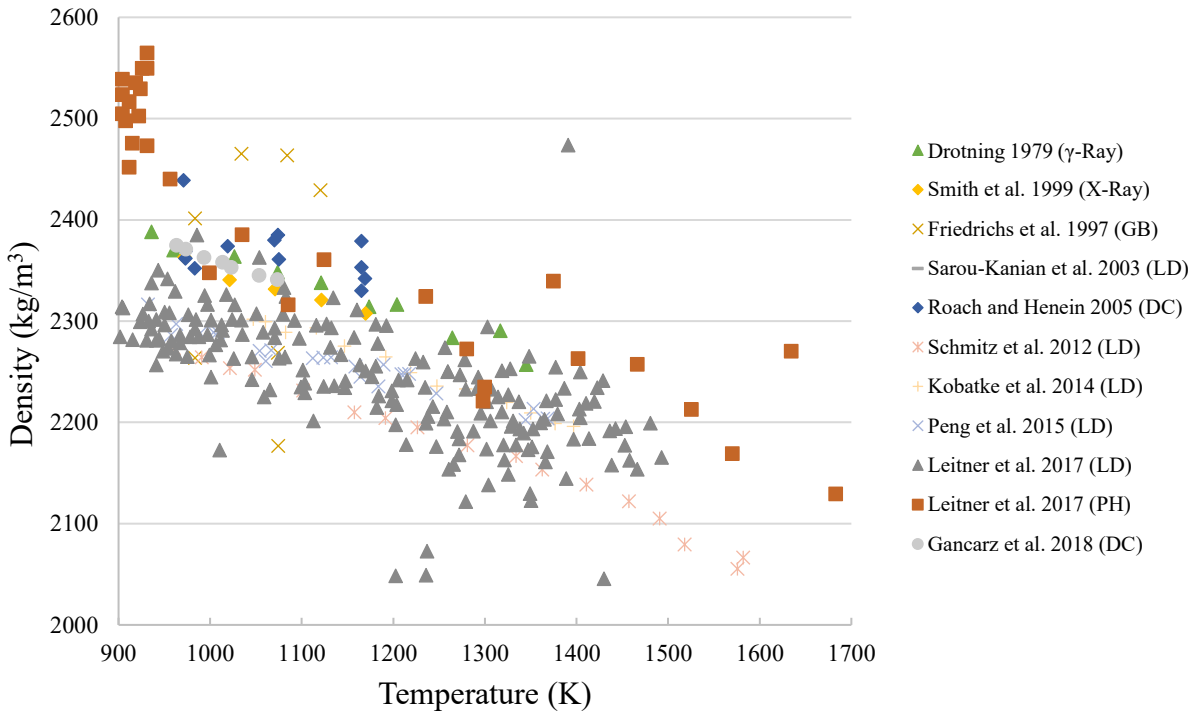

Figure 2.41: Experimental density of Al published in literature

2.5.2 Aluminum-Copper Literature Data

The Al-Cu alloy studied in this study has a composition of 22.5 wt.%. There have not been any prior published studies measuring the thermophysical properties of the exact same alloy; however, there have been several studies with Al-Cu of very similar compositions. This data will be used to verify that the results obtained in this study are valid. The experimental viscosity, surface tension, and density of liquid Al-Cu obtained from literature are summarized in Tables 2-5, 2-6, and 2-7, respectively.

The viscosity of Al-Cu published in various studies measured using the gas bubble viscometer and oscillating vessel methods are given per the Arrhenius constants in Table 2-5. All experiments were conducted in a protective atmosphere, but none of the studies reported O content. The quoted uncertainties for values published in the literature range between 1% and 10%. The data obtained by Friedrichs *et al.* [131], Plevachuk *et al.* [165], Schick *et al.* [3] and Konstantinova *et al.* [187] for Al-Cu of approximately 20 wt.% Cu were plotted on Figure 2.42.

Table 2-5: Viscosity of liquid Al-Cu alloys published in literature

Authors	Year	Method	x_{Cu} (wt.%)	Atmosphere	Container	Temp. Range (K)	Arrhenius Constants		Quoted Uncertainty (%)
							A (Pa·s)	E_a (J/mol)	
Friedrichs *et al.* [131]	1997	GB	21	Argon	Steel	1025 - 1250	9.73×10^{-6}	4776	6.8
Plevachuk *et al.* [165]	2008	OV	20	Helium	Boron Nitride	875 - 1200	2.09×10^{-4}	15295	3
Schick *et al.* [3]	2012	OV	21	Argon	Alumina	873 - 2100	3.05×10^{-4}	16014	10
Schick *et al.* [3]	2012	OV	21	Argon	Alumina	873 - 2100	3.80×10^{-4}	15640	10
Konstantinova *et al.* [187]	2016	OV	21	Helium	Berylium Oxide	873 - 1373	2.74×10^{-4}	15142	2

GB = gas bubble viscometer; OV = oscillating vessel

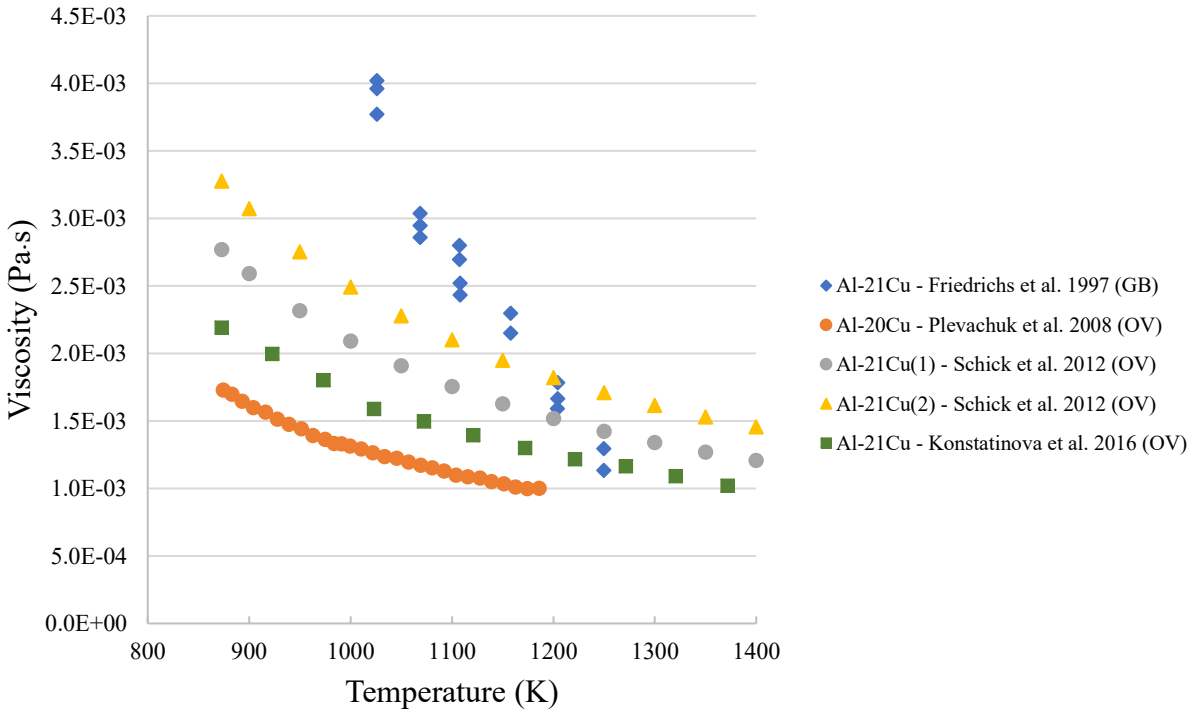

Figure 2.42: Experimental viscosity of Al-Cu published in literature

The surface tension measurements of Al-Cu using various methods are given in Table 2-6 and plotted in Figure 2.43. Surface tension can be significantly affected by surface-active agents, like O. None of the studies presented in Table 2-6 report the O content in the protective atmosphere,

therefore, it is difficult to assess whether the surface tension represents the pure alloy. It is probable that the Al-Cu liquid alloys are saturated with O. The quoted uncertainties are also given in Table 2-6 and the reported errors are generally relatively small.

Table 2-6: Surface tension of liquid Al-Cu alloys published in literature

Authors	Year	Method	x_{Cu} (wt.%)	Atmosphere	Container	Temp. Range (K)	σ_m (N/m)	-dσ/dT (N/mK)	Quoted Uncertainty (%)
Laty *et al.* [180]	1977	SD	20	Argon	Boron Nitride	920 - 1224	0.906	1.69×10^{-4}	0.5
Laty *et al.* [180]	1977	MBP	20	Argon	Alumina	950 - 1224	0.882	1.36×10^{-4}	0.2
Friedrichs *et al.* [131]	1997	GB	21	Argon	Steel	1025 - 1365	0.771	9.74×10^{-5}	5.4
Schmitz *et al.* [15]	2009	LD	21	Helium / Hydrogen	*Containerless*	1100 – 1600	0.871	1.20×10^{-4}	1

SD = sessile drop; MBP = maximum bubble pressure; GB = gas bubble viscometry; LD = levitated drop

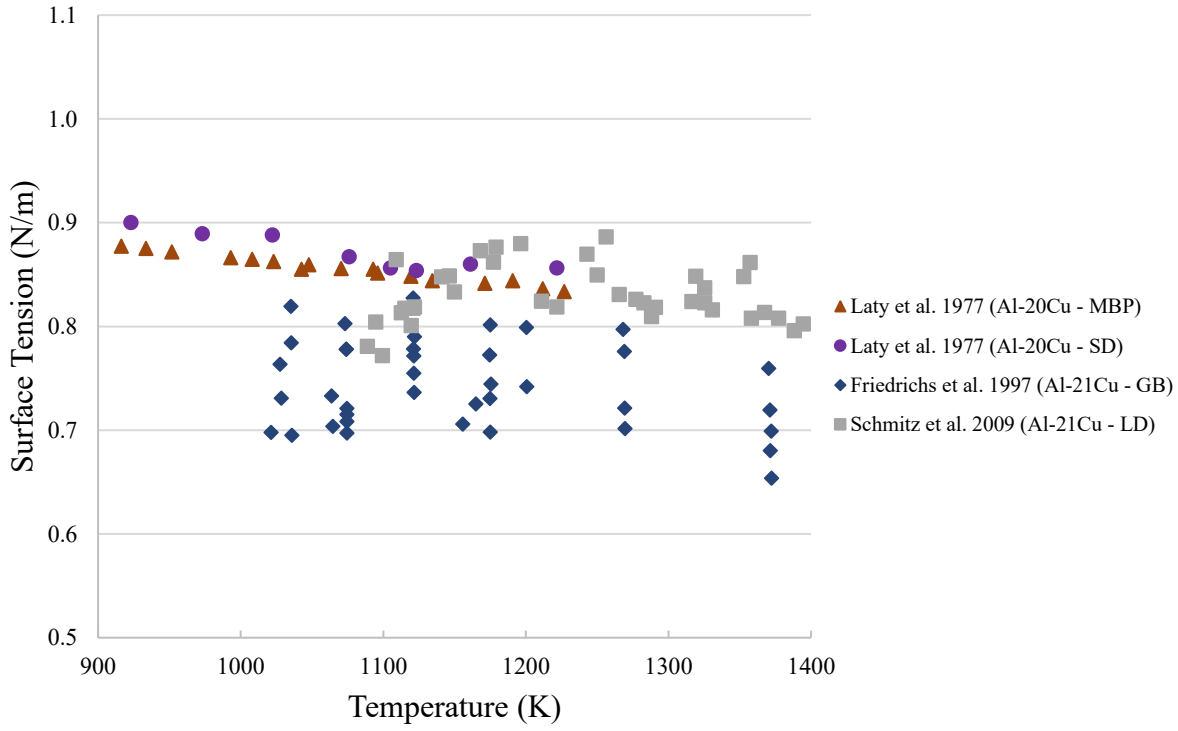

Figure 2.43: Experimental surface tension of Al-Cu published in literature

Lastly, the literature for density measurements of Al-Cu was reviewed and the studies summarized in Table 2-7 and shown in Figure 2.44. The measurements were performed with minimal reported error, as shown by the quoted uncertainties.

Table 2-7: Density of liquid Al-Cu alloys published in literature

Authors	Year	Method	x_{Cu} (wt.%)	Atmosphere	Container	Temp. Range (K)	ρ_m (kg/m^3)	-dρ/dT (kg/m^{3}K)	Quoted Uncertainty (%)
Friedrichs *et al.* [188]	1997	GB	21	Argon	Steel	1025 - 1365	2869	6.27×10^{-1}	5
Plevachuk *et al.* [165]	2008	SD	20	Argon / Hydrogen	Graphite	885 - 1290	2710	4.05×10^{-1}	3

GB = gas bubble viscometer; SD = sessile drop

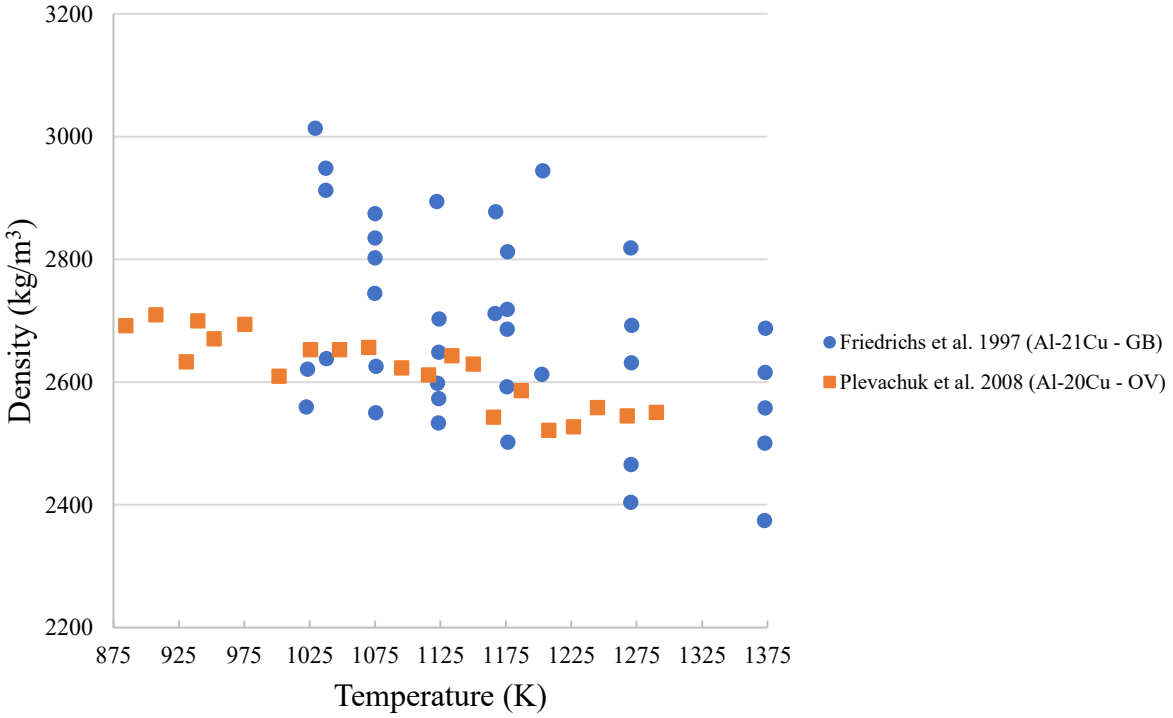

Figure 2.44: Experimental density of Al-Cu published in literature

2.6 Summary

An urgent need to measure the thermophysical properties of alloys exists so that metallurgical processes may be accurately modelled. There is however a lack of reliable data, due to the difficulty of measurement using conventional techniques. These challenges were summarized in this chapter, and primarily arise from technical and mathematical complications. Conventional measurement techniques are hindered by the compatibility between the equipment components and the highly reactive metallic liquids. Often refractories must be used which are difficult to fabricate and machine to high tolerances, especially for complex parts like fine and long-bore capillary tubes, thin oscillating plates and suspension wires. As a consequence, many of these measurement techniques are limited to low and narrow temperature ranges. Furthermore, many techniques require challenging post-processing, like the oscillating vessel which relies on second-order differentiation, or the sessile drop method which requires complicated computer curve fitting to measure the dimensions of the drop. Several theoretical and semi-empirical models have been proposed to predict the viscosity, surface tension and density of metallic liquids. These could facilitate the determination of thermophysical properties, but first these models need to be better studied and evaluated by testing on different metals and alloys. The numerical models reviewed in Section 2.1.1 and Section 2.2.3 could also prove useful in better understanding the relationships between thermophysical properties and fundamental thermodynamic principles.

In addition, conventionally, measuring viscosity, surface tension and density of metallic liquids requires separate individual methods, with a few exceptions. This incurs higher costs and significantly more time and effort. Several methods were developed to simultaneously measure these properties for high-temperature metallic liquids; however, each have their own individual challenges. The gas bubble viscometer, although theoretically sound, fails to accurately measure the thermophysical properties when compared to other data published in literature. Conversely, EML-LD offers the advantage of eliminating container to liquid contamination, and it provides very accurate measurements. But viscosity can only be reliably measured in microgravity conditions. This is obviously expensive, and incredibly complicated. Moreover, EML-LD tends to evaporate volatile elements (like Al and Mn), which will significantly affect the composition of measured alloys, potentially compromising the measurement accuracy for certain liquid alloys.

The DC method is a ground-based technique that could potentially resolve these aforementioned issues. It is a relatively simple design, thus economical, and able to simultaneously measure viscosity, surface tension and density over a wide range of temperatures. It also offers a statistical advantage over conventional methods since a vast amount of data is used to calculate the properties. Furthermore, as described by the Gibbs adsorption isotherm, surface contamination by surface-active agents can significantly impact the surface tension of the liquid. The DC method relies on a flowing stream; this highly dynamic situation creates continuous replenishment of the surface, potentially able to measure surface tension without O contamination. This will be confirmed in the results that follow.

The aim of the present work is to extend and improve the DC method previously introduced by Roach and Henein [7]. Measurements will be made on Al and Al-Cu, and checked against reported viscosity, surface tension and density data in literature as a function of temperature. This data was presented in Sections 2.5.1 and 2.5.2. Eventually, when data is made available, the Al-Cu results will be compared to data obtained onboard the ISS using EML-LD. Ultimately, more data will help add to an ever growing database for Al and Al-based alloys, and hopefully provide a better understanding of various metallurgical processes. The present work will also implement experimental and analytical improvements to eliminate possible difficulties associated with prior DC measurements. These include challenges related with O contamination, head measurement and temperature instability. Additionally, an effort will be made to outline the DC data analysis process so that future measurements can be reproduced reliably. Finally, a thorough evaluation of theoretical and semi-empirical models will be conducted, and the results calculated using selected models will be compared to results measured experimentally. This will all be addressed shortly in Chapter 3 and Chapter 4.

CHAPTER 3 : EXPERIMENTAL

This chapter will describe equipment used in measuring the thermophysical properties of metallic liquids using the modified Bernoulli formulation outlined in Section 2.4.3. Prior to conducting experiments at high temperatures, certain preliminary calibrations at low temperatures must be completed. These include ultrasonic calibration which converts volume left in the crucible to head, load cell calibration which converts the load cell voltage signal to mass (or cumulative mass), and discharge coefficient calibration which determines the frictional characteristics of the crucible. With the necessary calibration completed, the properties of low-temperature liquids, like water or ethylene glycol, can be measured using the modified Bernoulli formulation.

This chapter also includes a detailed description of the equipment used to measure the properties of high-temperature liquids, namely metals and alloys, as well as a detailed procedure for high-temperature experiments. The equipment used for high-temperature measurements includes an orificed crucible, stopper, collection vessel, oxygen analyzer, and two-color pyrometer. The goal of this chapter is to give sufficient information on the experimental setup, so that experiments may be easily reproduced in the future. A more detailed discussion of potential experimental challenges will be presented in Appendix A.

3.1 Crucible and Orifice Design

A key consideration when setting up the DC method are the crucible and orifice design. The crucible is essential for both preliminary calibrations and high-temperature experiments and the orifice size is particularly important in determining whether the classical or modified Bernoulli formulation should be applied (as discussed in Section 2.4.3). This section will provide an in-depth description of the crucibles used for all experiments conducted in this work.

3.1.1 Crucibles

The crucibles were fabricated from flat closed one end Al_2O_3 tubes (FCOE AD-998 high-alumina tubes, supplied by CoorsTek). They were used because of their ability to withstand very high temperature (up to 1750 °C) under inert atmosphere. The AD-998 is made of 99.8% pure Al_2O_3 and offers high resistance to chemical attack and proves to be inert with pure and alloyed Al and Fe at and above the melting temperature. It should be noted that the AD-998 is sensitive to

thermal shock, so the crucibles must be fully dried before use, and when heated, the heating rate must not exceed 150 °C/hour for the first 1 – 1.5 hours of heating. It is also important handle the crucibles carefully and to inspect it for micro-cracks prior to use. Refer to Table 3-1 for the properties of AD-998. For crucible dimensions, refer to Figure 3.1. These crucibles are single-use because the crucibles will crack when cooled quickly once the furnace is shut off due to rapid thermal contraction. Thus, for each experiment at high temperature, a new crucible must be calibrated, per procedures outlined in Section 3.2.

Table 3-1: CoorsTek AD-998 high-Al_2O_3 properties

Property	Units	Value
Maximum Use Temperature	℃	1750
Flexural Strength, MOR (20 ℃)	MPa	300 – 550
Fracture Toughness, K_{IC}	MPa $m^{1/2}$	4.0 – 5.0
Hardness	HR45N	79
Density	kg/m^3	3900
Thermal Conductivity (20 ℃)	W/m K	18.0 – 37.1
Coefficient of Thermal Expansion	1 x 10^{-6} / ℃	8.2 – 9.0
Dielectric Strength (6.35 mm)	Ac-kV/mm	8.7 – 19.7
Dielectric Loss (tan δ)	1MHz, 25 ℃	1 x 10^{-4} to 4 x 10^{-4}
Volume Resistivity (25 ℃)	Ω-cm	> 10^{14}

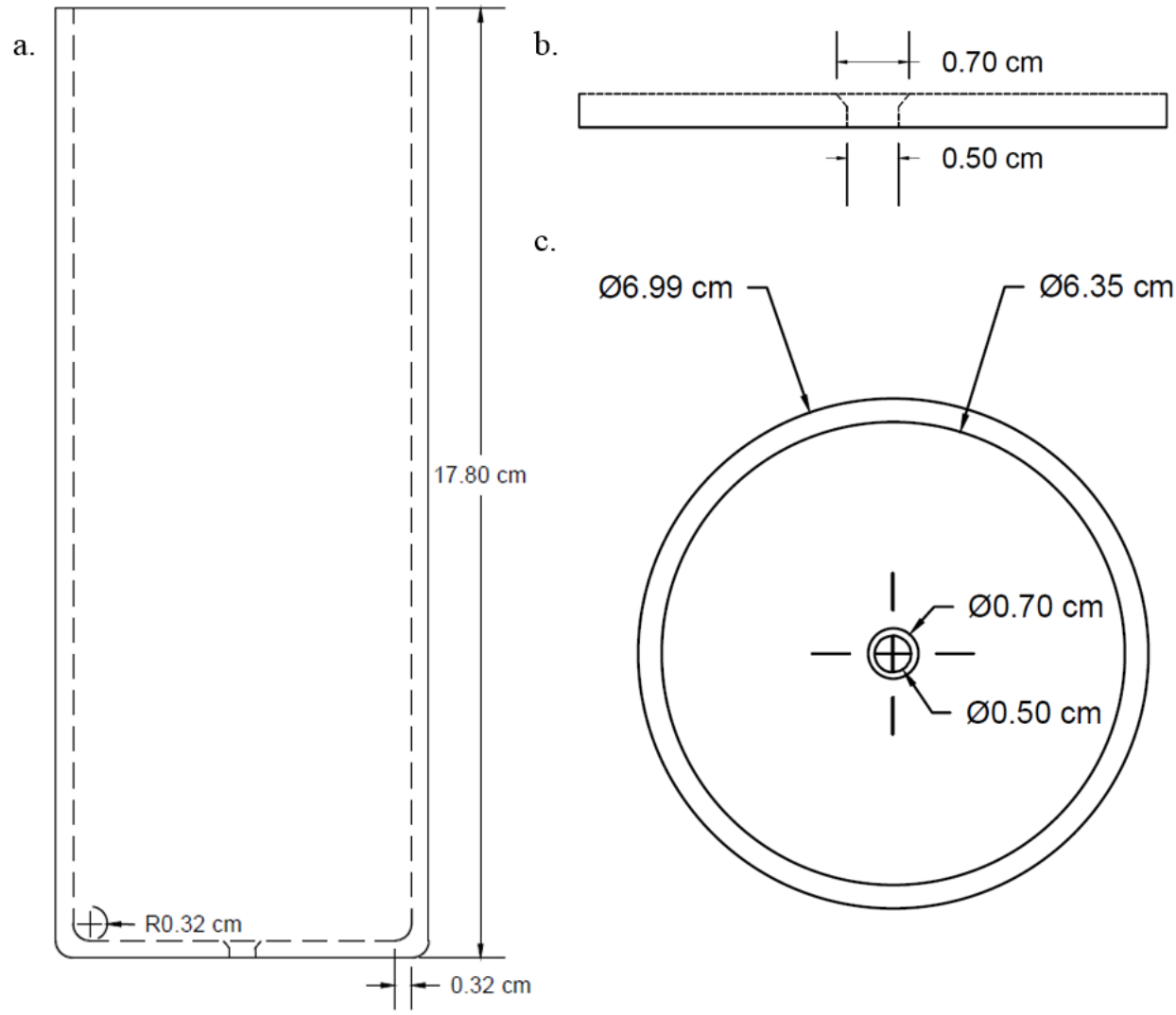

Figure 3.1: Dimensions of Al_2O_3 crucible; a) side view, b) orifice and c) top view

3.1.2 Orifice

To determine the optimal size of the orifice, an analysis can be conducted using dimensionless equations outlined in Section 2.4.3. For the analysis conducted on liquid Al at melting temperature, shown in Figure 3.2, when an orifice radius of 2.5 mm is chosen, and the liquid drains from a head of 15 cm to 2.5 cm, $(1\text{-}1/\mathrm{Bo})^{1/2}$ will range from 0.95 to 0.65. These are favorable conditions because it indicates that surface tension effects should be included (i.e. $(1-1/Bo)^{1/2}$ is never equal to 1) and that the stream will continue to flow (i.e. $(1-1/Bo)^{1/2}$is never equal to 0) throughout the entirety of the crucible height. If the surface

tension effects are too large, i.e. metallic system paired with a small orifice, the stream may break-up before impacting load cell resulting in an erratic signal. If the surface tension forces surpass gravitational forces, a continuous stream is not formed at all and dripping ensues [189].

To ensure that multiple different liquid metals and alloys could be measured with favorable flow conditions, the orifice size chosen for this work was approximately 5 mm in diameter, or 2.5 mm in radius, similar to experiments conducted by Roach and Henein [7]. The orifices were drilled into the AD-998 tubes using a 5 mm diamond hole saw (Milwaukee Diamond Plus Mini Hole Saw supplied by Home Depot) and chamfered using diamond countersink drill bit (OAL Diamond Countersink w/ 82 Degree Angle supplied by Triatic). The reason that the orifices were chamfered is discussed in Appendix A. Note that it is important to measure that orifice with a Vernier caliper after fabricating the hole because, often, the orifices end up larger than the hole saw dimensions (e.g. 5.3 mm versus 5.0 mm).

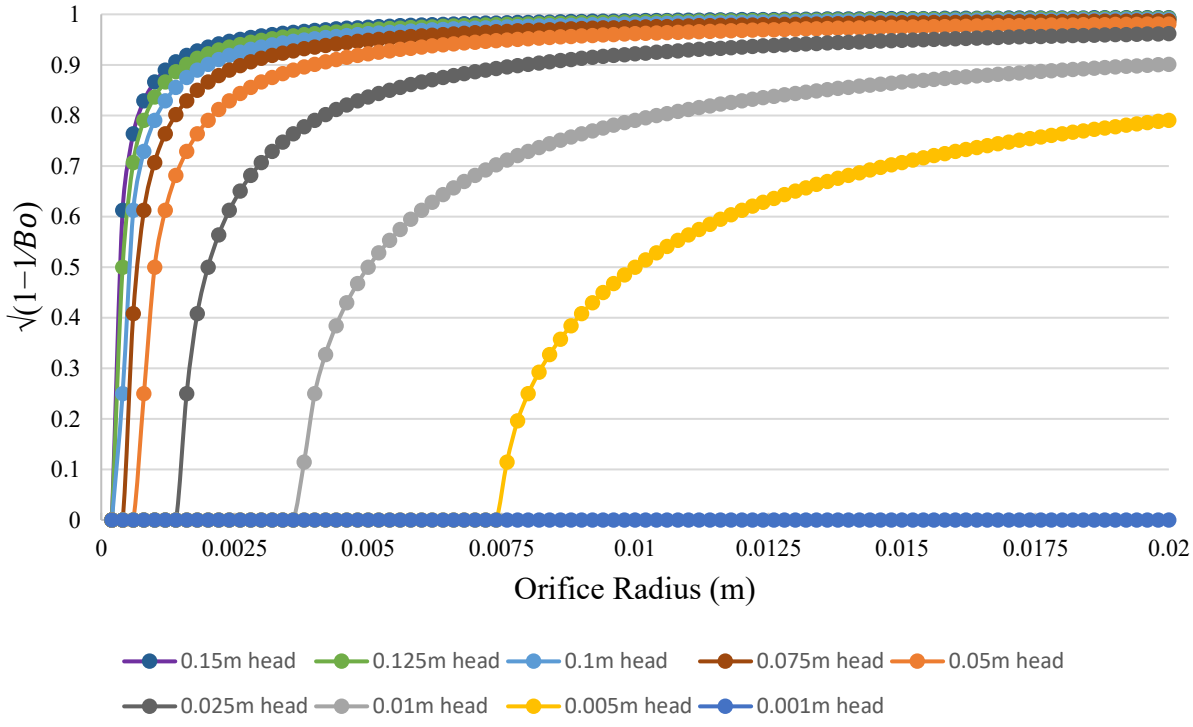

Figure 3.2: Dimensionless analysis used to determine appropriate orifice dimension

3.2 Preliminary Calibrations

There are multiple preliminary calibrations that must be performed prior to conducting high-temperature experiments. These include ultrasonic calibrations to relate the volume of the crucible with the head, load cell calibrations to convert the electrical strain signal to cumulative mass, and C_d versus Re calibrations to determine the frictional characteristics of the crucible. This section will describe all calibration experimental details further.

3.2.1 Ultrasonic Calibration

The head of the fluid is measured through careful calibration of the crucible geometry. The setup for ultrasonic calibrations is shown in Figure 3.3. Prior to experimentation, deionized water (ASTM Type II supplied by Fischer Scientific) samples of known volume are related to head measured in the crucible. The volume is measured indirectly by measuring the weight of the water, using a scale (OHAUS GT-800 Scale). The temperature is measured using a thermometer (Fisherbrand™ Traceable™ Lollipop™ Shock/Waterproof Thermometer) throughout the calibration so that volume can be calculated using accurate density values. The thermometer has an accuracy of ±1 °C between 0 to 100 °C.

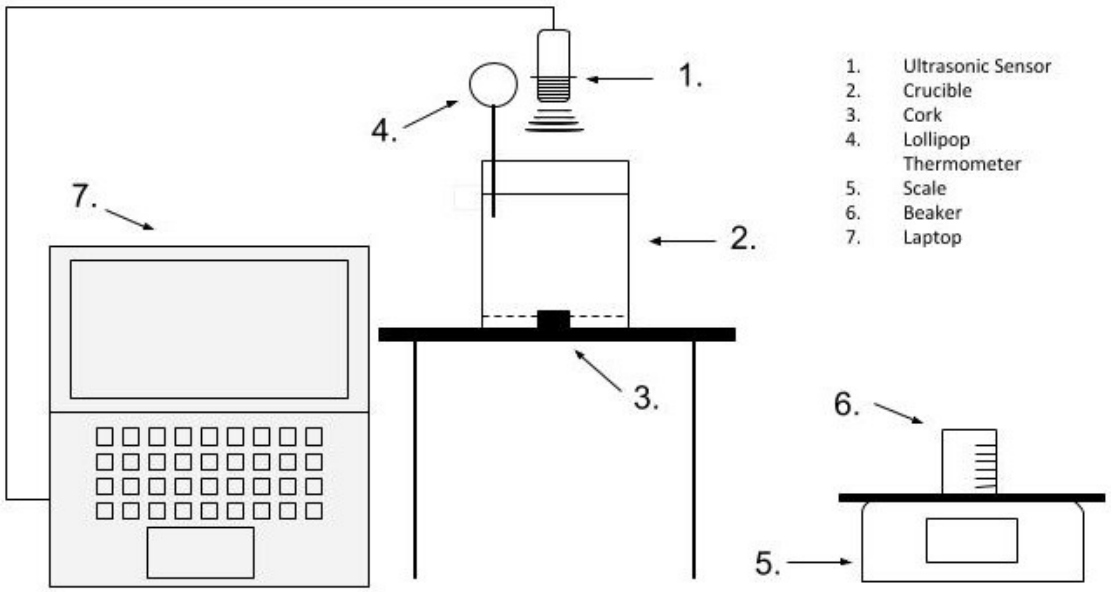

Figure 3.3: Ultrasonic calibration setup

An ultrasonic level sensor (ToughSonic® 14, RS-232 supplied by Senix) is used to directly measure head of the water, with an accuracy of ± 0.001 mm. The ultrasonic level sensor (shown in Figure 3.4) has a range between of 3.0 m and 4.3 m, with a deadband of < 100 mm. It is fabricated from 316 stainless steel, and can operate at temperatures ranging from -40 to 70 °C [190]. It is temperature compensated and has a resolution of 0.086 mm. It can detect flat or curved objects, and is unaffected by target color, light, transparency, or other optical characteristics.

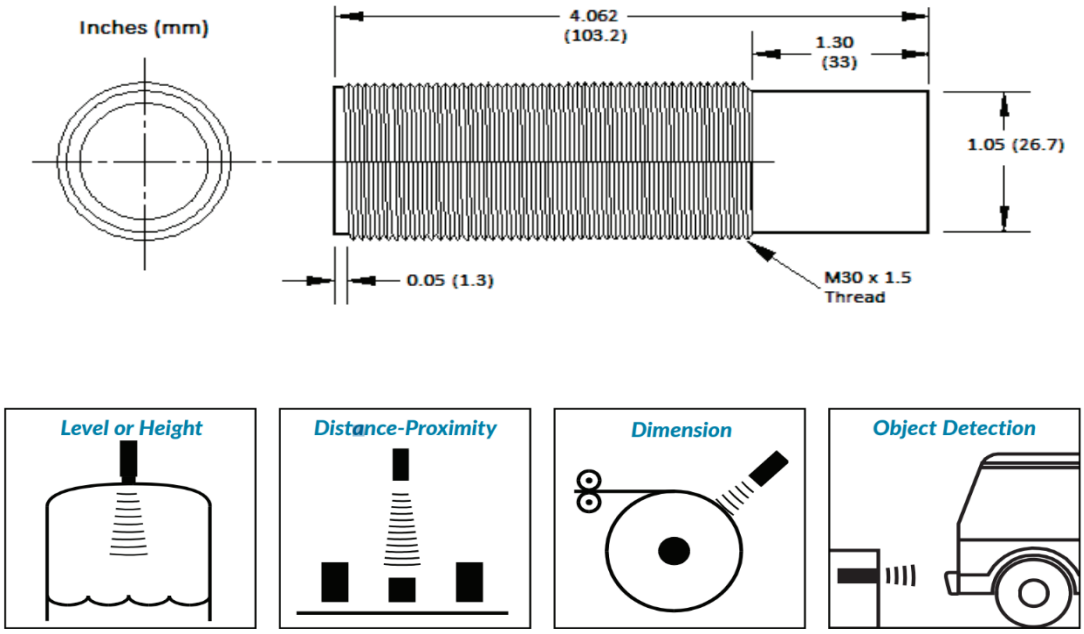

Figure 3.4: Schematic of dimensions and applications of ultrasonic level sensor [190]

The head measurements of the deionized water samples are plotted as a function of volume, as shown in a sample calibration given in Figure 3.5. Recall, the volume of the water is calculated by dividing the scaled mass by density. A linear fit of the head is generated and is used in future experiments to determine the head of the draining crucible with time. Each head measurement is an average of a total of 500 ultrasonic measurements (counts). The ultrasonic data is analyzed using the SenixView software. The software can measure the standard deviations for each head measurement, which were found to range from 0.03 to 0.08 mm, or approximately 0.2 to 0.4 %, for any given calibration. An example of the calculated standard deviations versus head measurements can be seen in Figure 3.6.

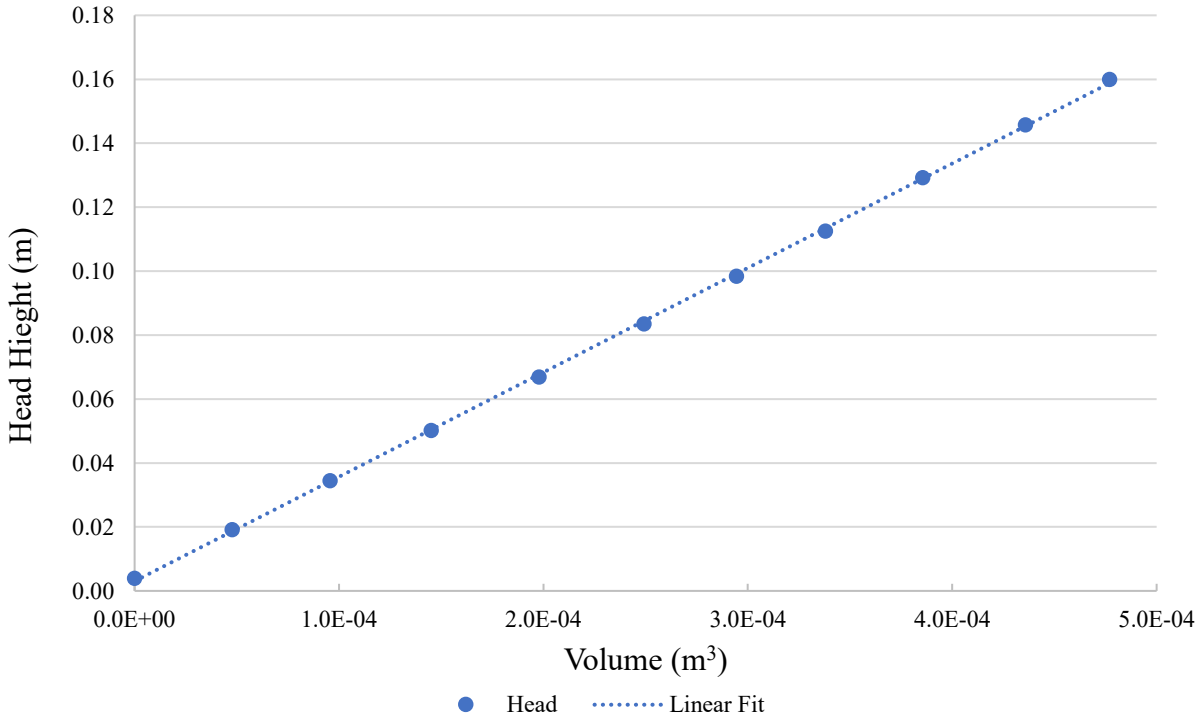

Figure 3.5: Volume of deionized water within the crucible corresponding to a different head height

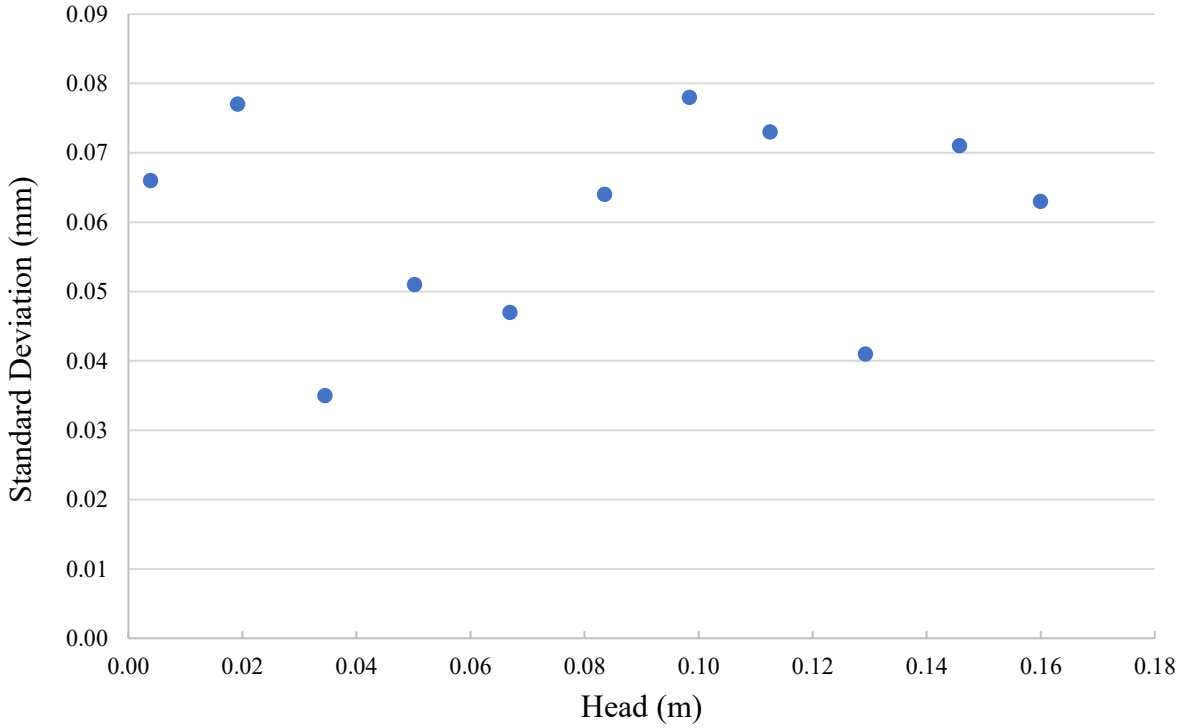

Figure 3.6: Standard deviations of ultrasonic sensor at different head heights

3.2.2 Load Cell Calibration

A load cell (LCCA-25 high accuracy S-beam load cell, supplied by Omega) is used to measure both the experimental head and flow rate of the fluid draining through the crucible orifice. A schematic of the load cell is shown in Figure 3.7. The load cell has a capacity of up to 11 kg (25 lbs.), using an excitation of 10 Vdc, and outputting 3 mV/V ± 0.0075 mV/V [191].

When fluid is poured into the collection vessel, weight acts on the load cell's metal spring element and causes elastic deformation. The strain, which is either positive or negative, is converted into an electrical signal by a strain gauge. The voltage signal is detected and recorded in a LabVIEW 7.1 software. The voltage signal is converted to mass by generating a linear fit on a load versus voltage signal graph. The graph is generated by placing a range of calibration weights (Troemner Stainless Steel Class 7 Weight Sets supplied by Fisher Scientific) onto the load cell and recording the output voltage signal. The accuracy of the load cell is ±0.001 g. An example of a load cell calibration can be seen in Figure 3.8.

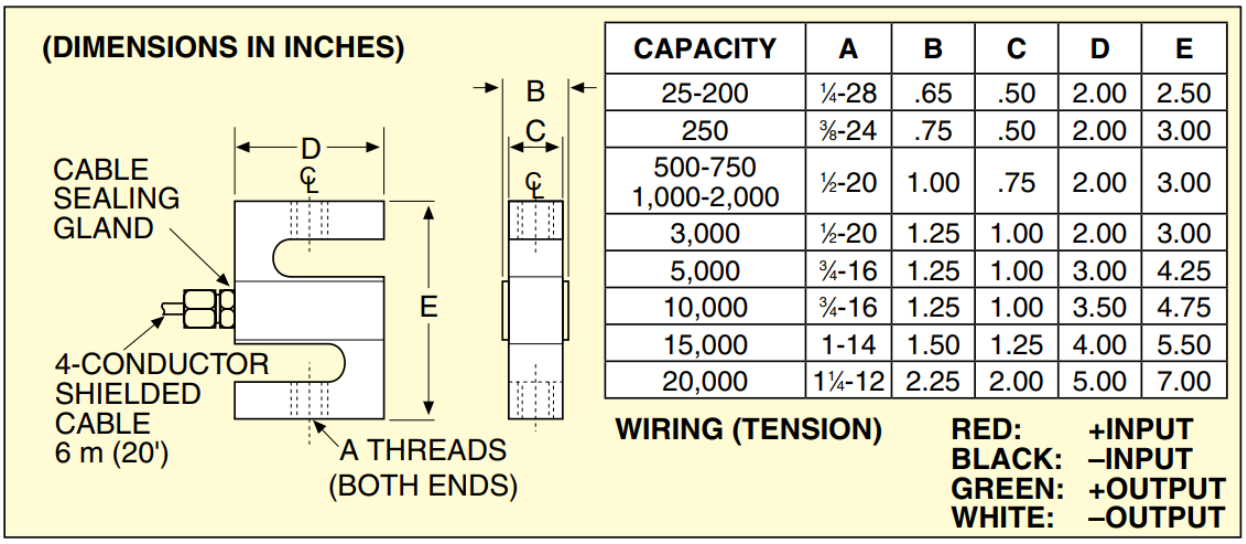

CAPACITY	A	B	C	D	E
25-200	¼-28	.65	.50	2.00	2.50
250	⅜-24	.75	.50	2.00	3.00
500-750 1,000-2,000	½-20	1.00	.75	2.00	3.00
3,000	½-20	1.25	1.00	2.00	3.00
5,000	¾-16	1.25	1.00	3.00	4.25
10,000	¾-16	1.25	1.00	3.50	4.75
15,000	1-14	1.50	1.25	4.00	5.50
20,000	1¼-12	2.25	2.00	5.00	7.00

Figure 3.7: Schematic of LCCA high accuracy S-beam load cell [191]

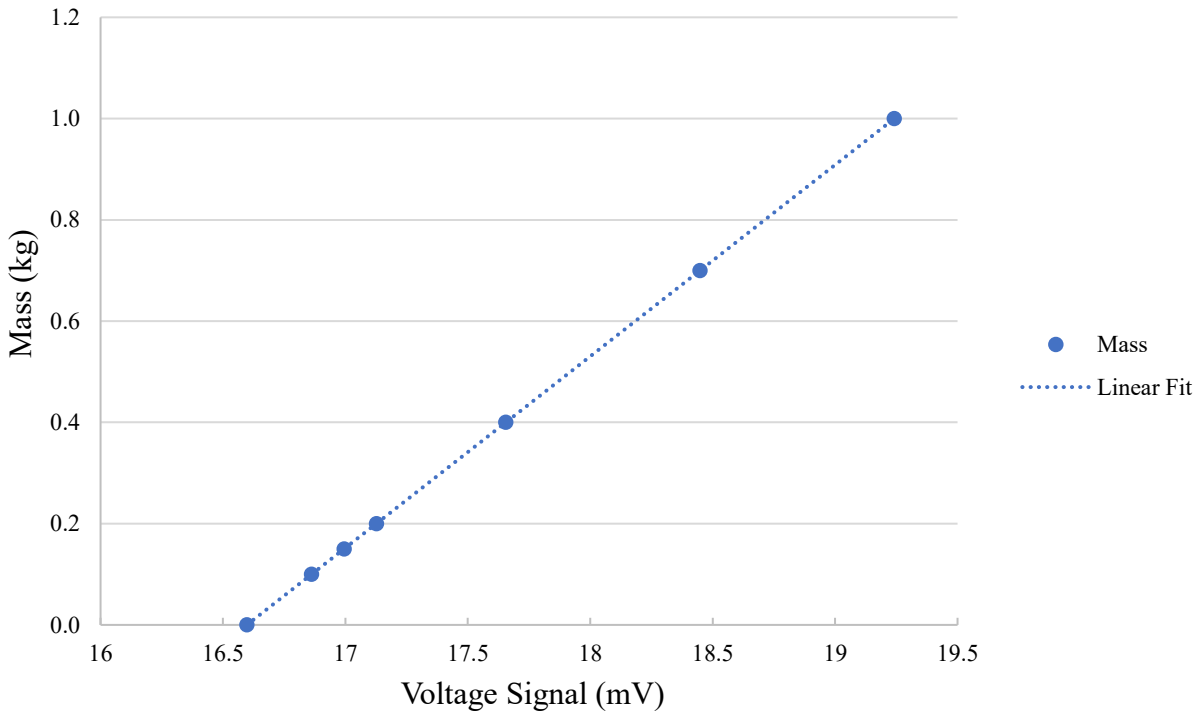

Figure 3.8: Calibration results for the load cell showing the linear relationship of mass versus voltage signal

3.2.3 Discharge Coefficient Calibration

As previously discussed in Section 2.4.3, a calibration curve of C_d versus Re for a specific crucible must be generated. The curve is used to calculate the surface tension, viscosity and density for a metallic liquid at a specific temperature. In this study, deionized water (ASTM Type II supplied by Fischer Scientific) was used as the calibration fluid because the property values across varying temperatures are well known, and, when calculated, shares a similar Re number range with liquid metals, like Al and Fe. Likewise, ethylene glycol can be used as another calibration fluid for systems exhibiting lower Re number ranges. The frictional characteristics (i.e. C_d versus Re curves), are dependent on the specific crucible used, thus, calibrations must be performed on each individual crucible used at high temperature. Note that crucibles are not reused between different measurements. The design of the crucibles used at high temperature is described in Section 3.1. The apparatus for calibrations is illustrated in Figure 3.9.

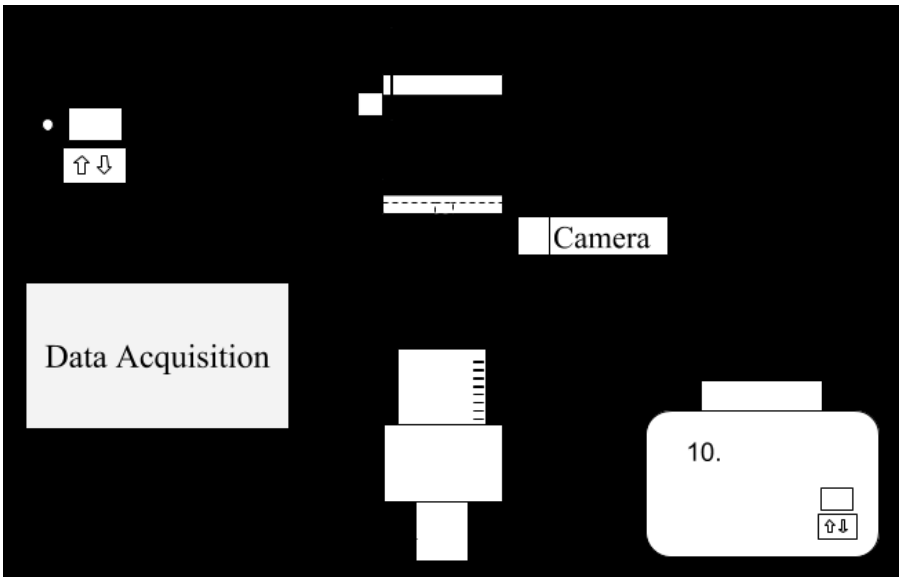

1.	Crucible	2.	Orifice Hole	3.	Stopper Rod	4.	Beaker	5.	Collection Vessel
6.	Load Cell	7.	Heating Blanket	8.	Thermocouple	9.	Temperature Controller	10.	Heat Bath

Figure 3.9: Schematic of low temperature apparatus

Prior to calibrating, the base of the crucible is sprayed with a hydrophobic coating (Nikwax TX. Direct® Spray-On supplied by MEC) to reduce wetting of water at the orifice. The challenges associated with wetting during calibrations will be discussed in Appendix A. Then, deionized water, of a known mass and temperature, drains through the crucible (Figure 3.9, Item 1) and collected by a beaker (Item 4), which sits on the load cell (Item 6). The temperature is measured using a lollipop thermometer or thermocouple (Item 8) immediately before removing the stopper, and the mass measured using a scale (Item 6). When calibrating with deionized water at a temperature above room temperature, the water is uniformly heated with a water bath (Digital Water Bath Model HW-2L supplied by Walter Inc., Item 10), and the temperature is maintained using an electric beaker heater (BriskHeat 1000-1 Silicone Beaker Heater supplied by Cole Parmer) connected to a temperature controller (DIGI-SENSE TC5000 Single-Zone Temperature Controller supplied by Cole Parmer, Item 7). As a precaution, the stopper is only removed once the water is perfectly still; any stirring prior to draining will affect the flow conditions (e.g. vortexing). It is important that the beaker is placed no greater than 0.06 m below the exit of the orifice so that the stream does not break-up before being collected. The break-up of the stream leads to the creation of discrete droplets that impact the load cell at irregular intervals, ultimately resulting in erratic load cell signals. This is shown in Appendix A.

The load cell signal is converted to mass (discussed in Section 3.2.2) and recorded using a LabVIEW 7.1 software. The data acquisition rate is 40 Hz (or 0.025 s per data point). A DLSR camera (EOS Rebel T7i DSLR supplied by McBain Cameras) is used to film the exit of the orifice; if any wetting is observed, additional hydrophobic coating is applied, or the load cell data is discarded at the time at which wetting begins. A second order polynomial is fitted to the cumulative mass that is plotted as a function of time. This will be further described in Section 4.1. This polynomial is differentiated, yielding a new function that describes the mass flow rate as a function of time, which was described in Section 2.4.3. The head is calculated by relating the volume of liquid left in the crucible, which is determined using the cumulative mass curve, and the ultrasonic calibration curve (described in Section 3.2.1). Note that since the crucible used is opaque, it is not possible to make visual observations of the head during calibrations (or during actual measurements). Using the experimental flow rate, the experimental head, and the known properties of the deionized water, C_d as a function of Re is calculated. Multiple calibrations at the same temperature are conducted so that the C_d versus Re curves can be averaged (and to ensure that the calibrations are consistent). This procedure will be discussed in more detail in Section 4.1.

3.2.4 Procedure for Low Temperature Experiments

1. Spray the base of the crucible with hydrophobic coating and let dry overnight. Test to see if coating worked as advertised; water should bead off surface.
2. Pour approximately 500 ml of deionized water into a beaker and weigh the calibration fluid using scale. The volume of the deionized water should not exceed the volume of the crucible or the volume at which the maximum height of the crucible was calibrated to.
3. If conducting calibrations at temperatures higher than room temperature, place the beaker of deionized water into the water bath until it has reached the desired temperature. Hold at constant temperature for at least 10 minutes.
4. Screw the collection vessel to the load cell and connect the load cell to the data acquisition system by connecting the 9-pin connector.
5. Place another beaker into the collection vessel so that the drained water can be removed easily following the experiment. Place the beaker as close as possible to the orifice exit while still being able to remove the stopper without impacting the load cell.
6. Place the crucible on the platform above the load cell, collection vessel and beaker.

7. Use a bubble level to ensure that the crucible is level. Ensure that the platform is rigid.
8. If conducting calibrations at temperatures higher than room temperature, wrap the beaker heater around the crucible and place a Type K thermocouple inside the crucible.
9. Connect both the heat blanket and thermocouple to the temperature controller and set the temperature to the desired calibration temperature.
10. Insert the stopper rod to ensure that the fluid does not begin draining out once added to the crucible. The stopper rod can be either made of cork, or you can use your finger if temperature allows.
11. Pour the calibration fluid into the crucible using a funnel.
12. Record the temperature of the calibration fluid using a water-resistance thermometer, or thermocouple. It is important that the thermometer is removed before the stopper rod is removed to avoid any stirring.
13. Run the data acquisition LabVIEW program to register and record the load cell data. A sample rate of 40 Hz (0.025 s per data point) is selected.
14. If conducting calibrations at temperatures higher than room temperature, turn off the heat blanket to avoid any heat induced stirring or convection.
15. Wait 10 s for the fluid to become still and for the load cell to tare. Any stirring or convection in the fluid can severely interfere with the dynamics of the experiment.
16. Remove the stopper to allow the fluid to drain through the orifice and flow into the beaker placed on the load cell. To minimize wetting, remove the stopper rod quickly and straight-out.
17. Import the load cell data into MATLAB from a .csv file; the data is trimmed, tared, a second order polynomial is fitted to the cumulative mass versus time data, and the function is differentiated to obtain the experimental flow rate.
18. Use the UT calibration curve and the cumulative mass data to determine the head of the deionized water as a function of time.
19. Using the time, head and experimental flow rate, generate the C_d versus Re number curve for the deionized water at a specific temperature.

3.3 High Temperature Experiments

Once all necessary calibrations are performed, a high-temperature apparatus is used to measure the viscosity, surface tension and density of a desired metallic liquid. In this study, liquid Al and Al-Cu alloys were measured using the DC method. The equipment and process that measures head and flow rate accurately is very similar to what was described for calibrating the crucibles in Section 3.2; however, for high-temperature experiments, the apparatus must provide enough heat to melt the material and reduce the oxygen content in the atmosphere. There are a variety of design and implementation challenges associated with measuring the thermophysical properties of metallic liquids. These challenges are discussed in more detail in Appendix A. See Figure 3.10 for a schematic of the high temperature apparatus.

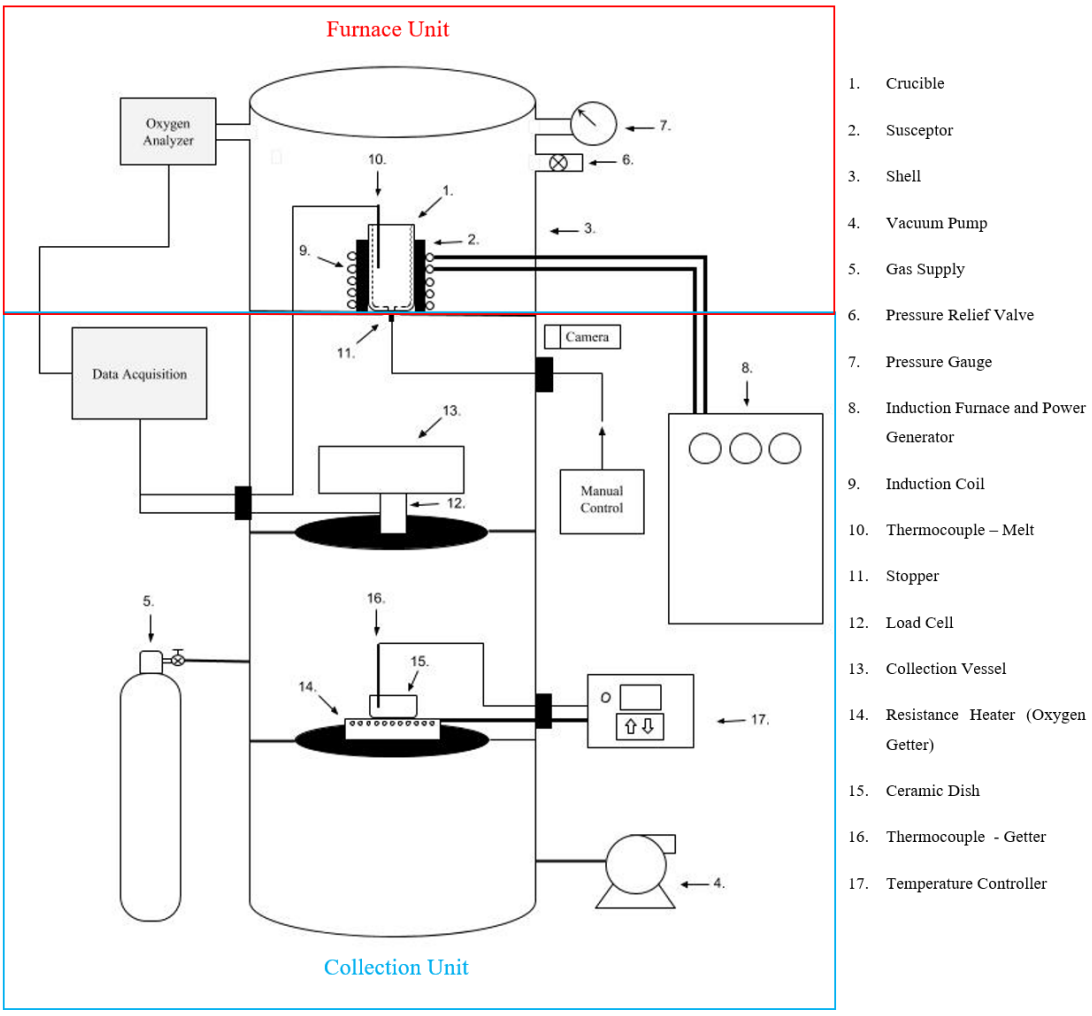

Figure 3.10: Schematic of high-temperature apparatus

The apparatus consists of two main units: the furnace unit and the collection unit. The furnace unit consists of a coreless induction furnace, which is simply an induction coil (inside is a crucible to hold the melt) connected to a power supply, the cooling system, and an outer shielding shell. The material to be melted is placed in a crucible (Figure 3.10, Item 1) that rests on a stainless-steel water-cooled bottom plate that measures 0.6 m in diameter, and 0.04 m in thickness. The water-cooled bottom plate has a hole in the center, allowing the melt to drain through to the collection unit. The crucible is encircled with a cylindrical graphite susceptor (Item 2) with an outer diameter of 0.1 m, a height of 0.1 m and a 0.04 m hole machined at the base. Small granules of graphite are used to fill the empty gap between the crucible and the susceptor. A susceptor is used because the crucible material is a poor heat conductor, therefore the graphite ensures more efficient and uniform heating. The susceptor is surrounded by a 0.0127 m (0.5 in.) diameter Cu induction coil consisting of 9 coil turns, which provides sufficient coupling to the susceptor. A 0.003175 m (0.25 in.) thick ceramic fibre blanket (Kaowool 3000 supplied by Inproheat), with a continuous use temperature of 1538 °C, separates the susceptor from the coil, and the blanket is placed between each coil turn to prevent any short circuiting between neighboring coil turns. To further mitigate this issue, the copper coil is coated with an Al_2O_3 paint (Pyro-Paint 634-AL supplied by Aremco) able to withstand temperature up to 1760 °C. An insulating annulus is cut from the Kaowool 3000 and placed between the susceptor and the water-cooled bottom plate. The Cu coil is connected to a 20 kW induction furnace (Inducto 20 supplied by Inductotherm Corp., Item 8) through induction leads which provides cooling-water and an alternating current to the coil. The temperature in the crucible is monitored using a Type C thermocouple wire, sheathed in Mo with hafnia insulation (Item 10), which is protected by a 99.5% Al_2O_3 thermocouple tube, and recorded as function of time using LabVIEW. Further temperature monitoring is performed using a two-color fiber optic pyrometer (Fluke EF1RH-F2-1-0-0-03BL Endurance Fiber Optic Two Color Pyrometer supplied by ITM Instruments). The reason that both temperature measurement methods are employed is due to the poor reliability of the thermocouple at higher temperatures. The pyrometer acts as a safeguard in case the thermocouple fails during the experiment. These issues are discussed in more detail in Appendix A.

The collection unit consists of three main parts: the stopper (Figure 3.10, Item 11) and stopper rod, the collection vessel (Item 13) and load cell (Item 12), and the oxygen getter (Items

14, 15 and 16). These components will be discussed in detail is the sections to follow. Both units are enclosed by a 0.003 m thick stainless-steel shell that contains the inert atmosphere. The high-temperature apparatus also includes a vacuum pump (Speedivac supplied by Edward High Vacuum Ltd., Item 4) to evacuate the air, inlet and outlet valves for the inert gas, an oxygen monitor (Oxygen Sensor Model 2D-220 supplied by Centorr Vacuum Industries), and a safety release valve (Item 6) to ensure that the unit never exceeds a pressure of 1103 kPa (5 psig).

Before closing the shell, both the furnace and collection units must be set up according to the procedure outlined in Section 3.3.7. Most importantly, the stopper rod must be placed through the bottom of the orifice, so that the melt does not drain until the temperature is uniform throughout the crucible. After the units are set up, the shell is closed and the air in the apparatus is evacuated. Then, either He (pre-purified 99.999% supplied by Praxair) or Ar (pre-purified 99.998% supplied by Praxair) gas enters the shell until an overpressure of 34000 Pa (5 psig) is read on the pressure gauge. The oxygen monitor then analyzes the atmosphere, and if the oxygen content is above 300 ppm, the shell is evacuated and filled again. Once the oxygen content is below 300 ppm, the shell is continuously purged with He or Ar, by opening the inlet and outlet valves halfway, until the oxygen content reaches 10 ppm. Over one experiment, one cylinder containing 19 MPa of gas is consumed. At this point, the oxygen getter is turned on, and the atmosphere is gettered until the oxygen monitor reads an oxygen content below $1x10^{-8}$ ppm. Note that the gas is kept at an overpressure of 5 psig so that air is not able to enter the system. The induction furnace is then turned on, and the material heated by slowly increasing the power until the melt reaches a superheat temperature at least 300 °C above the melting or liquidus temperature. The melt is held at superheat for at least 1 hour to ensure that all the material has melted; this is especially important when melting Al which easily forms an oxide layer. Then, the furnace power is decreased until the melt temperature reaches the desired draining temperature. Once the melt temperature equilibrates at the desired draining temperature, the induction furnace is shut off, the stopper rod is manually removed, and the melt captured in a collection vessel that is attached to a load cell. All load cell data and temperature data are recorded using a LabVIEW 7.1 software. The data acquisition rate is 40 Hz. Like the calibration experiments, the load cell data is used to calculate both the flow rate of the draining metallic liquid, and the head of the metallic liquid, as a function of time. Recall that the head is calculated using the UT calibration curve. These experimental parameters are used

to calculate the surface tension, viscosity and density of a metallic liquid at a specific draining temperature.

3.3.1 Stopper

The stopper assembly consists of the plug, the rod and the locking mechanism, as illustrated in Figure 3.11.

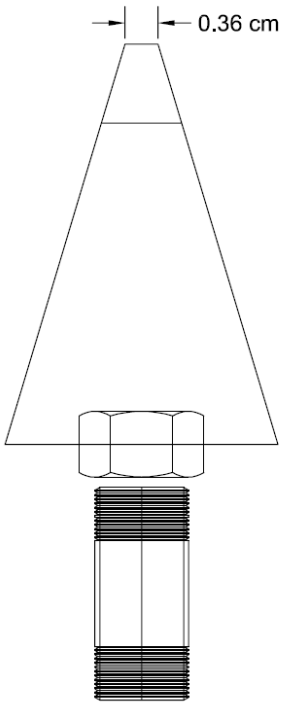

Figure 3.11: Schematic of cross-section of stopper

Since the plug is in contact with the metallic liquid over a large duration of time, it is important that it is made of material that does not react with the liquid and has a continuous use temperature above the temperature at which the metallic liquids are being tested (or superheated). Thus, the plug was custom made using a combination of castable ceramic (Ceramacast 510 supplied by Aremco), consisting of Al_2O_3 filler and a CaO-Al_2O_3 binder, and a 99.6% Al_2O_3 conical sample pan (Al-6402 Conical Shaped Sample Pan supplied by AdValue Technology). The castable ceramic was cast into a cone using a metallic mold (Tin-Plated Steel Cream Horns Set of 6 supplied by Bed, Bath and Beyond). In addition, a steel pipe cap (1/8” F-NPT 150lb Merchant Steel Pipe Cap supplied by Fastenal) was set into the base of the castable ceramic cone, which was place into

a box furnace (Hotpack Supermatec Oven, powered by a GE 5KCP 32GN28S AC Motor, with a Eurotherm Temperature Controller) to bake at 93°C for 4 hours, proceeded by a final cure at 121°C for 1 hour. The sample pan was then glued to the casted cone using a ceramic high temperature adhesive (Ceramabond 503 supplied by Aremco) which was step cured for 2 hours at 93°C, 260°C and 370°C. The plug is set and released manually with a stainless steel rod that exits the apparatus shell. The plug is connected to the rod using a stainless steel pipe nipple (1/8" x 1-1/2: Schedule 40 316 Stainless Steel Welded Pipe Nipple supplied by Fastenal) which is threaded to the steel pipe cape, casted into the plug. The castable ceramic is very brittle once cured, especially at the cone tip, therefore, a locking mechanism was designed to prevent the stopper from moving during setup. It also acts as a lock so that the stopper remains in place (i.e. secured through the orifice) during melting. Refer to Figure 3.12 for an image of the locking mechanism.

Figure 3.12: Stopper locking mechanism

3.3.2 Collection Vessel

The collection vessel initially used to capture the metallic liquid once the stopper rod released is made of stainless steel and measures 12.72 cm (5 in.) in diameter and 10.16 cm (4 in.) in height. The collection vessel was lined with Kaowool 3000 and partially filled with SiO_2 (sand) for the purpose of dissipating heat. The collection pan is tightly threaded to the LCCA-25 load

cell, which in turn is threaded to a steel platform that sits in the collection unit. The LCCA-25 load cell has a suggested maximum operating temperature of 65°C, therefore, Kaowool 3000 is placed between the load cell and collection vessel for further heat protection. It was found that at melting temperatures exceeding 1200°C, the temperature of the load cell, measured with a Type K thermocouple (KMQSS-040U-12 supplied by Omega Canada), exceeded 65°C. Thus, another collection pan was made, but with a greater height of 20.32 cm (8 in.). This would allow for more SiO_2 to be filled in the collection vessel which would result in more heat dissipation. The larger collection vessel is used for collecting metallic liquid drained at temperature above 1200°C. A schematic of both collections vessels is shown in Figure 3.13.

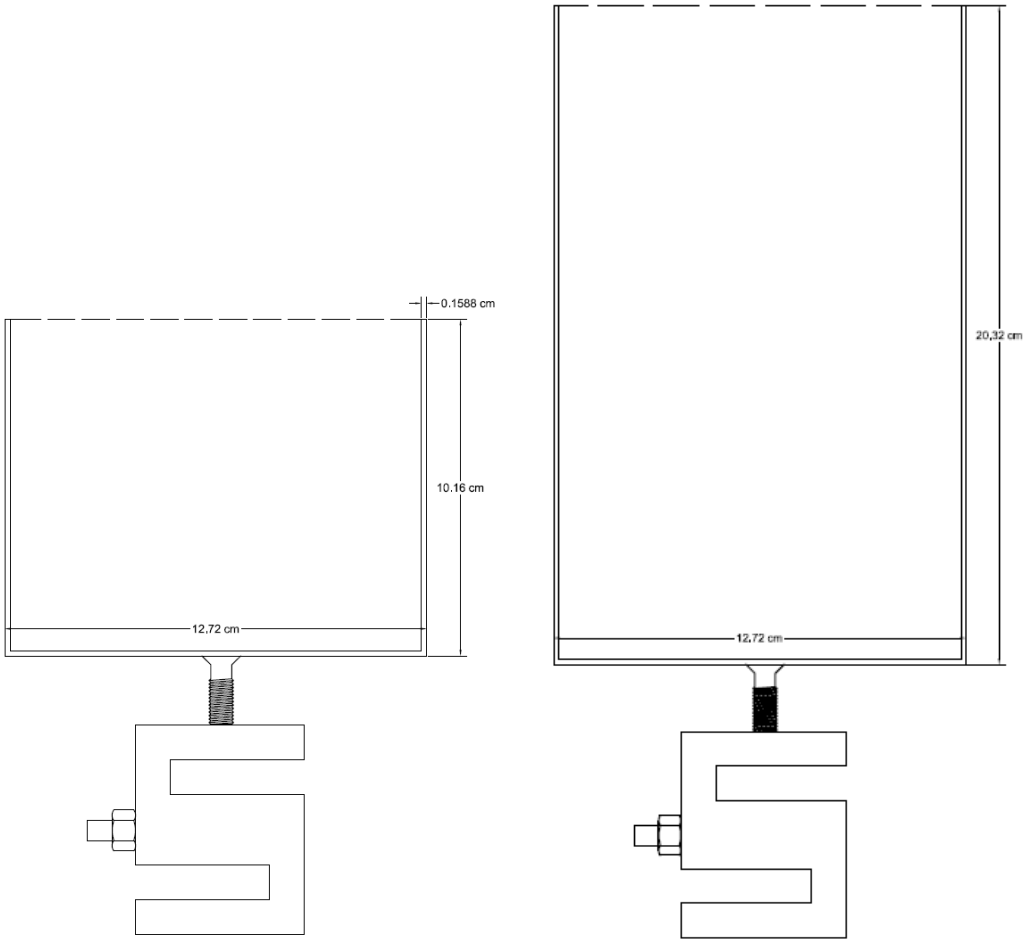

Figure 3.13: Schematic of cross-sections of the small (12.72 cm x 10.16 cm) and large (12.72 cm x 20.32 cm) collection vessels

3.3.3 Oxygen Getter

A getter is simply a reactive material that is deliberately placed inside a system for the purpose of purifying the atmosphere by scavenging oxygen. As previously discussed in Section 2.5, Al readily reacts with O to form an oxide at the surface of the sample. This can have a drastic effect on the property values measured. With a getter system in place, when O_2 gas molecules strike the getter material, they combine with it chemically or by adsorption to be removed from the environment. In this work, Ti-sponge (3-19 mm, 99.95% purity, supplied by Alfa Aesar) was used as a gettering material. When choosing a gettering material, it is key that the material will react strongly with the contaminant. This can be verified using an Ellingham diagram, and assessing the Gibb free energy of the reaction.

To promote the reaction between the Ti and O, before heating the Al sample, but after the unit has been purged and filled with inert gas, the Ti-sponge is heated using a resistance heating element (Flate Plate Without Flange Heating Element supplied by Applied Test Systems). The heating element has a maximum operating temperature of 1200 ºC, power of 575 W, and voltage of 115 V. A temperature controller (ZESTA Benchtop Controller Model ZVP11K000), connected to a Type K thermocouple and the element leads, is used to set the getter temperature. The Ti-sponge is placed in a rectangular Al_2O_3 crucible (99.6% purity, Al-3150 supplied by AdValue Technology), and insulated with insulating firebrick (JM30 supplied by Inproheat).

3.3.4 Oxygen Analyzer

The Model 2D-220 supplied by Centorr Vacuum Industries is a single phase, 220 VAC, 300 W, ZrO_2 O_2 sensor with an O_2 monitoring range of $1x10^{-15}$ to $2x10^5$ ppm. The principle behind the sensor lies with the voltaic cell that is used to measure the O_2 concentration in the gas stream being monitored. The voltaic cell is a solid electrolyte comprised of ZrO_2. At temperatures exceeding 800°C, the mobility of oxygen in the ZrO_2 is high, which allows O^{2-} ions to migrate through the electrolyte, with the driving force being a difference in concentrations. The migration of O^{2-} results in a voltage difference between the two electrodes; the concentration of O_2 in the air establishes the potential for the reference electrode, and the concentration in the sample establishes the potential in the second electrode. The magnitude of the voltage difference increases as the ratio of the O_2 concentration between the two electrodes is increased; therefore, the voltage difference

increases as the sample gas decreases in O_2 content. A high impedance electronic circuit monitors the voltage in the ZrO_2 solid electrolyte. The voltage signal can be translated to ppm using fundamentals based on the Nernst Equation. The ZrO_2 has been proven the be the most reliable oxygen sensor. It has a very long useful life, and the response of the sensor does not change over many years, thus, never requiring recalibration. The oxygen content of the high-temperature apparatus atmosphere is recorded manually through the experiment. When the furnace reaches temperatures above 350°C, the monitor should be turned off to avoid any lasting damage. Therefore, the last recorded O_2 concentration is well before the crucible is drained; however, since the shell is filled to an overpressure, and the getter remains on during the course of the experiment, it is assumed that the O_2 content remains constant throughout the run.

3.3.5 Two-color Pyrometer

The two-color pyrometer used is a Fluke EF1RH Endurance Fiber-Optic Two-Color Pyrometer supplied by ITM Instruments. It can measure temperatures ranging from 1000 - 3200°C, and has an optical resolution of 65:1, spectral response of 1.0 μm, accuracy of ±(0.3%$T_{meas.}$+2°C), repeatability of ±1°C, and response time of 10 milliseconds. The fiber-optic cable and optical head have standard temperature rating of 0 to 315°C. The pyrometer is connected to a laptop via Ethernet cable, and the temperatures of both the crucible and optical head are monitored and recorded using the Endurance software.

The two-color pyrometer consists of two one-color pyrometers in the same package. It uses two detectors, operating at two separate wavelengths, but both detectors see the same hot target. The advantages of using a two-color pyrometer over a one-color pyrometer include:

1. Ability to measure small objects (too small to fill the cone-of-vision).
2. Ability to measure when the line of sight is obscured by dust, smoke or steam.
3. Ability to measure through windows that get dirty or are difficult to clean.
4. Ability to measure targets that have changing emissivity (due to change in alloy or surface condition)

The principle of a two-color is that it relies on two detectors, having two separate wavelengths, as shown in Figure 3.14.

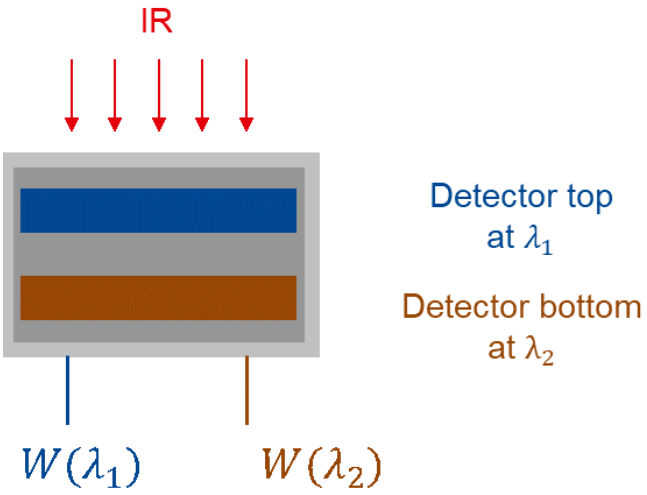

Figure 3.14: Implementation scheme for a ratio pyrometer using two detectors in a sandwhich structure [192]

The reason that that the two-color pyrometer is unaffected by dusk, smoke, steam or a dirty window is that the temperature is calibrated to a ratio of emitted energy. Consider the example in Figure 3.15: when the wavelengths, from a blackbody with a temperature of 1500°C and effective emissivity of 1.0, are detected through a clean window, λ_1 will emit an energy of 1000 units, and λ_2 an energy of 500 units.

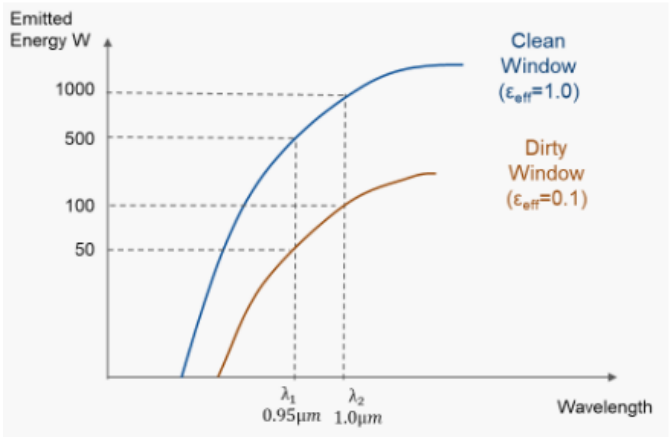

$$\frac{W_1(\lambda_1)}{W_2(\lambda_2)} = \frac{1000 \text{ energy units}}{500 \text{ energy units}} = 2 \rightarrow 1500°C$$

$$\frac{W_1(\lambda_1)}{W_2(\lambda_2)} = \frac{100 \text{ energy units}}{50 \text{ energy units}} = 2 \rightarrow 1500°C$$

Figure 3.15: Planck curves for the ratio thermometer looking with two detectors at a blackbody at a temperature of 1500 °C [192]

The ratio of the energy is then calculated and is equal 2; the instrument is calibrated in a way to read 1500°C when it sees a ratio of 2. If, the window becomes dirty, reducing the signal from the blackbody by 90% and effective emissivity to 0.1, λ_1 will only emit an energy of 100 units, and λ_2

an energy of 50 units. Now, with a one-color pyrometer, if the effective emissivity decreases, so will the temperature reading. However, with a ratio pyrometer, no matter what the effective emissivity, the ratio of 100 to 50 energy units will still yield 2, and thus, read a temperature of 1500°C. This is so, as long as the emissivity of the two wavelengths is the same. When measuring molten metals, the object emissivity is different for the two wavelengths. Thus, the signal ratio, or slope, will be incorrect and an error will occur in the temperature reading. The correct temperature and signal ratio can be confirmed using an in-situ thermocouple.

3.3.6 Metal and Alloy Selection

The Al used in these experiments was supplied by Alfa Aesar and came in the form of flattened shots. Two purities of Al were used: 99.9 wt.% for measurements of Al, and 99.99 wt.% for measurements of Al-Cu. The 99.9 wt.% Al shot measured at a diameter of 15 mm or less, while the 99.99 wt.% Al, 9.5 mm or less. The Cu shots used to make the Al-Cu alloy was also supplied by Alfa Aesar, had a purity of 99.99 wt.% and measured 13 mm in diameter. The compositions of the Alfa Aesar metals were provided from their Certificate of Analysis, and are shown in Tables 3-2, 3-3 and 3-4.

Table 3-2: Al shot, 99.9 wt.% composition

Element	Metal Basis (wt.%)	Element	Metal Basis (wt.%)
Al	> 99.92	Fe + Si	0.073
Fe	0.032	Si	0.041
Ga	0.007	Zn	0.014
V	0.002		

Table 3-3: Al shot, 99.99 wt.% composition

Element	Metal Basis (wt.%)	Element	Metal Basis (wt.%)
Al	99.99	Zn	<0.0000
Si	0.0001	V	<0.0000
Fe	0.0002	Pb	<0.0000
Cu	0.0001	Ga	<0.0000

Table 3-4: Cu shot, 99.99 wt.% composition

Element	Metal Basis (wt.%)	Element	Metal Basis (wt.%)
Cu	99.997	P	<0.0001
S	0.0003	Sn	<0.0001
Ni	ND	Pb	<0.0001
Zn	ND	As	0.0001

3.3.7 Procedure for High Temperature Experiments

3.3.7.1 Pre-Experimental Set-Up

- Fabricate stopper rod by first casting Ceramacast 510 castable ceramic with pipe cap into conical mold. Let dry at room temperature for 16 – 24 hours. Then, bake at 93°C for 3-4 hours, proceeded by a final cure at 121°C for 3 hours. After the castable ceramic has cured, glue the Al_2O_3 sample pan to tip of the cone using Ceramabond 503, and cure in box furnace at 93°C, 260°C and 370°C for 2 hours each.
- Place crucible in box furnace and let dry for 12 hours at 300°C at a heating rate of no more than 150°C/hour.
- Paint induction coil with Pyro-Paint 634-AL and let air set for 2 hours and then cure at 93°C for another 2 hours.
- Weigh both the charge and oxygen getter materials. Record in Excel sheet.

3.3.7.2 Experimental Set-Up

1. Open the furnace unit of the apparatus by unbolting 16 bolts. The shell can be raised using an overhead crane.
2. Clean crucible with compressed air.
3. Place and center crucible in the graphite susceptor. Fill the gap between the crucible and susceptor with small granules of graphite.
4. Insert a Type K thermocouple into an Al_2O_3 tube and place the tube vertically in the crucible until it is 1 to 2 mm from the bottom and roughly 1 cm to the side of the orifice so that it does not interfere with the flow characteristics of the melt exiting the crucible.
5. Connect the thermocouple to LabVIEW and test to see if it is reading properly.

6. Add the pre-weighed charge material to the crucible.
7. Place the painted Cu induction coils around the susceptor and crucible. Make sure that the coil turns do not touch each other by placing ceramic blanket inserts in between each coil turn. Also, separate the susceptor from the coil by wrapping the susceptor with ceramic blanket.
8. Place ceramic blanket annulus between susceptor and bottom plate.
9. Turn on the cooling water valve and pump to make sure that there are no leaks, especially at the Swagelok connections.
10. Install two-color pyrometer above the crucible and use pyrometer laser feature to confirm that it is pointed at the crucible.
11. Briefly turn on induction furnace by pressing the start button, followed by the on button, and slowly increased the percent power dial. Let temperature rise to 30 °C to confirm that crucible is heating and to check for short circuiting.
12. Close the top section of the apparatus. The 16 bolts need to be fastened tightly so there is no gas leakage during heating.
13. Open the bottom section of the apparatus by unbolting 16 bolts. Use overhead crane to lift furnace unit out of the way.
14. Install the getter. This includes placing an electric resistance heating element on the bottommost platform and placing an Al_2O_3 dish with a Type C thermocouple on top of the heating element. Note that the thermocouple is glued to the Al_2O_3 dish using Ceramabond 503. To further insulate the resistance heater, place the heating element on an JM30 insulating firebrick and surround with additional JM30 insulating firebricks and Denka Alcen ceramic blanket.
15. Test the oxygen getter by turning on the temperature controller and verify if the thermocouple temperature matches the set temperature. Add the pre-weighed getter material to the Al_2O_3 dish.
16. Install the load cell and collection vessel. This includes screwing the load cell on the uppermost platform and screwing the collection vessel onto the load cell.
17. Line the collection vessel with Kaowool 3000, and partially fill the vessel with SiO_2.
18. Connect the load cell the to a 9-pin connector. Calibrate load cell using LabVIEW per the procedure outlined in Section 3.2.2.

19. Align the stopper rod in the bottom of the orifice. Use locking mechanism to secure in place.
20. Close the bottom section of the apparatus.

3.3.7.3 Setting the Atmosphere

1. Switch on the power for the oxygen analyzer (it takes 15 minutes to initialize).
2. Switch on the vacuum pump and open the valves until full vacuum is obtained by reading -100 kPa on the pressure gauge.
3. Close the vacuum valve, and pump Ar or He into the apparatus until the apparatus pressure reaches 34 kPa (5 psig) and check the O_2 level. If the O_2 level is greater than 300 ppm, check for leakage, tighten nuts, then vacuum and refill again.
4. If O_2 level is less than 300 ppm, begin purging the tower in a continuous way by half opening the vacuum valve and regulating the gas flow rate (partially opening the valve) so that the pressure is held constant despite partial evacuation.
5. Continuously measure the O_2 level and stop purging when the O_2 level reaches 10 ppm. This includes closing all gas and vacuum valves and shutting off the vacuum pump.
6. Turn on the getter at a prescribed temperature and record the final oxygen level prior to shutting off the O_2 sensor. Note that the O_2 analyzer must be turned off once the crucible reaches a temperature of 300°C.

3.3.7.4 Sample Heating and Discharge

1. Turn on the data acquisition system and run program to record melt temperature and load cell data.
2. Turn on the induction furnace by switching on the auxiliary power supply and apply approximately 1 kW (power = voltage * current in induction coil) to the crucible for every 100 °C until the desired temperature is reached.
3. When the melt approaches the desired superheat temperature, turn down the induction power until the temperature remains steady. The temperature is held for 1 hour to ensure that the system is stabilized in terms of temperature and oxygen content.
4. Reduce the power of the induction furnace so that the temperature decreases from superheat to desired draining temperature. Let stabilize for 30 minutes.

5. Reset the data acquisition system and allow 60 seconds for the tare to be recorded.
6. Turn off the induction furnace when the melt is ready to pour. Induction heating induces electromagnetic forces that causes convection within the melt, which could seriously impact the dynamics of the experiment
7. Untighten locking mechanism and remove the stopper rod and wait for the melt to flow through the orifice into the collection mold.
8. The load cell and thermocouple data are recorded and saved to a USB drive. The sample rate is 40 Hz (0.025 s per data point).

3.4 Summary

The low and high temperature equipment was designed to provide minimal uncertainty for measurement of head and flow rate. This was achieved via calibration of the head versus volume in the crucible using an ultrasonic sensor and calibration of the load cell. The high temperature apparatus provides efficient control of heat using an induction furnace and of the atmosphere using multiple Ar or He purges, a Ti-sponge getter and an O_2 analyzer. Further, an Al_2O_3 crucible was used to facilitate the measurement of high melting point metals and alloys. In turn, an Al_2O_3 stopper rod was designed for compatibility with reactive and high-temperature liquids. The equipment was also designed to perform the necessary calibrations for determination of the frictional characteristics of the crucible, which along with head and flow rate, is an important parameter for the calculation of viscosity, surface tension and density using the modified-Bernoulli formulation. A major component of property measurement using the DC method is post-experiment analysis of the load-cell data. This will be discussed in detail in Chapter 4 and will include the analysis of the determination of the crucible frictional characteristics, and liquid flow rate, head, and temperature.

CHAPTER 4 RESULTS AND DISCUSSION

The viscosity, surface tension and density of Al and an Al-Cu alloy (containing 22.5 wt.% Cu) were measured using the DC method. The alloy will be frequently referred to as simply Al-Cu. The properties were determined by draining the liquid through an orifice under the influence of gravity, and then implementing a multiple non-linear regression, using the Gauss-Newton algorithm. This regression minimizes the residuals between experimentally measured head and the calculated head predicted by the modified Bernoulli formulation (described in Section 2.3). To do this, knowledge of experimental flow rate, head, orifice radius, and frictional characteristics of the crucible are required. In this section, first, the manner in which the experimental data (primarily cumulative mass) is processed (prior to performing the multiple non-linear regression) will be discussed in detail. Then, the Al and Al-Cu viscosity, surface tension and density results will be presented, and these results will be compared to experimental data published in literature (see Section 2.5) and calculated values obtained from numerical models (see Sections 2.1.1 and 2.2.3). This analysis ultimately revealed some inconsistencies between the results from this study and those published in literature, therefore, a major goal of this discussion is to determine why and examine if wetting of the liquid at the exit of the orifice is the cause.

4.1 Data Analysis

The DC method uses the Gauss-Newton algorithm to iteratively determine the values of viscosity, surface tension and density of a liquid at a specific temperature. The algorithm minimizes the sum of squares of residuals by subtracting the theoretical head, $f\left(V_{i,exp},\beta\right)$, from the experimentally measured head of the liquid inside the crucible. The theoretical head is determined using the modified Bernoulli formulation, which requires knowledge of mass flux (calculated from flow rate), radius of the orifice hole, C_d versus Re calibration curve coefficients, and the viscosity, surface tension and density of the metallic liquid. Recall:

$$f\left(V_{i,exp},\beta\right)=\frac{1}{2g}\left(\frac{V_{i,exp}}{\left(a\left(\frac{2\rho r_o V_{i,exp}}{\pi r_o^2\eta}\right)^3+b\left(\frac{2\rho r_o V_{i,exp}}{\pi r_o^2\eta}\right)^2+c(\frac{2\rho r_o V_{i,exp}}{\pi r_o^2\eta})+d\right)\rho}\right)^2+\frac{\sigma}{\rho g r_o} \quad (2.116)$$

Since the thermophysical properties are considered unknown, $f(V_{i,exp}, \beta)$ is determined iteratively by updating the three properties until they converge within a specified tolerance. Or, in other words, until the modified Bernoulli formulation adequately predicts the experimental head conditions of the system.

The following section will describe the process of measuring and calculating flow rate, head and temperature using experimental data. It will also outline how to calibrate the C_d versus Re curves, which determines the frictional characteristics of each individual crucible. Finally, since viscosity, surface tension and density are determined iteratively until they reach a specific tolerance, an analysis will be performed to confirm the rate of convergence for the Gauss-Newton algorithm. The data presented in this section corresponds to 99.9 wt.% Al measured at 1032 K. A total mass of 568 g of Al was melted and drained from a high-purity Al_2O_3 cylindrical crucible with a 5.3 mm diameter orifice at the base. Note, the same data analysis (outlined in this section) was performed for every measurement presented in Section 4.2, and this analysis is provided for all Al and Al-Cu measurements in Appendix B.

4.1.1 Calibrating Discharge Coefficient

A key variable in the theoretical calculation of head using the modified Bernoulli formulation is the polynomial relationship between C_d and Re. This curve describes the unique frictional characteristics of the orificed crucible, and thus needs to be calibrated for each individual crucible. To determine C_d as a function of Re for the specific Al_2O_3 crucible used to measure the thermophysical properties of Al at 1032 K, four individual calibration curves were calculated using experimental flow rate and head measured by draining deionized water at 298 K (see Section 3.2.3). ASTM Type II deionized water was used as the calibration fluid for all experiments conducted in this study. The thermophysical properties of water, which are required to calculate both the C_d and Re, were referenced from "Yaws' Transport Properties of Chemicals and Hydrocarbons Handbook" [2]. It should be noted that water has a very large surface tension relative to other liquids at room temperature. Thus, special care was taken to prevent wetting at the orifice (see Section 3.2.3). The challenges associated with wetting and calibrations are discussed in Appendix A. The individual calibration curves were calculated and plotted on Figure 4.1. The C_d and Re data for deionized water were computed using MATLAB, with the code given in Appendix

C. Note, each crucible is single-use only, and therefore, a brand-new crucible must be calibrated before each individual high-temperature experiment (e.g. draining of Al or Al-Cu). The curves shown in Figure 4.1 are for one specific crucible, which in this case, was used to measure the thermophysical properties of Al at 1032 K.

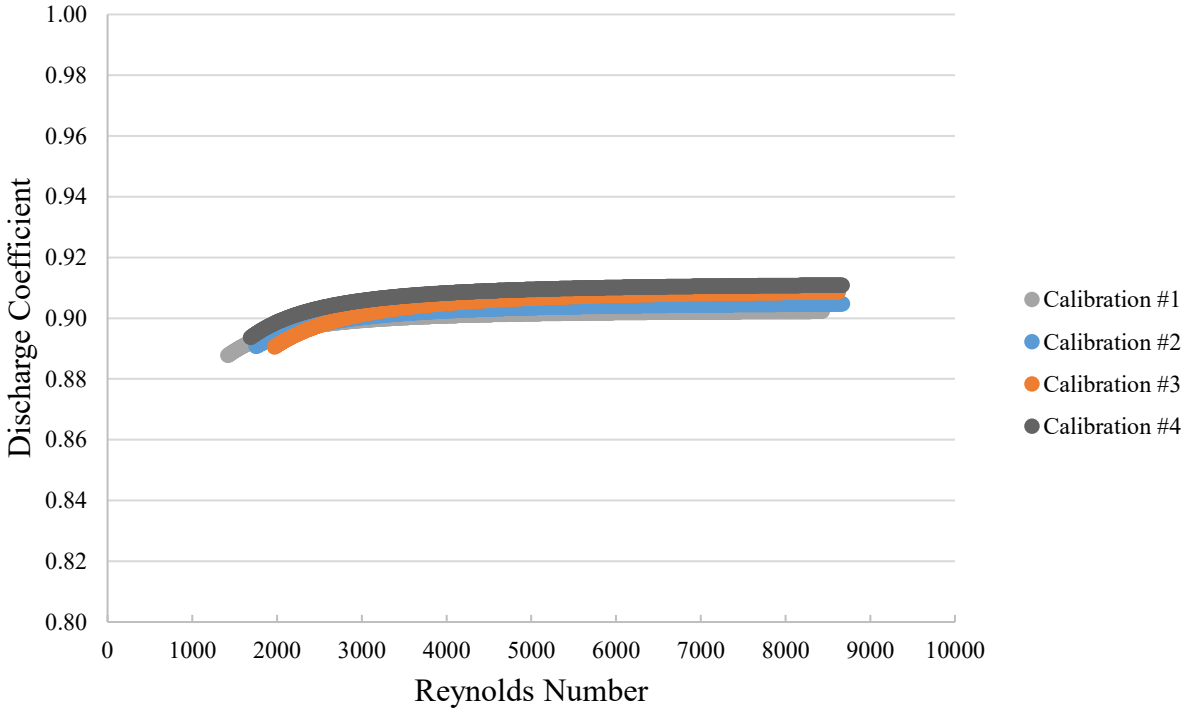

Figure 4.1: C_d versus Re calibration of Al_2O_3 crucible used for measurement of Al at 1032 K

It is clear from Figure 4.1 that there are small differences between different individual calibration curves at the same temperatures even though they are generated under identical conditions. This is a result of the propagation of systematic errors in the analytical expression of cumulative mass [7]. Consequently, the individual calibration curves were averaged and fitted together using a 3rd order polynomial fit, as shown below in Equation 4.1:

$$C_d = 1.392 \cdot 10^{-13}(Re)^3 - 2.593 \cdot 10^{-9}(Re)^2 + 1.612 \cdot 10^{-5}(Re) + 8.724 \cdot 10^{-1} \quad (4.1)$$

$$R^2 = 0.5851$$

The calibration for this specific crucible was valid for 1500 < Re < 9000. In previous studies, it was determined that a third order polynomial adequately describes the calibration data and an increasing polynomial order does not increase accuracy [16]. For the calibration data given in

Figure 4.1, a third order polynomial fit had an R^2 of 0.5851, compared to 0.4229, 0.5467 and 0.5882 when fitted to a first, second and fourth order equations, respectively.

It is also important to consider the Froude number, Fr. As discussed in Section 2.4.3.2, when Fr is equal to 1, surface tension effects (i.e. induced by Laplace pressure) should not be considered, or the classical Bernoulli formulation should be applied rather than the modified version. This effect of surface tension was also validated experimentally in Appendix D. For Al at 1032 K, Fr was predicted to range between 0.08 and 0.74, as shown in Figure 4.2. This confirmed that the modified Bernoulli formulation is appropriate in describing the liquid flow. As such, all three thermophysical properties, including surface tension, may be determined using the DC method.

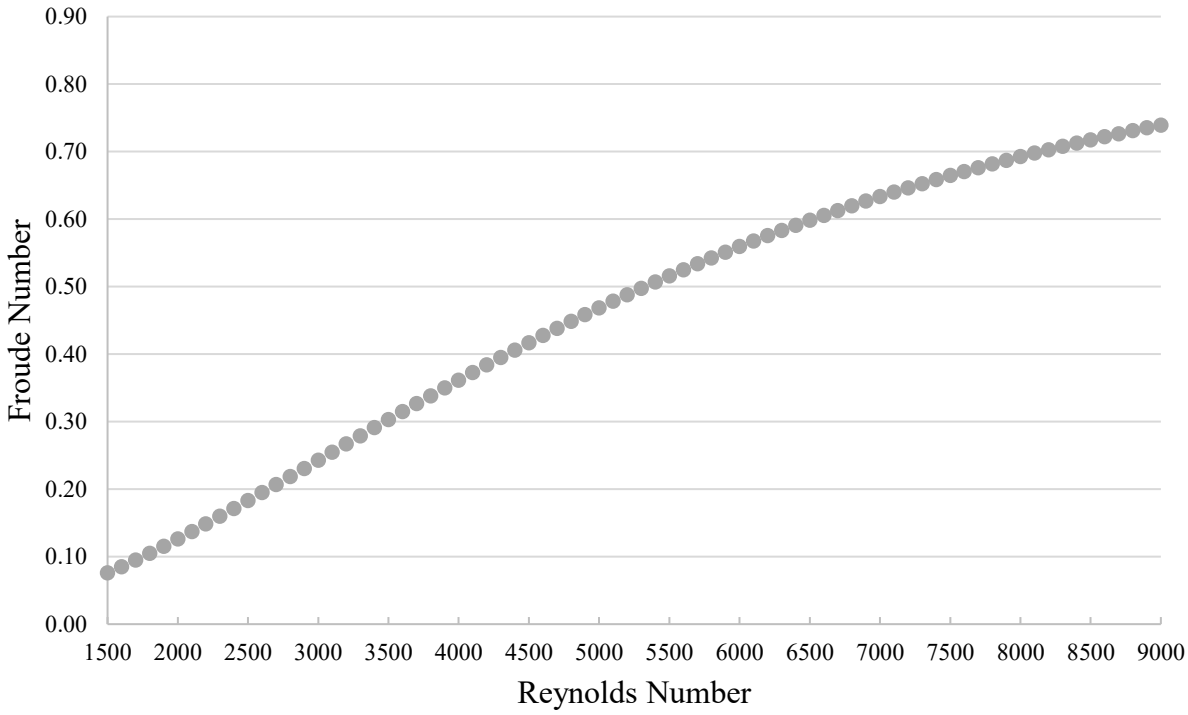

Figure 4.2: Predicted Fr of Al at 1032 K for 1500 < Re < 9000

4.1.2 Measuring Flow Rate

The mass flow rate was measured by placing a load cell beneath the melt crucible. The excitation voltage of the load cell was collected as a function of time. This process was described in Section 3.2.2. The data acquisition rate of the load cell is equal to 1 data point per 0.025 seconds.

The load was then tarred by subtracting the calculated average of the measured load (of the empty collection vessel) in the first 60 seconds of the data acquisition. Note, it is important that the load cell and collection vessel are undisturbed at the beginning of the experiment. The tared load versus time data for Al at 1032 K is shown in Figure 4.3.

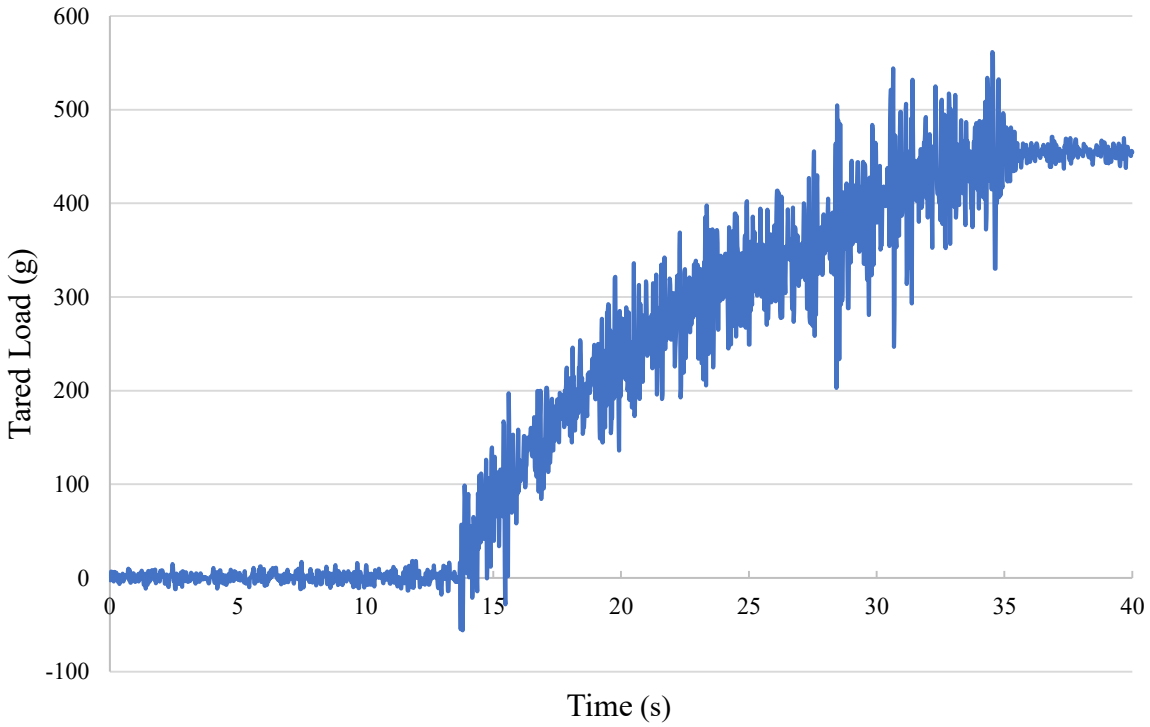

Figure 4.3: Tared output of load cell for liquid Al at 1032 K

Now, since flow rate and head are ultimately determined by curve fitting the load versus time curve, the back end of the curve (i.e. once continuous flow ends) and the front end of the curve (i.e. prior to draining) must be trimmed. The point at which continuous (or free stream) flow stops can be qualitatively pinpointed based on the evident decrease in load cell noise; in Figure 4.3, this occurs at approximately 35 seconds. All data recorded after this point was removed prior to conducting further analysis. Note, the scatter registered by the load cell was primarily created by the turbulent impact of the stream on the collection vessel. This issue is further exacerbated by the fact that the load cell needs to be placed at a minimum distance from the crucible to prevent overheating. Another source of scatter was the transfer of vibrations from the induction power supply via the induction coil leads. These issues are further discussed further in Appendix A. An additional 1 second was trimmed from the end of the time series to ensure that the data does not

include dripping (recall the assumption that the flow must be quasi-steady state). To accurately determine the time when draining (or more accurately, collection) begins, the data was smoothed using the Savitzky-Golay (second order polynomial) filter in the MATLAB Curve Fitting Toolbox, which is described in Appendix E. As previously mentioned, scatter observed in the dataset originates from the turbulent impact of the metallic liquid stream on the collection vessel. The scatter is not a reflection of the method, but rather the sensitivity of the load cell, and therefore should not be the focus of the analysis. To illustrate the impact load scatter has on the reported "accuracy" of the property measurements, see the example of the calculated error for surface tension of Al at 1032 K determined before and after the data is smoothed using the Savitzky-Golay filter, which is shown in Figure 4.4.

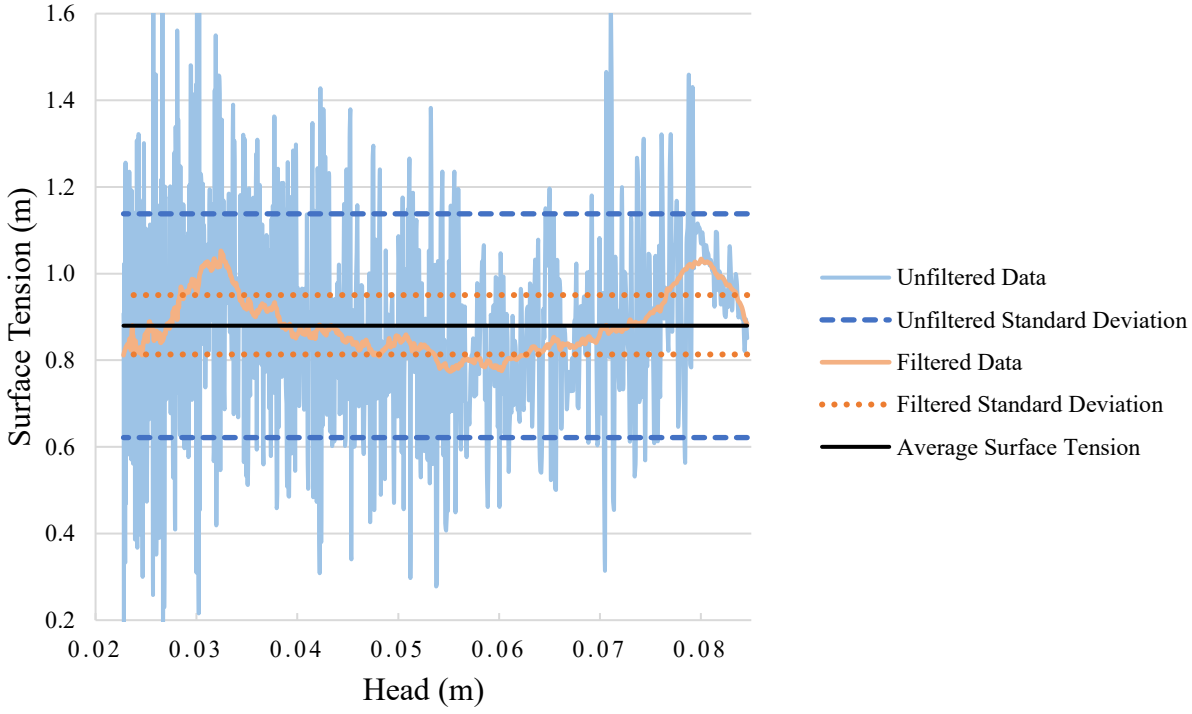

Figure 4.4: The experimental surface tension determined for Al at 1032 K with standard deviations calculated using and filtered (smoothed) and unfiltered load cell data

Here, the mean or average the surface tension measurements gives the measured surface tension result and the standard deviation is the measurement error. The large scatter from the unprocessed data results in a large standard deviation (or measurement error) of ±0.258 N/m (29%). This is not a good representation of the actual error in property measurement; rather, the standard deviation of ±0.069 N/m calculated using filtered data is a far more reasonable estimate

and more consistent with prior DC studies. The Savitzky-Golay filter was chosen because the loss and/or distortion of vital information is comparatively less than other filters, like the moving-average filter. A frame length of 95 data points was selected based on an analysis conducted in Appendix E. Both the filtered and unfiltered load for Al at 1032 K are shown in Figure 4.5.

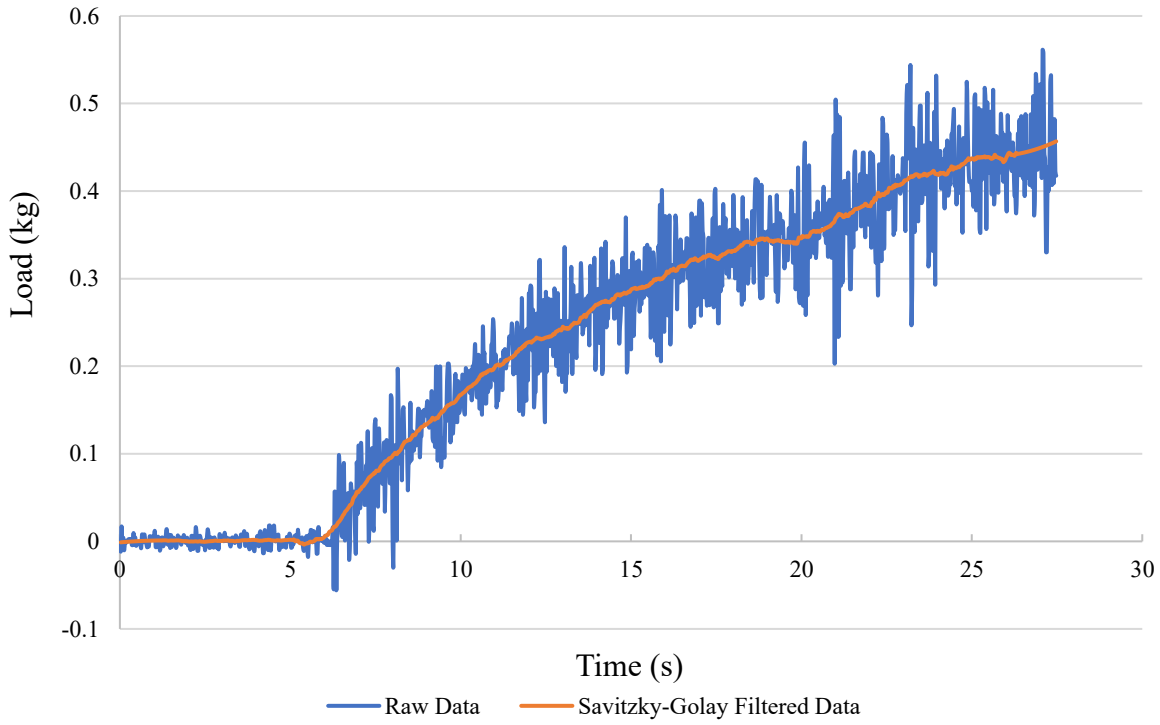

Figure 4.5: Filtered and unfiltered cumulative mass versus time of Al at 1032 K

Once smoothed using the Savitzky-Golay filter, a second order polynomial was fitted to the tared load versus time data. This was performed using MATLAB, with the code provided in Appendix F. Then, the beginning (or front-end) of the data was trimmed until the fitted equation had an intercept near zero (specifically < 0.001 kg or 1 g); this was performed iteratively using MATLAB (see Appendix F). In reality, the cumulative mass polynomial should have a zero intercept since liquid has yet to contact the collection vessel. Figure 4.6 shows the cumulative mass data of liquid Al drained at 1032 K before and after trimming the beginning of the time series.

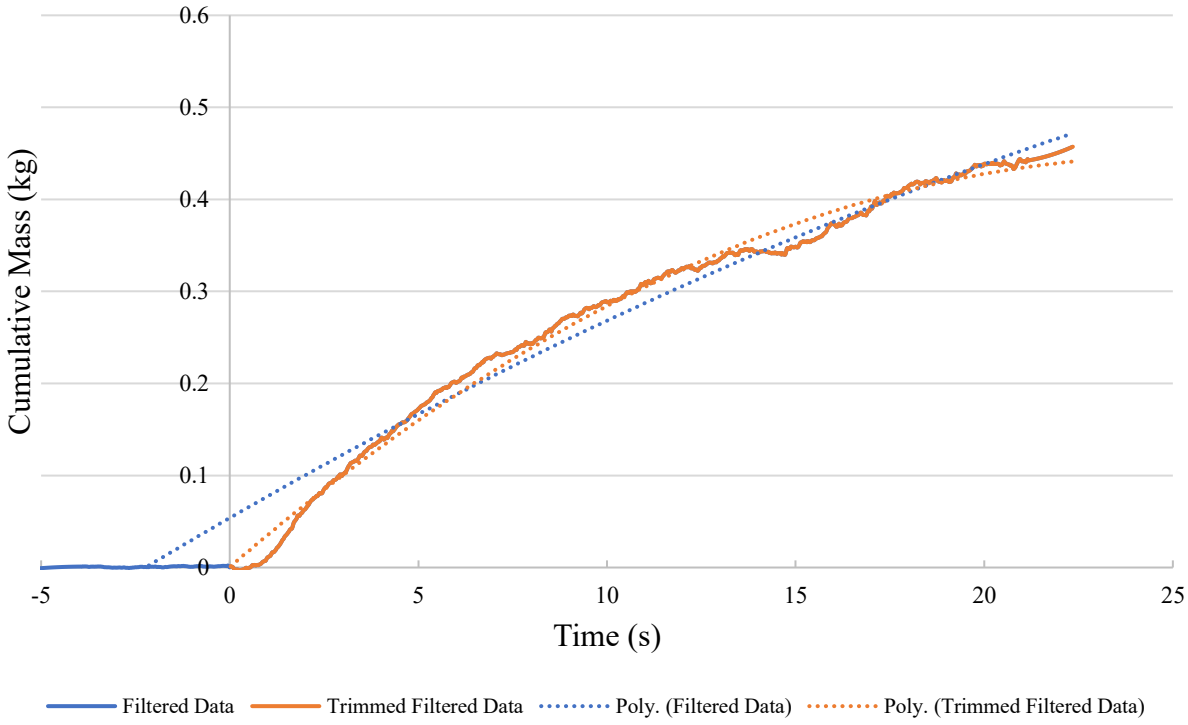

Figure 4.6: Filtered cumulative mass of Al at 1032 K trimmed so that y-intercept is near zero

A linear least-squares model (with an intercept near zero) was fitted to the trimmed, filtered cumulative mass data yielding a second order polynomial function that describes the fitted cumulative mass, $C_{m,poly}$ (kg), versus time, t (s). The function for Al at 1032 K is provided below, and shown in Figure 4.7:

$$C_{m,poly}(filtered) = -7.0 \cdot 10^{-4}(t)^2 + 3.5 \cdot 10^{-2}(t) + 4.8 \cdot 10^{-4} \quad \text{(kg)}$$
$$R^2 = 0.99 \tag{4.2}$$

The mass flow rate, $\dot{m}$ (kg/s), was calculated by differentiating Equation 4.2:

$$\dot{m} = \frac{d(C_{m,poly})}{dt} = -1.4 \cdot 10^{-3}(t) + 3.5 \cdot 10^{-2} \quad \text{(kg/s)} \tag{4.3}$$

The mass flow rate, $\dot{m}$ (kg/s), at each timestep was converted to volumetric flow rate, Q_{exp} (m^3/s), by dividing with an assumed density, ρ (kg/m^3), of the Al:

$$Q_{exp} = \frac{\dot{m}}{\rho} \tag{4.4}$$

Note, the density of the liquid Al was obtained from published values reported in a comprehensive review by Assael *et al.* [6]. Alternatively, since density is considered unknown, the mass flux, V_{exp} (kg/s·m^2), can be obtained by dividing Equation 4.4 by the cross-sectional area of the orifice, where r_o (m) is the radius of the orifice:

$$V_{exp} = \frac{\rho Q_{exp}}{\pi r_o^2} \tag{4.5}$$

This quantity was eventually used in Equation 2.116, described in Section 2.4.3.1, which was then used as an input parameter for the multiple non-linear regression analysis which calculates the unknown viscosity, surface tension and density values of, in this case, liquid Al at 1032 K. This regression analysis was performed using MATLAB, as seen in Appendix F.

A concern related to using the Savitzky-Golay filter is that the data smoothing has an effect on the relationship between load and time, and that the calculated flow rate does not accurately represent the actual flow rate of the system. To investigate, a second order polynomial was fitted to the raw (or un-filtered) load versus time series, and compared to the polynomial equation calculated from the filtered dataset:

$$C_{m,poly}(filtered) = -7.0 \cdot 10^{-4}(t)^2 + 3.5 \cdot 10^{-2}(t) + 4.8 \cdot 10^{-4} \quad \text{(kg)} \tag{4.2}$$

$$R^2 = 0.99$$

$$C_{m,poly}(raw) = -7.0 \cdot 10^{-4}(t)^2 + 3.5 \cdot 10^{-2}(t) + 6.2 \cdot 10^{-4} \quad \text{(kg)} \tag{4.6}$$

$$R^2 = 0.89$$

Equations 4.2 and 4.6 show that the first and second terms of both polynomials are identical, and the intercepts are only slightly different (less than 0.03% of the initial total Al charge). Both curves are presented in Figure 4.7. This adequately demonstrates that data filtering has little impact on the measured flow rate of the draining liquid and is only used to facilitate data trimming and error calculation.

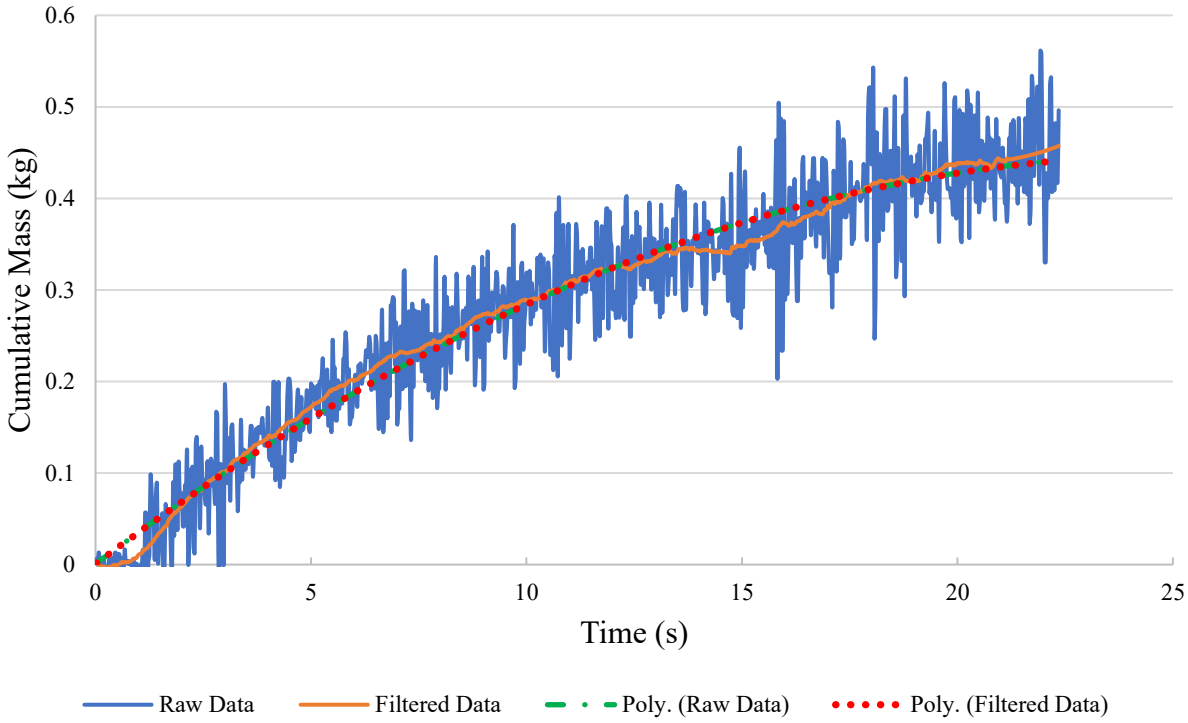

Figure 4.7: Cumulative mass of Al at 1032 K with fitted polynomial to raw data and filtered data

4.1.3 Measuring Head

In this study, the crucibles, made of high-density Al_2O_3, are opaque, meaning direct visual observations of head are not possible. Also, unlike experiments using graphite crucibles (conducted by Roach and Henein [7]), the head of the draining liquid cannot be determined by simply relating mass to the volume of a cylinder. Al_2O_3 was selected because it is an extremely stable compound, even at elevated temperatures. However, unlike graphite, Al_2O_3 cannot be precisely machined; it is highly brittle and needs to be cast or hot-isostatically pressed. The crucibles used in this study were cast, which often lead to geometrical issues. For example, the crucibles purchased from CoorsTek had specified tolerances on the inner diameter of ±1.6 mm and straightness of ±0.07 mm per 25.4 mm of height (the height of the crucible is approximately 17 cm), therefore, potential total deviations in straightness of nearly ±12 mm (0.5 in.) are conceivable. To add, there is the possibility of added geometrical issues, like an uneven base, dents, localized shrinkage etc. So, an ultrasonic level sensor was used to determine the relationships between the liquid head in the crucible and the volume of the liquid. Regrettably, the ultrasonic sensor cannot be used in-situ during the experiment, but rather, only to determine a calibration curve prior to

measuring the high-temperature liquid. The reason for this is that the sensor would need to be placed directly above the crucible, and the temperature of the atmosphere exceeds the maximum operating temperature of the device, which is 70 ºC.

An example of the head calibration curve for the crucible used to measure Al at 1032 K is given in Figure 4.8. The curve was obtained by plotting the ultrasonic measured head of water (at a specific temperature) versus the calculated volume of the water (based on mass and density) contained in the specific crucible prior to being used for high temperature measurements. This procedure is given in detail in Section 3.2.1. Recall that crucibles are not reusable and must be calibrated before each individual high-temperature measurement. A linear trendline was fitted to the data to relate the calibrated head, h_{cal} (m), to any liquid volume, V (m^3), in the crucible:

$$h_{cal} = 3.320x10^2(V) + 4.312x10^{-3} \quad \text{(m)}$$
$$R^2 = 0.9998 \tag{4.7}$$

To justify the use of the ultrasonic sensor to determine the head of the liquid inside the crucible, theoretical head, h_{theo} (m), was calculated using the volume of a cylinder equation (i.e. $h = \left(V/\pi\left(\frac{D}{2}\right)^2\right) + h_{base}$) where D (m) is the diameter of the crucible and h_{base} (m) is the height of the base plate of the crucible:

$$h_{theo} = 3.158x10^2(V) + 6.400x10^{-3} \quad \text{(m)}$$
$$R^2 = 1 \tag{4.8}$$

The head values calculated in Equations 4.7 and 4.8 were plotted in Figure 4.8, highlighting the difference and possible inaccuracies inherent when assuming that the head of the liquid can be calculated using the specified dimensions of the crucible.

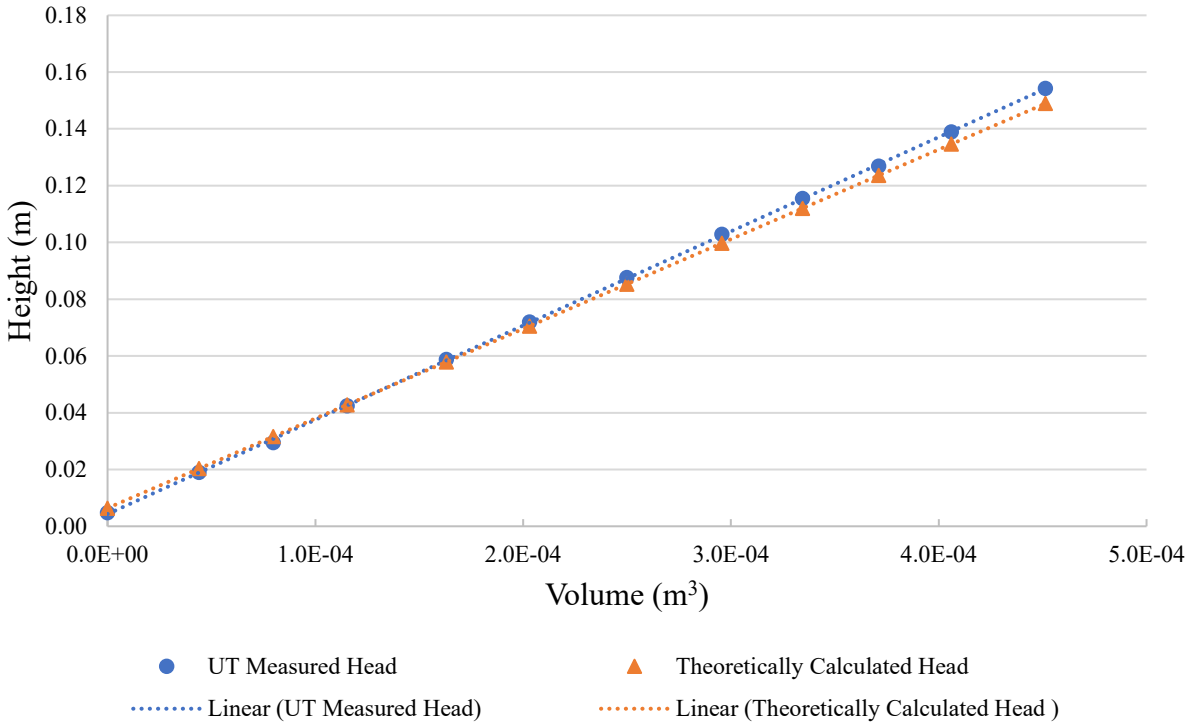

Figure 4.8: Head versus volume of crucible used to measure properties of Al at 1032 K

To determine the experimental head, h_{exp} (m^3), of Al at 1032 K as a function of time, first the liquid volume poured, V_{poured} (m^3), from the crucible was determined:

$$V_{poured} = \frac{C_{m,poly}}{\rho} \tag{4.9}$$

Where ρ (kg/m^3) is the density of the liquid Al obtained from published values reported by Assael *et al.* [193]. The liquid volume left, V_{left} (m^3), in the crucible was determined by subtracting the initial liquid volume, $V_{initial}$ (m^3), by V_{poured}:

$$V_{left} = V_{initial} - V_{poured} \tag{4.10}$$

Where,

$$V_{initial} = \frac{m_0}{\rho} \tag{4.11}$$

And m_0 (kg) is the initial mass of the liquid in the crucible. In this particular example (i.e. Al at 1032 K) h_{exp} as a function of V_{left} (or as a function of time) was determined using the calibration curve given by Equation 4.7:

$$h_{exp} = 3.320x10^{2}\left(V_{left}\right) + 4.312x10^{-3} \tag{4.12}$$

The results calculated in Equation 4.12 were plotted as a function of time and shown in Figure 4.9. An obvious paradox exists in using a density value published in literature to calculate experimental head, although, prior studies have indicated that this method yields accurate results [7], [77]. However, possibilities for advancement in building an apparatus capable of directly measuring of head of the liquid are certainly feasible.

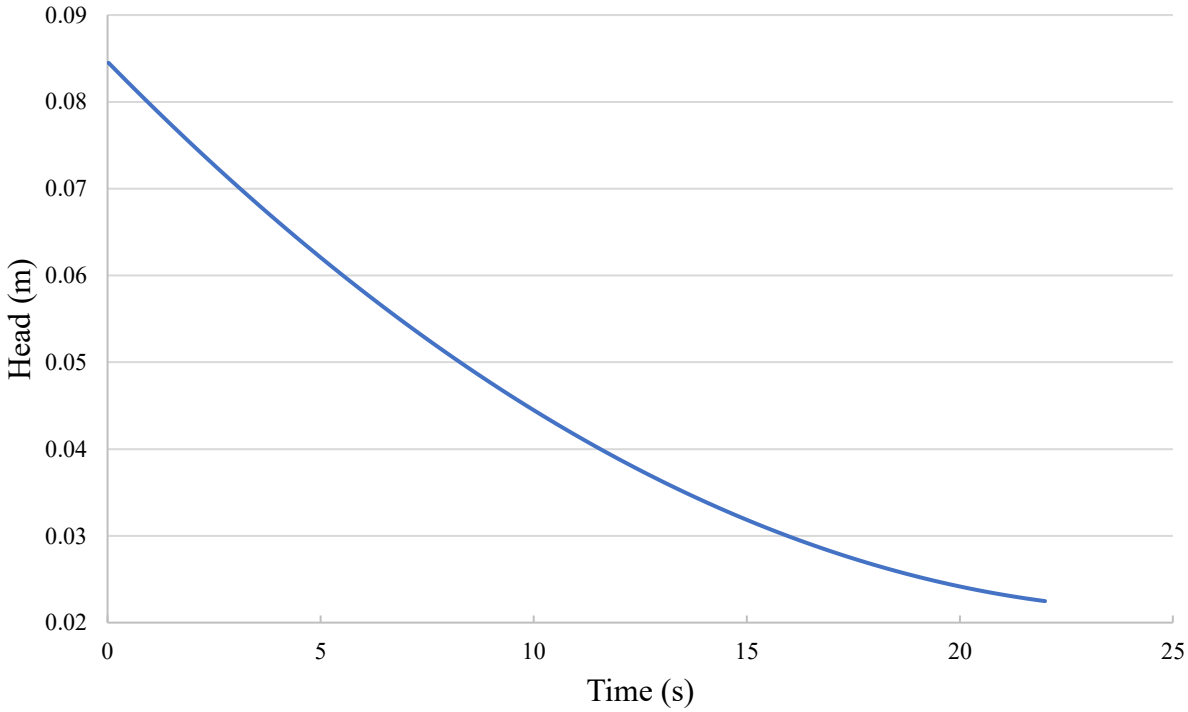

Figure 4.9: Experimental head of Al at 1032 K

4.1.4 Measuring Temperature

The temperature of the liquid Al was measured using a Type C thermocouple and recorded in LabVIEW. Additional monitoring of temperature was also performed using a two-color

pyrometer. Over the course of the 22 seconds in which the liquid Al drained, the temperature decreased from 1032 K to 1028 K, as shown in Figure 4.10.

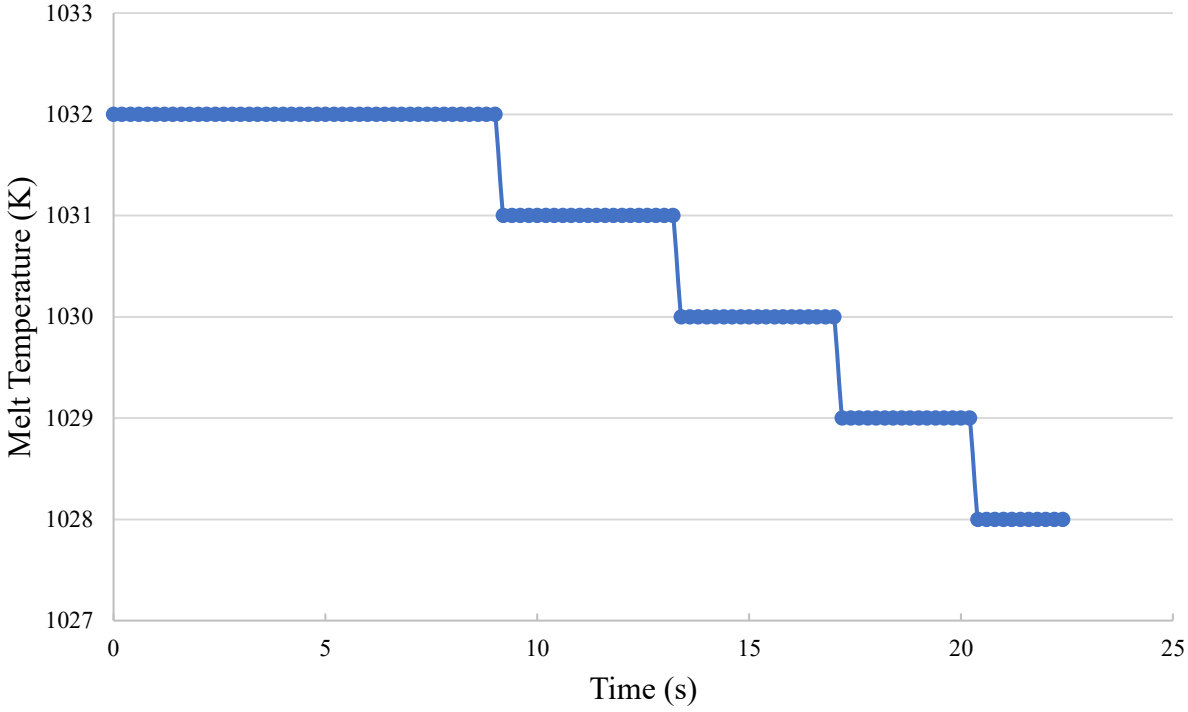

Figure 4.10: Recorded melt temperature during the draining of liquid Al at an initial drain temperature of 1032 K

A major assumption in the modified Bernoulli formulation is that the temperature of the metallic liquid remains constant over the course of the experiment (i.e. as the liquid drains). Typically, however, the temperature of the metallic liquid will slightly decrease by roughly 5 degrees. It is assumed that this change in temperature is negligible, and that the thermophysical properties of the metallic liquid remain essentially constant. This is further proven in the analysis conducted in Table 4-1. Here, the difference between viscosity, surface tension and density at 1032 and 1028 K is 0.90%, 0.12% and 0.04% respectively. This observed difference is considered negligible, and is in fact well within the measurement error, or accuracy, of the DC setup.

Table 4-1: Difference between thermophysical properties of Al at 1028 K versus 1032 K

	Temperature		% Difference
	1032 K	1028 K	
Viscosity (Pa·s)	1.11×10^{-3}	1.12×10^{-3}	0.90%
Surface Tension (N/m)	0.857	0.858	0.12%
Density (kg/m^3)	2347	2348	0.04%

This conclusion is valid for experiments conducted at temperatures below 1000ºC, for materials such as Al and Al-Cu. But, for measurement of higher melting point liquids, such as Fe, there is a larger temperature drop from the start to the end of the experiment, and the intrinsic change in property values must be accounted for. A modified DC model was developed to account for significant temperature losses and is presented in Appendix G. The viscosity, surface tension and density of the liquid can be calculated as a function of temperature using MATLAB, with the code provided in Appendix H. This model may be useful in future studies that use the DC method at higher temperatures, to measure high melting point liquids.

4.1.5 Gauss-Newton Convergence Analysis

A convergence analysis was performed on the Gauss-Newton model (described in Section 2.4.3.3) used to calculate the surface tension, viscosity and density of Al at 1032 K. The Gauss-Newton regression was executed using code written in MATLAB, provided in Appendix F. This method is used to solve non-linear least squares problems and consists of an algorithm that iteratively finds the value of the variables that minimizes the sum of squares of the residuals (described in Section 2.4.3.3). The residuals are linearized using a first order Taylor series expansion, and the viscosity, surface tension and density are determined iteratively using the Gauss-Newton algorithm. Plots of the mean square error of the residuals, $r_i(\beta)$, and viscosity of Al at 1032 K versus iteration count are given in Figures 4.11 and 4.12, respectively. This analysis reveals that the regression converges rapidly, i.e. within 9 iterations, with the surface tension, viscosity and density guesses of 1 N/m, 0.001 Pa·s, and 2500 kg/m^3, respectively. Note the convergence criterion is 1×10^{-10}.

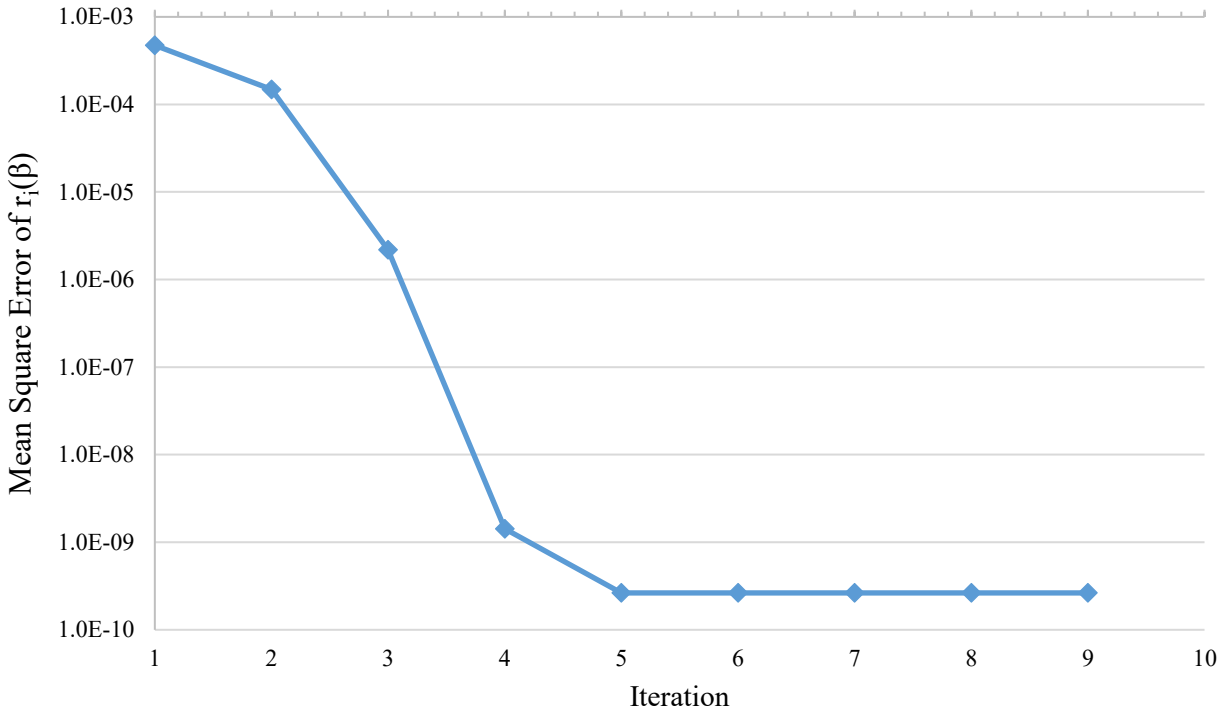

Figure 4.11: Mean square error of residuals of Al at 1032 K as a function of iteration count

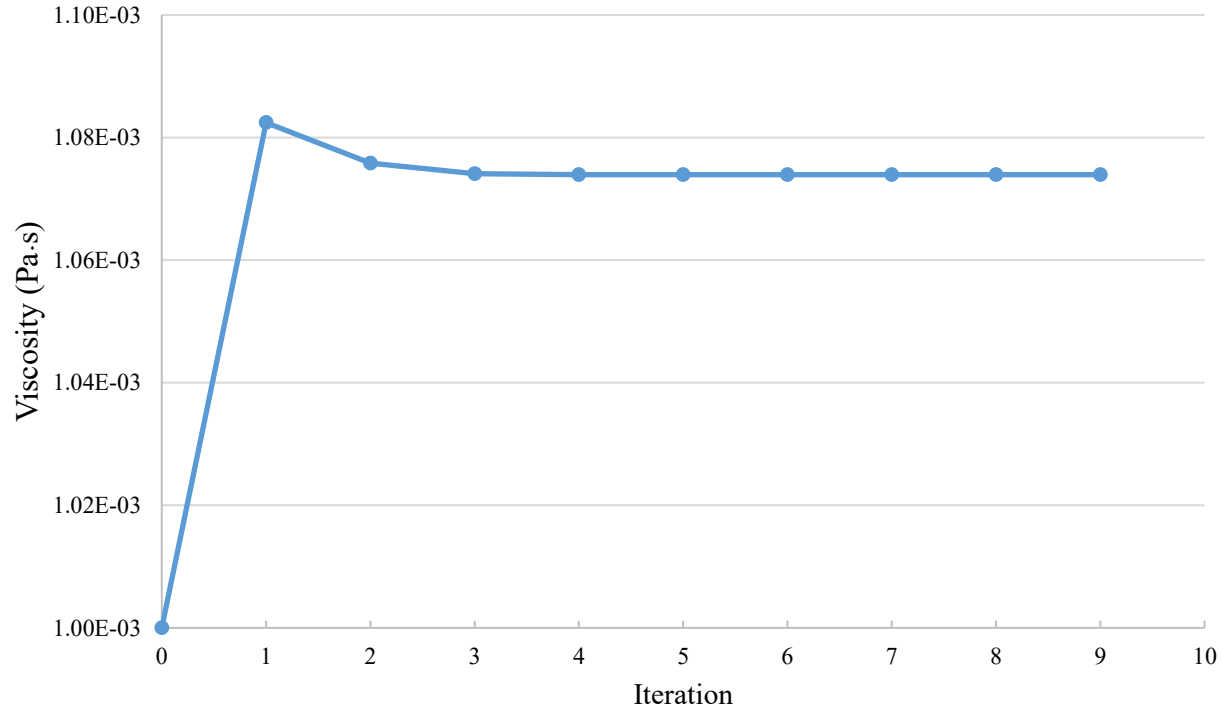

Figure 4.12: Viscosity of Al at 1032 K as a function of iteration count; initial guess of 0.001 Pa·s

There appears to be a distinct local minimum, which would suggest that there are unique solutions to the calculation (i.e. there is one set of properties that best minimize the residuals). Nevertheless, recall that this is a local statement, so if the guesses are far away from the local minimum, the regression might not converge, or might converge to a different local minimum. An example of this is shown in Figure 4.13, which shows the viscosity versus iteration count when the initial viscosity guess for Al at 1032 K is increased to 0.005 Pa·s .

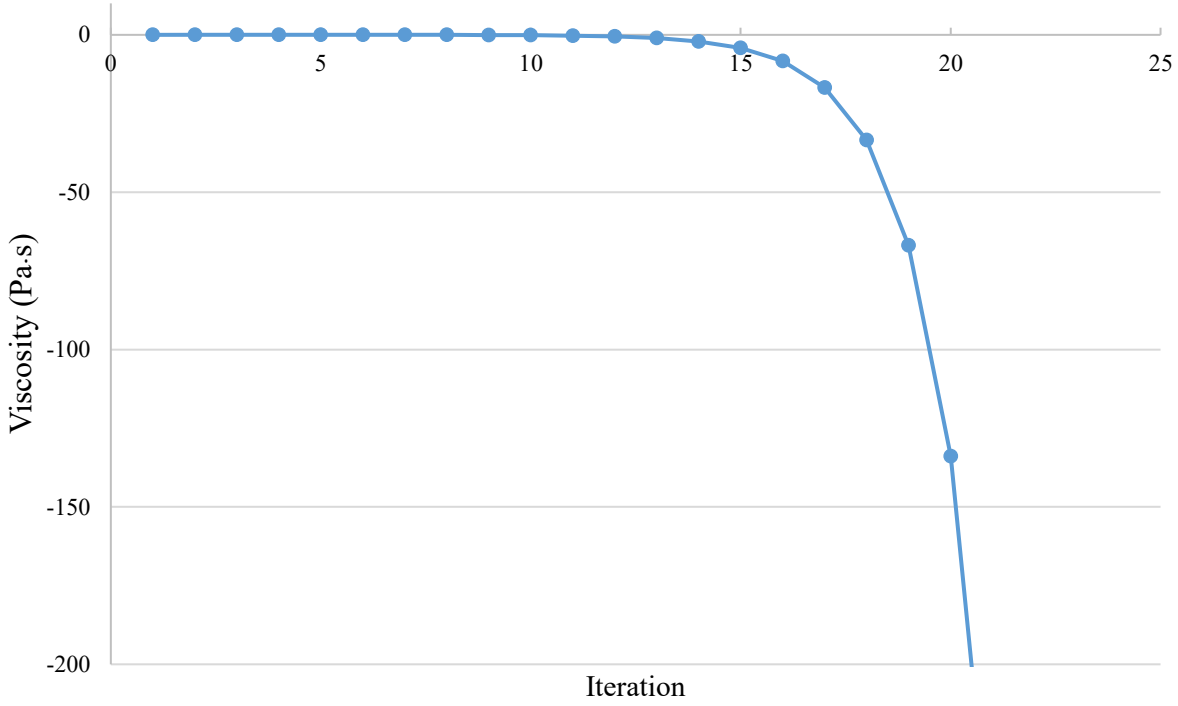

Figure 4.13: Viscosity of Al at 1032 K as a function of iteration count; initial guess of 0.0025 Pa·s

Figure 4.13 reveals that if the initial viscosity guess is not close enough to the local minimum, the viscosity will simply decrease with each iteration until the script times out (i.e. iteration reaches maximum set iteration count defined by the user). Note, a similar phenomenon occurred when the initial viscosity guess was set to 0.00004 Pa·s. Consequently, it important to have a reasonable prediction of actual surface tension, viscosity and density values to be used for initial guesses. For unknown liquids, there are theoretical or empirical models that provide good estimations of the properties of interest, which can be used to determine reasonable initial guesses. These models will be discussed further in Section 4.3 and were previously outlined in Sections

2.1.2 and 2.2.3. Otherwise, different initial guesses may be made by trial and error until they yield reasonable predictions when compared to literature.

4.2 Experimental Results

Thermophysical property measurements using the DC method at various temperatures were conducted on 99.9 wt.% Al as well as an Al-Cu alloy with a composition of 77.5 wt.% Al and 22.5 wt.% Cu. Experiments on Al were performed at 1032, 1120 and 1174 K. Previously, Roach and Henein [7] and Gancarz *et al.* [8] measured Al using the DC method [7], [8], so the main goal of these experiments was to validate the current experimental setup. It was also a useful exercise in testing the consistency and reproducibility of the DC method when performed by different users. There are four significant experimental differences between the Al experiments conducted in this study and the experiments conducted by Roach and Henein [7] and Gancarz *et al.* [8]*:*

1. The head is determined using a calibration obtained with an UT level sensor
2. The crucible is made of high-purity Al_2O_3 as opposed to graphite.
3. The purity of Al used is 99.9 wt.%, whereas as Gancarz *et al.* [8] measures Al with a purity of 99.999 wt.%.
4. The O_2 content in the atmosphere in this study is reduced using an Ti-sponge getter, resulting in a concentration of less than $1x10^{-8}$ ppm, versus 20 ppm [7] and 1 ppm [8]. Despite the reduction of oxygen partial pressure, the liquid was found to be O saturated.

Measurements were also performed on an Al-Cu alloy at 1029, 1076, 1123, 1180 and 1174 K. The composition of the Al-Cu alloy was 77.5 wt.% Al and 22.5 wt.% Cu, which is equivalent to 89 at.% Al and 11 at.% Cu. The alloy consisted of 99.99 wt.% Al and 99.99 wt.% Cu shots. This alloy was chosen because it is also currently being measured onboard the ISS with EML-LD. Once these results are made public, this study will facilitate the comparison between two different measurement techniques able to simultaneously measure the viscosity, surface tension and density of metallic liquids. All the results from these experiments will be discussed below.

The measurements for surface tension, viscosity and density of Al and Al-Cu are presented in Table 4-2. The minimum measured O_2 content, initial charge mass, and start and end heads are also all shown in the Table 4-2. The results were determined using a Gauss-Newton multiple non-

linear regression, which is performed using MATLAB, and the code is provided in Appendix F. Each experiment required a single crucible, and separate C_d calibration curves were obtained for each crucible using deionized water. On average, Re ranged between $1500 < Re < 9000$ for Al and $1500 < Re < 14000$ for Al-Cu. The calibrations curves for Al and Al-Cu experiments were determined using water at 298 K and/or 320 K. The radii of each orifice were determined prior to beginning the experiment and all measured 2.65 mm.

Table 4-2: Viscosity, surface tension and density of Al and Al-Cu determined experimentally at various temperatures using the DC method

Melt Material	Mass (kg)	Temperature (K)	O_2 Content (ppm)	Start Head (cm)	End Head (cm)	Viscosity (Pa·s)	Surface Tension (N/m)	Density (kg/m^3)
Al	0.568	1032	$1x10^{-8}$	8.45	2.25	$1.07x10^{-3}$	0.881	1588
Al	0.600	1120	$4x10^{-10}$	8.31	1.87	$8.62x10^{-4}$	0.859	1994
Al	0.544	1174	$2x10^{-9}$	8.24	1.98	$1.10x10^{-3}$	0.847	1804
Al-Cu	0.665	1029	$3x10^{-9}$	8.12	1.47	$1.66x10^{-3}$	0.877	2357
Al-Cu	0.600	1076	$1x10^{-9}$	7.32	1.55	$1.64x10^{-3}$	0.867	2433
Al-Cu	0.600	1123	$2x10^{-9}$	7.37	1.71	$9.32x10^{-4}$	0.842	2121
Al-Cu	0.671	1180	$8x10^{-10}$	8.14	1.84	$9.66x10^{-4}$	0.824	2133
Al-Cu	0.586	1224	$4x10^{-10}$	7.57	1.40	$7.24x10^{-4}$	0.808	2529

To facilitate the comparison between the experimental results reported in Table 4-2 and comparable data published in literature reviewed in Section 2.5, the thermophysical property (i.e. viscosity, surface tension and density) measurements reported in literature as a function of temperature were elaborated by a simple linear regression performed using the Fit Regression Model in Minitab 19 Statistical Software. Note, viscosity data was fitted to a linearly transformed Arrhenius equation using natural logarithms. The regression analysis was also performed on the measured experimental results to determine the temperature dependencies of the measurements

and to estimate the measurement error for the DC experiments. The regression equation parameters, temperature ranges and standard errors (SE) are given below in Tables 4-3, 4-4 and 4-5 for viscosity, surface tension and density, respectively. This includes the regression parameters for both fitted Al and Al-Cu combined literature data and experimental results provided in Table 4-2. Note, the full Minitab regression outputs for viscosity, surface tension and density are provided in Appendix I.

The standard error of the regression (SE) represents the average distance that the observed values fall from the regression line (e.g. SE becomes smaller when the data points are closer to the regression line). It is calculated from the mean square error (MSE) of the regression:

$$\mathrm{SE} = \sqrt{MSE} \tag{4.13}$$

Where,

$$\mathrm{MSE} = \frac{\sum\left(Y_i - \widehat{Y}_i\right)^2}{(N - P - 1)} \tag{4.14}$$

Y_i is the i[th] observed response value, $\widehat{Y}_i$ is the i[th] fitted response, N is the number of number of observations, and P is the number of coefficients in the model, not including the constant. This statistic provides an overall measure on how well the model fits the data and is also useful in determining whether the experimental results measured in this study fit the regression model on average as close as the literature data used to fit the model. Visually, this will be shown by plotting $\widehat{Y}_i$ with SE intervals (e.g. $\widehat{Y}_i \pm$ SE).

An additional statistic that will be used to determine the consistency between the measured results and published literature data is the 95% prediction interval (PI). This measure defines the range that is likely to contain the response value of a single new observation given specified settings of the predictors in the regression model. In other words, we can expect that 95% of the time, the next data point sampled will fall within the 95% PI of the regression model. Also, approximately 95% of the observations used to create the regression fit should fall within these bounds. The 95% PI is calculated as follows:

$$\widehat{Y}_0 = t_{(1-\alpha/1,\ N-P)} \cdot \sqrt{MSE}\left(1 + \boldsymbol{X_0'}(\boldsymbol{X'X})^{-1}\boldsymbol{X_0}\right) \tag{4.15}$$

Where $\widehat{Y_0}$ is the fitted response value for a given set of predictor values, t is the t-score, α is the level of significant (0.05 for 95% PI), $\boldsymbol{X}$ is the predictor matrix, and $\boldsymbol{X_0}$ is the matrix of given predictor values. The 95% PI (i.e. $\widehat{Y_i} \pm \widehat{Y_0}$) will be used to determine the consistency between the experimental results listed in Table 4-2 and comparable data published in literature (e.g. if the measured viscosity results fall within the 95% PI, they are, at a minimum, within the range at which the literature data regression model is able predict viscosity as a function of temperature at a 95% confidence).

4.2.1 Viscosity Measurements

The Al and Al-Cu measurements were plotted alongside comparable viscosity data (i.e. similar composition) published in literature in Figure 4.14 and Figure 4.15, respectively. The literature sources were previously summarized in Section 2.5. As stated above, the combined literature data were also fitted to a linearized Arrhenius equation (for both Al and Al-Cu) by performing a linear regression in Minitab 19, with the summarized regression output given in Table 4-3. The regression equation parameters were used to plot the best-fit Arrhenius curve for the combined literature data, as well as the plus and minus SE bounds and the 95% PI, as shown in Figures 4-14 and 4-15.

Table 4-3: The coefficients of linearized Arrhenius equations in relation to the temperature dependence of viscosity for Al and Al-Cu experimental results and collected literature data

Melt Materials	$\ln \eta = \ln \eta_\infty + \frac{E_a}{RT}$ (ln[Pa·s])				
	N	Temp. Range (K)	$\ln \eta_\infty$ ln(Pa·s)	E_a (J)	SE ln(Pa·s)
Al Literature Data	139	933 – 1225	-7.96	13700	0.65
Al	3	1032 – 1174	-7.10	1810	0.19
Al-Cu Literature Data	81	873 – 1400	-7.56	10400	0.33
Al-Cu	5	1029 – 1224	-11.73	46000	0.16

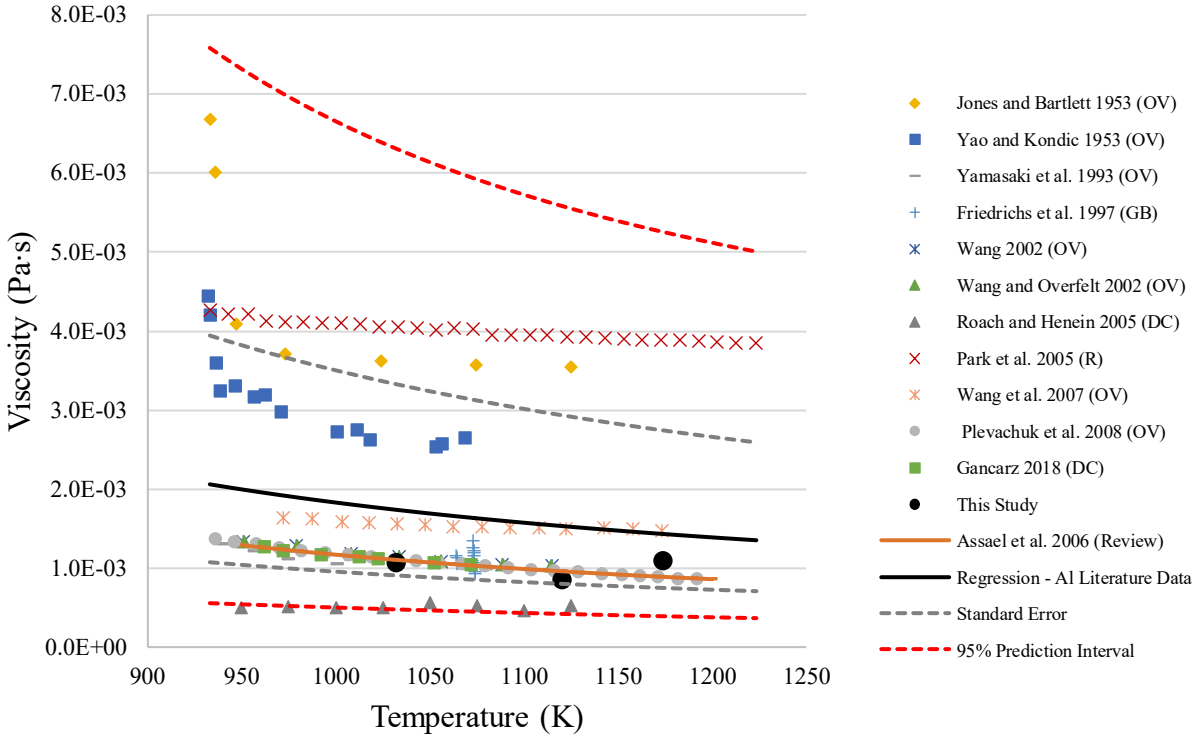

Figure 4.14: Viscosity of Al versus temperature compared with sources in the literature and regression of all combined Al literature data

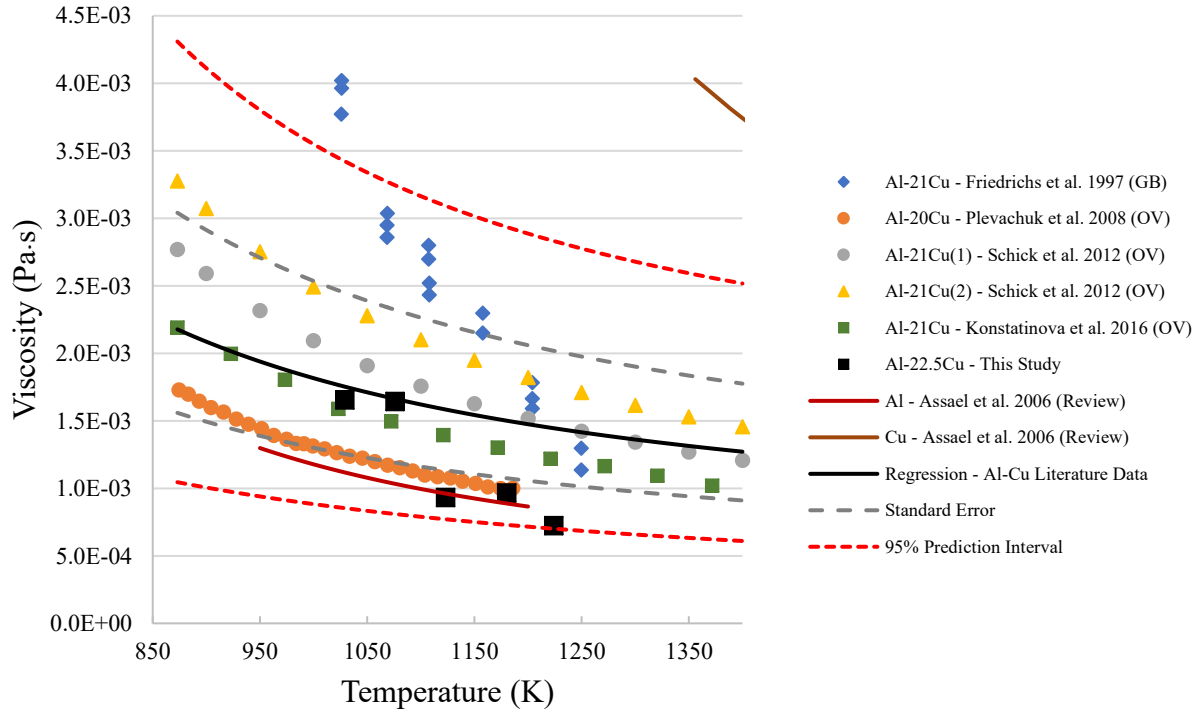

Figure 4.15: Viscosity of Al-Cu versus temperature compared with sources in the literature and regression of all combined Al-Cu literature data

The Al and Al-Cu results measured using the DC method all lie within the 95% PI of the literature data regression model, indicating good agreement with literature. Furthermore, the Al results are in even better agreement with comparable literature data, with all measurements falling within plus or minus one SE. The Al measurements agree particularly well with values reported by Gancarz *et al.* [8], Plevachuk *et al.*[165], Wang [39], and Yamasaki *et al.* [171], and suggested values by Assael *et al.* [6] – Assael *et al.* is considered a very accurate source because they reviewed experimental results from multiple different sources and determined suggested values accordingly–they fit a viscosity trendline to eight different experimental datasets, and a density trendline to five different datasets [6].

All Al-Cu measurements determine using the DC method are bound by 95% PI of the literature regression model; although, they do not all fall within plus or minus one SE, as shown in Figure 4.15. This is not to say that the DC measurements are inaccurate or not consistent with other data published in literature, but rather several measurements deviate from the regression fit by more than the average spread of the literature observations. There is considerable scatter between data obtained by different researchers (as indicated by the large 95% PI), therefore it is difficult to conclude whether the regression fit of the literature is a good predictor of the true Al-Cu viscosity as a function of temperature. Generally, the viscosity data for Al-Cu alloys published in literature is limited, and often contradictory. For example, Schick *et al.* [3] performed duplicate Al-Cu measurements on the same alloy composition (21wt.% Cu), but one study shows results up to 22% higher than the other. Overall, the Al-Cu results obtained in this study agree very well with data published by Plevachuk *et al.* [165], Schick *et al.* [3] and Konstantinova *et al.* [187].

The aforementioned scatter between measurements published in different studies in literature may be caused by challenges associated with melt contamination at high temperatures. Researchers have shown that superficial oxide films affect the measured viscosity of Al and Al alloys [22]. Furthermore, for DC experiments, solid oxide particles may form and can be trapped between the liquid and the orifice, drastically affecting the flow profile, and therefore the viscosity [194]. Dinsdale [22] suggests that the viscosity of Al decreases as the purity of the metal increases, due to various experimental factors, like the choice of crucible material. All of these observations are supported by experiments revealing that the apparent viscosity of Al increases as the oxygen content in the atmosphere increases [6]. This is validated in Figure 4.14, where very early studies

(i.e. 1950s, by Jones and Bartlett [42] and Yao and Kondic [170]) reported much higher Al viscosity measurements; highlighting recent technological advancements with regards to O_2 control, metal purity and experimental design.

4.2.2 Surface Tension Measurements

Much like viscosity, the experimental surface tension results of Al and Al-Cu and the combined data published in literature were fitted to a linear regression model using Minitab 19. The summarized outputs of the regression analysis are provided in Table 4-4, with additional statistics provided in Appendix I. The Al and Al-Cu surface tension results were plotted alongside comparable data published in literature and the regression fit of the combined literature data (including SE bounds and 95% PI). This is shown in Figure 4.16 and Figure 4.17 for Al and Al-Cu, respectively. The surface tension measurements reported in literature are in excellent agreement with each other; the SE for all Al literature data is 3.99×10^{-2} N/m (N=179), which is equivalent to 5% error at T_m, and is 5.95×10^{-2} (N=96) for Al-Cu, equivalent to 7% at T_m. This highlights the consistency of surface tension measurements between various researchers and measurement methods.

Table 4-4: The coefficients of linear temperature dependand nce of surface tension for Al and Al-Cu experimental results and collected literature data

Melt Material	$\sigma_t = \sigma_m + \frac{d\sigma}{dT}(T - T_m)$ (N/m)					
	N	Temp. Range (K)	T_m (K)	σ_m (N/m)	$\frac{d\sigma}{dT}$ (N/m·K)	SE (N/m)
Al Literature Data	179	900 – 1560	933	0.859	-9.26×10^{-5}	3.99×10^{-2}
Al	3	1032 – 1174	933	0.904	-2.39×10^{-4}	6.01×10^{-4}
Al-Cu Literature Data	96	915 – 1500	867	0.837	-1.09×10^{-4}	5.95×10^{-2}
Al-Cu	5	1029 – 1224	867	0.940	-3.70×10^{-4}	3.57×10^{-3}

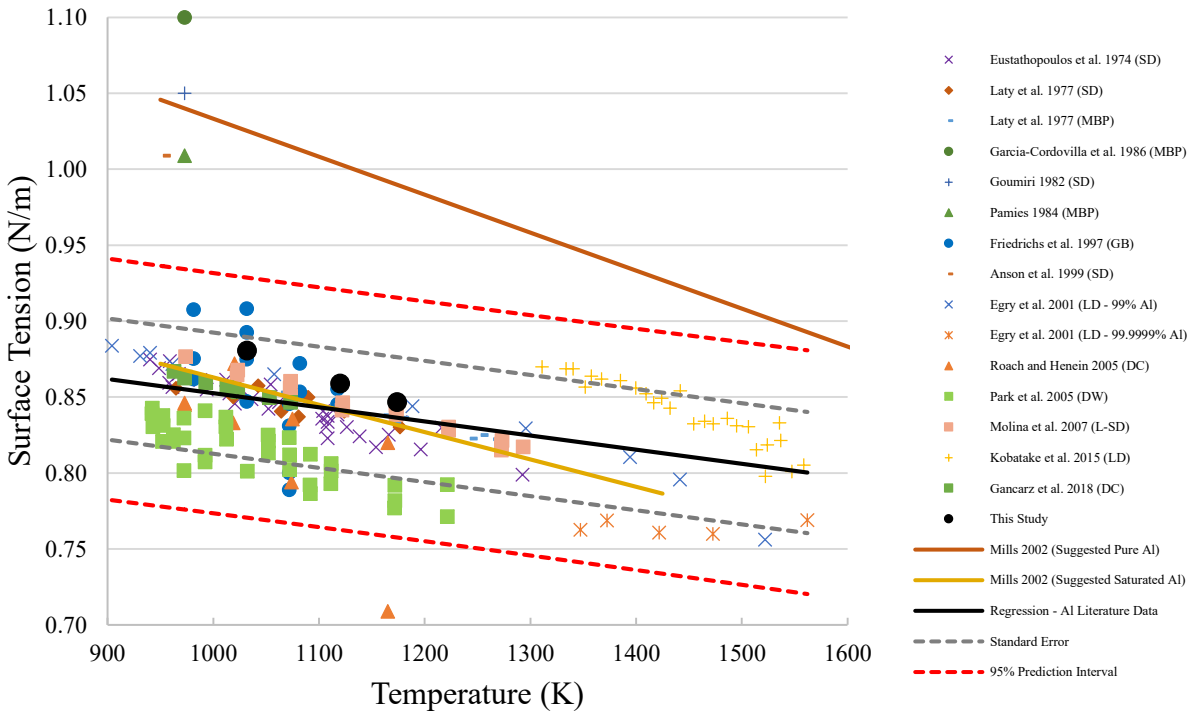

Figure 4.16: Surface tension of Al versus temperature compared with sources in literature and regression of all combined Al literature data

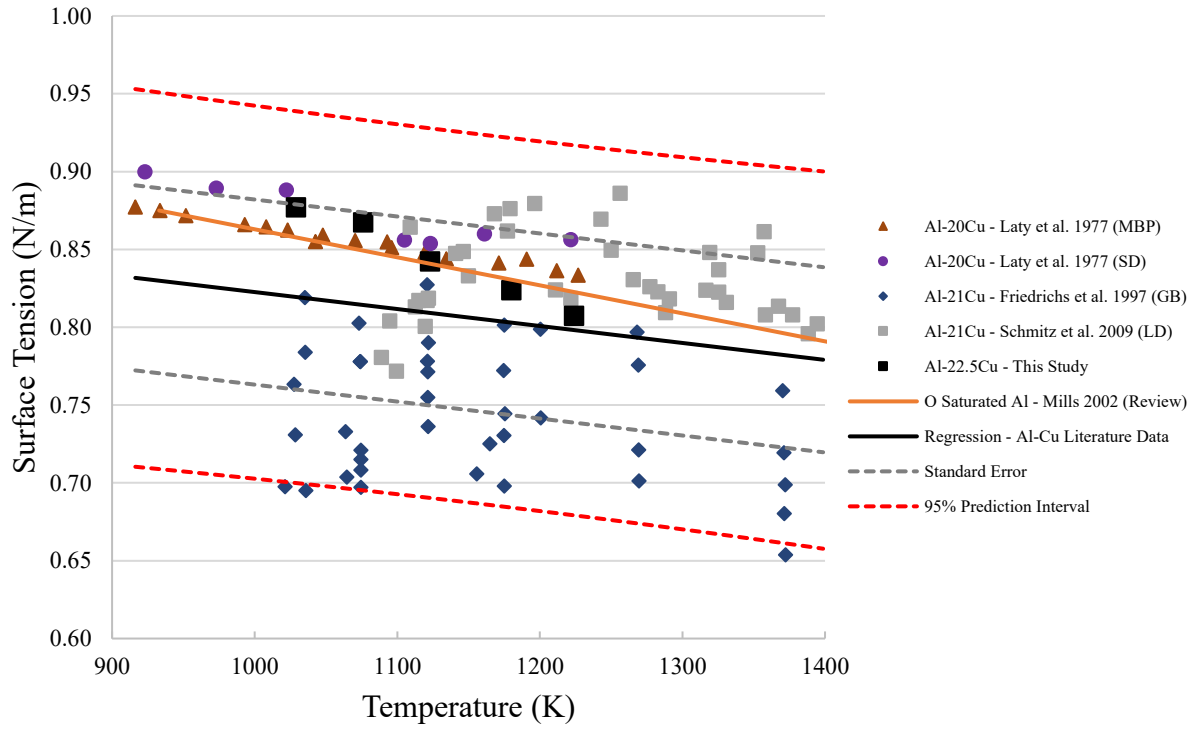

Figure 4.17: Surface tension of Al-Cu versus temperature compared with sources in literature and regression of all combined Al-Cu literature data

All Al surface tension measurements conducted in this study fall within plus or minus one SE and the 95% PI of the fitted literature regression model, as shown in Figure 4.16. Unlike with reported viscosity data, the surface tension data published in literature is in much better agreement, especially when only considering oxygen saturated samples. Mills [56] reported a confidence level 2% across four separate surface tension datasets which were used to calculate suggested values provided for O saturated Al. In considering results measured at 1032, 1120 and 1174 K, the difference between Mills and this study are no greater 3%. Garcia-Cordovilla [178], Goumiri [195], Anson *et al.* [175] and Pamies [177] all took extraordinary measures to determine the surface tension of effectively pure Al, or non O saturated Al. These results, as shown in Figure 4.16, are all much higher in magnitude. Although the O_2 content measured in this study were less that $1x10^{-8}$ ppm, or roughly a O_2 partial pressure of $1.36x10^{-9}$ atm, O managed to segregate to the surface, effectively reducing the Al surface tension. This phenomenon was explained in detail in Section 2.2.1 using the Gibbs absorption isotherm. Prior reports by Anson *et al.* [175] have stated that a O_2 partial pressure of $1x10^{-50}$ atm is required to avoid oxide contamination; this is clearly much lower than the partial pressure attained in this study, suggesting that the measurements in this study solely describe an O saturated system. Note that at sufficiently high temperatures, O will also diffuse from the Al_2O_3 crucible into the metallic liquid.

Additionally, all Al-Cu results lie within the SE and 95% PI of the combined literature linear regression. There is good consistency between Al-Cu results from this study and results obtained using EML-LD (Schmitz *et al.* [15]), SD (Laty *et al.* [180]) and MBP (Laty *et al.* [180]). As shown in Figure 4.17, the surface tension of Al-rich Al-Cu is very similar to pure O saturated Al. To reduce the energy at the surface, Al will segregate to the surface since it has a lower surface tension than Cu. Moreover, O will also absorb to the surface, further reducing surface tension. Consequently, the surface tension for Al-rich Al-Cu alloys are only marginally larger than the surface tension of O saturated Al.

Lastly, the surface tension temperature coefficients for both measured Al and Al-Cu are significantly more negative than those calculated using literature data (see Table 4-4). This is, however, not conclusive due to the limited number of datapoints (N=3 for Al and N=5 for Al-Cu) used to calculate the regression equation parameters for results published in this study.

4.2.3 Density Measurements

The regression outputs for both Al and Al-Cu results and comparable combined literature data are provided in Table 4-5. The density measurements determined in this study as well as results published in literature are shown in Figures 4-18 and 4-19 for Al and Al-Cu, respectively, along with the fitted regression models and the 95% PI and SE intervals.

Table 4-5: The coefficients of linear temperature dependance of density for Al and Al-Cu experimental results and collected literature data

Melt Material	$\rho = \rho_m + \frac{d\rho}{dT}(T - T_m)$ (kg/m^3)					
	N	Temp. Range (K)	T_m (K)	ρ_m (kg/m^3)	$\frac{d\rho}{dT}$ (kg/m^3·K)	SE (kg/m^3)
Al Literature Data	293	930 – 1680	933	2335	-0.31	58
Al	3	1032 – 1174	933	1474	1.83	220
Al-Cu Literature Data	58	885 – 1375	867	2769	-0.40	126
Al-Cu	5	1029 – 1224	867	2296	0.07	210

The densities measured in this study are significantly lower than data reported in literature, falling well outside plus or minus one SE of the literature data regression models. Further, all Al results lie outside the 95% PI, and three of five Al-Cu measurements as well. The slopes for both the measured Al and Al-Cu as a function of temperature are also, incorrectly, positive, per Table 4-5. The density values published in literature for both Al and Al-Cu (presented in Section 2.5) are in excellent agreement across various studies; the SE of the regression for Al literature values is only 58 kg/m^3 (N=298) while Al-Cu is 126 kg/m^3 (N=58); equivalent to only 2% and 5% at T_m, respectively. Note, this is a better fit than combined surface tension data published in literature. Conversely, the measured density results determined using DC are up to 31% lower for Al and 20% lower for Al-Cu than the corresponding regression model predicted values. Historically, density measurements of metallic liquids do not exhibit much scatter [21]. Thus, there are obviously issues with the experiments performed in this study. Or, the formulation used to calculate the thermophysical properties may not accurately model the flow.

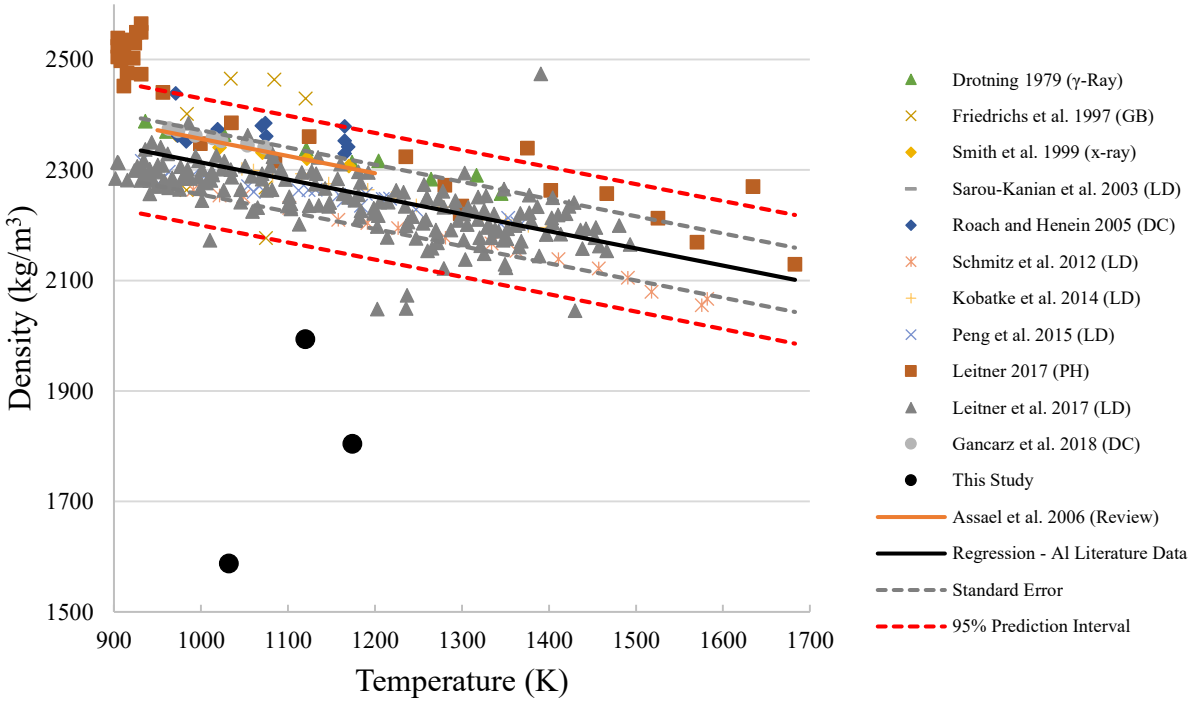

Figure 4.18: Density of Al versus temperature compared with sources in the literature and regression of all combined Al literature data

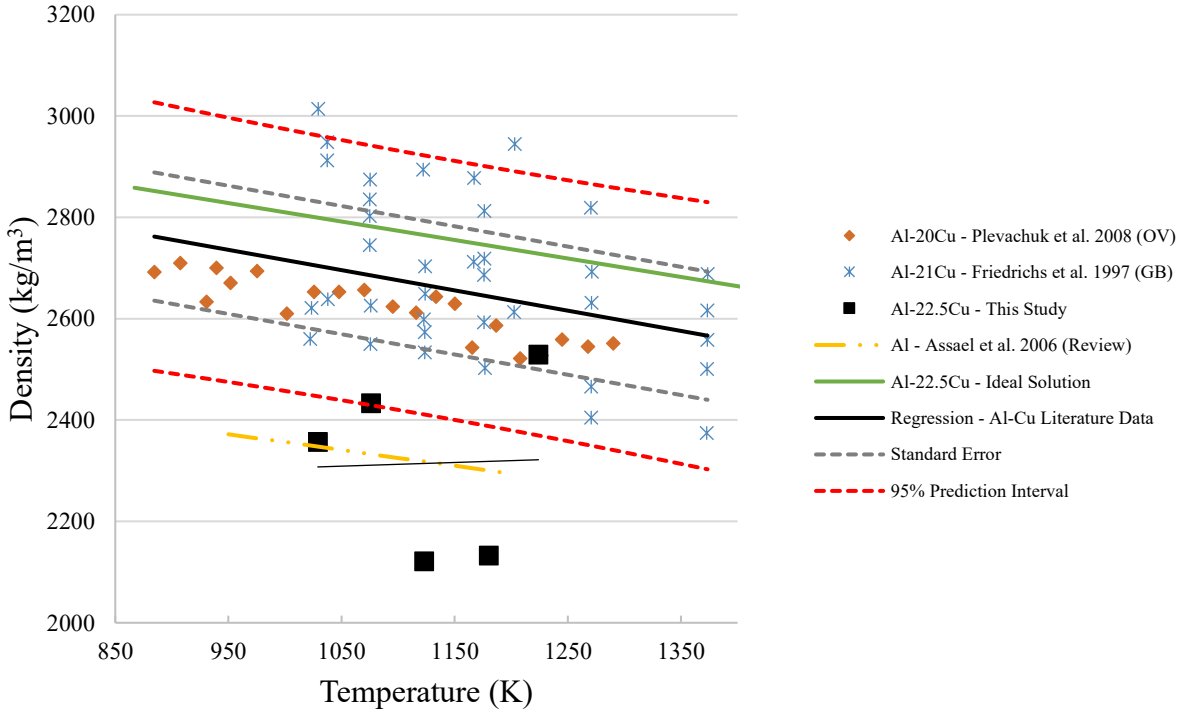

Figure 4.19: Density of Al-Cu versus temperature compared with sources in the literatures and regression of all combined Al-Cu literature data

4.2.4 Summary of the Comparison of Experimental Results and Literature Data

The results presented in this section have achieved, with varying degrees of success, the goal of measuring the thermophysical properties of Al and Al alloys using the DC method. The results for viscosity and surface tension have provided an important validation to the technique and are in good agreement with previous studies. All viscosity and surface tension results fall within the 95% PI of the corresponding regression fit of the combined published literature data. Further, all surface tension measurements fell within plus or minus one SE of the regression fits, indicating excellent agreement with literature data. There is considerable scatter between viscosity data published by different researchers, even when using the same measurement technique. This further reinforces the need to continue to conduct viscosity measurements on metallic liquids, specifically multi-component alloys. Additionally, the measured surface tension of both Al and Al-Cu likely reflect oxidized values, despite the highly dynamic nature of these experiments. When comparing the Al results to the O saturated Al surface tension – temperature equation proposed by Mills [56], the measurements obtained by the DC method all deviated by less than 3% from the suggested values.

On the other hand, the result for density determined using the DC method were consistently lower than values published in literature, with most measurements outside the 95% PI of the literature data regression fits. While the SE of the regression for the Al and Al-Cu literature data were only 58 kg/m^3 (N=298) for Al and 126 kg/m^3 for Al-Cu, the results determined in this study were at least 283 kg/m^3 lower for Al and 97 kg/m^3 lower for Al-Cu than corresponding (same temperature) regression estimates. The most pronounced difference was observed for Al at 1032 K where the density measurement was 716 kg/m^3 or 31% lower than the value calculated from the linear regression of the literature data. Despite the accuracy of the viscosity and surface tension measurements, the density results appear to be inconsistent with literature and are cause for concern. Perhaps, this is a clue of the flow rate not being correctly modelled by the modified Bernoulli formulation. Further discussion and analysis will provide a definitive understanding as to why these density results are so low.

4.3 Theoretical and Empirical Models

To further validate the–what appears to be–successful viscosity and surface tension measurements of oxygen-saturated Al and Al-Cu, the values reported in Section 4.2 will be compared to theoretical and empirical models described in Chapter 2. Note, literature review conducted on models predict the surface tension temperature dependency of metallic liquids and is limited to binary alloys (see Section 2.2.3), therefore, analysis of the Al using numerical models is not included in this section. Furthermore, a thorough analysis of these models may aid in the selection of an accurate non-experimental method to predict the thermophysical properties of Al and Al-Cu alloys best. Ultimately, the goal of this thesis is to grant researchers and industry the ability to accurately model metallurgical processes, which rely on accurate thermophysical property data.

4.3.1 Theoretical Viscosity of Aluminum

The viscosity of pure liquid Al was calculated using several semi-empirical models. These models were discussed in detail in Section 2.1.1. The theoretically predicted viscosity versus temperature curves were plotted alongside experimental data published in literature and measured in this study. This is shown in Figure 4.20. Both the Arrhenius (Equation 2.8) and the Hildebrand equations (Equation 2.13) were calculated using empirical parameters determined by Chhabra *et al.* [30] for pure liquid Al. They found that the activation energy, E_a, and pre-exponential factor, A, of the Arrhenius equation for pure liquid Al were 26.12 kJ and 0.1245 mPa·s, respectively. They also calculated that the intrinsic volume, V_0, and the characteristic constant, B, of the Hildebrand Free Volume equation for pure liquid Al as 10.76 cm^3/mol and 5.719, respectively. The Kaptay unified equation (Equation 2.13) and the Hirai model (Equation 2.11) are two additional semi-empirical models that require knowledge of empirical constants to determine the viscosity as a function of temperature. Due to the high reactivity of Al, these empirical constants were likely determined based on oxygen saturated conditions, though this is not confirmed in literature. Kaptay tested their equation of 15 different pure liquid metals and obtained values for constants A_K and B_K of (1.80 ± 0.39) x 10^{-8} $(J/Kmol^{1/3})^{1/2}$ and 2.34 ± 0.20, respectively. Many of these equations require knowledge of the molar volume, V_M (m^3/mol), which is calculated using the density values proposed by Assael *et al.* [6]. As for experimental data, Assael *et al.* [6] performed a thorough

review of various literature sources, and calculated a regression fit to estimate the viscosity of pure Al. This, along with the regression fit for all combined literature data (provided in Table 4-3) will be used for comparison in Figure 4.20.

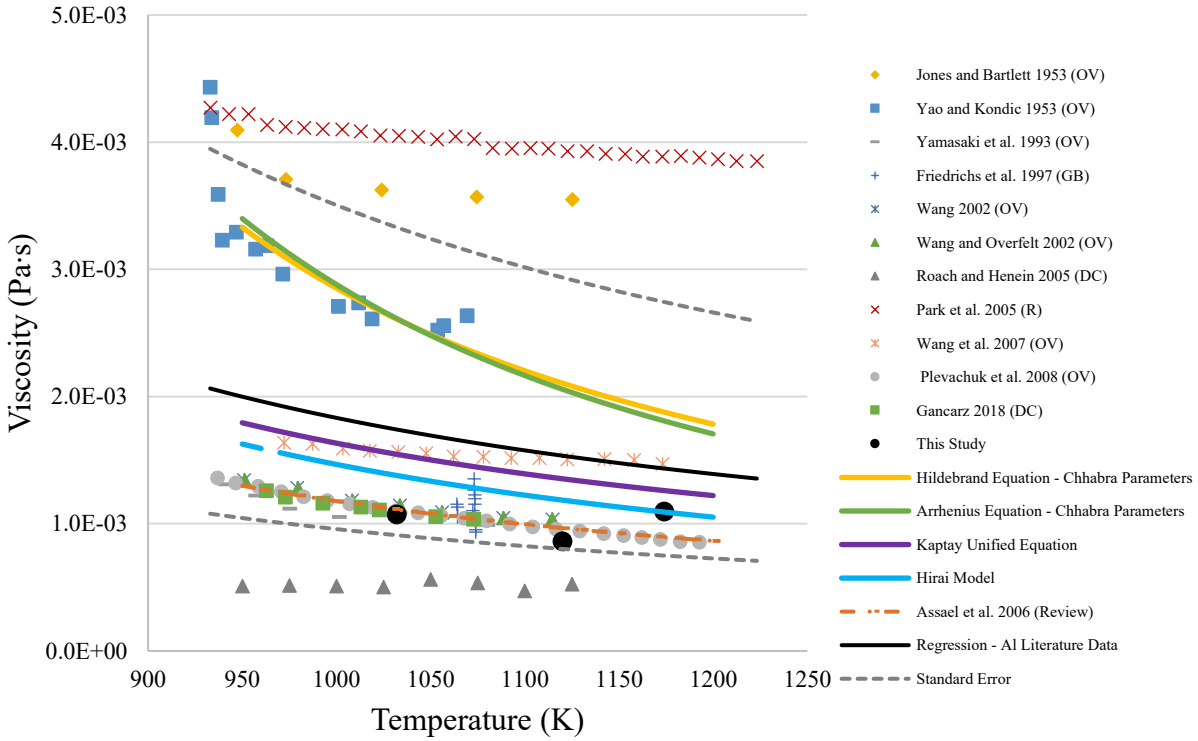

Figure 4.20: Viscosity data of Al as a function of temperature from experimental measurements (markers) and theoretical calculations (solid lines)

All theoretical models lie within plus or minus one SE of the combined literature data regression (for 933 K $\leq T \leq$ 1225 K) from Table 4-3, while the values proposed by Assael *et al.* [6] agree best with the Hirai model. Similarly, the Al viscosity results obtained in this study agree well the Hirai model, ranging between 0 – 27% lower than the predicted values. The Hirai model also slightly overestimates experimental viscosity measurements published by Yamasaki [171], Wang [39], Plevachuk [165], and Gancarz [8]. Again, the models require input from parameters that were derived empirically, and therefore, it is likely that they reflect oxygen saturated liquids, considering the high oxygen affinity of Al. Conversely, predictions based on parameters obtained by Chhabra *et al.* [30] appear to be grossly inaccurate*;* not only are the values overestimated, but the slope of the curves are noticeably different. The validity of the empirical constants used in these models depend on the accuracy of the data used to calculate the constants. As previously mentioned, Chhabra *et al.* derived values for E_a and A from various experimental data, however,

considering this work was published in 1990, the experimental data referenced may not have been reliable; see data published by Jones and Bartlett [42] and Yao and Kondic [170]. In conclusion, not only are the Al viscosity results presented consistent with recent data published in literature, but they agree reasonably well with values calculating using Hirai model. Improvements are warranted to derive more accurate empirical constants so that these semi-empirical models can be employed as a more reliable tool.

4.3.2 Theoretical Viscosity of Aluminum Copper

The viscosity of liquid Al-Cu as a function of the concentration of Cu was calculated using the Hirai model (Equation 2.11), the Moelwyn-Hughes model (Equation 2.14), the BBK model (Equation 2.18), the Schick model (Equation 2.20), and the Zhang model (Equation 2.23). The Hirai model is a very simple calculation that correlates the activation energy with the melting temperature, T_m (K), of the alloy. The model only requires knowledge of the density, molar mass, and melting temperature of the liquid alloy. These variables were obtained from an experimental study conducted by Brillo *et al.* [153] where they employed EML-LD on Al-Cu samples with various compositions. The density fit parameters are given in Table 4-6. The molar mass was calculated based on a weighted average of the individual molar masses of Al and Cu.

The Moelwyn-Hughes model relates the deviation of the viscosity from ideal behavior to the enthalpy of mixing, ΔH (kJ/mol), of the two components, Al and Cu. The viscosities of the two pure components are needed for this model, and were taken from review studies conducted by Assael *et al.* [6], [193]. The enthalpy of mixing was calculated using an equation proposed by Kanibolotsky *et al.* [196] based on direct calorimetric data, and given in Figure 4.21:

$$\Delta H = x_{Cu}(1 - x_{Cu})(-37.72 - 18.45x_{Cu} - 60.67x_{Cu}^2) \quad \text{(kJ/mol)} \qquad (4.16)$$

It should be noted that this equation assumes no temperature dependence. The Al-Cu system is characterized by considerably negative enthalpies of mixing, and the function's minima is skewed towards the Cu-enriched area, as shown in Figure 4.21. This fact is explained by the existence of a high-temperature intermetallic compound, β ($AlCu_3$), which melts at approximately 1300 K [196], as shown in the Al-Cu phase diagram in Figure 4.22. It is speculated that the strong

interaction between the Al and Cu atoms remains as the solid phase transitions to liquid, resulting in binary cluster formation, or short-range ordering in the liquid [167], [197]–[201].

Table 4-6: Fit parameters for the density Al–Cu samples investigated using EML-LD [153]

System (at. %)	T_m (°C)	ρ_m (g·cm^{-3})	$\frac{\partial\rho}{\partial T}$ (10^{-4} g·cm^{-3}K^{-1})
Al	660	2.35	8.5
$Al_{80}Cu_{20}$	562	3.32	16.0
$Al_{70}Cu_{30}$	592	3.76	12.9
$Al_{60}Cu_{40}$	627	4.44	12.3
$Al_{50}Cu_{50}$	814	5.05	12.0
$Al_{40}Cu_{60}$	960	5.49	12.6
$Al_{30}Cu_{70}$	1041	6.17	13.8
$Al_{20}Cu_{80}$	1042	6.66	11.6
Cu	1085	2.92	9.7

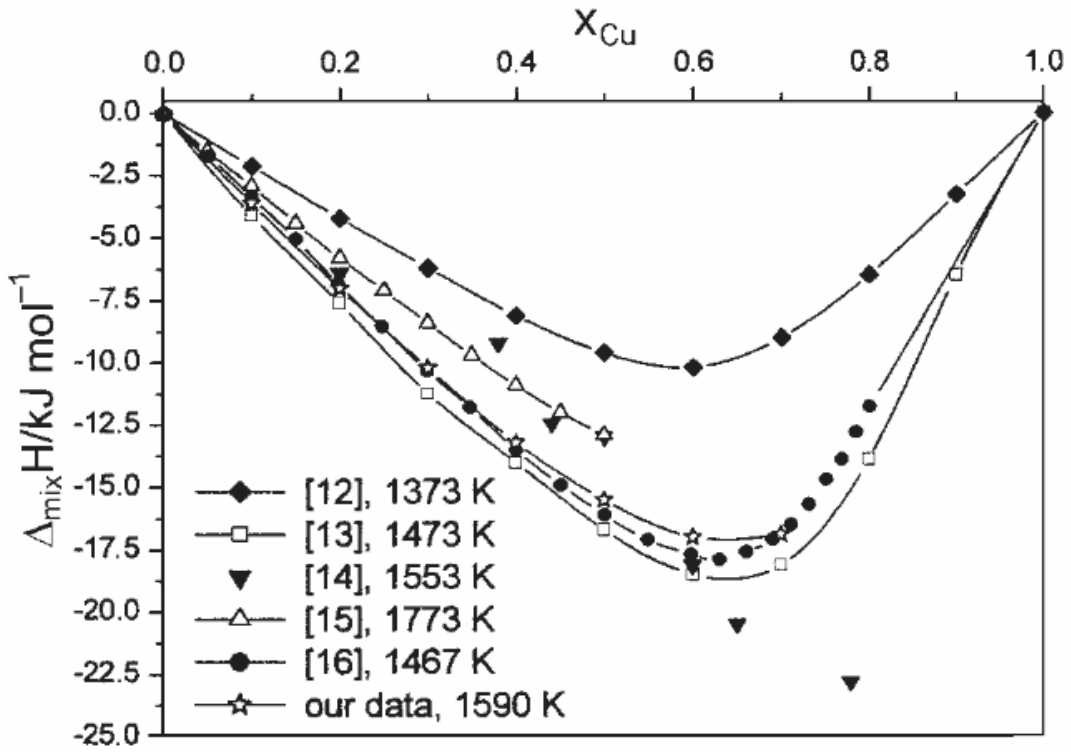

Figure 4.21: Enthalpy of mixing in liquid Al-Cu alloys [196]

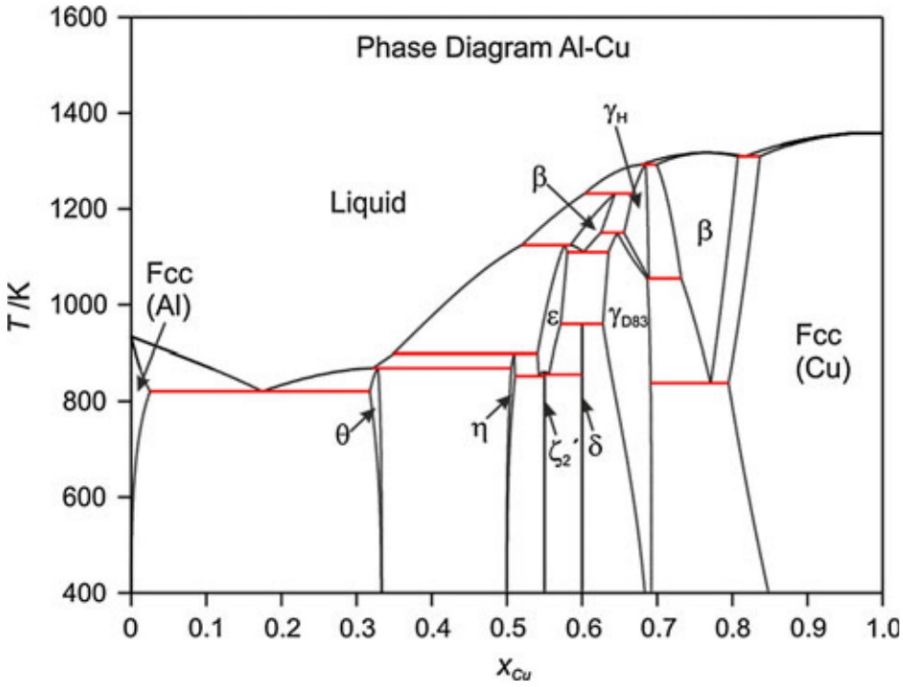

Figure 4.22: Phase diagram of Al-Cu [3]

The BBK model is useful in that it calculates the viscosity of multi-component liquids without knowledge of the pure viscosities of Al and Cu. In this study, the molar volumes of Al and Cu were calculated using density values from Assael *et al.* [6], [193], and the excess molar volume was taken as zero. The constants used for this model were given in Section 2.1.1.7.

The Schick model is based on the simple assumption that the activation energy of viscous flow is larger when the interactions between neighboring atoms are greater. Much like the Moelwyn-Hughes model, the Schick model relies on the enthalpy of mixing to characterize the interactions between Al and Cu. It also requires the pre-exponential factor, A (mPa·s), and activation energy, E_a(kJ/mol), of the pure liquid components, Al and Cu, which were measured by Schick *et al.* [3], and are given in Table 4-7.

Table 4-7: Arrhenius equation parameters calculated for pure Al and Cu [3]

Pure Component	A (mPa·s)	E_a (kJ/mol)
Al	0.247	13100
Cu	0.520	23570

Finally, the Zhang model was developed to properly characterize the effect of associates, i.e. clustering or short-range ordering, on the viscosity of the Al-Cu system. According to the Zhang model, the viscosity of a binary liquid can be simply defined as two parts; one is the ideal mixture, and the other is the excess viscosity. The excess viscosity, η_E (mPa·s), is related to the concentration and the thermodynamic property of the liquid phase, expressed using the Redlich-Kister polynomial. The Redlich-Kister parameters, A_k (mPa·s), used to calculate the viscosity of liquid Al-Cu were provided by Zhang *et al.* [36] and are given in Table 4-8. The model also requires the pure viscosities of liquid Al and Cu, which were once again taken from Assael *et al* [6], [193]. In addition, similar to the BBK model, the molar volume was considered ideal, with the excess volume taken as zero.

Table 4-8: Redlich-Kister parameters for Al-Cu [36]

k	A_k (mPa·s)
0	4.248
1	-16.750
2	2.866
3	9.807

Since each of these models are expected to be able to accurately predict the viscosity of Al-Cu alloys (considering oxygen saturation) with different Cu concentrations, an analysis was conducted to calculate the viscosity of Al-Cu for $0 \leq x_{Cu} \geq 1$ at a constant temperature of 1500 K. The results are given in Figure 4.23. The experimental viscosity data of Al-Cu obtained by Schick *et al.* using the OV method at 1500 K is also plotted [155]. This temperature was chosen because experimental data of Al-Cu could be easily extracted from Schick *et al.* [3] journal article. From this analysis, it appears as the concentration of Cu increases, several models begin to fail; this includes the Hirai and BBK models. The Hirai and BBK models are not able to predict the viscosity maxima at approximately $x_{Cu} = 0.75$. The Moelwyn-Hughes model predicts the position of the maximum viscosity correctly but overestimates the values published by Schick *et al.* considerably. According to Schick *et al.* [3], the viscosity maxima, or viscosity hump, observed in the Al-Cu experimental data can be explained by the large amount of intermetallics present in the Al-Cu phase diagram at this particular Cu concentration. This is shown in Figure 4.22. This same

phenomenon was also observed for Al-Ni, In-Sn and In-Bi liquid alloys [63]. This theory lines up well with the enthalpy of mixing curve, which exhibits a minimum at approximately the same composition. Clearly, the presence of a strong Al-Cu interaction has a large impact on the viscosity, whether it be from clustering, or intensified short-range ordering in the liquid. This logic is reasonable since shear flow can only occur if the nearest neighbor bonds are constantly broken; thus, as the interaction between Al-Cu increases, shear flow will decrease, and viscosity will increase. Both the Schick and Zhang models were actually proposed to address this phenomenon [3], [36]. The main difference between the models are that the Zhang model directly considers the effect of "associates", or compound formation via excess energy, whereas the Schick model attempts to simply relate the activation energy of viscous flow with the attractiveness between atoms, i.e. enthalpy of mixing. At 1500 K, it appears that both models are extremely effective in predicting the viscosity of Al-Cu over the entire range of compositions. It also indicates that the viscosity of Al-Cu can be predicted with sufficient precision without considering compound formation

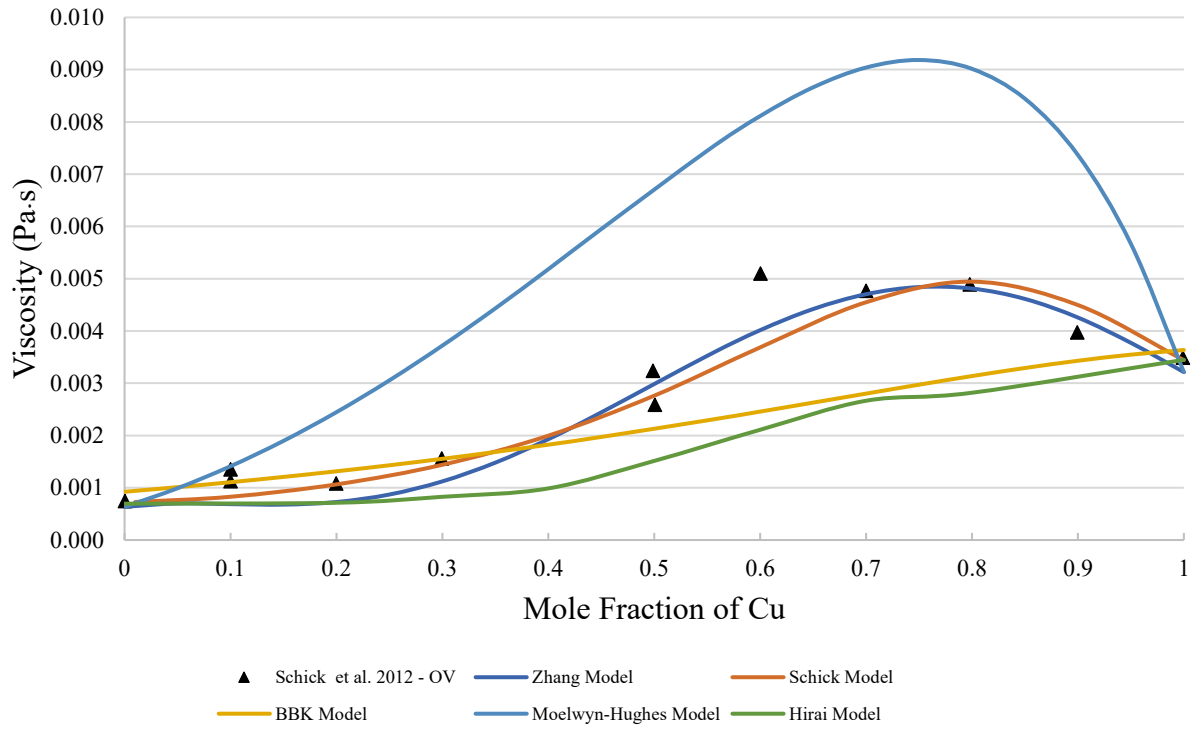

Figure 4.23: Viscosity of Al-Cu as a function of the atomic percent Cu at a constant temperature of 1500 K

To further evaluate the Schick and Zhang models, the viscosity of Al-Cu as a function of concentration was calculated at 1200 K. The results of these calculations are shown in Figure 4.24. The model results are compared to experimental viscosity measurements obtained by Schick *et al.* [3] for Al-Cu alloys at 1200 K. At 1200 K, the Schick model predicts the experimental data sufficiently well, while the Zhang model greatly underestimates the maximum viscosity of Cu-rich Al-Cu alloys. One possible reason for this discrepancy is that the Redlich-Kister parameters, A_k, is assumed to be constant, i.e. does not change with temperature. However, Zhang *et al.* [36].even suggested that A_k is not necessarily constant for all temperatures and all systems. Thus, for the Zhang model to be considered valid for high-Cu Al-Cu alloys, additional work needs to be done to parametrize excess viscosity as a function of temperature.

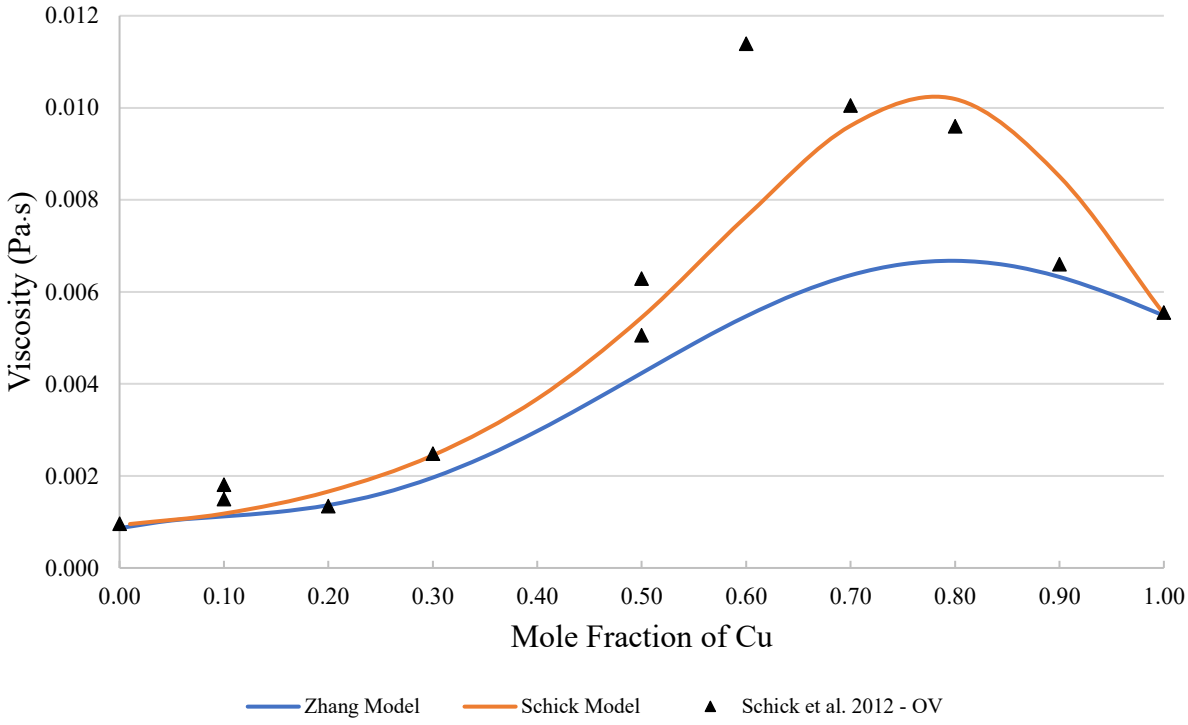

Figure 4.24: Viscosity of Al-Cu as a function of the atomic percent Cu at a constant temperature of 1200 K

To summarize, due to the presence of stable intermetallic phases in high-Cu Al-Cu alloys, the Schick model is most accurate for the entire range of Cu concentrations. The viscosities of the pure liquid components and the enthalpy of mixing of Al-Cu have been extensively studied, therefore, the Schick model can be easily applied. Unfortunately, as much as the Schick model can accurately predict the viscosity of Al-Cu liquids, this is not always the case for other alloy systems.

An example of this is shown in Figure 4.25 for Al-Mg where the Schick model actually underestimates the viscosity by predicting a concave shape versus a convex shape. This reveals that the connections between thermodynamic potentials and viscosity are not yet perfectly understood, and future work is required to investigate these relationships.

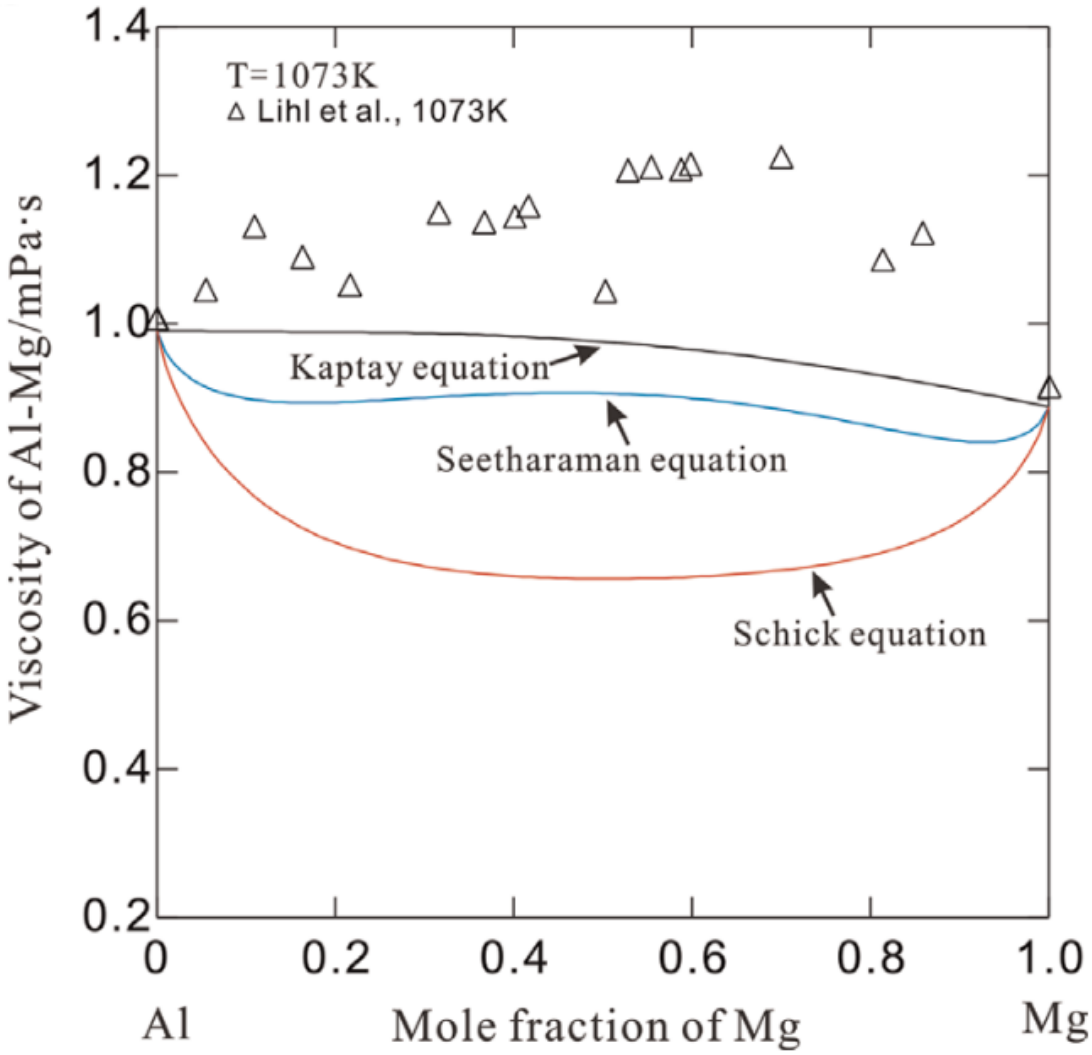

Figure 4.25: Calculated viscosities of Al–Mg system at 1073 K using three equations, compared with the experimental data [36]

Nevertheless, for low-Cu Al-Cu alloys, like the alloy measured in this work, most models appear to be accurate in estimating viscosity accounting for O saturation. Thus, the viscosities of Al-22.5wt.%Cu (or Al-11at.%Cu) obtained at various temperatures in this study were compared to the theoretical models described above. This is shown in Figure 4.26. Viscosity data published

in literature with roughly the same Cu content (see Section 2.5) along with the regression fit and SE (provided in Table 4-3) were also included in Figure 4.26.

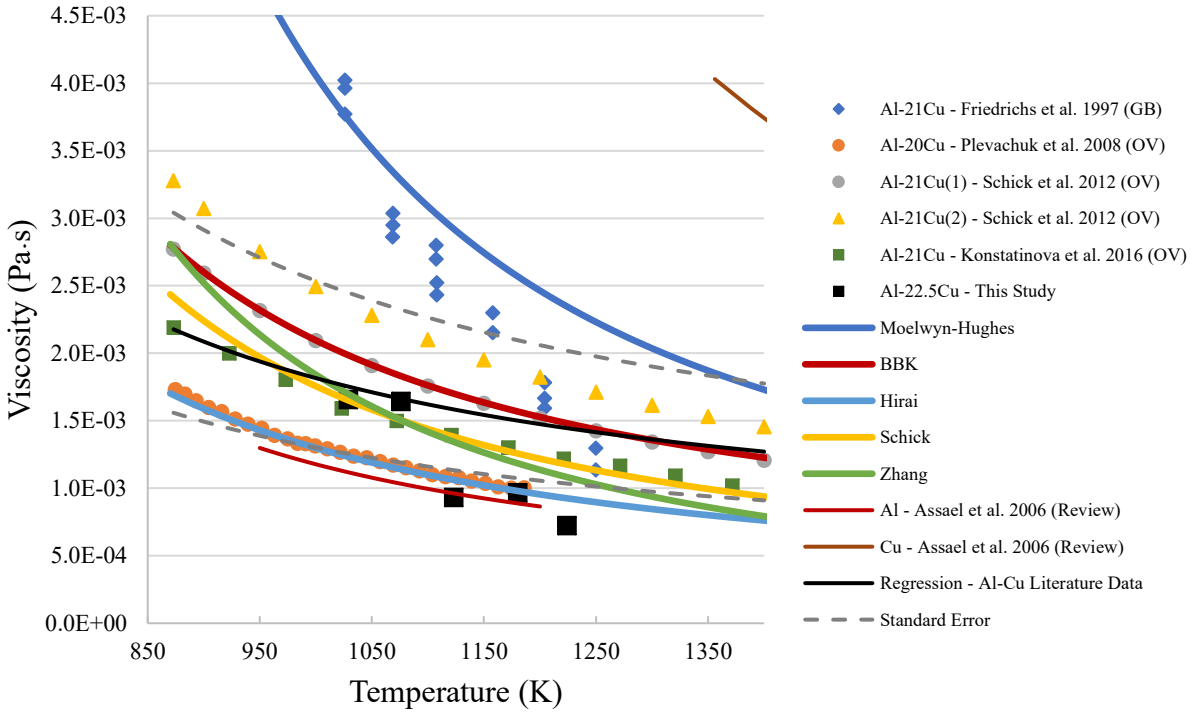

Figure 4.26: Viscosity data of Al-Cu as a function of temperature from experimental measurements (markers) and theoretical calculations (solid lines)

It appears that the accuracy of the models depends significantly on the source of data that is it being compared to. For example, the measurements published by Plevachuk *et al.* [165] agree very well with the Hirai model (within ± 2%), while Friedrichs *et al.* [131] tends to line up better with the Moelwyn-Hughes model. The Al-Cu measurements recorded in this work agree reasonably well with predictions calculated using the Schick, Zang and Hirai models, although only the BBK model lies completely within plus or minus one SE of the literature regression fit (for 873 K $\leq T \leq$ 1400 K) provided in Table 4-3. Nevertheless, for the most part, values calculated using the BBK, Hirai, Schick and Zang models primarily lie within or very close to plus or minus SE of the regression model, showing good agreement with experimental results published in literature. Going forward, particularly when measuring Al-Cu alloys with different Cu compositions, the Schick model should be used to compare with experimental results, considering its ability to accurately model the effect of complex Al – Cu interactions observed over the entire Cu concentration range.

4.3.3 Theoretical Surface Tension of Aluminum Copper

The Butler and Chatain models were previously investigated for the Al-Cu system by Schmitz *et al.* [15], and the parameters to solve surface tension using Equation 2.44, $\sigma_t = \sigma_m + d\sigma/dT\ (T - T_m)$, are given in Table 4-9. Using these parameters, both models were employed to calculate surface tension of oxygen saturated Al-22.5wt.%Cu (11at.%) as a function of temperature. The model results were compared to the O saturated surface tension results obtained by Laty *et al.* [180], Friedrichs *et al.* [131] and Schmitz *et al.* [15] with similar compositions. The comparison is given in Figure 4.27.

Table 4-9: Surface tension parameters of Al-Cu calculated using Butler and Chatain equations compared to experimental data

	This Study (22.5wt%)	Laty *et al.* (20wt.%)	Friedrichs *et al.* (20.08 wt.%)	Schmitz *et al.* (21 wt.%)	Butler Model	Chatain Model
σ_m (N/m)	0.940	0.868	0.850	0.870	0.870	0.870
$\frac{d\sigma}{dT}$ (10^{-4} N/mK)	-3.70	-1.40	-0.94	-1.20	-1.78	-1.67

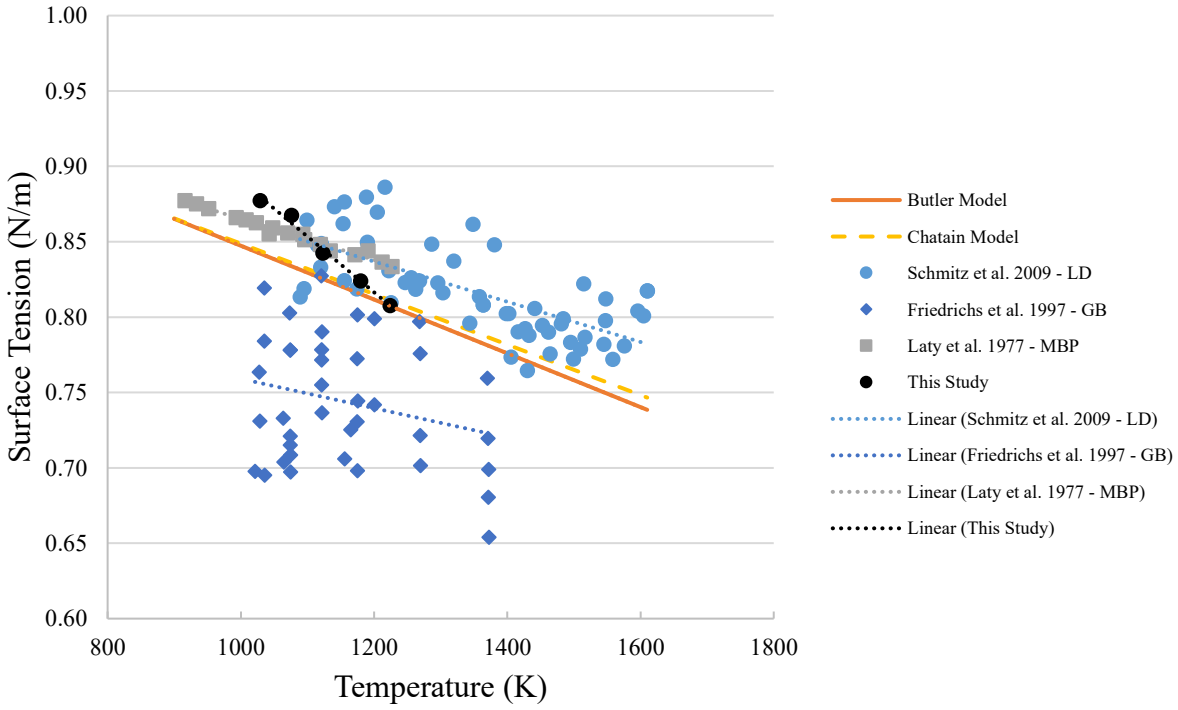

Figure 4.27: Surface tension data of Al-Cu as a function of temperature from experimental measurements (markers) and theoretical calculations (lines)

The Butler model had a slightly more negative slope than the Chatain model, so to further investigate this difference, the surface tension temperature coefficients, $d\sigma/dT$ (N/m·K), of both models were plotted versus the mole fraction of Al in the bulk of the liquid. This is shown Figure 4.28 and also includes temperature coefficients published by Laty et al. [180], Friedrichs et al. [131], Schmitz et al. [15] and determined in this study. Overall, the temperature coefficients are negative; this is due to the fact that the Al-Cu system has a negative excess Gibbs free energy, ${}^{E}G$ (see Figure 4.29). This has been repeatedly reported by numerous researchers [32], [202]. However, by examining Figure 4.28, as the bulk mole fraction of Al decreases to approximately 60 at.%, the temperature coefficient increases. This is particularly apparent with the Chatain model as well as the experimental results reviewed in literature. This phenomenon however conflicts with Figure 4.29 since there is an obvious decrease in free energy at this composition.

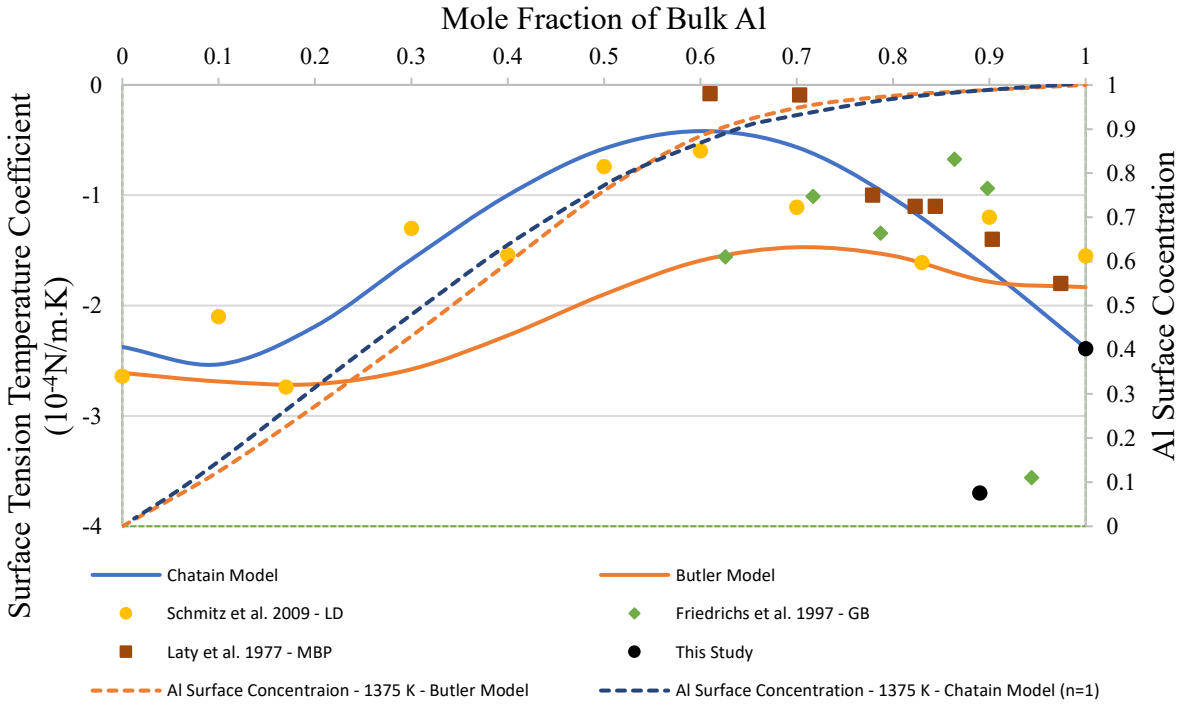

Figure 4.28: Surface tension temperature coefficient of Al-Cu as a function of bulk Al concentration determined experimentally and with the Butler and Chatain models

One possible explanation for this increase in temperature coefficient is that the Al appears to strongly segregate at rich-Al concentration. This is shown by the Al segregation profile plotted in Figure 4.28. Lee *et al.* [202] conducted a simulation to study the surface tension temperature coefficient of liquid Sn-X alloys in which they concluded that temperature coefficient is

determined by the surface enhancement, or surface segregation. The Al segregation in Al-Cu is largely due to the large difference of the pure Al and Cu surface tensions. Brillo [32] showed that the surface segregation factor, S_e, of an ideal binary liquid (with components A and B) increases exponentially as the difference in pure component surface tensions is increased:

$$S_e = e^{\frac{(\sigma_a - \sigma_b)A}{RT}} \tag{4.17}$$

Where $A_A = A_B = A$. For Al-Cu alloys, the surface tension at the melting temperature of pure Al is 0.87 N/m and pure Cu is 1.30 N/m.

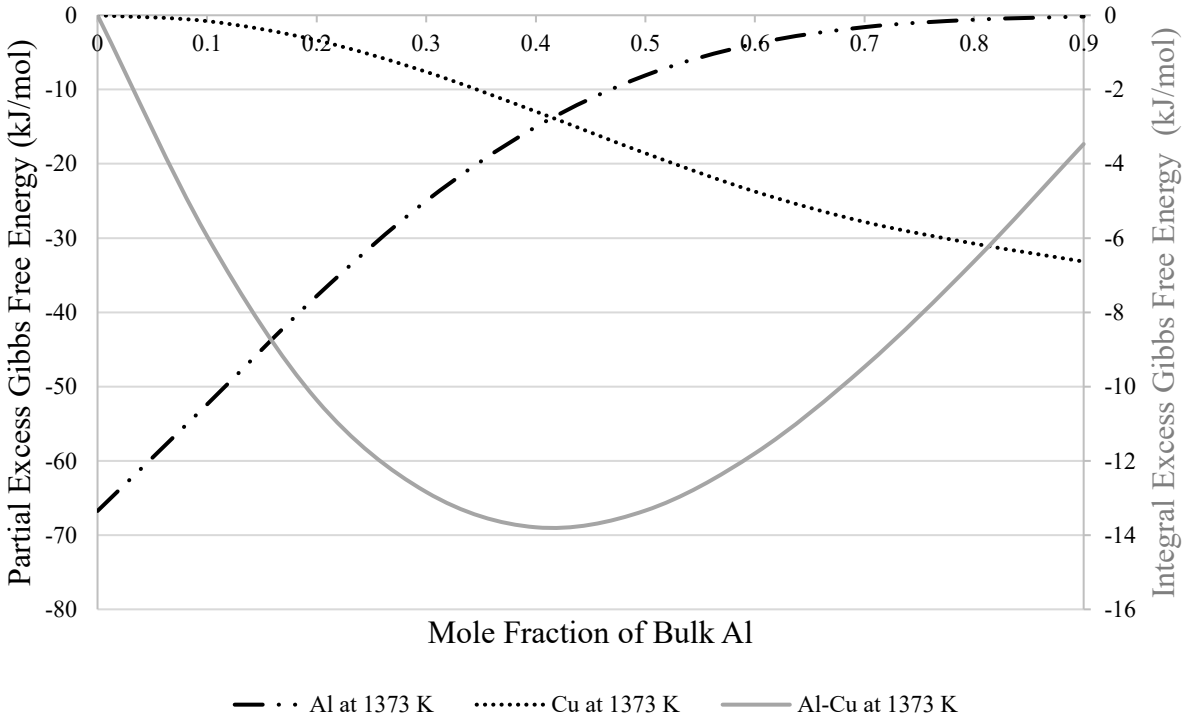

Figure 4.29: Partial and Integral excess Gibbs free energies of Al-Cu system [196]

The effect that surface segregation has on the temperature coefficient is determined by applying the Gibbs absorption equation to calculate the surface tension temperature dependence of a multicomponent system, which was previously discussed for pure liquid in Section 2.4.1 [202]:

$$\frac{d\sigma}{dT} = -s^s - \sum_{i=2,3\ldots} \Gamma_i \frac{d\mu_i}{dT} \tag{4.18}$$

Here, as entropy at the surface decreases, the magnitude of the surface tension temperature coefficient decreases. Or, in the case of Al-Cu, as the entropy at the surface decrease, the temperature coefficient becomes less negative. The entropy represents the ordering effect at the surface, therefore, when Al segregates to the surface, the surface becomes a more ordered monolayer of Al atoms. This theory also helps explain the difference between the Butler and Chatain models. In Figure 4.28, there is a more significant increase in temperature coefficient when the Chatain model, or multilayer model, is applied. Schmitz *et al.* [15] suggested that this discrepancy is caused by chemical layering. Using the Chatain model, they were able to calculate the Al surface concentration at the monolayer nearest to the surface, and the 10 subsequent layers. The results for Al-60at.%Cu are shown for temperatures of 1175 and 1375 K in Figure 4.30.

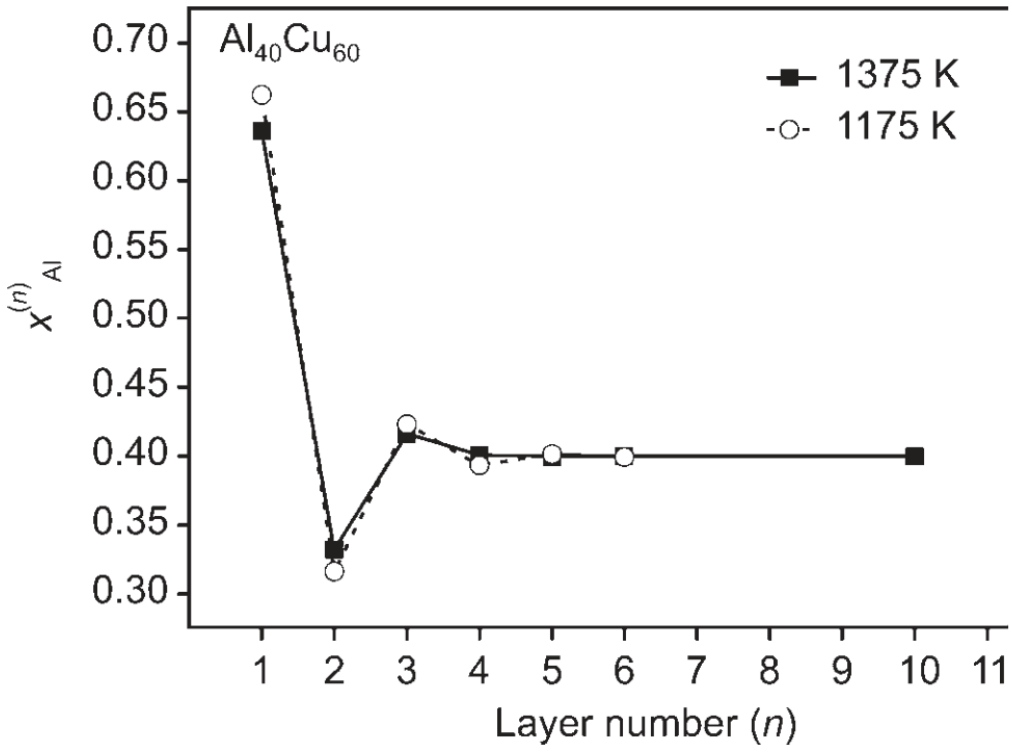

Figure 4.30: Calculated concentration profile of Al in surface near layers of Al40Cu60 alloy for 1375 K and 1175 K [15]

In contrast to the top layer, the Al concentration significantly lower in the second layer, and is in fact lower than the bulk Al concentration. This oscillation is caused by attractive interaction between Al and Cu atoms, where the Cu atoms preferentially segregate the second layer. The surplus of Cu in the second layer is energetically favored due to the negative excess enthalpy and negative excess free energy, which were shown in Figure 4.21 and Figure 4.29, respectively. In other words, the Cu atoms are strongly attracted to the Al atoms; this affects the overall temperature coefficient results through additional contribution to the surface entropy. Thus, a possible reason for the Chatain model better predicting both the surface tension and the surface tension temperature coefficient of results reported by Laty *et al.* [180] and Schmitz *et al.* [15] could be because it more accurately models the layering of alloy components near the free surface.

Per Figure 4.27, the Butler and Chatain models appear to predict the experimental results with high accuracy. Both models were able to predict values within ± 10% of the results published in literature by Laty *et al.* [180] and Schmitz *et al.* [15]. The surface tension results for Al-Cu reported in this study are also in good agreement with both models, deviating by no more than ± 4%. The Chatain model appears to better represent surface tension versus temperature relationship in data published in literature. On the other hand, the temperature coefficient calculated using results for Al-Cu (determined using the DC method) was found to be much more negative than predicted by both models, and even compared to data published on alloys with nearly identical composition. Additional measurements are needed to draw any legitimate conclusions regarding the temperature coefficient considering Laty *et al*, Friedrichs *et al.,* and Schmitz *et al.* all reported at least 18 measurements over a wide span of temperatures.

4.3.4 Summary of the Comparison of Experimental Results and Theoretical Models

The measured viscosities of Al and Al-Cu (both determined using the DC method) were compared to various theoretical and empirical models, which were described in Section 2.1.1. The Al results agreed well with the Hirai model, while the Al-Cu results agreed best with Schick, Zang and Hirai models. Considering the large spread in experimental agreement between various viscosity measurements (see standard errors reported in Table 4-3 for Al and Al-Cu), the outcome of this analysis contributes to the merits of the DC technique. Clearly, the data is within reasonable agreements with most theoretical models, excluding a few which rely on antiquated empirical data. Note that for higher-concentration Cu alloys, researchers should use the Schick model [32] for

comparison. This model successfully characterizes the activation energy of viscous flow caused by the interactions between Al and Cu atoms. Still, the validity of the Schick model to predict other types of binary alloys is still under debate [36].

Similarly, the measured surface tensions for Al-Cu (along with comparable data published in literature) were compared to predicted values determined using both the Butler and Chatain models. Overall, the results determined in this study were in excellent agreement with both models, deviating by less than ± 4%. The data published in literature tend to agree better with the Chatain model (particularly in terms of temperature coefficient), potentially due to its ability model the layering of alloy components near the free surface. The calculated surface tension temperature coefficient shown in Table 4-9, using the combined Al-Cu results listed in Table 4-2 and, was significantly more negative than predicted by both models; however, further data points would need to be obtained before making any noteworthy conclusions.

4.4 The Effect of Wetting

The results presented in Section 4.2, particularly the density measurements, do not agree well with data collected from literature. This is especially evident in contrast to recent measurements performed by Gancarz *et al.* [8] using the DC method on Al, where they reported observed differences compared to literature of < 1% and < 0.3% for surface tension and density, respectively. Roach and Henein [7] cautioned: "If wetting is an issue, the liquid may spread along the orifice exit effectively altering the radius of the exiting stream". The modified Bernoulli formulation assumes a constant radius and a cylindrical exit stream; therefore, wetting would likely cause errors in measurement. This section will investigate if wetting has an effect on the accuracy of the DC method, and if so, why.

4.4.1 Issues with Data Selection

The modified Bernoulli formulation assumes that the flow of a draining liquid exiting an orifice under the influence of gravity is steady-state and that the properties do not change with time. However, results show otherwise; the measurements presented in Section 4.2 were found to vary depending on the range of flow rate (or mass flux) and experimental head data used as inputs in the multiple non-linear regression model. To investigate, the viscosity, surface tension and

density of Al or Al-Cu were calculated iteratively using input data selected at different experimental end times. For example, say the full experimental dataset ranged from 0 to 14 seconds, the regression would then calculate the properties only using data from 0 to 13 seconds, 0 to 12 seconds, 0 to 11 seconds, and onwards. This analysis is shown for Al at 1032 K, and the results are given in Table 4-10. To add, the individual results for viscosity, surface tension and density as a function of selected end time were plotted in Figures 4.31, 4.32 and 4.33, respectively. Note that all experiments conducted in this study (i.e. both Al and Al-Cu at different temperatures) exhibited similar trends involving data selection.

Table 4-10: Effect of data trimming on the properties of Al at 1032 K (h_0 = 8.45 cm)

Time Trimmed (s)	Final Head (cm)	Data Points	Viscosity (Pa·s)	Surface Tension (N/m)	Density (kg/m^3)
0	2.25	880	1.07×10^{-3}	0.881	1587.5
4	2.66	720	1.08×10^{-3}	0.880	1587.3
8	3.40	560	1.10×10^{-3}	0.881	1587.8
12	4.45	400	1.14×10^{-3}	0.883	1588.5
16	5.82	240	1.23×10^{-3}	0.884	1589.1
20	7.50	80	1.32×10^{-3}	0.885	1589.4

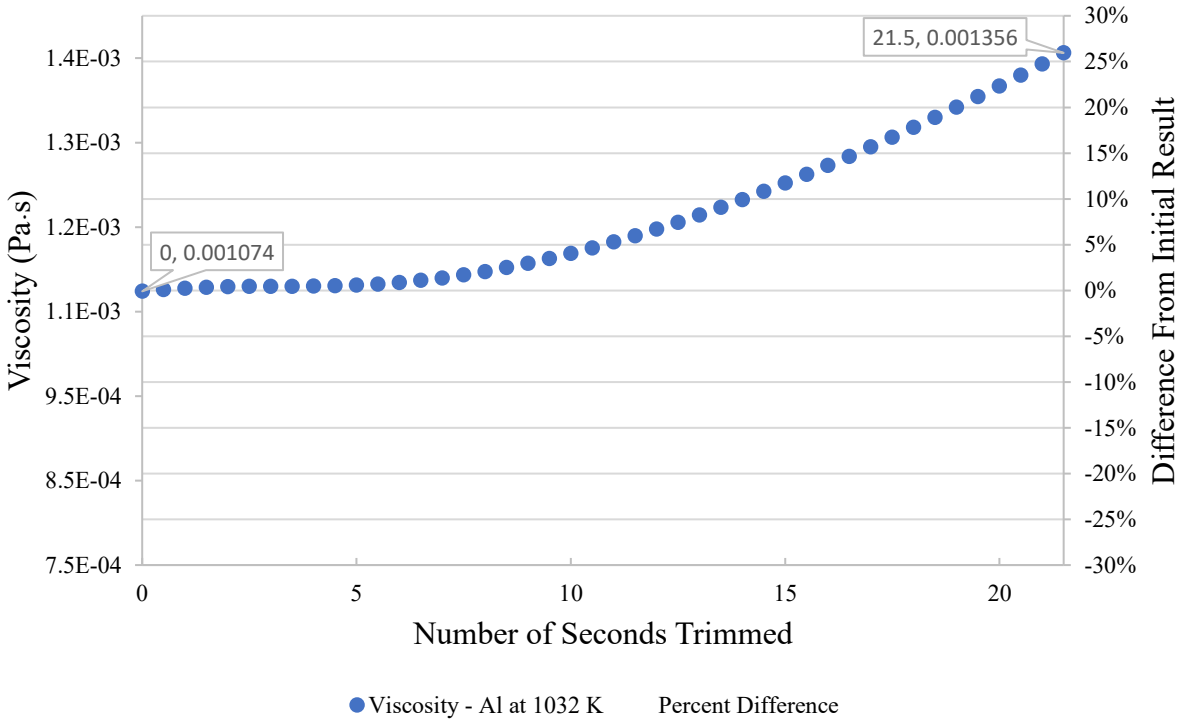

Figure 4.31: Calculated viscosity of Al at 1032 K vs time trimmed off end of dataset

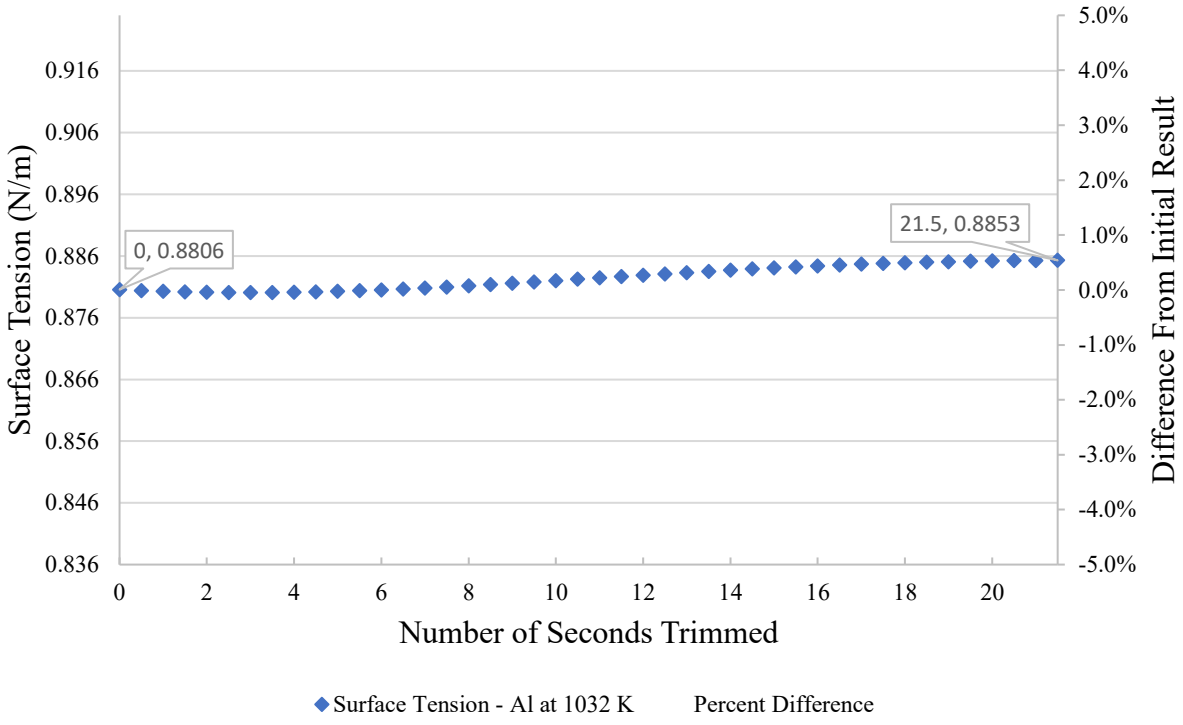

Figure 4.32: Calculated surface tension of Al at 1032 K vs time trimmed off end of dataset

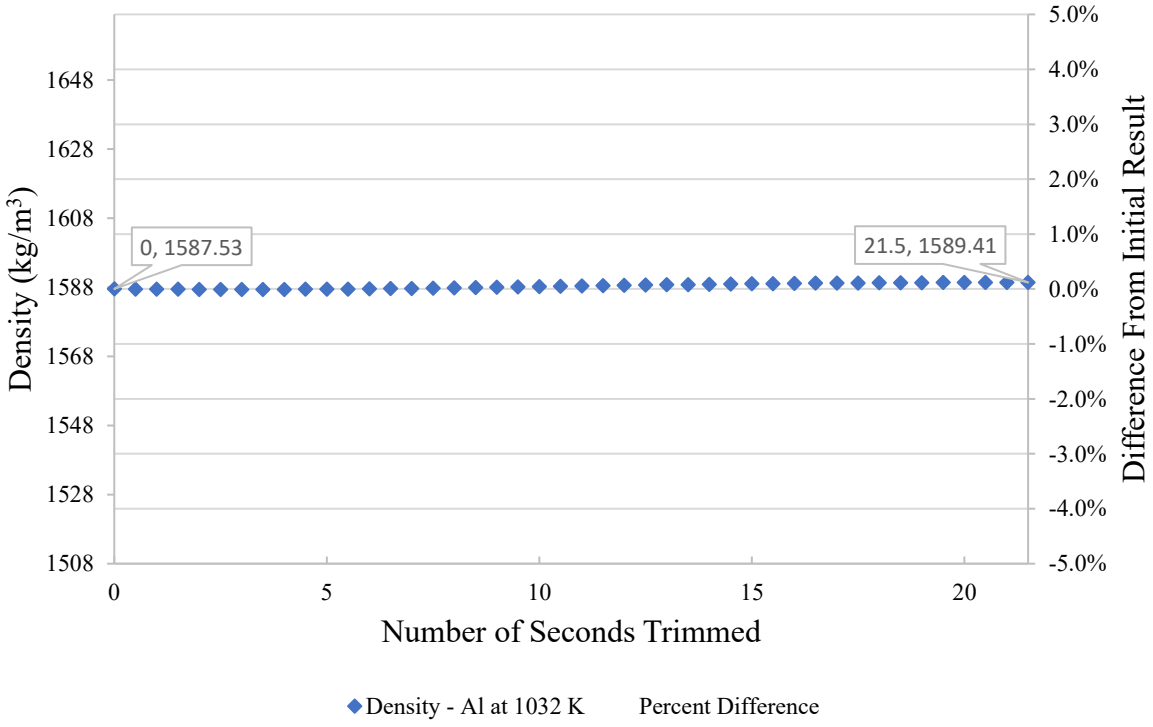

Figure 4.33: Calculated density of Al at 1032 K vs time trimmed off end of dataset

In this example, it is obvious that depending on the range of data selected, the results of the regression will differ. This is especially true for viscosity; the results for viscosity are volatile an vary by upwards of 25%. On the other hand, the results for surface tension and density are much more stable, varying by less than 1%. The fact that the apparent viscosity changes so much as a function of time is troublesome considering the nature of the DC method; recall, the modified Bernoulli formulation assumes that the thermophysical properties remain constant over the course of the experiment. Experimentally, considering that the temperature remains relatively constant, so should viscosity, surface tension and density. This is obviously not the case in this study.

Great effort was made to control experimental parameters, like calibrating the load cell and calibrating head measurements using ultrasonic, but wetting of the exit of the orifice was not a factor that was heavily controlled nor monitored. A possible reason for why the results found in this study do not align with those of extent literature may be due to wetting. This phenomenon was observed during preliminary calibrations where water was found to spread along the bottom of the Al_2O_3 crucible (see Appendix A). This abnormality may have also occurred between Al or Al-Cu and the Al_2O_3 crucible, which perhaps has an unforeseen effect on flow rate–not considered in the modified Bernoulli formulation and ultimately skewing the iteratively calculated viscosity, surface tension and density results.

4.3.2 Wetting Effect on Flow Rate

Ferrand [203] considered the effect of wetting on a liquid draining from an orifice under the influence of gravity. He addresses what happens if the flowing liquid wets the surface surrounding the orifice. They constructed an experimental device consisting of a square tank (made of two Dural plates and two glass plates) that is placed on a raised shelf. The temperature of the liquid within the tank is controlled using heating elements on both Dural plates. The liquid jet is recorded using a CCD camera and an electronic scale placed below the orifice measures the drained mass as a function of time, which is then converted in drained volume using the liquid density. The bottom plate is removable allowing change of the orifice size or even plate material.

This last feature allowed Ferrand [203] to change the wettability of the bottom plate by using plate materials like glass, Dural, Plexiglas, PVC, hydrophobic-coated glass and Teflon. They conducted an experiment where the tank was filled with water to a set volume and was heated to

25 °C and left at rest for a few minutes. The orifice was then opened and both jet shape and drained mass were recorded as a function of time. Figure 4.34 shows measurements of the drained volume, V (L), versus time, t (s), for two different initial volumes (1 L and 0.5 L) and three bottom plates made of different materials and having different wetting properties. The materials used were glass, Plexiglas, and glass made hydrophobic (by coating with Rain-X® Original Glass Water Repellent) with static contact angles, θ_s, of 13.2º ± 1.5, 63.8º ± 1.9º and 87.7º ± 5.3, respectively. The results show that for the various bottom plates, the experimental curves are all different even though the liquid, vessel, temperature and initial volume are all the same. Thereby, suggesting that the flow rate depends on the bottom plate, or explicitly wetting. Furthermore, Ferrand [203] determined that the lowest flow rates are for $\theta_s \sim 60°$. They concluded that wetting strongly affects the rate of drainage that goes through a minimum as the outside surface of the tank bottom plate transitions from hydrophilic to hydrophobic and proposed that this "nonmonotonic effect of wetting lies in the meniscus that forms at the hole outlet" [203].

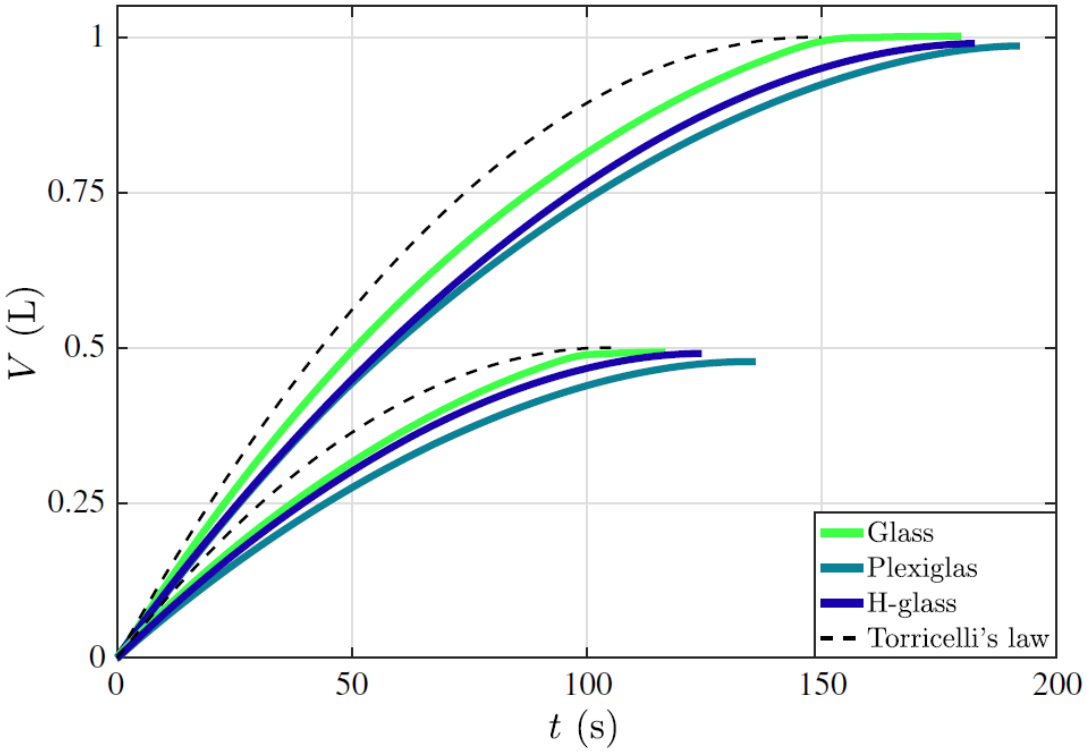

Figure 4.34: Drained volume versus time of 1 L and 0.5 L of water; the different colors represent the different bottom plates, from dark, the more hydrophobic (coated glass) to light, the more hydrophilic (glass) [204]

Ferrand [203] suggested that "for all materials, regardless of hydrophobicity, a thin ring of water close to the wall, right at the exit of the hole, spreads outwards, radially and perpendicularly to the main flow, to wet the surface around the opening". The shape of this meniscus evolves continuously with wettability; its lateral extension on the plate $r_{jet}(z=0)$ increases as θ_s decreases (i.e. increases with hydrophilicity), as illustrated in Figure 4.35. He postulated that the meniscus either accelerates or decelerates the flow depending upon its shape.

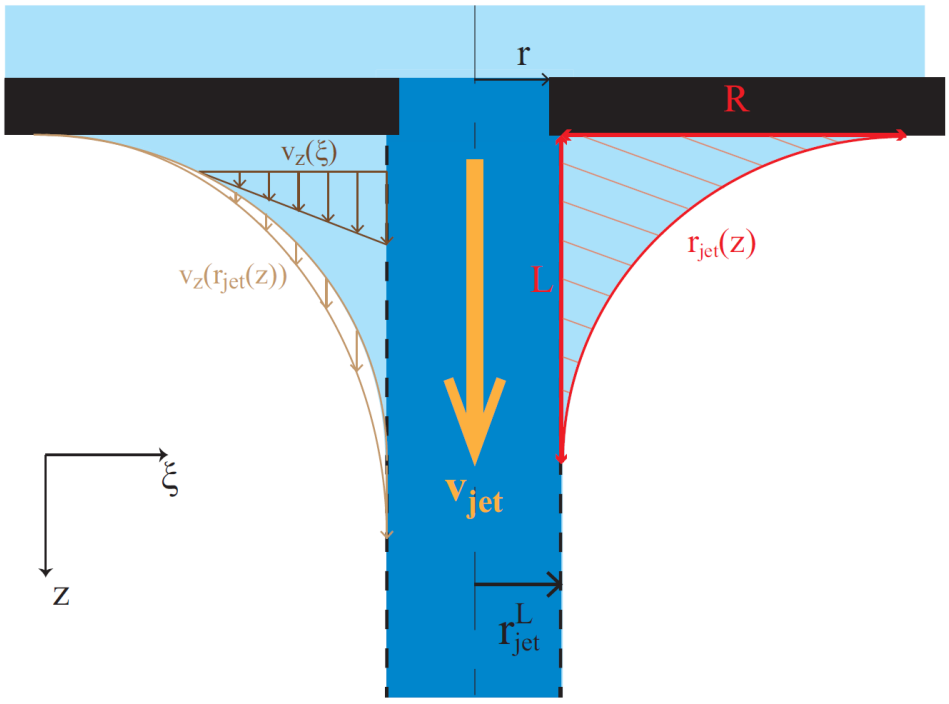

Figure 4.35: Schematic of the meniscus at the exit of an orifice with model parameters [203]

The meniscus always has a cylindrical symmetry and its outer shape follows a parabolic $r_{jet}(z)$ (m) that goes from $r_{jet}(0)$ at the plate level ($r_{jet}(0) = r_{jet}^L + R$) to $r_{jet}(L) = r_{jet}^L$ at the point where the meniscus vanishes and connects to the jet (at $z = L$). The meniscus profile can be expressed in terms of the distance from the plate as follows:

$$r_{jet}(z) = (R/L^2)z^2 - (2R/L)z + R + r_{jet}^L \tag{4.19}$$

The meniscus is considered made of two distinct parts in which flow is different: the meniscus (with velocity profiles $v_z(\xi)$ and $v_z(r_{jet}(z))$) and the principal cylindrical jet having a radius r_{jet}^L (where the flow has an assumed speed of $v_{jet}(t)$). With these profiles, Ferrand [203] developed a

hydrodynamic model of the meniscus by using the Navier-Stokes equation that calculates the variation of the kinetic energy, E_k (μW), within the meniscus which further confirmed the nonmonotonic effect of wetting on flow, as shown in Figure 4.36.

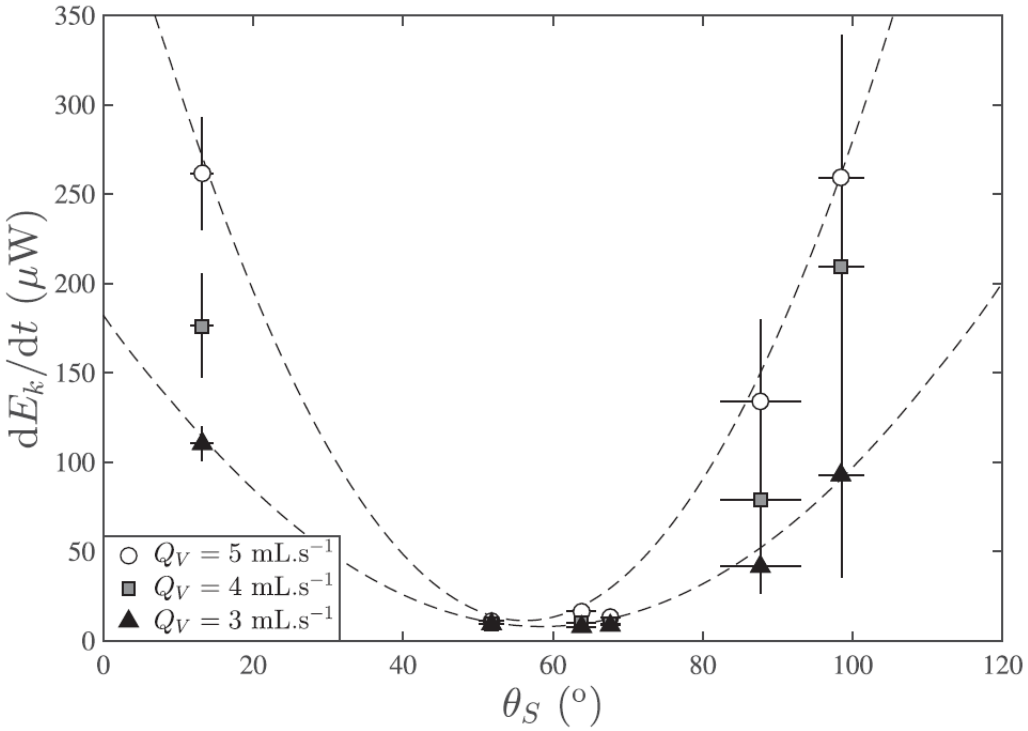

Figure 4.36: Calculated instantaneous variation of kinetic energy within the meniscus as a function of static contact angle for different volumetric flow rates [203]

The model identified three significant mechanisms that effect kinetic energy within the meniscus (and thus flow rate): nonlinear convection, local pressure, and hydrostatic pressure. This model is not perfectly accurate but does provide a basic understanding of how the shape of the meniscus has an effect of the flow rate of a liquid draining through an orifice under the influence of gravity. Further, it shows that no matter the shape, the meniscus always accelerates the flow with respect to the flow rate of simple cylindrical jet, with a minimum acceleration for materials having a $\theta_s \sim 60°$. More specifically, by examining E_k calculated for various circumstances in Figure 4.37, Ferrand [203] determined that:

- For highly wetting surfaces, R is large and $L/R \approx 1$, then acceleration caused by nonlinear convection, local pressure, and hydrostatic pressure are all important, particularly that of the nonlinear convection term; flow rate is high.

- As wetting decreases, R decreases while L/R grows up to approximately 4, then acceleration caused by nonlinear convection, local pressure, and hydrostatic pressure all decline sharply; flow rate is small.
- For non-wetting surfaces, meniscuses are small, R is large and $L/R \approx 2$, and consequently the contribution of local pressure term within the meniscus becomes significant, resulting in an increase in flow rate.

When modelling the dynamics of liquid draining through an orifice under the influence of gravity, potential, kinetic and viscous forces are conventionally considered using the traditional Bernoulli formulation. This formulation was later modified to consider both viscous losses and surface tension induced pressure at the orifice and used to quantify the flow rate of the draining liquid as a function of head above the orifice, i.e. $Q_{theo} = \pi r_o^2 \sqrt{2g(h - \sigma/\rho g r_o)}$; the derivation of this equation was performed by Roach and Henein [16] and described in Section 2.3. The modified Bernoulli formulation is valid for inviscid flow only, so viscous losses through the orifice were characterized by the discharge coefficient, $C_d = Q_{exp}/Q_{theo}$, which calibrates the ratio between the experimental flow rate and flow rate modelled using Bernoulli's principles. Plotting C_d versus Reynolds number, $Re = 2\rho Q_{exp}/\pi\, r_o \eta$, provides a measure of frictional characteristics of the orifice. A major assumption in application of the modified Bernoulli formulation in the measurement of thermophysical properties is that the C_d consistently follows a dependence on Re, and that this trend is continuous no matter the properties of the liquid. In other words, C_d is assumed to depend only on the specific geometry of the crucible. Ferrand [203], however, showed that when draining an identical liquid, at the same temperature with the same properties and the same initial volume, from a vessel and orifice with the same geometry, the flow rate would vary depending on the type or material at the exit of the orifice, i.e. the wettability of the base plate. Therefore, the modified Bernoulli C_d intrinsically characterizes not only viscous losses, but also but also the effect of wetting on the flow rate. Further, the modified Bernoulli formulation assumes that the effective radius of the stream remains constant over the course of the experiment, and that the stream has a cylindrical shape. These assumptions are obviously not valid if a meniscus is formed.

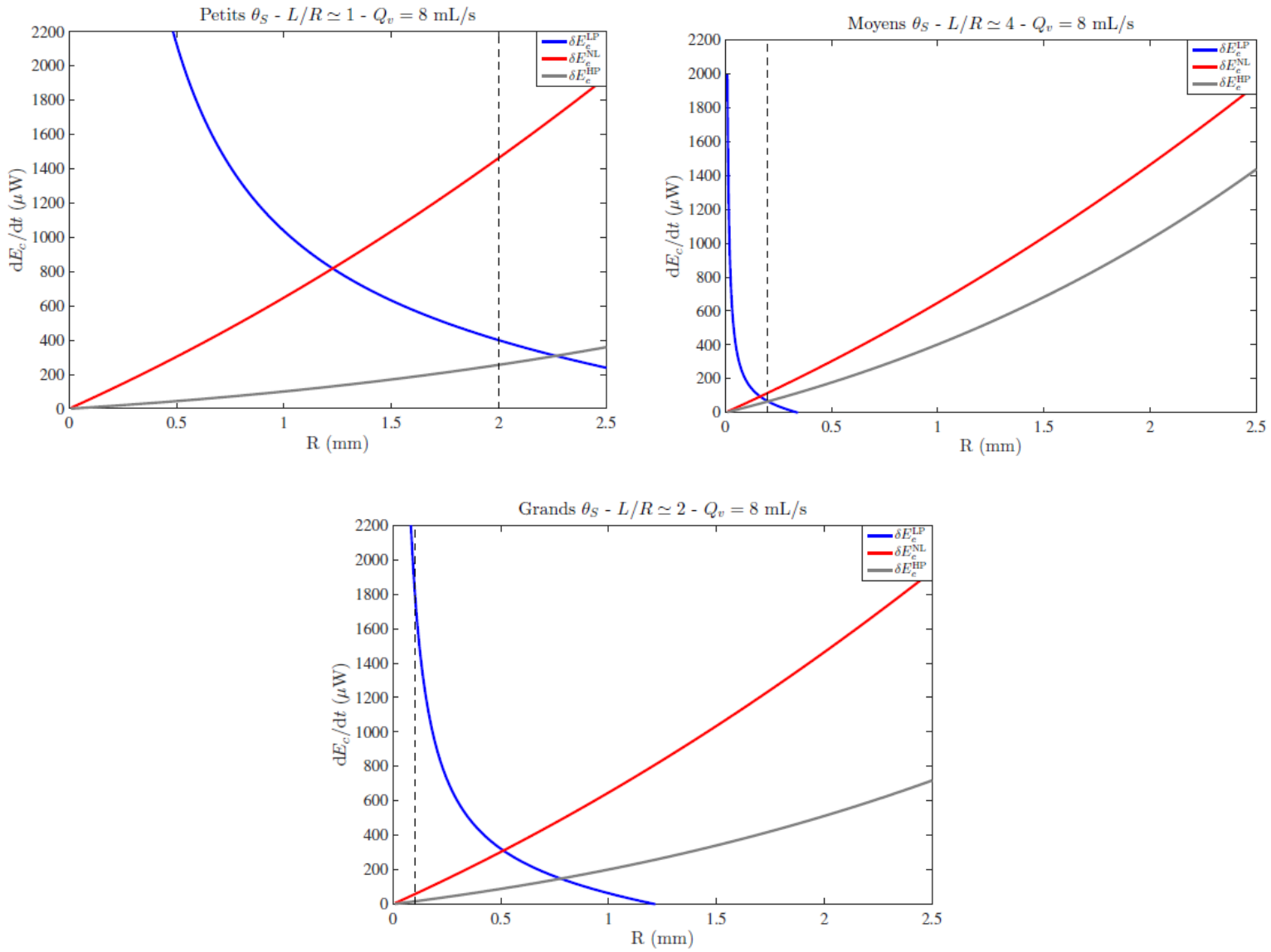

Figure 4.37: Calculations of the contributions of kinetic energy as a function of meniscus length, L, radius, R, and flow rate, Qv [203]

C_d versus Re calibrations were obtained for conditions of minimal or no wetting between the water and the orifice plate. A hydrophobic coating was used on the base of the Al_2O_3 crucibles at the exit of the orifice to mitigate wetting of the liquid around the orifice edges (see Appendix A). However, if Al and Al-Cu are likely to wet the Al_2O_3 crucible, particularly at the measurement temperatures recorded in Section 4.2 (i.e. $\geq$ 1029 K), the flow should be affected. Bao *et al.* [205] determined that near melting temperature, Al does not wet Al_2O_3, however, as the temperature of Al increases, wettability increases, exhibiting $\theta_s < 90°$, as shown in Figure 4.38. Likewise, Klinter *et al.* [206] measured the θ_s between an Al-Cu alloy and Al_2O_3 and noted a similar trend given in Figure 4.39.

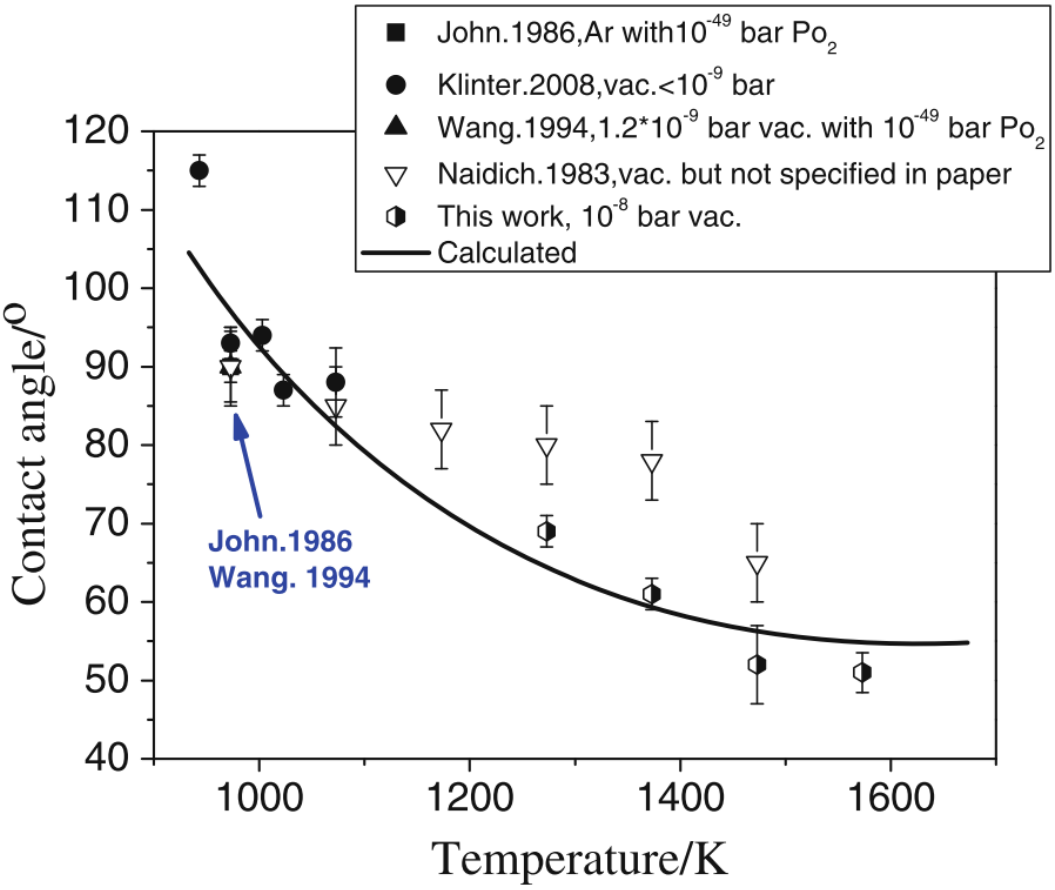

Figure 4.38: Calculated and measured contact angle versus temperature for Al on Al_2O_3 [205]

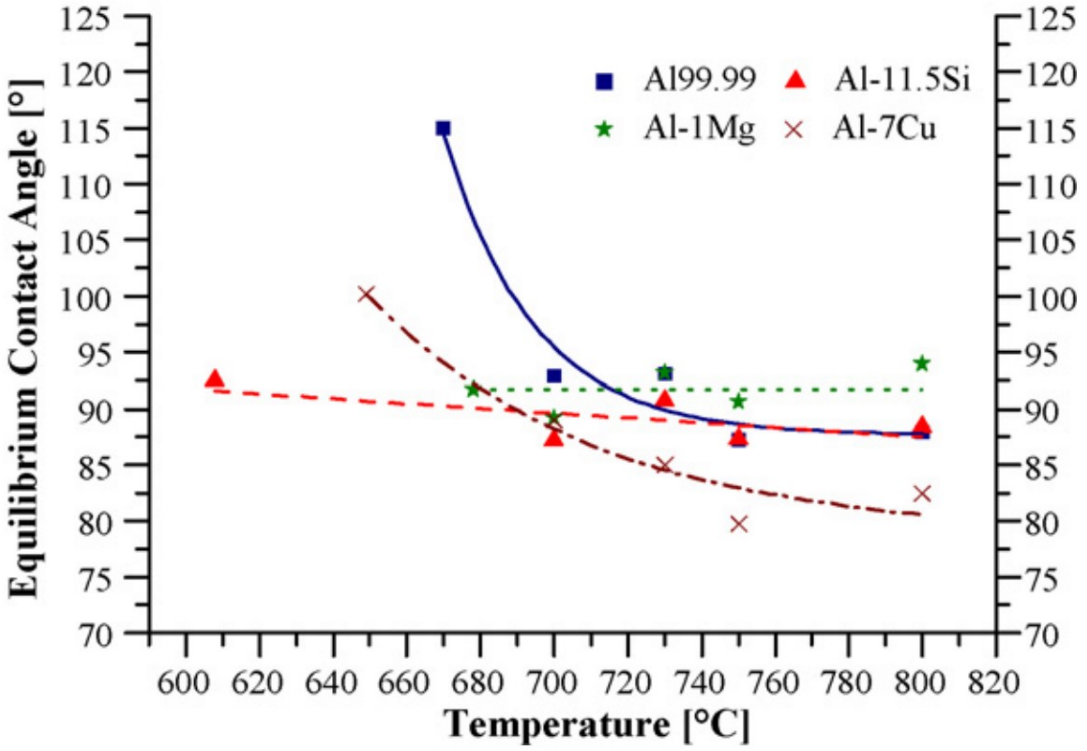

Figure 4.39: Wetting behavior of Al, Al-Mg, Al-Si and Al-Cu on Al_2O_3 [206]

Recall that Ferrand [203] concluded that the meniscus at the exit of the orifice always accelerates the flow with respect to a simple cylindrical jet, and this acceleration contribution decreases with increasing wetting, where it reaches a minimum for materials with $\theta_s \sim 60°$. They explained that when $\theta_s > 60°$, this effect is due to local pressure gradients, which vary depending on the size of the meniscus (i.e. length and radius). Thus, C_d versus Re calibrations obtained using water (and a hydrophobic-coated base plate) likely exhibited less wetting than with Al or Al-Cu on the same crucible (i.e. the length and radius of the meniscus during calibration was likely different than observed during the high-temperature experiment). Thus, the accelerative contribution to flow rate provided by the kinetic energy of the meniscus would be less when draining Al or Al-Cu (probable wetting) relative to water calibrations (no wetting). As mentioned earlier, the model used for the DC method to predict the flow rate of the of stream exiting the crucible does consider this added accelerative term caused by wetting/meniscus growth. Nevertheless, if the experimental flow is indeed affected by this phenomenon, C_d would intrinsically account of this, in addition to viscous losses. This means that C_d would no longer be

valid for liquids exhibiting different wetting characteristics, and therefore should not be used to predict the flow rate of Al or Al-Cu. To illustrate this dilemma, the expected experimental flow rate, $Q_{literature}$ (m^3/s), of Al at 1032 K and Al-Cu at 1029 were calculated using properties values published in literature. Since discharge coefficient, $C_d = a(Re)^3 + b(Re)^2 + c(Re) + d$, was calibrated using a hydrophobic-coated orifice plate (and solely characterizes these conditions) $Q_{literature}$ is assumed to be the flow rate of Al or Al-Cu if no wetting exists between the liquid and the crucible:

$$Q_{literature} = C_d \cdot \pi r_o^2 \sqrt{2g\left(h - \frac{\sigma_{lit}}{\rho_{lit} g r_o}\right)} \tag{4.20}$$

Where σ_{lit} (N/m) was provided by Mills [172] and Schmitz *et al.* [15] and ρ_{lit} (kg/m^3) from Assael *et al.* [6] and Plevachuk *et al.* [165] for Al and Al-Cu, respectively. Recall that h (m) was measured experimentally as described in Section 4.1.2. $Q_{literature}$ of Al and Al-Cu–if no wetting occurred– is compared to the actual measured flow rate, $Q_{measured}$ (m^3/s). These flow rates were plotted for the same Re ranges in Figure 4.40 (Al at 1032 K) and Figure 4.41 (Al-Cu at 1029 K).

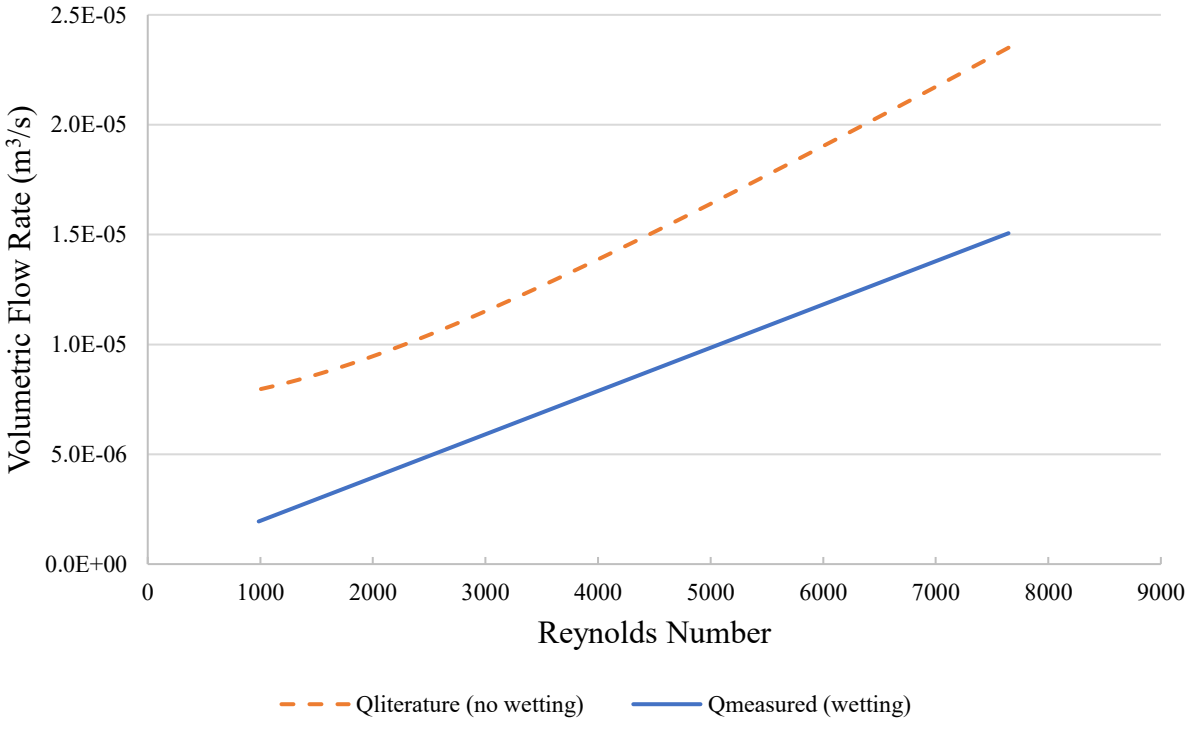

Figure 4.40: $Q_{literature}$ and $Q_{measured}$ of Al at 1032 K

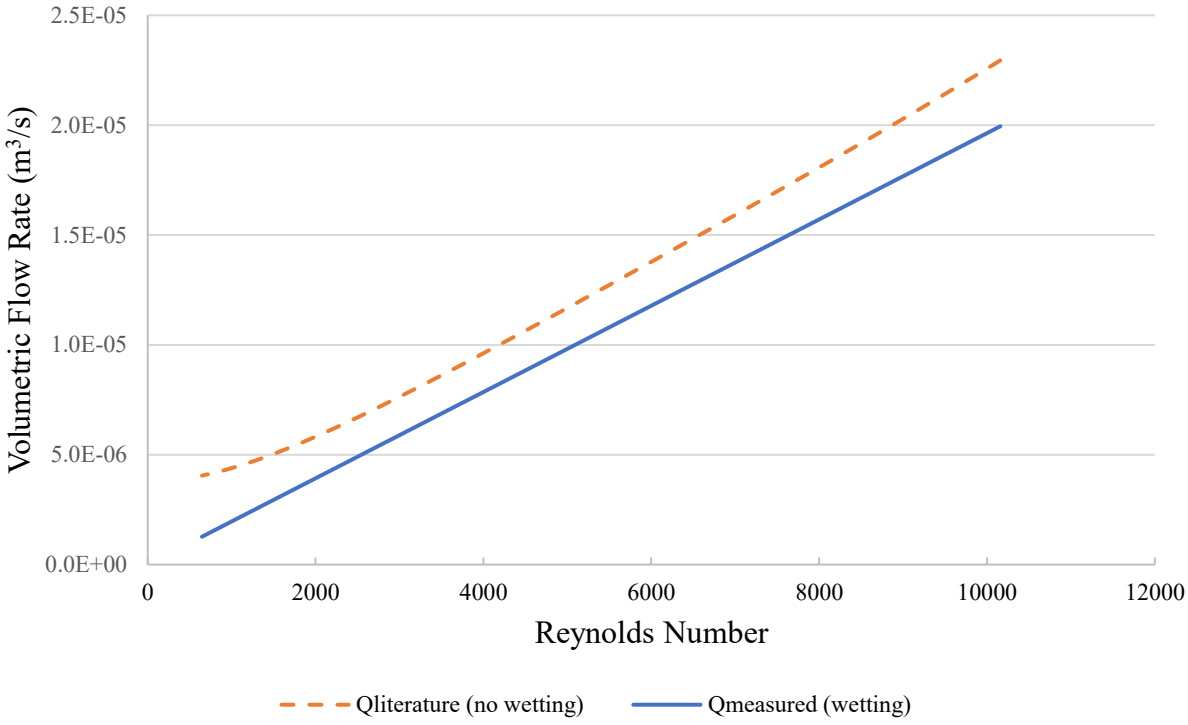

Figure 4.41: $Q_{literature}$ and $Q_{measured}$ of Al-Cu at 1029 K

In Figure 4.40 and Figure 4.41, $Q_{measured}$ is clearly lower than $Q_{literature}$. This is consistent with conclusions made by Ferrand [203], because $Q_{literature}$ represents flow with assumed no (or minimal) wetting, which they showed equates to larger accelerative contribution from the meniscus, or consequently higher relative flow rates. Clearly, wetting at the exit of the orifice has an effect on the flow rates observed during both Al and Al-Cu experiments; there is strong evidence that suggests wetting reduces the flow rate relative to non-wetting conditions. This finding helps substantiate the inaccurate results presented in Section 4.2–particularly the Al and Al-Cu density measurements, which were ~30% lower than other values published in literature. The modified Bernoulli formulation omits the accelerative contribution provided by the meniscus to main flow and does not differentiate the difference between flow from an orifice with low and high wettability. Consequently, the Gauss-Newton regression converges to a lower density in Al or Al-Cu experiments to compensate for the lower measured flow rates (than expected for no wetting conditions). The analysis presented in Figure 4.40 and Figure 4.41 also reveals that wetting has an effect on flow rate as soon as flow begins (i.e. at t = 0 seconds or Re ~ 10000). It is also understood that a ring of liquid at the exit of the orifice spreads outwards, radially and

perpendicularly to the main flow, wetting the base of the crucible surrounding the orifice. The dynamic contact angle, θ_d, is the contact angle which occurs in the course of wetting (advancing angle) or de-wetting (receding angle) of a solid. Generally, the θ_d of a liquid decreases with time; an example of this is shown in Figure 4.42 from a study conducted by Bao *et al.* [205].

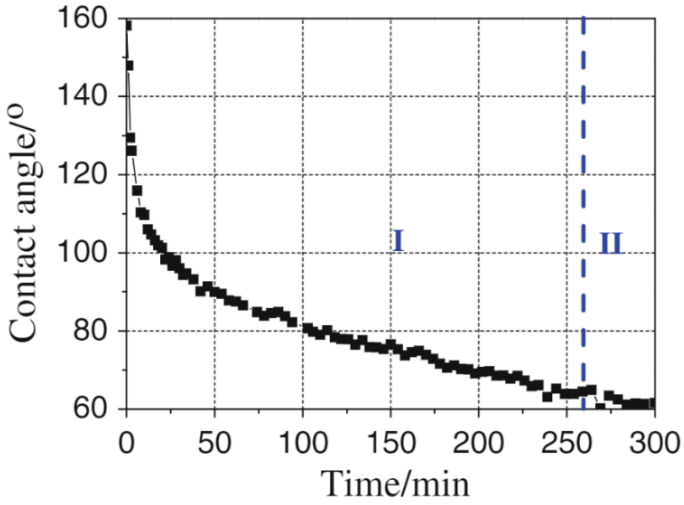

Figure 4.42: Contact angle vs time for Al on Al_2O_3 at 1373 K in 10^{-8} bar vacuum [205]

Bao *et al.* [205] concluded that the time required to reach the equilibrium contact angle depends on the removal of the oxide layer on the Al sessile drop surface. The surface of the draining stream observed during DC experiments is assumed to be continuously replenished, nullifying the effect of an oxide layer. In such cases, spreading of the liquid metal is a very fast process. Eustathopoulos [207] explains: "As the viscosity of liquid metals and alloys is very low—a few mPa·s—spreading of this type of liquid is a very fast process. As a general rule, for θ_s > 20°, the "spreading time" (defined as the time needed for a millimeter sized droplet to attain the equilibrium contact angle) is around 10 milliseconds". It is therefore expected that the liquid Al or Al-Cu spreads rapidly outwards from the orifice, and the dynamic contact angle quickly approaches the equilibrium contact angle, which for Al and Al-Cu (for temperatures measured in this study) ranges approximately between 90º and 70º. Ferrand [203] claimed that the local pressure gradients that create the accelerative effect of the meniscus decreases as the meniscus grows. Therefore, the added contribution to flow rate from the meniscus for Al or Al-Cu experiments ought to decrease as a function of how much the liquid wets the crucible, which evolves over time. To substantiate this theory, the ratio of actual experimental flow rate versus expected flow rate without wetting

($Q_{measured}/Q_{literature}$) was calculated for all experiments conducted and presented in Section 4.2. This measure is a good indicator of the extent of the effect of wetting on the flow rate of the liquid compared to if theoretically no wetting occurred. The ratio of both flow rates as a function of time for Al and Al-Cu experiments were plotted in Figure 4.43 and Figure 4.44, respectively. With the exception of Al-Cu at 1224 K, the ratios for all Al and Al-Cu experiments decrease with drain time. This analysis is further evidence towards conclusions made by Ferrand [203] that:

1. A thin ring of liquid spreads outwards, radially and perpendicularly to the main flow and wets the surface around the opening on the base of the crucible
2. As the liquid spreads outwards, the radius of the meniscus decreases; in turn reducing the accelerative effect on flow rate caused by local pressure within the meniscus.

Ultimately, since θ_d decreases with time, and the flow rate changes depending on the size of the meniscus (wetting), the assumptions used to develop the modified Bernoulli formulation (discussed in Section 2.4.3) that the flow is "quasi-steady state", the radius remains constant, and the stream is cylindrical are no longer valid. This should be revisited in future studies, and the model should be further modified to account of these unsteady state conditions.

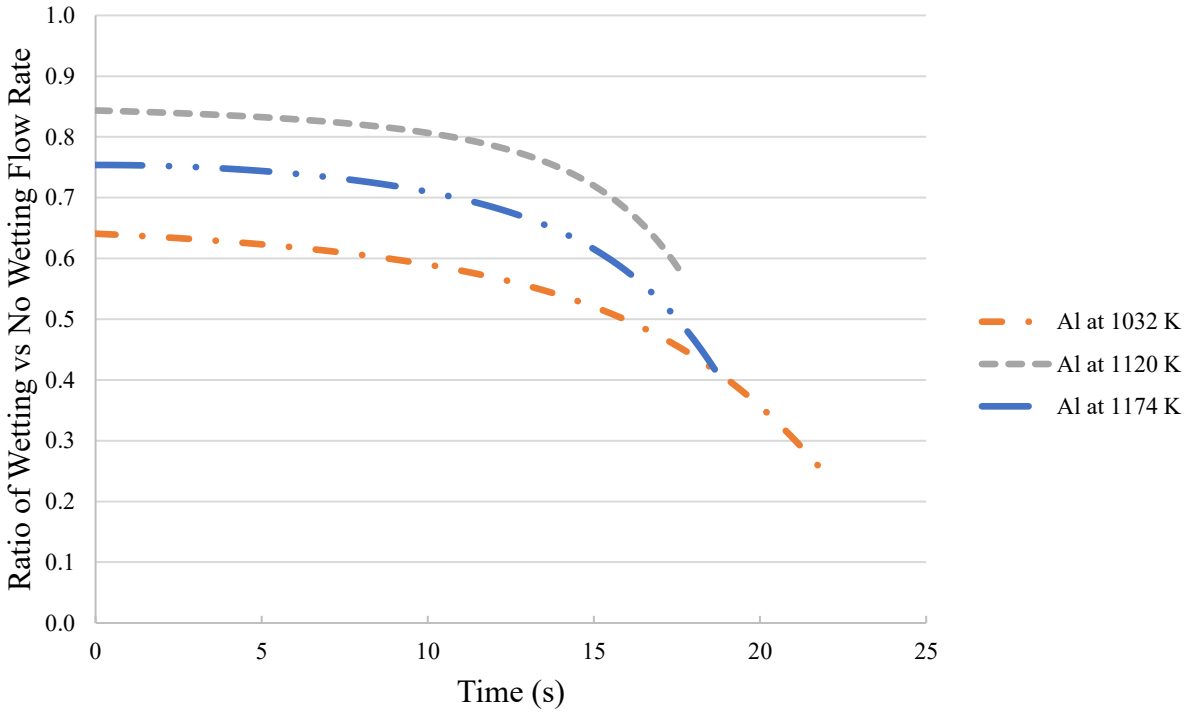

Figure 4.43: ($Q_{measured}/Q_{literature}$) as a function of time for Al at various temperature

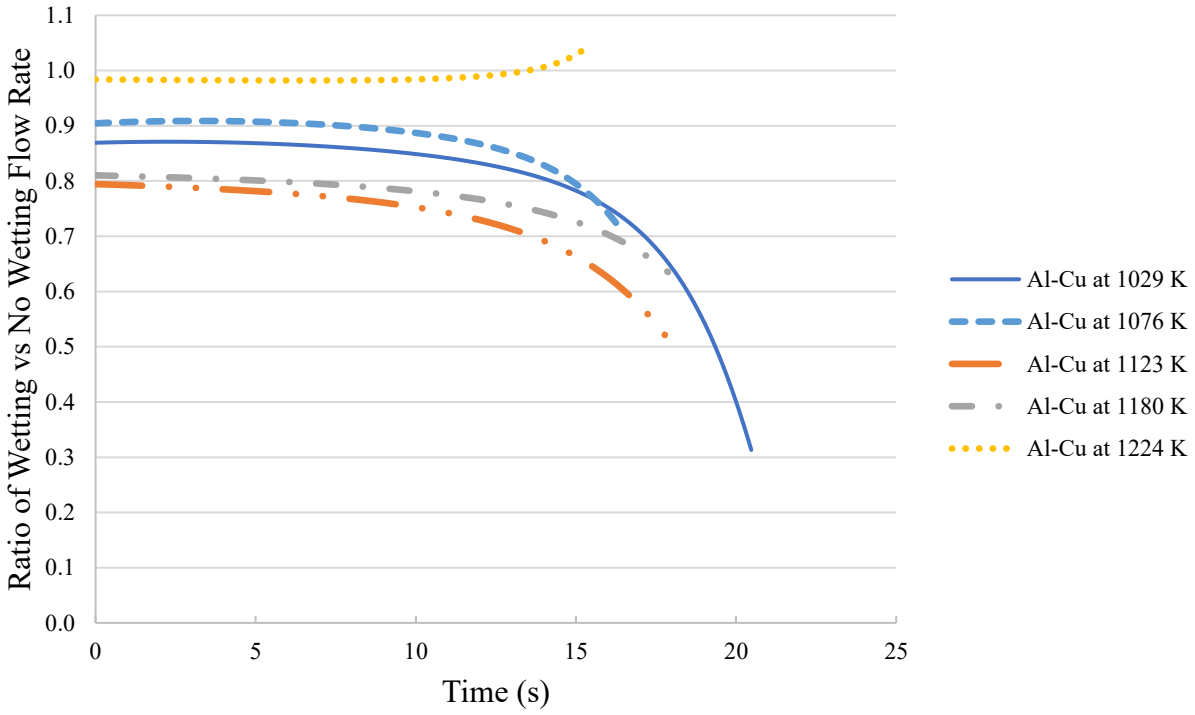

Figure 4.44: ($Q_{measured}/Q_{literature}$) as a function of time for Al-Cu at various temperature

4.3.3 Dimensionless Number Analysis

The meniscus at the exit of the orifice forms due to capillary action, where adhesion occurs between the Al or Al-Cu and the Al_2O_3 crucible and spreads along the surface until gravitational forces overcome the liquid cohesion. The combination of surface tension (cohesion within the liquid) and the adhesive forces between the liquid and the solid will propel the meniscus outwards. In Section 4.3.2, the relationship between wetting of the crucible base and the flow rate of the draining liquid was studied. There is strong evidence that suggests wetting slows the flow, which is correlated to the size of the growing meniscus which evolves with drain time. Figure 4.43 and Figure 4.44 reveal that this phenomenon becomes more and more dominant near the end of the experiments–the ratio between wetting and non-wetting flow rates sharply drops off at ~ 15 seconds for both Al and Al-Cu experiments.

To better understand the effect of wetting on flow rate, particularly as a function of drain time, it is useful to look at opposing forces, which can be achieved using dimensionless numbers.

The Weber number, We, relates the inertia forces to the forces resulting from surface tension of the liquid:

$$We = \frac{2\rho r_o \left({Q_{theo}}/{\pi r_o^2}\right)^2}{\sigma} = \frac{\text{inertial forces}}{\text{surface tension}} \tag{4.21}$$

Where Q_{theo} (m^3/s) is the theoretical flow rate, ρ (kg/m^3) and σ (N/m) are the density and surface tension of the liquid, respectively (obtained from published literature data), and r_o (m) is the radius of the orifice. The ratio of wetting flow rate (experimentally measured) and non-wetting flow rate (determined with properties published in literature), i.e. $Q_{measured}/Q_{literature}$, for Al at 1032 was plotted as a function of We, shown in Figure 4.45. Here, $Q_{measured}/Q_{literature}$ sharply decreases with decreasing We. This highlights that the decrease in flow rate caused by wetting becomes more dominant as surface tension forces overcome the inertial forces of the flowing stream.

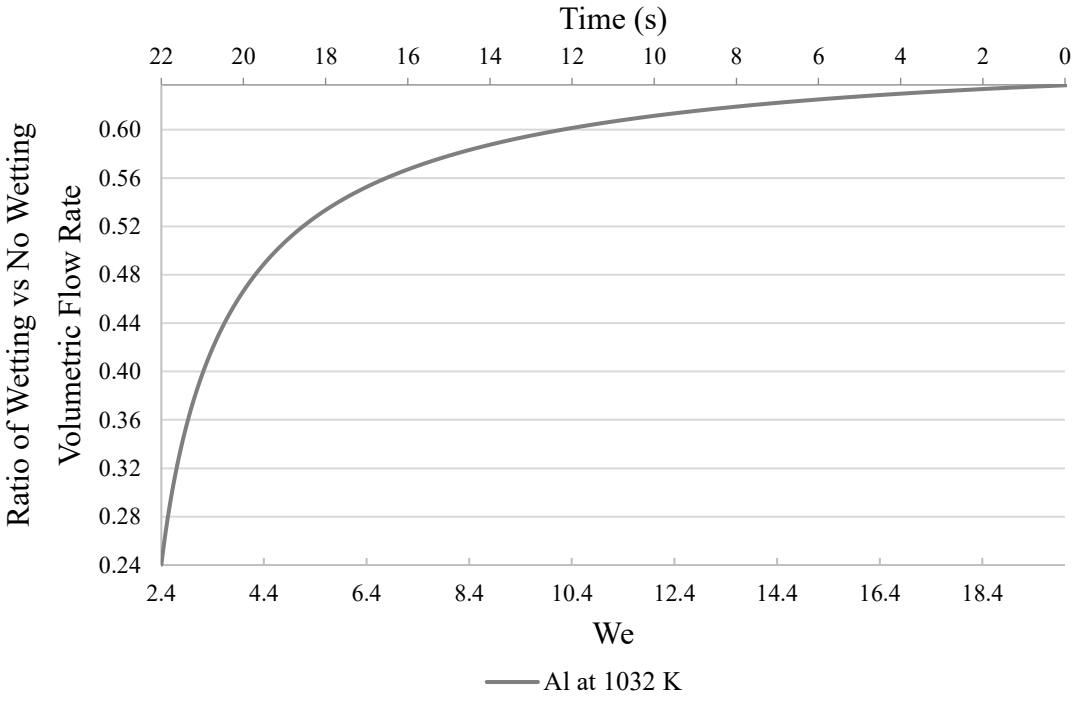

Figure 4.45: ($Q_{measured}/Q_{literature}$) as a function of We for Al at 1032 K

Now, as previously mentioned, the meniscus will spread radially outwards, perpendicular to the flow, until gravity overcomes the liquid surface tension. To investigate this phenomenon, $Q_{measured}/Q_{literature}$ was plotted as a function of We/Fr. Recall, the Froude number, Fr:

$$Fr = \frac{\left({}^{Q_{theo}}/_{\pi r_o^2}\right)^2}{2gh} = \frac{\text{inertial forces}}{\text{potential (gravitational) forces}} \tag{2.96}$$

By dividing We by Fr, the potential or gravitational forces exerted on the liquid can be approximately related to the surface tension forces:

$$\frac{We}{Fr} \propto \frac{\text{potential (gravitational) forces}}{\text{surface tension}} \tag{4.22}$$

The $Q_{measured}/Q_{literature}$ ratio was plotted against We/Fr for Al at 1032 K in Figure 4.46. This analysis is consistent with the theory that wetting (i.e. growth of the meniscus) decreases the flow rate relative to non-wetting conditions. As time passes, surface tension or cohesion of the liquid becomes increasingly dominant relative to gravity forces, which would promote extension of the meniscus via capillary action. Figure 4.40 shows that the flow rate of Al at 1032 K that wets Al_2O_3 decreases sharply compared to the flow rate expected when no wetting occurs. This seems to further reinforce the relationship between meniscus size and flow rate.

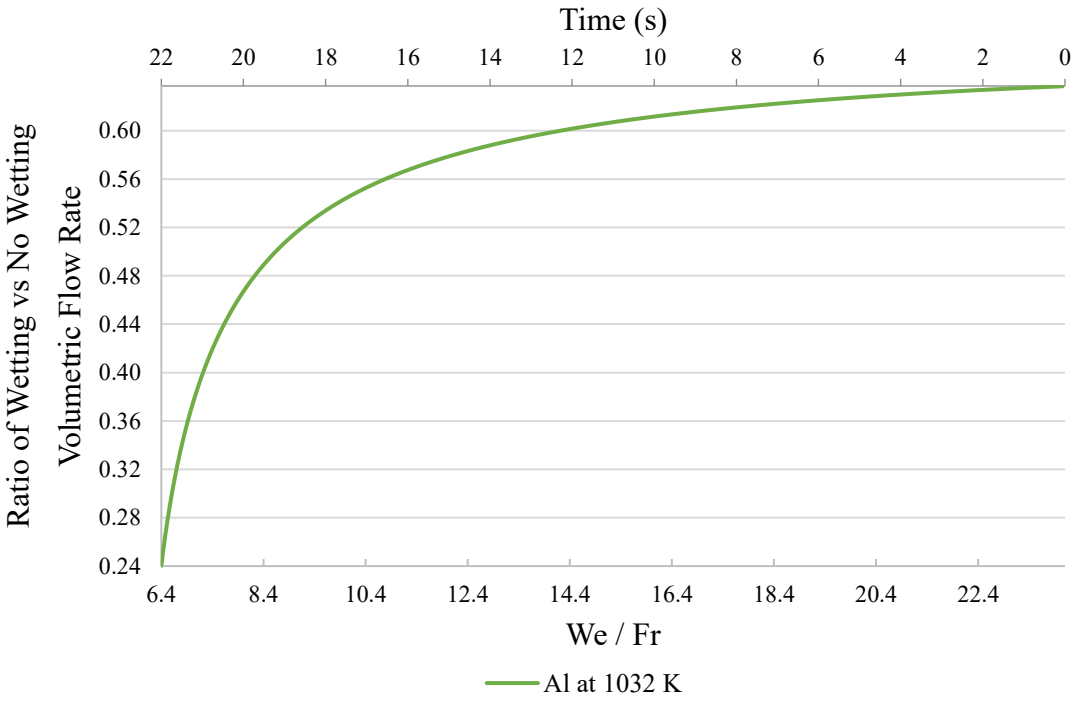

Figure 4.46: ($Q_{measured}/Q_{literature}$) as a function of We/Fr for Al at 1032 K

Literature has shown that dynamic contact angle, θ_d, formed between a flowing liquid (advancing or receding) and the solid is not constant but reflects the balance between capillary and viscous forces [208]. The relationship between forces is defined by the Capillary number, Ca:

$$Ca = \frac{\eta\left({}^{Q_{theo}}/_{\pi r_o^2}\right)}{\sigma} = \frac{\text{viscous forces}}{\text{surface tension}} \tag{4.23}$$

Where η (Pa·s) is the viscosity of the liquid obtained from published literature. The θ_d is related to small Ca values using Tanner's law [208]:

$$\theta_d \sim Ca^{1/3} \tag{4.24}$$

In theory, this law is valid over a wide range of Ca, with θ_d decreasing and converging to an equilibrium contact angle as Ca approaches 0 [208]. This is shown in Figure 4.47. There are also numerous other models that were developed and are in good agreement which each other that describe the same trend [209]. These are shown in Figure 4.48.

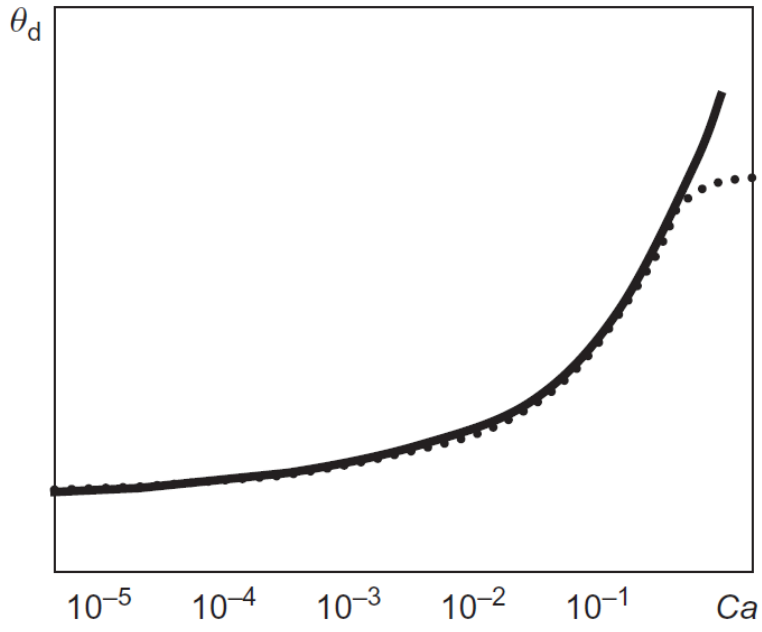

Figure 4.47: Experimental results for the dynamic contact angle versus capillary number (dots) and Tanner's relation (continuous line) [208]

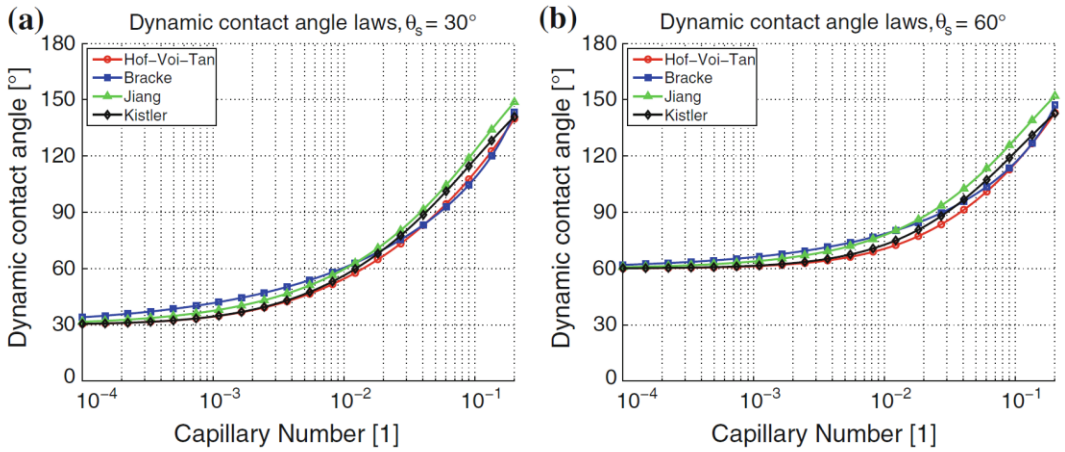

Figure 4.48: Dynamic contact angles as a function of capillary number, showing the agreement among literature models: a) $\theta_s = 30°$ b) $\theta_s = 60°$ [209]

Simply put, for low Ca values, flow is dominated by capillary or surface tension forces, whereas high Ca values, the capillary forces are negligible compared to viscous forces. A decreasing θ_d fundamentally describes an advancing meniscus front. It was also shown in Section 4.3.2 that for both liquid Al and Al-Cu on Al_2O_3, the θ_d decreases with time. The $Q_{measured}/Q_{literature}$ of Al at 1032 K was plotted versus Ca, given in Figure 4.49.

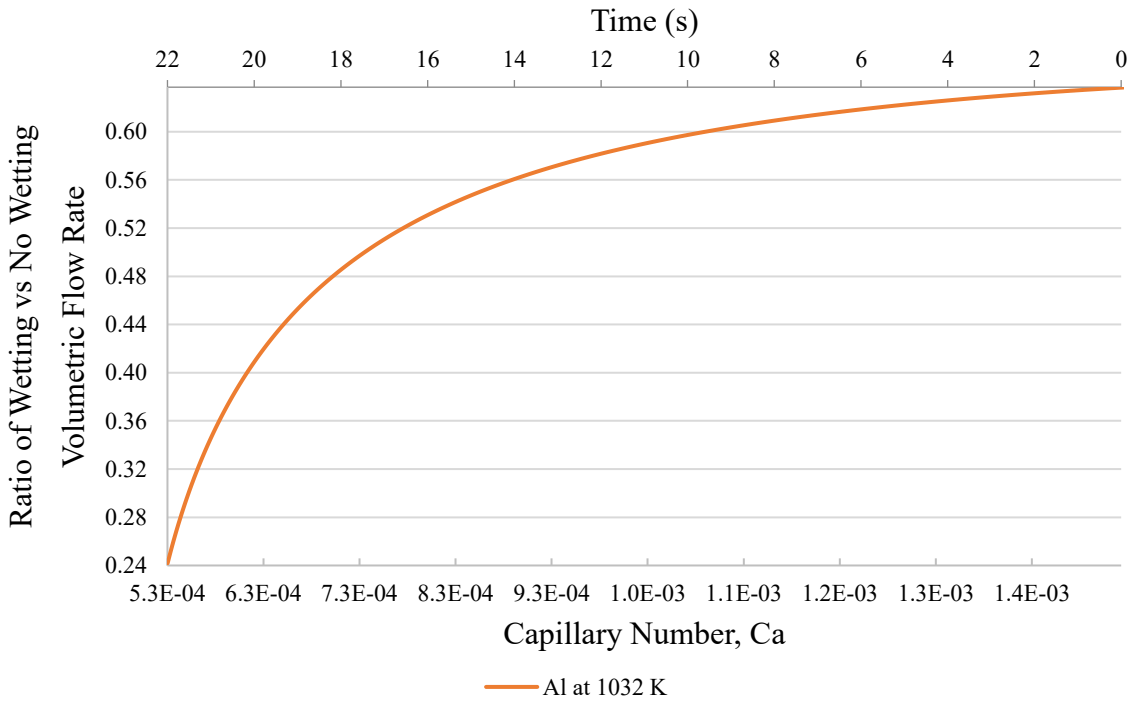

Figure 4.49: ($Q_{measured}/Q_{literature}$) as a function of Ca for Al at 1032 K

The flow rate of Al relative to the expected non-wetting flow rate appears to decrease with decreasing Ca. Since Ca decreases proportionally with θ_d, Figure 4.49 strongly suggests that the lower $Q_{measured}$ of Al (relative to $Q_{literature}$) is related to θ_d, supporting the theory that flow rate is affected by wetting of the liquid near the orifice exit when draining under the influence of gravity. In summary, the ratio of the experimentally measured flow rate (assumed wetting) to the expected flow rate calculated using literature values (assumed no wetting) appears to be strongly related to capillary forces. These forces were shown to be the driving force behind the growth of the meniscus as a function of time. The meniscus size was previously shown to have an effect of the flow rate of a draining liquid using a similar setup as the DC method [203]. Since the modified Bernoulli formulation does not consider the effect of the meniscus size on the flow rate, wetting is most likely the root cause for the inaccurate density measurements presented in Section 4.2.

4.5. Summary

The viscosity, surface tension and density of 99.9 wt.% Al and Al-Cu (~22.5 wt.% Cu) consisting of 99.99% wt.% Al and Cu shots were determined using a multiple non-linear regression model. Al was measured at 1032, 1120 and 1174 K and Al-Cu at 1029, 1076, 1123, 1180 and 1174 K. The modified Bernoulli model relates experimental quantities of head and flow rate, with surface tension, viscosity, and density, facilitating the calculation of all three properties. The formulation also requires input of the relationship between of C_d versus Re which was calibrated using deionized water. The results presented in this chapter were largely successful, with the exception of density measurements, which were 31% and 20% lower for Al and Al-Cu, respectively, compared to the linear regression fits of data from comparable liquids reported in literature. All density results were well outside plus or minus one SE of the predicted regression values, and for the most part, outside of the 95% PI of the regression. Typically, the agreement between experimental densities, regardless of the experimental method, is excellent, which raises questions regarding the ability of the modified Bernoulli to consistently model flow of the liquid through an orifice under the influence of gravity. Note, the temperature dependencies of surface tension was significantly more negatively correlated than shown in literature, though it is expected that this is simply a result of an insufficient number of datapoints (measurements) at a limited number of temperatures.

Next, the experimentally determined viscosity and surface tension results were compared to various theoretical and empirical models. The measured viscosity of Al agreed best with predictions by the Hirai model, which was described in Section 2.1.1.3. Meanwhile, the Schick model was found to be the best predictor of the viscosity of Al-Cu over the entire range of Cu concentration since it adequately describes the relationship between viscosity and atomic interactions. Nevertheless, at Cu concentrations ≤ 20 at.% or ~ 40 wt.%, all models (with the exception of the Moelwyn-Hughes) were relatively comparable to experimental measurements. Ultimately, however, the Schick, Zhang and Hirai models agreed best with Al-Cu results obtained using the DC method. The measured surface tensions of Al-Cu were compared to, and found to agree very well with, predictions calculated using the Butler and Chatain models. However, when compared other experimental data published in literature, the Chatain model, or multilayer model, fit the best as it is believed it can accurately predict the chemical layering phenomenon.

Roach and Henein [7] previously cautioned that if wetting is an issue, the liquid may spread along the orifice plate, changing the radius of the exiting stream. Analysis revealed that the results output by the Gauss-Newton regression vary depending on the range of experimental data (time series) selected. Previously, the flow rate was assumed to be quasi-steady state, and therefore the properties of the liquid assumed to remain constant over the short duration of the experiment. Both Al and Al-Cu wet solid Al_2O_3, but since the low-temperature calibrations used to determine the frictional characteristics of the crucible were obtained in non-wetting conditions, the C_d versus Re curves were assumed to not be valid for the high-temperature experiments. Wetting appears to have an effect on the flow rate as soon as the liquid begins to drain, and Ferrand [203] suggested that the effect of wetting on flow, very likely, is related to the shape of the meniscus that forms at the outlet of the orifice. By comparing the experimental flow rates of Al and Al-Cu to the "expected" flow rate calculated using literature properties, the effect of wetting versus non-wetting was quantified. With this, strong evidence was produced to indicate that the effect of wetting on decreasing the rate of flow becomes more dominant with time (i.e. as the head of the draining liquid in the crucible approaches 0). Intuitively, and by examining the dynamics of Al and Al-Cu contact angles on Al_2O_3, one can deduce that the shape of the meniscus evolves with time, generating unsteady state flow conditions. Dimensionless number analysis helped identify which forces promote the outwards growth of the meniscus at the exit of the orifice.

CHAPTER 5 : CONCLUSIONS

A thorough literature review was performed on different methods to determine the viscosity, surface tension and density of metallic liquids. These included both experimental techniques and numerical models. There are numerous challenges associated with performing high-temperature thermophysical property measurements, both technically and computationally. For example, most conventional measurement methods are hindered by the compatibility between equipment components and the reactive liquid being measured–refractory materials are required, which introduces high fabrication costs, especially for complex parts like capillary tubes and oscillating plates for viscosity measurement techniques. Further challenges exist mathematically, particularly with surface tension measurements where computational curve-fitting and video processing is required. Another significant hurdle is that most conventional techniques only measure a single property (e.g. one of viscosity, surface tension or density) resulting in higher costs if one needs to set up numerous experimental apparatus. The EML-LD method has therefore become the industry standard by using electromagnetic levitation to simultaneously measure viscosity, surface tension and density (among other properties). And, although it offers several advantages over conventional techniques, there are several insurmountable challenges, like requiring microgravity to measure viscosity. Alternatively, Roach and Henein [7] developed a ground-based technique coined the discharge crucible (DC) method that relates experimental parameters of a liquid flowing under the influence of gravity through an orifice to the several thermophysical properties. Apart from being able to simultaneously measure viscosity, surface tension and density, another major advantage is its simple, and therefore cost-effective, design.

To build upon the work performed by Roach and Henein [7], the DC apparatus was redesigned for the goal of improving on its ability to measure higher melting point and more reactive metallic liquids. This included using an Al_2O_3 crucible able to withstand temperatures up to 1750ºC and adding a Ti getter to reduce O_2 contamination. Further improvements included calibrating the head versus volume of the crucible using an ultrasonic level sensor and incorporating a two-color pyrometer for enhanced temperature monitoring reliability. Ultimately, this high-temperature DC apparatus was simple to operate, and relatively inexpensive to prototype. Unfortunately, at this time, only Al and Al-Cu were measured using this apparatus, which are

considering relatively low-melting point liquids, although the eventual goal is for this piece of equipment to be used on liquids like molten Fe and steel.

The viscosity, surface tension and density of 99.9wt.% Al and Al-Cu alloy (consisting of 22.5wt.% Cu) were measured using the DC method with an Al_2O_3 crucible and determined using a multiple non-linear Gauss-Newton regression model. The flow was modelled using the modified Bernoulli formulation, which relates experimental parameters of head and flow rate with viscosity, surface tension and density. The frictional characteristics of the crucible were characterized by performing calibration experiments with deionized water to determine the C_d versus Re relationship. Al was measured at 1032, 1120 and 1174 K and Al-Cu at 1029, 1076, 1123, 1180 and 1174 K.

The viscosity and surface tension results for both Al and Al-Cu were in relatively good agreement with comparable results published in literature determined using conventional techniques. Linear regression analyses using Minitab 19 Statistical Software were performed on the combined individual data points published in literature (which were originally presented in Section 2.5), yielding regression equation parameters and SE and 95% PI of the regression. Note, viscosity data was fitted to a linearly transformed Arrhenius equation. All viscosity and surface tension results were found to lie within the 95% PI of their corresponding combined literature data regression fits. Further, the viscosity results for Al as well as surface tension results for both Al and Al-Cu were all within plus or minus one SE of the regression models. It is clear that the surface tension for both Al and Al-Cu liquids reflects an O saturated liquid when comparing the results to data published in literature. For example, the Al surface tension results deviate by only ±3% from the suggested values proposed by Mills [56] for O saturated Al.

Additionally, the viscosity results of Al and Al-Cu measured in this study, as well as reported in literature, were compared to various numerical models, with most models providing relatively accurate predictions of viscosity. The results reported for Al were in closest agreement with values calculated using the Hirai model, while Al-Cu correlated well with values calculated using the Schick, Zhang and Hirai models. All of the numerical models for Al viscosity successfully predicted values within plus or minus one SE of the combined literature data linear regression model. Moreover, the Al-Cu surface tension results were compared to values predicted by both the Butler and Chatain models, showing excellent agreement, within ± 4%. However, the

temperature dependencies (i.e. surface tension temperature coefficients) for Al-Cu (and Al) were significantly more negative than calculated from experimental data published in literature or by predictions using theoretical models. Further efforts are needed to investigate this discrepancy, although it is likely that simply more measurements are needed to yield a more statistically significant surface tension-temperature relationship.

In contrast to viscosity and surface tension results, Al and Al-Cu density measurements for were in poor agreement with comparable data published in literature (they were significantly lower). For example, the largest difference between measured results and the linear regressions obtained from literature data was -31% for Al and -20% for Al-Cu. This is of substantial concern seeing as the spread between density data for both Al and Al-Cu in literature is relatively low. The SE of the regression for combined Al literature data was only 58 kg/m^3 (N=298) while Al-Cu was 126 kg/m^3 (N=58), which at T_m is equivalent to ± 2% and ± 5%, respectively. The large difference between measured results by the DC method and data obtained from literature reveals that perhaps the modified Bernoulli formulation did not accurately model the actual flow of the draining liquids using established assumptions.

Roach and Henein [7] previously cautioned that if wetting is an issue, the liquid may spread along the orifice plate, changing the effective radius of the exiting stream. The modified Bernoulli formulation assumes that the size of the radius remains constant over the duration of the experiment and that the stream is perfectly cylindrical, therefore, any change to the radius size would result in a different actual flow rate compared to what was anticipated. Ferrand [203] also suggested that, with liquid draining through an orifice under the influence of gravity, a thin ring of liquid spreads outwards, radially and perpendicularly to the main flow and wets the surface around the opening of the orifice and as the liquid spreads outwards, the radius of the meniscus decreases; in turn reducing the accelerative effect on flow rate caused by local pressure within the meniscus. Through analysis, it was determined that the actual measured flow rate of Al and Al-Cu experiments was indeed lower than the expected flow rate based on the modified Bernoulli formulation and the expected thermophysical properties of the liquid found in literature. It was concluded that the C_d versus Re relationship not only characterizes frictional losses, but also the effect of wetting on the flow rate. And, since these calibrations were obtained using a deionized water and a hydro-phobic coated crucible, the characterization of the effect of wetting would not

translate to high-temperature experiments where the liquid significantly wets the orifice. This gap ultimately led to the modified Bernoulli formulation predicting a higher flow rate than measured since it did not account for accelerative losses caused by a larger meniscus. Additionally, analysis revealed that the wetting immediately had an effect on the flow rate of the draining liquid, and the effect became more dominant with increasing drain time. This was supported using dimensionless analysis, where it was determined that the relative difference between measured flow rate and flow rate modelled using the modified Bernoulli formulation increased as a function of dynamic contact angle, which in turn is related to the Capillary number.

In conclusion, although the DC method (using an Al_2O_3 crucible) was able to successfully measure, despite wetting at the orifice tip, the viscosity and surface tension of both O saturated Al and an Al-Cu alloy at various temperatures, it was not capable of accurately measuring density. It was determined that discrepancies between measured density and comparable data published in literature were caused by the effect that wetting at the tip of the orifice has on the actual measured flow rate of the draining liquid. As part of the European Space Agency THERMOLAB project, further work is warranted to acquire additional Al-Cu measurements, and eventually compare these results to thermophysical property measurements obtained for a batch of samples with the same composition that were measured using the EML-LD technique onboard the ISS.

CHAPTER 6 : FUTURE WORK

In this work, significant steps were made to further validate the DC method as a suitable and reliable alternative to conventional thermophysical property measurement techniques. Efforts were also made to redesign the experimental equipment to facilitate measurement of higher melting point metals and alloys by, namely, using an Al_2O_3 crucible. In doing so, the results from this study, particularly density measurements, differed from previous studies that employed the DC method to measure liquid Al. There is some evidence that suggests that these discrepancies exist due to wetting of Al and Al-Cu at the Al_2O_3 orifice tip. Further efforts are required to investigate this issue, whether it be by performing tests of the same liquid at the same temperature, but using different crucible materials exhibiting different wettability (e.g. graphite, boron nitride), or by installing a suitable video camera capable of imaging and recording the meniscus of the liquid as it drains. Additionally, despite wetting, both viscosity and surface tension results were in good agreement with prior data published in literature. It would be of interest to better understand why only density is affected by wetting, and if this holds true for other alloy compositions. Finally, due to the material compatibility constraints when selecting an appropriate crucible material, it may be impossible to fully eliminate wetting, and the effect it has on flow. Therefore, the modified-Bernoulli formulation should be further modified to account for the effect of wetting, specifically to include the unsteady state effect that the continuously growing meniscus has on flow rate over the course of the experiment. Analysis in Section 4.4.1 revealed that the viscosity results varied depending on the amount of data included in the Gauss-Newton regression (i.e. as a function of drain time). Perhaps this is also due to wetting at the orifice tip and can be used to quantify the effect that the growth of the meniscus has on property measurement by means of back-calculation.

Furthermore, although individual surface tension results agreed very closely with data published in literature, the overall temperature dependencies of the results were significantly more negative. This may simply be due to a lack of experimental measurements; therefore, additional experiments should be conducted to increase the number of data for both Al and Al-Cu, and then use these results to calculate the surface tension temperature coefficients. The Al-Cu data should then be compared to results reported from the ESA Batch 2 experiments, so the effectiveness of the DC method can be compared to that of the EML-LD. Further experiments should also be conducted on various metals and alloys, and even slags, particularly those that have higher melting

points, since the experimental equipment was designed specifically for this. This would be a good opportunity to test the varying-temperature DC model, provided in Appendix G and H, to verify if it can accurately measure the change in thermophysical properties if the temperature changes due to heat loss. Additionally, it would be of interest to measure different Al-Cu alloys with varying Cu concentrations. By comparing these results with empirical models discussed in Section 4.3, the relationships between thermodynamic potentials and viscosity may be better understood.

Lastly, a number of improvements to the design of the equipment can be made to facilitate more accurate measurements. For example, there is value in incorporating direct measurement of the head using a laser; independent measurement of head and cumulative mass would reduce systematic errors. This would require a cooling sleeve and proper calibrations. Also, there are some concerns regarding the amount of scatter output by the load cell. Efforts should be made to reduce the scatter by means of reducing vibrations in the apparatus. Finally, although significant measures were taken to reduce O_2 contamination, the results, particularly surface tension, reflected O saturated values. Future work should investigate the feasibility of using a reducing atmosphere by incorporating CO:CO2 or even H_2 mixture with Ar or He. Such improvements are recommended to improve upon the potential of the DC method as a simple and cost-effective alternative means of high-temperature thermophysical property measurements.

REFERENCES

[1] H. Kvande, "The Aluminum Smelting Process," *J. Occup. Environ. Med.*, vol. 56, no. 5, pp. 2–4, 2014.

[2] I. F. Bainbridge and J. A. Taylor, "The Surface Tension of Pure Aluminum and Aluminum Alloys," *Metall. Mater. Trans. A*, vol. 44, no. 8, pp. 3901–3909, 2013.

[3] M. Schick, J. Brillo, I. Egry, and B. Hallstedt, "Viscosity of Al-Cu liquid alloys: measurement and thermodynamic description," *J. Mater. Sci.*, vol. 47, no. 23, pp. 8145–8152, 2012.

[4] J. J. Wessing and J. Brillo, "Density, Molar Volume, and Surface Tension of Liquid Al-Ti," *Metall. Mater. Trans. A*, vol. 48, no. 2, pp. 868–882, 2017.

[5] E. Louvis, P. Fox, and C. J. Sutcliffe, "Selective laser melting of aluminium components," *J. Mater. Process. Tech.*, vol. 211, no. 2, pp. 275–284, 2011.

[6] M. J. Assael *et al.*, "Reference Data for the Density and Viscosity of Liquid Aluminum and Liquid Iron," *J. Phys. Chem. Ref. Data*, vol. 35, no. 1, pp. 285–300, 2006.

[7] S. J. Roach and H. Henein, "A New Method to Dynamically Measure the Surface Tension, Viscosity, and Density of Melts," *Metall. Mater. Trans. B*, vol. 36, no. 5, pp. 667–676, 2005.

[8] T. Gancarz, J. Jourdan, W. Gasior, and H. Henein, "Physicochemical properties of Al, Al-Mg and Al-Mg-Zn alloys," *J. Mol. Liq.*, vol. 249, pp. 470–476, 2018.

[9] T. Gancarz and W. Gasior, "Density, Surface Tension, and Viscosity of Liquid Pb-Sb Alloys," *J. Chem. Eng. Data*, vol. 63, no. 5, pp. 1471–1479, 2018.

[10] T. Gancarz, W. Gąsior, and H. Henein, "The Discharge Crucible Method for Making Measurements of the Physical Properties of Melts: An Overview," *Int J Thermophys*, vol. 35, no. 9–10, pp. 1725–1748, 2014.

[11] T. Gancarz, W. Gąsior, and H. Henein, "Physicochemical Properties of Sb, Sn, Zn, and Sb-Sn System," *Int. J. Thermophys.*, vol. 34, no. 2, pp. 250–266, 2013.

[12] T. Gancarz, "Physicochemical Properties of Sb-Sn-Zn Alloys," *J. Electron. Mater.*, vol. 43, no. 12, pp. 4374–4385, 2014.

[13] T. Gancarz, "Density, surface tension and viscosity of Ga-Sn alloys," *J. Mol. Liq.*, vol. 241, pp. 231–236, 2017.

[14] T. Gancarz, "Density, surface tension and viscosity of liquid ZnAl + X (X = Li, Na, Si) alloys," *Fluid Phase Equilib.*, vol. 427, pp. 97–103, 2016.

[15] J. Schmitz, J. Brillo, I. Egry, and R. Schmid-Fetzer, "Surface tension of liquid Al–Cu binary alloys," *Int. J. Mater. Res.*, vol. 100, no. 11, pp. 1529–1535, 2009.

[16] S. Roach and H. Henein, "A Dynamic Approach to Determining the Surface Tension of a Fluid," *Can. Metall. Q.*, vol. 42, no. 2, pp. 175–186, 2003.

[17] J. Bergendahl, “Fluid Properties,” in *Treatment System Hydraulics*, American Society of Civil Engineers (ASCE), 2008, pp. 13–31.

[18] E. J. Shaughnessy, I. M. Katz, and P. Schaffer, James, “Fluid Properties,” in *Introduction to Fluid Mechanics*, New York, NY, USA: Oxford University Press, 2005, pp. 43–102.

[19] N. de Nevers, *Fluid Mechanics for Chemical Engineers*, 2nd ed. New York, NY, USA: McGraw-Hill, 1991.

[20] M. Jeyakumar, M. Hamed, and S. Shankar, “Rheology of liquid metals and alloys,” *J. Nonnewton. Fluid Mech.*, vol. 166, no. 14–15, pp. 831–838, 2011.

[21] T. Iida and R. I. L. Guthrie, *The Thermophysical Properties of Metallic Liquids*, 1st ed. Oxford, UK: Oxford University Press, 2015.

[22] R. F. Brooks, A. T. Dinsdale, and P. N. Quested, “The measurement of viscosity of alloys—a review of methods, data and models,” *Meas. Sci. Technol.*, vol. 16, no. 2, pp. 354–362, 2005.

[23] I. Budai, M. Z. Benkő, and G. Kaptay, “Comparison of Different Theoretical Models to Experimental Data on Viscosity of Binary Liquid Alloys,” *Mater. Sci. Forum*, vol. 537–538, pp. 489–496, 2007.

[24] J. Cheng, J. Gröbner, N. Hort, K. U. Kainer, and R. Schmid-Fetzer, “Measurement and calculation of the viscosity of metals—a review of the current status and developing trends,” *Meas. Sci. Technol.*, vol. 25, no. 6, 2014.

[25] G. Kaptay, “A unified equation for the viscosity of pure liquid metals,” *Zeitschrift für Met.* , vol. 96, no. 1, pp. 24–31, 2005.

[26] T. Iida, R. Guthrie, M. Isac, and N. Tripathi, “Accurate predictions for the viscosities of several liquid transition metals, plus barium and strontium,” *Metall. Mater. Trans. B*, vol. 37, no. 3, pp. 403–412, 2006.

[27] E. N. da C. Andrade, “XLI. A theory of the viscosity of liquids.—Part I.,” *London, Edinburgh, Dublin Philos. Mag. J. Sci.*, vol. 17, no. 112, pp. 497–511, 1934.

[28] L. Battezzati and A. L. Greer, “The viscosity of liquid metals and alloys,” *Acta Metall.*, vol. 37, no. 7, pp. 1791–1802, 1989.

[29] E. N. da C. Andrade, “LVIII. A theory of the viscosity of liquids.—Part II,” *London, Edinburgh, Dublin Philos. Mag. J. Sci.*, vol. 17, no. 113, pp. 698–732, 1934.

[30] R. P. Chhabra and D. K. Sheth, “Viscosity of molten metals and its temperature dependence,” *Zeitschrift fur Met.*, vol. 81, no. 4, pp. 264–271, 1990.

[31] M. Hirai, “Estimation of viscosities of liquid alloys,” *ISIJ Int.*, vol. 33, no. 2, pp. 251–258, 1993.

[32] J. Brillo, *Thermophysical Properties of Multicomponent Liquid Alloys*. Berlin, Germany: Walter de Gruyter GmbH & Co KG, 2016.

[33] J. H. Hildebrand, *Viscosity and Diffusivity: A Predictive Treatment*. John Wiley & Sons,

1977.

[34] E. A. Moelwyn-Hughes, *Physical Chemistry*, 2nd ed. New York, NY, USA: Pergamon Press, 1961.

[35] T. Iida, M. Ueda, and Z. Morita, "On the Excess Viscosity of Liquid Alloys and the Atomic Interaction of Their Constituents," *Tetsu-to-Hagane*, vol. 62, no. 9, pp. 1169–1178, 1976.

[36] F. Zhang, Y. Du, S. Liu, and W. Jie, "Modeling of the viscosity in the AL-Cu-Mg-Si system: Database construction," *Calphad Comput. Coupling Phase Diagrams Thermochem.*, vol. 49, pp. 79–86, 2015.

[37] A. J. Lewis, "The absolute measurement of the viscosity of liquid tin," *Proc. Phys. Soc.*, vol. 48, no. 1, pp. 102–110, 1936.

[38] R. F. Brooks, A. P. Day, R. J. L. Andon, L. A. Chapman, K. C. Mills, and P. N. Quested, "Measurement of viscosities of metals and alloys with an oscillating viscometer," *High Temp. - High Press.*, vol. 33, no. 1, pp. 73–82, 2001.

[39] Y. Wang, Y. Wu, and X. Bian, "Composition dependence of viscosity for Al(1-x)Mgx(0≤x≤0.10) alloys," *Chinese Sci. Bull.*, vol. 52, no. 11, pp. 1441–1445, 2007.

[40] Y. Sato, K. Sugisawa, D. Aoki, and T. Yamamura, "Viscosities of Fe–Ni, Fe–Co and Ni–Co binary melts," *Meas. Sci. Technol. Meas. Sci. Technol*, vol. 16, no. 2, pp. 363–371, 2005.

[41] R. J. L. Andon, L. A. Chapman, A. P. Day, and K. C. Mills, "Viscosities of liquid metals and commercial alloys," Middlesex, UK, 1999.

[42] W. Jones and W. Bartlett, "The Viscosity of Aluminum and Binary Aluminum Alloys," *J. Inst. Met.*, vol. 81, no. 3, pp. 145–152, 1952.

[43] T. Iida, T. Tanaka, and M. Koike, "Effect of Reflected Wave from the Wall of a Vessel and End Effect of the Plate in the Oscillating-plate Method," *ISIJ Int.*, vol. 33, no. 1, pp. 218–223, 1993.

[44] M. Tokuda, T. Yamamoto, K. Nakajima, H. Nakajima, and K. Kawaguchi, "Development and utilization of new oscillating-plate type viscometer for mould powder evaluation," *The Sumitomo Search*, no. 44, p. 368, 1990.

[45] T. Dubberstein, M. Schürmann, H. Chaves, H. P. Heller, and C. G. Aneziris, "A Novel Vibrating Finger Viscometer for High-Temperature Measurements in Liquid Metals and Alloys," *Int. J. Thermophys.*, vol. 37, no. 10, pp. 1–12, 2016.

[46] D. S. Viswanath, T. K. Ghosh, D. H. L. Prasad, N. V. K. Dutt, and K. Y. Rani, *Viscosity of Liquids: Theory, Estimation, Experiment, and Data*. Dordrecht, the Netherlands: Springer Science & Business Media, 2007.

[47] W. H. Herschel, "Determination of absolute viscosity by short-tube viscosimeters," *US Gov. Print. Off.*, no. 100, 1917.

[48] ASTM International, "Standard Test Method for Saybolt Viscosity," in *ASTM Standard D88-07*, 2013.

[49] ASTM International, “ASTM Viscosity Tables for Kinematic Viscosity Conversions and Viscosity Index Calculations,” in *ASTM Standard STP43B*, 1957.

[50] W. H. Herschel, “Standardization of the Saybolt Universal Viscometer,” *United States Am. Dept. Commer.*, no. 112, 1918.

[51] M. K. Khan, “Introduction to Fluids and Fluid Mechanics,” in *Fluid Mechanics and Machinery*, Oxford University Press, 2015.

[52] J. William D. Callister and David G. Rethwish, *Materials Science and Engineering: An Introduction*, 9th ed. John Wiley & Sons, 2013.

[53] B. J. Keene, “Review of data for the surface tension of pure metals,” *Int. Mater. Rev.*, vol. 38, no. 4, pp. 157–192, 1993.

[54] W. F. Gale and T. C. Totemeier, *Smithells Metals Reference Book*, 8th ed. Burlington, MA, USA: Elsevier Butterworth-Heinemann, 2004.

[55] H.-J. Butt, K. Graf, and M. Kappl, *Physics and Chemistry of Interfaces*. Weinheim, Germany: WILEY-VCH Verlag GmbH & Co., 2013.

[56] K. C. Mills and Y. C. Su, “Review of surface tension data for metallic elements and alloys: Part 1 – Pure metals,” *Int. Mater. Rev.*, vol. 51, no. 6, pp. 329–351, 2006.

[57] M. A. Floriano and C. A. Angell, “Surface tension and molar surface free energy and entropy of water to -27.2.degree.C,” *J. Phys. Chem.*, vol. 94, no. 10, pp. 4199–4202, 1990.

[58] J. A. V. Butler, “The Thermodynamics of the Surfaces of Solutions,” *Proc. R. Soc. London. Ser. A, Contain. Pap. a Math. Phys. Character*, vol. 135, no. 827, pp. 348–375, 1932.

[59] J. Brillo, D. Chatain, and I. Egry, “Surface tension of liquid binary alloys – theory versus experiment,” *Int. J. Mater. Res.*, vol. 100, no. 1, pp. 53–58, 2009.

[60] T. Tanaka and T. Iida, “Application of a thermodynamic database to the calculation of surface tension for iron-base liquid alloys,” *Steel Res.*, vol. 65, no. 1, pp. 21–28, 1994.

[61] M. Hillert, “Partial Gibbs energies from Redlich-Kister polynomials,” *Thermochim. Acta*, vol. 129, no. 1, pp. 71–75, 1988.

[62] I. Egry, “Surface tension of compound forming liquid binary alloys: A simple model,” *J. Mater. Sci.*, vol. 39, no. 20, pp. 6365–6366, 2004.

[63] I. Egry, J. Brillo, D. Holland-Moritz, and Y. Plevachuk, “The surface tension of liquid aluminium-based alloys,” *Mater. Sci. Eng. A*, vol. 495, no. 1–2, pp. 14–18, 2008.

[64] B. C. Allen, “The interfacial free energies of solid chromium, molybdenum and tungsten,” *J. Less-Common Met.*, vol. 29, no. 3, pp. 263–282, 1972.

[65] G. Kaptay, “A unified model for the cohesive enthalpy, critical temperature, surface tension and volume thermal expansion coefficient of liquid metals of bcc, fcc and hcp crystals,” *Mater. Sci. Eng. A*, vol. 495, no. 1–2, p. 255, 2008.

[66] R. J. Hunter, “Foundations of Colloid Science,” 2nd ed., Oxford University Press, 2001, pp.

44–80.

[67] F. Bashforth and J. C. Adams, “An Attempt to Test the Theories of Capillary Action by Comparing the Theoretical and Measured Forms of Drops of Fluid.” Cambridge: At the University Press, pp. 1–158, 1883.

[68] D. N. Staicopolus, “The computation of surface tension and of contact angle by the sessile-drop method,” *J. Colloid Sci.*, vol. 17, no. 5, pp. 439–447, 1962.

[69] J. Lee, A. Kiyose, S. Nakatsuka, M. Nakamoto, and T. Tanaka, “Improvements in Surface Tension Measurements of Liquid Metals Having Low Capillary Constants by the Constrained Drop Method,” *ISIJ Int.*, vol. 44, no. 11, pp. 1793–1799, 2004.

[70] T. Dubberstein and H. P. Heller, “Surface tension and density of liquid gold, silver, and tin,” *High Temp. - High Press.*, vol. 44, no. 5, pp. 393–406, 2015.

[71] W. D. Kingery and J. Humenik, M., “Surface Tension at Elevated Temperatures. I. Furnace and Method for Use of the Sessile Drop Method; Surface Tension of Silicon, Iron and Nickel,” *J. Phys. Chem.*, vol. 57, no. 3, pp. 359–363, 1953.

[72] F. Halden and W. Kingery, “Surface Tension at Elevated Temperatures. II. Effect of C, N, O and S on Liquid Iron Surface Tension and Interfacial Energy with Al2O3,” *J. Phys. Chem.*, vol. 59, no. 6, pp. 557–559, 1955.

[73] T. Dubberstein and H. Heller, “Determination of Surface Tension for FeCrMnNi Alloy with Varying Sulfur and Phosphorous Relevant to Gas Atomization,” in *5th International Symposium on High-Temperature Metallurgical Processing*, 2014, pp. 161–168.

[74] A. Sharan and A. W. Cramb, “Surface Tension and Wettability Studies of Liquid Fe-Ni-O Alloys,” *Metall. Mater. Trans. B*, vol. 28, no. 3, pp. 475–472, 1997.

[75] D. Giuranno, A. Tuissi, R. Novakovic, and E. Ricci, “Surface Tension and Density of Al-Ni Alloys,” *J. Chem. Eng. Data*, vol. 55, no. 9, pp. 3024–3028, 2010.

[76] E. Schrödinger, “Notiz über den Kapillardruck in Gasblasen,” *Ann. Phys.*, vol. 351, no. 3, pp. 413–418, 1915.

[77] S. J. Roach, “Determination of the Physical Properties of Melts,” M.S. thesis, Department of Chemical & Materials Engineering, University of Alberta, Edmonton, Canada, 2001.

[78] J. Goichoechea, E. Garcia-Cordovilla, E. Louis, and A. Pamies, “Effects of Wetting and Surface Oxidation on the Measurement of the Surface Tension of Al by the Maximum Bubble Pressure Method,” *Scr. Metall. Mater.*, vol. 25, no. 2, pp. 479–484, 1991.

[79] T. Dubberstein and H. P. Heller, “The Thermophysical Properties of Liquid TRIP/TWIP-Steel Alloys Using the Maximum Bubble Pressure Method,” *Adv. Eng. Mater.*, vol. 15, no. 7, pp. 583–589, 2013.

[80] T. Yoshikawa, “Surface Tensions of Fe--(30-40 mol%) Si-C Alloys at 1523-1723 K,” *Mater. Trans.*, vol. 54, no. 10, pp. 1968–1974, 2013.

[81] S. Fordham, “On the calculation of surface tension from measurements of pendantd drops,”

Proc. R. Soc. A Math. Phys. Eng. Sci., vol. 194, no. 1036, pp. 1–16, 1948.

[82] D. B. Thiessen and K. F. Man, "A Quasi-Containerless Pendant Drop Method for Surface Tension Measurments of Molten Metals and Alloys," *Int. J. Thermophys.*, vol. 16, no. 1, pp. 245–255, 1995.

[83] G. J. Abbaschian, "Surface tension of liquid gallium," *J. Less-Common Met.*, vol. 40, no. 3, pp. 329–333, 1975.

[84] K. Astakov, N. Penin, and E. D. Zh, "Surface Tension and Density of Liquid Selenium," *Zh. Fiz. Khim*, vol. 20, pp. 403–408, 1946.

[85] K. F. Man, "Surface Tension Measurements of Liquid Metals by the Quasi-containerless Pendant Drop Method," *Int. J. Thermophys.*, vol. 21, no. 3, pp. 793–804, 2000.

[86] B. Vinet, J. P. Garandet, and L. Cortella, "Surface tension measurements of refractory liquid metals by the pendant drop method under ultrahigh vacuum conditions: Extension and comments on Tate's law," *J. Appl. Phys.*, vol. 73, no. 8, pp. 3830–3834, 1993.

[87] E. Ricci *et al.*, "Surface tension and density of Si-Ge melts," *J. Chem. Phys.*, vol. 140, no. 214704, pp. 1–6, 2014.

[88] D. Giuranno, E. Ricci, R. Nowak, and N. Sobczak, "Surface tension of high melting metals by PD/SD combined method," *High Temp. - High Press.*, vol. 40, no. 3–4, pp. 215–223, 2011.

[89] E. Ricci, D. Giuranno, and N. Sobczak, "Further Development of Testing Procedures for High Temperature Surface Tension Measurements," *J. Mater. Eng. Perform.*, vol. 22, no. 11, pp. 3381–3388, 2013.

[90] T. Tate, "XXX. On the magnitude of a drop of liquid formed under different circumstances," *London, Edinburgh, Dublin Philos. Mag. J. Sci.*, vol. 27, no. 181, pp. 176–180, 1864.

[91] W. D. Harkins and F. E. Brown, "The determination of surface tension (free surface energy), and the weight of falling drops: The surface tension of water and benzene by the capillary height method," *J. Am. Chem. Soc.*, vol. 41, no. 4, pp. 499–524, 1919.

[92] T. R. Hogness, "The surface tensions and densities of liquid mercury, cadmium, zinc, lead, tin and bismuth," *J. Am. Chem. Soc.*, vol. 43, no. 7, pp. 1621–1628, 1921.

[93] M. Wilkinson and M. Aronson, "Applicability of the drop-weight technique to the determination of the surface tensions of liquid metals," *J. Chem. Soc. Faraday Trans. 1 Phys. Chem. Condens. Phases*, vol. 60, no. 0, pp. 474–480, 1973.

[94] T. Dubberstein, M. Hötzel, R. Hagemann, P. Heller, and P. R. Scheller, "Some Thermophysical Properties of Liquid Cr-Mn-Ni-Steels," *Steel Res. Int.*, vol. 82, no. 9, pp. 1122–1128, 2011.

[95] B. Vinet, J. P. Garandet, B. Marie, L. Domergue, and B. Drevet, "Surface Tension Measurements on Industrial Alloys by the Drop-Weight Method," *Int. J. Thermophys.*, vol. 25, no. 3, pp. 869–883, 2004.

[96] B. Vinet, S. Schneider, J. P. Garandet, B. Marie, B. Drevet, and I. Egry, “Surface Tension Measurements on CMSX-4 Superalloy by the Drop-Weight and Oscillating-Drop Methods,” *Int. J. Thermophys.*, vol. 25, no. 6, pp. 1889–1903, 2004.

[97] A. Horibe, S. Fukusako, and M. Yamada, “Surface tension of low-temperature aqueous solutions,” *Int. J. Thermophys.*, vol. 17, no. 2, pp. 483–493, 1996.

[98] G. Jones and W. A. Ray, “The Surface Tension of Solutions of Electrolytes as a Function of the Concentration. III. Sodium Chloride,” *J. Am. Chem. Soc.*, vol. 63, no. 1, pp. 3262–3263, 1941.

[99] T. P. Hoar and D. A. Melford, “The surface tension of binary liquid mixtures: lead + tin and lead + indium alloys,” *Trans. Faraday Soc.*, vol. 53, pp. 315–326, 1957.

[100] K. Hellström, A. Diószegi, and L. Diaconu, “A Broad Literature Review of Density Measurements of Liquid Cast Iron,” *Metals (Basel).*, vol. 7, no. 5, p. 165, 2017.

[101] J. Brillo and I. Egry, “Density of Multicomponent Melts Measured by Electromagnetic Levitation,” *Jpn. J. Appl. Phys.*, vol. 50, no. 11S, p. 11RD02, 2011.

[102] K. T. Jacob, S. Raj, and L. Rannesh, “Vegard’s law: a fundamental relation or an approximation?,” *Int. J. Mater. Res.*, vol. 98, no. 9, pp. 776–779, 2007.

[103] S. D. Veazey and W. C. Roe, “Review: Density Measurements in Liquid Metals and Liquid Binary Alloy Systems — A Survey,” *J. Mater. Sci.*, vol. 7, no. 4, pp. 445–466, 1972.

[104] A. F. Crawley, “Densities of Liquid Metals and Alloys,” *Int. Mater. Rev.*, vol. 19, no. 1, pp. 32–48, 1974.

[105] A. D. Kirshenbaum and J. A. Cahill, “The density of liquid iron from the melting point to 2500 K,” *Trans. Met. Soc. AIME*, vol. 224, p. 816, 1962.

[106] L. Wang and A.-P. Xian, “Density Measurement of Sn-40Pb, Sn-57Bi, and Sn-9Zn by Indirect Archimedean Method,” *J. Electron. Mater.*, vol. 34, no. 11, pp. 1414–1419, 2005.

[107] H. Sasaki, E. Tokizaki, K. Terashima, and S. Kimura, “Density Variation of Molten Silicon Measured by an Improved Archimedian Method,” *Jpn. J. Appl. Phys.*, vol. 33, no. Part 1, No. 7A, pp. 3803–3807, 1994.

[108] B. Dang, Z. Jian, J. Xu, and S. Li, “Density and solidification shrinkage of hypereutectic Al–Si alloys,” *Int. J. Mater. Res.*, vol. 108, no. 10, pp. 815–819, 2017.

[109] A. Crawley and D. Kiff, “The Density and Viscosity of Liquid Antimony,” *Metall. Mater. Trans. B*, vol. 3, no. 1, pp. 157–159, 1972.

[110] A. J. Davis, M. P. Harding, and P. M. Robinson, “The Densities of Some Zinc-Aluminium Alloys,” *Mater. Sci. Eng.*, vol. 15, no. 1, pp. 67–73, 1974.

[111] A. F. Crawley, “Densities and Viscosities of Some Liquid Alloys of Zinc and Cadmium,” *Metall. Mater. Trans. B*, vol. 3, no. 4, pp. 971–975, 1972.

[112] B. B. Alchagirov, T. M. Shamparov, and A. G. Mozgovoi, “Experimental Investigation of the Density of Molten Lead-Bismuth Eutectic,” *High Temp.*, vol. 41, no. 2, pp. 210–215,

2003.

[113] Y. Sato, T. Nishizuka, K. Hara, T. Yamamura, and Y. Waseda, “Density Measurement of Molten Silicon by a Pycnometric Method,” *Int. J. Thermophys.*, vol. 21, no. 6, pp. 1463–1471, 2000.

[114] T. K. Sandeep Kumar, N. N. Viswanathan, H. M. Ahmed, C. Andersson, and B. Björkman, “Estimation of Sintering Kinetics of Magnetite Pellet Using Optical Dilatometer,” *Metall. Mater. Trans. B*, vol. 47, no. 1, pp. 309–319, 2016.

[115] E. J. Westcot, C. Binet Andrandall, and M. German, “*In situ* dimensional change, mass loss and mechanisms for solvent debinding of powder injection moulded components,” *Powder Metall.*, vol. 46, no. 1, pp. 61–67, 2003.

[116] N. Yamada, R. Abe, and M. Okaji, “A calibration method for measuring thermal expansions with a push-rod dilatometer,” *Meas. Sci. Technol.*, vol. 12, no. 12, pp. 2121–2129, 2001.

[117] M. Piasecki *et al.*, “Temperature operated infrared nonlinear optical materials based on Tl4HgI6,” *J. Mater. Sci. Mater. Electron.*, vol. 24, no. 4, pp. 1187–1193, 2013.

[118] J. Brillo and I. Egry, “Density Determination of Liquid Copper, Nickel, and Their Alloys,” *Int. J. Thermophys.*, vol. 24, no. 4, pp. 1155–1170, 2003.

[119] J. Brillo and I. Egry, “Density and excess volume of liquid copper, nickel, iron, and their binary alloys,” *Zeitschrift für Met.*, vol. 95, no. 8, pp. 691–697, 2004.

[120] I. Jimbo and A. W. Cramb, “The Density of Liquid Iron-Carbon Alloys,” *Metall. Trans. B*, vol. 24, no. 1, pp. 5–10, 1993.

[121] H. Mizukami, A. Yamanaka, and T. Watanabe, “Prediction of Density of Carbon Steels,” *ISIJ Int.*, vol. 42, no. 4, pp. 375–384, 2002.

[122] T. Dubberstein, H.-P. Heller, J. Klostermann, R. Schwarze, and J. Brillo, “Surface tension and density data for Fe–Cr–Mo, Fe–Cr–Ni, and Fe–Cr–Mn–Ni steels,” *J. Mater. Sci.*, vol. 50, no. 22, pp. 7227–7237, 2015.

[123] P. M. Nasch and S. G. Steinemann, “Density and thermal expansion of molten manganese, iron, nickel, copper, aluminum and tin by means of the gamma-ray attenuation technique,” *Phys. Chem. Liq.*, vol. 29, no. 1, pp. 43–58, 1995.

[124] P. M. Smith, J. W. Elmer, and G. F. Gallegos, “Measurement of the density of liquid aluminum alloys by an X-ray attenuation technique,” *Scr. Mater.*, vol. 40, no. 8, pp. 937–941, 1999.

[125] C. Sanloup, F. Guyot, P. Gillet, G. Fiquet, M. Mezouar, and I. Martinez, “Density measurements of liquid Fe-S alloys at high pressure,” *Geophys. Res. Lett.*, vol. 27, no. 6, pp. 811–814, 2000.

[126] H. Terasaki *et al.*, “Density measurement of Fe3C liquid using X-ray absorption image up to 10 GPa and effect of light elements on compressibility of liquid iron,” *J. Geophys. Res.*, vol. 115, no. B6, pp. 1–7, 2010.

[127] S. Mehmood, U. E. Klotz, and G. Pottlacher, “Thermophysical Properties of Platinum-Copper Alloys,” *Metall. Mater. Trans. A*, vol. 43, no. 13, pp. 5029–5037, 2012.

[128] T. Hüpf, C. Cagran, E. Kaschnitz, and G. Pottlacher, “Thermophysical properties of Ni80Cr20,” *Thermochim. Acta*, vol. 494, no. 1–2, pp. 40–44, 2009.

[129] H. A. Friedrichs, L. W. Ronkow, P. Vermot, and S. A. Bliznjukow, “New method for simultaneous measurement of viscosity, density and surface tension of metallic melts at high temperatures,” *Steel Res.*, vol. 66, no. 12, pp. 509–515, 1995.

[130] ASTM International, “Standard Test Method for Viscosity of Transparent Liquids by Bubble Time Method,” in *ASTM Standard D1545*, 2017.

[131] H. A. Friedrichs, L. W. Ronkow, and Y. Zhou, “Measurement of viscosity, density and surface tension of metal melts,” *Steel Res.*, vol. 68, no. 5, pp. 209–214, 1997.

[132] S. I. Bakhtiyarov and R. A. Overfelt, “Measurement of liquid metal viscosity by rotational technique,” *Acta Mater.*, vol. 47, no. 17, pp. 4311–4319, 1999.

[133] M. Iguchi, T. Nakatani, and H. Tokunaga, “The Shape of Bubbles Rising near the Nozzle Exit in Molten Metal Baths,” *Metall. Mater. Trans. B*, vol. 28, no. 3, pp. 417–423, 1997.

[134] P. F. Paradis *et al.*, “Materials properties measurements and particle beam interactions studies using electrostatic levitation,” *Mater. Sci. Eng. R Reports*, vol. 76, no. 1, pp. 1–53, 2014.

[135] H. Ä. Fecht and R. Wunderlich, “The ThermoLab Project: Thermophysical Property Measurements in Space for Industrial High Temperature Alloys,” *J. Jpn. Soc . Microgravity Appl.*, vol. 27, no. 4, pp. 190–198, 2010.

[136] I. Egry, G. Lohöfer, I. Seyhan, S. Schneider, and B. Feuerbacher, “Viscosity and Surface Tension Measurements in Microgravity,” *Int. J. Thermophys.*, vol. 20, no. 4, pp. 1005–1015, 1999.

[137] D. M. Matson, X. Xiao, J. Rodriguez, and R. K. Wunderlich, “Preliminary Experiments Using Electromagnetic Levitation On the International Space Station,” *Int. J. Microgravity Sci. Appl.*, vol. 33, no. 2, pp. 1–11, 2016.

[138] R. K. Wunderlich, H.-J. Fecht, and G. Lohöfer, “Surface Tension and Viscosity of the Ni-Based Superalloys LEK94 and CMSX-10 Measured by the Oscillating Drop Method on Board a Parabolic Flight,” *Metall. Mater. Trans. B*, vol. 48, no. February, pp. 1–10, 2016.

[139] T. Matsushita and S. Seetharaman, “Thermolab Project: Results on Thermophysical Properties Data of Iron Alloys,” *High Temp. Mater. Process.*, vol. 27, no. 6, pp. 1–18, 2008.

[140] R. K. Wunderlich and H.-J. Fecht, “Surface tension and viscosity of NiAl catalytic precursor alloys from microgravity experiments,” *Int. J. Mater. Res.*, vol. 102, no. 9, pp. 1164–1173, 2011.

[141] R. F. Brooks, I. Egry, S. Seetharaman, and D. Grant, “Reliable data for high-temperature viscosity and surface tension: results from a European project,” *High Temp. - High Press.*, vol. 33, no. 6, pp. 631–637, 2001.

[142] I. Egry and I. Seyhan, “The Surface Tension of Undercooled Binary Iron and Nickel Alloys and the Effect of Oxygen on the Surface Tension of Fe and Ni,” *Int. J. Thermophys.*, vol. 20, no. 4, pp. 1017–1028, 1999.

[143] J. Brillo and I. Egry, “Density and Surface Tension of Electromagnetically Levitated Cu-Co-Fe Alloys,” *Int. J. Thermophys.*, vol. 28, no. 3, pp. 1004–1016, 2007.

[144] J. Brillo and I. Egry, “Surface tension of nickel, copper, iron and their binary alloys,” *J. Mater. Sci.*, vol. 40, no. 9–10, pp. 2213–2216, 2005.

[145] I. Egry and J. Brillo, “Surface Tension and Density of Liquid Metallic Alloys Measured by Electromagnetic Levitation,” *J. Chem. Eng. Data*, vol. 54, no. 9, pp. 2347–2352, 2009.

[146] H. G. Kim, J. Choe, T. Inoue, S. Ozawa, and J. Lee, “Surface Tension of Super-Cooled Fe-O Liquid Alloys,” *Metall. Mater. Trans. B*, vol. 47, no. 4, pp. 2079–2081, 2016.

[147] R. K. Wunderlich, H. J. Fecht, M. Schick, and I. Egry, “Time Dependent Effects in Surface Tension Measurements of an Industrial Fe-alloy,” *Steel Res. Int.*, vol. 82, no. 6, pp. 746–752, 2011.

[148] F. Schmidt-Hohagen and I. Egry, “Surface tension measurements of industrial alloys,” *Mater. Sci. Forum*, vol. 508, pp. 573–578, 2006.

[149] S. Ozawa, K. Morohoshi, and T. Hibiya, “Influence of Oxygen Partial Pressure on Surface Tension of Molten Type 304 and 316 Stainless Steels Measured by Oscillating Droplet Method Using Electromagnetic Levitation,” *ISIJ Int.*, vol. 54, no. 9, pp. 2097–2103, 2014.

[150] J. Choe *et al.*, “Surface Tension Measurements of 430 Stainless Steel,” *ISIJ Int.*, vol. 54, no. 9, pp. 2104–2108, 2014.

[151] T. Hibiya and I. Egry, “Thermophysical property measurements of high temperature melts: results from the development and utilization of space,” *Meas. Sci. Technol.*, vol. 16, no. 2, pp. 317–326, 2005.

[152] M. Watanabe, M. Adachi, and H. Fukuyama, “Densities of Fe–Ni melts and thermodynamic correlations,” *J. Mater. Sci.*, vol. 51, no. 7, pp. 3303–3310, 2016.

[153] J. Brillo, I. Egry, and I. Ho, “Density and thermal expansion of liquid Al–Ag and Al–Cu alloys,” *Int. J. Mater. Res.*, vol. 99, no. 2, pp. 162–167, 2008.

[154] J. Brillo, I. Egry, H. S. Giffard, and A. Patti, “Density and Thermal Expansion of Liquid Au-Cu Alloys,” *Int. J. Thermophys.*, vol. 25, no. 6, pp. 1881–1888, 2004.

[155] M. Schick, J. Brillo, and I. Egry, “Thermophysical properties of liquid Co–Cu–Ni alloys,” *Int. J. Cast Met. Res.*, vol. 22, no. 1–4, pp. 82–85, 2009.

[156] J. Brillo, R. Brooks, I. Egry, and P. Quested, “Density and viscosity of liquid ternary Al-Cu-Ag alloys,” *High Temp. - High Press.*, vol. 37, no. 4, pp. 371–381, 2008.

[157] H. Kobatake and J. Brillo, “Density and thermal expansion of Cr-Fe, Fe-Ni, and Cr-Ni binary liquid alloys,” *J. Mater. Sci.*, vol. 48, no. 14, pp. 4934–4941, 2013.

[158] H. Kobatake, J. Schmitz, and J. Brillo, “Density and viscosity of ternary Al-Cu-Si liquid

alloys," *J. Mater. Sci.*, vol. 49, no. 9, pp. 3541–3549, 2014.

[159] P. Wu, Y. Yang, M. Barati, and A. Mclean, "Thermodynamic and Kinetic Aspects of Sulfur Evaporation from Fe-C Alloy Droplets," *ISIJ Int.*, vol. 55, no. 4, pp. 717–722, 2015.

[160] I. Egry, G. Lohöfer, and D. Matson, "EML Processing Measurement Techniques," *High Temp. Mater. Process.*, vol. 27, no. 6, pp. 389–400, 2008.

[161] I. Egry, "Surface Tension Measurements in Microgravity and their Relevance to Marangoni Convection," *ChemPhysChem*, vol. 4, no. 4, pp. 329–333, 2003.

[162] D. L. Cummings and D. A. Blackburn, "Oscillations of magnetically levitated aspherical droplets," *J. Fluid Mech.*, vol. 224, pp. 395–416, 1991.

[163] R. W. Hyers, "Fluid flow effects in levitated droplets," *Meas. Sci. Technol.*, vol. 16, no. 2, pp. 394–401, 2005.

[164] M. Shimoji, "Liquid Metals: An Introduction to the Physics and Chemistry of Metals in the Liquid State," *Berichte der Bunsengesellschaft für Phys. Chemie*, vol. 83, no. 7, pp. 749–749, 1979.

[165] Y. Plevachuk, V. Sklyarchuk, A. Yakymovych, S. Eckert, B. Willers, and K. Eigenfeld, "Density, Viscosity, and Electrical Conductivity of Hypoeutectic Al-Cu Liquid Alloys," *Metall. Mater. Trans. A*, vol. 39, no. 12, pp. 3040–3045, 2008.

[166] P. Neuhaus, I. Egry, and G. Lohöfer, "Aspects of High-Temperature Pyrometry for Measurements in Ultrahigh Vacuum," *Int. J. Thermophys.*, vol. 13, no. 1, pp. 199–210, 1992.

[167] J. Schmitz, B. Hallstedt, J. Brillo, I. Egry, and M. Schick, "Density and thermal expansion of liquid Al–Si alloys," *J. Mater. Sci.*, vol. 47, no. 8, pp. 3706–3712, 2012.

[168] R. L. Daugherty, B. Franzini, and J. Finnemore, *Fluid Mechanics with Engineering Application*. New York, NY, USA: McGraw-Hill, 1985.

[169] A. Bjorck, *Numerical Methods for Least Squares Problems*. .

[170] T. P. Yao and V. Kondic, "The viscosity of molten tin, lead, zinc, aluminium, and some of their alloys," *J. Inst. Met.*, vol. 81, pp. 17–24, 1952.

[171] T. Yamasaki, S. Kanatani, Y. Ogino, and A. Inoue, "Viscosity measurements for liquid Al-Ni-La and Al-Ni-Mm (Mm: Mischmetal) alloys by an oscillating crucible method," *J. Non. Cryst. Solids*, vol. 156–158, pp. 441–444, 1993.

[172] K. C. Mills, *Recommended values of thermophysical properties for selected commercial alloys*. Cambridge, UK: Woodhead Publishing Limited, 2002.

[173] D. Wang and R. A. Overfelt, "Oscillating Cup Viscosity Measurements of Aluminum Alloys: A201, A319 and A356," *Int. J. Thermophys.*, vol. 23, no. 4, pp. 1063–1076, 2002.

[174] S. H. Park, Y. S. Um, C. H. Kum, and B. Y. Hur, "Thermophysical properties of Al and Mg alloys for metal foam fabrication," *Colloids Surfaces A Physicochem. Eng. Asp.*, vol. 263, no. 1–3, pp. 280–283, 2005.

[175] J. P. Anson, R. A. L. Drew, and J. E. Gruzleski, "The Surface Tension of Molten Aluminum and Al-Si-Mg Alloy under Vacuum and Hydrogen Atmospheres," *Metall. Mater. Trans. B*, vol. 30, no. 6, pp. 1027–1032, 1999.

[176] L. Gourmiri and J. C. Joud, "Auger electron spectroscopy study of aluminium-tin liquid system," *Acta Metall.*, vol. 30, no. 7, pp. 1397–1405, 1982.

[177] A. Pamies, C. Garcia-Cordovilla, and E. Louis, "The measurement of surface tension of liquid aluminum by means of the maximum bubble pressure method: the effect of surface oxidation," *Scr. Metall.*, vol. 18, no. 9, pp. 869–872, 1984.

[178] C. Garcia-Cordovilla, E. Louis, and A. Pamies, "The surface tension of liquid pure aluminium and aluminium-magnesium alloy," *J. Mater. Sci.*, vol. 21, no. 8, pp. 2787–2792, 1986.

[179] N. Eustathopoulos, J. C. Joud, P. Desre, and J. M. Hicter, "The wetting of carbon by aluminium and aluminium alloys," *J. Mater. Sci.*, vol. 9, no. 8, pp. 1233–1242, 1974.

[180] P. Laty, J. C. Joud, P. Desré, and G. Lang, "Tension superficielle d'alliages liquid aluminum-cuivre," *Surf. Sci.*, vol. 69, no. 2, pp. 508–520, 1977.

[181] I. Egry, S. Schneider, I. Seyhan, and T. Volkmann, "Surface Tension Measurements of High Temperature Metallic Melts," *Trans. JWRI*, vol. 30, pp. 195–200, 2001.

[182] J. M. Molina, R. Voytovych, E. Louis, and N. Eustathopoulos, "The surface tension of liquid aluminium in high vacuum: The role of surface condition," *Int. J. Adhes. Adhes.*, vol. 27, no. 5, pp. 394–401, 2007.

[183] H. Kobatake, J. Brillo, J. Schmitz, and P. Y. Pichon, "Surface tension of binary Al–Si liquid alloys," *J. Mater. Sci.*, vol. 50, no. 9, pp. 3351–3360, 2015.

[184] W. D. Drotning, "Thermal expansion and density measurements of molten and solid materials at high temperatures by the gamma attenuation technique," Sandia National Laboratories, Albuquerque, NM, USA, 1979.

[185] V. Sarou-Kanian, F. Millot, and J. C. Rifflet, "Surface Tension and Density of Oxygen-Free Liquid Aluminum at High Temperature," *Int. J. Thermophys.*, vol. 24, no. 1, pp. 277–286, 2003.

[186] M. Leitner, T. Leitner, A. Schmon, K. Aziz, and G. Pottlacher, "Thermophysical Properties of Liquid Aluminum," *Metall. Mater. Trans. A*, vol. 48, no. 6, pp. 3036–3045, 2017.

[187] N. Y. Konstantinova, A. R. Kurochkin, A. V. Borisenko, V. V. Filippov, and P. S. Popel', "Viscosity of aluminum–copper melts," *Russ. Metall.*, vol. 2016, no. 2, pp. 144–149, 2016.

[188] A. Kostov and B. Friedrich, "Selection of crucible oxides in molten titanium and titanium aluminum alloys by thermo-chemistry calculations," *J. Min. Metall.*, vol. 41, no. 1, pp. 113–125, 2005.

[189] H. Henein, "The Transition From Free Stream Flow To Dripping in Draining Vessels," *Can. Metall. Q.*, vol. 44, no. 2, pp. 261–264, 2005.

[190] Senix Distance and Level Sensors, “ToughSonic 14 Ultrasonic Sensor,” 2020. [Online]. Available: https://senix.com/ultrasonic-sensor-product-lines/general-purpose-sensors/toughsonic-14/.

[191] Omega Engineering, “High Accuracy ‘S’ Beam Load Cells,” 2019. [Online]. Available: https://assets.omega.com/pdf/test-and-measurement-equipment/load-and-force/load-cells/LCCA.pdf.

[192] Fluke Process Instruments, “How Do Ratio Pyrometers Work?,” 2019. [Online]. Available: https://www.flukeprocessinstruments.com/en-us/service-and-support/knowledge-center/infrared-technology/how-do-ratio-pyrometers-work.

[193] M. J. Assael, A. E. Kalyva, K. D. Antoniadis, M. R. Banish, and W. A. Wakeham, “Reference Data for the Density and Viscosity of Liquid Copper and Liquid Tin,” *J. Phys. Chem. Ref. Data*, vol. 39, no. 3, pp. 1–8, 2010.

[194] N. Jakse and A. Pasturel, “Liquid Aluminum: Atomic diffusion and viscosity from ab initio molecular dynamics,” *Sci. Rep.*, vol. 3, no. 1, pp. 1–8, 2013.

[195] L. Goumiri, J. C. Joud, and P. Desre, “Tensions superficielles d’alliages liquides binaires présentant un caractère dimmiscibilité: Al-Pb, Al-Bi, Al-Sn et Zn-Bi,” *Surf. Sci.*, vol. 83, no. 2, pp. 471–486, 1979.

[196] D. S. Kanibolotsky, O. A. Bieloborodova, and N. V. Kotova, “Thermodynamic properties of liquid Al-Si and Al-Cu alloys,” *J. Therm. Anal. Calorim.*, vol. 70, no. 3, pp. 975–983, 2002.

[197] S. K. Das, J. Horbach, M. M. Koza, S. M. Chatoth, and A. Meyer, “Influence of chemical short-range order on atomic diffusion in Al-Ni melts,” *Appl. Phys. Lett.*, vol. 86, no. 1, pp. 1–4, 2005.

[198] M. E. Trybula, T. Gancarz, and W. Gąsior, “Density, surface tension and viscosity of liquid binary Al-Zn and ternary Al-Li-Zn alloys,” *Fluid Phase Equilib.*, vol. 421, pp. 39–48, 2016.

[199] M. E. Trybula, P. W. Szafrański, and P. A. Korzhavyi, “Structure and chemistry of liquid Al–Cu alloys: molecular dynamics study versus thermodynamics-based modelling,” *J. Mater. Sci.*, vol. 53, no. 11, pp. 8285–8301, 2018.

[200] F. Sommer, “Thermodynamic properties of supercooled compound forming liquid alloys,” *Mater. Sci. Eng. A*, vol. 133, pp. 434–437, 1991.

[201] J. Brillo *et al.*, “Local structure in liquid binary Al–Cu and Al–Ni alloys,” *J. Non. Cryst. Solids*, vol. 352, no. 38–39, pp. 4008–4012, 2006.

[202] J. Lee, W. Shimoda, and T. Tanaka, “Surface Tension and its Temperature Coefficient of Liquid Sn-X(X=Ag,Cu) Alloys,” *Mater. Trans.*, vol. 45, no. 9, pp. 2864–2870, 2004.

[203] J. Ferrand, “Écoulements et écrasements de fluides: effet du mouillage et de la rhéologie,” Ph.D. dissertation, École Doctorale de Physique et d’Astrophysique de Lyon, l’École Normale Supérieure de Lyon, Lyon, France, 2017.

[204] J. Ferrand, L. Favreau, S. Joubaud, and E. Freyssingeas, “Wetting Effect on Torricelli’s

Law," *Phys. Rev. Lett.*, vol. 117, no. 24, pp. 1–5, Dec. 2016.

[205] S. Bao, K. Tang, A. Kvithyld, M. Tangstad, and T. A. Engh, "Wettability of aluminum on alumina," *Metall. Mater. Trans. B*, vol. 42, no. 6, pp. 1358–1366, Dec. 2011.

[206] A. J. Klinter, G. Mendoza-Suarez, and R. A. L. Drew, "Wetting of pure aluminum and selected alloys on polycrystalline alumina and sapphire," *Mater. Sci. Eng. A*, vol. 495, no. 1–2, pp. 147–152, 2008.

[207] N. Eustathopoulos, "Wetting by liquid metals—application in materials processing: The contribution of the grenoble group," *Metals*, vol. 5, no. 1. MDPI AG, pp. 350–370, 10-Mar-2015.

[208] J. Berthier, *Micro-Drops and Digital Microfluidics*, 2nd ed. Oxford, UK: William Andrew, 2012.

[209] P. Lambert, *Surface Tension in Microsystems: Engineering Below the Capillary Length*. Berlin, Germany: Springer-Verlag, 2013.

[210] L. Gillespie, *Countersinking Handbook*, 1st ed. New York, NY, USA: Industrial Press, 2008.

[211] S. J. Roach and H. Henein, "Physical Properties of AZ91D Measured Using the Draining Crucible Method: Effect of SF6," *Int. J. Thermophys.*, vol. 33, no. 3, pp. 484–494, 2012.

[212] A. S. Utada, A. Fernandez-Nieves, J. M. Gordillo, and D. A. Weitz, "Absolute Instability of a Liquid Jet in a Coflowing Stream," *Phys. Rev. Lett.*, vol. 100, no. 1, pp. 1–4, 2008.

[213] A. Smalcerz and R. Przylucki, "Impact of Electromagnetic Field upon Temperature Measurement of Induction Heated Charges," *Int. J. Thermophys.*, vol. 34, no. 4, pp. 667–679, 2013.

APPENDIX A : EXPERIMENTAL DESIGN CHALLENGES

This appendix presents certain challenges with conducting DC experiments to determine the thermophysical properties of liquids. These challenges are associated with both the low temperature and high temperature apparatuses. They include issues with orifice design, wetting at the orifice tip, head measurement, load cell scatter, load cell operating temperature, thermocouple, induction coil and stopper rod. The goal of outlining these challenges is to facilitate future studies using the DC method and to explain certain design choices made and highlighted in Chapter 3.

A.1 Orifice Design

The geometry of the orifice was found to have a significant effect on the scatter of the cumulative mass data measured by the load cell. An orifice with sharp edges was found to produce high scatter, as shown in Figure A.1.

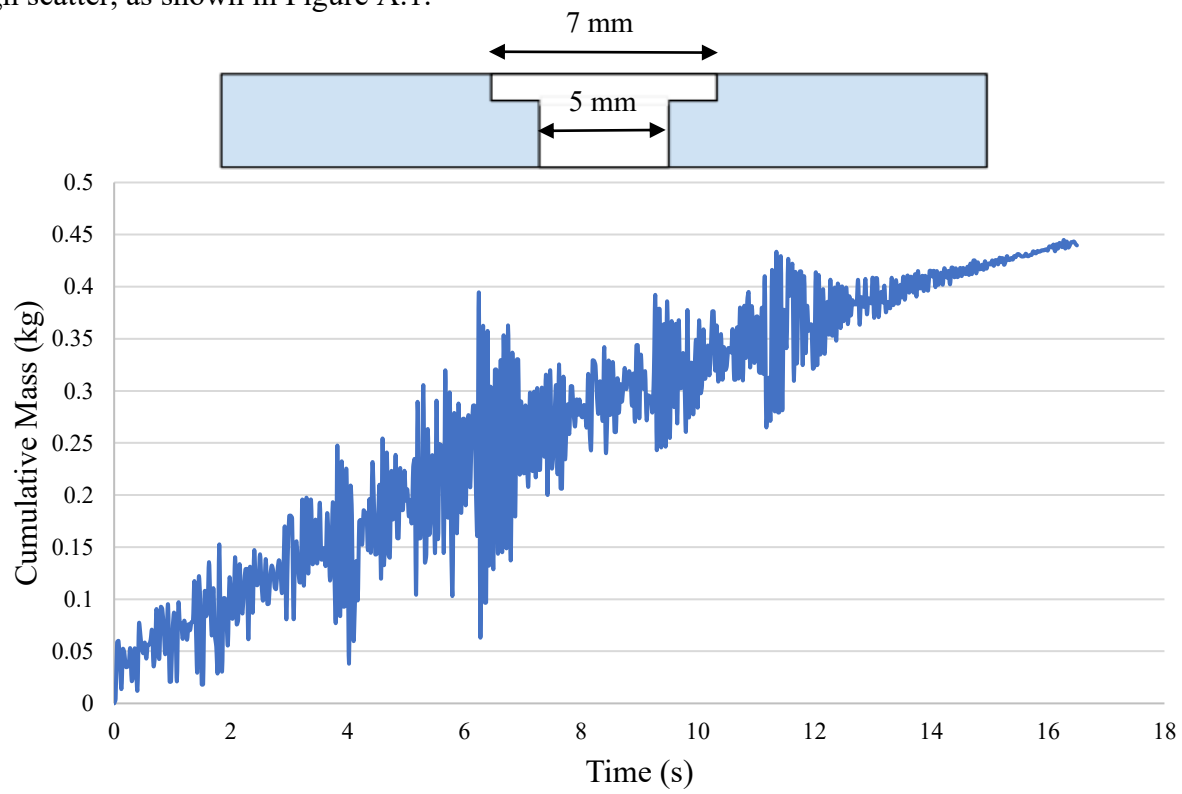

Figure A.1: Flow characteristics using a non-chamfered orifice

To remediate this, the orifice was chamfered using a diamond countersink drill bit (OAL Diamond Countersink w/ 82 Degree Angle supplied by Triatic), ultimately providing much less scatter, as shown in Figure A.2.

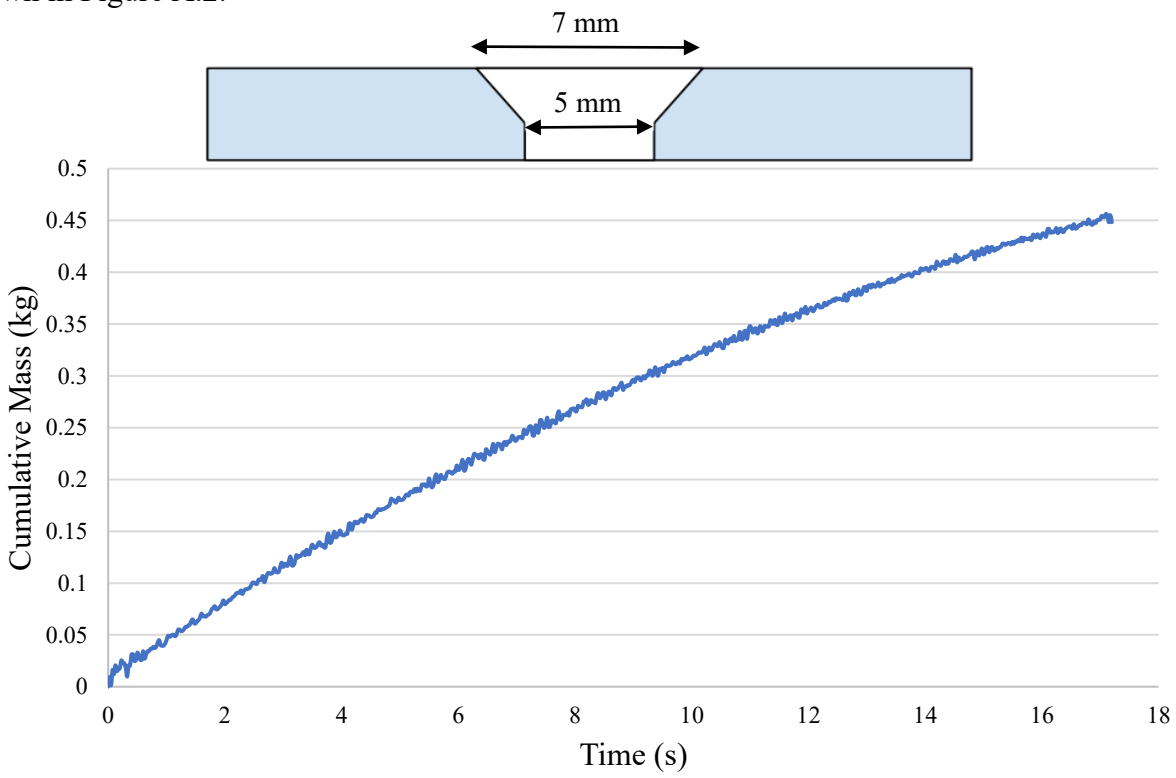

Figure A.2: Flow characteristics using a chamfered orifice hole

As liquids exit the orifice, the entrance and exit orifice geometry will affect the flow conditions. The discharge coefficient, C_d, is especially sensitive to orifice geometry. An orifice with shape-edged entrance has a C_d of 0.6 and an orifice with a chamfered orifice has a C_d of 0.9 [210].

A.2 Wetting at Orifice Tip

During calibration, it was observed that water gradually wets the base of the Al_2O_3 crucible as it exits orifice. This is shown in Figure A.3 over the course of 30 seconds. As the water wets the orifice, the effective radius of the orifice increases. This will alter the calculation of both the calculated discharge coefficient and theoretical flow rate. Since the formulation determines viscosity, surface tension and density based on these values, wetting will have a significant effect on the output of the non-linear regression.

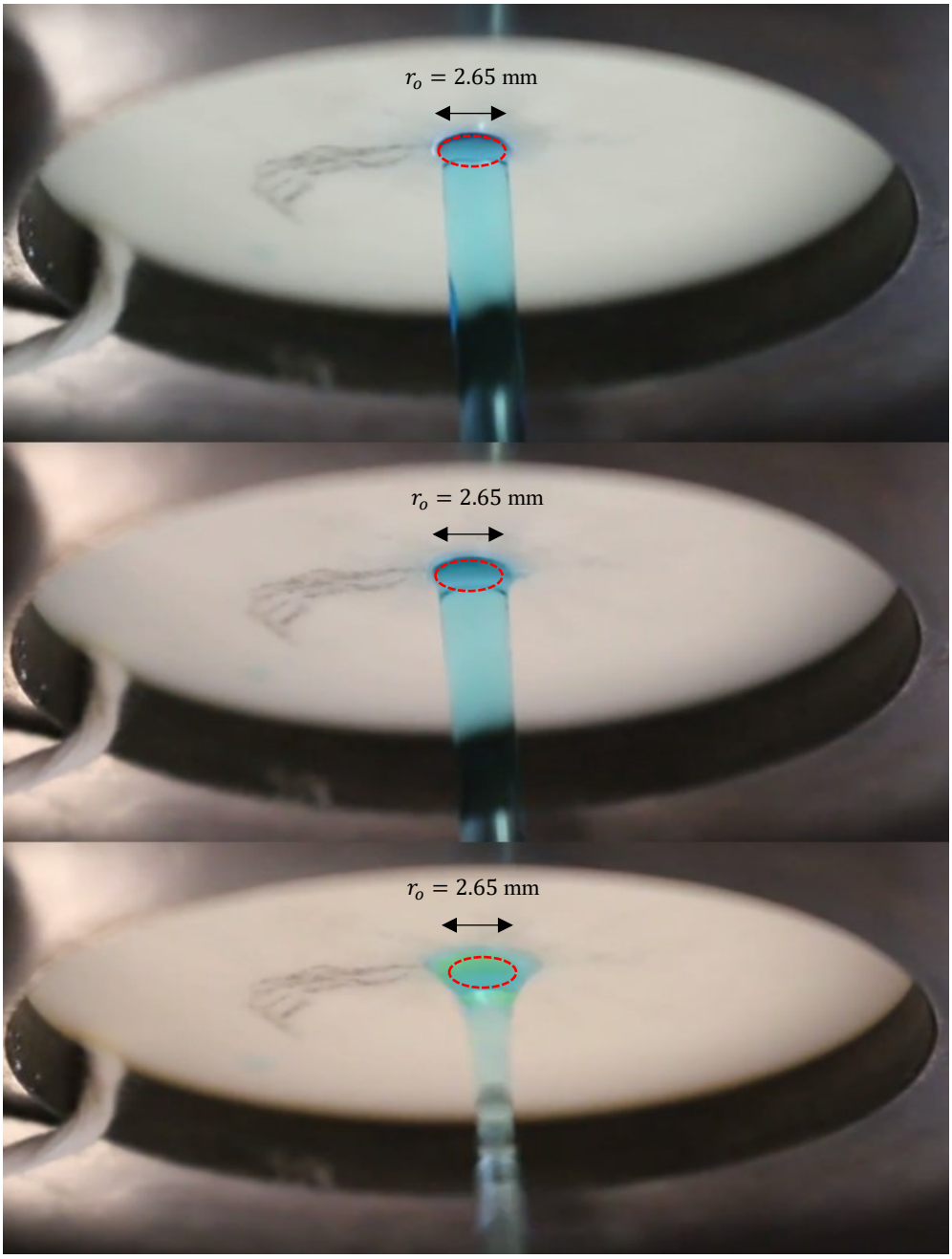

Figure A.3: Wetting at the orifice at a) 5 seconds, b) 15 seconds, and c) 30 seconds

To reduce wetting during water calibrations, the base of the crucibles were coated with a with hydrophobic spray (NIKWAX TX.DIRECT SPRAY-ON supplied by MEC). Unfortunately, this spray cannot be used for high-temperature applications. Thus, wetting is likely to have occurred when performing experiments on Al and Al-Cu.

A.3 Head Measurement

Previous studies determined the head of the liquid using the geometry of the crucible, i.e. based on the volume equation of a cylinder [211]. They, however, used a graphite crucible, which can be machined to high tolerances, and thus, the dimensions of the crucible can be easily measured, or are precisely known. In this study, Al_2O_3 was used for as the crucible material, but since the only way to manufacture these crucibles is by casting, geometrical deviations will exist. Therefore, using geometry of the crucible is not a reliable way to determine the head of the liquid draining the crucible. To remediate this, an ultrasonic level sensor was employed to measure the liquid level, or head of the water as a function of volume. The difference between the head measured from geometry and ultrasonic is presented in Figures A.4 and A.5.

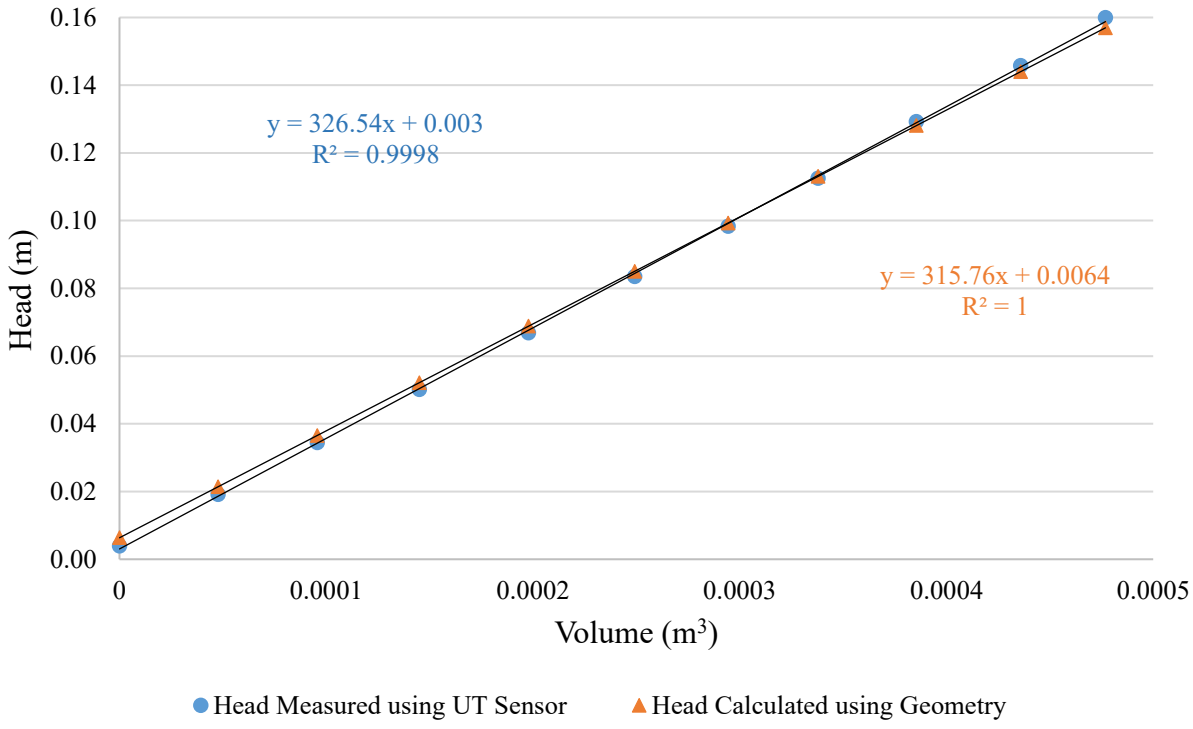

Figure A.4: Head of liquid water in Al_2O_3 crucible measured with UT sensor and calculated based on geometry of crucible

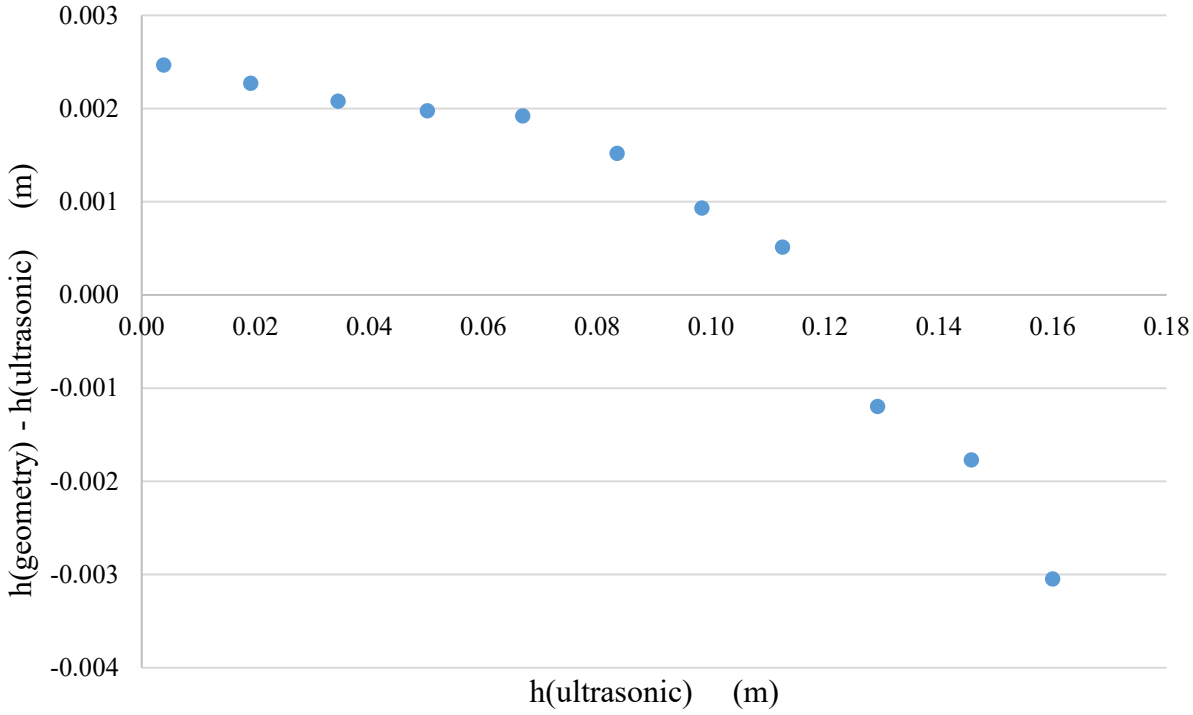

Figure A.5 Difference between head of liquid water in Al_2O_3 crucible measured with UT sensor and calculated based on geometry of crucible

A.4 Load Cell Scatter

Load cell scatter can impact curve fitting, and thus the determination of cumulative mass which is used to calculate the flow rate of the liquid exiting the orifice. This is an important parameter used to calculate the thermophysical properties of the liquid, and thus it is important that scatter is reduced. It was observed that when the collection vessel, which is attached to the load cell, is placed closer to the orifice exit, the scatter is reduced. The contrast between load cell scatter of the collection vessel being placed 50 cm versus 30 cm from the orifice exit is shown in Figures A.6 and A.7, respectively. The raw cumulative mass in both figures was fitted with a polynomial curve; the trendline for the cumulative mass with the collection vessel placed 30 cm away fit better, yielding a calculated R^2 value of 0.993 versus 0.986 when the collection was placed 50 cm away.

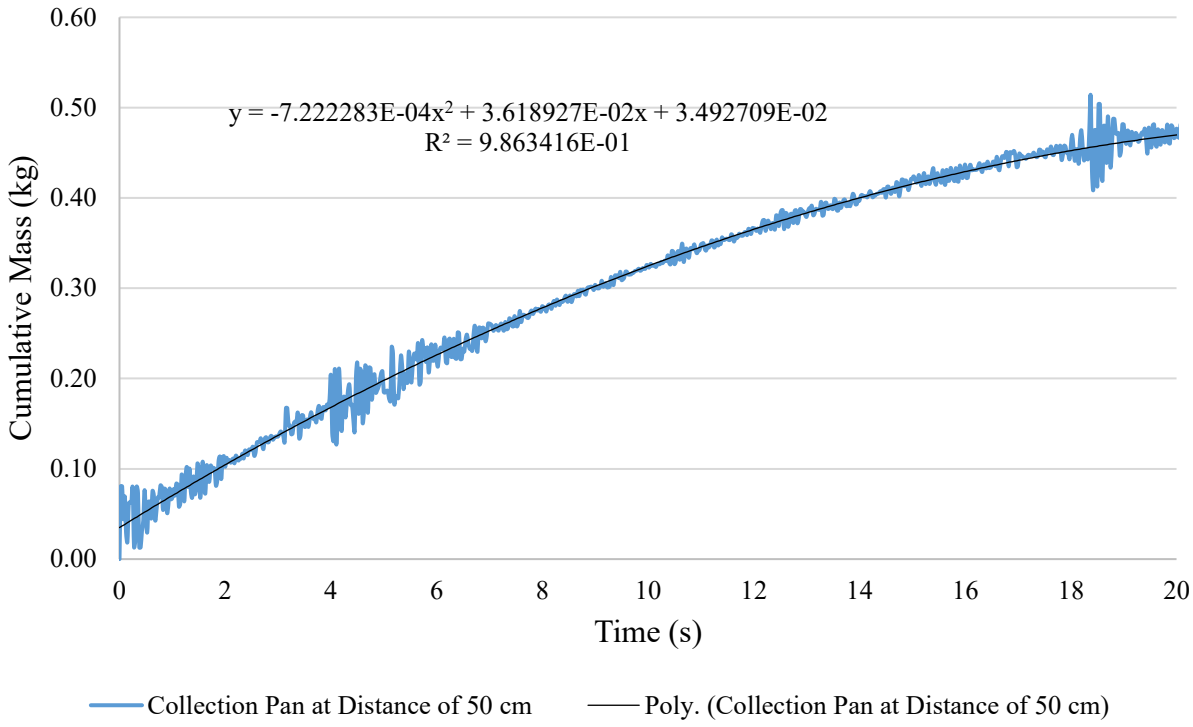

Figure A.6: Load cell scatter when collection vessel is placed 50 cm from the orifice exit

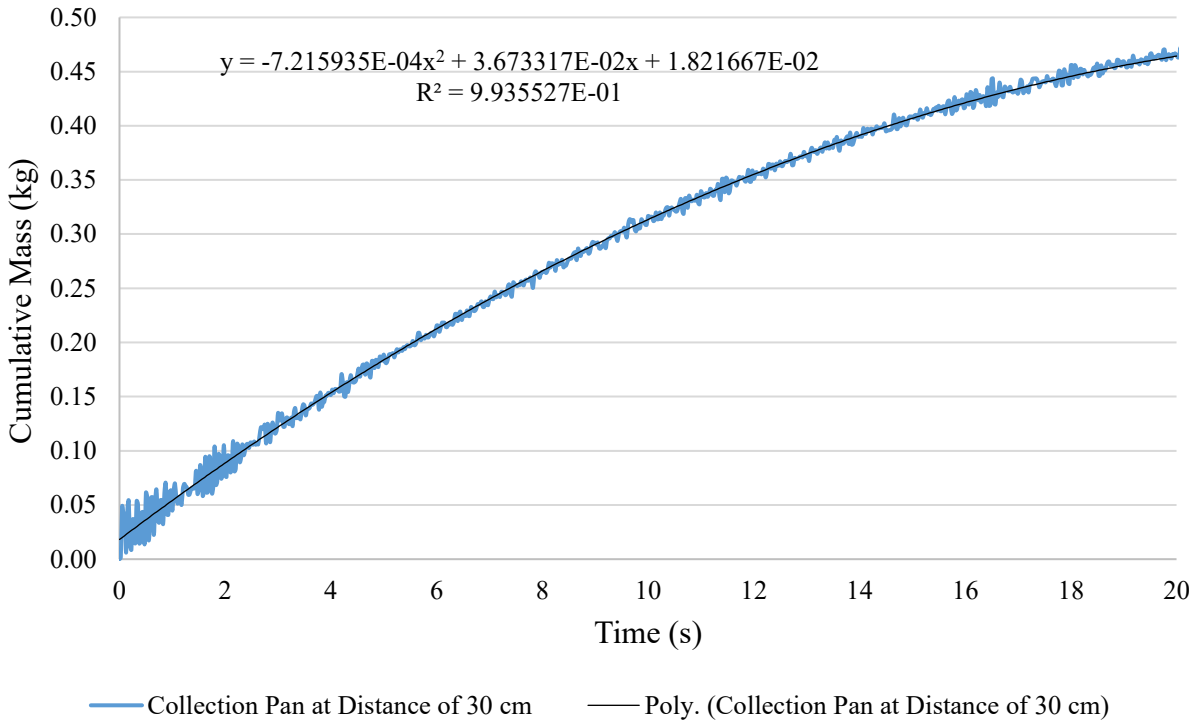

Figure A.7: Load cell scatter when collection vessel is placed 30 cm from the orifice exit

The increased scatter observed when the collection vessel is placed at a larger distance is caused by surface-tension driven Plateau-Rayleigh instability [212]. The stream of Newtonian fluid becomes unstable, i.e. growing perturbations, and eventually breaks up into droplets at a certain breakup time. The stream breakup time can be calculated as a function of initial stream radius and the liquid-gas surface tension. In this scenario, when the collection vessel is placed further away from the orifice exit, the cylindrical stream flows for a longer period of time before contacting the collection vessel. This increases the likelihood of perturbations becoming more dominant, or of the stream beginning to breakup and form droplets. Increased instability will increase the turbulence of the stream hitting the collection vessel, which in turn, will increases the scatter registered by the load cell.

Another source of load cell scatter originates from the design of the collection vessel. When a heavier, larger collection vessel was used to collect the draining fluid, as shown in Figure A.8, cumulative mass scatter increased. This is shown in Figure A.9. The cause of this is that the moment of the force created by the weight of the liquid increases as the collection vessel extends past the connection between the load cell and the collection vessel. This will create an imbalance, and any additional movement by the collection vessel will be registered by the load cell. Also, when the collection vessel becomes heavier, the moment will be larger, and hence more scatter will be observed. This was the case with the heavier collection vessel utilized to collect Al-Cu at 1029 and 1076 K.

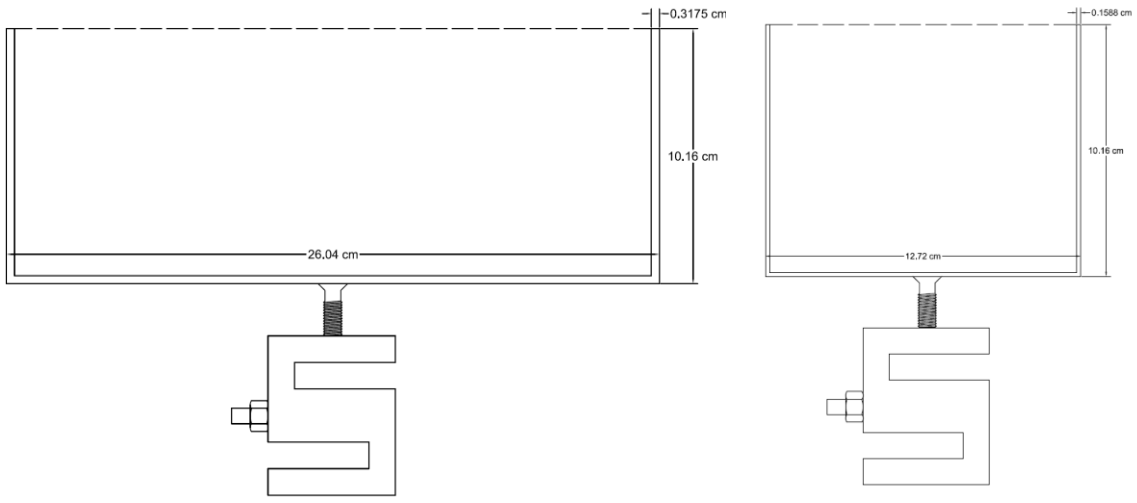

Figure A.8: a) large rectangular collection vessel and b) small cylindrical collection vessel

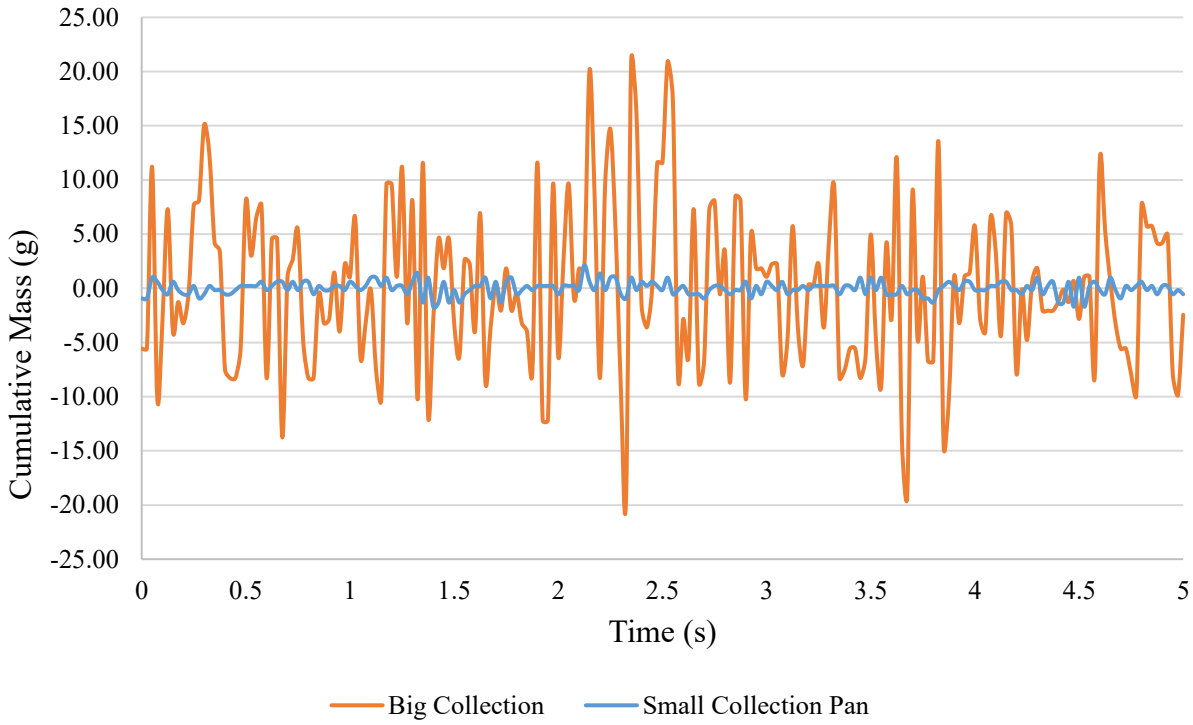

Figure A.9: Load cell scatter of unloaded collection vessels

A.5 Load Cell Temperature

The load cell used in this study (LCCA-25 supplied by Omega) has a maximum operating temperature of 65ºC. When the ambient temperature surrounding the load cell reaches this temperature, the load cell readings become compromised. This is shown in Figure A.10. To resolve this issue, a thermocouple was placed near the load cell to continuously monitor the load cell temperature. Also, Kaowool 3000 (supplied by Inproheat) and SiO_2 was placed in the base of the collection vessel to insulate the load cell from the heat emitted by the high-temperature metallic liquid.

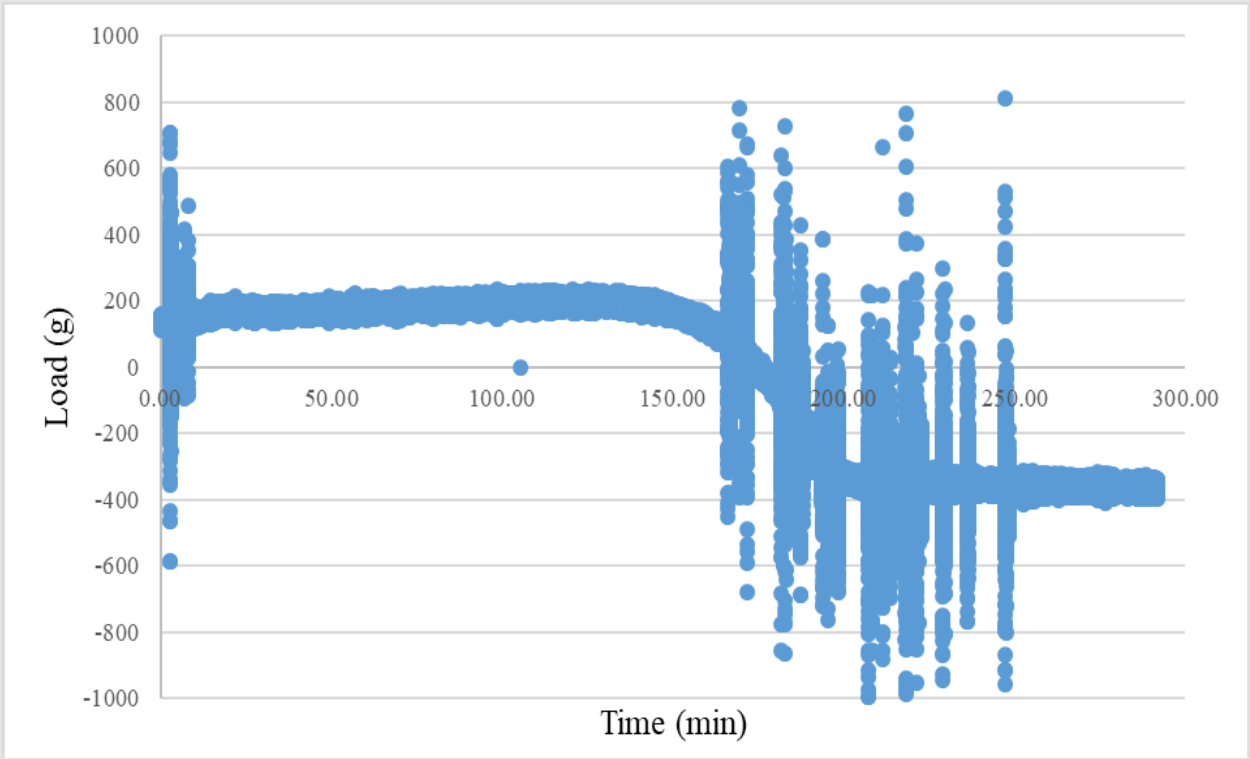

Figure A.10: Load cell failure when load cell is subject to temperatures above maximum operating temperature

A.6 Thermocouple Issues

Thermocouples perform reliably in most environments and are able to tolerate extreme temperatures and vibrations. However, they are susceptible to the effects of electromagnetic fields because of the nature and design of a transducer [213]. In this work, an induction furnace is used to heat the crucible, and therefore, electromagnetic fields are unavoidable. Electromagnetic fields affect thermocouple readings in two ways:

- Induced voltage in the thermocouple wire
- Inductive heating of the thermocouple

Faraday's law dictates that an electric conductor moving through a magnetic field results in the generation of electrical potential. This can create voltage in the thermocouple wires, and since the thermocouple works by outputting voltage (caused by the resistance between two dissimilar metals), this can have a tremendous effect on the thermocouple readings. Furthermore, the premise of inductive heating is that the electromagnetic field creates eddies giving rise to heating. Since

tungsten is uses in Type C thermocouples, which are used to measure the temperature of the metallic liquid, the alternating magnetic field created by the induction furnace may heat the thermocouple itself. This will result in a signal that does not accurately portray the temperature being measured.

An example of possible electromagnetic interference involving a thermocouple is given in Figure A.11. Here, when the power of the induction furnace was increases to raise the temperature of Al above 1600ºC, the thermocouple began to act sporadically. The temperature of the metallic liquid needs to be measured accurately to properly measure the thermophysical properties of the liquid. Thus, to mitigate the risk of unreliable temperature readings, a two-color pyrometer (Fluke EF1RH Endurance Fiber-Optic Two-Color Pyrometer supplied by ITM Instruments) was purchased and implemented to measure the temperature of the metallic liquid.

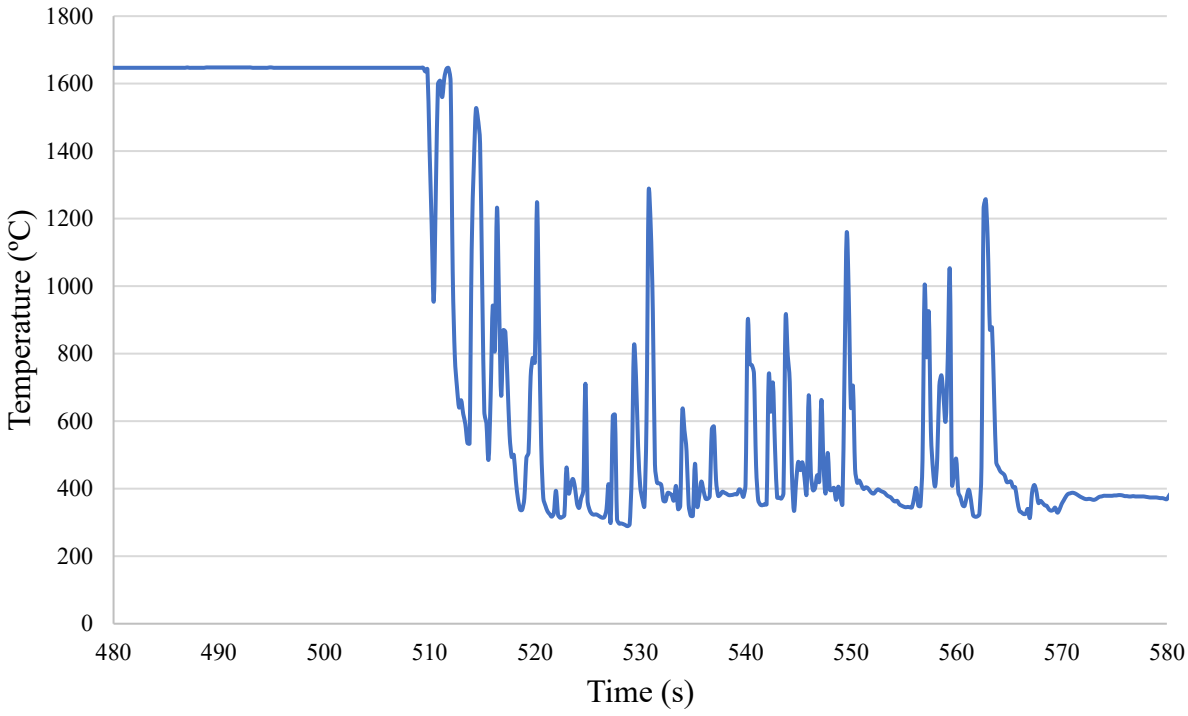

Figure A.11: Type K thermocouple failure when measuring liquid Al above 1600ºC

Another challenge associated with temperature measurement is at high enough temperatures, the temperature of the metallic liquid will significantly drop when the induction furnace is shut off. Induction heating must be shut off before the liquid is drained, otherwise the electromagnetic field will induce stirring in the liquid, negatively impacting the flow of the liquid

exiting the orifice. An example of this is given in Figure A.12 where Al was heated to above 1600ºC and then the temperature drastically decreases because the induction furnace was turned off. Once the induction furnace was turned off, the cooling rate was found to equal -100 ºC /min, and the temperature of the metallic liquid decreased by 50ºC from the beginning to the end of the pour. Since the thermophysical properties of Al changes as a function of temperature, this decrease in temperature would have a significant effect on the measurement results. In the work presented in this study, the measurements were not performed at temperatures high enough for a significant temperature drop to occur. However, an expanded varying temperature DC model was developed (see Appendix H) for situations like presented in Figure A.12.

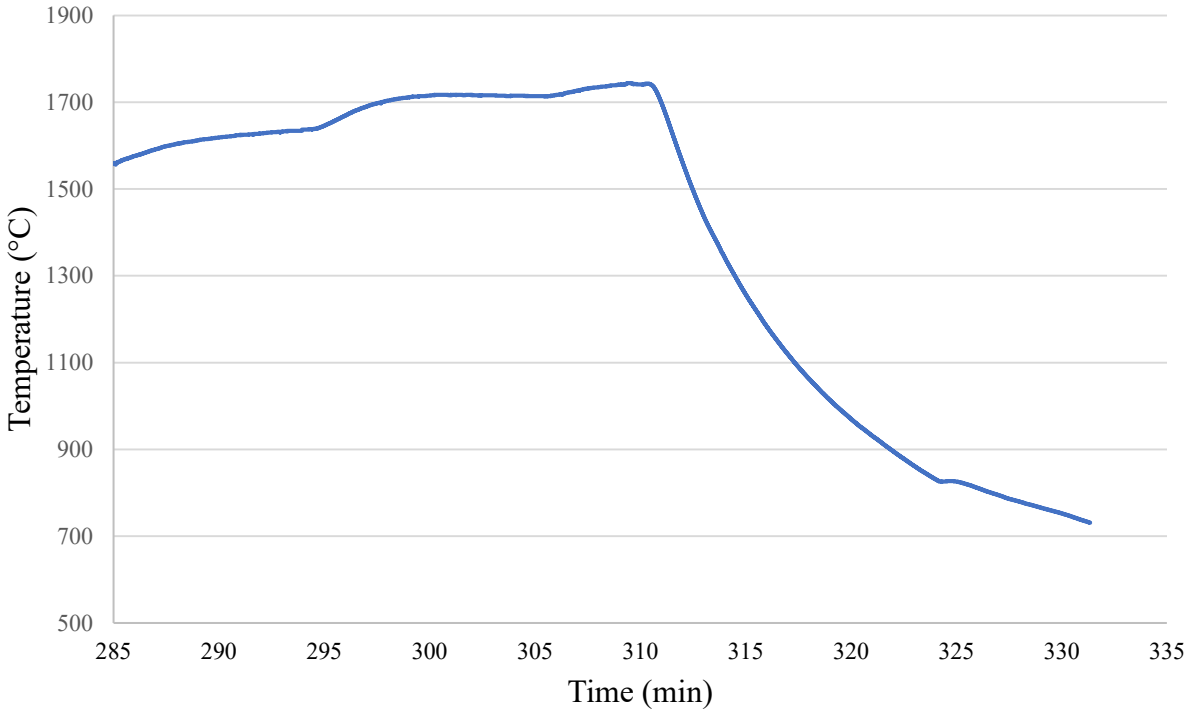

Figure A.12: Temperature drop of liquid Al after induction furnace is shut off

A.7 Stopper Failure

Lastly, at extreme temperatures, the stopper rod was found to fuse with the Al_2O_3 crucible. Numerous efforts were made to fabricate stopper rods from different materials, including high-temperature ceramic blanket (Kaowool 3000 supplied by Inproheat) and castable ceramic (Ceramacast 510 supplied by Aremco). Unfortunately, these materials would fuse to the crucible,

which prevented the stopper from being removed from the orifice. Other times, the ceramic would break down, and the liquid would drain from the crucible before the draining temperature was achieved. Examples of this are given in Figures A.14 and A.15.

Figure A.13: Failed stopper rod made of high-temperature Kaowool ceramic blanket

Figure A.15: Failed stopper rod made of cast Ceramacast 510

APPENDIX B : CALIBRATION AND EXPERIMENTAL DATA

This appendix provides the calibration data and experimental data for all measurements reported in Section 4.2. The calibration data consists of the discharge coefficient versus Reynolds number curves for each individual crucible used, and the ultrasonic calibration of heat versus volume. The experimental data includes the cumulative mass and the head of the draining liquid as a function of time. Both of these were determined using data measured by a load cell, as described in Section 4.1.

B.1 Aluminum at 1032 K

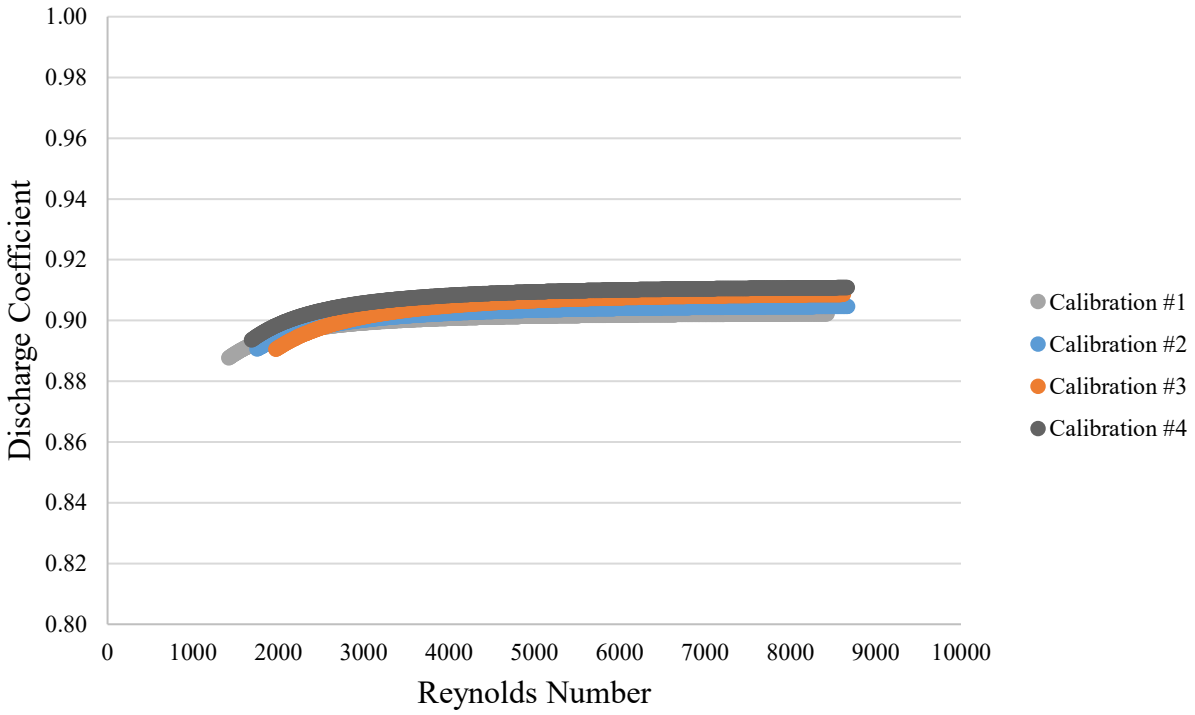

Figure B.1: C_d versus Re calibration for Al at 1032 K

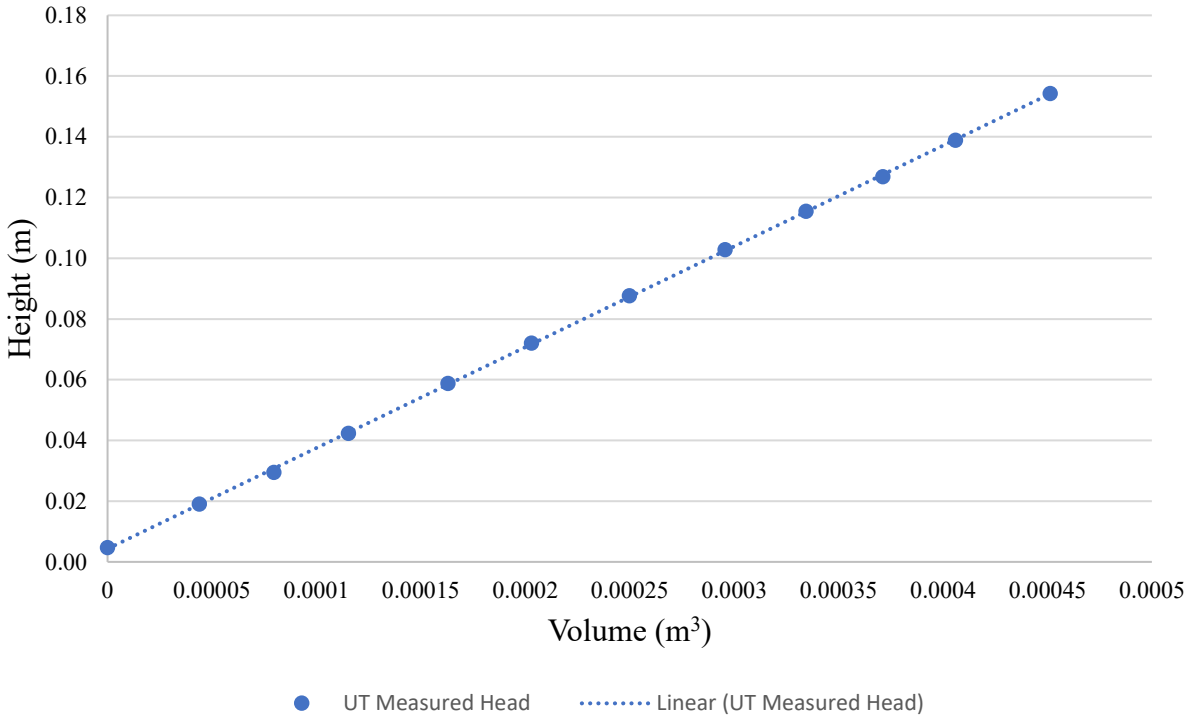

Figure B.2: Head versus volume calibration of crucible for Al at 1032 K

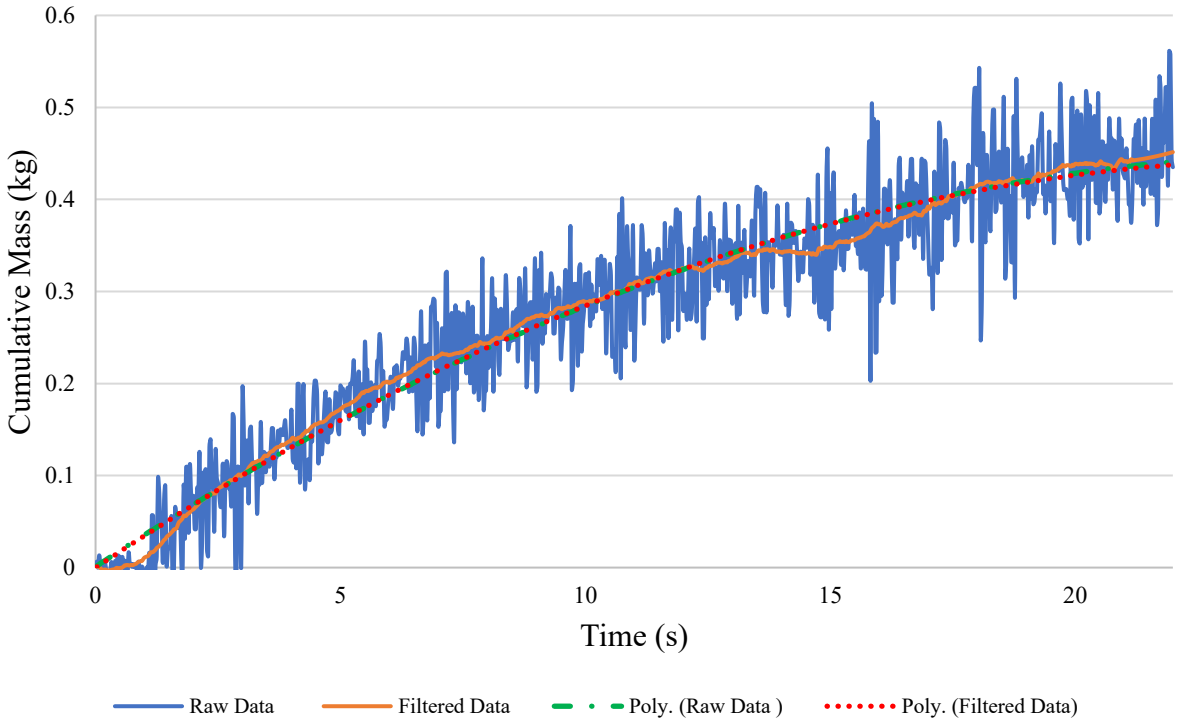

Figure B.3: Cumulative mass of Al at 1032 K with fitted polynomial to raw data and filtered data

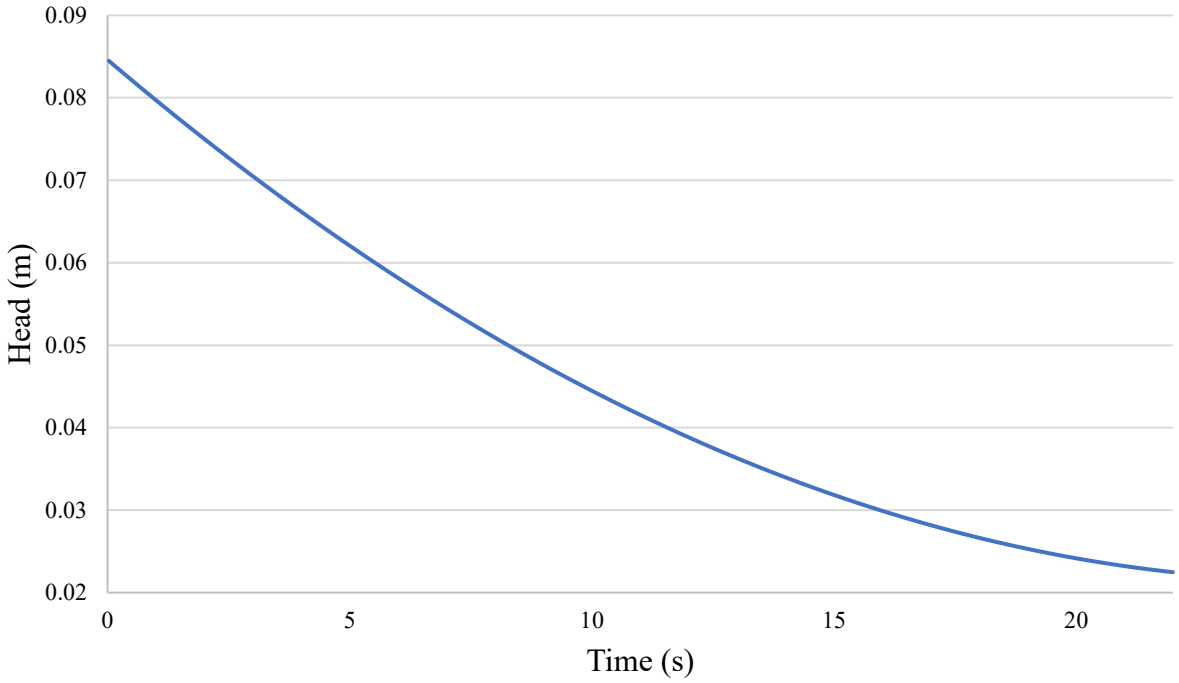

Figure B.4: Experimental head of Al at 1032 K.

B.2 Aluminum at 1120 K

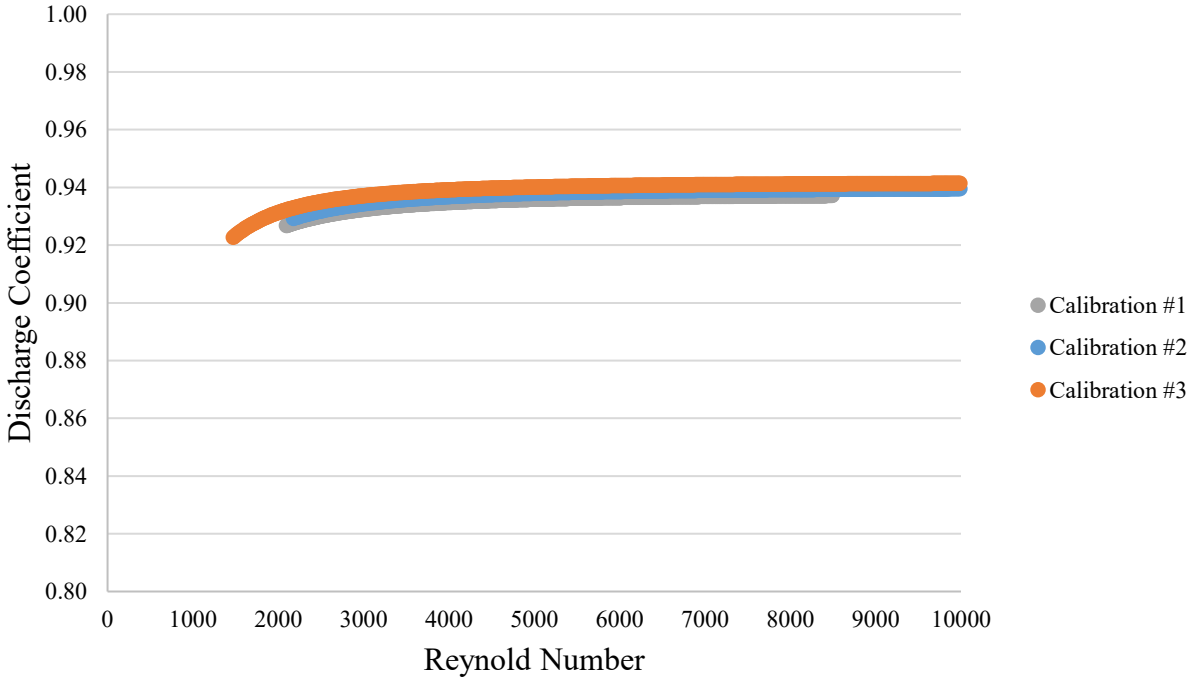

Figure B.5: C_d versus Re calibration for Al at 1120 K

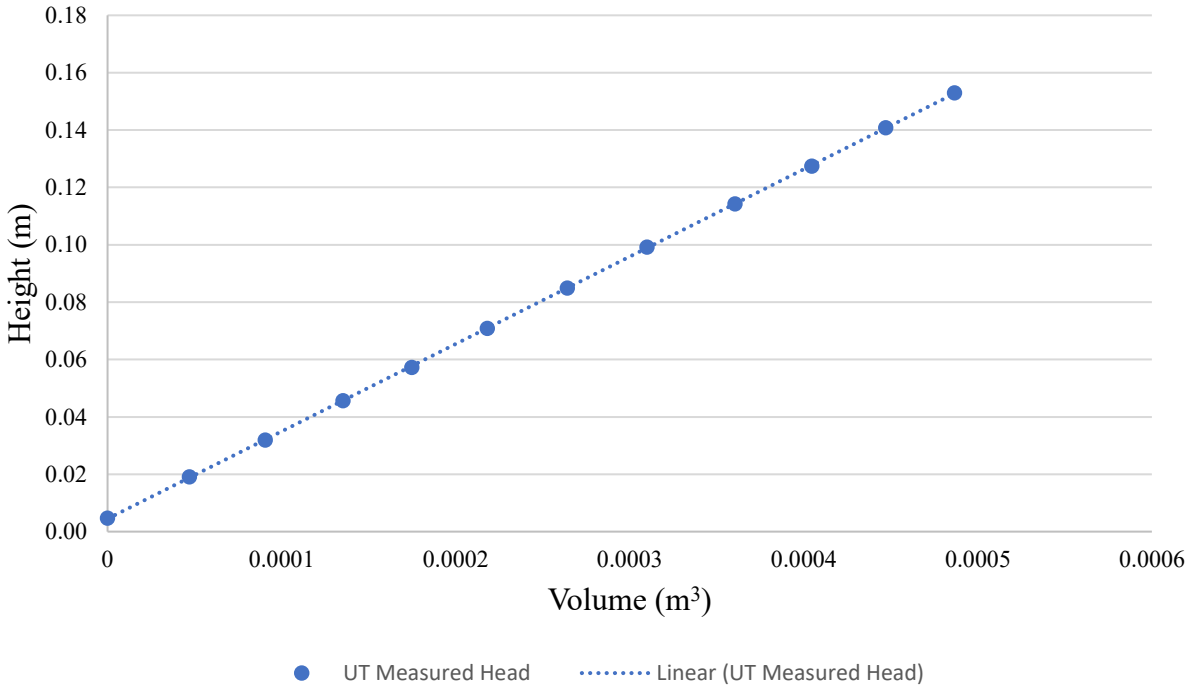

Figure B.6: Head versus volume calibration of crucible for Al at 1120 K

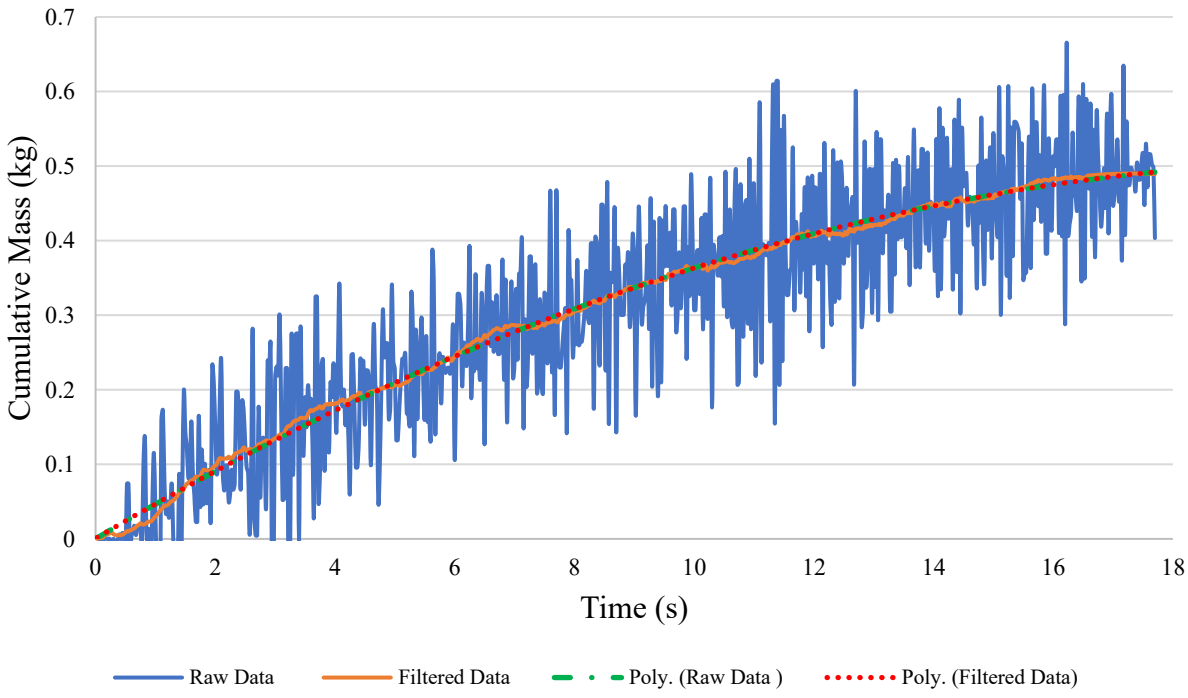

Figure B.7: Cumulative mass of Al at 1120 K with fitted polynomial to raw data and filtered data

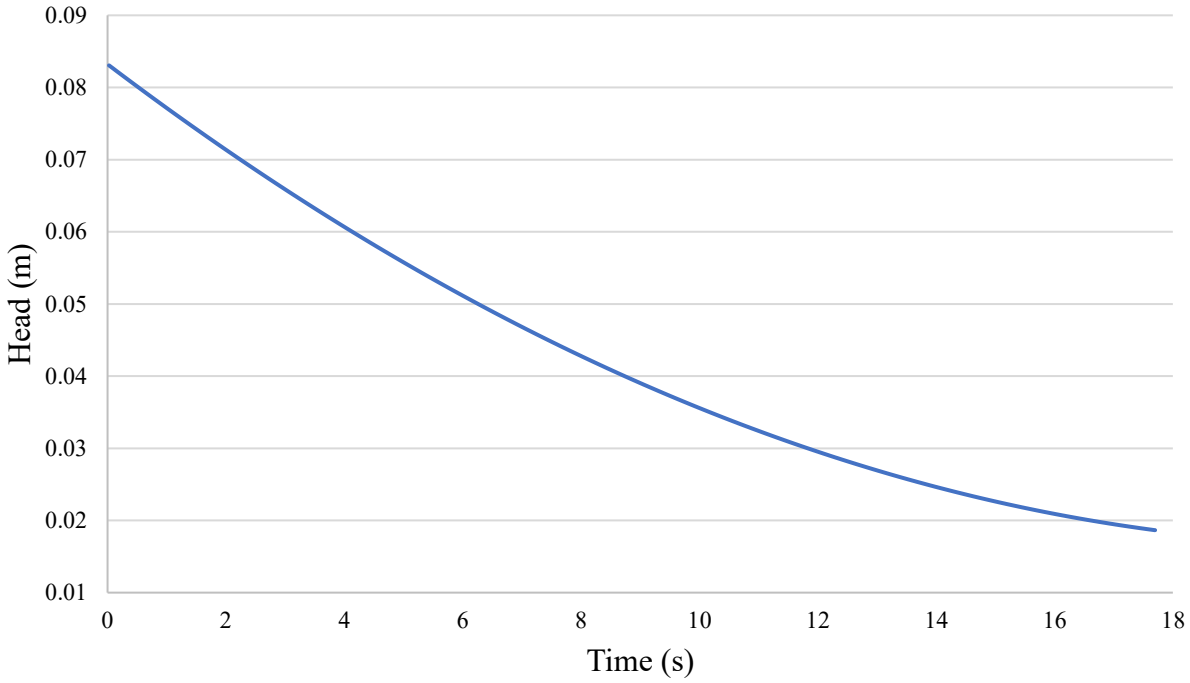

Figure B.8: Experimental head of Al at 1120 K.

B.3 Aluminum at 1174 K

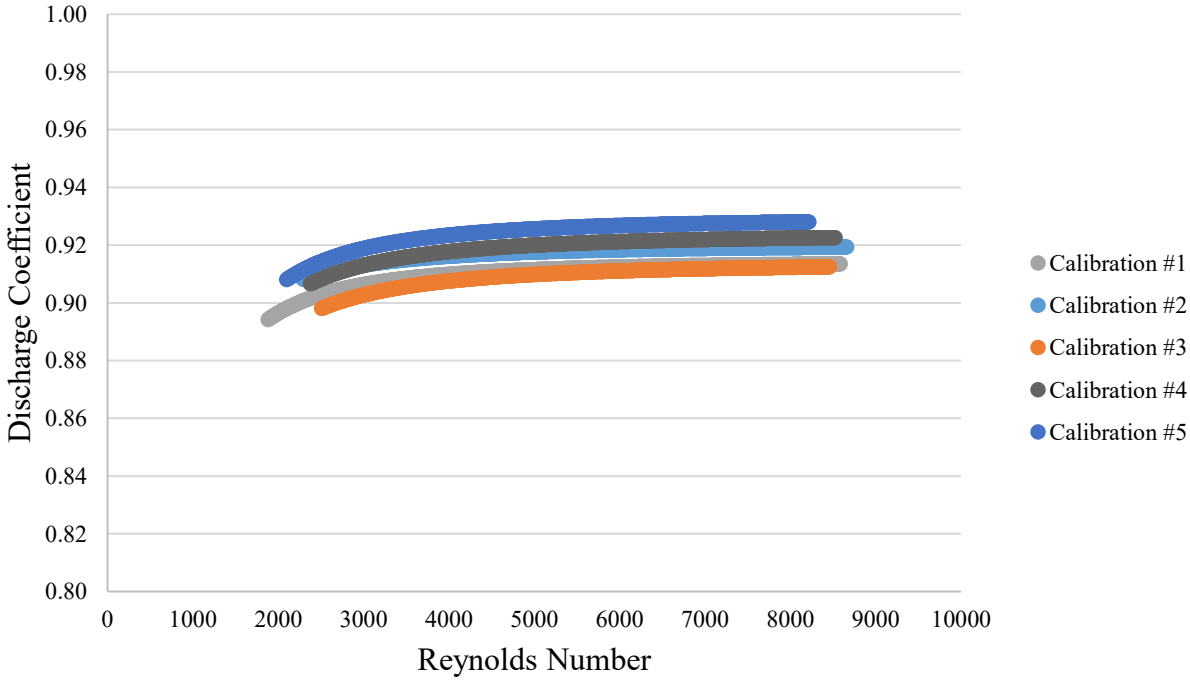

Figure B.9: C_d versus Re calibration for Al at 1174 K

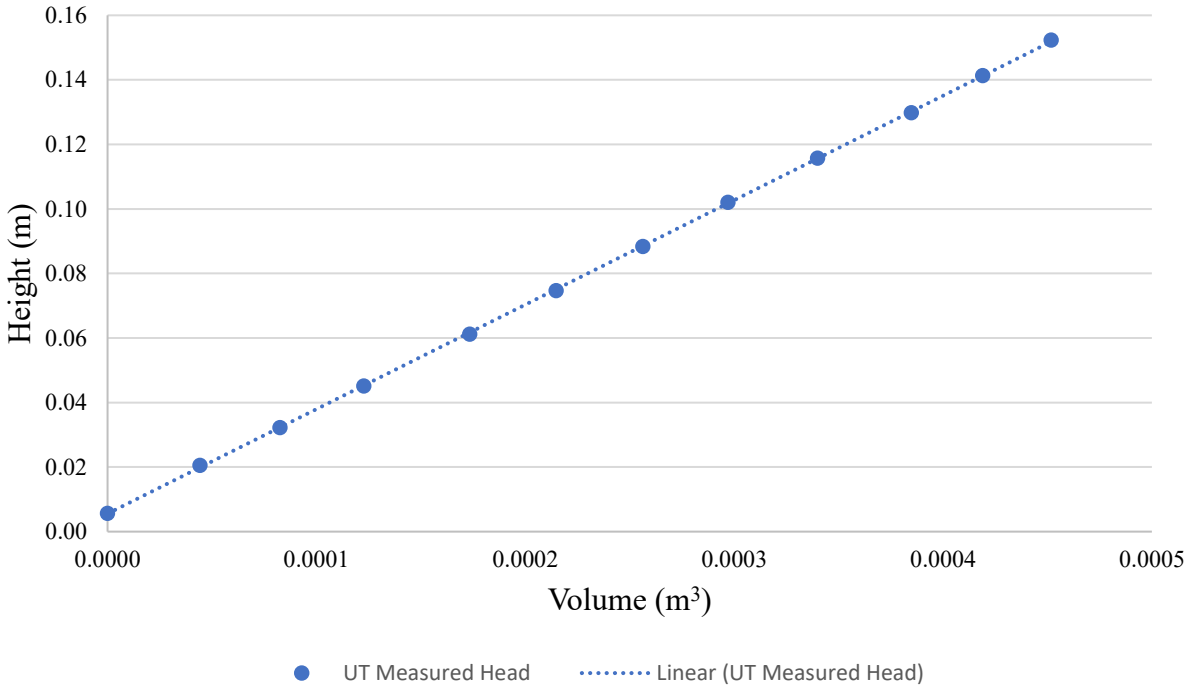

Figure B.10: Head versus volume calibration of crucible for Al at 1174 K

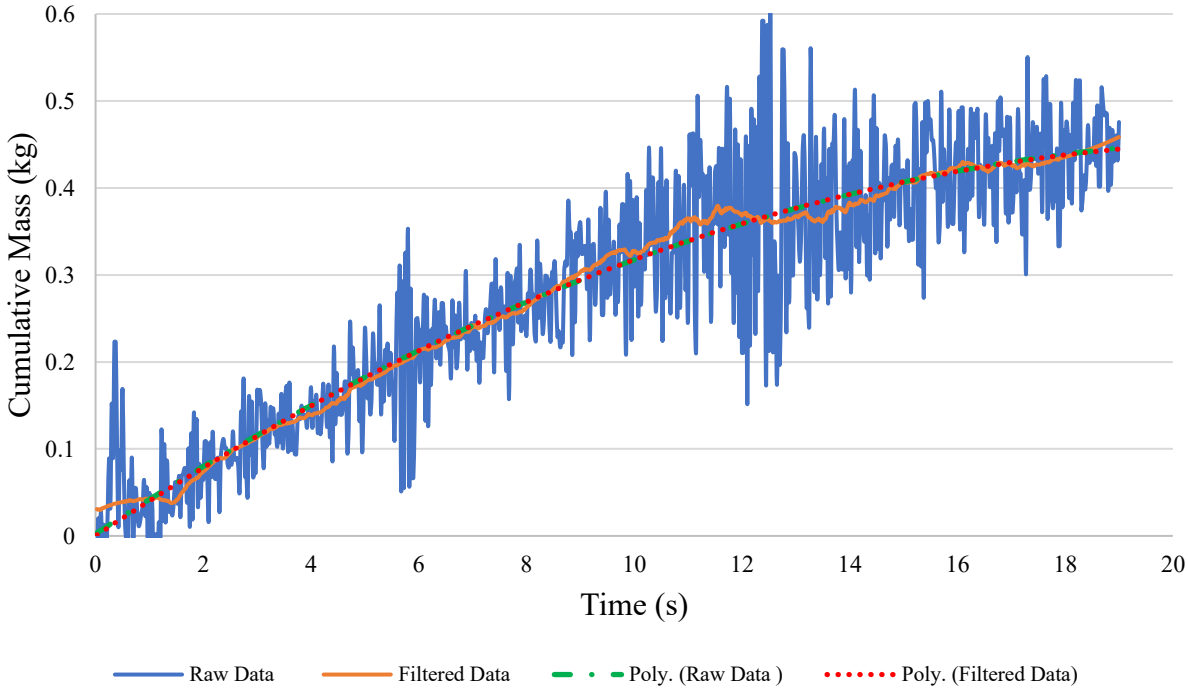

Figure B.11: Cumulative mass of Al at 1174 K with fitted polynomial to raw data and filtered data

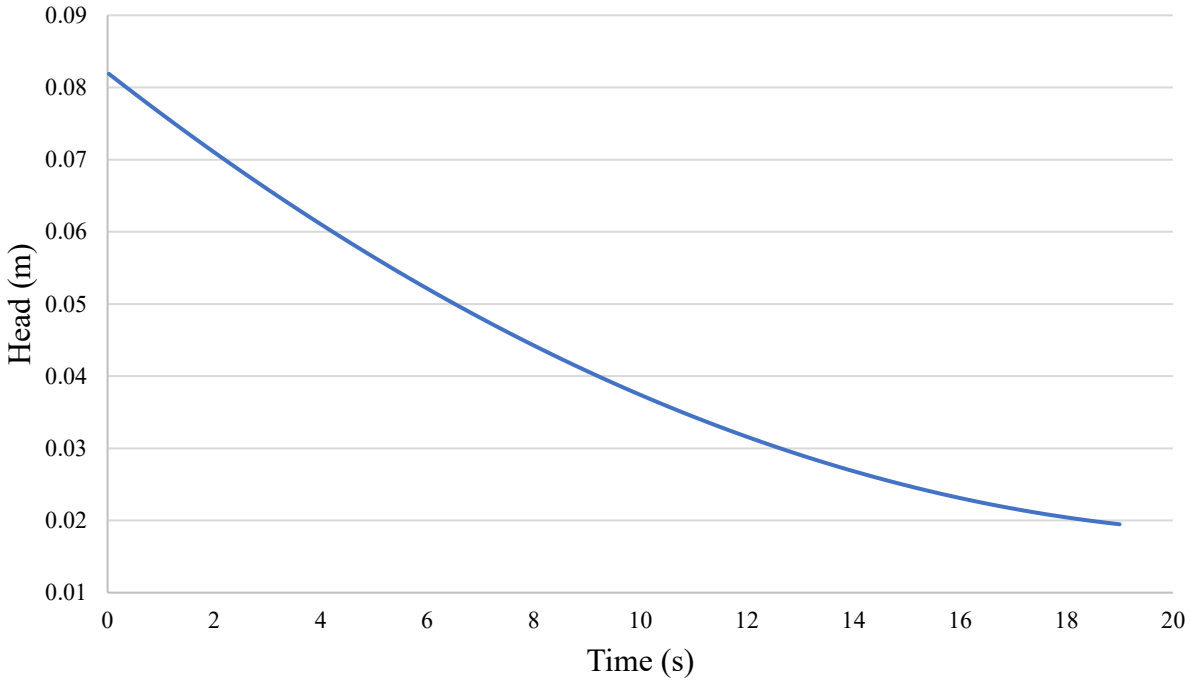

Figure B.12: Experimental head of Al at 1174 K.

B.4 Aluminum Copper at 1029 K

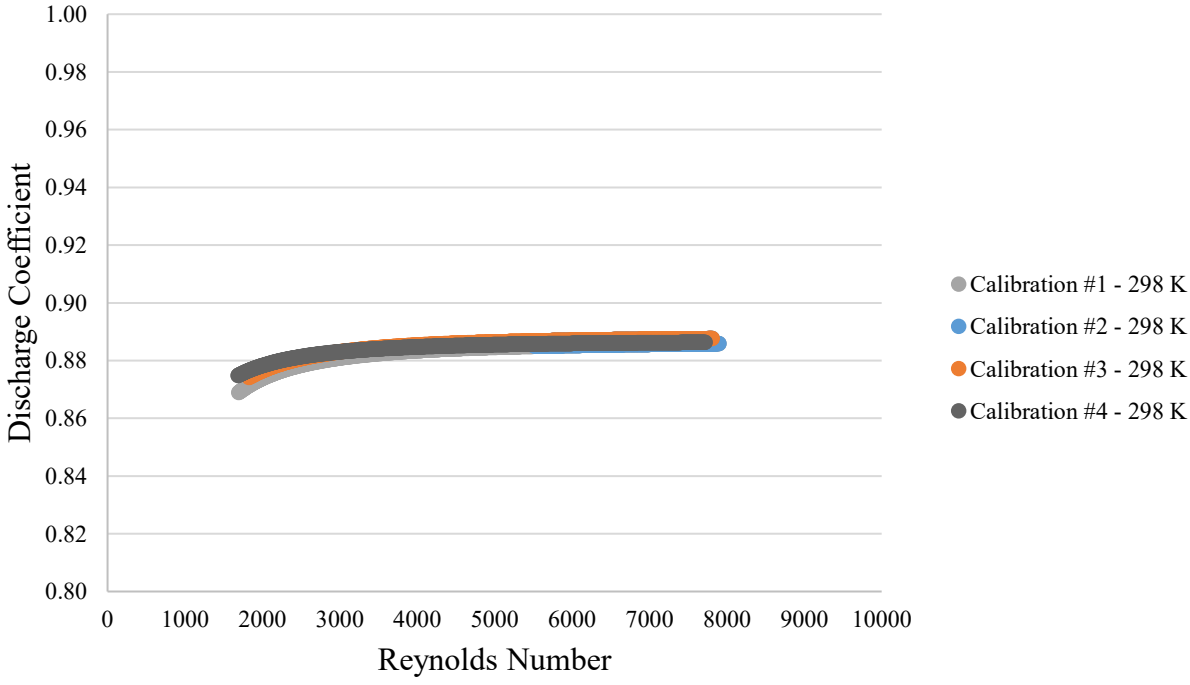

Figure B.13: C_d versus Re calibration for Al-Cu at 1029 K

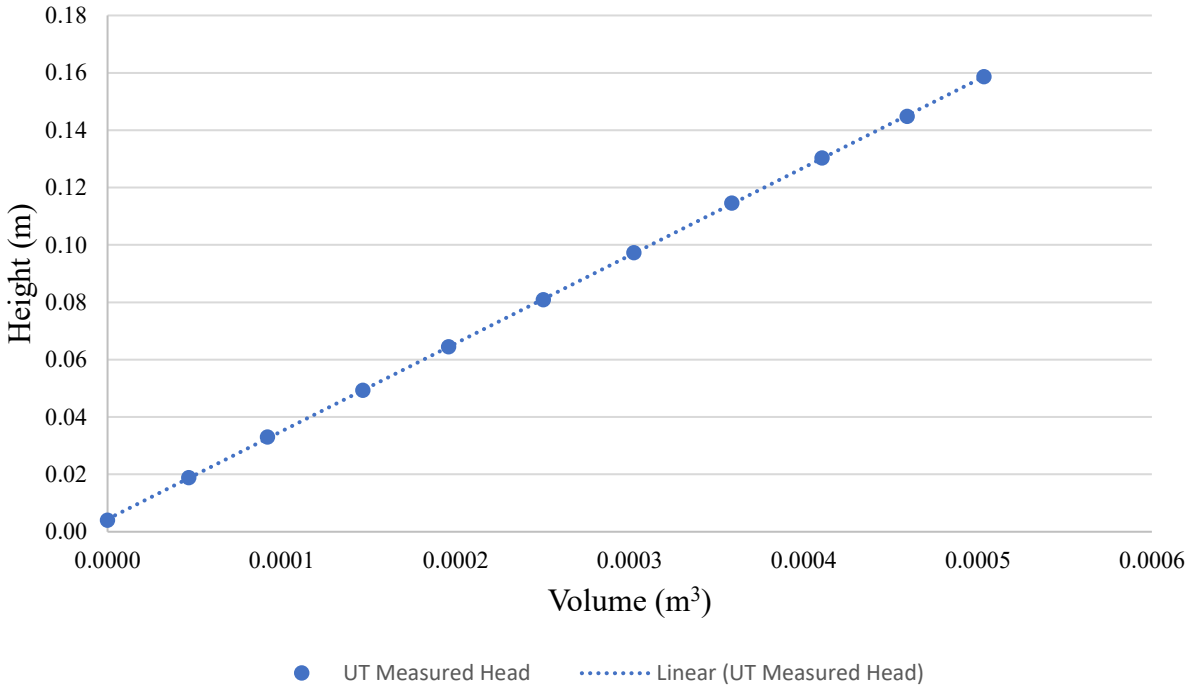

Figure B.14: Head versus volume calibration of crucible for Al-Cu at 1029 K

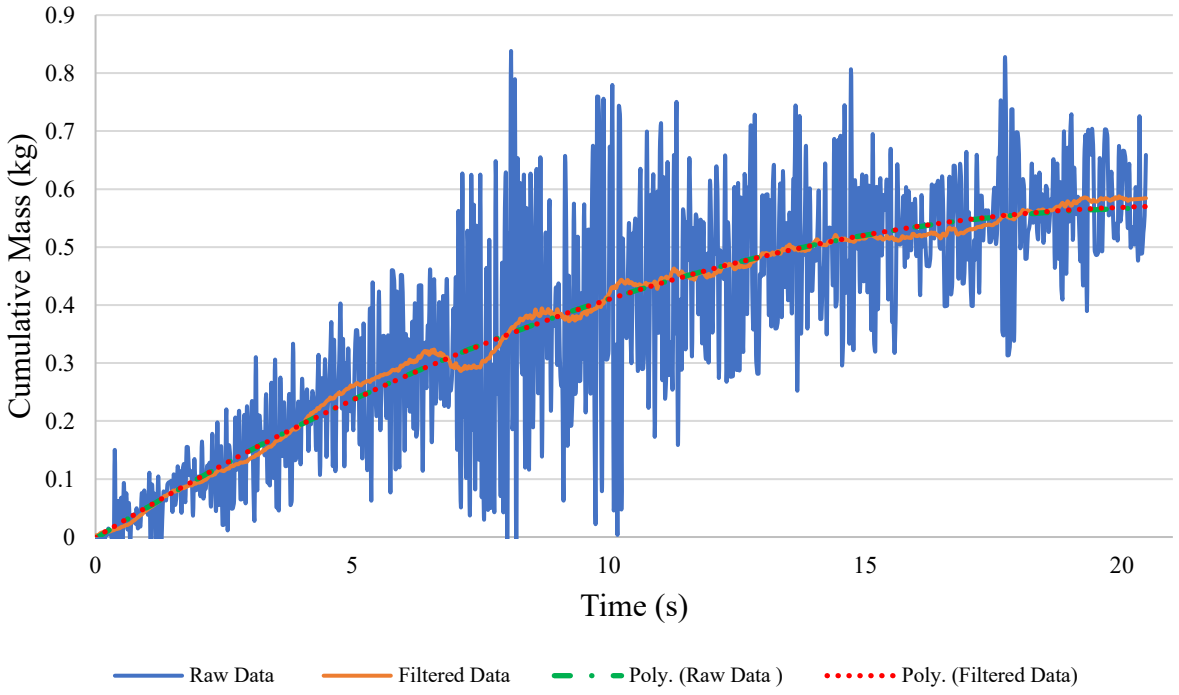

Figure B.15: Cumulative mass of Al-Cu at 1029 K with fitted polynomial to raw data and filtered data

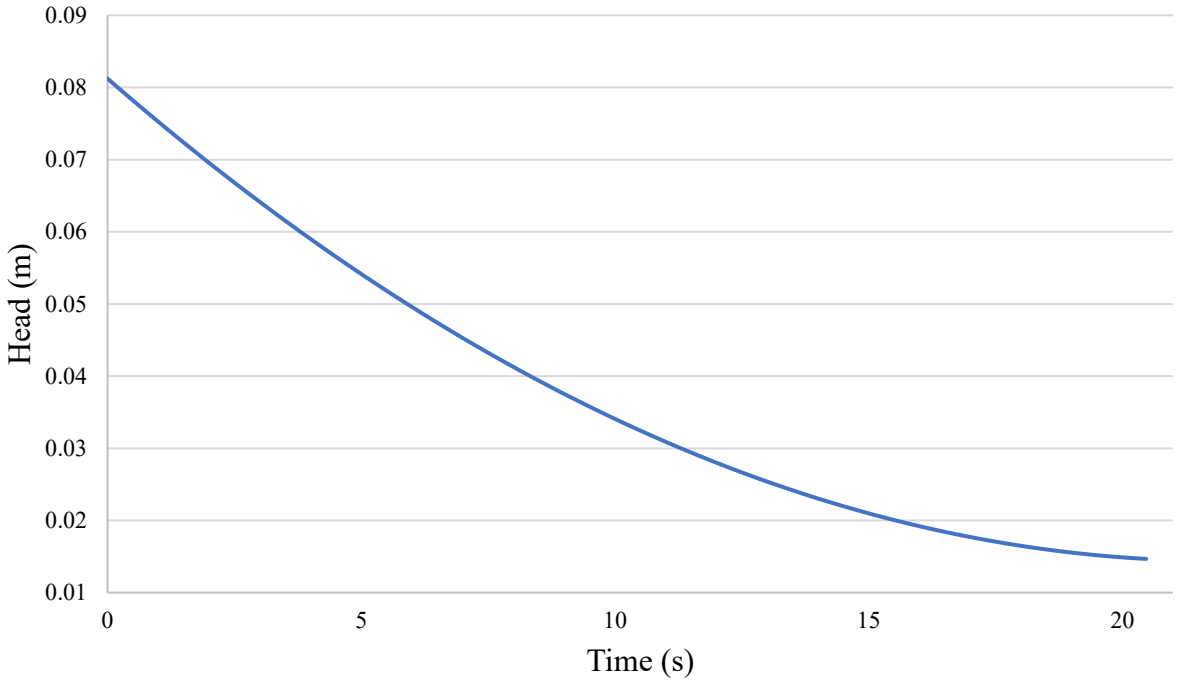

Figure B.16: Experimental head of Al-Cu at 1029 K.

B.5 Aluminum Copper at 1076 K

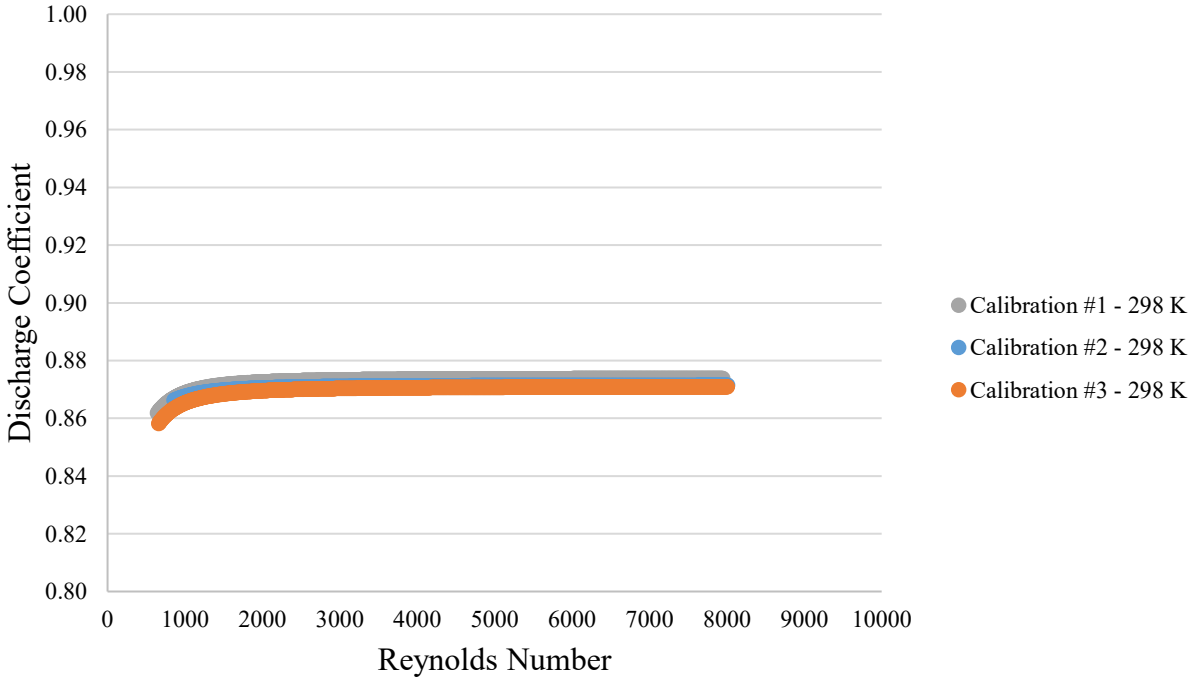

Figure B.17: C_d versus Re calibration for Al-Cu at 1076 K

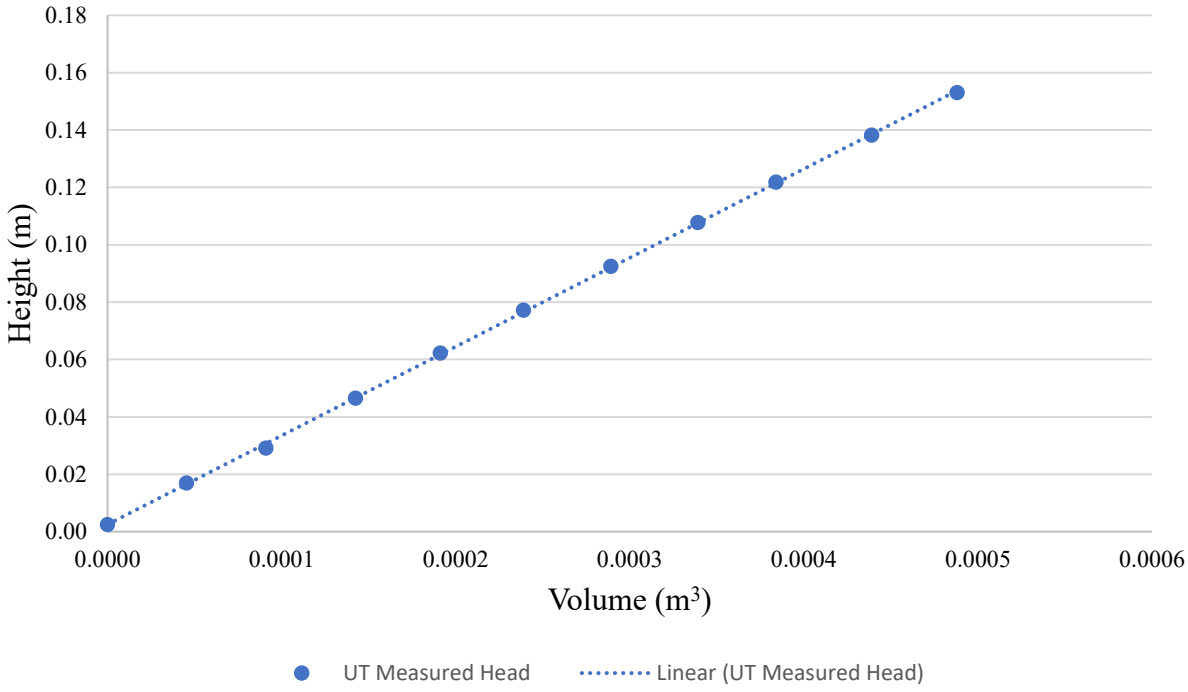

Figure B.18: Head versus volume calibration of crucible for Al-Cu at 1076 K

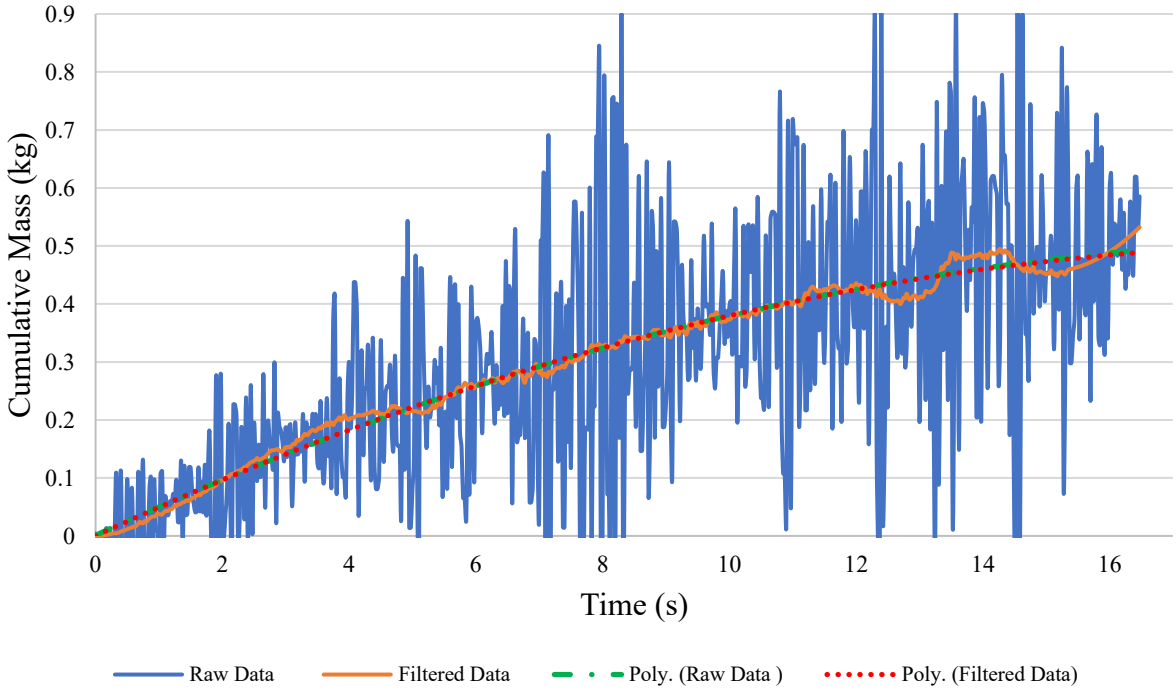

Figure B.19: Cumulative mass of Al-Cu at 1076 K with fitted polynomial to raw data and filtered data

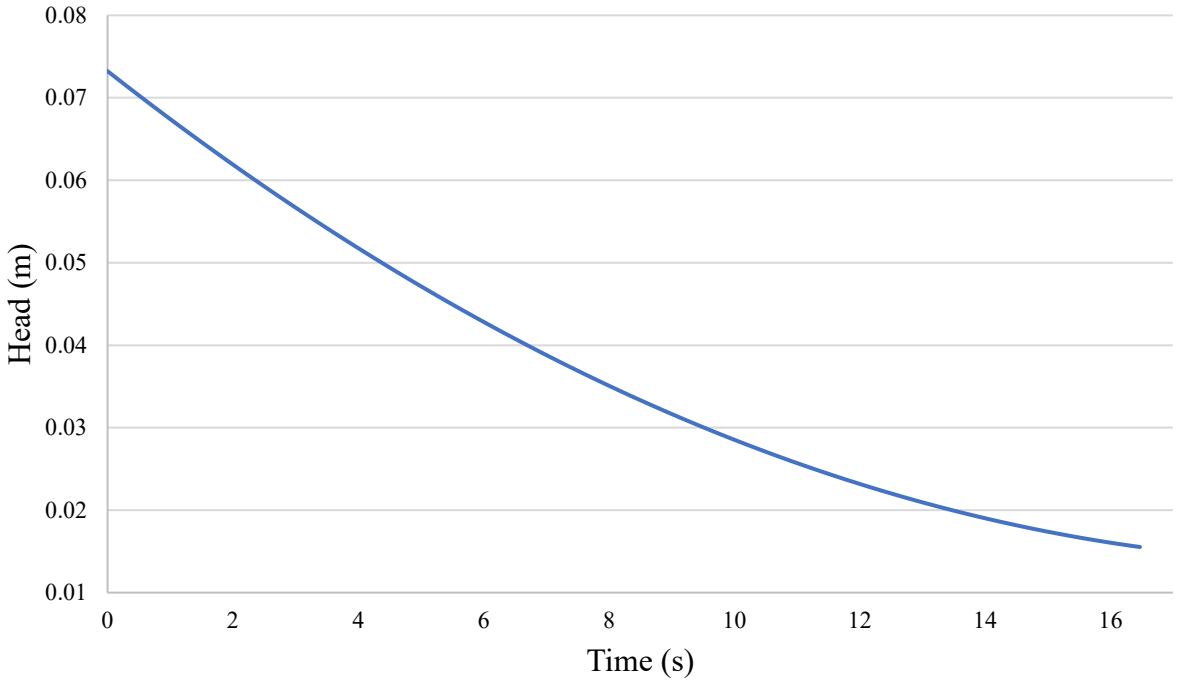

Figure B.20: Experimental head of Al-Cu at 1076 K.

B.6 Aluminum Copper at 1123 K

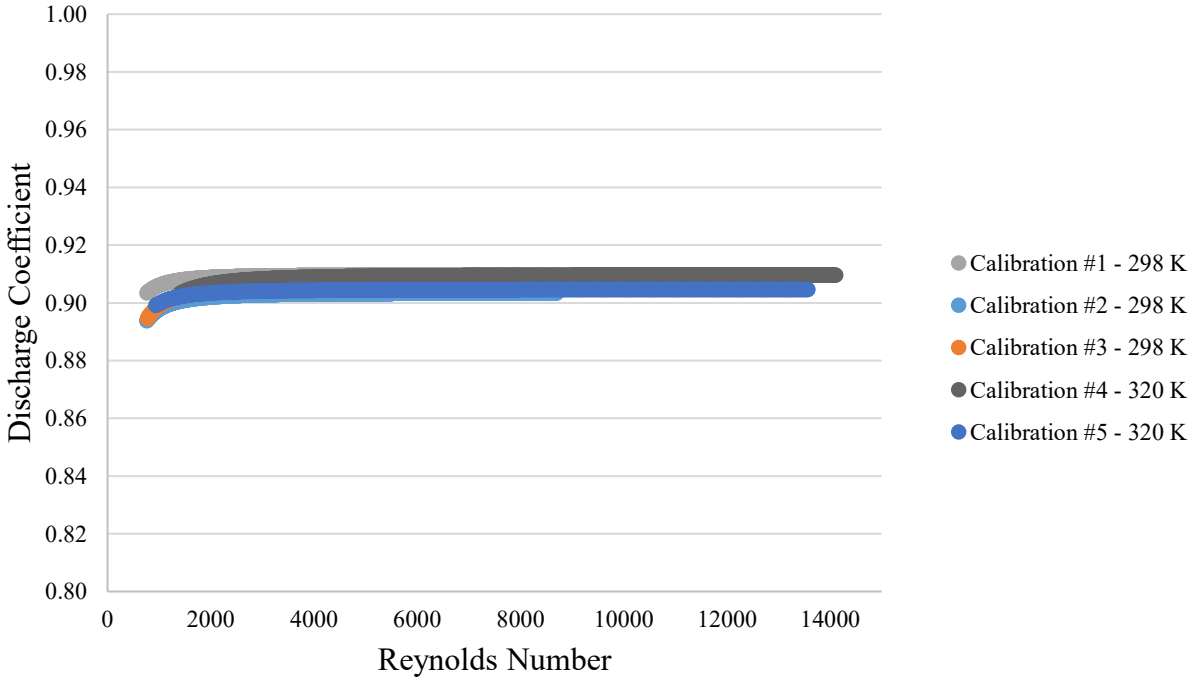

Figure B.21: C_d versus Re calibration for Al-Cu at 1123 K

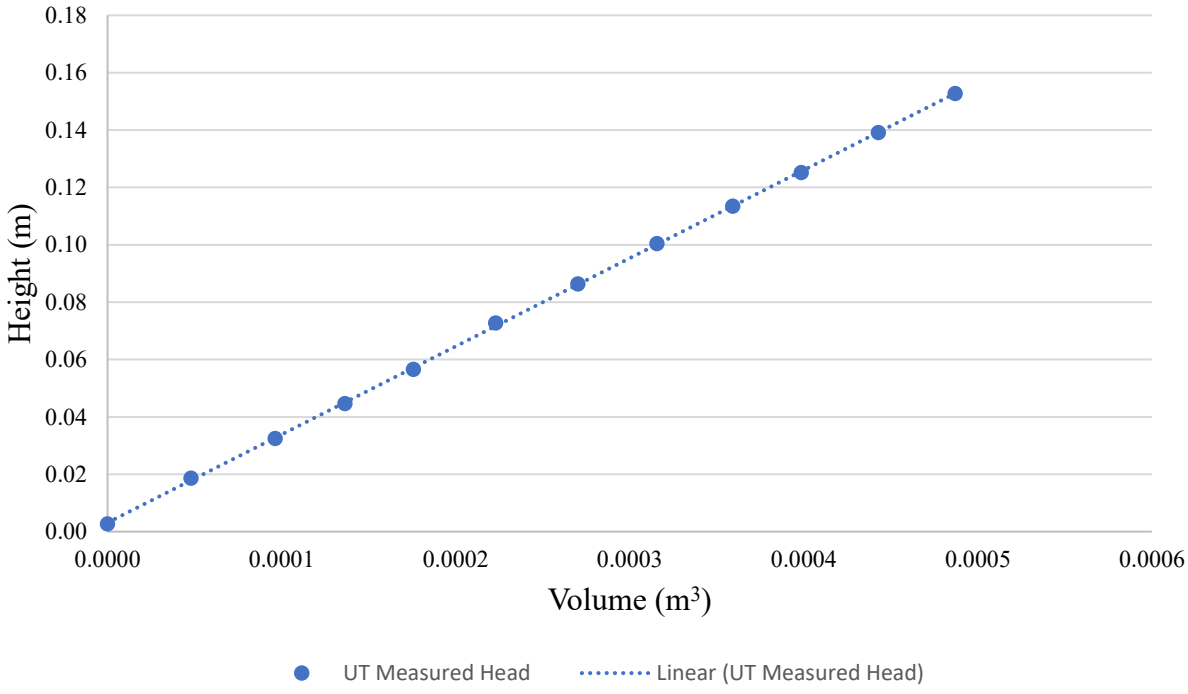

Figure B.22: Head versus volume calibration of crucible for Al-Cu at 1123 K

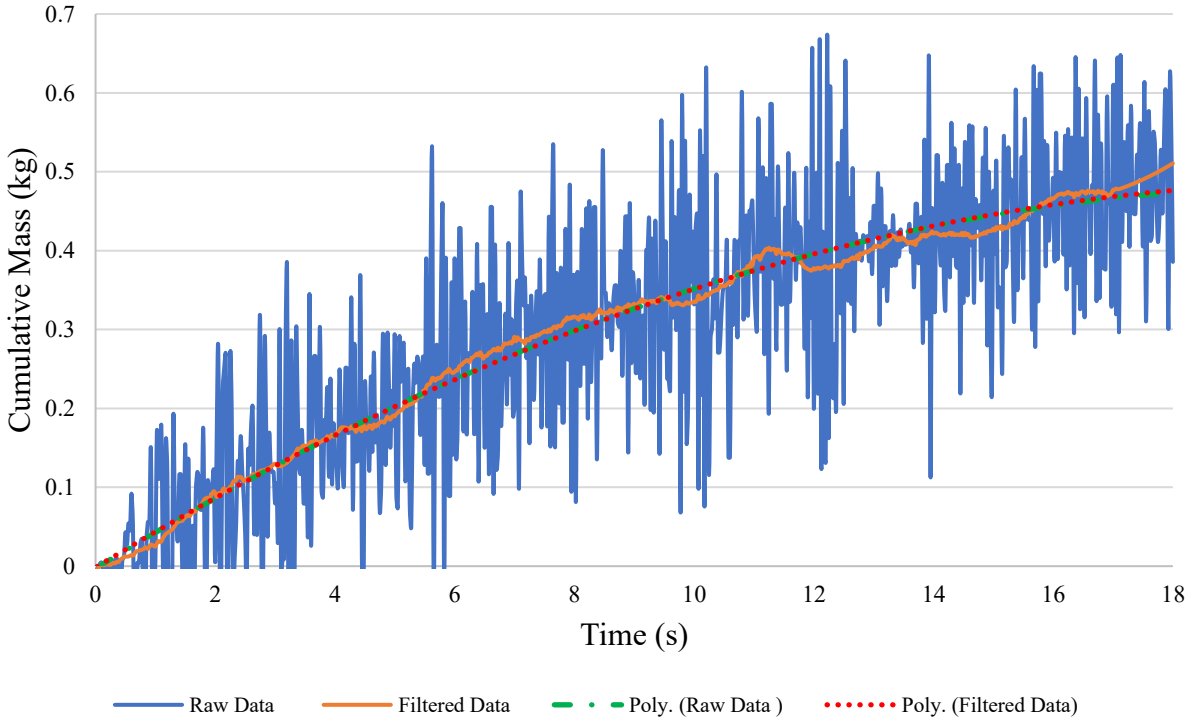

Figure B.23: Cumulative mass of Al-Cu at 1123 K with fitted polynomial to raw data and filtered data

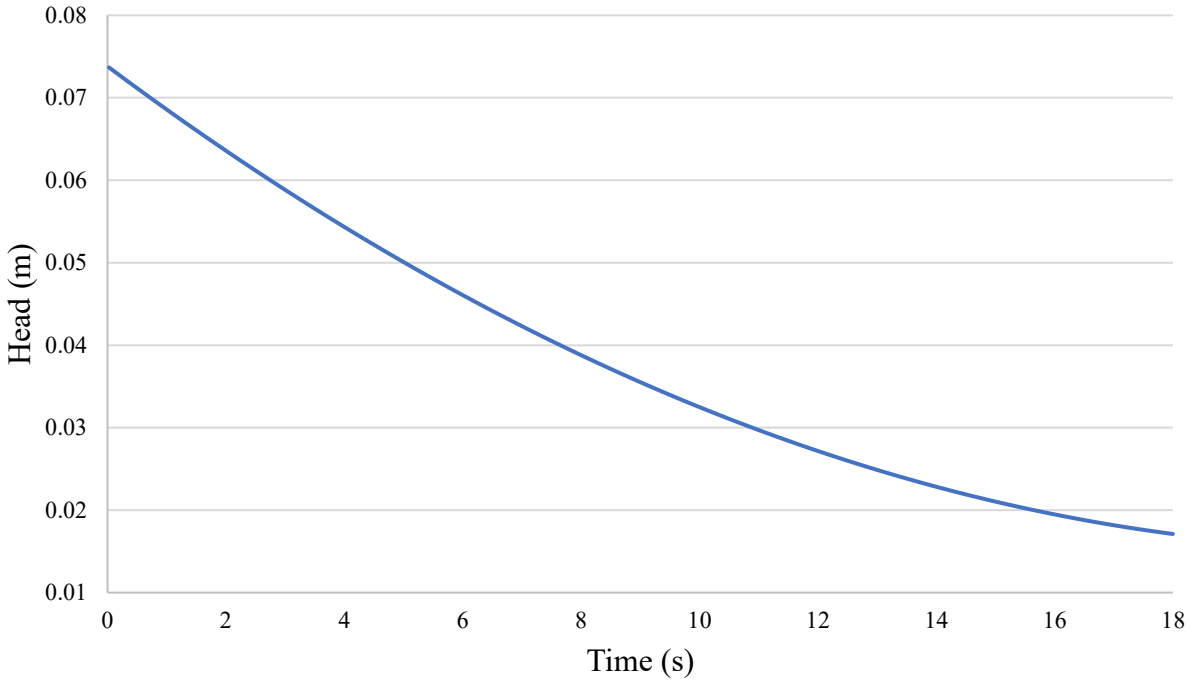

Figure B.24: Experimental head of Al-Cu at 1123 K.

B.7 Aluminum Copper at 1180 K

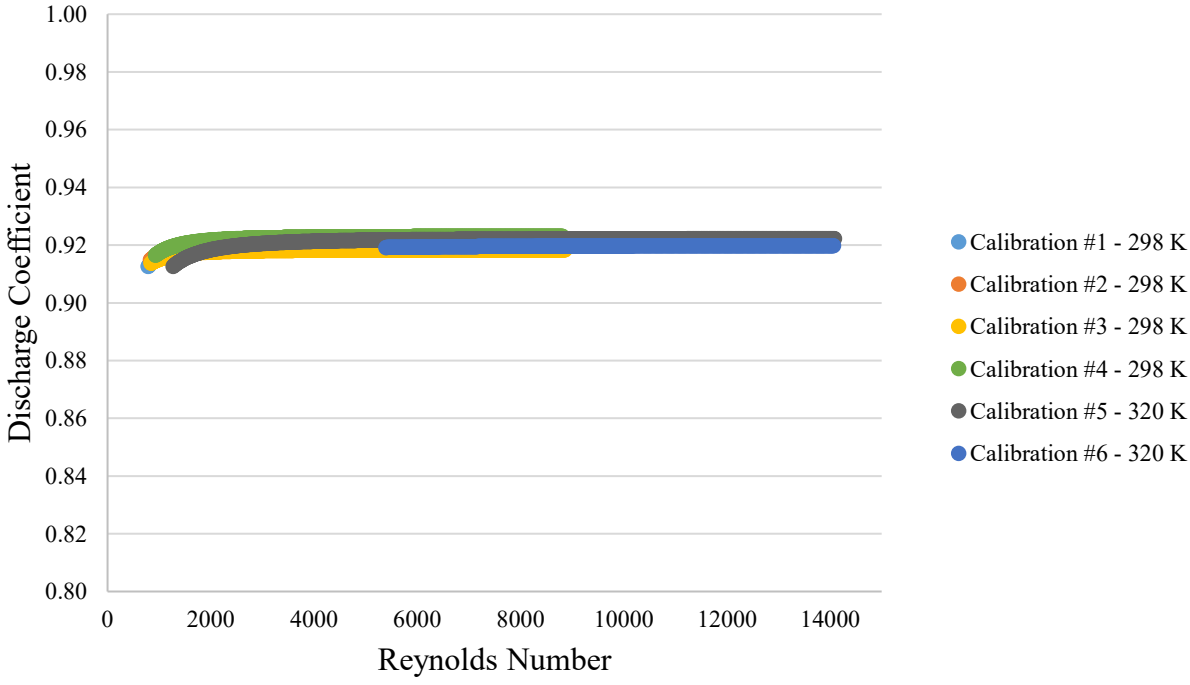

Figure B.25: C_d versus Re calibration for Al-Cu 1180 K

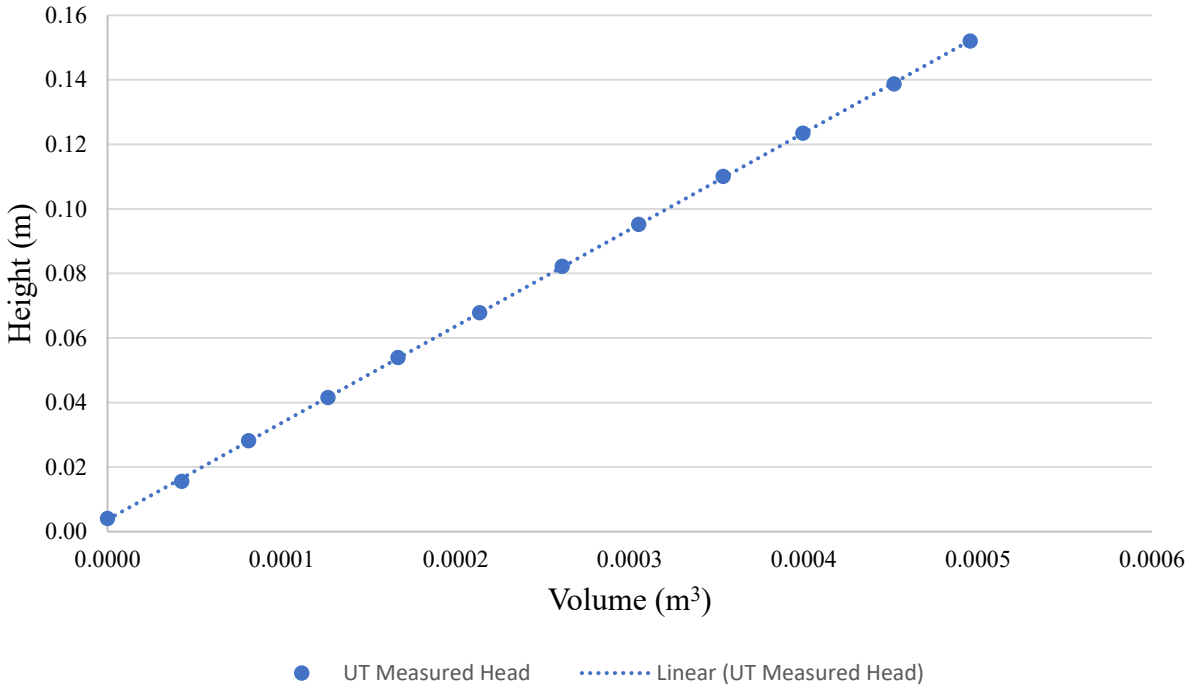

Figure B.26: Head versus volume calibration of crucible for Al-Cu at 1180 K

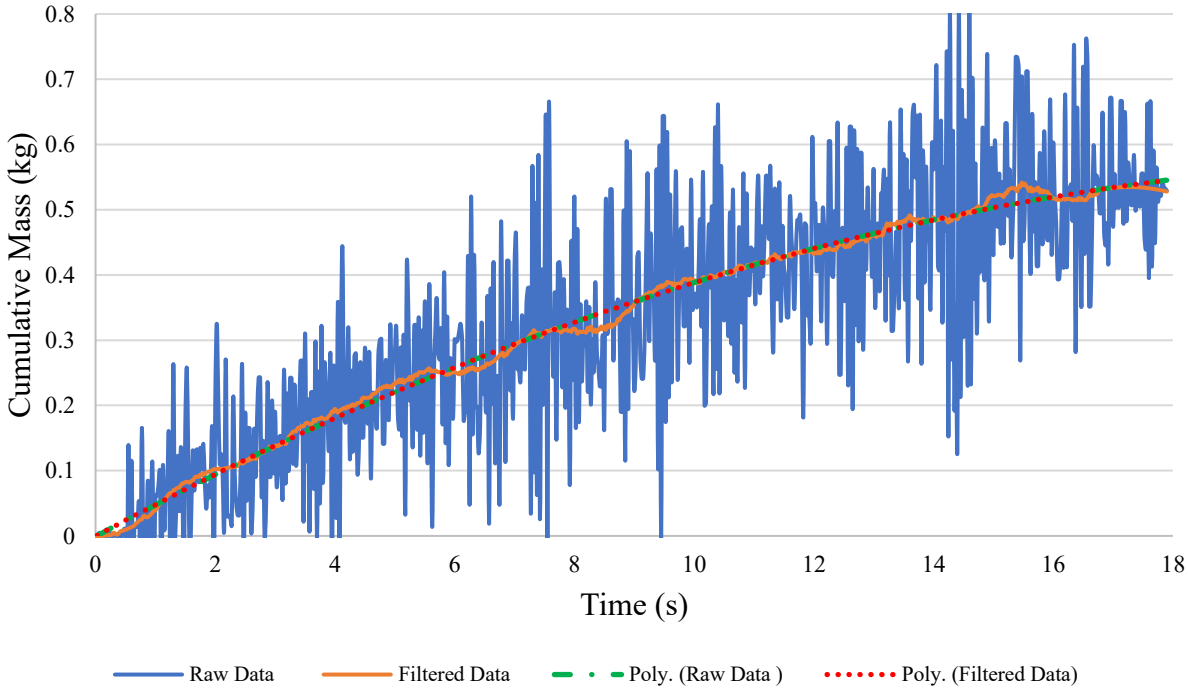

Figure B.27: Cumulative mass of Al-Cu at 1180 K with fitted polynomial to raw data and filtered data

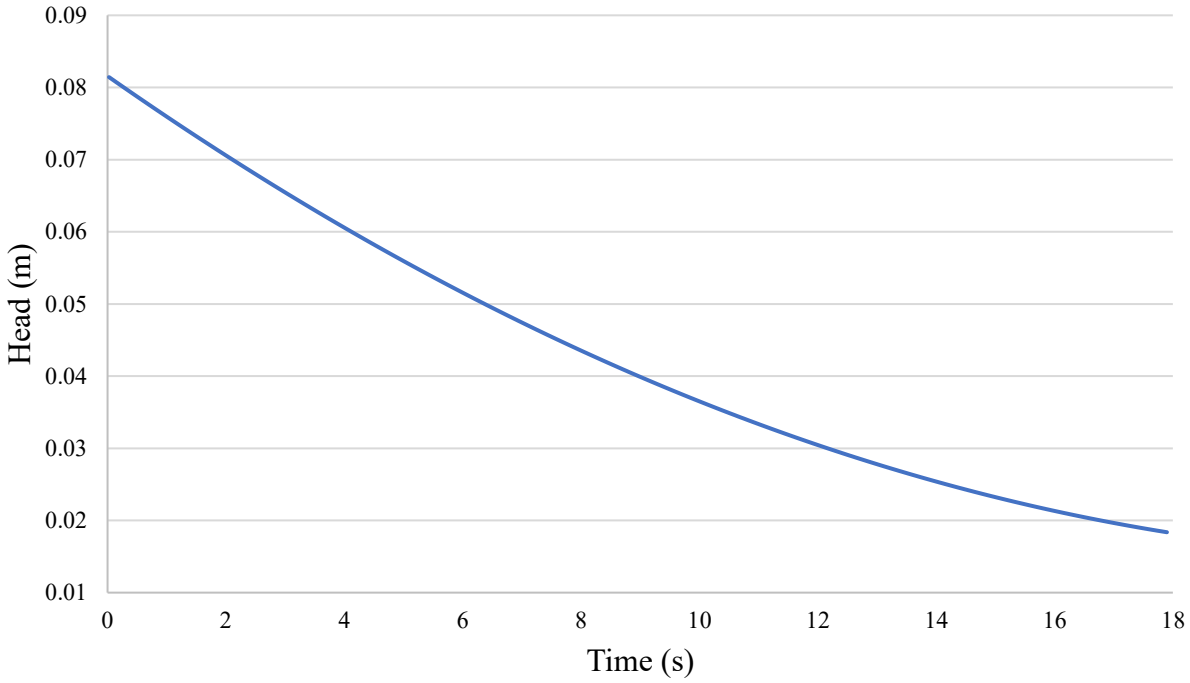

Figure B.28: Experimental head of Al-Cu at 1180 K.

B.8 Aluminum Copper at 1224 K

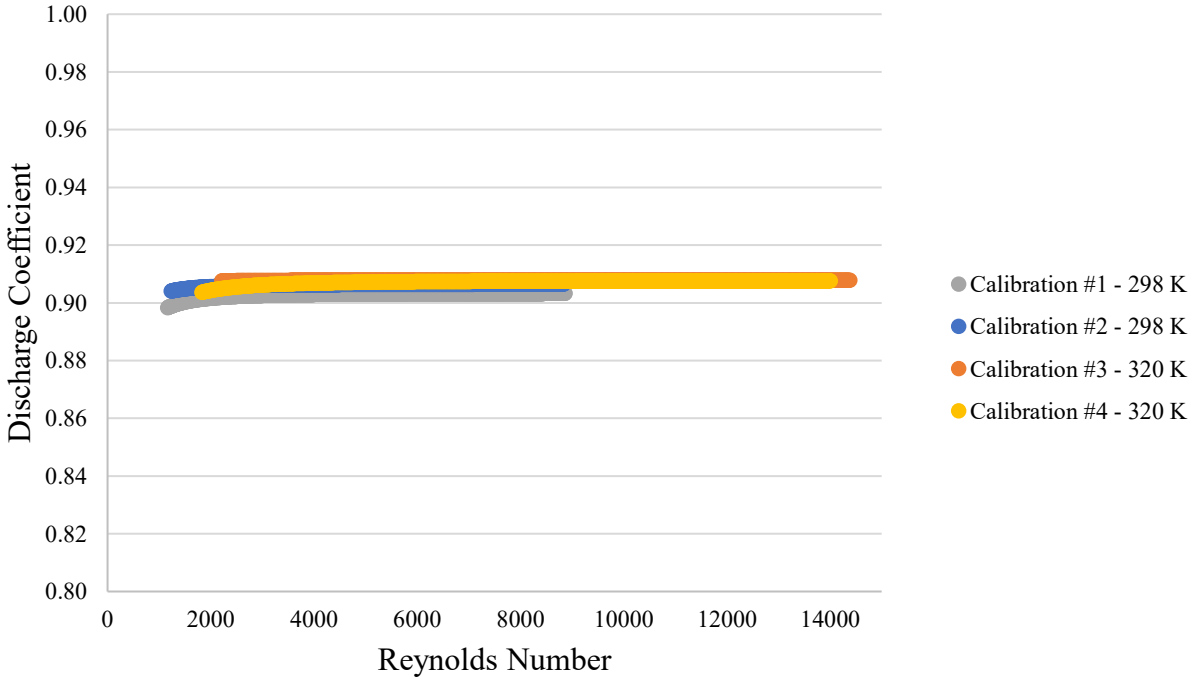

Figure B.29: C_d versus Re calibration for Al-Cu at 1224 K

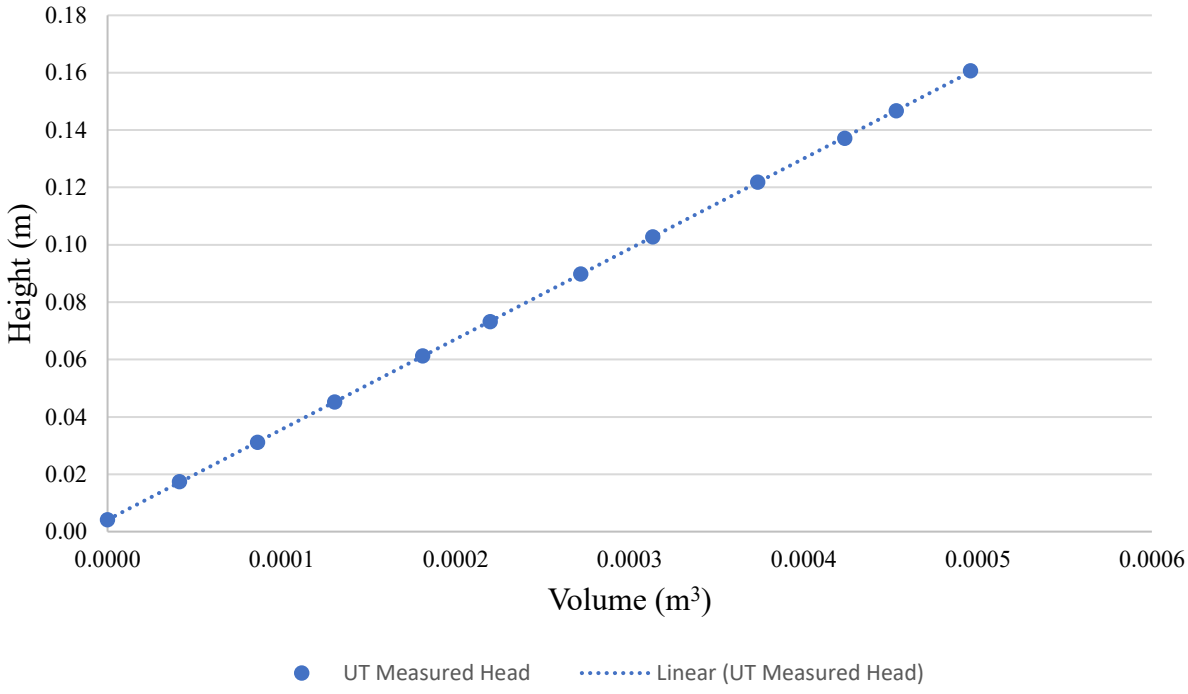

Figure B.30: Head versus volume calibration of crucible for Al-Cu at 1224 K

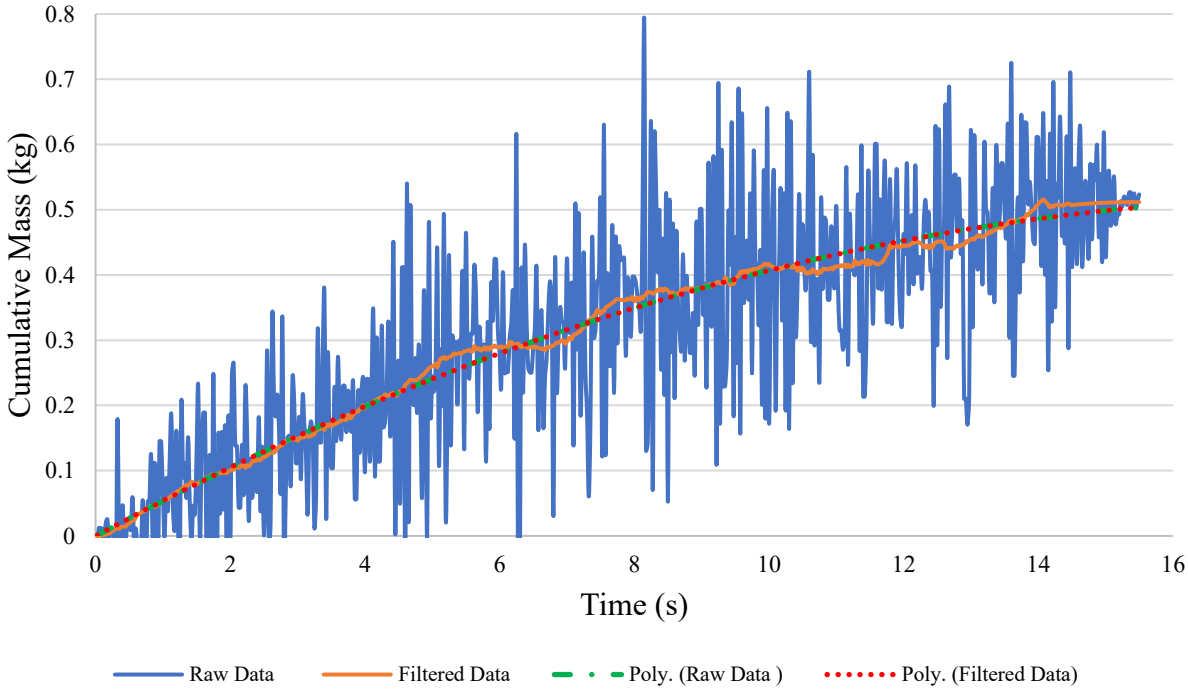

Figure B.31: Cumulative mass of Al-Cu at 1224 K with fitted polynomial to raw data and filtered data

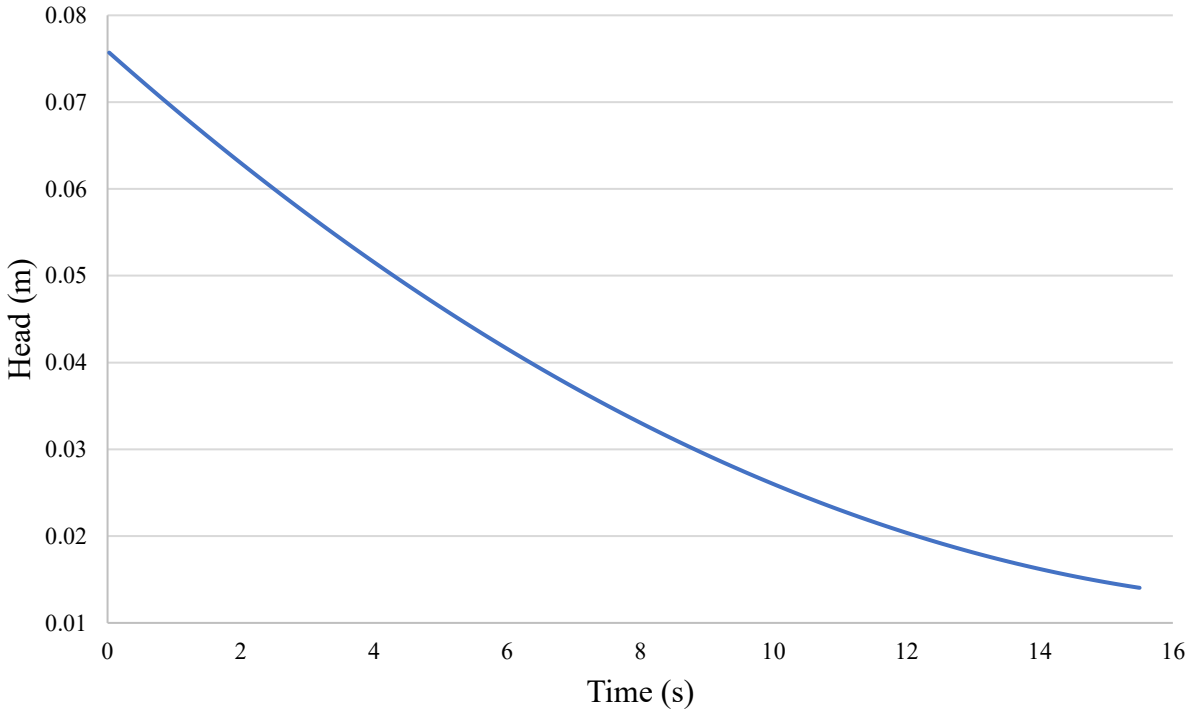

Figure B.32: Experimental head of Al-Cu at 1224 K.

APPENDIX C : CODE FOR LOW TEMPERATURE CALIBRATIONS

```
%% Import and clear:
close all
clear
clc, format compact

%% Settings and prefill:
% Imports raw load vs time data at the specified file location
raw = csvread('[]');

b_trim = []; % Number of data seconds to remove at the end of the experiment
tarewin = 5; % Seconds of lead-time/trail-time for tare
tint = 0.025; % How often (in s) the weight is measured

%Literature values
dens =  []; % kg/m3
surft =  []; % N/m
visc =  []; % Pa.s

o_diam = []; % Diameter (in mm) of the orifice
m_in = []; % Mass in (in g)

% Constants related to calibrated head (in m) vs. volume (in m^3) equation:
% h = h1*V + h2
h1 = [];
h2 = [];

% %Initial sepreparation of data:
% Seperate raw input into time and load vectors saved in the Workspace:
raw_time = raw(:,1);
raw_load = raw(:,2)./1000; % Converts immediately to kg
```

```
t = raw_time;
t = t/10; % Correct for labview counting issue
t = round(t,3); % Helps calculations since we know this as our time resolution

Cm = raw_load;

% If the load vector has a zero as its first value, the second value will
replace the first
if Cm(1) == 0
    Cm(1) = Cm(2);
end

% For communications errors, negative values may be present; this averages the
following and preceding points to fill the gaps (note: just taking the previous
is safer in case of consecutives)
gaps = find(Cm < 0 );
if isempty(gaps) == 0 % Skips step if find function returns an empty vector
    for n = 1:length(gaps)
        Cm(gaps(n)) = Cm(gaps(n)-1); % Safer code
    end
end

%% Tareing:
taresize = tarewin/tint; % Turn into number of indices from tint
tarevals = Cm(1:taresize); % Imports values for tare
tare = mean(tarevals); % Calculates a tare value
Cm = Cm(taresize:end); % Trims out tare values
t = t(taresize:end); % Trims out tare values
Cm = Cm - tare; % Tares the load data
t_tarecut = t(1); % Store tare time
t = t - t_tarecut; % Tare time
negs = find(sign(Cm) == -1); % Find negative tared values
for n = 1:length(negs)
```

```
    Cm(negs) = 0; % Sets negative values to a load of 0
end

%% Front and back data trimming:
% Looks for the beginning of the experiment and trims the data to there
% Flip data so data is clipped off the end
Cm = flip(Cm);
t = flip(t);
front_cut = find( Cm == 0 , 1); % Clips data at the first point the script sees
a weight of 0

% Reflip
Cm = flip(Cm(1:front_cut)); % Trims and flips
t = flip(t(1:front_cut)); % Trims and flips

t_frontcut = t(1); % Store amount of seconds
t = t - t_frontcut; % Set t = 0 at start

%% Additional back data selection:
Trim additional data at end of experiment to ensure that only data associated
with free flow is included
Cm = Cm(1:(b_trim*40));
t = t(1:(b_trim*40));

%% Calculate mass flow rate, dCm/dt:
Cmpoly = fit(t,Cm,'poly2'); % Generate polynomial for Cm
disp(Cmpoly) % Display it to user for coefficient information
dCmpolydt = differentiate(Cmpoly,t); % Generate dCmdt
dCmpolydt_fit = fit(t,dCmpolydt,'poly1');
disp(dCmpolydt_fit) % Display it to user for coefficient information

% Plots cumulative mass and mass flow rate versus time:
figure
hold on
```

```
title('Cumulative Mass (Cm) and Mass Flow Rate (dCm/dt) as a Function of Time')
xlabel('Time [s]')
ylabel('Cumulative Load [kg]')
plot(t,Cm,'k');
plot(t,Cmpoly(t),'y');
ylim([0 inf])
yyaxis right
plot(t,dCmpolydt,'red')
ax = gca;
ax.YColor = 'k';
ylabel('dCm/dt [kg/s]')
legend('Cm','Cmpoly(t)','dCmpolydt');
grid minor
hold off

Cm = Cmpoly(t); % Sets Cm to the polynomial values

%% Calculates head:
m_in = m_in/1000; % Converts to kg
vol_in = m_in/dens; % Calculates the initial volume in crucible

vol_poured = Cm / dens; % Calculates the the volume poured from crucible
vol_left = vol_in - vol_poured; % Calculated volume left in crucible

h = (h1*vol_left) + h2; % Calculates head from UT head vs volume equation

%Plots head versus time:
figure
hold on
title('Head as a Function of Time')
xlabel('Time [s]')
ylabel('Head [m]')
plot(t,h)
```

```
ax = gca;
ax.YColor = 'k';
grid on
hold off

hpoly = fit(t,h,'poly2'); % Generate polynomial for h
disp(hpoly) % Display it to user for coefficient information

%% Store process parameter results:
process_results(:,1) = t(:,1);
process_results(:,2) = Cm(:,1);
process_results(:,3) = dCmpolydt(:,1);
process_results(:,4) = h(:,1);

%% Calculate Cd vs. Re:
% Calculation of flow:
r = o_diam/2000; % Convert diameter to radius

Qexp = dCmpolydt./(dens); % Calculates experimnetal flow rate

Qtheo = zeros(length(Cm),1); % Initializes theoretical flow rate

for n = 1:length(Cm)
%Calculates theoretical flow rate
    Qtheo(n) = (pi*(r^2)*sqrt(2*9.81*(h(n)-(surft/(dens*9.81*r)))));
end

% Cd versus Re calculation:
Cd = zeros(length(Cm),1);
for n = 1:length(Cm)
    Cd(n) = Qexp(n)/Qtheo(n); % Calculates discharge coefficient
end
```

```
Re = zeros(length(Cm),1);
for n = 1:length(Cm)
    Re(n) = 2*dens*Qexp(n)/(pi*visc*r); % Calculates Reynolds number
end

% Plots Cd versus Re calibration curve:
figure
hold on
title('Discharge Coefficient (Cd) as a Function of the Reynolds Number (Re)')
xlabel('Re')
ylabel('Cd')
plot(Re,Cd)
ax = gca;
ax.YColor = 'k';
grid on
hold off

%% Fr(1/Bo):
Fr = zeros(length(Cm),1);
for n = 1:length(Cm)
    Fr(n) = (Qexp(n)/(Cd(n)*pi*r^2))^2/(2*9.81*h(n)); % Calculates Fr number
end

Bo = zeros(length(Cm),1);
for n = 1:length(Cm)
    Bo(n) = (dens*9.81*r*h(n))/surft; % Calculates Bo number
end

invBo = 1./Bo;

% Checks that Fr + 1/Bo = 1:
Check = round(Fr+invBo,4);
model_chk = find(Check ~= 1);
```

```
if isempty(model_chk) == 0
    disp('Not all portions of the model are correct.')
else
    disp('Fr + 1/Bo = 1 is consistent')
end

% Plots Fr and 1/Bo versus time:
figure
title('Froude (Fr) and Bond (Bo) Numbers as a Function of Time')
hold on
xlabel('Time [s]')
ylabel('Fr')
ylim([0 1])
plot(t,Fr)
yyaxis right
ylabel('1/Bo')
plot(t,invBo)
ylim([0 1])
ax = gca;
ax.YColor = 'k';
legend('Fr','1/Bo')
grid on
hold off

%% Store Cd versus Re calibration curve data:
CdRe_results(:,1) = Re(:,1);
CdRe_results(:,2) = Cd(:,1);
```

APPENDIX D : VALIDATION OF SURFACE TENSION EFFECT

This appendix outlines the validation the effect of surface tension on the prediction of flow rate. The discharge coefficient versus Reynold's number of water samples at varying temperature, i.e. with different thermophysical properties, were calculated using both the classical and modified Bernoulli's formulation, previously outlined in Section 2.4.3.1.2. It should be noted that this analysis was previously conducted in prior study, so this analysis solely acts a further proof that the formulation is indeed valid. Both the discharge coefficient and Reynold's number were calculated using the steps outlined in Section 4.1.1.2. Once again, the viscosity, surface tension, and density of water at different temperatures were taken from Yaws' Transport Properties of Chemicals and Hydrocarbons Handbook. Figure D.1 shows the discharge coefficient versus Reynolds number calculated without considering surface tension effects, and Figure D.2 shows the same calculations, but this time, including the effect of Laplace pressure at the orifice tip.

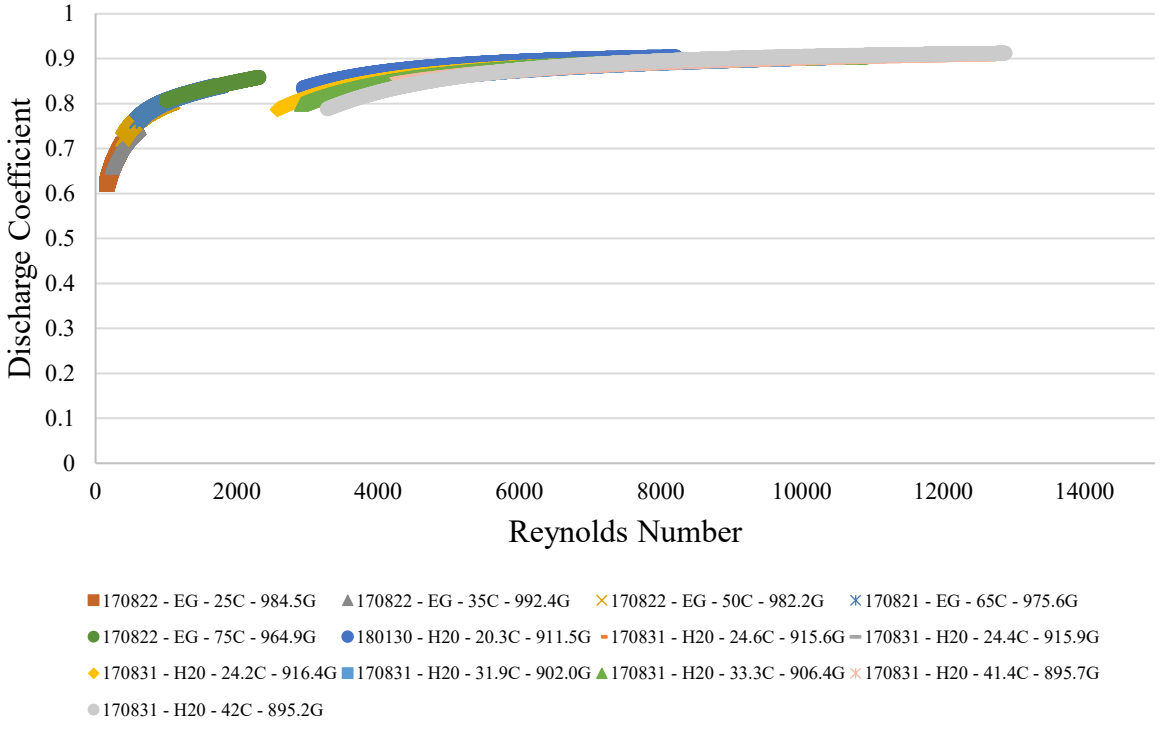

Figure D.1: C_d versus Re calculated without considering surface tension effects for a Mo crucible with a 0.005 m orifice.

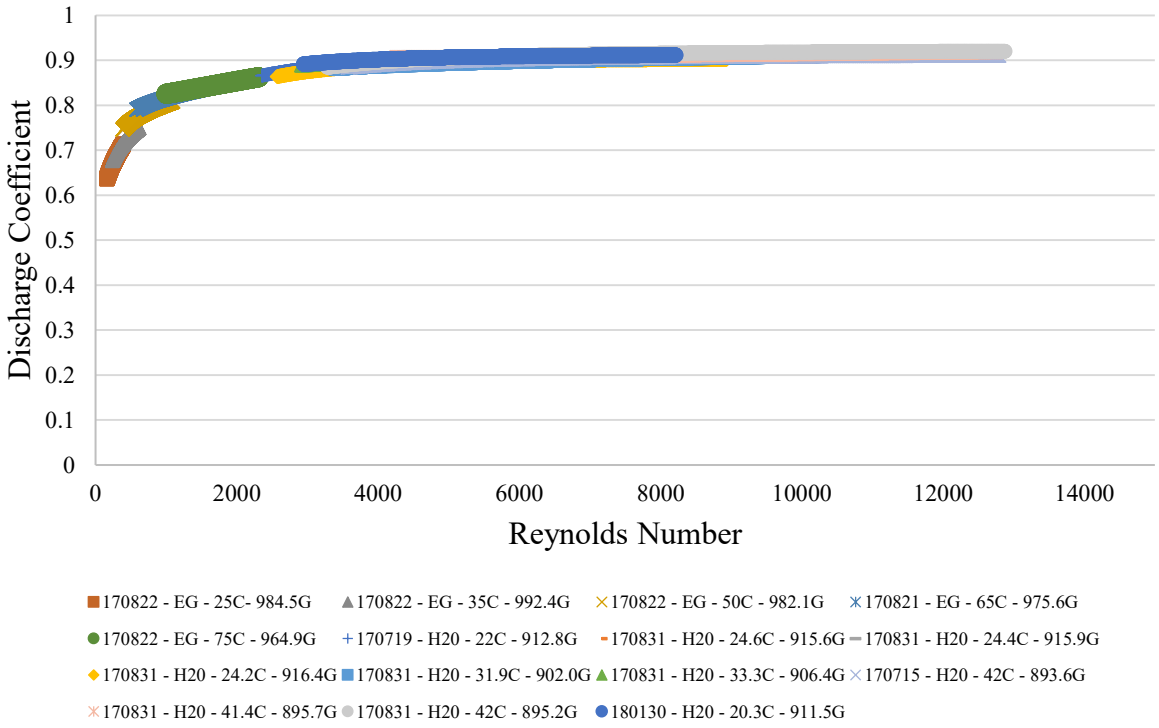

Figure D.2: Cd versus Re calculated considering surface tension effects for a Mo crucible with a 0.005 m orifice.

The trends depicted in Figure B.1 indicates that when water at different temperatures is used, varying frictional effects are observed for each calibration. Since the frictional effects are dependent on the geometry of the crucible and orifice, and the material of the crucible. Figure B.2 clearly follows, more consistently, a dependence of Reynold's number. This indicates that the effect of surface tension better describes the system, and that the frictional characteristics of the crucible does not depend on the properties of the liquid measured.

APPENDIX E : SAVITZKY-GOLAY FILTERING

The cumulative mass data was smoothed using the Savitzky-Golay (2^{nd} order polynomial) filter in the MATLAB Curve Fitting Toolbox. Savitzky-Golay filter is a generalized moving average filter, and the coefficients are derived by performing an unweighted linear least-square fit using a polynomial of the specified degree. A high degree of polynomial allows one to achieve a high level of smoothing without loss of data features. To use this smoothing method by using the Curve Fitting Toolbox:

- the span must be odd,
- the polynomial degree must be less than the span, and
- the data points are not required to have uniform spacing.

The Savitzky-Golay syntax in MATLAB is specified as:

$$y = \text{sgolayfilt}(x, \text{order}, \text{framelen}) \tag{E.1}$$

Where order is the polynomial order (or degree) and framelen is the frame length (or span), specified by a positive integer. The frame length was chosen as 95 for smoothing in this study based on analysis provided in Figure E.1, which was performed using MATLAB with the code provided below in Section E.1. Here, the sum of absolute differences (SAD) between the filtered and raw data and the slope between neighboring SAD values becomes constant at approximately 100. This implies that there is no additional value in increasing the frame length past this point since the smoothing does not further improve. If too large of a frame length is chosen, one might lose data features. On average, for all Al and Al-Cu datasets, this flat line occurred at approximately 95.

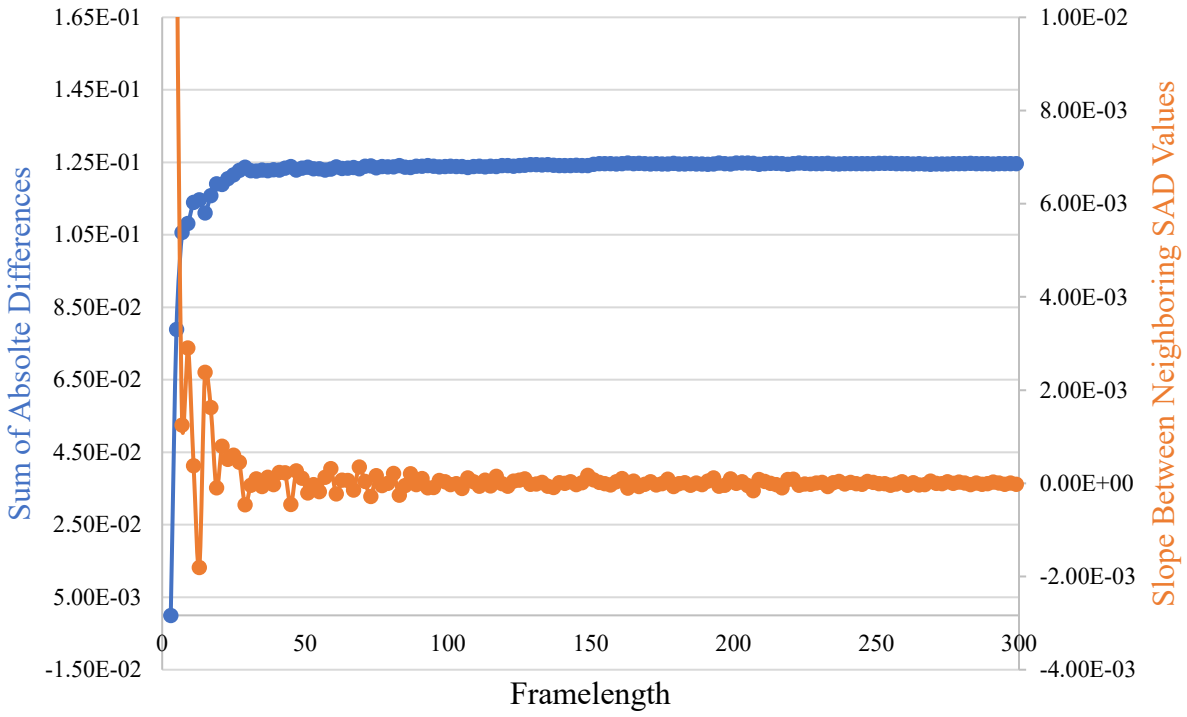

Figure E.1: Sum of Absolute Differences (and slope between neighboring SAD values) of filtered cumulative mass calculated using the Savitzky-Golay filter versus framelength

E.1 Savitzky-Golay SAD Analysis

```
close all
clear
clc, format compact

raw = csvread('[]'); %Raw load cell data; time and mass

%Constants related to calibrated head (in m) vs. volume (in m^3) equation:
%h = h1*V + h2
h1 = [];
h2 = [];

dens_lit = []; %Density of liquid at experiment temperature per literature
m_in = []; %Initial mass of charge in (in g)

%Separate raw input into time and load vectors saved in the Workspace:
t = raw(:,1)./10; %Converts to seconds
```

```
Cm = raw(:,2)./1000;%Converts kilograms

order = 2; %Define polynomial order for filtering

%% Sum of absolute differences calculation:
framelen = 3:2:301; %Sets frame length range
for k = 1:length(framelen)%Begins iterations using each frame length value

    FilteredCmPerSecond = sgolayfilt(Cm, order, framelen(k)); %Calculates
filtered cumulative mass
    Cm_filtered = FilteredCmPerSecond; %Stores filtered cumulative mass
    Cm_raw = Cm; %Defines raw cumulative mass from raw data file

    SAD(k) = (sum(abs(Cm_filtered - Cm_raw)))/length(Cm_filtered);%Calculates
sum of absolute differences between filter and raw cumulative mass
end

SAD = SAD';
framelen = framelen';

%% Stores SAD and frame length arrays:
FilterAnalysis(:,1) = SAD(:,1);
FilterAnalysis(:,2) = framelen(:,1);
```

APPENDIX F : CODE FOR HIGH-TEMPERATURE EXPERIMENTS

```
%% Import and clear:
close all
clear
clc, format compact

%% Settings and prefill:
%Import raw load vs time data at the specified file location
raw = csvread('[]');

m_in =[]; % Initial mass in crucible in g
r = 0.00265; % Radius of orifice in m
g = 9.81; % Gravitational constant in m^2/s
T_exp = []; % Temperature at which liquid was drained in K

% Thermophysical property values as published in literature
surft_lit = [];
visc_lit = [];
dens_lit = [];

framelen = []; % Size of filter window for Savitzky-Golay filter; specified as
positive odd integer
order = []; % Polynomial order for Savitzky-Golay filter; specified as a
positive integer order must be smaller than framelen. If order = framelen - 1,
the filter produces no smoothing
dataselec = 22; %Number of seconds selected to be used in Gauss-Newton
regression; must be in fraction of 0.025.

% Constants related to calibrated head (in m) vs. volume (in m^3) equation:
% h = h1*V + h2
h1 = [];
h2 = [];
```

```
%Constants related to averaged calibrated Cd vs. Re curve:
% Cd=c1*Re^3+c2%Re^2+c3*Re+c4
cd1 = [];
cd2 = [];
cd3 = [];
cd4 = [];

%% Input initial physical property guesses:
% Min and max can be specified (optional)
% Initial guess for surface tension in N/m:
surft_guess = [];
surft_min = -Inf;
surft_max = Inf;
% Initial guess for viscosity in Pa*s:
visc_guess = [];
visc_min = -Inf;
visc_max = Inf;
% Initial guess for density in kg/m^3:
dens_guess = [];
dens_min = -Inf;
dens_max = Inf;

%% Gauss Newton method prefill:
% Tolerance that Gauss-Newton regression calculation must reach for convergence
criterion:
surft_tol = 1e-10; % Tolerance for convergence of surface tension
visc_tol = 1e-10; % Tolerance for convergence of viscosity
dens_tol = 1e-10; % Tolerance for convergence of density
ntol = 1; % Condition where all three properties converge within tolerance limit
iter_max = 5000; % Set the maximum number of iterations allowed
iter_min = 0; % Set the minimum number of iterations allowed

%% Initial separation of data:
% Separate raw input into time and load vectors saved in the Workspace
```

```
t = raw(:,1)./10; %Converts immediately to s
Cm = raw(:,2)./1000; %Converts immediately to kg


%% Filter raw data:
Cm_filter = sgolayfilt(Cm_raw, order, framelen); % Applie Savitzky-Golay finite impulse response (FIR)smoothing filter of polynomial order "order" and frame length "framelen" to the data in vector "Cm_raw"

%% Trim data points at the beginning of the dataset so Cm(t = 0s)~ 0kg
tr_tol = 1; % Convergence check loop
inter_tol = 0.001; % Convergence tolerance for selection of trim range
iteration = 0; % Initialize iteration count
trim = zeros(1000,1); % Initialize trim vector

while tr_tol == 1

    iteration = iteration + 1;
    trim(1) = 10;

    t_test = t(1:(end - (trim(iteration)))); % Trim time for n iteration
    Cm_test = Cm_filter(1+trim(iteration):end); % Trim Cm for n iteration

    Cmpoly = fit(t_test,Cm_test,'poly2'); % Generate polynomial for Cm
    coeff = coeffvalues(Cmpoly); % Store polynomial coefficients


%Check if intercept coeff(3) is within specified tolerances

    tr_sum = 0;

    if coeff(3) > 0 && coeff(3) < inter_tol
        tr_sum = 1;
    end

    if tr_sum == 1
        tr_tol = 0;
    end
     trim(iteration+1) = trim(iteration) + 1;
```

```
end

trimtime = trim(iteration); % Specify number of seconds to be trimmed based
on iteration analysis

t = t(1:(end - (trimtime))); % Trim time
Cm_filter = Cm_filter(1+trimtime:end); % Trim filtered Cm
Cm_raw = Cm_raw(1+trimtime:end); % Trim raw Cm


%% Calculate mass flow rate, dCm/dt:
Cmpoly = fit(t,Cm_filter,'poly2'); % Generate polynomial for Cm
dCmpolydt = differentiate(Cmpoly,t); % Generate dCm/dt
Cm = Cmpoly(t); % Set Cm to the polynomial values
figure
hold on
title('Cumulative Mass')
xlabel('Time [s]')
ylabel('Cumulative Mass [kg]')
plot(t,Cm_filter,t,Cm)
plot(t,Cmpoly(t))
hold off


%% Calculate head height:
m_in = m_in/1000; % Convert mass to kg
vol_in = m_in/dens_lit; % Calculate the initial volume
vol_poured = Cm / dens_lit; % Calculate the volume poured using curve fitted
data
vol_poured_filter = Cm_filter / dens_lit; % Calculate the volume poured using
only filtered data
vol_left = vol_in - vol_poured; % Calculate volume left in vessel
vol_leftraw = vol_in - vol_pouredraw; % Calculate volume left in vessel using
only filtered data
h = (h1*vol_left) + h2; % Calculate head from UT calibration linear equation
h_filter = (h1*vol_leftraw) + h2; % Calculate head from UT calibration linear
equation using only filtered data
```

```
%% Additional back data trimming:
% Trim additional data at end of experiment to ensure that only data associated
with free flow is included
t = t(1:(dataselec*40));
Cm = Cm(1:(dataselec*40));
dCmpolydt = dCmpolydt(1:(dataselec*40));
h = h(1:(dataselec*40));
h_filter = h_filter(1:(dataselec*40));
h_raw = h_raw(1:(dataselec*40));


%% Initiate iterations:
iter = 0; % Set the iteration counter
n = length(dCmpolydt); % Determine the size of problem

%% Matrices and vectors of appropriate size are created:
Vexp = zeros(n,1); % Mass flux
hcalc = zeros(n,1); % Theoretical head
Z = zeros(n,3); % Partial derivatives matrix
Y = zeros(n,1); % Experimental head minus theoretical head residuals
surft = zeros(iter_max,1); % Surface tension matrix
visc = zeros (iter_max,1); % Viscosity matrix
dens = zeros(iter_max,1); % Density matrix
MSE_Y = zeros(iter_max,1); % Mean square error of residuals

%% Calculate mass flux from the mass flow rate data:
for i=1:n
    Vexp(i)= dCmpolydt(i)/(pi*(r)^2);
end

%% Solution to Gauss-Newton regression:
while ntol==1 % Convergence check loop
    % Set initial iteration values as initial guesses
```

```
surft(1) = surft_guess;

visc(1) = visc_guess;

dens(1) = dens_guess;

% Set up matrices to be solved:

% Set up calculated head equation

for i = 1:n

  hcalc(i,1)=
  1/(2*g)*((Vexp(i)/(dens(iter)*((cd1*((2*r*Vexp(i))/visc(iter))^3)      +
  (cd2*((2*r*Vexp(i))/visc(iter))^2) + (cd3*((2*r*Vexp(i))/visc(iter)))  +
  cd4)))^2) + (surft(iter)/(dens(iter)*g*r));

end

% Set up residuals' matrix:

for i = 1:n

    Y(i) = h(i)-hcalc(i);

end

MSE_Y(iter)= (sum(Y(:).^2))/n; % Calculate mean square error

% Set up partial derivatives matrix:

for i = 1:n

    Z(i,1) = 1/(dens(iter)*g*r); %surface tension differential


    Z(i,2)=        (Vexp(i)^2*((8*cd2*r^2*Vexp(i)^2)/visc(iter)^3        +
        (24*cd1*r^3*Vexp(i)^3)/visc(iter)^4                              +
    (2*cd3*r*Vexp(i))/visc(iter)^2))/(dens(iter)^2*g*(cd4                +
    (4*cd2*r^2*Vexp(i)^2)/visc(iter)^2                                   +
    (8*cd1*r^3*Vexp(i)^3)/visc(iter)^3 + (2*cd3*r*Vexp(i))/visc(iter))^3);
    %viscosity differential


    Z(i,3)=               -Vexp(i)^2/(dens(iter)^3*g*(cd4                +
    (4*cd2*r^2*Vexp(i)^2)/visc(iter)^2                                   +
    (8*cd1*r^3*Vexp(i)^3)/visc(iter)^3  +  (2*cd3*r*Vexp(i))/visc(iter))^2)
    - surft(iter)/(dens(iter)^2*g*r); %density differential

end

    %Gauss-Newton algorithm:

    x = ((Z')*Z)\((Z')*Y);

%Maximum number of iterations allowed:

if iter > iter_max

       disp('Script timed out.')

    return
```

```
end

%Update values for surface tension, viscosity and density:
%Surface tension
surft(iter+1) = surft(iter)+(x(1,1));
if surft(iter+1) < surft_min
    surft(iter+1) = surft_min;
elseif surft(iter+1) > surft_max
    surft(iter+1) = surft_max;
end
%Viscosity
visc(iter+1) = visc(iter)+(x(2,1));
 if visc(iter+1) < visc_min
    visc(iter+1) = visc_min;
elseif visc(iter+1) > visc_max
    visc(iter+1) = visc_max;
 end
 %Density
 dens(iter+1) = dens(iter)+(x(3,1));
 if dens(iter+1) < dens_min
    dens(iter+1) = dens_min;
elseif dens(iter+1) > dens_max
    dens(iter+1) = dens_max;
 end

%Tolerance check:
nsum = 0;

if abs((surft(iter) - surft(iter+1))/surft(iter)) < surft_tol
    nsum = nsum + 1;
end

if abs((visc(iter) - visc(iter+1))/visc(iter)) < visc_tol
```

```
        nsum = nsum + 1;
    end

    if abs((dens(iter) - dens(iter+1))/dens(iter)) < dens_tol
        nsum = nsum + 1;
    end

    if nsum ==3 %if all variables meet convergence then:
        if iter < iter_min
            continue
        else
            ntol = 0;
        end
    end
end

%% Final properties solved using Gauss-Newton method:
SurfaceTension = surft(iter+1);
Viscosity = visc(iter+1);
Density = dens(iter+1);

%% Calculation of measurement error:
h_poly = fit(t,h_filter,'poly2'); % Generate polynomial for h
h_poly = h_poly(t);

stdev_head = sqrt((sum((h_poly-h_filter).^2))/(length(h_filter)-3));

surft_h = zeros(length(h_filter),1);
for n = 1:length(h_filter)
    surft_h(n) = (Density*9.81*r)*(h_filter(n)-
((1/(2*9.81))*((Qexp(n)/(Cd_reg(n)*pi*(r^2)))^2)));
end
surft_error = std(surft_h); % Calculate surface tension error

dens_h = zeros(length(h_filter),1);
```

```
for n = 1:length(h_filter)
    dens_h(n) = SurfaceTension/((9.81*r)*(h_filter(n)-
((1/(2*9.81))*((Qexp(n)/(Cd_reg(n)*pi*(r^2)))^2))));
end
dens_error = std(dens_h); % Calculate density error

visc_h = zeros(length(h_filter),1);
for n = 1:length(h_filter)
    visc_h(n) =
(2*cd3*Density*r*Qexp(n))/((Qexp(n)/(sqrt(2*9.81*(h_filter(n)-
(SurfaceTension/(Density*9.81*r))))))-(pi*(r^2)*cd4));
end
visc_error = std(visc_h); % Calculate viscosity error

%% Difference between measured values and values published in literature:
surft_literror = 100*abs(surft(iter+1)-surft_theo)/surft_theo;
visc_literror = 100*abs(visc(iter+1)-visc_theo)/visc_theo;
dens_literror = 100*abs(dens(iter+1)-dens_theo)/dens_theo;
average_literror = (surft_literror+visc_literror+dens_literror)/3;

%% Output results:
message1 = ['Final value for surface tension is ', num2str(SurfaceTension), '
N/m.' newline 'Associated error for surface tension is ',
num2str(surft_error), ' N/m' newline];
    disp(message1)
message2 = ['Final value for viscosity is ', num2str(Viscosity), ' Pa*s'
newline 'Associated error for viscosity is ', num2str(visc_error), ' Pa*s'
newline];
    disp(message2)
message3 = ['Final value for density is ', num2str(Density), ' kg/m^3'
newline 'Associated error for density is ', num2str(dens_error), ' kg/m^3'
newline];
    disp(message3)

message4 = ['The standard deviation for head measurements is ',
num2str(stdev_head,'%10.5e'),' m' newline];
disp(message4)
```

```
message5 = ['The percent difference for surface tension compared to
literature is ', num2str(surft_literror), '%'];
disp(message5)

message6 = ['The percent difference for viscosity compared to literature is
', num2str(visc_literror), '%'];
disp(message6)

message7 = ['The percent difference for density compared to literature is ',
num2str(dens_literror), '%'];
disp(message7)

message8 = ['The average percent difference for all three properties compared
to literature is ', num2str(average_literror), '%'];
disp(message8)
```

APPENDIX G : VARYING TEMPERATURE MODEL

One main assumption made when conducting a DC measurement is that the decrease of temperature as the liquid drains from the crucible is negligible, and thus, the viscosity, surface tension and density of the liquid remain constant as the crucible empties. This is true when measuring liquids at relatively low temperatures, such as the temperatures reported in this study; however, at temperatures exceed 1800 K this is not the case. For high-melting point metals and alloys, like Fe and steel this becomes an issue. In an experimental trial where the DC apparatus was heated to 2000 K, once the induction furnace was turned off, the cooling rate was found to equal -100 K/min. Recall that the induction furnace must be shut off before the stopper is removed to reduce electromagnetic stirring. Typically, it takes 30 seconds for a 600 g charge to completely drain from the crucible; and if heated to 2000 K, the temperature would decrease by roughly 50 K by the time the crucible completely emptied. For the case of pure Fe, a 50 K decrease in temperature, from 2000 to 1950 K, marks an 8% change in viscosity [6].

To account for this issue, a new model was developed to account for possible temperature changes. Rather than defining the thermophysical properties as constants, the viscosity, surface tension and density are defined as a function of temperature:

$$\eta(T) = \eta_A T^2 + \eta_B T + \eta_C \tag{G.1}$$

$$\sigma(T) = \sigma_A T + \sigma_B \tag{G.2}$$

$$\mu(T) = \rho_A T + \rho_B \tag{G.3}$$

Now, similar to described in Section 2.4.3.2, the residuals, $r_i(\beta)$, are given as:

$$r_i(\beta) = h_{i,exp} - f\left(V_{i,exp}, \beta\right) \tag{G.4}$$

And, the unknowns, β, in the formulation consist of:

$$\beta = \begin{bmatrix} \eta_A \\ \eta_B \\ \eta_C \\ \sigma_A \\ \sigma_C \\ \rho_A \\ \rho_B \end{bmatrix} \tag{G.5}$$

The modified Bernoulli equation must now be written as:

$$f(V_{i,exp}, \beta) = \frac{1}{2g} \cdot \left(\frac{V_{i,exp}}{\left(a\left(\frac{2r_o V_{i,exp}}{\left(\eta_A {T_{i,exp}}^2 + \eta_B T_{i,exp} + \eta_C\right)} \right)^3 + b\left(\frac{2r_o V_{i,exp}}{\left(\eta_A {T_{i,exp}}^2 + \eta_B T_{i,exp} + \eta_C\right)} \right)^2 + c\left(\frac{2r_o V_{i,exp}}{\left(\eta_A {T_{i,exp}}^2 + \eta_B T_{i,exp} + \eta_C\right)} \right) + d \right) (\rho_A T_{i,exp} + \rho_B)} \right)^2 + \frac{\sigma_A T_{i,exp} + \sigma_B}{(\rho_A T_{i,exp} + \rho_B) g r_o} \tag{G.6}$$

Where h_{exp} (m) is experimental head, Q_{exp} (m^3/s) is experimental volumetric flow rate, and T_{exp} (K) is the experimental temperature, which is measured using a pyrometer or thermocouple:

$$h_{exp} = \begin{bmatrix} h_{1,exp} \\ \cdot \\ \cdot \\ h_{i,exp} \\ h_{m,exp} \end{bmatrix} \tag{G.7}$$

$$Q_{exp} = \begin{bmatrix} Q_{1,exp} \\ \cdot \\ \cdot \\ Q_{i,exp} \\ Q_{m,exp} \end{bmatrix} \tag{G.8}$$

$$T_{exp} = \begin{bmatrix} T_{1,exp} \\ \cdot \\ \cdot \\ T_{i,exp} \\ T_{m,exp} \end{bmatrix} \tag{G.9}$$

The Gauss-Newton algorithm is given below:

$$\Delta\boldsymbol{\beta}_{\boldsymbol{j}} = \left(\boldsymbol{J_{i,j}}^{T}\boldsymbol{J}_{\boldsymbol{i,j}}\right)^{-1}\boldsymbol{J_{i,j}}^{T}\Delta\boldsymbol{y_i} \tag{G.10}$$

Where now,

$$\Delta\boldsymbol{\beta}_{\boldsymbol{j}} = \begin{bmatrix} \eta_A{}^{(s+1)} - \eta_A{}^{(s)} \\ \eta_B{}^{(s+1)} - \eta_B{}^{(s)} \\ \eta_C{}^{(s+1)} - \eta_C{}^{(s)} \\ \sigma_A{}^{(s+1)} - \sigma_A{}^{(s)} \\ \sigma_B{}^{(s+1)} - \sigma_A{}^{(s)} \\ \rho_A{}^{(s+1)} - \rho_A{}^{(s)} \\ \rho_B{}^{(s+1)} - \rho_B{}^{(s)} \end{bmatrix} \tag{G.11}$$

$$\boldsymbol{J}_{\boldsymbol{i,j}} = \begin{Bmatrix} \frac{\partial f(V_{1,exp})}{\partial \eta_A} & \frac{\partial f(V_{1,exp})}{\partial \eta_B} & \frac{\partial f(V_{1,exp})}{\partial \eta_C} & \frac{\partial f(V_{1,exp})}{\partial \sigma_A} & \frac{\partial f(V_{1,exp})}{\partial \sigma_B} & \frac{\partial f(V_{1,exp})}{\partial \rho_A} & \frac{\partial f(V_{1,exp})}{\partial \rho_B} \\ \vdots & \vdots & \vdots & \vdots & \vdots & \vdots & \vdots \\ \frac{\partial f(V_{i,exp})}{\partial \eta_A} & \frac{\partial f(V_{i,exp})}{\partial \eta_B} & \frac{\partial f(V_{i,exp})}{\partial \eta_C} & \frac{\partial f(V_{i,exp})}{\partial \sigma_A} & \frac{\partial f(V_{i,exp})}{\partial \sigma_B} & \frac{\partial f(V_{i,exp})}{\partial \rho_A} & \frac{\partial f(V_{1,exp})}{\partial \rho_B} \\ \frac{\partial f(V_{m,exp})}{\partial \eta_A} & \frac{\partial f(V_{m,exp})}{\partial \eta_B} & \frac{\partial f(V_{m,exp})}{\partial \eta_C} & \frac{\partial f(V_{m,exp})}{\partial \sigma_A} & \frac{\partial f(V_{m,exp})}{\partial \sigma_B} & \frac{\partial f(V_{m,exp})}{\partial \rho_A} & \frac{\partial f(V_{1,exp})}{\partial \rho_B} \end{Bmatrix}_s \tag{G.12}$$

$$\Delta\boldsymbol{y}_{\boldsymbol{i}} = \begin{bmatrix} h_{1,exp} - f\left(V_{1,exp}, \beta^s\right) \\ \vdots \\ h_{i,exp} - f\left(V_{i,exp}, \beta^s\right) \\ h_{i,exp} - f\left(V_{i,exp}, \beta^s\right) \end{bmatrix} \tag{G.13}$$

The derivatives of $\partial f\left(V_{1,exp}\right)$ as a function of η_A, η_B, η_C, σ_A, σ_B, ρ_A and ρ_B were calculated, and provided below:

$$\frac{\partial f(V_{i,exp})}{\partial \eta_A} = \frac{V_{i,exp}{}^2\left(\frac{8br_o^2T_{i,exp}^2V_{i,exp}^2}{(\eta_AT_{i,exp}^2+\eta_BT_{i,exp}+\eta_C)^3}+\frac{24ar_o^3T_{i,exp}^2V_{i,exp}^3}{(\eta_AT_{i,exp}^2+\eta_BT_{i,exp}+\eta_C)^4}+\frac{2cr_oT_{i,exp}^2V_{i,exp}}{(\eta_AT_{i,exp}^2+\eta_BT_{i,exp}+\eta_C)^2}\right)}{g\left(\rho_AT_{i,exp}+\rho_B\right)^2\left(d+\frac{4br_o^2V_{i,exp}^2}{(\eta_AT_{i,exp}^2+\eta_BT_{i,exp}+\eta_C)^2}+\frac{8ar_o^3V_{i,exp}^3}{(\eta_AT_{i,exp}^2+\eta_BT_{i,exp}+\eta_C)^3}+\frac{2cr_oV_{i,exp}}{(\eta_AT_{i,exp}^2+\eta_BT_{i,exp}+\eta_C)}\right)^3} \tag{G.14}$$

$$\frac{\partial f(V_{i,exp})}{\partial \eta_B} = \frac{{V_{i,exp}}^2\left(\frac{8br_o^2T_{i,exp}V_{i,exp}^2}{(\eta_A T_{i,exp}^2+\eta_B T_{i,exp}+\eta_C)^3}+\frac{24ar_o^3T_{i,exp}V_{i,exp}^3}{(\eta_A T_{i,exp}^2+\eta_B T_{i,exp}+\eta_C)^4}+\frac{2cr_oT_{i,exp}V_{i,exp}}{(\eta_A T_{i,exp}^2+\eta_B T_{i,exp}+\eta_C)^2}\right)}{g\left(\rho_A T_{i,exp}+\rho_B\right)^2\left(d+\frac{4br_o^2V_{i,exp}^2}{(\eta_A T_{i,exp}^2+\eta_B T_{i,exp}+\eta_C)^2}+\frac{8ar_o^3V_{i,exp}^3}{(\eta_A T_{i,exp}^2+\eta_B T_{i,exp}+\eta_C)^3}+\frac{2cr_oV_{i,exp}}{(\eta_A T_{i,exp}^2+\eta_B T_{i,exp}+\eta_C)}\right)^3} \quad \text{(G.15)}$$

$$\frac{\partial f(V_{i,exp})}{\partial \eta_C} = \frac{{V_{i,exp}}^2\left(\frac{8br_o^2V_{i,exp}^2}{(\eta_A T_{i,exp}^2+\eta_B T_{i,exp}+\eta_C)^3}+\frac{24ar_o^3V_{i,exp}^3}{(\eta_A T_{i,exp}^2+\eta_B T_{i,exp}+\eta_C)^4}+\frac{2cr_oV_{i,exp}}{(\eta_A T_{i,exp}^2+\eta_B T_{i,exp}+\eta_C)^2}\right)}{g\left(\rho_A T_{i,exp}+\rho_B\right)^2\left(d+\frac{4br_o^2V_{i,exp}^2}{(\eta_A T_{i,exp}^2+\eta_B T_{i,exp}+\eta_C)^2}+\frac{8ar_o^3V_{i,exp}^3}{(\eta_A T_{i,exp}^2+\eta_B T_{i,exp}+\eta_C)^3}+\frac{2cr_oV_{i,exp}}{(\eta_A T_{i,exp}^2+\eta_B T_{i,exp}+\eta_C)}\right)^3} \quad \text{(G.16)}$$

$$\frac{\partial f(V_{i,exp})}{\partial \sigma_A} = \frac{T_{i,exp}}{gr_o\left(\rho_A T_{i,exp}+\rho_B\right)} \quad \text{(G.17)}$$

$$\frac{\partial f(V_{i,exp})}{\partial \sigma_B} = \frac{1}{gr_o\left(\rho_A T_{i,exp}+\rho_B\right)} \quad \text{(G.18)}$$

$$\frac{\partial f(V_{i,exp})}{\partial \rho_A} = \frac{-T_{i,exp}V_{i,exp}^2}{g\left(\rho_A T_{i,exp}+\rho_B\right)^3\left(d+\frac{4br_o^2V_{i,exp}^2}{(\eta_A T_{i,exp}^2+\eta_B T_{i,exp}+\eta_C)^2}+\frac{8ar_o^3V_{i,exp}^3}{(\eta_A T_{i,exp}^2+\eta_B T_{i,exp}+\eta_C)^3}+\frac{2cr_oV_{i,exp}}{(\eta_A T_{i,exp}^2+\eta_B T_{i,exp}+\eta_C)}\right)^2} - \frac{T_{i,exp}\left(\sigma_A T_{i,exp}+\sigma_B\right)}{gr_0\left(\rho_A T_{i,exp}+\rho_B\right)^2} \quad \text{(G.19)}$$

$$\frac{\partial f(V_{i,exp})}{\partial \rho_B} = \frac{-V_{i,exp}^2}{g\left(\rho_A T_{i,exp}+\rho_B\right)^3\left(d+\frac{4br_o^2V_{i,exp}^2}{(\eta_A T_{i,exp}^2+\eta_B T_{i,exp}+\eta_C)^2}+\frac{8ar_o^3V_{i,exp}^3}{(\eta_A T_{i,exp}^2+\eta_B T_{i,exp}+\eta_C)^3}+\frac{2cr_oV_{i,exp}}{(\eta_A T_{i,exp}^2+\eta_B T_{i,exp}+\eta_C)}\right)^2} - \frac{\left(\sigma_A T_{i,exp}+\sigma_B\right)}{gr_0\left(\rho_A T_{i,exp}+\rho_B\right)^2} \quad \text{(G.20)}$$

Using the Jacobian matrix, the updated values can be calculated after each iteration:

$$\eta_A{}^{(s+1)} = \eta_A{}^{(s)} + \Delta\beta_1 \quad \text{(G.21)}$$

$$\eta_B{}^{(s+1)} = \eta_B{}^{(s)} + \Delta\beta_2 \quad \text{(G.22)}$$

$$\eta_C{}^{(s+1)} = \eta_C{}^{(s)} + \Delta\beta_3 \tag{G.23}$$

$$\sigma_A{}^{(s+1)} = \sigma_A{}^{(s)} + \Delta\beta_4 \tag{G.24}$$

$$\sigma_B{}^{(s+1)} = \sigma_B{}^{(s)} + \Delta\beta_5 \tag{G.25}$$

$$\rho_A{}^{(s+1)} = \rho_A{}^{(s)} + \Delta\beta_6 \tag{G.26}$$

$$\rho_B{}^{(s+1)} = \rho_B{}^{(s)} + \Delta\beta_7 \tag{G.27}$$

The iterations continue until the following quantities are less than the specified tolerance, ε:

$$\varepsilon_{\eta_A} = \frac{\eta_A{}^{(s+1)} - \eta_A{}^{(s)}}{\eta_A{}^{(s+1)}} \tag{G.28}$$

$$\varepsilon_{\eta_B} = \frac{\eta_B{}^{(s+1)} - \eta_B{}^{(s)}}{\eta_B{}^{(s+1)}} \tag{G.29}$$

$$\varepsilon_{\eta_C} = \frac{\eta_C{}^{(s+1)} - \eta_C{}^{(s)}}{\eta_C{}^{(s+1)}} \tag{G.30}$$

$$\varepsilon_{\sigma_A} = \frac{\sigma_A{}^{(s+1)} - \sigma_A{}^{(s)}}{\sigma_A{}^{(s+1)}} \tag{G.31}$$

$$\varepsilon_{\sigma_B} = \frac{\sigma_B{}^{(s+1)} - \sigma_B{}^{(s)}}{\sigma_B{}^{(s+1)}} \tag{G.32}$$

$$\varepsilon_{\rho_A} = \frac{\rho_A{}^{(s+1)} - \rho_A{}^{(s)}}{\rho_A{}^{(s+1)}} \tag{G.33}$$

$$\varepsilon_{\rho_B} = \frac{\rho_B{}^{(s+1)} - \rho_B{}^{(s)}}{\rho_B{}^{(s+1)}} \tag{G.34}$$

This model was tested on 613 g of Al-22.5Cu at 1076 K, which had a temperature decrease of approximately 10 K, measured using a thermocouple. The Gauss-Newton regression was performed using MATLAB, and the code specific to the varying temperature model is provided in Appendix H. The results for viscosity, surface tension and density as a function of temperature are given in Figures G.1, G.2 and G.3, respectively.

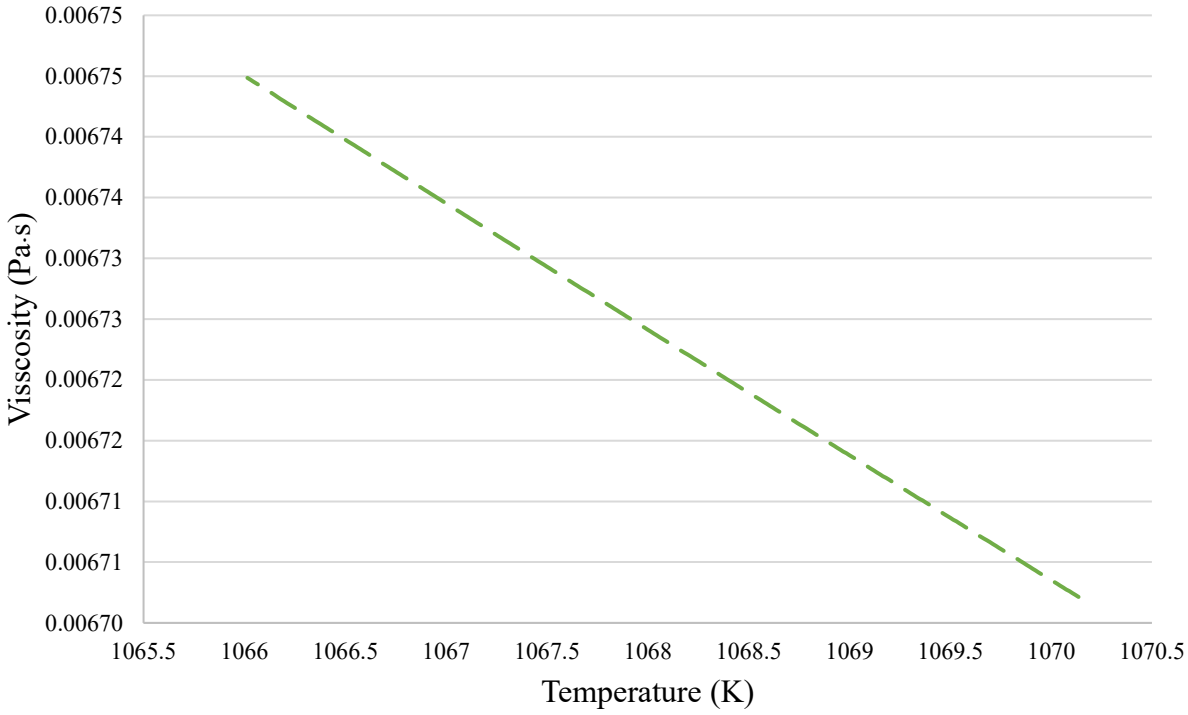

Figure G.1: Viscosity of Al-Cu determined using a varying temperature regression model

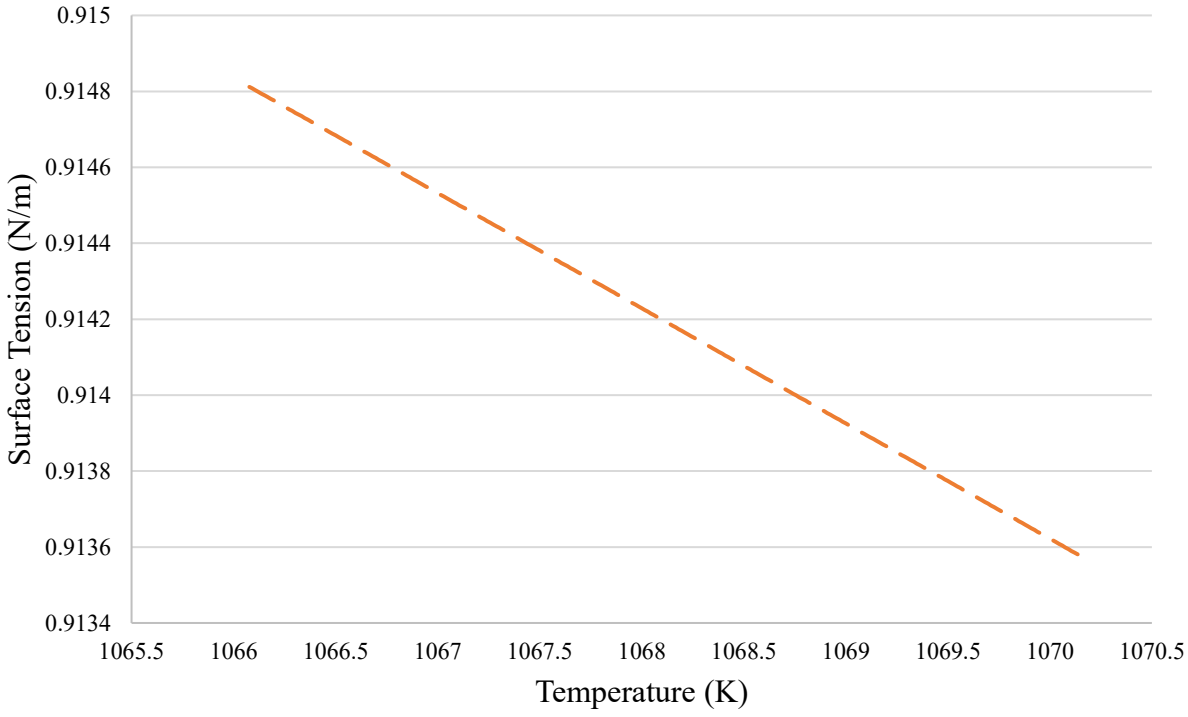

Figure G.2: Surface tension of Al-Cu determined using a varying temperature regression model

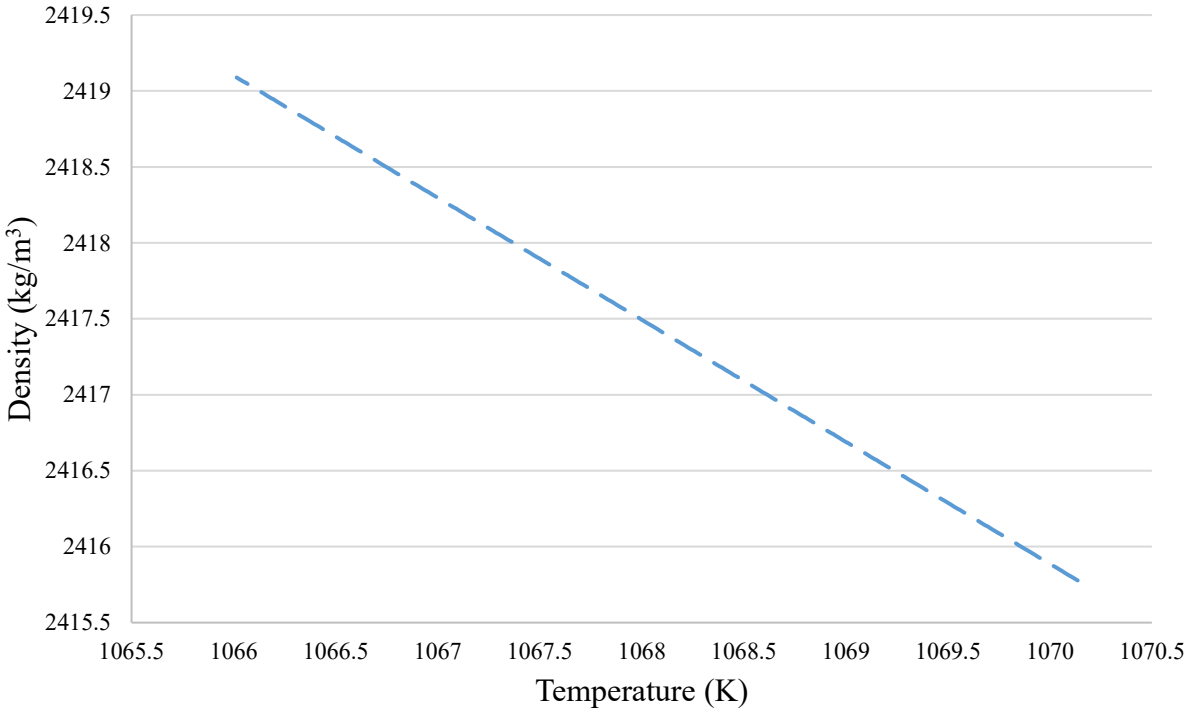

Figure G.3: Density of Al-Cu determined using a varying temperature regression model

All three properties have a negative temperature dependence slope, and both the surface tension and density agree well with values obtained from literature. The viscosity, however, is overestimated. It would be interesting to apply this model to experiments conducted at higher temperatures since the temperature range would be much larger, and there would be a significant discrepancy in properties at the beginning and end of the experiment. Overall, at a first glance, the varying temperature model appears to work, however, additional testing is required, especially with DC experiments conducted as high temperatures.

APPENDIX H : CODE FOR VARYING TEMPERATURE MODEL

```
%% Import and clear

close all
clear
clc, format compact


%% Settings and prefill:
% Import raw load vs time and temperature data at the specified file location

raw = csvread('[]');
temp = csvread('[]');

%% Settings and prefill

m_in =[]; % Initial mass in crucible (in g)
r = 0.00265; % Radius of orifice (in m)
g = 9.81; % Gravitational constant (in m^2/s)
T_exp = []; % Temperature at which liquid was drained in K

% Thermophysical property values as published in literature
dens_lit = [];

framelen = []; % Size of filter window for Savitzky-Golay filter; specified as
positive odd integer
order = []; % Polynomial order for Savitzky-Golay filter; specified as a
positive integer order must be smaller than framelen. If order = framelen - 1,
the filter produces no smoothing
dataselec = []; % Number of seconds selected to be used in Gauss-Newton
regression; must be in fraction of 0.025.


% Constants related to calibrated head (in m) vs. volume (in m^3) equation:
%h = h1*V + h2
h1 = [];
h2 = [];
```

```
% Constants related to averaged calibrated Cd vs. Re curve:
%Cd=c1*Re^3+c2%Re^2+c3*Re+c4
cd1 = [];
cd2 = [];
cd3 = [];
cd4 = [];

%% Input initial physical property guesses:
% Initial guess for surface tension parameters; surft = surftA + surftB*T:
surftA = 1;
surftA_min = -Inf;
surftA_max = Inf;
surftB = -0.0001;
surftB_min = -Inf;
surftB_max = Inf;
% Initial guess for viscosity parameters; visc = viscA*T^2 + viscB*T + viscC:
viscA = 1E-09;
viscA_min = -Inf;
viscA_max = Inf;
viscB = -1E-06;
viscB_min = -Inf;
viscB_max = Inf;
viscC = 0.001;
viscC_min = -Inf;
viscC_max = Inf;
% Initial guess for density parameters; dens = densA + densB*T:
densA = 2000;
densA_min = -Inf;
densA_max = Inf;
densB = -0.1;
densB_min = -Inf;
densB_max = Inf;
```

```
%% Gauss Newton method prefill:

% Tolerance that Gauss-Newton regression calculation must reach for convergence
criterion:
tol = 1e-6; % Tolerance for convergence

ntol = 1; % Condition where variables converge within tolerance limit

iter_max = 5000; % Set the maximum number of iterations allowed

iter_min = 0; % Set the minimum number of iterations allowed

lambda = 1; % Damping gain - start with 1

k1 = 0.01; % Damping parameter - has to be less than 1; changing this will

affect rate of covergence

Y_old = 100000; % Better to leave this number big


%% Initial separation of data:

% Separate raw input vectors saved in the Workspace

t = raw(:,1)./10;

Cm_raw = raw(:,2)./1000; % CONVERTS IMMEDIATELY TO KG

T = temp(:,2);


%% Filter raw data:

Cm_filter = sgolayfilt(Cm_raw, order, framelen); % Applie Savitzky-Golay finite
impulse response (FIR)smoothing filter of polynomial order "order" and frame
length "framelen" to the data in vector "Cm_raw"

%% Trim data points at the beginning of the dataset so Cm(t = 0s)~ 0kg

tr_tol = 1; % Convergence check loop

inter_tol = 0.001; % Convergence tolerance for selection of trim range

iteration = 0; % Initialize iteration count

trim = zeros(1000,1); % Initialize trim vector


while tr_tol == 1

    iteration = iteration + 1;

    trim(1) = 10;


    t_test = t(1:(end - (trim(iteration)))); % Trim time for n iteration

    Cm_test = Cm_filter(1+trim(iteration):end); % Trim Cm for n iteration
```

```
    Cmpoly = fit(t_test,Cm_test,'poly2'); % Generate polynomial for Cm
    coeff = coeffvalues(Cmpoly); % Store polynomial coefficients


%Check if intercept coeff(3) is within specified tolerances

    tr_sum = 0;

    if coeff(3) > 0 && coeff(3) < inter_tol
        tr_sum = 1;
    end

    if tr_sum == 1
        tr_tol = 0;
    end
     trim(iteration+1) = trim(iteration) + 1;
end

trimtime = trim(iteration); % Specify number of seconds to be trimmed based
on iteration analysis

t = t(1:(end - (trimtime))); % Trim time
Cm_filter = Cm_filter(1+trimtime:end); % Trim filtered Cm
Cm_raw = Cm_raw(1+trimtime:end); % Trim raw Cm
T = T(1+trimtime:end); % Trim T

%% Calculate mass flow rate, dCm/dt:
Cmpoly = fit(t,Cm_filter,'poly2'); % Generate polynomial for Cm
dCmpolydt = differentiate(Cmpoly,t); % Generate dCm/dt
Cm = Cmpoly(t); % Set Cm to the polynomial values
figure
hold on
title('Cumulative Mass')
xlabel('Time [s]')
ylabel('Cumulative Mass [kg]')
plot(t,Cm_filter,t,Cm)
plot(t,Cmpoly(t))
hold off
```

```
%% Calculate head height:

m_in = m_in/1000; % Convert mass to kg

vol_in = m_in/dens_lit; % Calculate the initial volume

vol_poured = Cm / dens_lit; % Calculate the volume poured using curve fitted
data

vol_poured_filter = Cm_filter / dens_lit; % Calculate the volume poured using
only filtered data

vol_left = vol_in - vol_poured; % Calculate volume left in vessel

vol_leftraw = vol_in - vol_pouredraw; % Calculate volume left in vessel using
only filtered data

h = (h1*vol_left) + h2; % Calculate head from UT calibration linear equation

h_filter = (h1*vol_leftraw) + h2; % Calculate head from UT calibration linear
equation using only filtered data


%% Additional back data trimming:

% Trim additional data at end of experiment to ensure that only data associated
with free flow is included

t = t(1:(dataselec*40));

Cm = Cm(1:(dataselec*40));

dCmpolydt = dCmpolydt(1:(dataselec*40));

h = h(1:(dataselec*40));

h_filter = h_filter(1:(dataselec*40));

h_raw = h_raw(1:(dataselec*40));

T = T(1:(dataselec*40));


%% Initiate iterations:

iter = 0; % Set the iteration counter

n = length(dCmpolydt); % Determine the size of problem


%% Matrices and vectors of appropriate size are created:

Vexp = zeros(n,1); % Mass flux

hcalc = zeros(n,1); % Theoretical head

Z = zeros(n,3); % Partial derivatives matrix

Y = zeros(n,1); % Experimental head minus theoretical head residuals

surft = zeros(iter_max,1); % Surface tension matrix
```

```
visc = zeros (iter_max,1); % Viscosity matrix
dens = zeros(iter_max,1); % Density matrix
MSE_Y = zeros(iter_max,1); % Mean square error of residuals

%% Set conditions for convergence, i.e. previous iterated property values:
surftA_j = 1000;
surftB_j = -1000;
viscA_j = 1000;
viscB_j = -1000;
viscC_j = 1000;
densA_j = 1000;
densB_j = -1000;

%% Solution to linear regression:
while ntol==1 % Convergence check loop
    iter = iter+1;
    %Set up matices to be solved
    %Set up calculated head equation:
    for i = 1:n
        hcalc(i,1) =
((1/(2*g))*(Vexp(i)/((densA+(densB*T(i)))*((cd1*((2*r*Vexp(i))/((viscA*(T(i)^
2))+(viscB*T(i))+viscC))^3)+(cd2*((2*r*Vexp(i))/((viscA*(T(i)^2))+(viscB*T(i)
)+viscC))^2)+(cd3*((2*r*Vexp(i))/((viscA*(T(i)^2))+(viscB*T(i))+viscC))) +
cd4)))^2)+((surftA+(surftB*T(i)))/((densA+(densB*T(i)))*g*r));
    end


    % Set up residuals' matrix:

    for i = 1:n
        Y(i) = h(i)-hcalc(i);
    end
    MSE_Y(iter)= (sum(Y(:).^2))/n; % Calculates mean square error
    % Set up partial derivatives matrix:
    for i = 1:n
        Z(i,1) = 1/(g*r*(densA + densB*T(i))); % surftA differential
        Z(i,2) = T(i)/(g*r*(densA + densB*T(i))); % surftB differential
        Z(i,3) = (Vexp(i)^2*((8*cd2*r^2*T(i)^2*Vexp(i)^2)/(viscA*T(i)^2 +
viscB*T(i) + viscC)^3 + (24*cd1*r^3*T(i)^2*Vexp(i)^3)/(viscA*T(i)^2 +
```

```
viscB*T(i) + viscC)^4 + (2*cd3*r*T(i)^2*Vexp(i))/(viscA*T(i)^2 + viscB*T(i) +
viscC)^2))/(g*(densA + densB*T(i))^2*(cd4 +
(4*cd2*r^2*Vexp(i)^2)/(viscA*T(i)^2 + viscB*T(i) + viscC)^2 +
(8*cd1*r^3*Vexp(i)^3)/(viscA*T(i)^2 + viscB*T(i) + viscC)^3 +
(2*cd3*r*Vexp(i))/(viscA*T(i)^2 + viscB*T(i) + viscC))^3); % viscA
differential
        Z(i,4) = (Vexp(i)^2*((8*cd2*r^2*T(i)*Vexp(i)^2)/(viscA*T(i)^2 +
viscB*T(i) + viscC)^3 + (24*cd1*r^3*T(i)*Vexp(i)^3)/(viscA*T(i)^2 +
viscB*T(i) + viscC)^4 + (2*cd3*r*T(i)*Vexp(i))/(viscA*T(i)^2 + viscB*T(i) +
viscC)^2))/(g*(densA + densB*T(i))^2*(cd4 +
(4*cd2*r^2*Vexp(i)^2)/(viscA*T(i)^2 + viscB*T(i) + viscC)^2 +
(8*cd1*r^3*Vexp(i)^3)/(viscA*T(i)^2 + viscB*T(i) + viscC)^3 +
(2*cd3*r*Vexp(i))/(viscA*T(i)^2 + viscB*T(i) + viscC))^3); % viscB
differential
        Z(i,5) = (Vexp(i)^2*((8*cd2*r^2*Vexp(i)^2)/(viscA*T(i)^2 + viscB*T(i)
+ viscC)^3 + (24*cd1*r^3*Vexp(i)^3)/(viscA*T(i)^2 + viscB*T(i) + viscC)^4 +
(2*cd3*r*Vexp(i))/(viscA*T(i)^2 + viscB*T(i) + viscC)^2))/(g*(densA +
densB*T(i))^2*(cd4 + (4*cd2*r^2*Vexp(i)^2)/(viscA*T(i)^2 + viscB*T(i) +
viscC)^2 + (8*cd1*r^3*Vexp(i)^3)/(viscA*T(i)^2 + viscB*T(i) + viscC)^3 +
(2*cd3*r*Vexp(i))/(viscA*T(i)^2 + viscB*T(i) + viscC))^3); % viscC
differential
        Z(i,6) = - Vexp(i)^2/(g*(densA + densB*T(i))^3*(cd4 +
(4*cd2*r^2*Vexp(i)^2)/(viscA*T(i)^2 + viscB*T(i) + viscC)^2 +
(8*cd1*r^3*Vexp(i)^3)/(viscA*T(i)^2 + viscB*T(i) + viscC)^3 +
(2*cd3*r*Vexp(i))/(viscA*T(i)^2 + viscB*T(i) + viscC))^2) - (surftA +
surftB*T(i))/(g*r*(densA + densB*T(i))^2); % densA differential
        Z(i,7) = - (T(i)*Vexp(i)^2)/(g*(densA + densB*T(i))^3*(cd4 +
(4*cd2*r^2*Vexp(i)^2)/(viscA*T(i)^2 + viscB*T(i) + viscC)^2 +
(8*cd1*r^3*Vexp(i)^3)/(viscA*T(i)^2 + viscB*T(i) + viscC)^3 +
(2*cd3*r*Vexp(i))/(viscA*T(i)^2 + viscB*T(i) + viscC))^2) - (T(i)*(surftA +
surftB*T(i)))/(g*r*(densA + densB*T(i))^2); % densB differential
    end
        % Gauss-Newton algorithm:
        x = ((Z')*Z)\((Z')*Y);
        Y_new = norm(Y);
```

```
% Maximum number of iterations allowed:
if iter > iter_max
       disp('Script timed out.')
    return
end

%Determine new values for surftA/B, viscA/B/C/D and densA/B:
surftA = surftA+(lambda*x(1,1));
if surftA < surftA_min
    surftA = surftA_min;
elseif surftA > surftA_max
    surftA = surftA_max;
end
surftB = surftB+(lambda*x(2,1));
if surftB < surftB_min
    surftB = surftB_min;
elseif surftB > surftB_max
    surftB = surftB_max;
end
viscA = viscA+(lambda*x(3,1));
 if viscA < viscA_min
    viscA = viscA_min;
elseif viscA > viscA_max
    viscA = viscA_max;
 end
viscB = viscB+(lambda*x(4,1));
 if viscB < viscB_min
    viscB = viscB_min;
elseif viscB > viscB_max
    viscB = viscB_max;
 end
viscC = viscC+(lambda*x(5,1));
 if viscC < viscC_min
    viscC = viscC_min;
elseif viscC > viscC_max
    viscC = viscC_max;
 end
densA = densA+(lambda*x(6,1));
```

```
 if densA < densA_min
    densA = densA_min;
elseif densA > densA_max
    densA = densA_max;
end
   densB = densB+(lambda*x(7,1));
 if densB < densB_min
    densB = densB_min;
elseif densB > densB_max
    densB = densB_max;
 end

 % This is to make sure that the error is decreasing with every iteration
    if Y_new <= Y_old
    lambda = lambda - k1*lambda;
else
    lambda = k1*lambda;
end

% Tolerance check:
nsum = 0;

if abs((surftA_j - surftA)/surftA_j) < tol
    nsum = nsum + 1;
end

 if abs((surftB_j - surftB)/surftB_j) < tol
    nsum = nsum + 1;
end

if abs((viscA_j - viscA)/viscA_j) < tol
    nsum = nsum + 1;
end

if abs((viscB_j - viscB)/viscB_j) < tol
    nsum = nsum + 1;
end
```

```
    if abs((viscC_j - viscC)/viscC_j) < tol
        nsum = nsum + 1;
    end

    if abs((densA_j - densA)/densA_j) < tol
        nsum = nsum + 1;
    end

    if abs((densB_j - densB)/densB_j) < tol
        nsum = nsum + 1;
    end


    if nsum ==7 % if all variables meet convergence then:
        if iter < iter_min
            continue
        else
            ntol = 0;
        end
    end

    % Redefine surft_j, visc_j and dens_j for subsequent iteration:
    surftA_j = surftA;
    surftB_j = surftB;
    viscA_j = viscA;
    viscB_j = viscB;
    viscC_j = viscC;
    densA_j = densA;
    densB_j = densB;
    Y_old = Y_new;
end


%% Final properties solved using Gauss-Newton method:

surft = zeros(n,1);
visc = zeros(n,1);
dens = zeros(n,1);
```

```
for i = 1:n
    surft(i,1) = surftA + (surftB*T(i));
    visc(i,1) = (viscA*(T(i)^2))+(viscB*T(i))+viscC;
    dens(i,1) = densA + (densB*T(i));

end

% Output results:

message1 = ['Surface Tension = ',num2str(surftA),' + ',num2str(surftB),'T', '
(N/m)'];
    disp(message1)
message2 = ['Viscosity = ',num2str(viscA),'T^2',' + ',num2str(viscB),'T',' +
',num2str(viscC), ' (Pa*s)'];
    disp(message2)
message3 = ['Density = ',num2str(densA),' + ',num2str(densB),'T', ' (kg/m^3)'
newline];
    disp(message3)

SurfaceTension = surftA + (surftB*T_errorcalc);
message4 = ['Final value for surface tension at ',num2str(T_errorcalc),'
degrees Kelvin is ', num2str(SurfaceTension), ' N/m.' newline 'Associated
error for surface tension is ', num2str(surft_error), '%' newline];
    disp(message4)
Viscosity = (viscA*(T_errorcalc^2))+(viscB*T_errorcalc)+viscC;
message5 = ['Final value for viscosity at ',num2str(T_errorcalc),' degrees
Kelvin is ', num2str(Viscosity), ' Pa*s' newline 'Associated error for
viscosity is ', num2str(visc_error), '%' newline];
    disp(message5)
Density = densA + (densB*T_errorcalc);
message6 = ['Final value for density at ',num2str(T_errorcalc),' degrees
Kelvin is ', num2str(Density), ' kg/m^3' newline 'Associated error for
viscosity is ', num2str(dens_error), '%' newline];
    disp(message6)
```

APPENDIX I : MINITAB REGRESSION ANALYSIS

I.1 Al Viscosity Tension Literature Data Regression Output

AL VISCOSITY LITERATURE DATA

Regression Analysis: ln(η) versus 1/(T*R)

Regression Equation

ln(η) = -7.955 + 13742 1/(T*R)

Coefficients

Term	Coef	SE Coef	T-Value	P-Value	VIF
Constant	-7.955	0.796	-10.00	0.000	
1/(T*R)	13742	6893	1.99	0.048	1.00

Model Summary

S	R-sq	R-sq(adj)	R-sq(pred)
0.648557	2.82%	2.11%	0.00%

Analysis of Variance

Source	DF	Adj SS	Adj MS	F-Value	P-Value
Regression	1	1.672	1.6715	3.97	0.048
1/(T*R)	1	1.672	1.6715	3.97	0.048
Error	137	57.626	0.4206		
Lack-of-Fit	133	54.331	0.4085	0.50	0.904
Pure Error	4	3.295	0.8237		
Total	138	59.297			

Fits and Diagnostics for Unusual Observations

Obs	ln(η)	Fit	Resid	Std Resid	
27	-7.5811	-6.2562	-1.3249	-2.06	R
54	-7.6585	-6.3345	-1.3241	-2.05	R

R Large residual

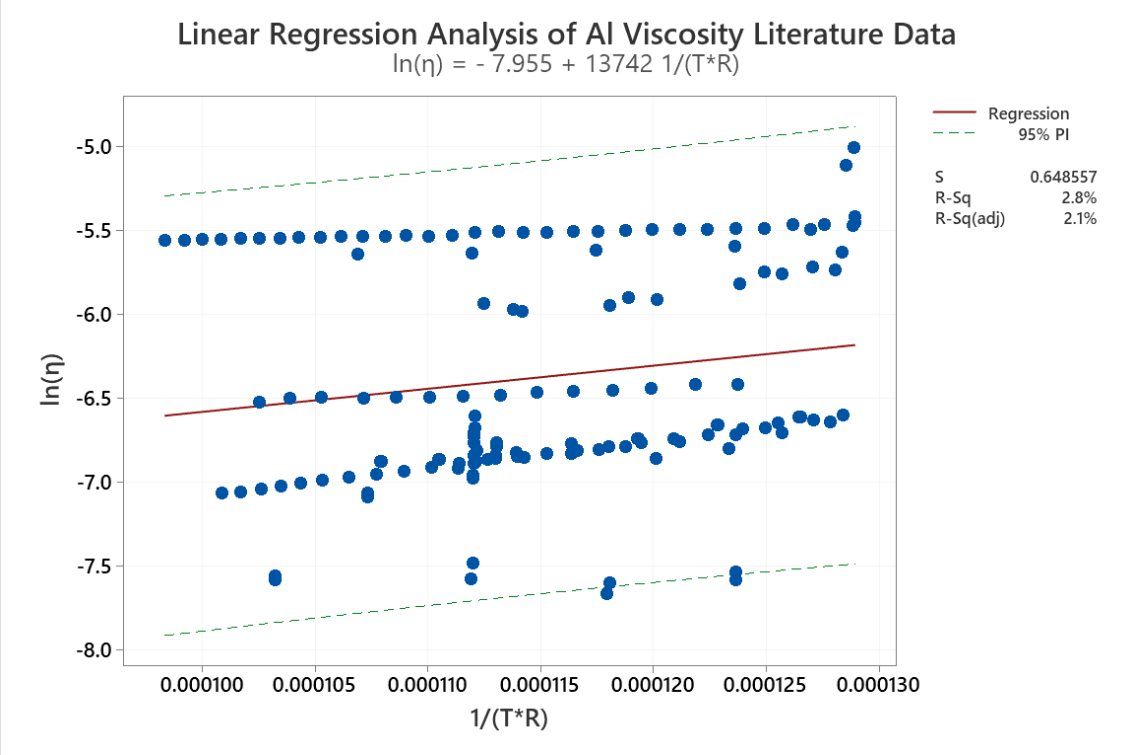

Figure I.1: Linear Regression Analysis of Al Viscosity Literature Data

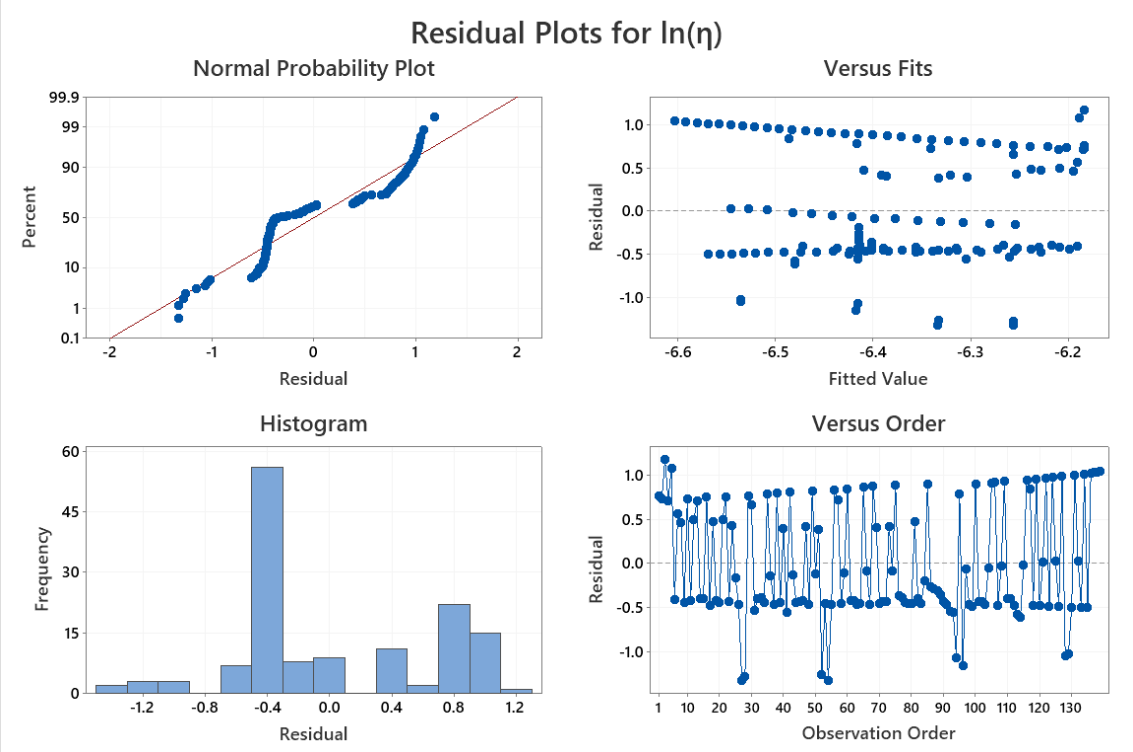

Figure I.2: Residual Plots for Al Viscosity Literature Data

I.2 Al Viscosity Results Regression Output

AL VISCOSITY

Regression Analysis: ln(η) versus 1/(T*R)

Regression Equation

ln(η) = -7.10 + 1813 1/(T*R)

Coefficients

Term	Coef	SE Coef	T-Value	P-Value	VIF
Constant	-7.10	2.02	-3.52	0.176	
1/(T*R)	1813	18523	0.10	0.938	1.00

Model Summary

S	R-sq	R-sq(adj)	R-sq(pred)
0.187379	0.95%	0.00%	0.00%

Analysis of Variance

Source	DF	Adj SS	Adj MS	F-Value	P-Value
Regression	1	0.000336	0.000336	0.01	0.938
1/(T*R)	1	0.000336	0.000336	0.01	0.938
Error	1	0.035111	0.035111		
Total	2	0.035447			

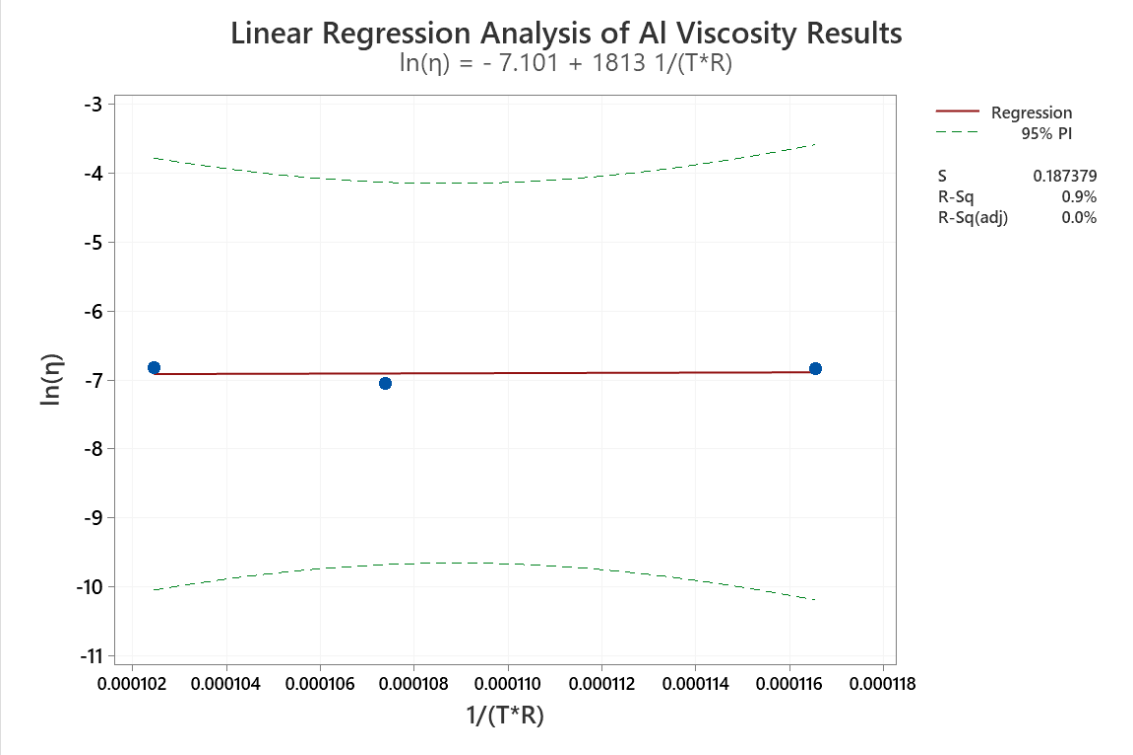

Figure I.3: Linear Regression Analysis of Al Viscosity Results

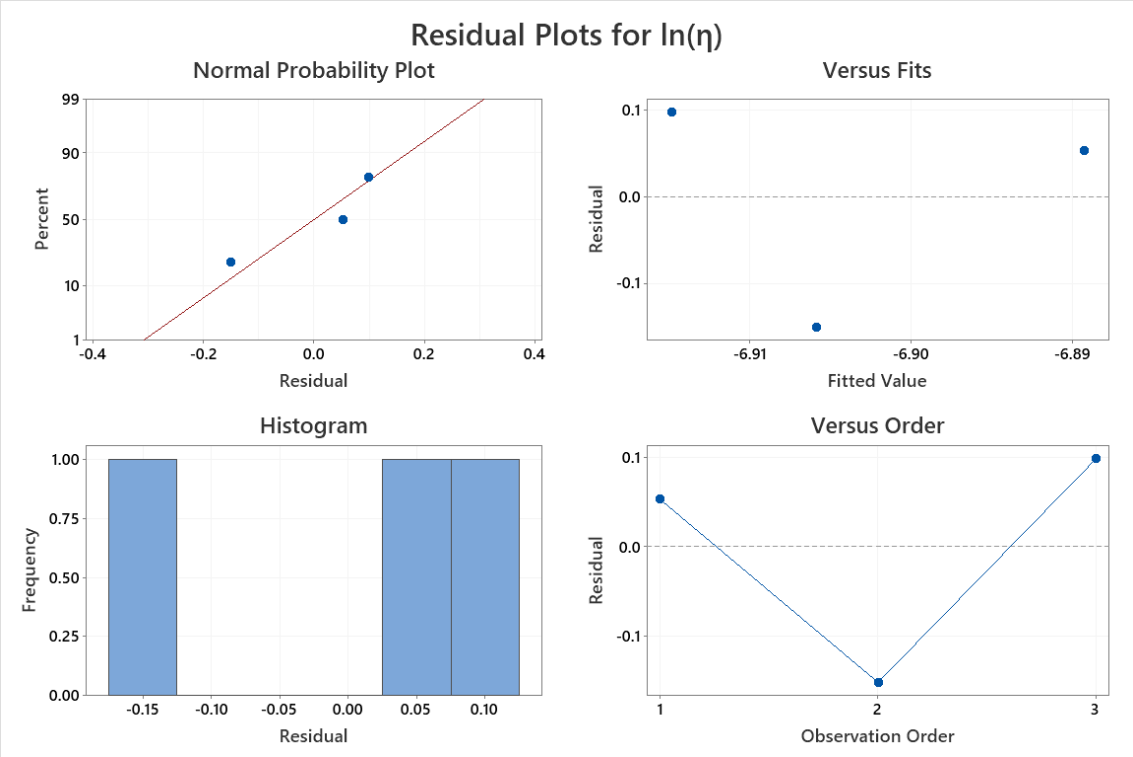

Figure I.4: Residual Plots for Al Viscosity Results

I.3 Al-Cu Viscosity Literature Data Regression Output

AL-CU VISCOSITY LITERATURE DATA

Regression Analysis: ln(η) versus 1/(T*R)

Regression Equation

ln(η) = -7.559
+ 10375 1/(T*R)

Coefficients

Term	Coef	SE Coef	T-Value	P-Value	VIF
Constant	-7.559	0.304	-24.84	0.000	
1/(T*R)	10375	2697	3.85	0.000	1.00

Model Summary

S	R-sq	R-sq(adj)	R-sq(pred)
0.334028	15.78%	14.72%	12.50%

Analysis of Variance

Source	DF	Adj SS	Adj MS	F-Value	P-Value

Regression	1	1.6517	1.65171	14.80	0.000
1/(T*R)	1	1.6517	1.65171	14.80	0.000
Error	79	8.8144	0.11157		
Lack-of-Fit	67	8.6219	0.12869	8.02	0.000
Pure Error	12	0.1925	0.01604		
Total	80	10.4661			

Fits and Diagnostics for Unusual Observations

Obs	ln(η)	Fit	Resid	Std Resid	
65	-5.5800	-6.3431	0.7631	2.30	R
66	-5.5307	-6.3432	0.8125	2.45	R
69	-5.5160	-6.3433	0.8272	2.49	R

R Large residual

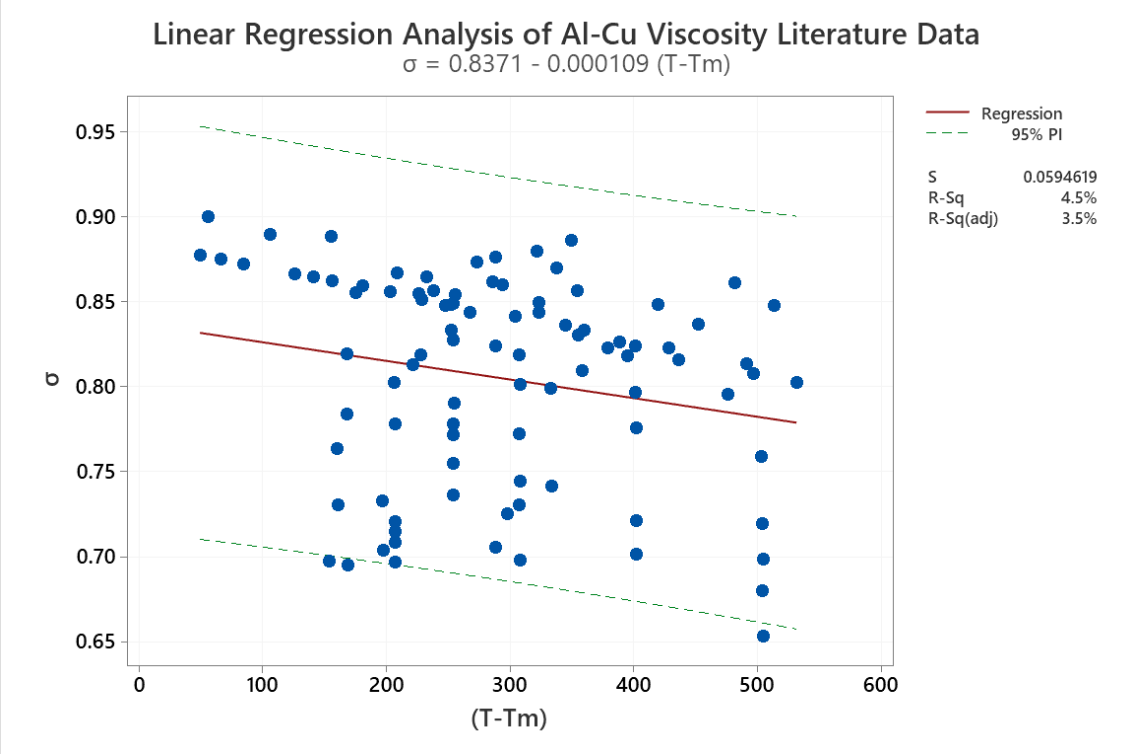

Figure I.5: Linear Regression Analysis of Al-Cu Viscosity Literature Data

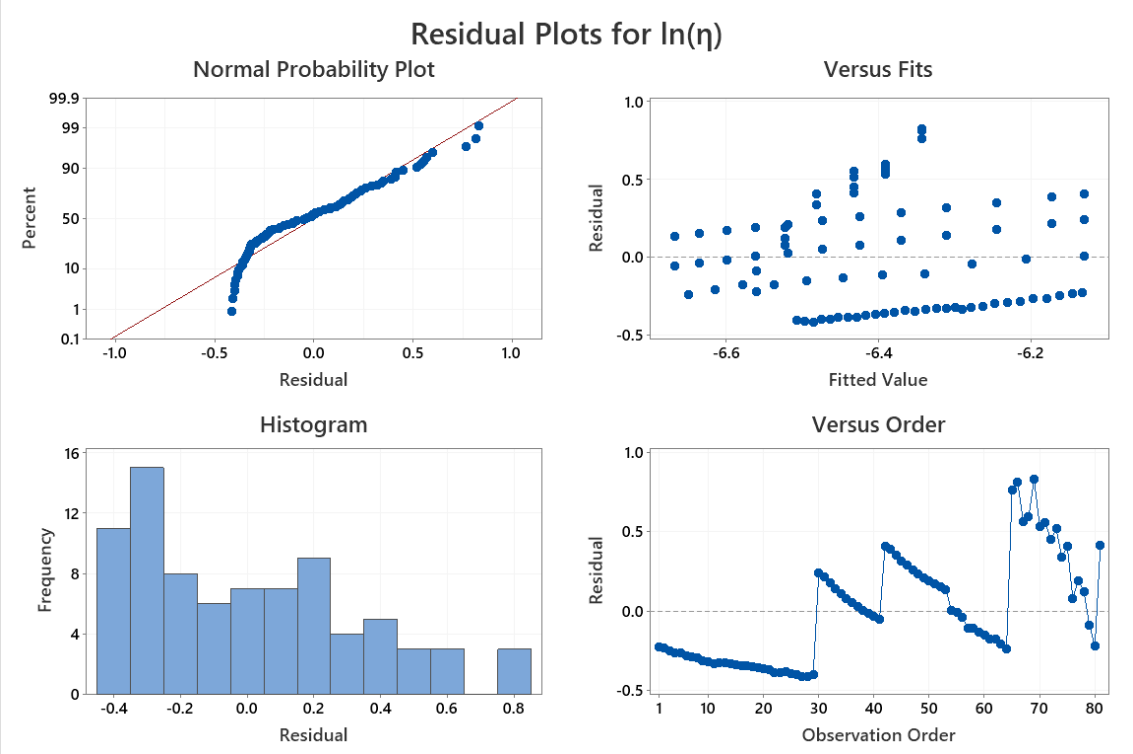

Figure I.6: Residual Plots for Al-Cu Viscosity Literature Data

I.4 Al-Cu Viscosity Results Regression Output

AL-CU VISCOSITY

Regression Analysis: ln(η) versus 1/(T*R)

Regression Equation

ln(η) = -11.73
+ 46035 1/(T*R)

Coefficients

Term	Coef	SE Coef	T-Value	P-Value	VIF
Constant	-11.73	1.13	-10.35	0.002	
1/(T*R)	46035	10545	4.37	0.022	1.00

Model Summary

S	R-sq	R-sq(adj)	R-sq(pred)
0.157284	86.40%	81.86%	71.76%

Analysis of Variance

Source	DF	Adj SS	Adj MS	F-Value	P-Value
Regression	1	0.47143	0.47143	19.06	0.022
1/(T*R)	1	0.47143	0.47143	19.06	0.022

Error	3	0.07421	0.02474
Total	4	0.54564	

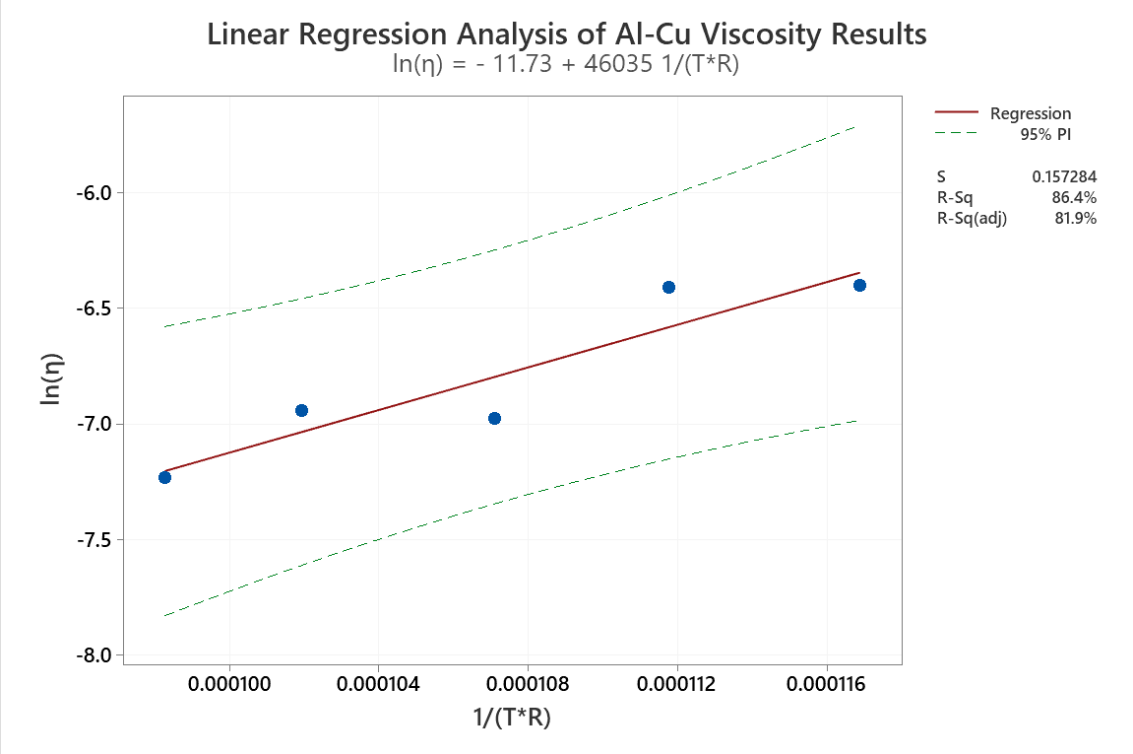

Figure I.7: Linear Regression Analysis of Al-Cu Viscosity Results

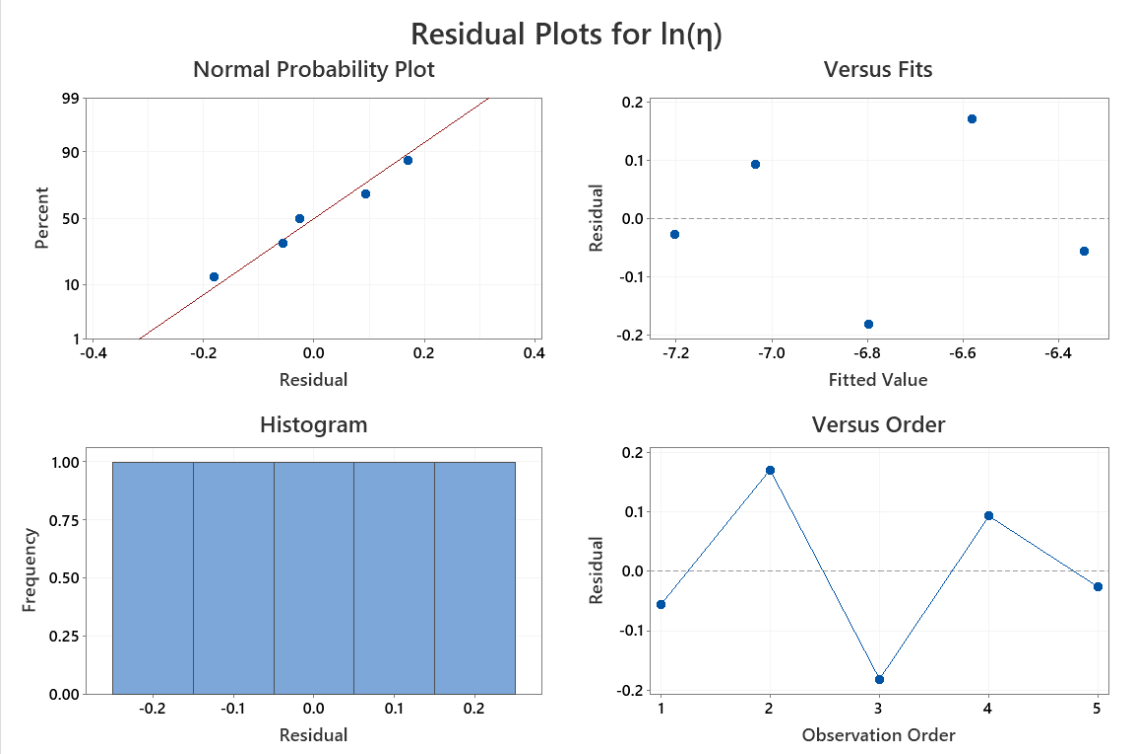

Figure I.8: Residual Plots of Al-Cu Viscosity Results

I.5 Al Surface Tension Literature Data Regression Output

AL SURFACE TENSION LITERATURE DATA

Regression Analysis: σ versus (T-Tm)

Regression Equation

σ = 0.85877 - 0.000093 (T-Tm)

Coefficients

Term	Coef	SE Coef	T-Value	P-Value	VIF
Constant	0.85877	0.00466	184.46	0.000	
(T-Tm)	-0.000093	0.000017	-5.35	0.000	1.00

Model Summary

S	R-sq	R-sq(adj)	R-sq(pred)
0.0398833	13.93%	13.45%	11.97%

Analysis of Variance

Source	DF	Adj SS	Adj MS	F-Value	P-Value
Regression	1	0.04557	0.045575	28.65	0.000
(T-Tm)	1	0.04557	0.045575	28.65	0.000
Error	177	0.28155	0.001591		

Lack-of-Fit	152	0.20412	0.001343	0.43	0.999
Pure Error	25	0.07743	0.003097		
Total	178	0.32712			

Fits and Diagnostics for Unusual Observations

Obs	σ	Fit	Resid	Std Resid	
12	1.00900	0.85692	0.15208	3.84	R
28	1.10000	0.85507	0.24493	6.17	R
29	1.05000	0.85507	0.19493	4.91	R
30	1.00900	0.85507	0.15393	3.88	R
117	0.70900	0.83730	-0.12830	-3.23	R
175	0.83293	0.80299	0.02994	0.76	X
176	0.82145	0.80287	0.01858	0.47	X
177	0.80091	0.80191	-0.00101	-0.03	X
178	0.80514	0.80086	0.00428	0.11	X
179	0.76887	0.80055	-0.03168	-0.81	X

R Large residual
X Unusual X

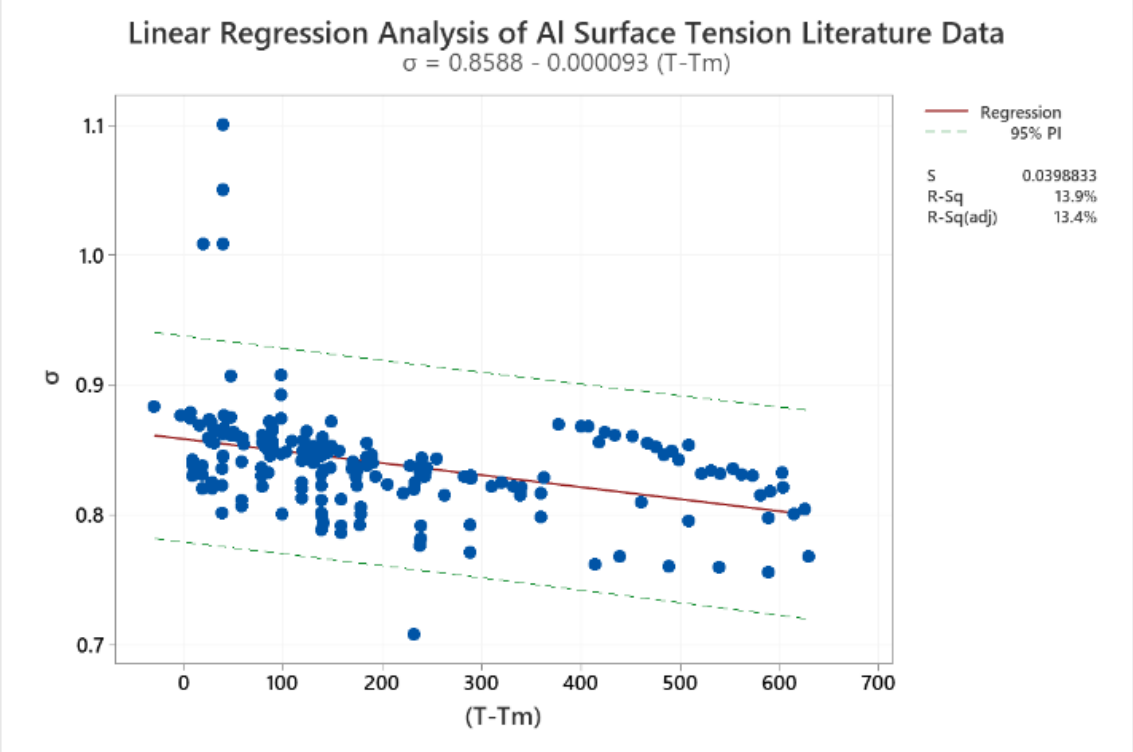

Figure I.9: Linear Regression Analysis of Al Surface Tension Literature Data

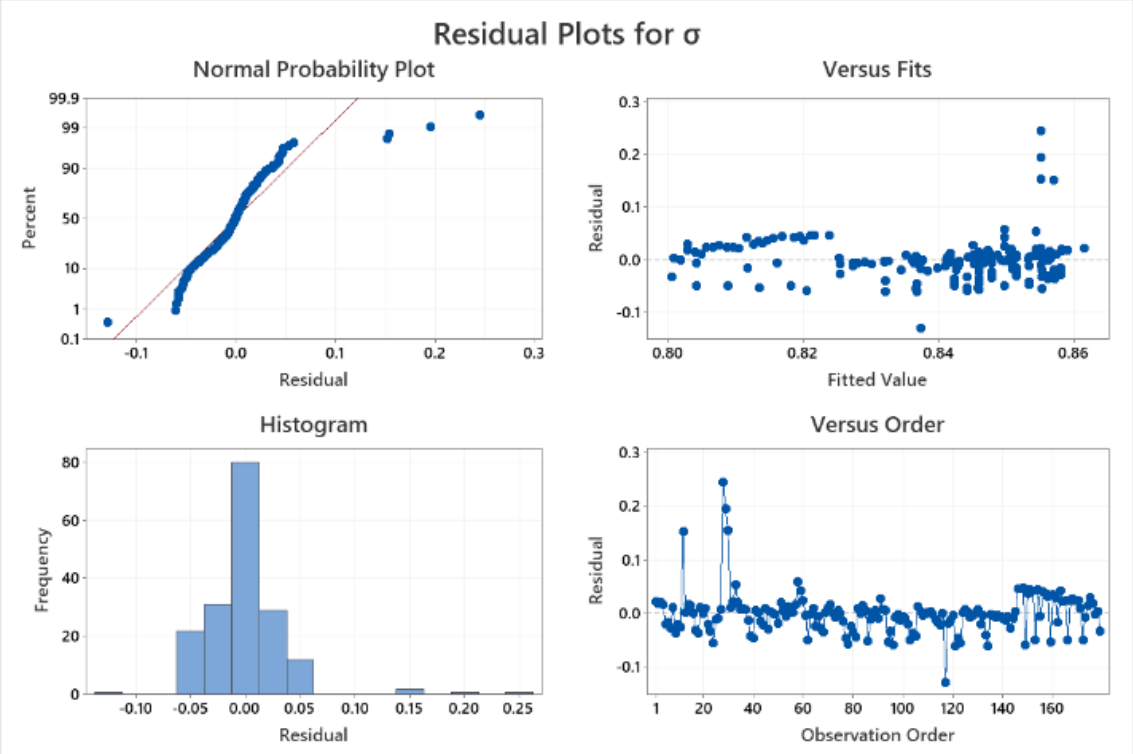

Figure I.10: Residual Plots of Al Surface Tension Literature Data

I.6 Al Surface Tension Results Regression Output

AL SURFACE TENSION

Regression Analysis: σ versus (T-Tm)

Regression Equation

σ = 0.90405 - 0.000239 (T-Tm)

Coefficients

Term	Coef	SE Coef	T-Value	P-Value	VIF
Constant	0.90405	0.00110	824.08	0.001	
(T-Tm)	-0.000239	0.000006	-40.37	0.016	1.00

Model Summary

S	R-sq	R-sq(adj)	R-sq(pred)
0.0006006	99.94%	99.88%	99.01%

Analysis of Variance

Source	DF	Adj SS	Adj MS	F-Value	P-Value
Regression	1	0.000588	0.000588	1629.92	0.016
(T-Tm)	1	0.000588	0.000588	1629.92	0.016
Error	1	0.000000	0.000000		

Total 2 0.000588

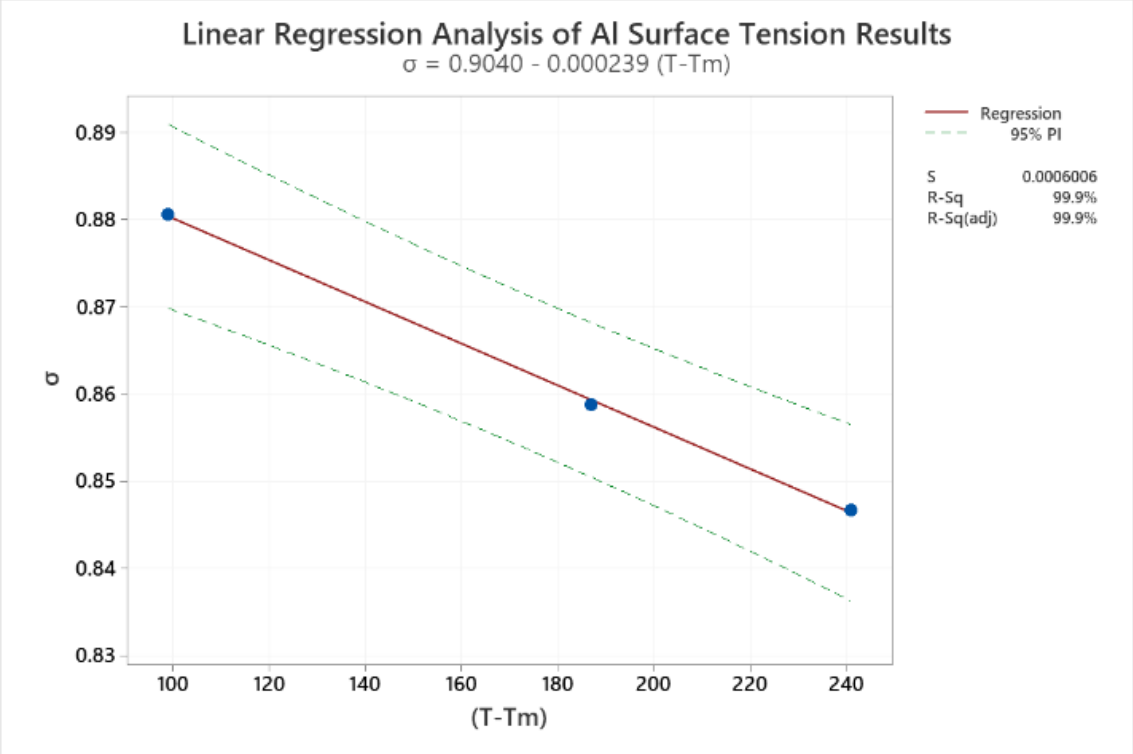

Figure I.11: Linear Regression Analysis of Al Surface Tension Results

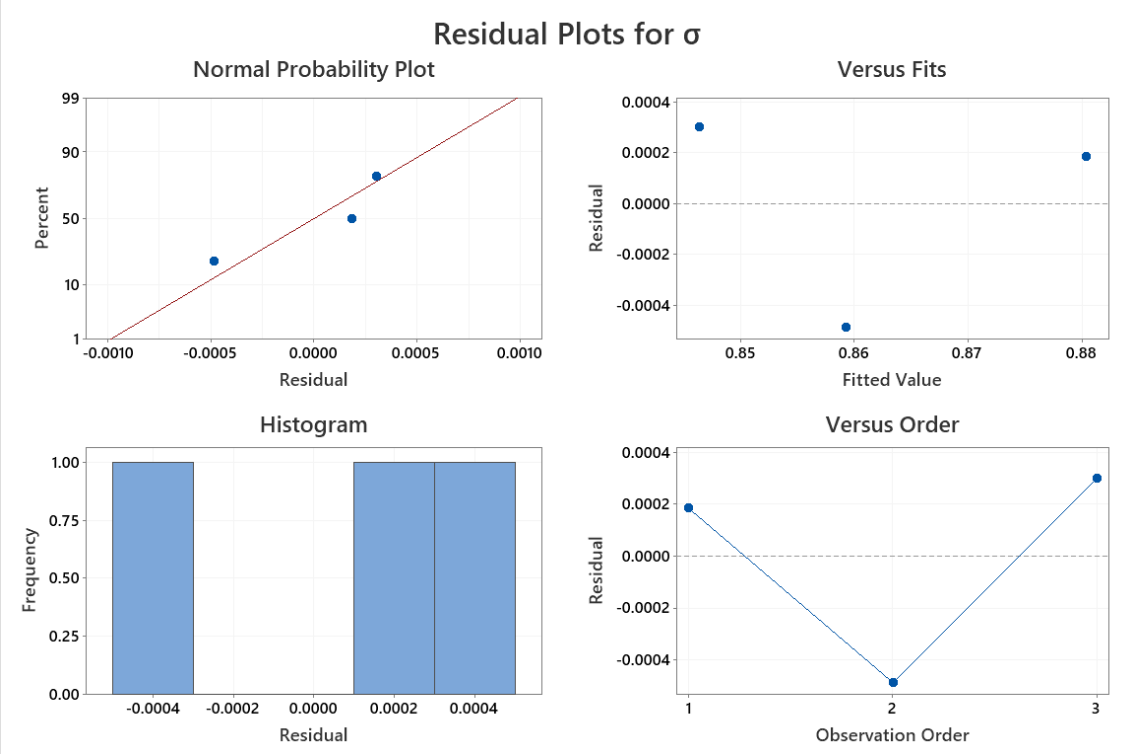

Figure I.12: Residual Plots of Al Surface Tension Results

I.7 Al-Cu Surface Tension Literature Data Regression Output

AL-CU SURFACE TENSION LITERATURE DATA

Regression Analysis: σ versus (T-Tm)

Regression Equation

σ = 0.8371 - 0.000109 (T-Tm)

Coefficients

Term	Coef	SE Coef	T-Value	P-Value	VIF
Constant	0.8371	0.0164	51.01	0.000	
(T-Tm)	-0.000109	0.000052	-2.10	0.038	1.00

Model Summary

S	R-sq	R-sq(adj)	R-sq(pred)
0.0594619	4.50%	3.48%	0.11%

Analysis of Variance

Source	DF	Adj SS	Adj MS	F-Value	P-Value
Regression	1	0.015652	0.015652	4.43	0.038
(T-Tm)	1	0.015652	0.015652	4.43	0.038
Error	94	0.332358	0.003536		

Lack-of-Fit	92	0.332358	0.003613	*	*
Pure Error	2	0.000000	0.000000		
Total	95	0.348010			

Fits and Diagnostics for Unusual Observations

Obs	σ	Fit	Resid	Std Resid	
8	0.6977	0.8202	-0.1225	-2.09	R
15	0.6951	0.8186	-0.1235	-2.10	R
94	0.6538	0.7818	-0.1280	-2.20	R

R Large residual

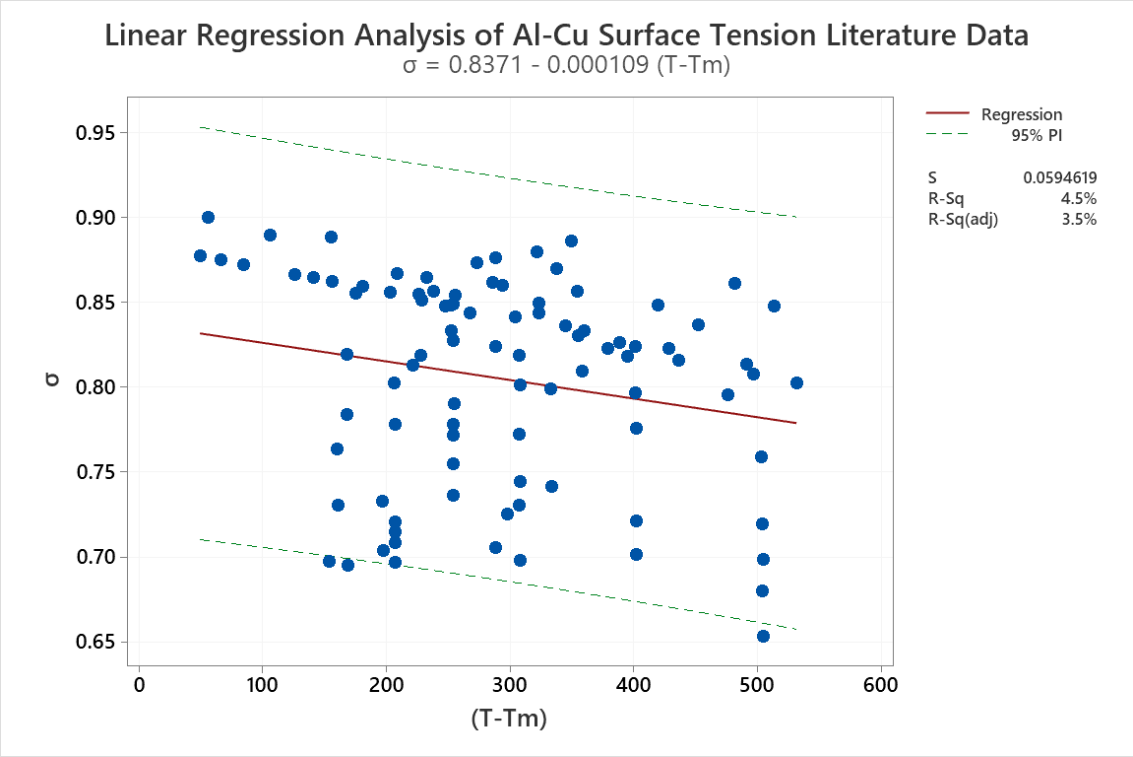

Figure I.13: Linear Regression Analysis of Al-Cu Surface Tension Literature Data

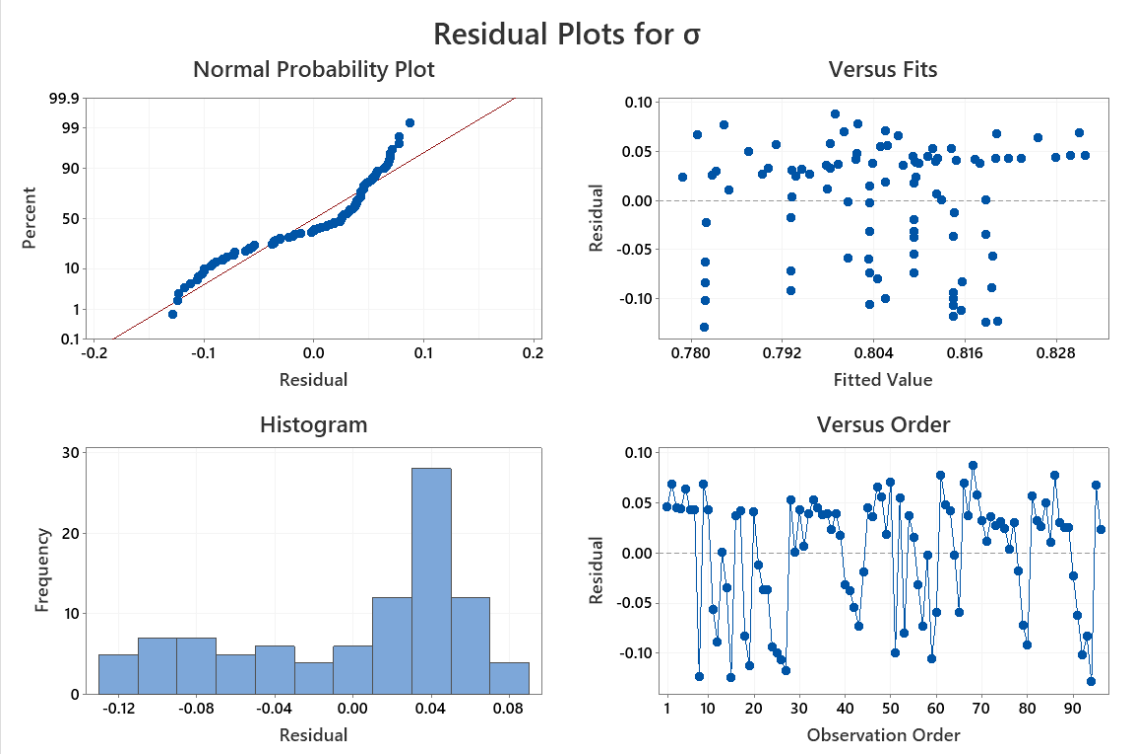

Figure I.14: Residual Plots of Al-Cu Surface Tension Literature Data

I.8 Al-Cu Surface Tension Results Regression Output

AL-CU SURFACE TENSION

Regression Analysis: σ versus (T-Tm)

Regression Equation

σ = 0.93964 - 0.000370 (T-Tm)

Coefficients

Term	Coef	SE Coef	T-Value	P-Value	VIF
Constant	0.93964	0.00614	153.00	0.000	
(T-Tm)	-0.000370	0.000023	-16.18	0.001	1.00

Model Summary

S	R-sq	R-sq(adj)	R-sq(pred)
0.0035736	98.87%	98.49%	97.02%

Analysis of Variance

Source	DF	Adj SS	Adj MS	F-Value	P-Value
Regression	1	0.003345	0.003345	261.89	0.001
(T-Tm)	1	0.003345	0.003345	261.89	0.001
Error	3	0.000038	0.000013		
Total	4	0.003383			

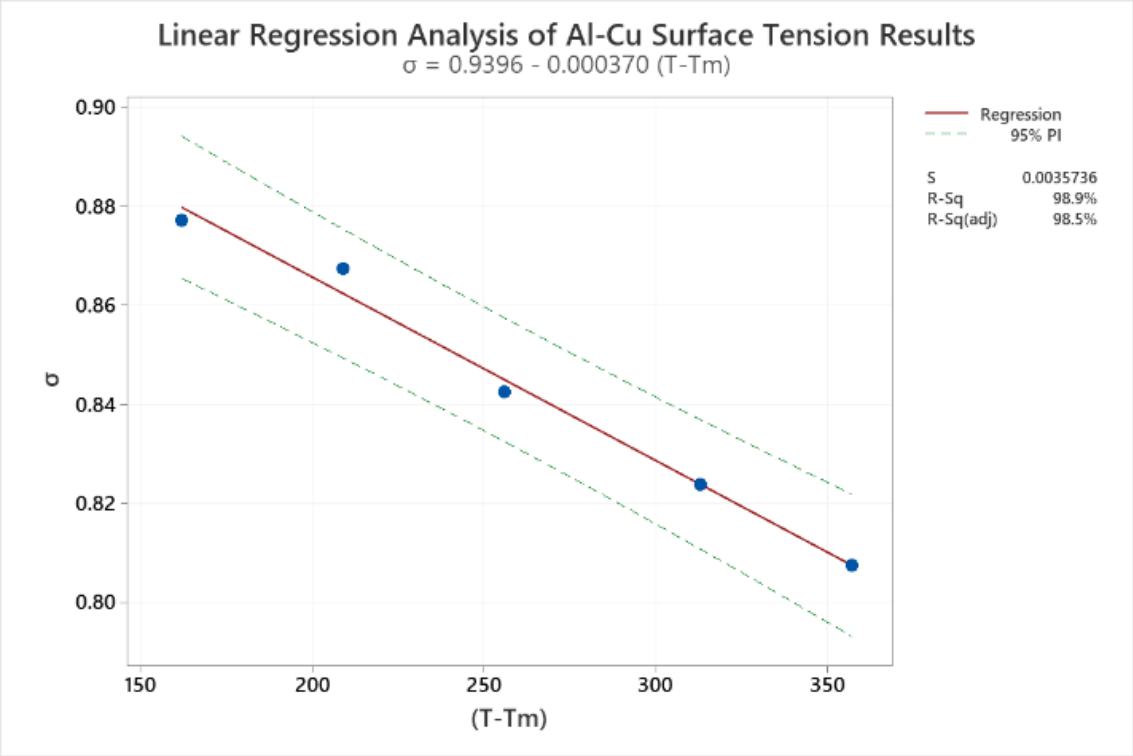

Figure I.15: Linear Regression Analysis of Al-Cu Surface Tension Results

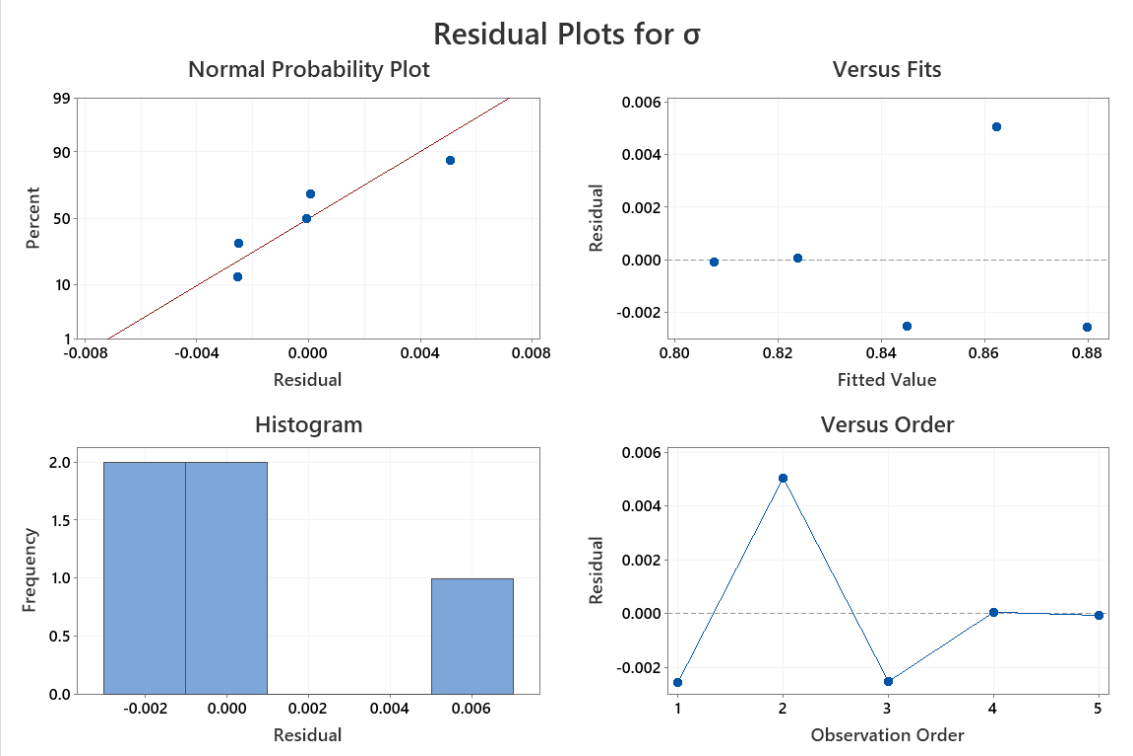

Figure I.16: Residual Plots of Al-Cu Surface Tension Results

I.9 Al Density Literature Data Regression Output

AL DENSITY LITERATURE DATA

Regression Analysis: ρ versus (T-Tm)

Regression Equation

ρ = 2335.63 - 0.3113 (T-Tm)

Coefficients

Term	Coef	SE Coef	T-Value	P-Value	VIF
Constant	2335.63	6.05	385.97	0.000	
(T-Tm)	-0.3113	0.0203	-15.31	0.000	1.00

Model Summary

S	R-sq	R-sq(adj)	R-sq(pred)
58.1688	44.60%	44.41%	43.73%

Analysis of Variance

Source	DF	Adj SS	Adj MS	F-Value	P-Value
Regression	1	792656	792656	234.26	0.000
(T-Tm)	1	792656	792656	234.26	0.000

Error	291	984629	3384		
Lack-of-Fit	264	937944	3553	2.05	0.014
Pure Error	27	46685	1729		
Total	292	1777285			

Fits and Diagnostics for Unusual Observations

Obs	ρ	Fit	Resid	Std Resid	
2	2473.24	2336.22	137.02	2.37	R
3	2564.79	2336.22	228.57	3.95	R
4	2549.53	2336.22	213.31	3.69	R
61	2172.71	2311.52	-138.81	-2.39	R
76	2465.35	2304.09	161.26	2.78	R
109	2463.78	2288.57	175.21	3.02	R
122	2429.25	2277.31	151.95	2.62	R
165	2048.37	2251.68	-203.31	-3.50	R
180	2049.14	2241.38	-192.24	-3.31	R
182	2072.91	2241.06	-168.15	-2.90	R
254	2339.44	2198.03	141.41	2.44	R
261	2473.87	2193.12	280.75	4.85	R

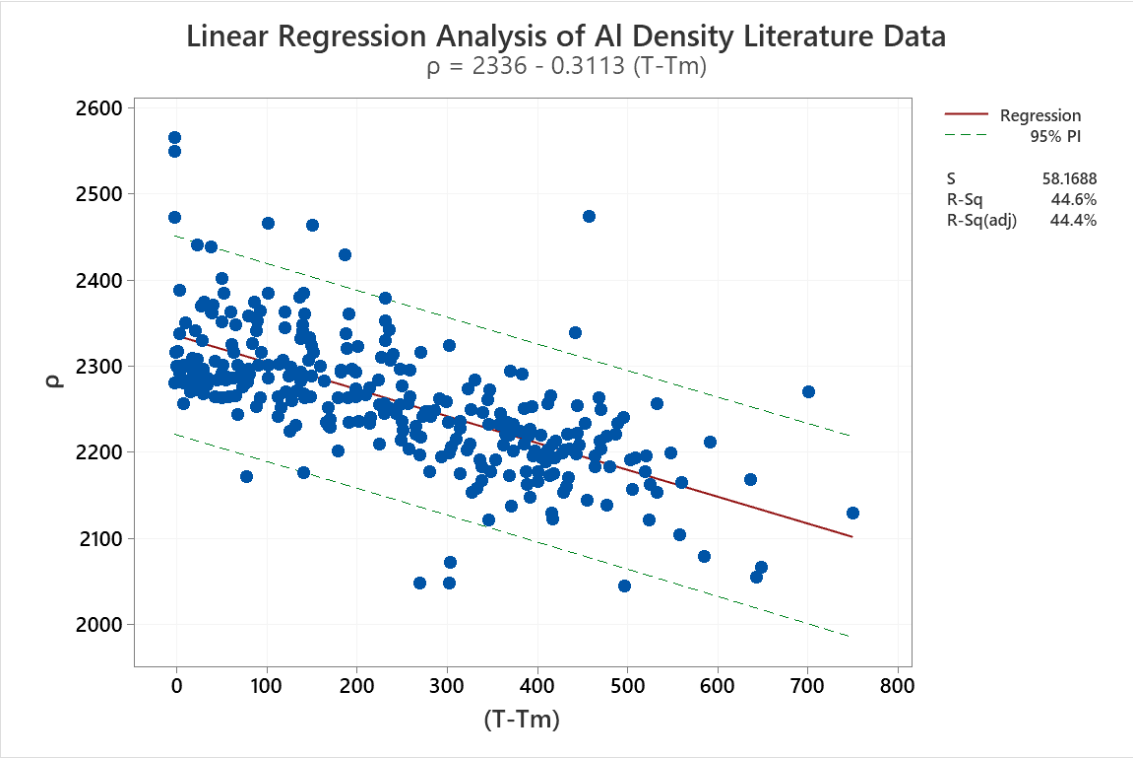

Figure I.17: Linear Regression Analysis of Al Density Literature Data

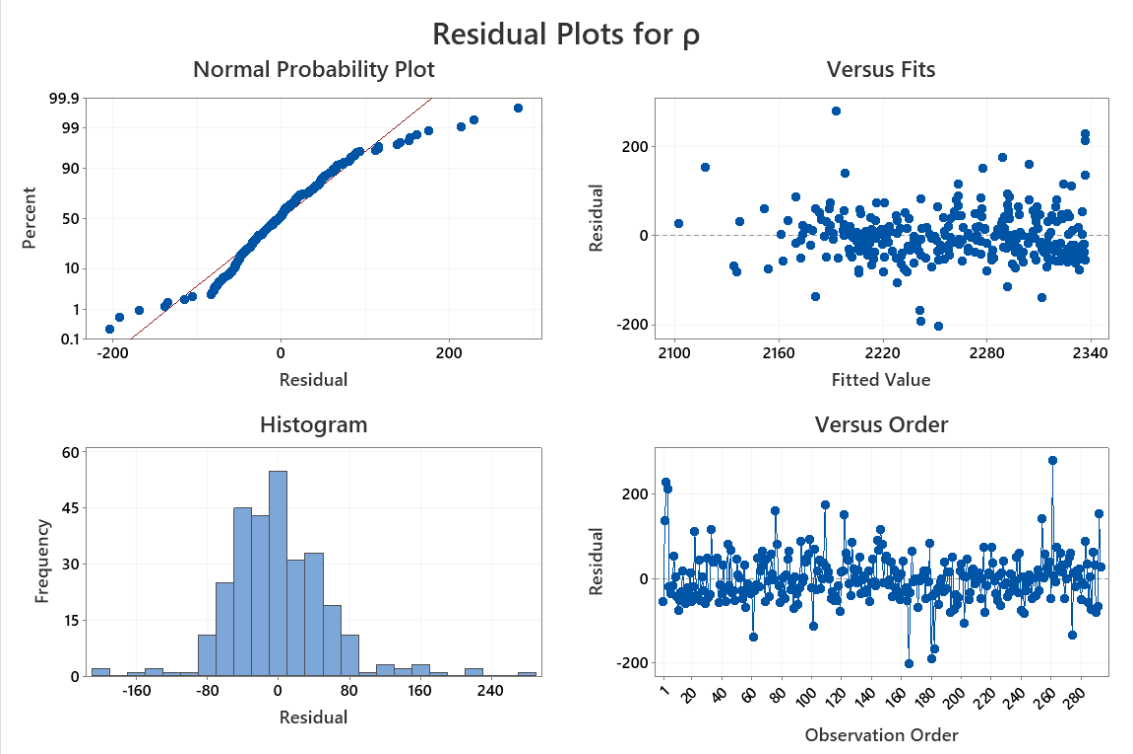

Figure I.18: Residual Plots of Al Density Literature Data

I.10 Al Density Results Regression Output

AL DENSITY

Regression Analysis: ρ versus (T-Tm)

Regression Equation

ρ = 1474 + 1.83 (T-Tm)

Coefficients

Term	Coef	SE Coef	T-Value	P-Value	VIF
Constant	1474	402	3.67	0.169	
(T-Tm)	1.83	2.17	0.84	0.555	1.00

Model Summary

S	R-sq	R-sq(adj)	R-sq(pred)
220.126	41.43%	0.00%	0.00%

Analysis of Variance

Source	DF	Adj SS	Adj MS	F-Value	P-Value
Regression	1	34273	34273	0.71	0.555
(T-Tm)	1	34273	34273	0.71	0.555
Error	1	48455	48455		
Total	2	82728			

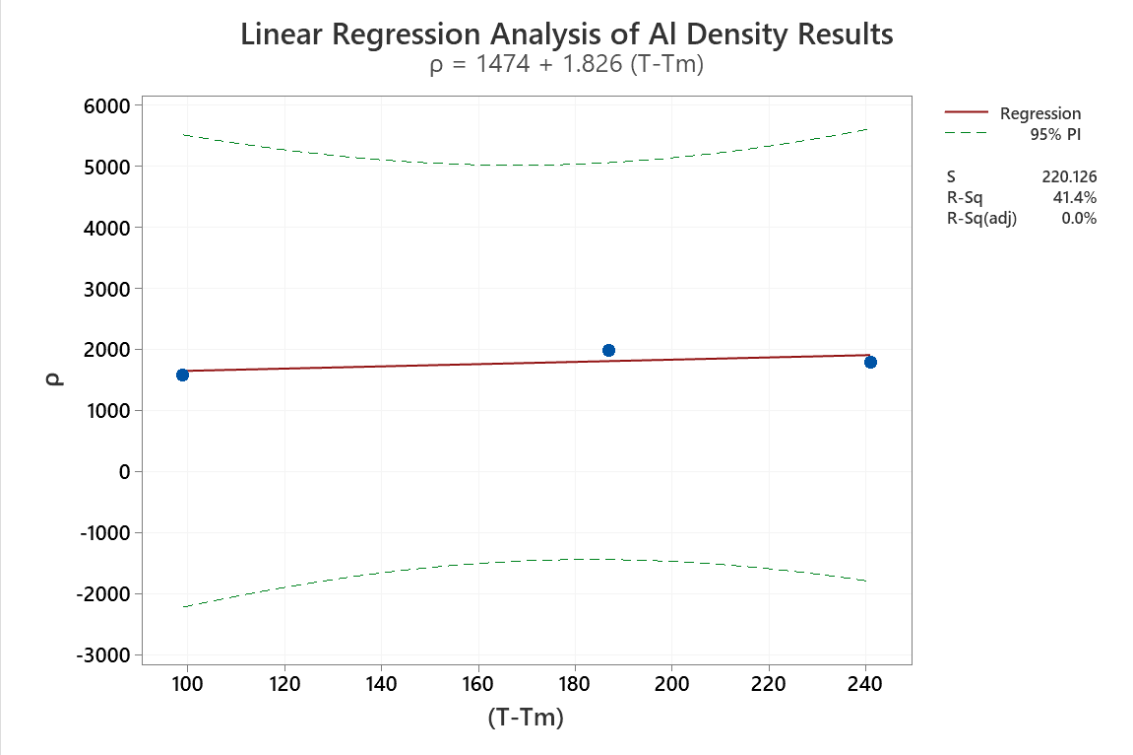

Figure I.19: Linear Regression Analysis of Al Density Results

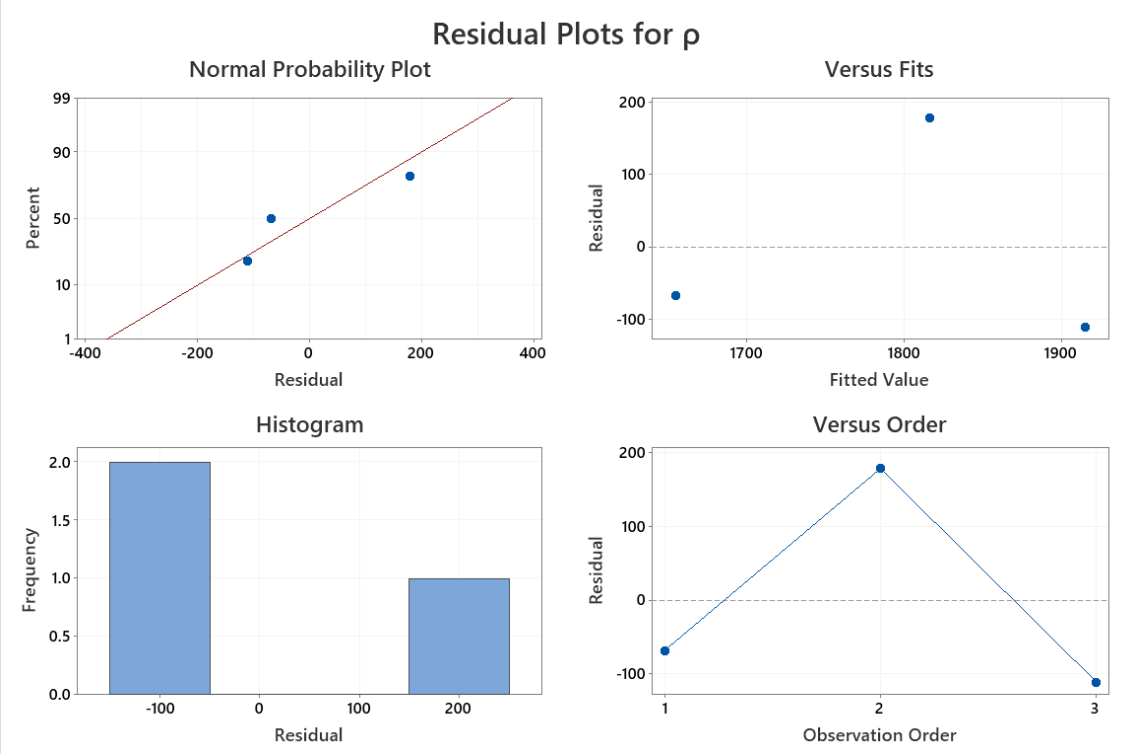

Figure I.20: Residual Plots of Al Density Results

I.11 Al-Cu Density Literature Data Regression Output

AL-CU DENSITY LITERATURE DATA

Regression Analysis: ρ versus (T-Tm)

Regression Equation

ρ = 2769.1 - 0.400 (T-Tm)

Coefficients

Term	Coef	SE Coef	T-Value	P-Value	VIF
Constant	2769.1	40.8	67.89	0.000	
(T-Tm)	-0.400	0.137	-2.92	0.005	1.00

Model Summary

S	R-sq	R-sq(adj)	R-sq(pred)
126.484	13.19%	11.64%	7.44%

Analysis of Variance

Source	DF	Adj SS	Adj MS	F-Value	P-Value
Regression	1	136148	136148	8.51	0.005
(T-Tm)	1	136148	136148	8.51	0.005
Error	56	895903	15998		

Total 57 1032051

Fits and Diagnostics for Unusual Observations

Obs	ρ	Fit	Resid	Std Resid	
11	3013.9	2704.1	309.7	2.49	R
43	2944.7	2634.6	310.1	2.48	R

R Large residual

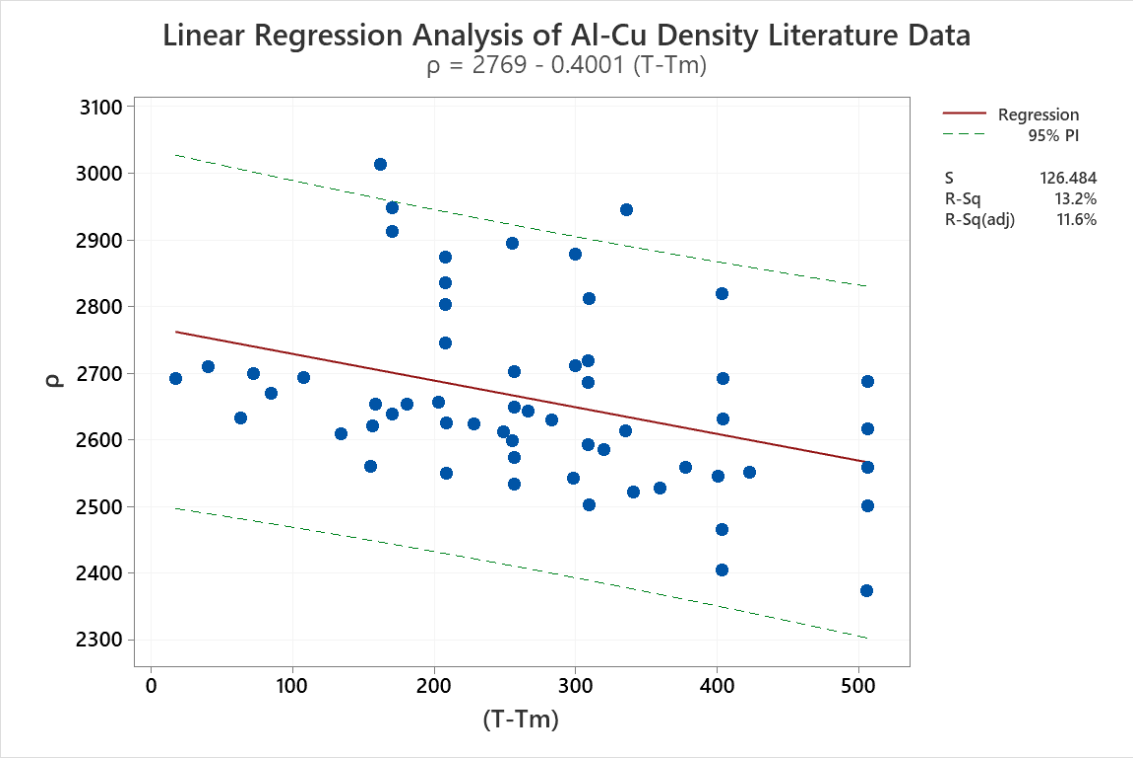

Figure I.21: Linear Regression Analysis of Al-Cu Density Literature Data

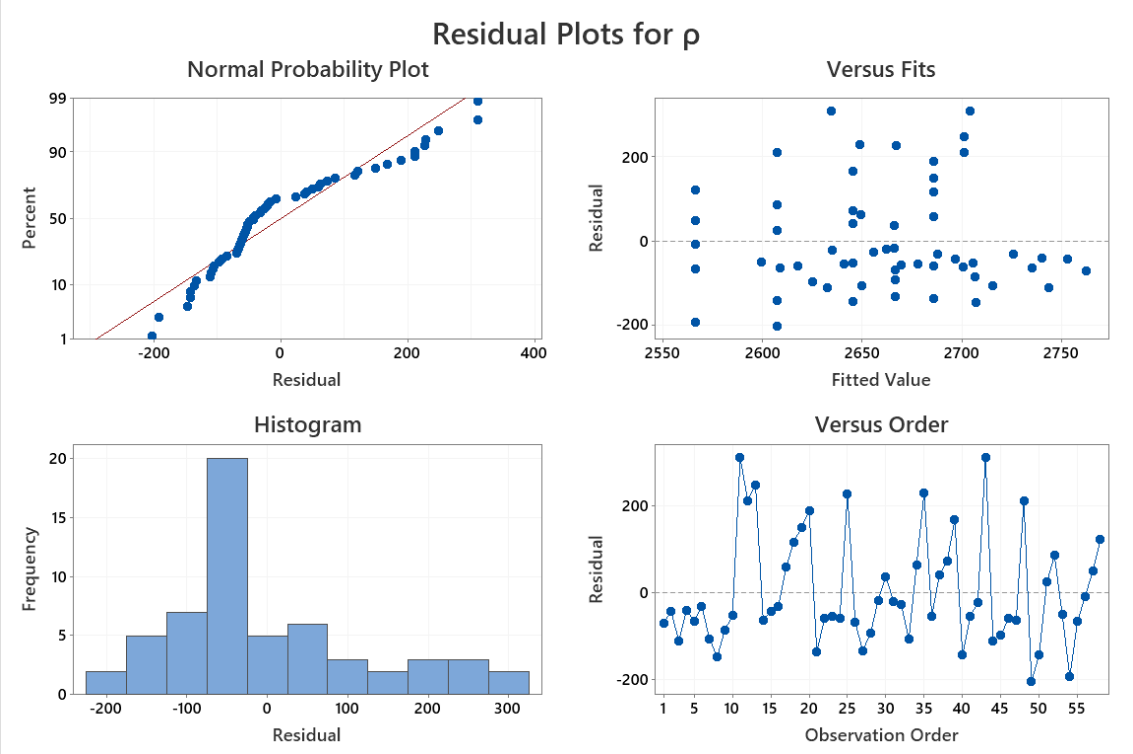

Figure I.22: Residual Plots of Al-Cu Density Literature Data

I.12 Al-Cu Density Results Regression Output

AL-CU DENSITY

Regression Analysis: ρ versus (T-Tm)

Regression Equation

ρ = 2296 + 0.07 (T-Tm)

Coefficients

Term	Coef	SE Coef	T-Value	P-Value	VIF
Constant	2296	361	6.36	0.008	
(T-Tm)	0.07	1.34	0.05	0.960	1.00

Model Summary

S	R-sq	R-sq(adj)	R-sq(pred)
210.053	0.10%	0.00%	0.00%

Analysis of Variance

Source	DF	Adj SS	Adj MS	F-Value	P-Value
Regression	1	129	129.0	0.00	0.960
(T-Tm)	1	129	129.0	0.00	0.960
Error	3	132366	44122.1		
Total	4	132495			

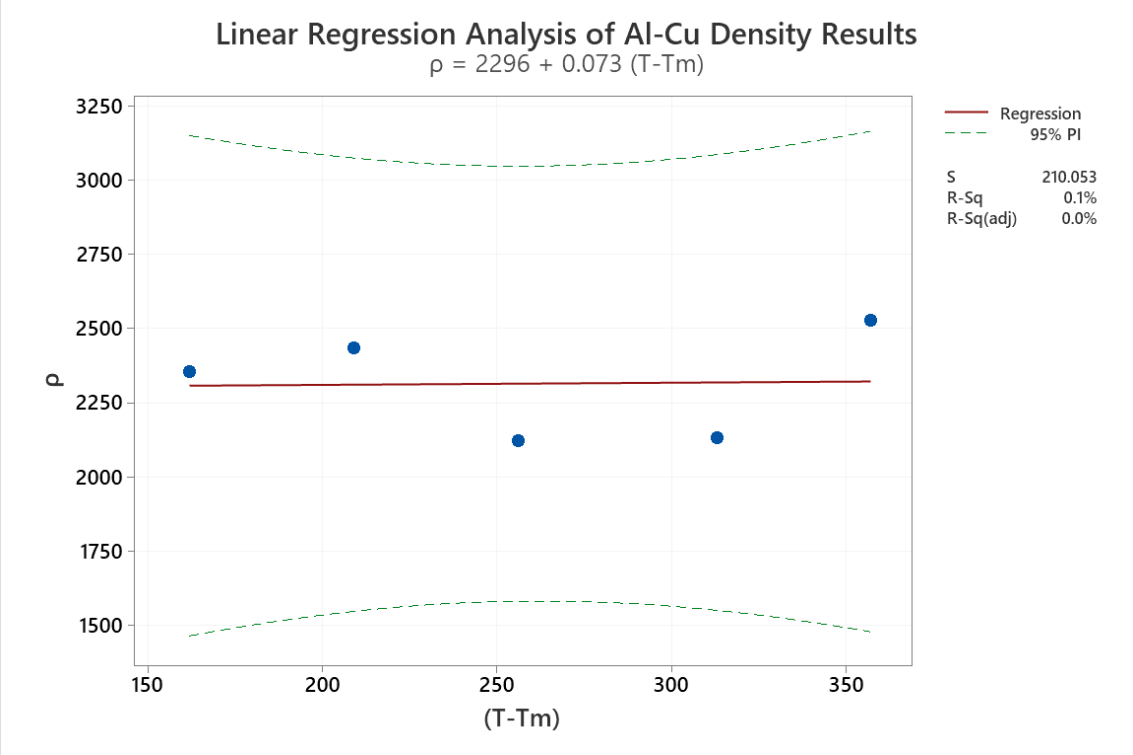

Figure I.23: Linear Regression Analysis of Al-Cu Density Results

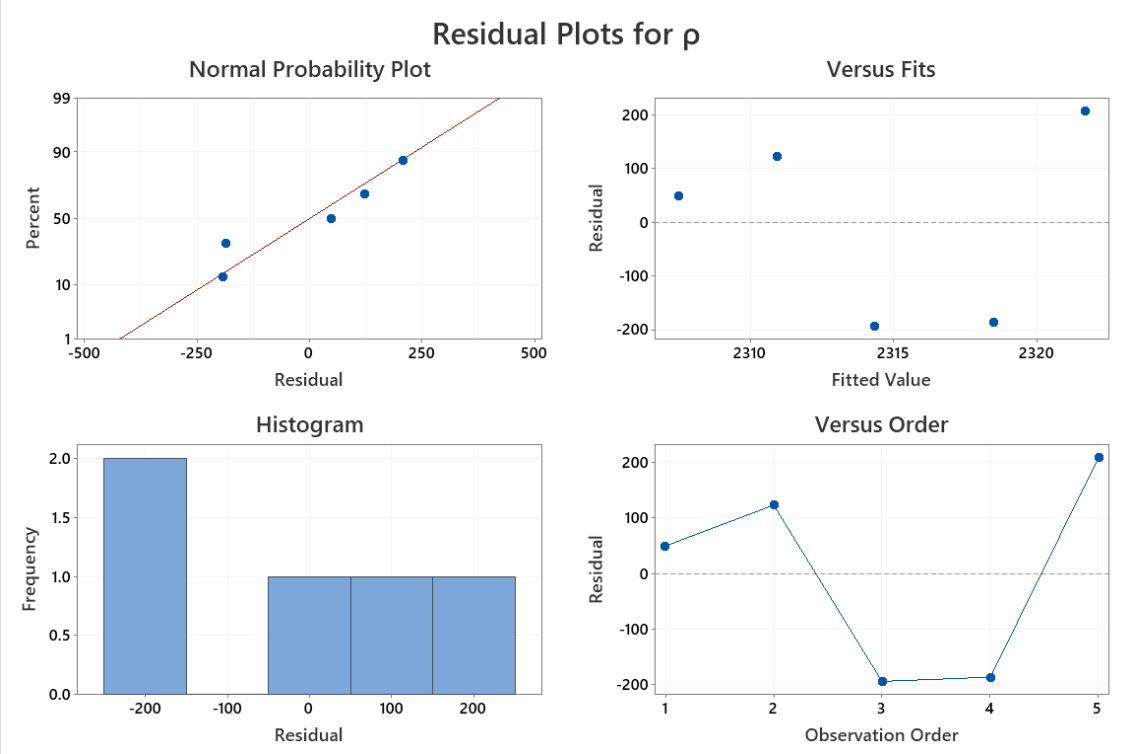

Figure I.24: Residual Plots of Al-Cu Density Results